

**REPUBLIC OF TURKEY
YILDIZ TECHNICAL UNIVERSITY
GRADUATE SCHOOL OF NATURAL AND APPLIED SCIENCES**

**PROPELLER JET INDUCED EROSION AROUND PILE
SUPPORTED BERTH STRUCTURES**

REMZİYE İLAYDA TAN

**PhD THESIS
DEPARTMENT OF CIVIL ENGINEERING
PROGRAM OF COASTAL AND HARBOR ENGINEERING**

**ADVISER
PROF. DR. YALÇIN YÜKSEL**

İSTANBUL, 2019

REPUBLIC OF TURKEY
YILDIZ TECHNICAL UNIVERSITY
GRADUATE SCHOOL OF NATURAL AND APPLIED SCIENCES

**PROPELLER JET INDUCED EROSION AROUND PILE
SUPPORTED BERTH STRUCTURES**

A thesis submitted by Remziye İlayda TAN in partial fulfillment of the requirements for the degree of **DOCTOR OF PHILOSOPHY** is approved by the committee on 16.01.2019 in the Department of Civil Engineering, Coastal and Harbor Engineering Program.

Thesis Adviser

Prof. Dr. Yalçın YÜKSEL
Yıldız Technical University

Approved by the Examining Committee

Prof. Dr. Yalçın YÜKSEL
Yıldız Technical University

Assoc. Prof. Dr. Yeşim ÇELİKOĞLU, Member
Yıldız Technical University

Assoc. Prof. Dr. Özgür Veysel Şadan KIRCA, Member
İstanbul Technical University

Prof. Dr. Esin ÇEVİK, Member
Yıldız Technical University

Prof. Dr. Cem AVCI, Member
Boğaziçi University

ACKNOWLEDGEMENTS

I would like to express my sincere gratitude to my adviser Prof. Dr. Yalçın YÜKSEL, Head of the Hydraulic Division. I am glad to have joined his team as Research Assistant. I thank for his continuous support of my Ph.D. study and related research, patience, motivation, and immense knowledge.

Besides my adviser, I would like to thank the rest of my thesis committee: Assoc. Prof. Dr. Ö.V. Şadan KIRCA for his insightful comments, but also for the hard question which incited me to widen my research from various perspectives. Assoc. Prof. Dr. Yeşim ÇELİKOĞLU for her motivation and support through my thesis.

I would like to thank Assoc. Prof. Mehmet ÖZTÜRK, and Asst. Prof. Cihan ŞAHİN, all the Hydraulics Division Researchers for their motivation and support in overcoming numerous obstacles and have been facing through my research.

I express my deep sense of gratitude to Emine YAKUT and Zafer KARAKÜTÜK for their invaluable advices and feedbacks during the final stage of my study.

I must also thank, in particular, the invaluable support and encouragement received from my co-worker, best friend, fellow doctoral student Res. Asst. Erdal KESGİN. It will be his turn soon.

Last but not the least, I would also like to extend my deepest gratitude to my family: my parents Akif TAN, Dilek TAN and to my brother Uluhan TAN for supporting me spiritually throughout writing this thesis and my life in general. I owe everything to my family who encouraged and helped me at every stage of my personal and academic life. I dedicate this work to my beloved grandmother Kerime Şekeroğlu, my generous father and my loving mother. I love you all.

January, 2019

Remziye İlayda TAN

TABLE OF CONTENTS

	Page
LIST OF SYMBOLS	vii
LIST OF ABBREVIATIONS.....	x
LIST OF FIGURES	xi
LIST OF TABLES.....	xxi
ABSTRACT.....	xxiii
ÖZET	xxv
CHAPTER 1	
INTRODUCTION	27
1.1 Literature Review.....	27
1.2 Objective of the Thesis	62
1.3 Hypothesis.....	63
CHAPTER 2	
EROSION AROUND BERTH STRUCTURES	67
2.1 Berthing Requirements and Effects on Seabed.....	64
2.1.1 Berth Structures.....	64
2.1.2 Berthing and Unberthing Operations	67
2.1.3 Erosion During Berthing and Unberthing Conditions.....	69
CHAPTER 3	
PROPELLER JET MECHANISM	71
3.1 Jet Diffusion Mechanism	71

3.1.1 Velocity Distribution of a Jet	72
3.1.2 Velocity Distribution of a Propeller Jet.....	73
CHAPTER 4	
SCOUR MECHANISM	83
4.1 Scour Mechanism.....	83
4.1.1 Scour Mechanism Induced by Jet Diffusion	83
4.1.2 Propeller Jet Induced Scour Mechanism.....	84
4.1.3 Scour Mechanism Around a Circular Pile.....	85
CHAPTER 5	
EXPERIMENTAL STUDY	89
5.1 Experimental Setup / Flume.....	89
5.1.1 Propeller Characteristics	93
5.1.2 Propellers Used in the Experiments	96
5.1.3 Sand Bed Characteristics Used in the Experiments	102
5.1.4 Distribution of the Propeller Jet Velocity	104
5.1.5 Scaling of the Experimental Model.....	115
CHAPTER 6	
SCOUR FORMATIONS INDUCED PROPELLER JET MECHANISM.....	122
6.1 Scouring Formations without Pile Cases	122
6.2 Scour Formation Around Pier Piles	148
6.2.1 Effects of the Pile Diameters, Bed Material Sizes, Propeller Diameters and Speeds.....	163
6.2.2 Effects of the Propeller Gap	178
6.2.3 Effects of the Pile Location	185
6.2.4 Estimation of Scour Depth Around a Pile	197

6.3 Scour Around Two - Pile Tandem Arrangements	204
6.4 Scour Protection Around a Pile Structure	209
CHAPTER 7	
RESULTS AND DISCUSSION	217
REFERENCES	221
APPENDIX-A	
SCOUR PROFILES.....	227
CURRICULUM VITAE.....	290



LIST OF SYMBOLS

A_p	Projected area of propeller
A_D	Developed area of propeller
A_E	Expanded area of propeller
A_o	Propeller disc area
B_{smax}	Maximum equilibrium scour width at equilibrium scour state
C	Clearance distance from seabed to the propeller tip
c	Chord length
C_c	Gradation coefficient
C_u	Uniformity coefficient
C_T	Propeller thrust coefficient
C_r	Ratio of the standard deviation of velocity
d_o	Diameter of pile
d_{10}	Effective grain size as 10% passing on the cumulative particle size
d_{16}	Effective grain size as 16% passing on the cumulative particle size
d_{50}	Median size of sediment bed
d_{84}	Effective grain size as 86% passing on the cumulative particle size
d_{90}	Effective grain size as 90% passing on the cumulative particle size
D_o	Diameter of circular jet
D_p	Diameter of propeller
D_r	Relative density of compaction
e	Void ratio
e_{max}	Maximum void ratio
e_{min}	Minimum void ratio
Fr_d	Densimetric Froude Number
Fr_{dc}	Critical Densimetric Froude Number
g	Acceleration of gravity
G	Gap; vertical distance from seabed to center of propeller axis, offset distance
h	Water depth
h_r	Height of deposition crest
j	Advance coefficient
K_Q	Propeller torque coefficient
L_m	Characteristic length of the propeller
L_s	Maximum length from the jet exit to the beginning of scour hole where formation starts

L_t	Maximum length of scour hole from the beginning of the scour to downstream edge of deposition zone for unconfined cases
L_{pt}	Maximum length of scour hole from the beginning of the scour to downstream edge of deposition zone for pile cases
L_{smax}	Maximum equilibrium scour length at equilibrium scour state for unconfined case
$L_{smax,c}$	Maximum equilibrium scour length from the propeller face at equilibrium scour state for confined case
L_{pmax}	Maximum length of the scour hole around pile at equilibrium state for pile obstructed case
n	Number of propeller revolutions per second
N	Number of a propeller's blade
n_d	Number of data
P	Pitch: Theoretical distance a propeller would move in one revolution
P_A	Pressure at point A
P_B	Pressure at point B
P_C	Pressure at point C
P_D	Pressure at point D
r	Radial distance from the propeller center
R_m	Location of maximum axial velocity
R_{mo}	Radial distance from the rotation axis to the location where the maximum thrust occurs
R_p	Radius of propeller
Re_f	Reynolds flow number
Re_j	Reynolds jet number
Re_p	Reynolds propeller number
S_{smax}	Maximum scour depth hole at equilibrium scour state
S	Depth of scour at any time
S_{max}	Maximum depth of scour hole at any time
S_o	Scour depth at the toe of pile
S_{o2}	Scour at the toe of the second pile
S_{10}	Scour depth at 10 cm away from propeller face
S_{20}	Scour depth at 20 cm away from propeller face
S_{30}	Scour depth at 30 cm away from propeller face
S_{40}	Scour depth at 40 cm away from propeller face
S_d	Scour depth at the downstream of pile in scour hole
T	Thrust
$t_{section}$	Thickness of the section
t	Thickness of sediment bed
t_b	Thickness of propeller's blade
t_s	Time needed to initiate scouring
U_0	Axial efflux velocity of the propeller
U'_a	Axial component of turbulence intensity
U'_r	Radial component of turbulence intensity
U'_t	Tangential component of turbulence intensity

U_r	Radial velocity
U_a	Axial velocity
U_t	Tangential velocity
U_{rot}	Rotational Velocity
U_{max}	Maximum axial velocity
U_A	Advanced velocity
U_B	Velocity at point B
U_C	Velocity at point C
U_D	Velocity at point D
U_{cr}	Critical flow velocity
$U_{b,max}$	Maximum velocity near the bed
w	Water content of soil
X	Horizontal distance from the center of the jet
X_{mu}	Longitudinal distance of maximum scour depth from the propeller's face for the unconfined case
X_m	Longitudinal distance of maximum scour depth from the propeller's face for the confined case
X_c	Horizontal distance from propeller face to the deposition crest
X_{pc}	Horizontal distance from pile face to the deposition crest
X_t	Toe distance
X_{max}	Location of the maximum scour depth
X_t	Toe distance
X_s	Distance between the propeller and the second pile
X_i	Impingement distance (Horizontal distance from the face of the propeller to the pile)
y	Vertical distance from the undisturbed bed level to the center of the jet axis
Y	Vertical distance from the bed level to the jet axis
z	Number of blades
β	Blade Area Ratio
ρ	Density of fluid
ρ_s	Density of the sediment
σ_0	Cavitation number
σ_g	Geometric standard deviation
Δ	Relative density
μ	Dynamic viscosity of fluid
ϕ	Porosity
γ_d	Dry unit weight of soil
γ_s	Saturated unit weight of soil
ν	Kinematic viscosity of fluid

LIST OF ABBREVIATIONS

ADV	Acoustic Doppler Velocimeter
BAR	Blade Area Ratio
BEM	Blade Element Method
CFD	Computational Fluid Dynamics
CPP	Controllable Pitch Propeller
CRP	Contra Rotating Propeller
FPP	Fixed Pitch Propeller
KC	Keulegan - Carpenter Number
KE	Kinetic Energy
KN	Knot
LDA	Laser Doppler Anemometry
MIN	Minutes
OBL	Original Bed Level
PIV	Particle Image Velocimeter
RPM	Revolutions Per Minute
RPS	Revolutions Per Second
RMSE	Root - Mean - Squared Error
SEC	Seconds
SWL	Still Water Level
USCS	Soil Classification System
ZFE	Zone of Flow Establishment
ZEF	Zone of Established Flow

LIST OF FIGURES

	Page
Figure 1.1 Sketch of scour formation by a submerged circular (a) wall jet (b) horizontal jet with gap (Chiew and Lim [2]).....	27
Figure 1.2 S_{smax}/D_o with Fr_d for circular wall jets in (a) air and (b) water (Chiew and Lim [2])	28
Figure 1.3 h_r/S variation with densimetric Froude number (Fr_d) (Chiew and Lim [2])	29
Figure 1.4 Variation of S_{smax}/D_o with offset height G/D_o for various Fr_d values for circular offset jets (Chiew and Lim [2])	29
Figure 1.5 Schematic scour formation owing to the propeller jet (Hong et al. [5]) ...	30
Figure 1.6 Scour hole formations (Hong et al. [5])	31
Figure 1.7 Scour profiles (a) low gap ratio with $G/D_p=0.5$ (b) high gap ratio with $G/D_p=1.0$ (Hong et al. [5]).....	32
Figure 1.8 (a) Comparison of (a) S_{smax}/D_o and Fr_d (b) S_{smax}/D_o and G/D_o with dashed line for Equation (1.10)) (Hong et al. [5])	34
Figure 1.9 Critical conditions for the scour induced by the propeller and submerged jets (Hong et al. [5]).....	34
Figure 1.10 Erosion of seabed induced by a ship propeller (Chin et al. [8]).....	35
Figure 1.11 Vertical flow distribution at the pile (Chin et al. [8]).....	35
Figure 1.12 Scour hole formation induced by wall jet around a vertical pile (Chin et al. [8])	36
Figure 1.13 Zero counter line and centerline profile (a) Type 1, (b) Type 2, (c) Type 3, (d) Type 4 (Chin et al. [8])	37
Figure 1.14 Boundary limits of centerline profiles (a) Type 1 and 3 (b) Type 2 and 4 (Chin et al. [8])	38
Figure 1.15 Variation of S_{smax}/D_o with Fr_d (Chin et al. [8])	38
Figure 1.16 Classification of the equilibrium scour profiles in terms of Fr_d and X_i/D_o (Chin et al. [8])	39
Figure 1.17 Jet flow deflection toward the bed and quay wall structures (Hamill et al. [9])	40

Figure 1.18	Comparison between confined and unconfined scour profiles with the quay wall placed at (a) $0.636X_s$ (b) $0.909X_s$ (c) $1.636X_s$ (d) $2.272X_s$ (e) $2.727X_s$ (f) $3.27X_s$ (Hamill et al. [9])	42
Figure 1.19	Axial, tangential and radial velocity components in coordinate system (Lam et al. [10]).....	43
Figure 1.20	Measured axial velocity with 2D LDA and 3D LDA (Lam et al. [10]) ...	44
Figure 1.21	Measured tangential velocity with 2D LDA and 3D LDA (Lam et al. [10])	45
Figure 1.22	Measured radial velocity with 2D LDA and 3D LDA (Lam et al. [10])..	45
Figure 1.23	Measurement of dimensionless velocity components (Lam et al. [10])...	46
Figure 1.24	Velocity components for different propeller geometry (Lam et al. [10]) .	46
Figure 1.25	Axial (U'_a), Tangential (U'_t) and, radial (U'_r) components of turbulence intensity (Lam et al. [10])	47
Figure 1.26	Schematic view of boundary layer development (Johnston et al. [19])	47
Figure 1.27	Velocity profiles at the propeller centerline (Johnston et al. [19]).....	48
Figure 1.28	Velocity profiles at the propeller centerline at $r/R_p=2.5$ (Johnston et al. [19])	48
Figure 1.29	Velocity profiles at the propeller centerline at 5mm above the bed ($r/R_p=3.6$) (Johnston et al. [19])	49
Figure 1.30	Expansion angle variation (Johnston et al. [19]).....	49
Figure 1.31	Seabed scouring parameters (Lam et al. [24]).....	53
Figure 1.32	Horizontal and vertical measurements for the propeller at 1000 rpm (Lam et al. [24])	54
Figure 1.33	Scour profile induced by twin propellers (Yew et al. [25]).....	56
Figure 1.34	Scour formation at constant a) clearance b) rotational speed (Yew et al. [25])	57
Figure 1.35	Schematic view of a typical scour formation in the presence of a quay slope (Wei and Chiew [26])	59
Figure 1.36	Comparisons of confined and unconfined scour profiles a) $X_t=2D_p$ b) $X_t=3D_p$ c) $X_t=4D_p$ d) $X_t=5D_p$ e) $X_t=6D_p$ f) $X_t=7D_p$ g) $X_t=8D_p$ h) $X_t=9D_p$ (Wei and Chiew [26])	60
Figure 1.37	Schematic view of the propeller jet's target point for a) unconfined b) near toe distance c) intermediate toe distance (Wei and Chiew [26]).....	61
Figure 2.1	Gravity wall structures a) monolithic b) block wall (PIANC [28])	65
Figure 2.2	Gravity wall structures a) caisson b) cantilever monolithic (PIANC [28])	65
Figure 2.3	Sheet pile structures a) cantilevered sheet-pile b) anchored sheet-pile c) Sheet-pile with platform (PIANC [28]).....	65

Figure 2.4	Examples of different kinds of open berth structures a) pile / column supported deck b) pile supported pier c) pile / column supported deck (PIANC [28]).....	66
Figure 2.5	Scour induced by the propeller jet near an open berth structure (Chin et al. [8])	67
Figure 2.6	Components of depth (Thoresen [29])	68
Figure 2.7	Illustration of possible berthing / unberthing operations (PIANC [28]) ...	70
Figure 3.1	Different forms of jets (Hoffmans and Verheij [35])	72
Figure 3.2	Schematized representation of a diffusing jet from an orifice (Albertson et al. [21])	73
Figure 3.3	Schematic view of the velocity component of a propeller (Hamill et al. [38])	73
Figure 3.4	Velocity distribution induced by a propeller jet (Lam et al. [4])	74
Figure 3.5	Velocity distribution of a 76 mm diameter propeller at 100 rpm (Hamill et al. [3])	74
Figure 3.6	Tip vortex sheet cavitation of a four-bladed propeller (Faltinsen [39])	75
Figure 3.7	Propeller's slip stream by an actuator disc model (Lam et. al. [4])	76
Figure 3.8	Velocity distribution induced by a ship's propeller (PIANC [28]).....	79
Figure 4.1	Demonstration of a local scour cycle a) Scour begins b) Digging stage c) Digging continues d) Maximum digging e) Filling phase g) Maximum fill h) Recurrence of a digging stage (Balachandar and Prashanth [43])	84
Figure 4.2	Definition sketch of the scour by a) an offset jet b) a propeller jet (Chiew et al. ([45])	85
Figure 4.3	Flow pattern and scour around a pile (Van Rijn [46])	87
Figure 4.4	Positions of separation points at critical and supercritical regimes (Sumer and Fredsøe [44]).....	88
Figure 4.5	(a) Prior to shedding Vortex A, Vortex B is being drawn across the wake (b) Prior to sheeding vortex B, vortex C is being drawn across the wake (Sumer and Fredsøe [44]	88
Figure 5.1	View of the experimental setup.....	90
Figure 5.2	Experimental setup in mm (Longitudinal-Section).....	90
Figure 5.3	Experimental setup in mm (Plan view)	91
Figure 5.4	Schematic view of the experimental setup	92
Figure 5.5	Schematic view of the plexiglass box system	93
Figure 5.6	General view of a propeller (Faltinsen [39]).....	93
Figure 5.7	View of the Propeller a) Back view b) Face view (aft side)	94
Figure 5.8	Travel path of a propeller's blade in one revolution [48]	94
Figure 5.9	Propeller's pitch angle and angle of attack [48]	95
Figure 5.10	Characteristic of propeller areas (Carlton [42])	96

Figure 5.11	Geometry of four bladed propellers used in the experiments	96
Figure 5.12	Propeller's computation geometry a) Propeller-65 mm b) Propeller-100 mm c) Propeller-130 mm.....	97
Figure 5.13	Design drawing for the propeller - 65 mm	98
Figure 5.14	Design drawing for the propeller - 100 mm	99
Figure 5.15	Design drawing for the Propeller - 130 mm.....	100
Figure 5.16	Open water diagram for Wageningen B5 - 75 screw series (Carlton [42])	101
Figure 5.17	Sediment beds (a) Material 1 (b) Material 2 (c) Material 3 (d) Material 4	102
Figure 5.18	Sieve analysis of Material 1	103
Figure 5.19	Sieve analysis of Material 2	104
Figure 5.20	Sieve analysis of Material 3	104
Figure 5.21	Sieve analysis of Material 4	104
Figure 5.22	ADV modules (NDV Operations Manual [50]).....	105
Figure 5.23	3D down - looking probes of ADV (NDV Operations Manual [50])	106
Figure 5.24	Distribution of the axial velocity at the face of the propeller - 130 mm at 590 rpm.....	107
Figure 5.25	Distribution of the axial velocity at the face of the propeller - 130 mm at 670 rpm.....	108
Figure 5.26	Distribution of the axial velocity at the face of the propeller - 130 mm at 745 rpm.....	108
Figure 5.27	Distribution of the axial velocity at the face of the propeller - 100 mm at 590 rpm.....	109
Figure 5.28	Distribution of the axial velocity at the face of the propeller - 100 mm at 670 rpm.....	109
Figure 5.29	Distribution of the axial velocity at the face of the propeller - 100 mm at 745 rpm.....	110
Figure 5.30	Distribution of the axial velocity at the face of the propeller - 65 mm at 670 rpm.....	110
Figure 5.31	Distribution of the axial velocity at the face of the propeller - 65 mm at 670 rpm.....	111
Figure 5.32	Distribution of the axial velocity at the face of the propeller - 65 mm at 745 rpm.....	111
Figure 5.33	Measured and predicted efflux velocity comparisons for the propeller - 65 mm.....	112
Figure 5.34	Measured and predicted efflux velocity comparisons for the propeller - 100 mm.....	113
Figure 5.35	Measured and predicted efflux velocity comparisons for the propeller - 130 mm.....	113

Figure 5.36	Comparison of measured and calculated efflux velocities	114
Figure 5.37	Relationship between power and diameter of the main and bow thruster (PIANC [28]).....	119
Figure 6.1	Time development of the maximum scour depth with $D_p = 6.5$ cm and 10 cm for $G = 10$ cm on sand bed, with $d_{50} = 0.52$ mm	123
Figure 6.2	Time dependent evolution of the scour profile without structure over the sediment bed sizes of $d_{50}=0.52$ mm with $D_p=10$ cm, $G=10$ cm at 745 rpm	124
Figure 6.3	Critical conditions for the initiation of the scour caused by the propeller jet flow	127
Figure 6.4	Critical curve for the initiation of scour	128
Figure 6.5	Comparisons of critical curves for the initiation of scouring	128
Figure 6.6	Plan view of the scour formation with $D_p=10$ cm, at 590 rpm and $G=10$ cm, on $d_{50}=0.52$ mm sediment bed	129
Figure 6.7	Scour profile with $D_p=10$ cm, at 745 rpm and $G=15$ cm, on the sediment bed of $d_{50}=0.52$ mm	129
Figure 6.8	Scour profile with $D_p=6.5$ cm, at 745 rpm and $G=15$ cm, on sediment bed of $d_{50}=0.52$ mm.....	130
Figure 6.9	Isometric view of scour hole with $D_p=6.5$ cm, at 745 rpm $G=15$ cm, on sediment bed of $d_{50}=0.52$ mm	130
Figure 6.10	Scour profiles with $D_p = 10$ cm and $G = 10$ cm at 45 Hertz propeller speed for different sediment bed materials	132
Figure 6.11	Scour profiles with or without small scour formation under the propeller in terms of Fr_d and G/D_p	132
Figure 6.12	Dimensions of the scour hole	133
Figure 6.13	Schematic diagram of scour formations owing to a propeller jet.....	133
Figure 6.14	Scour profiles with $D_p=10$ cm, $G=10$ cm, at 40 Hertz for different sediment beds	134
Figure 6.15	Scour profiles with $D_p=6.5$ cm, $G=10$ cm, at 40 Hertz over different sediment beds	134
Figure 6.16	Scour profiles with $D_p=10$ cm, $G=10$ cm, at 50 Hertz over different sediment beds	135
Figure 6.17	Scour profiles with $D_p=13$ cm, $G=10$ cm, at 50 Hertz over different sediment beds	135
Figure 6.18	X_c versus Re_f of the propellers over different sand bed materials at the constant gap	136
Figure 6.19	Scour profiles for different gaps of the propeller on $d_{50}=0.52$ mm beds ($D_p=10$ cm at 50 Hertz)	137
Figure 6.20	Scour profiles for different gaps of the propeller on $d_{50}=8.30$ mm beds ($D_p=13$ cm at 50 Hertz)	137

Figure 6.21	Scour profiles with different gaps of the propeller with $D_p=6.5$ cm, at 670 rpm on sediment bed of $d_{50}=0.52$ mm	138
Figure 6.22	X_c/G versus Re_f for $D_p=10$ cm over different sand beds	139
Figure 6.23	Relationship between S_{smax}/D_p and Fr_d for the propeller and circular wall jet conditions	140
Figure 6.24	Relationship between B_{smax}/D_p and Fr_d for the propeller and circular wall jets.....	141
Figure 6.25	Relationship between L_{smax}/D_p and Fr_d for the propeller and circular wall jets.....	141
Figure 6.26	Comparison between the observed and calculated scour depths using equations proposed by Hong et al. [5].....	143
Figure 6.27	Comparison between the observed and calculated scour depths using equations proposed by Hamill et al. [9].....	144
Figure 6.28	Relationship between S_{max}/D_p and G/D_p for the circular and square wall jet with included propeller jet data (Hong et al. [5])	146
Figure 6.29	Relationship between S_{smax}/D_p and G/D_p for the propeller jet mechanism	147
Figure 6.30	Comparison between the observed and calculated maximum scour depth location (X_{mu}) using the equation proposed by Hamill et al. [9].....	148
Figure 6.31	Scour profile measurements by using a limnimeter	151
Figure 6.32	Critical curve for the initiation of the scour with the presence of a pile type structure	151
Figure 6.33	Typical plan view of the scour profile without pile for the sediment bed of $d_{50}=0.52$ mm ($D_p=10$ cm at 590 rpm).....	152
Figure 6.34	Scour formations on the sediment bed of $d_{50}=0.52$ mm for $D_p=6.5$ cm the propeller at 590 rpm, $X=10$ cm and $G=20$ cm with (a) $d_o=9$ cm and (b) $d_o=4$ cm.....	154
Figure 6.35	Characteristics scour profiles induced by the propeller jet flow around a pile structure	155
Figure 6.36	Type 1, 2 and 3 scour formations with respect to the G/d_o versus Fr_d ...	158
Figure 6.37	Schematic view of the flow pattern around the vertical pile.....	159
Figure 6.38	Variation of S_o/D_p and S_{10}/D_p with Fr_d over the bed of $d_{50}=0.52$ mm ($D_p=6.5$ cm and 10 cm at the propeller speed of 590 rpm, 670 rpm and 745 rpm)	161
Figure 6.39	Variation of S_o/D_p and S_{10}/D_p with Re_p over bed of $d_{50}=0.52$ mm ($D_p=6.5$ cm and 10 cm at propeller speed of 590 rpm, 670 rpm and 745 rpm)	161
Figure 6.40	Variation of S_o/D_p and S_{10}/D_p with Re_f over bed of $d_{50}=0.52$ mm ($D_p=6.5$ cm and 10 cm at propeller speed of 590 rpm, 670 rpm and 745 rpm)	162
Figure 6.41	Variation of S_o/D_p and S_{10}/D_p with Fr_d over bed of $d_{50}=1.28$ mm ($D_p=6.5$ cm, 10 cm and 13 cm at propeller speed of 590 rpm, 670 rpm and 745 rpm)	162

Figure 6.42	Variation of S_o/D_p and S_{10}/D_p with Fr_d over bed of $d_{50}=4$ mm ($D_p=6.5$ cm, 10 cm and 13 cm at propeller speed of 590 rpm, 670 rpm and 745 rpm)	163
Figure 6.43	Variation of S_o/D_p and S_{10}/D_p with Fr_d over bed of $d_{50}=8.3$ mm ($D_p=6.5$ cm, 10 cm and 13 cm at propeller speed of 590 rpm, 670 rpm and 745 rpm)	163
Figure 6.44	Variation of S_o/d_o with Re_f on sediment bed of $d_{50}=0.52$ mm ($D_p=6.5$ cm and 13 cm at propeller speed of 590 rpm, 670 rpm and 745 rpm)	164
Figure 6.45	Variation of S_o/d_o with Re_p on sediment bed of $d_{50}=0.52$ mm ($D_p=6.5$ cm and 13 cm at propeller speed of 590 rpm, 670 rpm and 745 rpm)	164
Figure 6.46	Variation of S_o/d_o with Fr_d on sediment bed of $d_{50}=0.52$ mm ($D_p=6.5$ cm and 10 cm at propeller speed of 590 rpm, 670 rpm and 745 rpm)	165
Figure 6.47	Variation of S_o/d_o with Fr_d on sediment bed of $d_{50}=1.28$ mm ($D_p=6.5$ cm, 10 cm and 13 cm at propeller speed of 590 rpm, 670 rpm and 745 rpm)	165
Figure 6.48	Variation of S_o/d_o with Fr_d on sediment bed of $d_{50}=4$ mm ($D_p=6.5$ cm, 10 cm and 13 cm at propeller speed of 590 rpm, 670 rpm and 745 rpm)	166
Figure 6.49	Variation of S_o/d_o with Fr_d on sediment bed of $d_{50}=8.3$ mm ($D_p=6.5$ cm, 10 cm and 13 cm at propeller speed of 590 rpm, 670 rpm and 745 rpm)	166
Figure 6.50	Relationship between S_o/d_o with Fr_d on different sand beds for different speeds (590 rpm, 670 rpm, 745 rpm) of Propeller-65 mm at $X=10$ cm, $G=10$ cm	167
Figure 6.51	Relationship between S_o/d_o with Fr_d on different sand beds for different speeds (590 rpm, 670 rpm, 745 rpm) of Propeller-100 mm at $X=10$ cm, $G=10$ cm	167
Figure 6.52	Relationship between S_o/d_o with Fr_d on different sand beds for different speeds (590 rpm, 670 rpm, 745 rpm) of Propeller-130 mm at $X=10$ cm, $G=10$ cm	168
Figure 6.53	Schematic of the scour profile with a pile at the equilibrium state induced by the propeller jet.....	168
Figure 6.54	Scour profiles around 4 cm pile on different beds with $D_p=10$ cm and 745 rpm at $G=10$ cm.....	169
Figure 6.55	Scour profiles around 9 cm pile on different beds with $D_p=10$ cm and 745 rpm at $G=10$ cm.....	169
Figure 6.56	Scour profiles around 14 cm pile on different beds with $D_p=10$ cm and 745 rpm at $G=10$ cm.....	170
Figure 6.57	Scour profiles with and without pile cases on $d_{50}=0.52$ mm sediment bed ($D_p=10$ cm, $G=10$ cm, at 670 rpm).....	171
Figure 6.58	Scour profiles with and without pile cases on $d_{50}=1.28$ cm sediment bed ($D_p=10$ cm, $G=10$ cm, at 670 rpm).....	171
Figure 6.59	Scour profiles with and without pile cases on $d_{50}=4$ mm sediment bed ($D_p=10$ cm, $G=10$ cm, at 670 rpm).....	172
Figure 6.60	Scour profiles with and without pile cases on $d_{50}=8.3$ mm sediment bed ($D_p=10$ cm, $G=10$ cm, at 670 rpm).....	172

Figure 6.61	Relationship between B_{smax}/D_p and Fr_d with $d_o = 4$ cm, 9 cm, and 14 cm, with and without piles, based on propeller jet mechanisms on a sand bed, with $d_{50} = 0.52$ mm	173
Figure 6.62	Relationship between L_{smax}/D_p and Fr_d with $d_o = 4$ cm, 9 cm, and 14 cm, with and without piles, based on propeller jet mechanisms on a sand beds, with $d_{50} = 0.52$ mm, 1.28 mm, 4.0 mm and 8.3 mm.....	174
Figure 6.63	Relationship between S_{max}/D_p and Fr_d with $d_o = 4$ cm, 9 cm, and 14 cm, with and without piles, based on propeller jet mechanisms on a sand beds, with $d_{50} = 0.52$ mm, 1.28 mm, 4.0 mm and 8.3 mm.....	175
Figure 6.64	Variation of S_o/D_p with Fr_d on sediment bed of $d_{50}=0.52$ mm ($G=10$ cm)	176
Figure 6.65	Variation of S_o/D_p with Fr_d on the sediment bed of $d_{50}=0.52$ mm ($G=15$ cm).....	176
Figure 6.66	Variation of S_o/D_p with Fr_d on the sediment bed of $d_{50}=0.52$ mm ($G=20$ cm).....	176
Figure 6.67	Variation of S_o/D_p with Fr_d with $d_o= 4$ cm pile on the sediment bed of $d_{50}=0.52$ mm for different gaps of the propeller.....	177
Figure 6.68	Variation of S_o/D_p with Fr_d with $d_o= 9$ cm pile on the sediment bed of $d_{50}=0.52$ mm for different gaps of the propeller.....	177
Figure 6.69	Variation of S_o/D_p with Fr_d with $d_o= 14$ cm pile sediment bed of $d_{50}=0.52$ mm for different gaps of the propeller.....	177
Figure 6.70	Variation of S_o/D_p with Fr_d based on the propeller jet mechanism with and without pile cases for $G=10$ cm and $X/d_o=2.5$	182
Figure 6.71	Variation of S_o/D_p with Fr_d based on the propeller jet mechanism with and without pile cases for $G=10$ cm and $X/d_o=5.0$	183
Figure 6.72	Variation of S_o/D_p with Fr_d based on the propeller jet mechanism with and without pile cases for $G=10$ cm and $X/d_o=7.5$	183
Figure 6.73	Variation of S_o/D_p with Fr_d based on the propeller jet mechanism with and without pile cases for $G=10$ cm and $X/d_o=10$	184
Figure 6.74	Schematic view of the boundary layer development (Johnston et al. [19])	185
Figure 6.75	Scour profile without piles and scour depths at the toe of pile (S_o) for different locations at $X/d_o=2.5, 5, 7.5, 10$, $D_p=10$ cm, speed = 590 rpm, and $G=10$ cm	186
Figure 6.76	Scour profile without piles and scour depths at the toe of the pile (S_o) for different locations at $X/d_o=2.5, 5, 7.5, 10$, $D_p=10$ cm, speed = 670 rpm, and $G=10$ cm	187
Figure 6.77	Scour profile without piles and scour depths at the toe of the pile (S_o) for different locations at $X/d_o=2.5, 5, 7.5, 10$, $D_p=10$ cm, speed = 745 rpm, and $G=10$ cm	187
Figure 6.78	Scour profile without piles and scour depths at the toe of the pile (S_o) for different locations at $X/d_o=2.5, 5, 7.5, 10$, $D_p=6.5$ cm, speed = 590 rpm, and $G=10$ cm	189

Figure 6.79	Scour profile without piles and scour depths at the toe of the pile (S_o) for different locations at $X/d_o=2.5, 5, 7.5, 10$, $D_p=6.5$ cm, speed = 670 rpm, and $G=10$ cm	189
Figure 6.80	Scour profile without piles and scour depths at the toe of the pile (S_o) for different locations at $X/d_o=2.5, 5, 7.5, 10$, $D_p=6.5$ cm, speed = 745 rpm, and $G=10$ cm	190
Figure 6.81	Scour profile without piles and scour depths at the toe of the pile (S_o) for different locations at $X/d_o=2.5, 5, 7.5, 10$, $D_p=13$ cm, speed = 590 rpm, and $G=10$ cm	190
Figure 6.82	Scour profile without piles and scour depths at the toe of the pile (S_o) for different locations at $X/d_o=2.5, 5, 7.5, 10$, $D_p=13$ cm, speed = 670 rpm, and $G=10$ cm	191
Figure 6.83	Scour profile without piles and scour depths at the toe of the pile (S_o) for different locations at $X/d_o=2.5, 5, 7.5, 10$, $D_p=13$ cm, speed = 745 rpm, and $G=10$ cm	191
Figure 6.84	Scour profile without piles and scour depths at the toe of the pile (S_o) for different locations at $X/d_o=2.5, 5, 7.5, 10$, and different gaps of the propeller ($D_p=10$ cm with 590 rpm)	192
Figure 6.85	Scour profile without piles and scour depths at the toe of the pile (S_o) for different locations at $X/d_o=2.5, 5, 7.5, 10$, and different gaps of the propeller ($D_p=10$ cm with 670 rpm)	192
Figure 6.86	Scour profile without piles and scour depths at the toe of the pile (S_o) for different locations at $X/d_o=2.5, 5, 7.5, 10$, and different gaps of the propeller ($D_p=10$ cm with 745 rpm)	193
Figure 6.87	Relationship between S_o/d_o with Fr_d on sediment bed of $d_{50}=1.28$ mm for $G/d_o=2.5$	193
Figure 6.88	Relationship between S_o/d_o with Fr_d on sediment bed of $d_{50}=1.28$ mm for $G/d_o=3.75$	194
Figure 6.89	Relationship between S_o/d_o with Fr_d on sediment bed of $d_{50}=1.28$ mm for $G/d_o=5.0$	194
Figure 6.90	Comparison between measured and calculated relative scours at the toe of the pile (S_o/d_o) with 95% confidence interval	196
Figure 6.91	Comparison between measured and calculated relative scours at the toe of the pile (S_o/D_p) with 95% confidence interval.....	197
Figure 6.92	Comparison between measured and calculated relative scours at the toe of the pile (S_o/d_o).....	198
Figure 6.93	View of the flume at the beginning of the tests.....	202
Figure 6.94	Schematic view of the scour formation with a two - pile tandem arrangement	203
Figure 6.95	Scour profile of two - pile tandem arrangement for $X_t=2.5d_o$ (Set 1)	204
Figure 6.96	Scour profile of two - pile tandem arrangement for $X_t=5d_o$ (Set 1)	204
Figure 6.97	Scour profile of two - pile tandem arrangement for $X_t=7.5d_o$ (Set 1)	204

Figure 6.98	Scour profile without pile case and scour depths at the toe of 4 cm piles for two-pile tandem arrangement on the sediment bed of $d_{50}=0.52$ mm (Set 1)	205
Figure 6.99	Scour profile without pile case and scour depths at the toe of 4 cm piles for two-pile tandem arrangement on the sediment bed of $d_{50}=1.28$ mm (Set 3)	205
Figure 6.100	Scour profile without pile case and scour depths at the toe of 9 cm piles for two-pile tandem arrangement on the sediment bed of $d_{50}=0.52$ mm (Set 2)	206
Figure 6.101	Application of rock protection (Hawkswood et al. [77])	207
Figure 6.102	Cross-section of application for protection layer	207
Figure 6.103	Sieve analysis of rocks used in armor layer	208
Figure 6.104	Application of the armor layer in two layers around the pile diameter of (a) $d_o=4$ cm (b) $d_o=14$ cm	208
Figure 6.105	Idealised propeller jet flow (modified from Hawkswood et al. [77])	209
Figure 6.106	Relative bed velocity ($U_{b, \max}/U_0$) of the propeller jet as a function of gap ratio (G/D_p) (Modified from Hawkswood et al. [77])	210
Figure 6.107	Stone sizes related to maximum bed velocities ($U_{b, \max}$) (Hawkswood et al. [77])	211
Figure 6.108	Scour profile induced propeller jet with the absence of pile ($D_p=13$ cm, 745 rpm, $G=10$ cm)	212
Figure 6.109	Final scour profile without the protection layer around the pile of $d_o=4$ cm on the sediment bed of $d_{50}=8.30$ mm ($D_p=13$ cm, 745 rpm, $G=10$ cm)	214
Figure 6.110	Final scour profile without the protection layer around the pile of $d_o=14$ cm on the sediment bed of $d_{50}=8.30$ mm ($D_p=13$ cm, 745 rpm, $G=10$ cm)	214

LIST OF TABLES

		Page
Table 1.1	Summarized test conditions (Hong et al. [5]).....	30
Table 1.2	Summarized parameters that are effective on the scour formation given by researchers (Hong et al. [5])	33
Table 1.3	Parameters for the experiments (Hamill et al. [9])	40
Table 1.4	Measured and calculated efflux velocity values (Lam et al. [10])	43
Table 1.5	Position of efflux velocity values (Lam et al. [10]).....	44
Table 1.6	Propeller characteristics of Kee et al. [18] and Lam et al. [10]’s	46
Table 1.7	Coefficient values for maximum velocity (JJohnston et al. [19])	50
Table 1.8	Maximum velocity in the ZEF and ZFE (Lam et. al. [4])	51
Table 1.9	Axial velocity at any distance in the ZEF and ZFE (Lam et. al. [4])	52
Table 1.10	Propeller characteristics (Lam et al. [24])	53
Table 1.11	Efflux coefficients measured with LDA and correlation coefficients (R^2) (Lam et al. [24]).....	54
Table 1.12	Equations for different propeller (Lam et al. [24]).....	55
Table 1.13	The view of the stages of scour formations induced by twin propellers (Yew et al. [25]).....	56
Table 1.14	Summarized test conditions of Wei and Chiew’s [26] study	58
Table 3.1	Equations used for calculation the efflux velocity	81
Table 4.1	Flow around a cylinder in steady current (Sumer and Fredsøe [44])	86
Table 5.1	Characteristics of the propellers used in the present study.....	97
Table 5.2	Thrust coefficient (C_T) as the function of propeller pitch / diameter ratio (Carlton [42]).....	101
Table 5.3	Sediment bed material characteristics used in the present study.....	103
Table 5.4	Technial Specifications of ADV (NDV Operations Manual [51]).....	105
Table 5.5	Technial specifications of flowmeter (Nixon Operations Manual [52])..	106
Table 5.6	Measured efflux velocity values at three different speeds.....	112
Table 5.7	Descriptive statistical performance indices for datasets	115
Table 5.8	Dimensions of defined physical quantities	116

Table 5.9	Exponents for each dimension.....	116
Table 5.10	Dimensionless Π groups with defined exponents for each dimension....	119
Table 5.11	Summarized parameters for the prototype and model propellers.....	120
Table 6.1	Test conditions with the absence of structure.....	122
Table 6.2	Summarized test conditions.....	125
Table 6.3	Observations of small scour formations according to different test conditions.....	131
Table 6.4	Range of the data collected for the scours caused by a propeller jet in different studies.....	144
Table 6.5	Experimental conditions for tests with piles.....	150
Table 6.6	Scour formations with pile conditions.....	153
Table 6.7	Measured scour profiles for different pile diameters (d_o).....	156
Table 6.8	Scour profiles with different gaps of the propeller over the sediment bed material size of $d_{50}=0.52$ mm.....	178
Table 6.9	Scour profiles with different gaps of the propeller over the sediment bed material size of $d_{50}=1.28$ mm.....	179
Table 6.10	Scour profiles with different gaps of the propeller over the sediment bed material size of $d_{50}=4$ mm.....	180
Table 6.11	Scour profiles with different gaps of the propeller over the sediment bed material size of $d_{50}=8.3$ mm.....	181
Table 6.12	Propeller jet expansion angles for propeller gaps at 10 cm, 20 cm and 30 cm.....	185
Table 6.13	Descriptive statistical performance indices for the data sets.....	199
Table 6.14	Parameters used during experimental tests.....	203
Table 6.15	Scour protection types and failure mechanisms (Hawkswood et al. [78]).....	206
Table 6.16	Standard jet dispersion conditions (BAW [74]).....	209
Table 6.17	Maximum flow velocity at the bed ($U_{b,max}$).....	213
Table 6.18	Rock weights used in the armor layer.....	215

ABSTRACT

PROPELLER JET INDUCED EROSION AROUND PILE SUPPORTED BERTH STRUCTURES

Remziye İlayda TAN

Department of Civil Engineering

PhD Thesis

Adviser: Prof. Dr. Yalçın YÜKSEL

This thesis presents an improvement for the assessment of scour effects owing to propeller jet velocities with a direct application to prototype modeling by conducting a non-dimensional analysis. This study provides insights on the scouring problems owing to a propeller jet. In order to overcome the limitations found in the literature, expanded densimetric Froude numbers ($1.95 \leq Fr_d \leq 15.01$) were used. Experimental tests were developed for this purpose and formulae recommendations are provided to enhance the estimation of different relevant parameters of the scour process. In addition, the experimental conditions were extended, by ranging sand beds from finer to coarser that were $d_{50} = 0.52$ mm, 1.28 mm, 4.00 mm and 8.30 mm, and the Fr_d were compared with the ones stated in the previous studies. Hence, this study has proposed new formulae to predict the scouring owing to propeller jet flows. Scaling of the experimental model have been explained and the experimental conditions have been given. An acoustic Doppler velocimeter (ADV) was used to obtain the propeller velocity. In order to calculate the magnitude of efflux velocity a new equation is proposed, considering the propeller geometry and characteristics. Thus, it has been aimed to improve the level of knowledge that already exists in the literature. In addition, the scour induced by a propeller jet around a single pile was examined experimentally. The initiation of scour formation was found to be related to the densimetric Froude number (Fr_d), propeller diameter (D_p), and the gap of the propeller (G), which is defined as the vertical distance between the centerline of the propeller and the undisturbed sand bed. Three types of scour profiles were defined that can be classified according to a) the scour depth at the upstream toe of the pile (S_o), and b) the scour at the downstream section of the pile (S_d). Scour profiles were found to be highly dependent on the densimetric Froude number

(Fr_d) and pile diameter (d_o). Scour profiles and scour depths at the toe of the pile (S_o) were investigated at different distances between pile locations and propeller face (X), pile diameter, sediment bed material size, propeller diameter, speed, and gap. New empirical equations were proposed for the estimation of the scour depth at the toe of the pile. The locations of the pile (X) were also investigated to assess whether the predominant scouring mechanism was the propeller jet or the pile mechanism. Furthermore, scour formations around the two - pile tandem arrangements with different pile diameters ($d_o = 4$ cm and 9 cm) and sediment beds ($d_{50} = 0.52$ mm, 1.28 mm), and the application of rock protection around a pile case at a constant propeller diameter, speed and gap were investigated.

Key Words: Scour, Propeller Jet, Berth Structures, Propeller Wash, Water Jet, Pile



YILDIZ TECHNICAL UNIVERSITY
GRADUATE SCHOOL OF NATURAL AND APPLIED SCIENCES

PERVANE JETİ ETKİSİNDE KAZIK DESTEKLİ YANAŞMA YAPILARI ETRAFINDA MEYDANA GELEN OYULMA

Remziye İlayda TAN

İnşaat Mühendisliği Anabilim Dalı

Doktora Tezi

Tez Danışmanı: Prof. Dr. Yalçın YÜKSEL

Bu tez kapsamında seçilen prototip için yanaşma yapılarına yanaşan ve ayrılan gemilerin pervanelerinden çıkan jet akımlardan dolayı oluşan oyulma miktarları deneysel olarak incelenmiştir. Bu çalışmada geçmişte yapılan literatür çalışmalarında verilen Froude yoğunluk sayısı aralığı ($1.95 \leq Fr_d \leq 15.01$) genişletilerek kullanılmıştır. Bu amaçla daha önce yapılan deneysel çalışmalar geliştirilmiş ve oyulma sürecinde etkin olan ilgili parametreler ile ilgili bağıntılar önerilmiştir. Daha önce yapılan çalışmalar kapsamında yer alan esaslar da dikkate alınarak, bu çalışmada deney taban malzemesi ortalama tane çapı ($d_{50} = 0.52$ mm, 1.28 mm, 4.00 mm and 8.30 mm) ve Froude yoğunluk sayısı (Fr_d) aralıkları genişletilmiştir. Böylece, pervane jeti etkisinde tabanda beklenen oyulma miktarlarını tahmin edebilmek üzere yeni denklemler önerilmiştir. Deneyde kullanılan modele ait boyut analizi ve deney koşulları ayrıntılarıyla belirtilmiştir. Ayrıca Akustik Doppler hız ölçer (ADV) cihazı ile pervane jetinin meydana getirdiği hız dağılımları ve büyüklüğü belirlenmiştir. Pervanenin çıkış hızını hesaplayabilmek amacıyla seçilen pervane geometrisi ve özelliklerine bağlı olarak yeni bir denklem önerilmiştir. Ayrıca pervane jetinin yapı (tekil kazık) etrafında meydana getirdiği oyulma miktarları ve oyulma çukuru boyutları deneysel olarak incelenmiştir. Yapı etrafında meydana gelen oyulmanın Froude yoğunluk sayısı (Fr_d), pervane çapı (D_p) ve pervane açıklığına (pervane eksenini ile taban arasındaki düşey mesafeye, G) bağlı olarak değiştiği bulunmuştur. Üç farklı oyulma profili a) kazığın membasında meydana gelen (S_o) b) kazığın mansabında meydana gelen oyulma (S_d) miktarları dikkate alınarak sınıflandırılmıştır. Oyulma profillerinin Froude yoğunluk sayısı (Fr_d) ve kazık çapına bağlı olarak değiştiği görülmüştür. Oyulma profilleri ve kazık etrafında meydana gelen oyulma miktarları (S_o) kazığın pervaneden farklı

uzaklıktaki konumu (X), kazık apı, taban malzeme byklkleri, pervane apı, hızı ve aıklıęı aısından incelenmiřtir. Kazık topuęunda meydana gelen oyulma derinlięini tahmin edebilmek iin yeni ampirik denklemler nerilmiřtir. Kazıęın deęiřen konumları (X) iin oyulmayı kontrol eden mekanizmanın pervane jeti veya kazık mekanizması tarafından gerekleřtirildięi incelenmiřtir. Ayrıca $d_{50}=0.52$ mm ve 1.28 mm'lik taban malzemesi zerinde $d_o= 4$ cm ve 9 cm'lik kazıklar kullanılarak arka arkaya iki kazıęın yerleřtirildięi durum ve tekil kazık etrafında tař koruma uygulandıęı durum iin tabanda meydana gelen oyulma, pervanenin belirlenen sabit hızı, apı ve aıklıęı aısından incelenmiřtir.

Anahtar Kelimeler: Oyulma, Pervane Jeti, Yanařma Yapısı, Su Jeti, Kazık



INTRODUCTION

Propeller induced scour problems have been investigated by researchers such as Blaauw and Van de Kaa [1], Chiew and Lim [2], Hamill and Hughes [3], Lam et al. [4] etc. However, studies on the scour mechanism owing to three-dimensional propeller jet around a vertical pile still limited. This chapter provides an overview of previous researches.

1.1 Literature Review

Chiew and Lim [2] investigated the scour hole induced by a deeply submerged circular wall jet and an offset jet both in air and water with uniform noncohesive sediments (Figure 1.1). Series of experiments conducted by Chiew and Lim [2] showed that formation of the scour hole formation reached the equilibrium state approximately in 6 hours and 24 - 68 hours in air and water, respectively.

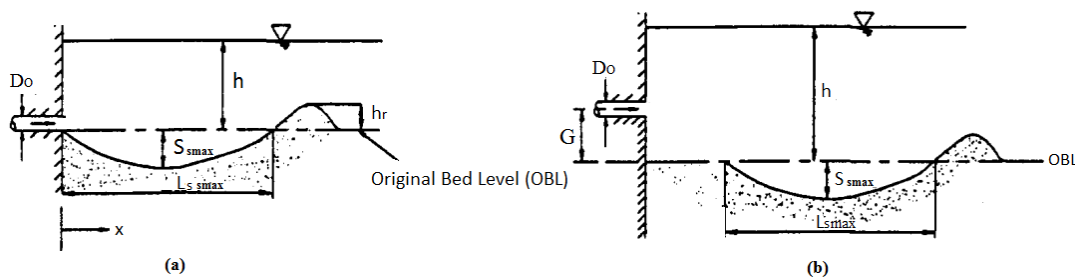


Figure 1.1 Sketch of scour formation by a submerged circular (a) wall jet (b) horizontal jet with gap (Chiew and Lim [2])

Chiew and Lim [2] found that the scour hole formations produced by the circular wall jet were highly dependent on the densimetric Froude number (Fr_d) that is one of the main characteristic of scouring parameter. They also defined characteristic

dimensionless parameters of scour formation due to a circular jet for both in air and water, by the Equation (1.1) and Equation (1.2) given below.

Scour hole formed in air for an equilibrium state ($2.7 \leq Fr_d \leq 32.5$)

$$S_{smax} = 0.15 \cdot Fr_d^{1.33}; \quad \frac{B_{smax}}{D_o} = Fr_d^{1.11}; \quad \frac{L_{smax}}{D_o} = 2.89 \cdot Fr_d^{1.11} \quad (1.1)$$

Scour hole formed in water for an equilibrium state ($4.8 \leq Fr_d \leq 85.3$)

$$S_{smax} = 0.21 \cdot Fr_d; \quad \frac{B_{smax}}{D_o} = Fr_d^{0.75}; \quad \frac{L_{smax}}{D_o} = 4.41 \cdot Fr_d^{0.75} \quad (1.2)$$

where S_{smax} is the maximum depth of scour hole at equilibrium state, B_{smax} is the maximum width of the scour hole at equilibrium state, L_{smax} is the maximum length from the jet exit to the initiation of the scour hole formation, D_o is the diameter of circular jet, Fr_d is the densimetric Froude number $Fr_d = U_0 / \sqrt{gd_{50}\Delta}$, U_0 is the efflux velocity, Δ is the relative density, g is gravitational acceleration, d_{50} is median grain size of the bed sediment.

Figure 1.2 shows the dimensionless parameters of S_{smax}/D_o , B_{smax}/D_o , and L_{smax}/D_o as a function of the densimetric Froude number. These parameters formed with the same Fr_d are always higher in air than in water.

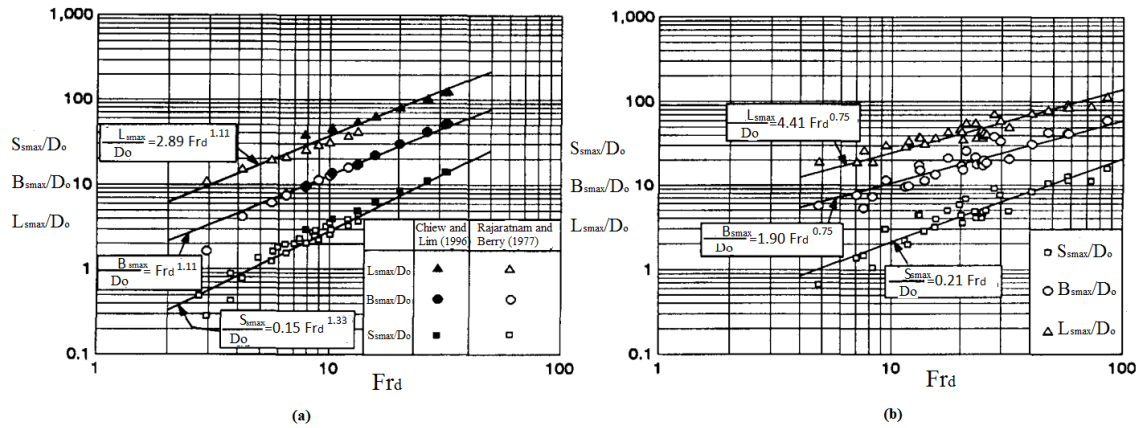


Figure 1.2 S_{smax}/D_o with Fr_d for circular wall jets in (a) air and (b) water (Chiew and Lim [2])

Chiew and Lim [2] also defined the correlation between the dimensionless deposition crest h_r/S_{smax} with Fr_d seen in (Figure 1.3). They observed that the eroded scour hole quickly formed a deposition mound while the scour hole was increasing.

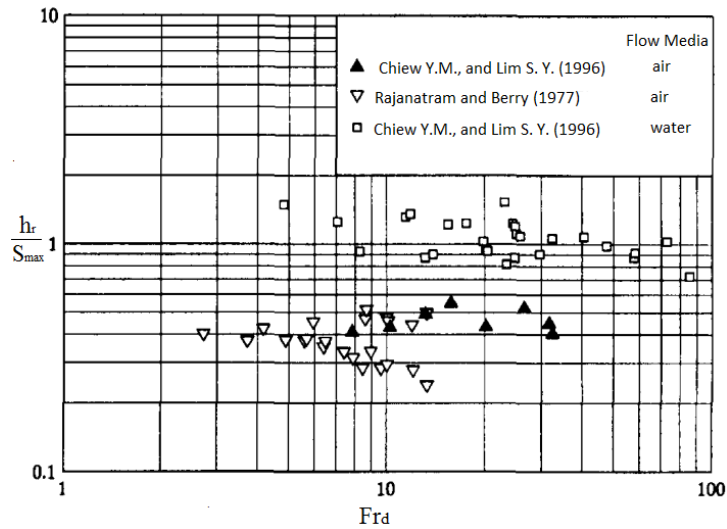


Figure 1.3 h_r/S variation with densimetric Froude number (Fr_d) (Chiew and Lim [2])

Chiew and Lim [2] stated that the eroded particles from the scour hole needed much more energy to overcome the potential energy created by higher the deposition mound height (h_r) formed in water than in air because the density difference between air / sediment and water / sediment directly affects the mode of sediment transport and the scour hole formation.

The gap between the sediment bed and water jet is also an additional parameter which is affective on scour formation. Figure 1.4 shows the variation of S_{smax}/D_o and G/D_o . They found that the higher gap (G) reduced the scour depth because most of the energy diffused into the flow instead of being used to erode the sediment bed.

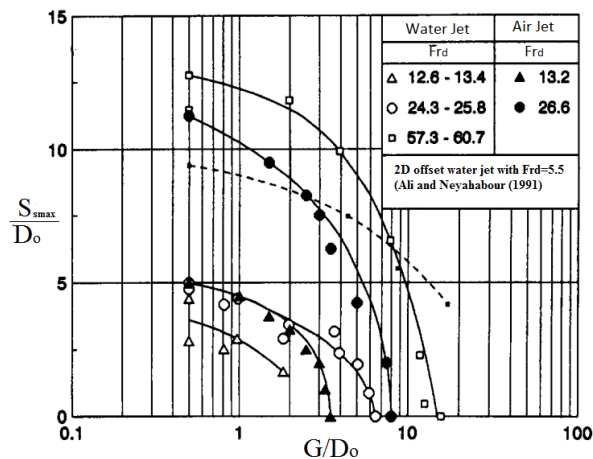


Figure 1.4 Variation of S_{smax}/D_o with offset height G/D_o for various Fr_d values for circular offset jets (Chiew and Lim [2])

Hong et al. [5] investigated the local scour hole induced by a rotating propeller for noncohesive sediment beds. They defined a schematic view for the scour formation

given in Figure 1.5. They tested different experimental parameters such as; propeller diameter (D_p), sediment bed material, gap ratio G/D_p , and propeller speed to define the affective parameters on scour formation.

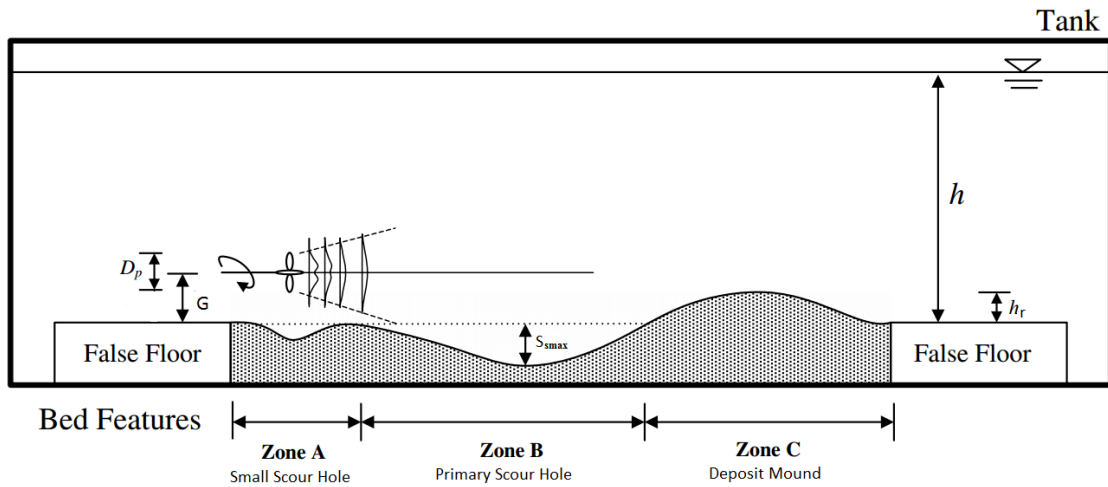


Figure 1.5 Schematic scour formation owing to propeller jet (Hong et al. [5])

Hong et al. [5]'s summarized experimental test conditions compared with Karki et al. [6]'s and Hamill [7]'s data in Table 1.1.

Table 1.1 Summarized test conditions (Hong et al. [5])

Test	D_p (cm)	d_{50} (cm)	G (cm)	h (cm)	U_0 (m/sec)	Fr_a	Re_j	h_r (cm)	Type of Scour
R-1	10	0.34	15	60	0.682	9.19	68.176	60	Propeller wash
R-2	10	0.34	15	60	0.484	6.53	48.443	60	Propeller wash
R-3	10	0.34	10	60	0.484	6.53	48.443	60	Propeller wash
R-4	21	0.24	10.5	60	0.379	6.08	79.58	45	Propeller wash
R-5	21	0.24	10.5	60	0.482	7.73	101.177	45	Propeller wash
R-6	21	0.24	10.5	60	0.557	8.94	117.014	45	Propeller wash
R-7	21	0.24	10.5	60	0.666	10.69	139.92	45	Propeller wash
R-8	21	0.24	21	60	0.379	6.08	79.58	45	Propeller wash
R-9	21	0.24	21	60	0.482	7.73	101.177	45	Propeller wash
R-10	21	0.24	21	60	0.557	8.94	117.014	45	Propeller wash
R-11	21	0.24	21	60	0.666	10.69	139.92	45	Propeller wash
H-1	6.1	0.76	12.5		1.219	10.99	74.355	-	Propeller wash
H-2	6.1	0.76	17.5		1.219	10.99	74.355	-	Propeller wash
H-3	6.1	1.46	7.5		1.689	10.99	103.058	-	Propeller wash
H-4	6.1	1.46	12.5		1.689	10.99	103.058	-	Propeller wash
H-5	6.1	1.46	17.5		1.689	10.99	103.058	-	Propeller wash
H-6	15.4	0.76	17.5		0.857	7.729	132.016	-	Propeller wash

Table 1.1 Summarized test conditions (cont'd)

H-7	15.4	0.76	17.5		1.285	11.59	197.965	-	Propeller wash
H-8	15.4	0.76	17.5		1.715	15.46	264.067	-	Propeller wash
H-9	15.4	1.46	17.5		0.853	5.548	131.344	-	Propeller wash
H-10	15.4	1.46	17.5		1.279	8.318	196.921	-	Propeller wash
H-11	15.4	1.46	17.5		1.706	11.095	262.664	-	Propeller wash
K-1	2.66	0.71	2.66		1.08	10.07	28.716	16	Squared offsetjet
K-2	2.66	0.71	3.99		1.08	10.07	28.716	16	Squared offsetjet
K-3	2.66	0.71	5.32		1.08	10.07	28.716	16	Squared offsetjet

R denotes the study by Hong et al. [5], K the study by Karki et al.[6]'s, H study by Hamill [7]'s

Hong et al. [5] divided scour hole formation into four stages as seen in Figure 1.6. The first one is the initial stage when is the primary scour hole is formed with small ripples. Then a small scour hole formed beneath the propeller while the primary hole was increasing in size at the developing stage. During stabilization stage, the small and the primary scours increase and the distance between them decrease. In the last asymptotic stage, both the small and primary scours merge together and remain still.

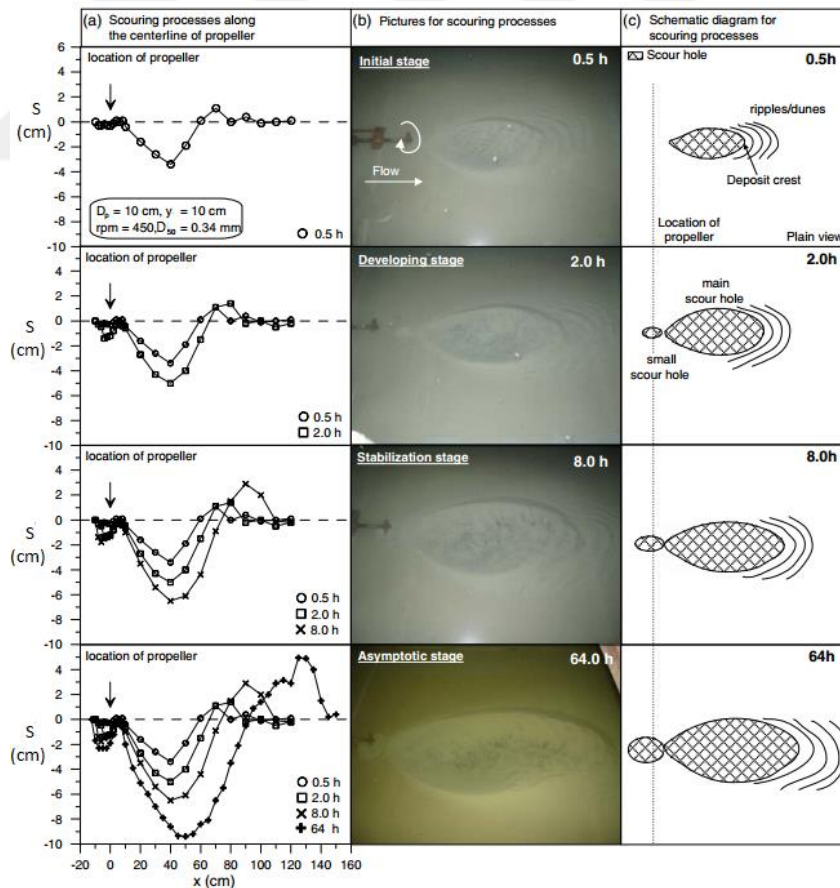


Figure 1.6 Scour hole formations (Hong et al. [5])

Figure 1.7 shows the scour depth differences at low and high gaps of the propeller. For the case with low gap ratio ($G/D_p = 0.5$) deeper scour hole and higher dune formations were observed than a higher gap ratio ($G/D_p = 1.0$).

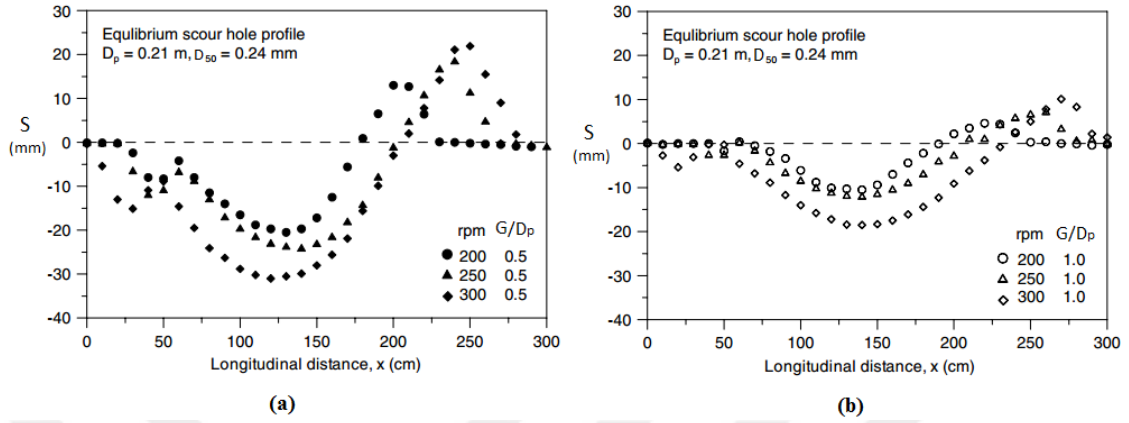


Figure 1.7 Scour profiles (a) Low gap ratio with $G/D_p = 0.5$ (b) High gap ratio with $G/D_p = 1.0$ (Hong et al. [5])

Hong et al. [5] expressed the scour depth using Buckingham Pi theorem by choosing, ρ and U_0 as the primary parameters;

$$\frac{S_{\max}}{D_p} = f\left(\text{Fr}_d, \frac{G}{d_{50}}, \frac{t}{(D_p/U_o)}\right) \quad (1.3)$$

where S_{\max} is the maximum depth of the scour hole at any time, D_p is the propeller diameter, Fr_d is the densimetric Froude number, d_{50} is median grain size of sediment bed, G is the vertical distance from the seabed to the center of the propeller axis, t is time.

Hong et al. [5] rearranged the formula with using experimental data for the time dependent scour hole formation both for the propeller jet and the submerged jet valid for $0.5 < G/D_p < 2.87$ and $5.55 < \text{Fr}_d < 11.1$ as follows:

$$\frac{S_{\max}}{D_p} = k_1 \left[\log_{10} \left(\frac{U_o t}{D_p} \right) - k_2 \right]^{k_3} \quad (1.4)$$

$$k_1 = 0.014 \cdot \text{Fr}_d^{1.120} \cdot \left(\frac{G}{D_p} \right)^{-1.740} \cdot \left(\frac{G}{d_{50}} \right)^{-0.170} \quad (1.5)$$

$$k_2 = 1.882 \cdot Fr_d^{-0.009} \cdot \left(\frac{G}{D_p} \right)^{2.302} \cdot \left(\frac{G}{d_{50}} \right)^{-0.441} \quad (1.6)$$

$$k_3 = 2.477 \cdot Fr_d^{-0.073} \cdot \left(\frac{G}{D_p} \right)^{0.53} \cdot \left(\frac{G}{d_{50}} \right)^{-0.045} \quad (1.7)$$

The rearranged Equation (1.4) was used to define the time needed to initiate the scouring t_s , for $S_{max}=0$;

$$\log_{10} \left(\frac{U_o t}{D_p} \right) = k_2 \quad (1.8)$$

$$\frac{t_s}{\left(\frac{D_p}{U_o} \right)} = 10^{k_2} = 10^{\left[1.882 \times Fr_d^{-0.009} \times \left(\frac{G}{D_p} \right)^{2.302} \times \left(\frac{G}{d_{50}} \right)^{-0.441} \right]} \quad (1.9)$$

The results showed that seabed scour formation due to propeller jet occurred within a very short time after the propeller began to rotate within the range of 0.06 to 12.1 sec in their experiments.

Hong et al. [5] defined the effective parameters on scour formation caused by propeller jet. Their defined parameters with the data from various researchers are summarized in Table 1.2.

Table 1.2 Summarized parameters that are effective on the scour formation given by researchers (Hong et al. [5])

Researchers	G/D _o	Fr _d	S _{max} /D _o	Jet Mechanism
Hamill [8]	1.14	5.55-7.73	0.91-1.00	Propeller jet
Chiew and Lim [2]	0.50 -15.75	13.14-60.4	0.47-12.76	Circular jet
Karki et. al. [6]	1.00 -2.00	10.00	2.03-2.87	Square jet
Hong et al. [5]	0.50 - 1.50	6.08-10.69	0.50-1.50	Propeller jet
D _o denotes nozzle diameter of the circular jet, width of square jet or propeller diameter				

They indicated that both Fr_d and gap ratio G/D_o are effective parameters for the depth of scour. Figure 1.8 (a) shows the parameters mostly associated with propeller jet scour for Fr_d ≤ 10 which tends to merge into the trend formed by the data for jet flow at higher Fr_d. Figure 1.8 (b) also shows that the dimensionless scour depth S_{max}/D_o decreases with an increasing of G/D_o. Hong et al. [5] expressed an empirical equation valid for

$0.5 < G/D_p < 2.87$ and $5.55 < Fr_d < 11.1$ by considering these parameters for the initiation of scouring as follows:

$$13 \cdot \frac{S_{\max}}{D_o} = 0.265 \left[Fr_d - \left(4.114 \cdot \frac{G}{D_o} \right) \right]^{0.955} \cdot \left(\frac{G}{D_o} \right)^{-0.022} \quad (1.10)$$

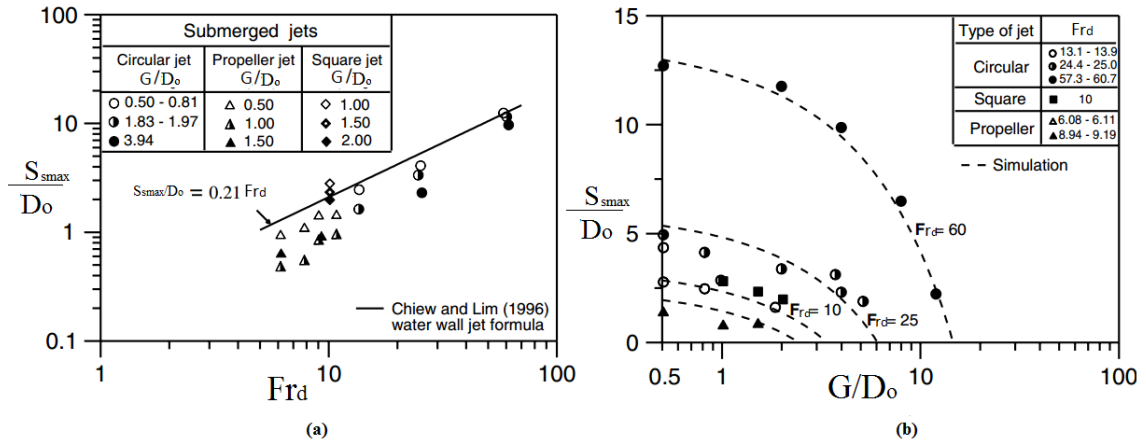


Figure 1.8 (a) Comparison of (a) S_{\max}/D_o and Fr_d (b) S_{\max}/D_o and G/D_o with dashed line for Equation (1.10) (Hong et al. [5])

They obtained critical densimetric Froude number Fr_{cd} by using Equation (1.10) for $G/D_o > 0.5$ given as follows:

$$Fr_{cd} = 4.114 \cdot \frac{G}{D_o} \quad (1.11)$$

Linearized plots of Equation (1.10) with their experimental data are given in Figure 1.9 that represents both no scour and scour conditions.

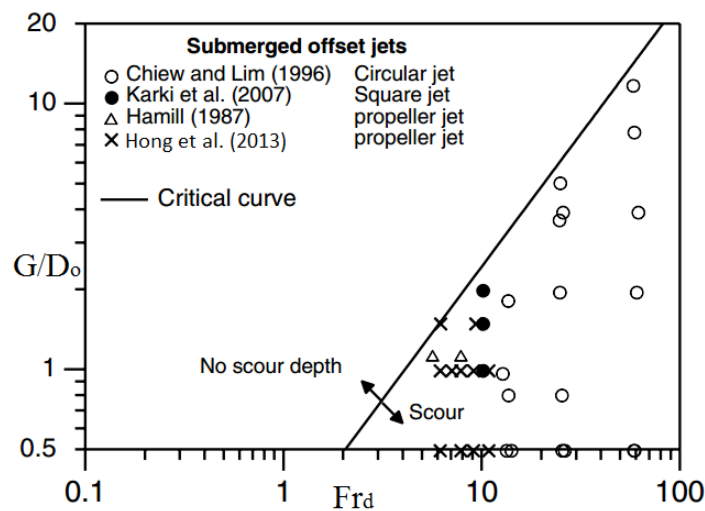


Figure 1.9 Critical conditions for scour induced by propeller and submerged jets (Hong et al. [5])

A local scour problem induced by propeller jet as seen in Figure 1.10 during a ship's berthing/unberthing and maneuvering operations may occur at the seabed and at the banks of navigation channels on the sloping banks of the harbor, near quay walls, and around pile structures (Chin et al. [8]).

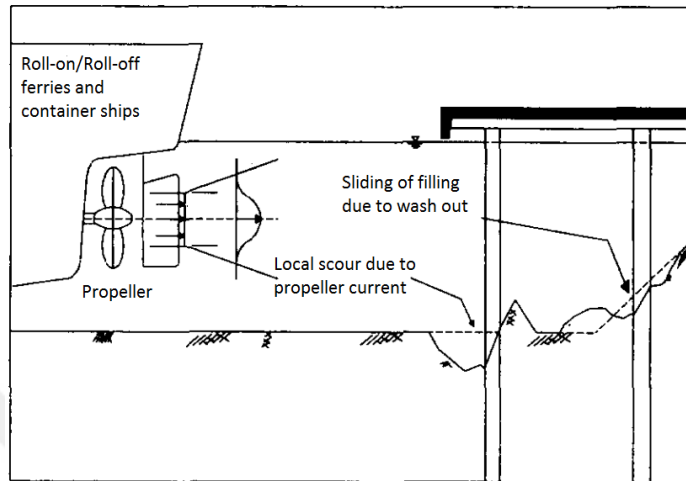


Figure 1.10 Erosion of seabed induced by a ship propeller (Chin et al. [8])

Chin et al. [8] identified the mechanism of scour induced by propeller jet into two categories; 'Pile obstruction mechanism' that occurred owing to impinging of jet flow onto the pile and 'Jet diffusion mechanism' that formed the scour hole under jet's diffusive velocity.

Chin et al. [8] observed the downflow due to the impinging and horseshoe vortex with the deflected flow. They stated that the downflow velocity increased with the deflected flow into scour hole while the scour hole at the pile was developing (Figure 1.11).

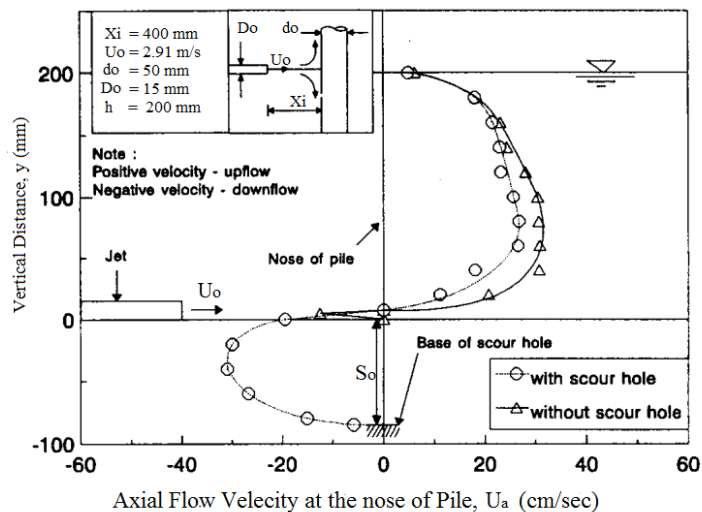


Figure 1.11 Vertical flow distribution at the pile (Chin et al. [8])

They investigated the formation of the scour hole mechanism owing to circular jet around a vertical pile (Figure 1.12).

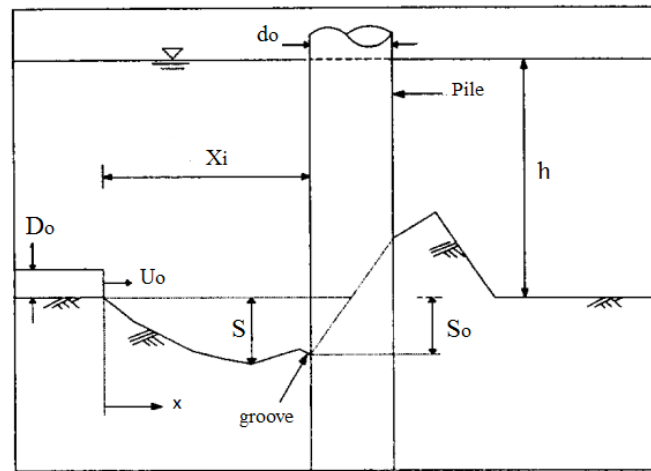


Figure 1.12 Scour hole formation induced by wall jet around a vertical pile (Chin et al. [8])

They defined different types of scour profiles by changing the values of impingement distances (X_i) as seen in Figure 1.13. Type 1 scour profiles occurred at the face of pile, that is $S_{\text{max}}=S_o$ and obstruction mechanism was dominant because of the small impingement distance. Jet mechanism was dominant for Type 2 profiles due to larger impingement distance and the scour hole had a similar formation produced by wall jet with no pile case ($S_o=0$). Type 3 scour profiles had two different scour formations one of them was produced due to jet mechanism as Type 2 profile and the other formation was produced by obstruction mechanism around the pile. The maximum scour depth occurred at the upstream toe of pile as $S_{\text{max}} \geq S_o$.

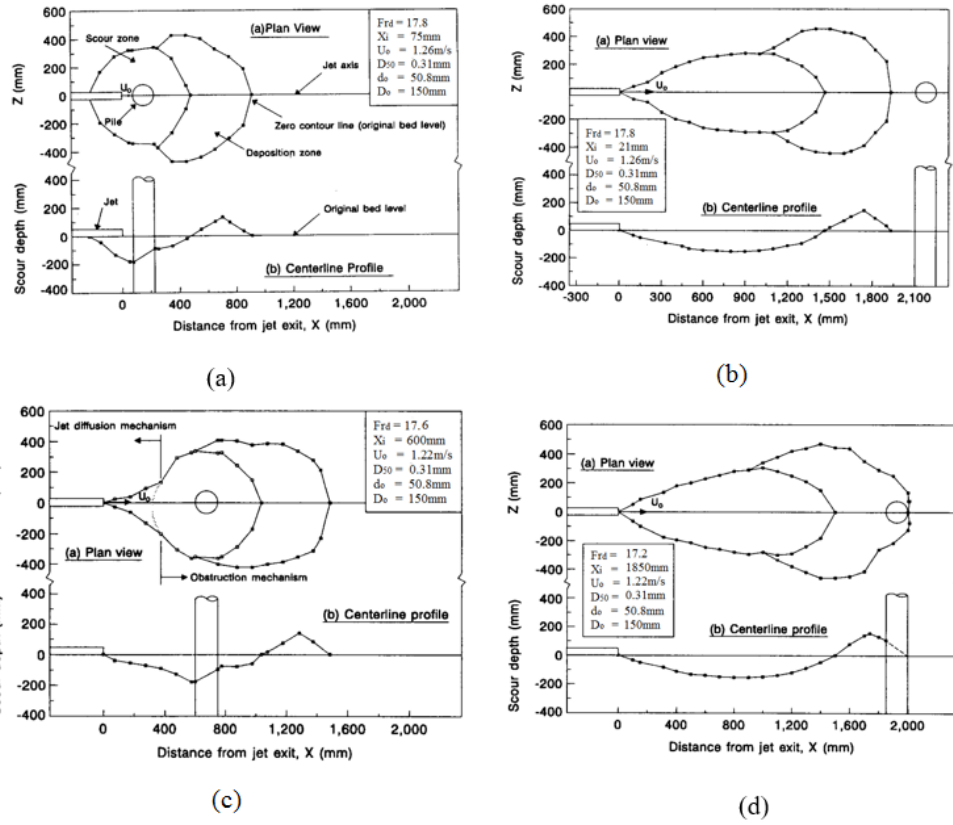


Figure 1.13 Zero counter line and centerline profile (a) Type 1, (b) Type 2, (c) Type 3, (d) Type 4 (Chin et al. [8])

Boundary limits of the scour profiles were expressed by Equations (1.12) and (1.13) for different type of scour profiles (Figure 1.14) by Chin et al. [8] as follows:

$$\text{Type 1 and 3 : } \tan\theta = \frac{S_o}{X_i} \quad (1.12)$$

$$\text{Type 2 and 4 : } X_i = L_t \quad (1.13)$$

where S_o is the depth of maximum scour hole at the pile, X_i is the impingement distance, L_t is the length of maximum scour hole from the initiation of the scour to downstream edge of deposition zone, θ is the angle of repose of the sediment bed.

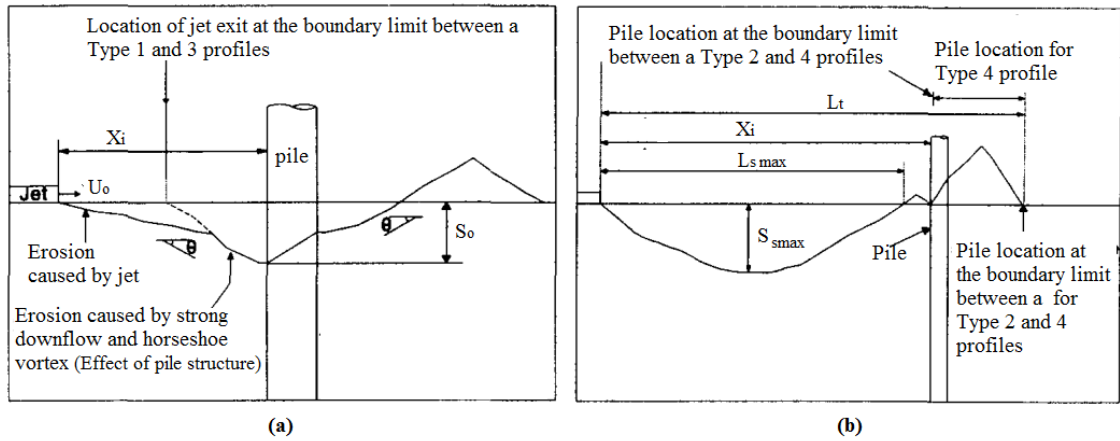


Figure 1.14 Boundary limits of centerline profiles (a) Type 1 and 3 (b) Type 2 and 4 (Chin et al. [8])

The functional relationship of Fr_d on S_{smax}/D_o with X_i/D_o ($=0.5-41.3$) and d_o/D_o ($=0-21$) in their study was given with Equation (1.14) in (Figure 1.15);

$$\frac{S_{smax}}{D_o} = 0.21 Fr_d \quad (1.14)$$

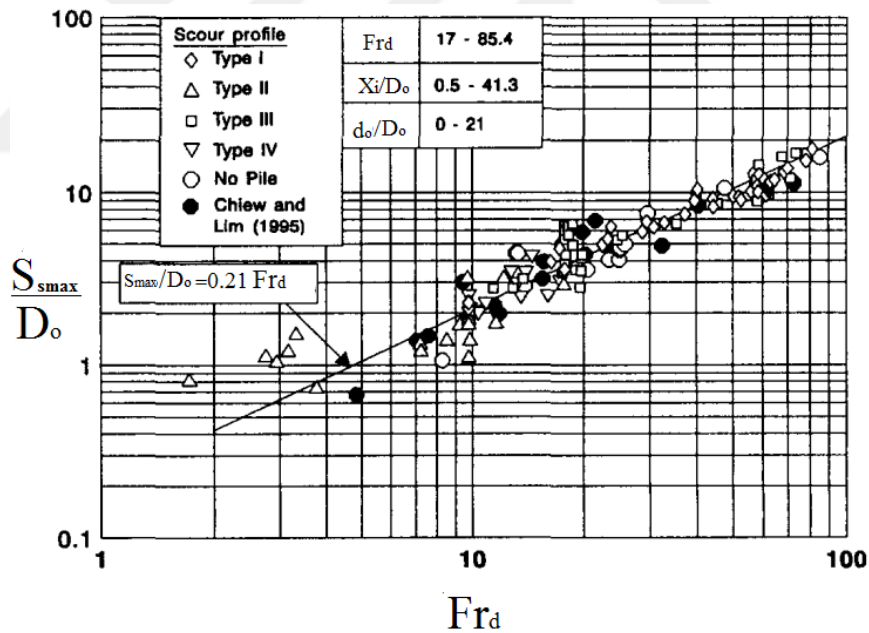


Figure 1.15 Variation of S_{smax}/D_o with Fr_d (Chin et al. [8])

The boundary limit between different types of scour profiles defined by Chin et al. [8] is as follows:

Type 1 and 3 scour profiles are formed with substituting Equation (1.14) into (1.12) for the average value of $\theta=31^\circ$;

$$Fr_d = 2.86 \cdot \frac{X_i}{D_o} \quad (1.15)$$

Type 3 and 4 scour profiles are formed with substituting Equation (1.14) into (1.13) for the value of $L_{smax}/S_{smax} = 9.8$;

$$Fr_d = 0.49 \cdot \frac{X_i}{D_o} \quad (1.16)$$

Type 2 and 4 scour profiles are formed with substituting Equation (1.14) into (1.13) for the value of $L_t/S_{smax} = 12.6$;

$$Fr_d = 0.38 \cdot \frac{X_i}{D_o} \quad (1.17)$$

Chin et al. [8] stated that Fr_d and X_i/D_o were the most important parameters in determining the formation of the scour type. These three boundary limits defined in Equation (1.15), (1.16) and (1.17) are classified in terms of Fr_d and X_i/D_o in Figure 1.16.

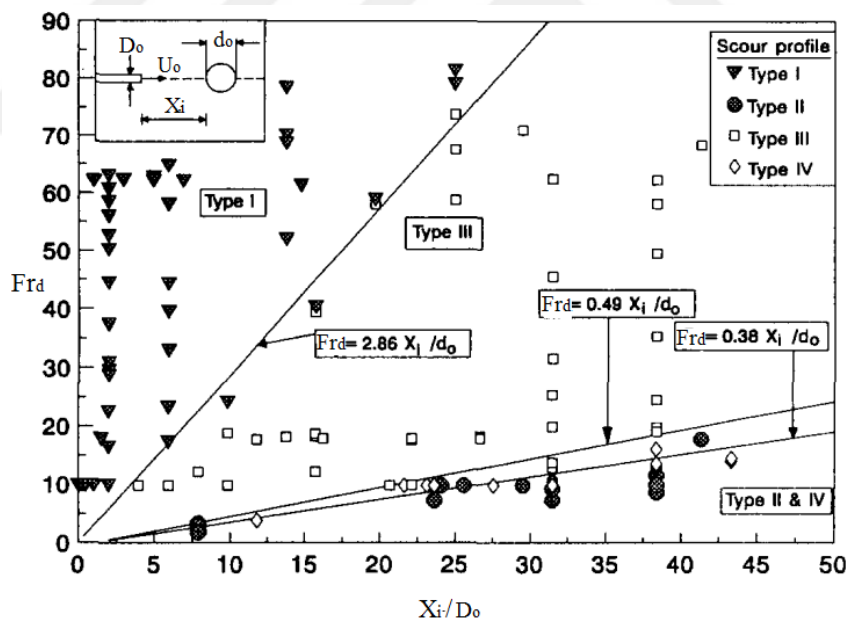


Figure 1.16 Classification of the equilibrium scour profiles in terms of Fr_d and X_i/D_o (Chin et al. [8])

Hamill et al. [9] investigated different positions of a solid vertical quay wall on scouring process induced by wall jet to simulate the propeller wash as seen in Figure 1.17.

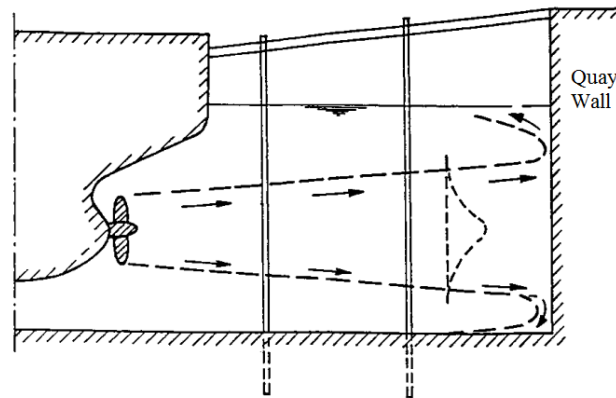


Figure 1.17 Jet flow deflection toward the bed and quay wall structures (Hamill et al. [9])

Characteristics of the propellers with some test parameters used in the experiments are summarized in Table 1.3.

Table 1.3 Parameters for the experiments (Hamill et al. [9])

D_p (m)	Pitch of the Blade	BAR	N	C_T	d_{50} (mm)	C (mm)	rpm	Fr_d
0.154	0.95	0.488	4	0.38	0.76-1.46	50-150	400-800	5.55-15.46
0.061	0.98	0.663	3	0.48	0.76-1.46	45-145	1,400-2,200	8.55-18.73
0.076	1.0	0.473	3	0.402	1.46-3.00	95-150	1,000-2,500	7.97-11.02
0.131	1.1352	0.922	6	0.558	1.46-3.00	60-150	350-800	6.08-8.33

In the table, BAR is the propeller's blade area ratio, N is the number of the propeller's blades, C_T is the propeller's thrust coefficient, C is the clearance distance from the sediment bed to the propeller tip.

They developed empirical equations for the estimation of scouring due to the propeller jet. Earlier researchers such as Blaauw and Van de Kaa [1] provided some methods for estimating the maximum scour depth without considering the effect of any berth structure and maximum scour depth (S_{smax}) was given as a function of; $S_{smax} = f(U_o, D_p, d_{50}, C, \rho, g, \Delta, \nu)$.

Maximum scour depth that is defined without considering berth structure as a logarithmic function of time is as follows:

$$S_{\max} = \Omega [\ln(t)]^{\Gamma} \quad (1.18)$$

$$\Gamma = 4.113 \left(\frac{C}{d_{50}} \right)^{0.742} \left(\frac{D_p}{d_{50}} \right)^{-0.552} Fr_d^{-0.682} \quad (1.19)$$

$$\Omega = 6.9 \cdot 10^{-4} \left(\frac{C}{d_{50}} \right)^{-4.63} \left(\frac{D_p}{d_{50}} \right)^{3.58} Fr_d^{4.535} \quad (1.20)$$

They expressed the maximum depth of scour by dimensional analysis without considering the effect of viscosity as follows:

$$\frac{S_{\max}}{D_p} = f \left(Fr_d, \frac{D_p}{d_{50}}, \frac{G}{d_{50}} \right) \quad (1.21)$$

where S_{\max} is maximum depth of scour hole at any time, D_p is the diameter of propeller jet, Fr_d is the densimetric Froude number, U_0 is the efflux velocity, Δ is the relative density, g is gravitational acceleration, d_{50} is median grain size of sediment bed.

Hamill et al. [9] rearranged Equation (1.18) as (1.22) with the k value for 38.97 and 70% of the data validated as $\pm 45\%$.

$$S_{\max} = k\Omega [\ln(t)]^{\Gamma} \quad (1.22)$$

Relationship between Γ and Ω was given in their study for $0.5 < G/D_p < 2.5$ is as follows:

$$\Omega = \Gamma^{-6.38} \quad (1.23)$$

$$\Gamma = \left(\frac{C}{d_{50}} \right)^{0.94} \left(\frac{D_p}{d_{50}} \right)^{-0.48} Fr_d^{-0.53} \quad (1.24)$$

Distance from the face of propeller to the location of maximum scour at equilibrium state (X_{μ}) was determined by Hamill et al. [9] as;

$$X_{\mu} = Fr_d^{0.94} C \quad (1.25)$$

Hamill et al. [9] also showed that scouring mechanism could be different in different positions of quay wall as seen in Figure 1.18. The scour holes started to develop similarly for the unconfined case; however, there was additional erosion observed close to the wall as seen in Figure 1.18 (a) and Figure 1.18 (b). In Figure 1.18 (c) there was a decrease in the amount of erosion that took place in the area that eroded in the

unconfined situation, although there was additional erosion at the beginning of the profile. Figure 1.18 (e) shows the situation in which the wall is removed away from the area affected by the unconfined scour. In this case the profile becomes slightly elongated with the crest and the position of the maximum scour moving farther away from the propeller. In Figure 1.18 (f), the maximum depth of scour tends to be reduced.

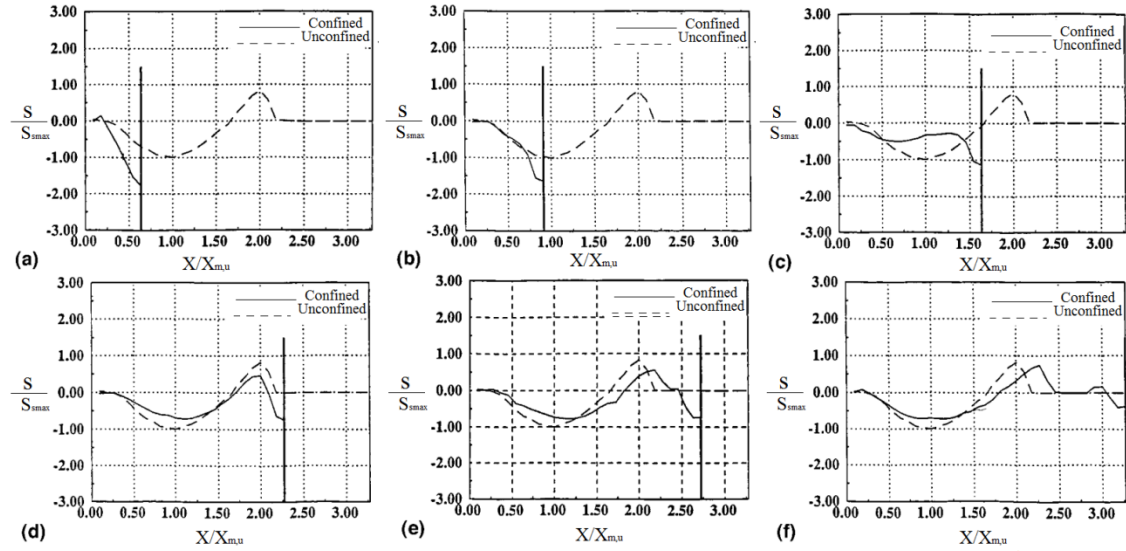


Figure 1.18 Comparison between confined and unconfined scour profiles with the quay wall placed at (a) $0.636X_s$ (b) $0.909X_s$ (c) $1.636X_s$ (d) $2.272X_s$ (e) $2.727X_s$ (f) $3.27X_s$ (Hamill et al. [9])

In the figure, S_{max} is the maximum eroded depth of scour, S_{smax} is the maximum depth of scour hole at the equilibrium state without quay structure, X_{mu} is the longitudinal location of maximum scour depth for unconfined case, X is the horizontal distance from the propeller's face.

Lam et al. [10] investigated the axial, tangential, radial components of velocity and the turbulence intensity caused by a ship's propeller. They measured three components of velocity with laser Doppler anemometry (LDA) according to the coordinate system as seen in Figure 1.19.

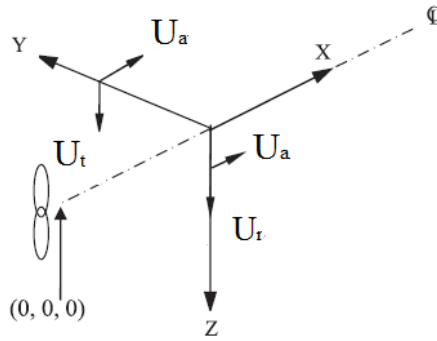


Figure 1.19 Axial, tangential and radial velocity components in the coordinate system (Lam et al. [10])

They used 76 mm propeller diameter (D_p) and 1000 rpm propeller speed to illustrate a typical ship propeller with a diameter 2.5 m, 200 rpm propeller speed with thrust coefficient (C_t) 0.61. According to a survey carried out at British ports and harbors by Qurrain [11], it was observed that having a propeller with the size of 1.5 – 3.0 m and with a 200 rpm rotation speed, a ship might cause seabed scouring.

Lam et al. [10] reported that the measured efflux velocity with the LDA is higher than the theoretical values of efflux velocity calculated with the equations given by various researchers seen in Table 1.4.

Table 1.4 Measured and calculated efflux velocity values (Lam et al. [10])

Source	Equation	Efflux Velocity, U_0 (m/sec)	Variation (%)
Lam et al. [10]	-	1.365	-
Axial Momentum Theory	$U_0 = 1.59 \cdot n \cdot D_p \cdot \sqrt{C_T}$ $n = 16.67$ Rps $D_p = 0.076$ m $C_T = 0.4$	1.274	6.7
Hamill [7]	$U_0 = 1.33 \cdot n \cdot D_p \cdot \sqrt{C_T}$	1.066	21.9
Stewart [12]	$U_0 = \zeta \cdot n \cdot D_p \cdot \sqrt{C_T}$ $\zeta = D_p^{-0.0686} \cdot P^{1.519} \cdot \beta^{-0.323}$ $P' = 1$ $\beta = 0.47$	1.230	9.9
Hashmi [13]	$U_0 = E_o \cdot n \cdot D_p \cdot \sqrt{C_T}$ $E_o = \left(\frac{D_p}{D_h} \right) \cdot C_T^{0.403} \cdot \beta^{-0.744}$ $D_h = 0.01492$ m	1.223	10.4

In the table, D_p is the propeller diameter, U_0 is the efflux velocity, n is the number of propeller revolutions per second (rps), C_T is propeller thrust coefficient, ζ is efflux velocity coefficient, P' is the propeller pitch ratio, D_h is the diameter of hub.

Lam et al. [10] found the position of the maximum velocity approximately 22.5 mm radial distance from the rotation axis for the radius of propeller (R_p) is 38 mm and radius of hub (R_h) is 7.46 mm. The variation between Lam et al. [10]'s and Berger et al. [14]'s results were 10% as seen in Table 1.5.

Table 1.5 Position of efflux velocity values (Lam et al. [10])

Researchers	Equation	Position (mm)	Variation (%)
Lam et al. [10]	-	22.5	10
Berger et al. [14]	$R_{mo} = 0.67 \cdot (R_p - R_h)$	20.46	-
Prosser [15]	$R_{mo} = 0.6 \cdot (R_p - R_h)$	18.32	10
Hamill [7]	$R_{mo} = 0.7 \cdot (R_p - R_h)$	21.38	4
Stewart [12]	Agreed with Berger et al. [14]'s Equation	-	2-5
McGarvey [16]	Agreed with Berger et al. [14]'s Equation	-	30

Hamill [7], Stewart [12] McGarvey [16] and Brewster [17] reported that the most dominant component of the velocity was the axial velocity (U_a). The axial velocity (U_a) distribution had two peak ridges with a low velocity core at the rotation axis and Lam et al. [10]'s results agreed with theirs as seen in Figure 1.20.

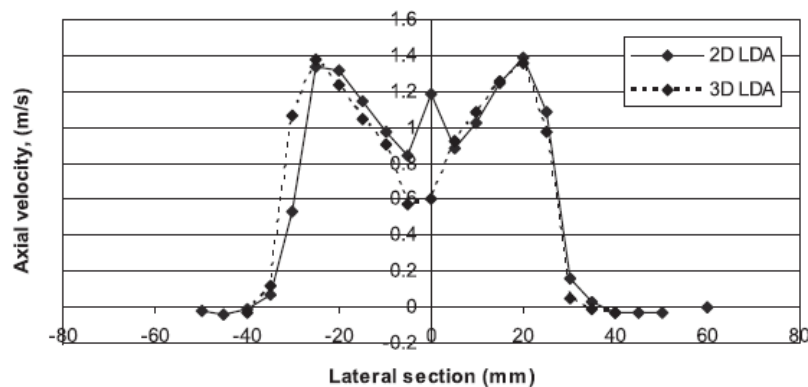


Figure 1.20 Measured axial velocity with 2D LDA and 3D LDA (Lam et al. [10])

The tangential velocity (U_t) was emphasized as the second largest component of the velocity by Stewart [12] which was confirmed with Lam et al. [10]'s measurement results as seen in Figure 1.21.

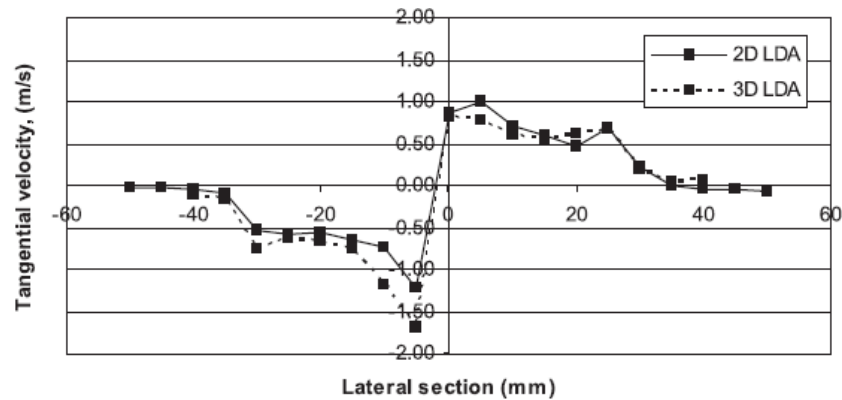


Figure 1.21 Measured tangential velocity with 2D LDA and 3D LDA (Lam et al. [10])

The location of the first peak of tangential velocity was determined at the point of the propeller hub and where the blades were joined, and the second peak was at the point near the tip of the blade. Lam et al. [10] found the distance of those peaks located at radial distance $r/R_p = 0.13$ and 0.66 , respectively.

The radial component of the velocity (U_r) was stated by McGarvey [16] as approximately 30% of the axial velocity. Likewise, Lam et al. [10] found that the radial velocity increased from the hub to a peak velocity and decreased towards the blade's tips (Figure 1.22).

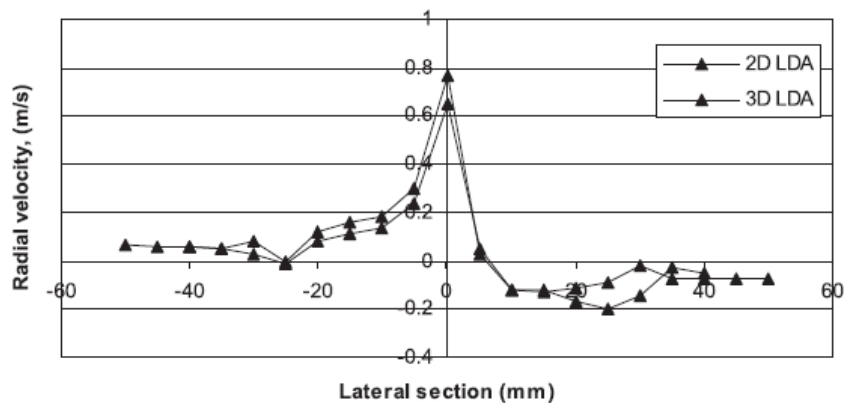


Figure 1.22 Measured radial velocity with 2D LDA and 3D LDA (Lam et al. [10])

All three components of the velocity measured by Lam et al. [10] are given in Figure 1.23. This figure shows that the axial velocity has two peaks between the rotation axis (r/R_p) and the jet boundary.

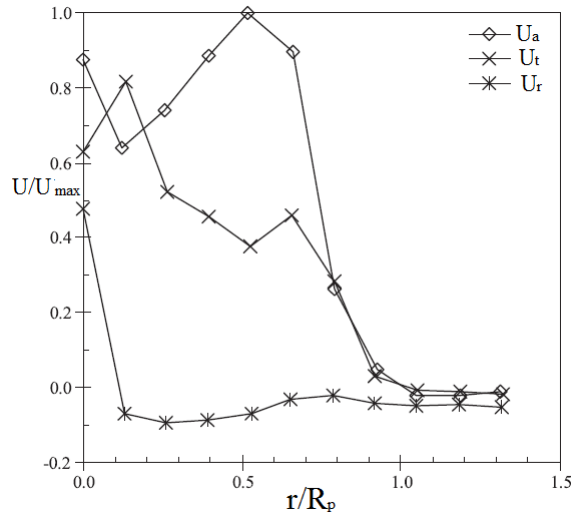


Figure 1.23 Measurement of dimensionless velocity components (Lam et al. [10])

In the figure, r is the radial distance from the propeller's center and R_p is the radius of the propeller.

Lam et al. [10] compared their results with Kee et al. [18]'s to determine the effects of the propeller geometry on all three components of velocity as seen in Figure 1.24. Comparison of the propeller parameters used in Kee et al. [18]'s and Lam et al. [10]'s is given in Table 1.6.

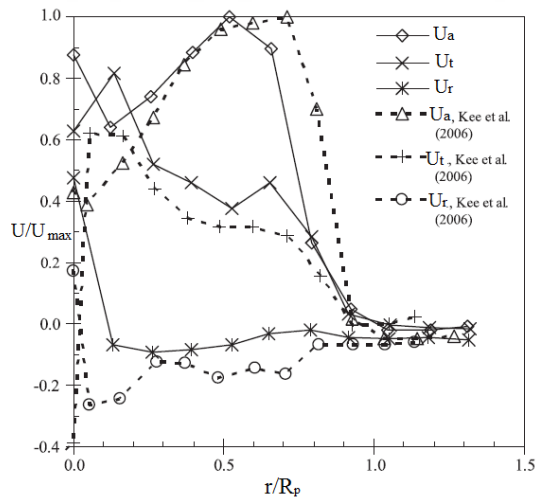


Figure 1.24 Velocity components for different propeller geometry (Lam et al. [10])

Table 1.6 Propeller characteristics of Kee et al. [18] and Lam et al. [10]

Researcher	D_p (mm)	D_h (mm)	N	P'	BAR	C_T
Kee et al. [18]	92	20.3	4	0.735	0.4525	0.2908
Lam et al. [10]'s	76	14.92	3	1	0.47	0.4

Hamill [7] stated that the turbulence intensity that we have little information about, flow pattern decreased along the rotation axis. Lam et al. [10] found that the axial (U'_a), tangential (U'_t) and, radial (U'_r) component of turbulence intensity showed three peaks at the propeller face as 0.28, 0.88, 0.56, respectively as seen in Figure 1.25. The maximum peak also observed at the rotation axis ($r/R_p=0$) is shown in this figure.

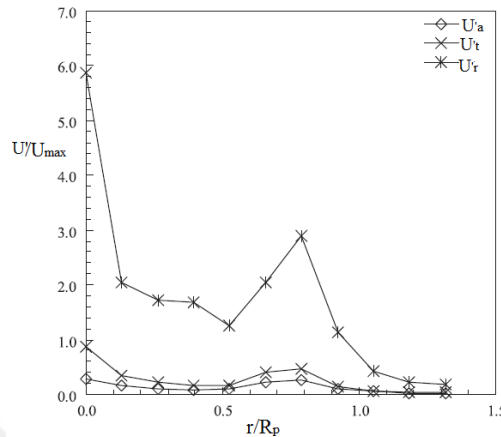


Figure 1.25 Axial (U'_a), Tangential (U'_t) and, radial (U'_r) component of turbulence intensity (Lam et al. [10])

Johnston et al. [19] tested different clearances of propeller, with and without sediment bed conditions to determine the expansion of propeller wash. The case of a propeller jet incident on an horizontal bed was proposed as three zones; zone prior to jet impact with the boundary, zone of boundary layer development and the zone of developed boundary layer flow as seen in Figure 1.26.

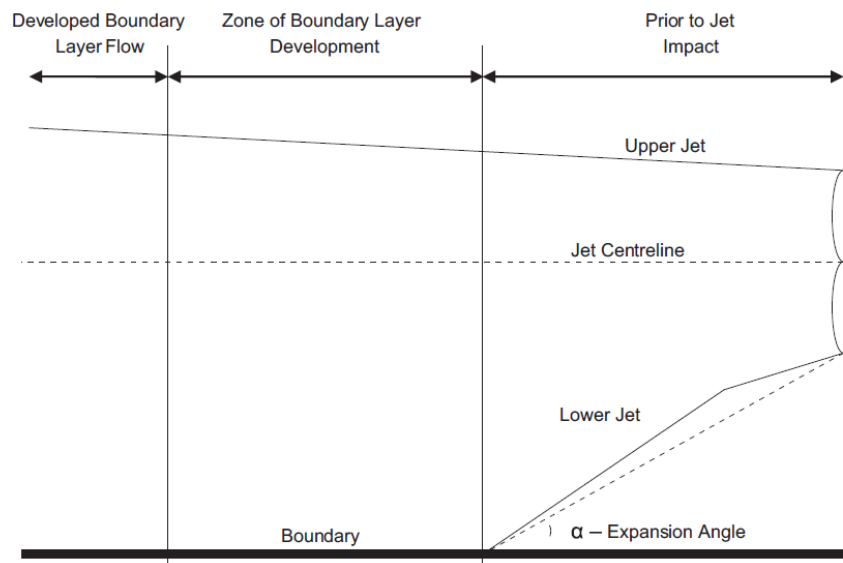


Figure 1.26 Schematic view of boundary layer development (Johnston et al. [19])

As a propeller, they used 76 mm diameter (D_p), 0.61 thrust coefficient (C_t), 0.47 blade area ratio (BAR), 14.92 mm hub diameter (D_h) to illustrate a typical small vessel.

They made velocity measurements by a particle image velocimeter (PIV) system at the propeller's face (1), farthest downstream (2) and at a point equidistant from (1) and (2). Velocity profile measurements for a constant clearance height at 96 mm with and without bed conditions at the propeller centerline are given in Figure 1.27, Figure 1.28, Figure 1.29. Figure 1.27 shows that the increasing distance to downstream from the face of propeller causes increasing velocity difference between with bed and without bed conditions.

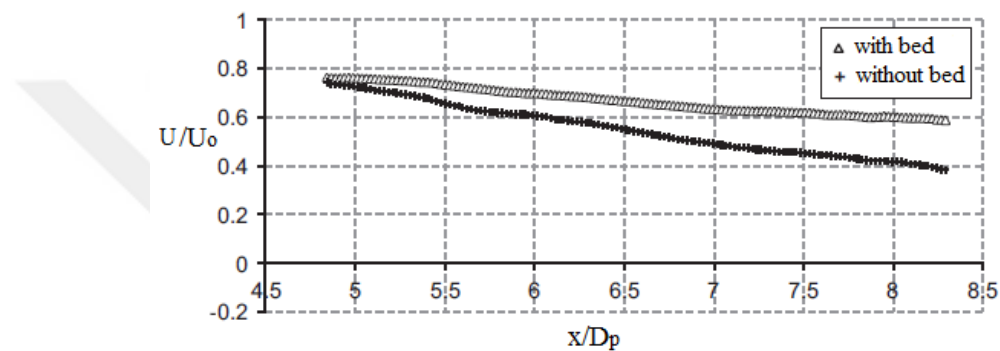


Figure 1.27 Velocity profiles at the propeller centerline (Johnston et al. [19])

Johnston et al. [19] measured the axial velocity approximately as 0.05 m/sec which remained low and constant for the unconfined bed at $r/R_p=2.5$ (Figure 1.28).

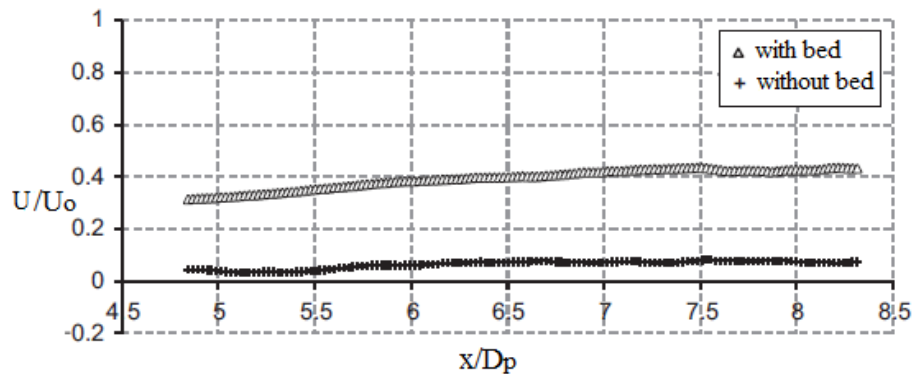


Figure 1.28 Velocity profiles at the propeller centerline at $r/R_p=2.5$ (Johnston et al. [19])

Close to the boundary at $r/R_p=3.6$ (5 mm above the bed) the axial velocity without bed conditions has negative values that represents a return flow whereas the velocity confined condition increases from 0.05 m/sec to 0.17 m/sec as seen in Figure 1.29. (Johnston et al. [19]).

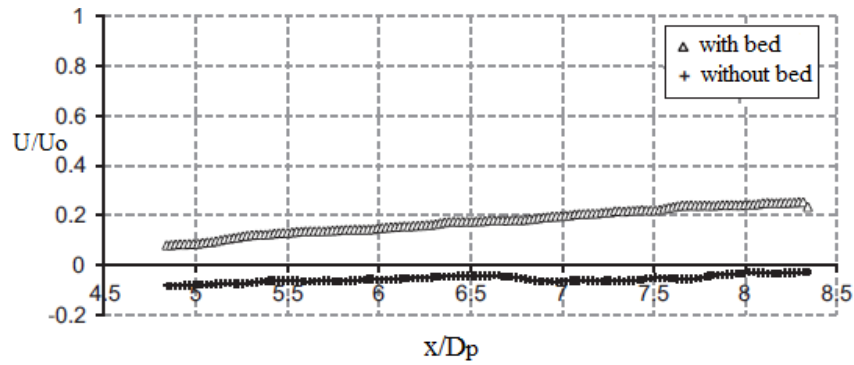


Figure 1.29 Velocity profiles at the propeller centerline at 5mm above the bed ($r/R_p=3.6$) (Johnston et al. [19])

According to all these three test results Johnston et al. [19] observed a change point at $7.2D_p$ in both at centerline and at $r/R_p=2.5$ in the longitudinal velocity as seen in Figure 1.27 and Figure 1.28. When they changed the clearance height at 121 mm, this point was observed at the centerline and boundary at $7.9D_p$ and $7.7D_p$, respectively. The clearance height for 146 mm was observed at $8.2D_p$ in both at the centerline of the propeller and at $r/R_p=2.5$. As the clearance height was increased, the expansion of the propeller jet increased up to 10° and 20° , for with bed and without bed conditions, respectively (Figure 1.30).

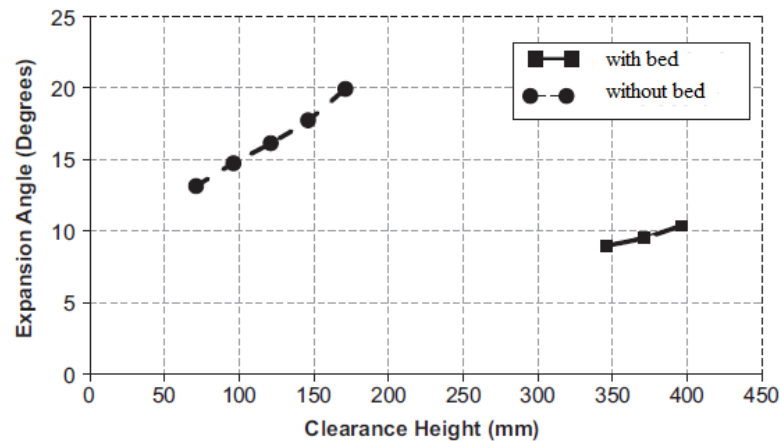


Figure 1.30 Expansion angle variation (Johnston et al. [19])

Johnston et al. [19] proposed Equation (1.26) to represent the expansion angle as follows:

$$\alpha = 66 \cdot 10^{-3} \cdot C + 8.3 \quad (1.26)$$

where α is the expansion angle of a propeller jet, C is the clearance height.

Their study showed that the maximum axial velocity decay with the increasing distance from the propeller as a function of the efflux velocity and clearance height is given in

Equation (1.27). According to different clearance heights, Johnston et al. [19]'s calculated A_z and B_z coefficient values are given in Table 1.7.

$$\frac{U_{\max}}{U_0} = A_z \left(\frac{x}{D_p} \right)^{B_z} \quad (1.27)$$

where U_{\max} is the maximum axial velocity, U_0 is the efflux velocity, A_z is the derived coefficient for a zone, B_z is derived coefficient for a zone, D_p is propeller diameter, x is axial distance from the face of propeller.

Table 1.7 Coefficient values for maximum velocity (Johnston et al. [19])

Clearance, C (m)	Up to Developed Boundary Layer Flow (z=1)		Developed Boundary Layer Flow (z=2)	
	A_1	B_1	A_2	B_2
0.071	2.1	-0.90	1.4	-0.70
0.096	1.8	-0.62	2.6	-0.78
0.121	1.8	-0.73	2.6	-0.91
0.146	1.3	-0.47	1.3	-0.50
0.171	0.8	-0.16	1.2	-0.40

Johnston et al. [19] produced Equations (1.28) and (1.29) with the results of Table 1.7.

$$A_1 = -102.9C^2 + 12.5C + 1.68 \quad , \quad B_1 = 49.1C^2 - 5.37C - 0.71 \quad (1.28)$$

$$A_2 = -445.7C^2 + 101.1C - 3.33 \quad , \quad B_2 = 102.9^2 - 21.4C + 0.29 \quad (1.29)$$

where C is the clearance height, A_1 , A_2 , B_1 , B_2 are the coefficients for a zone up to development layer flow $z=1$ and $z=2$.

Lam et al. [4] presented a detailed review of the equations that were used to calculate the velocity distribution. They gave Berger et al. [14]'s Equation (1.30) for the radial distance from the rotation axis to location where the maximum thrust occurs (R_{mo}) and Oebius and Schuster [20]'s Equation (1.31) for the location of the maximum axial velocity at the efflux plane given as follows:

$$R_{mo} = 0.67(R_p - R_h) \quad (1.30)$$

where R_h is the Propeller hub diameter, R_p is the radius of the propeller.

$$R_m = 0.3R_{mo} \left(\frac{x}{R_{mo}} \right)^{-0.3} \quad (1.31)$$

where R_m is the location of maximum axial velocity within the zone of flow establishment.

Lam et. al. [4] also summarized the equations to determine the maximum and axial velocity and its position along the longitudinal distance within the zone of flow establishment and the zone of established flow (Table 1.8 and Table 1.9).

Table 1.8 Maximum velocity in the ZEF and ZFE (Lam et. al. [4])

Zone	Researcher(s)	Equation	Remarks
Zone of Established Flow	Albertson et al. [21]	$\frac{U_{\max}}{U_0} = \frac{1}{2C_r} \left(\frac{x}{D_p} \right)^{-1}$	Researchers suggested equations with different C coefficients to determine the U_{\max} in terms of x/D_p .
	Fuehrer and Römisch [22]	$\frac{U_{\max}}{U_0} = 2.6 \left(\frac{x}{D_p} \right)^{-1.0}$	
	Blaauw and Van de Kaa [1]	$\frac{U_{\max}}{U_0} = 2.8 \left(\frac{x}{D_p} \right)^{-1.0}$	
	Berger et al. [14]	$\frac{U_{\max}}{U_0} = 1.025 \left(\frac{x}{D_p} \right)^{-0.6}$	
	Verhey [23]	$\frac{U_{\max}}{U_0} = 1.275 \left(\frac{x}{D_p} \right)^{-0.7}$	
	Hamill [7]	$\frac{U_{\max}}{U_0} = A' \left(\frac{x}{D_p} \right)^{B'}$ $A' = -11.4C_t + 6.65\beta + 2.16(P/D_p)$ $B' = -(1.0C_t)^{-0.216}\beta^{1.024} (P/D_p)^{-1.0}$	Takes account of the propeller characteristics by considering blade area ratio.
	Stewart [12]	$\frac{U_{\max}}{U_0} = 0.543 - 0.0281 \left(\frac{x}{D_p} \right)$	The maximum velocity decays in the ZFE to a downstream distance of $x/D_p=10$.
	Hashmi [13]	$\frac{U_{\max}}{U_0} = 0.638e^{-0.097 \left(\frac{x}{D_p} \right)}$	The ZEF can be extended up to $x/D_p=16$.

Table 1.8 Maximum velocity in the ZEF and ZFE (cont'd)

Zone of Flow Establishment	Hamill [7]	$\frac{U_{\max}}{U_0} = 1$	Valid up to $x/D_p = 0.35$ from the face of propeller.
		$\frac{U_{\max}}{U_0} = 0.87 \left(\frac{x}{D_p} \right)^{-(\beta/4)}$	After distance $x/D_p=0.35$ at the location downstream U_{\max} decays steadily.
	Stewart [12]	$\frac{U_{\max}}{U_0} = 1.0172 - 0.1835 \left(\frac{x}{D_p} \right)$	U_{\max} decays from the propeller face within the ZFE to be up to $x/D_p \leq 3.25$.

In the table, D_p is the propeller diameter, U_{\max} is the maximum velocity, β is the blade area ratio, x is axial distance, C_r is ratio of the standard deviation concerning velocity, P/D_p is pitch ratio.

Table 1.9 Axial velocity at any distance in the ZEF and ZFE (Lam et. al. [4])

Zone	Researcher(s)	Equation	Remarks
Zone of Flow Establishment	Albertson et al. [21]	$\frac{U_a}{U_{\max}} = e^{[-(r^2/2\sigma^2)]}$	$\sigma \cong 0.605U_{\max}$ on the axial distance from the propeller.
	Albertson et al. [21]	$\frac{U_a}{U_{\max}} = e^{[-((r+Cx-(D_o/2))^2/(2(Cx)^2)]}$	$\sigma=Cx$ $U_{\max}=U_o$
	Hamill [7]	$\frac{U_a}{U_{\max}} = e^{[-(1/2)((r-R_{mo})/(R_{mo}/2))^2]}$	Valid up to distace $0.5 D_p$ downstream of the propeller.
		$\frac{U_a}{U_{\max}} = e^{[-(1/2)((r-R_{mo})/(R_{mo}/2)+0.075(X-R))^2]}$	
	McGarvey [16]	$\begin{aligned} \frac{U_a}{nNR_p} = & 1.261 - 0.974 \left(\frac{P}{R_p} \right) + 0.733 \left(\frac{c}{R_p} \right) \\ & + 18.53 \left(\frac{t_b}{R_p} \right) + 5.028 \left(\frac{h_d}{R_p} \right) + 0.106 \left(\frac{P}{R_p} \right)^2 \\ & - 7.277 \left(\frac{h_d}{R_p} \right)^2 - 4.093 \left(\frac{h_t}{c} \right)^2 \end{aligned}$	Applicable only across the initial efflux plane for the propeller jet.
Zone of Established Flow	Albertson et al. [21]	$\frac{U_a}{U_{\max}} = e^{[-22.2(r/X)^2]}$	

In the table, U_a is the axial velocity at any distance, r is the radius of propeller rotation axis, σ is standard deviation, h_d is the helical distance from the blade section leading edge to rake datum line, h_t is the helical distance from the blade section leading edge to position of the maximum thickness, N is the number of blades, R_p is the radius of propeller, P is the pitch of blades, t_b is the thickness of blade, c is the chord length, R_{mo} is the radial distance from the rotation axis to the point where maximum thrust occurs.

Lam et al. [24] investigated the efflux velocity of a ship's propeller as the preliminary parameter of the seabed scouring due to propeller jet as illustrated in Figure 1.31.

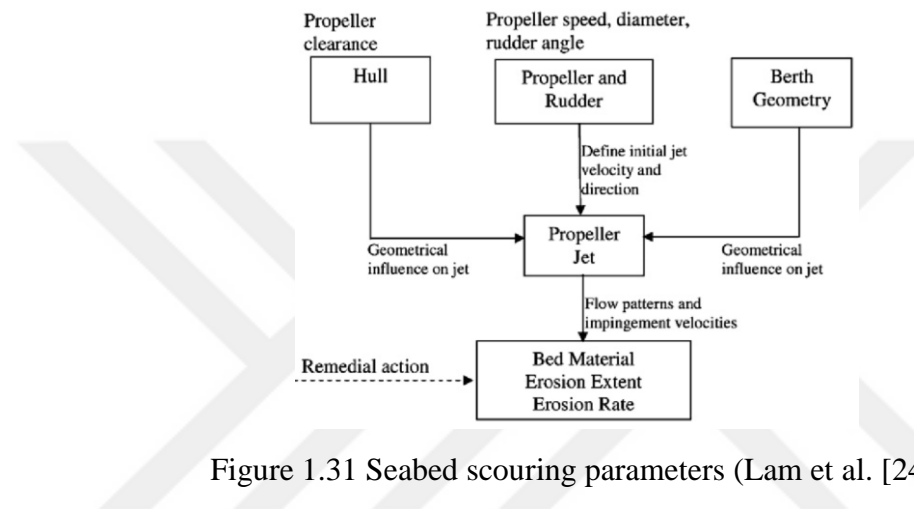


Figure 1.31 Seabed scouring parameters (Lam et al. [24])

They proposed semi-empirical methods for determining efflux velocity by using the laser Doppler anemometry (LDA) and computational fluid dynamics (CFD). Their results were compared with the theoretical equation for the efflux velocity derived from axial momentum theory.

They tested two different propeller geometry by using various propeller speeds (Table 1.10). The efflux velocity profile measurements at 750-1500 rpm propeller speeds with propeller - 76 and 350 - 100 rpm with propeller - 131.

Table 1.10 Propeller characteristics (Lam et al. [24])

Propeller Characteristics	Propeller - 76	Propeller - 131
Propeller Diameter (D_p)	76 mm	131 mm
Propeller Hub Diameter (D_h)	15.2 mm	35 mm
Propeller Blade Number (N)	3	6
Blade Area Ratio (BAR, β)	0.473	0.922
Thrust Coefficient (C_t)	0.4	0.56
Mean Pitch Ratio (P')	1	1.14

Measured efflux velocity profiles with LDA given by Lam et al. [24] showed two peaked ridges owing to the hub that are similar to Hamill [7], Stewart [12], Hashmi [13] and McGarvey [16]'s suggestion. However, they could not observe this peak in the CFD seen in Figure 1.32.

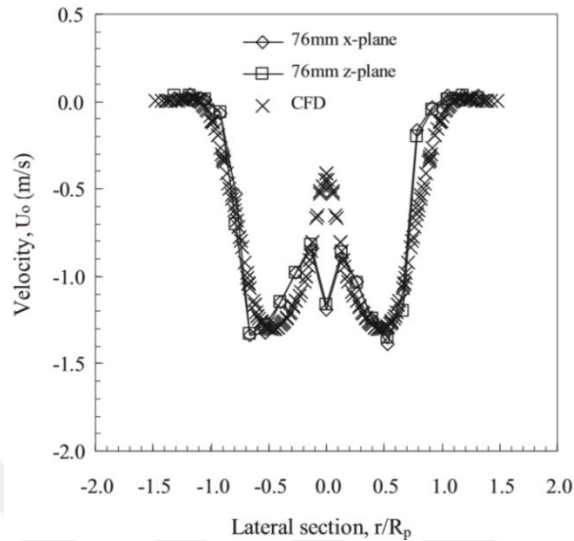


Figure 1.32 Horizontal and vertical experimental measurements in for the propeller - 76 at 1000 rpm (Lam et al. [24])

The theoretical equation to determine the efflux velocity derived from axial momentum theory with the consideration of zero advance speed of a ship is given in Equation (1.32).

$$U_0 = 1.59nD_p \sqrt{C_T} \quad (1.32)$$

Lam et al. [24] investigated the coefficient 1.59 given in Equation (1.32) by using their results. They plotted measured efflux velocity (U_0) values with LDA versus $nD_p C_T$ and obtained the efflux coefficients for two different propellers (Table 1.11).

Table 1.11 Efflux coefficients measured with LDA and correlation coefficients (R^2) (Lam et al. [24])

Location	Propeller - 76		Propeller - 171	
	Efflux Coefficient	R^2	Efflux Coefficient	R^2
On the left hand side, across the horizontal section	1.6901	0.9985	1.5589	0.9987
On the right hand side, across the horizontal section	1.7244	0.9973	1.5961	0.9990
On the top, across the vertical section	1.6959	0.9982	1.6426	0.9988
At the bottom, across the vertical section	1.7203	0.9963	1.6565	0.9957

Lam et al. [24] also investigated efflux coefficients with a CFD model results with a wider range of propeller speeds (250 - 1750 rpm) and proposed equations of the efflux velocity with different coefficients as given in Table 1.12.

Table 1.12 Equations for different propellers (Lam et al. [24])

Propeller	Source of Data	Equation
Propeller - 76	LDA	$U_0=1.71nD_p\sqrt{C_T}$
Propeller - 76	CFD	$U_0=1.46nD_p\sqrt{C_T}$
Propeller - 131	LDA	$U_0=1.61nD_p\sqrt{C_T}$
Propeller - 131	CFD	$U_0=1.41nD_p\sqrt{C_T}$
Both Propeller	LDA	$U_0=1.65nD_p\sqrt{C_T}$
Both Propeller	CFD	$U_0=1.41nD_p\sqrt{C_T}$
Modified Four Bladed Propeller - 76	CFD	$U_0=1.48nD_p\sqrt{C_T}$
Modified Five Bladed Propeller - 76	CFD	$U_0=0.89nD_p\sqrt{C_T}$

They compared efflux velocity values obtained from CFD values with LDA measurements and validated that the linear relationship with the efflux velocity (U_0) and $nD_p\sqrt{C_T}$. In their study it was stated that the efflux coefficient was reduced when the blade number increased.

Yew et al. [25] investigated scouring formation by using twin propellers instead of a single propeller. They conducted their experiments in a tank with a width of 1.2 m, length of 3.0 m and height of 1.0 m. Sediment bed material with median grain size of $d_{50}=0.1$ cm was used in the tank and propeller diameter of 22 cm was tested with rotation speeds of 400, 500 and 600 rpm.

Under these experimental conditions they stated that the scour profiles with twin-propellers had similar scour profiles in longitudinal axis when compared with single-propeller wash as in Hong et al. [5]'s study. However, in the plan view of scour formation with the tests conducted by using twin propellers, the right side had a larger scour impact than the left side as seen in Figure 1.33. The right side was expected to form a larger scouring impact attributed to the rotating directions (clockwise) of both propellers.

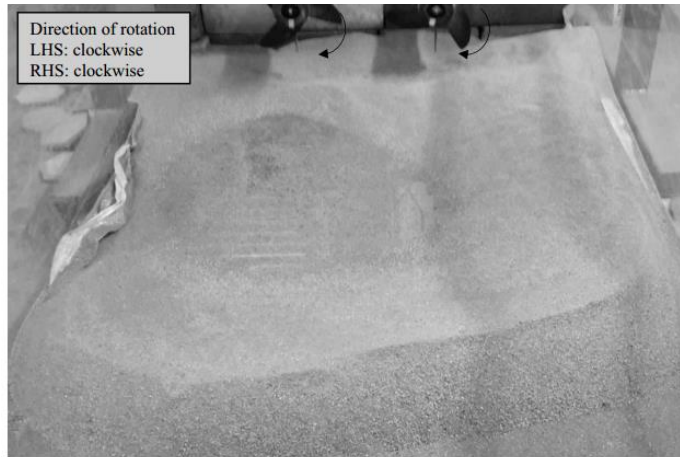


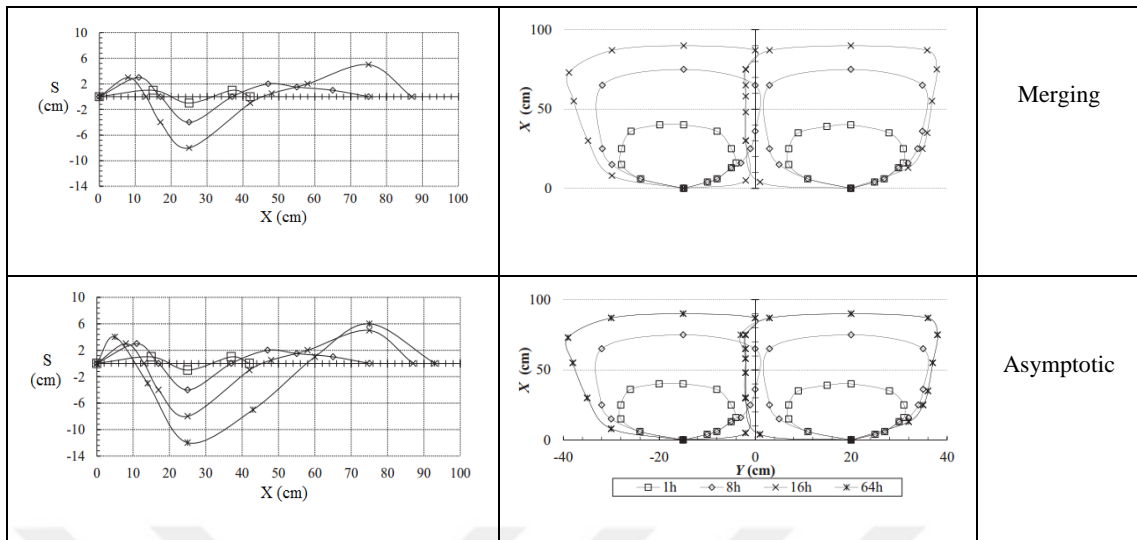
Figure 1.33 Scour profile induced by twin propellers (Yew et al. [25])

They also divided scour hole formations into four stages similar to the definitions given by Hong et al. [5] as seen in Table 1.13. In the initial stage; two small scour holes form with deposition crests in front and back of the holes, then the depths, widths and lengths of the scours increase at the developing stage. During the stabilization stage, both individual scour holes merge but they are still observed as individual scour holes. In the last asymptotic stage the scour depth reaches its maximum level and the length, width and, the depth remain still.

Table 1.13 The view of the stages of scour formations induced by twin propellers (Yew et al. [25])

Scour Profile in Longitudinal View	Scour Profile in Plan View	Stages
		Initial
		Developing

Table 1.13 The view of the stages of scour formations induced by twin propellers (cont'd)



In Figure 1.34 scour profiles are given at the asymptotic stage when scour formation reaches its equilibrium conditions for the constant clearance (C) and rotation speed (rpm). They stated that the maximum depth of the scour hole (S_{smax}) at the asymptotic stage, was low at lower rotational speeds of the propellers and it increased with the increasing rotational speeds. Width of the scour hole (B_{smax}) and height of the deposition crests (h_f) increased as the clearance of the propeller decreased at constant rotational speed.

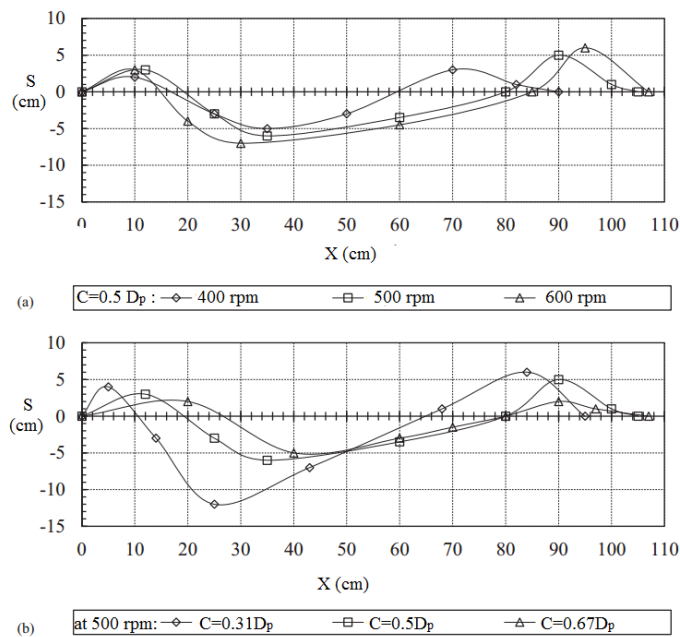


Figure 1.34 Scour formation at constant a) clearance b) rotational speed (Yew et al. [25])

Yew et al. [25] proposed an equation for the estimation of maximum scour depth (S_{\max}) owing to twin propeller wash at any time valid when $t \geq 1$ sec. The equation is given below.

$$S_{\max} = k(\log t)^{0.0231} \cdot \left(\frac{C}{D_p}\right)^{-0.488} \cdot \left(\frac{U_0 \cdot t}{C}\right)^{0.241} \quad (1.33)$$

Vis-a-vis the propeller (in centimeters), U_0 is the efflux velocity (in meter/second), t is the time (in seconds).

They also gave an equation for the maximum scour depth location (X_{\max}) induced by twin propellers for $X > 0.3D_p$ as follows:

$$X_{\max} = Fr_d^{0.9098} \cdot \left(\frac{C}{D_p}\right)^{0.1932} \quad (1.34)$$

Wei and Chiew [26] investigated temporal and spatial development of the scour hole induced by a confined jet near an open quay with slope. They conducted their experimental tests in a tank that was 1.8 m wide, 4.0 m long and 1.0 m deep. Summarized test conditions of their study are listed in Table 1.14.

Table 1.14 Summarized test conditions of Wei and Chiew [26]'s study

Test Number	D_p (cm)	d_{50} (cm)	G/D_p	X_i/D_p	rpm	U_0 (m/sec)	Fr_d	Type of Scour
A1-8	10	0.034	1	2, 3, 4, 5, 6, 7, 8, 9	450	0.778	10.5	Confined
B1-9	10	0.034	1	2, 3, 4, 5, 6, 7, 8, 9, 11	600	1.040	14.0	Confined
C1-9	15	0.034	1	2, 3, 4, 5, 6, 7, 8, 9, 10	450	1.053	14.2	Confined
*A0	10	0.034	1	∞	450	0.778	10.5	Unconfined
B0	10	0.034	1	∞	600	1.040	14.0	Unconfined
C0	15	0.034	1	∞	450	1.053	14.2	Unconfined
*A0 data set was obtained from Hong et al. [5]'s study								

Parameters in Table 1.14 are defined as; D_p is the propeller diameter, Fr_d is the densimetric Froude number, d_{50} is the median grain size of sediment bed material, G is the gap that is the vertical distance from the bed to the center of propeller's axis.

A typical scour profile is given in Figure 1.35 under summarized test conditions. They also examined various influences of toe distances (X_t) in their study, where; S_{smax} is the maximum depth of scour hole at equilibrium stage, B_{smax} is the maximum width of scour hole at the equilibrium state, $L_{smax,c}$ is the maximum length of scour hole at the equilibrium stage for confined conditions, X_t is the toe distance.

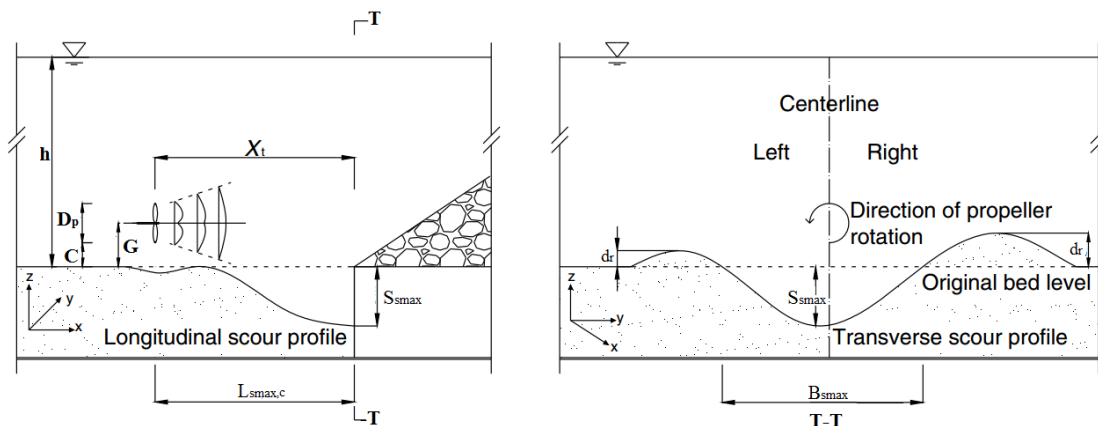


Figure 1.35 Schematic view of a typical scour formation in the presence of a quay slope (Wei and Chiew [26])

They determined each test duration as 128 hours to reach the equilibrium state and also divided the scouring into four stages that are similar to Hong et al. [5]'s as initial, developing, stabilization, and asymptotic stages. Wei and Chiew [26] examined the influence by the presence of the armored slope and vertical skirting on scour profiles with a different toe distance (X_t). In Figure 1.36 Wei and Chiew [26]'s scour profiles are given as compared to Hong et al. [5]'s. Hong et al. [5]'s profiles were obtained from the cases without obstruction.

The small and primary scour holes are lower for the confined cases when compared with Hong et al. [5]'s unconfined scour profiles for $X_t = 2D_p$ to $5D_p$ as seen in Figure 1.36. The small steeper local scour was observed at the face of vertical skirting with the scour profiles for $X_t = 6D_p$ to $7D_p$ whereas it disappeared for $X_t = 8D_p$. Wei and Chiew [26] concluded that the predominant effective mechanism on scouring process is due to the obstruction mechanism with $X_t = 6D_p$ to $7D_p$ while this effect changes to jet mechanism with $X_t = 8D_p$ that is similarly observed in Chin et al. [27]'s study. When

the scour profile reaches $X_t = 9D_p$ both small and primary scour holes are similar to the profile without obstructed cases.

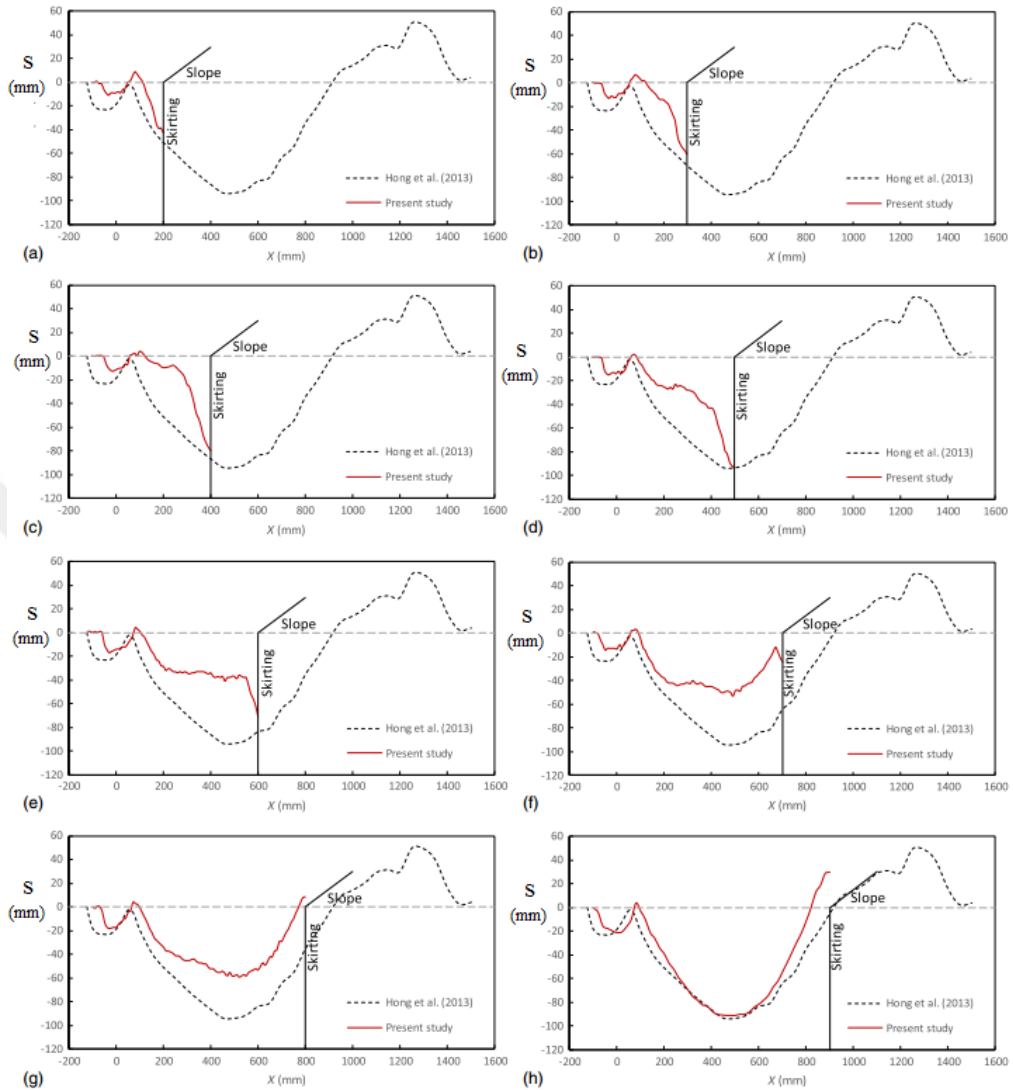


Figure 1.36 Comparisons of confined and unconfined scour profiles a) $X_t = 2D_p$ b) $X_t = 3D_p$ c) $X_t = 4D_p$ d) $X_t = 5D_p$ e) $X_t = 6D_p$ f) $X_t = 7D_p$ g) $X_t = 8D_p$ h) $X_t = 9D_p$ (Wei and Chiew [26])

Wei and Chiew [26] classified scour profiles with an open quay based on different toe distances as follows:

- Near toe field ($X_t = 2D_p$ to $5D_p$)
- Intermediate toe field ($X_t = 6D_p \sim 8D_p$)
- Far toe field ($X_t \geq 9D_p$)

They also used to relationship between X_t and X_{mu} in this classification. At the asymptotic stage, they found that the location of maximum scour depth (X_{mu}) for the unconfined case, was the limit of the downward jet diffusion and beyond this limit the

jet slipstream did not expand. Figure 1.37 (a) shows a target point considered which is the limit of the downward jet diffusion without obstruction. According to Figure 1.37 (b), in near toe distance field, target point of the jet diffusion mechanism must occur at $X = X_t$ where, $X_t \leq X_{mu}$. However, in the intermediate field, ($X_t > X_{mu}$) target point located at the upstream of the skirting as seen in Figure 1.37 (b) remains still as in the unconfined case, i.e., $X = X_{mu}$.

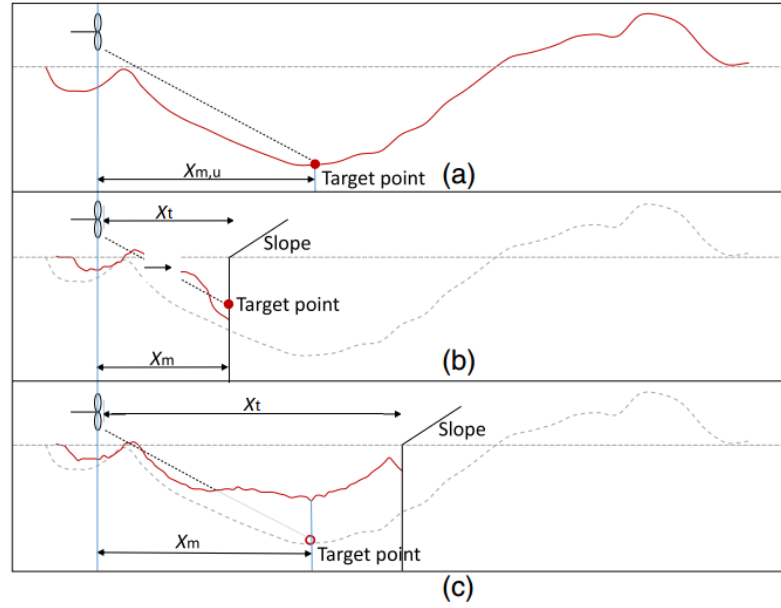


Figure 1.37 Schematic view of the the propeller jet's target point for a) unconfined case b) near toe distance c) intermediate toe distance (Wei and Chiew [26])

Parameters in Figure 1.37 are defined as; X_{mu} is the longitudinal location of maximum scour depth for the unconfined case, X_m is the longitudinal location of maximum scour depth for the confined case.

Based on these classifications, Wei and Chiew [26] also stated that the threshold between the near and intermediate field can be quantified as the location of the maximum scour depth (X_t) in the confined case corresponding to the unconfined case, i.e., $X_t / X_{mu} = 1$ while the threshold of the far toe distance field occurs at $X_t / X_{mu} = 1.9$. They also gave a linear equation between the lengths and locations of the maximum scour holes valid for the far toe distance field as given in Equation (1.35).

$$\frac{L_{smax,c}}{L_{smax}} = 0.523 \frac{X_t}{X_{mu}} + 0.018 \quad (1.35)$$

where $L_{s_{max,c}}$ is defined as the maximum length from the face of the propeller to the end of the primary scour hole in the confined case while $L_{s_{max}}$ is defined for the unconfined cases.

In this equation, the linear relationship is not valid for the far field because in this field $L_{s_{max,c}}$ reaches the same value as $L_{s_{max}}$ and remains unchanged for any increment of X_t .

They observed that within the intermediate field, the maximum scour depth and width decreased within the range of $X_t = X_{mu}$ to $1.5X_{mu}$. However, they increased when X_t is greater than $1.5X_{mu}$. Consequently, in the intermediate field, effective predominant mechanism caused due to the obstruction mechanism with increasing toe distance when $X_t > 1.5X_{mu}$ since after this distance its effect starts to decrease and in the far toe disatant field ($X_t / X_{mu} = 1.9$); the jet diffusion mechanism is predominantly affective on the scouring process.

1.2 Objective of the Thesis

The objective of this thesis is to give an overview over the subject of scouring formation to improve the understating of scouring process under a ship's propeller jet flow. The study objectives include:

- To investigate the scouring process and scour dimensions induced by a propeller jet on sediment bed with the absence and presence of berth structures;
- To examine effective parameters such as: location of berth structure from the propeller, propeller diameter, speed and gap, sediment bed material types;
- To examine the scour profile and the scouring process under different conditions and propose a critical curve for the initiation of scour;
- To determine the maximum scour depth and its location with the absence of a berth structure;
- To propose equations for the determination of the maximum scour depth at the toe of a pile by considering both fixed and changing pile locations from the propeller's face with the presence of a pile type berth structure;
- To examine the scouring process when a two-pile tandem arrangement is under propeller jet flow;
- To test an example of scour protection application around a pile induced by propeller jet.

1.3 Hypothesis

Investigations of scouring problems have been studied upon consideration of different types of berth structures. However, to the best of our knowledge, there is currently limited research reporting on propeller jet induced scour around piled berths as open-type structures. This is because scour formed near pile-supported structures is a more complex problem owing to pile obstruction and jet diffusion mechanisms, as reported by Chin et al. [8]. Consequently, this study aims to extend laboratory tests on scouring induced by ship propeller during berthing and/or unberthing operations for a pile-supported, pier type berth structure. Scour tests (without piles) were extended by considering the effect of the confinement of the propeller wash in the experimental flume induced by a vertical pile.



EROSION AROUND BERTH STRUCTURES

This chapter specifies the berth structures and scouring problems due to berthing and/or unberthing operations of vessels' near the structures.

2.1 Berthing Requirements and Effects on Seabed

Berthing requirements should be known for an understanding of scour mechanism induced by ships' propeller. Also types of berth structures and berthing/ unberthing operations are mentioned for a better understanding of this mechanism.

2.1.1 Berth Structures

There are many different berth structures in use throughout the world. Some of the main design parameters for berth structures are the site conditions such as geotechnical conditions, water levels, currents, waves, seabed, etc. and the characteristics of the design vessels (draft, length, propulsion system, etc.). Berth structures are divided into two main classifications as (Permanent International Association of Navigation Congresses (PIANC) [28]);

- Solid berth structures (Sheet pile structures and gravity structures)
- Open berth structures.

Gravity structures are based on the concept that the weight of the structure itself provides the resistance against forces that could result in movement such as sliding or tipping. The weight resisting movement of the structure can be provided either mainly by the structure itself (Figure 2.1) or by a combination of the structure and its fill (Figure 2.2).

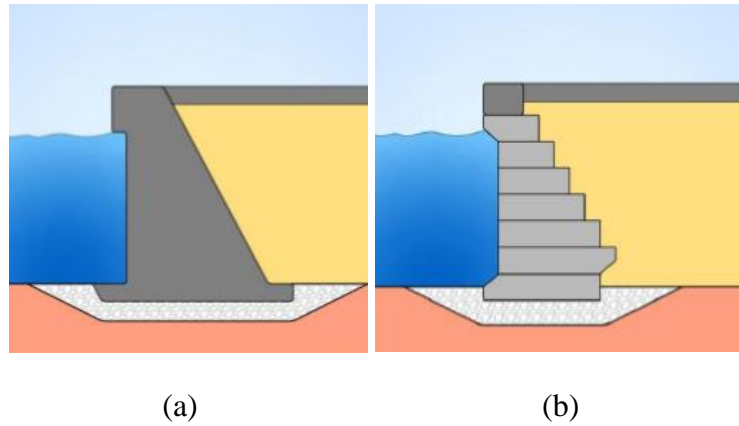


Figure 2.1 Gravity wall structures a) monolithic b) block wall (PIANC [28])

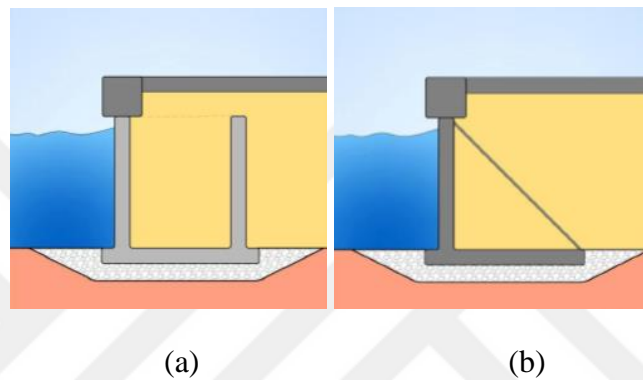


Figure 2.2 Gravity wall structures a) caisson b) cantilever monolithic (PIANC [28])

Sheet pile structures are the structures that retain the soil behind the structure by a vertical sheet-pile wall, normally the face of the berth. The following figures are examples of different types of sheet pile wall structures.

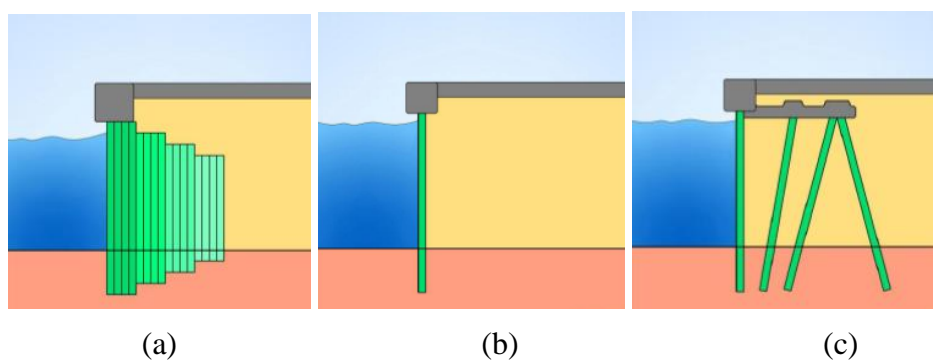


Figure 2.3 Sheet pile structures a) cantilevered sheet-pile b) anchored sheet-pile c) Sheet-pile with platform (PIANC [28])

Open type berth structures are classified according to how they transfer loads; horizontally and vertically (Figure 2.4). The soil resisting vertical loads is at some distance below the surfaces vulnerable to scour, but revetted slopes and piles (resisting horizontal loads in bending) are potentially at risk in the case of scour.

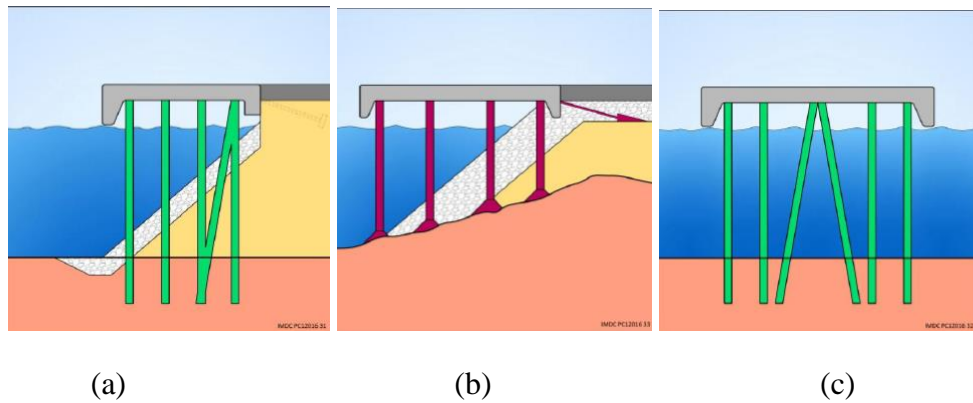


Figure 2.4 Examples of different kinds of open berth structures a) pile/column supported deck b) pile supported pier c) pile/column supported deck (PIANC [28])

Undergoing developments in marine transport with higher and larger size designs, aim to increase the capacity of ships with powerful thrusters. In the last few decades, growing size and capacities of ships have been designed with bow thrusters to increase the ships' maneuvering capacities that causes serious scour damages at the harbor basin, navigation channels and both near open and berth structures (PIANC [28]).

During a berthing and/or unberthing operations, a ship which is in proximity to the harbor structures, may cause serious scour to the sloping riprap banks, quay walls, or around piles (Figure 2.5) (Chin et al. [8]).

The propeller wash of a maneuvering ship in a confined waterway or harbor can cause serious problems. Some areas where the problems can occur are at (Chin et al. [8])

- the seabed banks of navigation channels,
- the sloping riprap banks of a harbor,
- quay walls,
- piled structures.

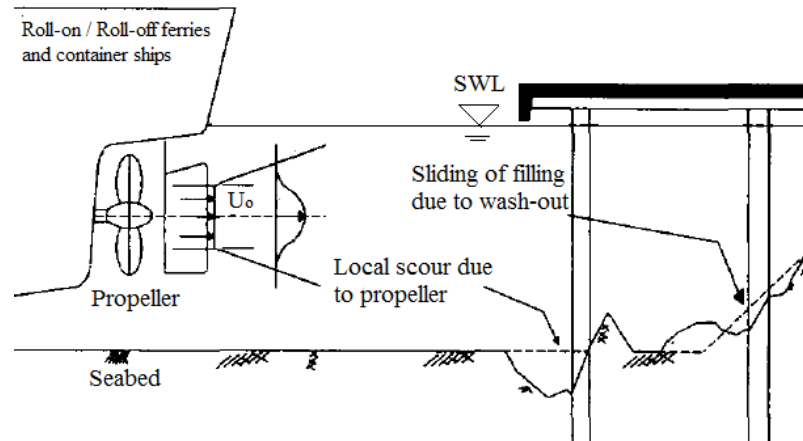


Figure 2.5 Scour induced by propeller jet near an open berth structure (Chin et al. [8])

Scour induced by propeller jet becomes an important issue in engineering problems due to high costs of the marine buildings and maintenance of the structures. Propeller induced scour problems have been investigated by researchers such as Blaauw and Van de Kaa [1], Chiew et al. [2], Hamill and Hughes [3], Lam et. al. [4]. However, studies on the scour mechanism due to the three-dimensional propeller jet around a vertical pile are still limited.

The main objective of this study is to investigate the characteristics of a three-dimensional scour hole without a berth structure. In addition by with considering an open type berth struture on noncohesive sediment beds owing to a submerged horizontal propeller jet has been investigated. Within the context of this study, there is an extensive amount of experimetal data by considering different conditions such as; changing diameter, gap, and speed of propeller on different sediment bed materials.

2.1.2 Berthing and Unberthing Operations

Generally ships are primarily designed and built for the open ocean, and therefore dramatic changes can occur in a ship's response characteristics in shallow water. Safemaneuvering, bertying and/or unberthing in confined waters require adequate design and layout of navigation channels, harbors, berth structures. In addition, it is a a must to have a comprehensive understanding of propellers and their working principles. (Thoresen [29]).

The total navigation operation ranging from arrival to departure can be sub-divided into following operations (Thoresen [29]) ;

- Arrival at the outer harbor basin,

- Preparation for berthing, maneuvering and pre-berthing procedures in the harbor basin,
- Berthing including mooring etc., to the berth structure,
- Loading and unloading operations when at berth,
- Unberthing from the berth structure,
- Departure from the harbor basin.

Water depth in front of and alongside the berth is one of the important design characteristics which for safe berthing and unberthing operations. The water depth should be based on the maximum loaded draft of the maximum ship design and must be determined by taking the following factors into consideration:

- draft of the maximum loaded ship,
- tidal variation,
- movement of the ship owing to the waves,
- trim due to the loading of the ship,
- squat,
- atmospheric pressure,
- character of the bottom,
- wrong applications in dredging.

The gross underkeel clearance shown in Figure 2.1 must be designed to allow the waves, trim, squat etc., in addition to a safety margin for unevenness of the bottom (Thoresen [29]).

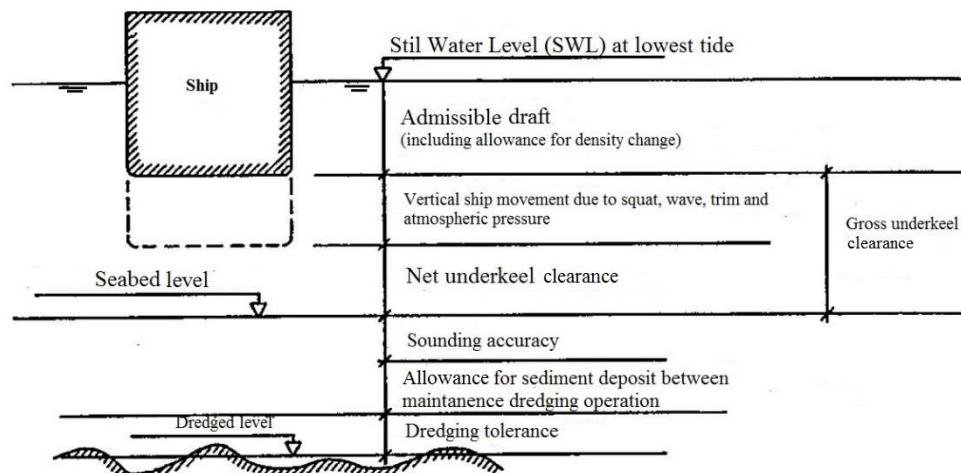


Figure 2.6 Components of depth (Thoresen [29])

Squat for the reduction of underkeel clearance, is due to the suction effect induced by the higher current velocity between the sea bottom and the ship. This causes a reduction in the water level near the the ship and ship therefore sinks bodily into the water. The longer/larger a ship is and faster it goes, the squat increases (Thoresen [29]).

Maneuvering during berthing and unberthing of a ship generally be done in one way or in a combination of the following ways;

- a) by using the ship's own engine, rudder, bow thruster and / or the ship's anchor,
- b) with the assistance of only one or more tugboats,
- c) by using the ship's own anchor, and with the assistance of one or more tugboats,
- d) with the use of bert or land-based winches, and with the assistance of one or more tugboats,
- e) with the use of mooring buoy, and with the assistance of one or more tugboats.

Berthing and unberthing operations are done after one of the cases; (a), (b) and (c) stated above. The decision where the arrival and the berthing operation should start, and where the required number of tugboats should meet and assist the ship to the berth, must be carried out by the local pilot or the port captain together with the ship's captain depending on the weather conditions, or according to the factor whether the ship has a bow thruster or not etc. Pilotage must be compulsory for all the gas and oil tankers and large ships (Thoresen [29]).

2.1.3 Erosion During Berthing and Unberthing Conditions

Erosion can occur near berth structures owing to natural currents and also berth structures which are vulnerable to erosion caused by vessels' propeller actions. Especially during berthing / unberthing, eroding forces on the seabed in front of the berth or on the slope under the berth can be substantial. An operating propeller of a vessel is a main eroding factor owing to the current velocities which can reach up to 8 m/sec near the bottom. The propeller currents are due to (Ghose and Gokarn [30]):

- The main propeller,
- The transverse thrusters located at the bow and / or stern.

The most severe erosion impact near the berth structure can usually be due to the main propeller or transverse thrusters. Impacts such as bottom erosion from the ships' main propeller are caused by on many factors. Ships are designed and built by taking these

factors into consideration: the propeller's closest position to the bottom, the ship's loaded condition at the lowest tide (Ghose and Gokarn [30]).

The impact area of the main propulsion system and thrusters (bow and stern) depends on the stage of the unberthing maneuver, position of the vessel, as seen in Figure 2.7.

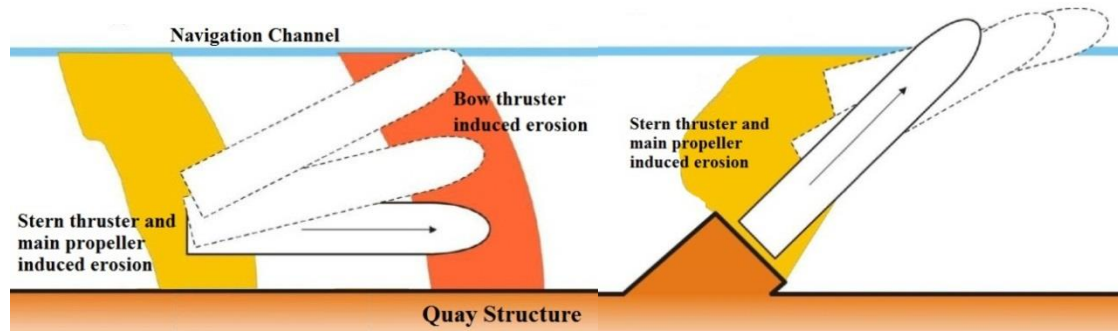


Figure 2.7 Illustration of possible berthing/unberthing operations (PIANC [28])

PROPELLER JET MECHANISM

Propeller induced scour problems have been investigated experimentally using physical models by many researchers such as; Blaauw and Van de Kaa [1], Bergh and Cederwall [31], Verhey [23], Schokking [32] and Lam et. al. [4], Yüksel et al. [33]. Most investigations have been carried out with circular wall jet instead of propeller jets to avoid the complexity flow around the propeller in the first place. This chapter is an introduction to circular and propeller jet flow mechanisms.

3.1 Jet Diffusion Mechanism

The term 'jet' in this context means a continuous stream of a fast moving fluid being discharged from some type of a nozzle (Tsinker [34]). In general, the following two-dimensional and / or three-dimensional jet forms can be considered as;

- downstream of hydraulic structures,
- equalizing water levels in locks,
- spillways,
- downstream of spurs in a river,
- diffusors,
- propeller jets of ships.

Horizontal two-dimensional flows are considered as the flows under barriers or gates which are infinitely, i.e. sufficiently wide (Figure 3.1). The jet form depends on a number of factors such as submergence, flow and turbulence patterns (Hoffmans and Verheij [35]).

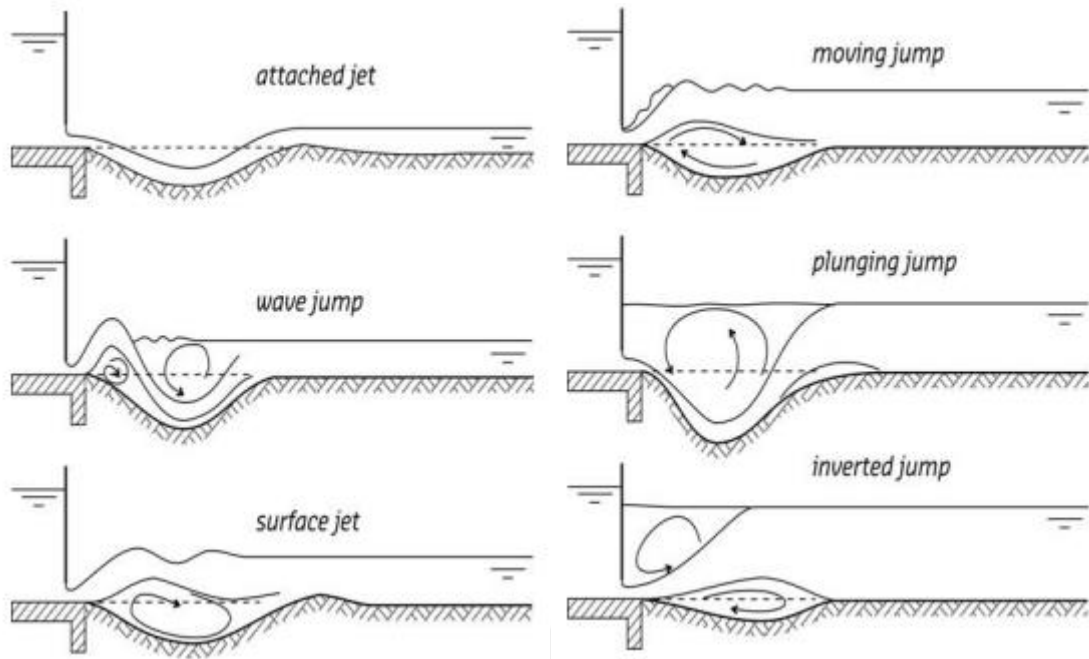


Figure 3.1 Different forms of jets (Hoffmans and Verheij [35])

3.1.1 Velocity Distribution of a Jet

Jet flow can be divided into two distinct regions (Albertson et al. [21]), namely a potential core and a diffused jet. Albertson et al. [21] classified diffusion under jet conditions into two categories called the zone of flow establishment (ZFE), and the zone of established flow (ZEF) as seen in Figure 3.2 (Situ et al. [37]). The velocity profile of a submerged water jet from an orifice varies also according to Gaussian normal distribution at each cross section (Figure 3.2). In the zone of flow establishment, the maximum velocity is constant while the lateral distribution is expanding. The region with constant maximum velocity has a pronounced potential core. The lateral section of potential core is contracting due to the turbulent mixing between the core and the surrounding fluid. In the zone of established flow, the maximum velocity starts to decay along the rotation axis. In this zone, the entrainment of the surrounding fluid is balanced by reduction in the jet velocity. In addition, the water jet is axisymmetrical with the entire jet being mirrored about the central axis (Lam et al. [4]).

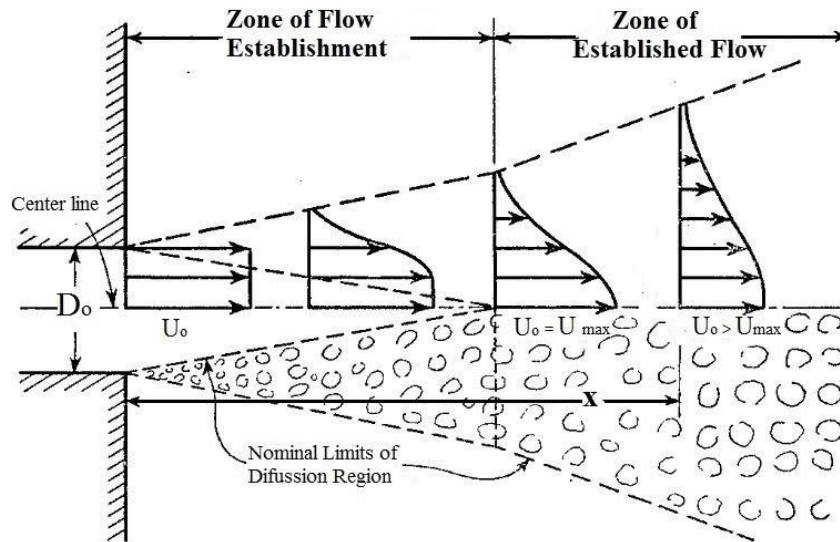


Figure 3.2 Schematized representation of a diffusing jet from an orifice (Albertson et al. [21])

3.1.2 Velocity Distribution of a Propeller Jet

Gaythwaite [36]’s proposed the velocity prediction within the ship’s propeller jet as the initial step to investigate the scouring made by the propeller jet. A rotating ship propeller generates a turbulent jet, with axial, radial, and tangential velocity components. The velocity distribution also differs from any other types of jets (Figure 3.3).

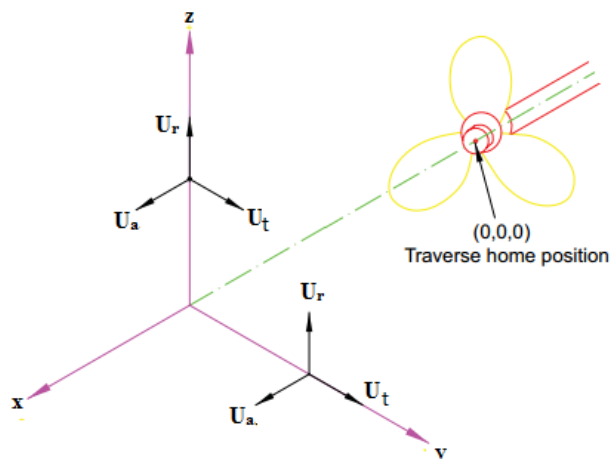


Figure 3.3 Schematic view of the velocity component of a propeller (Hamill et al. [38])

The velocity distribution of propellers differs from any other types of jets. The velocity distribution as the low-velocity core due to the hub on the propeller axis line, and the magnitudes of the velocities increase with the radial distance seen in Figure 3.4 (Hamill et al. [3]).

The cross-sectional velocity distribution of a propeller within the zone of ZFE has two-peak ridges as seen in Figure 3.3. In the ZEF mean axial velocity profile defined as a Gaussian normal distribution and the maximum velocity is constant while the lateral distribution is expanding (Lam et al. [4]).

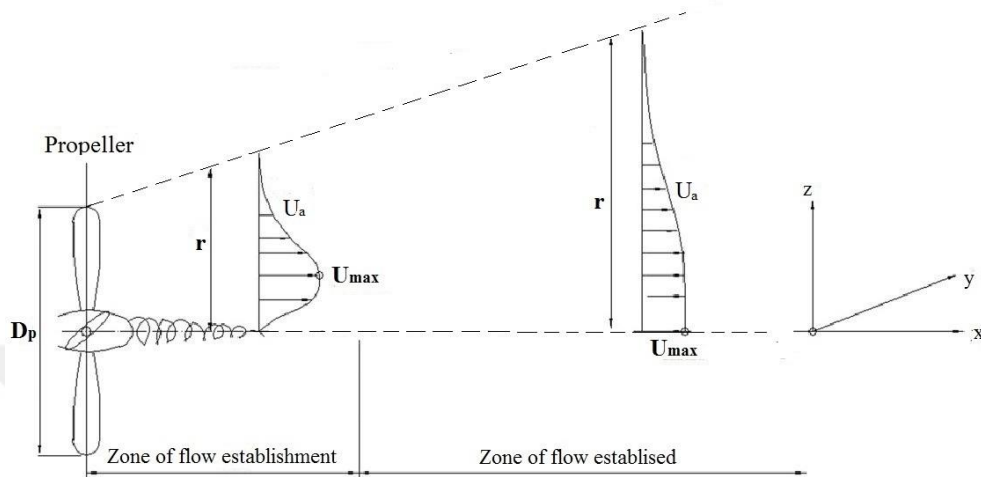


Figure 3.4 Velocity distribution induced by a propeller jet (Lam et al. [4])

where r is the radial distance from the axis, U_a is the axial velocity and X is the axial distance from the propeller's face.

Lam et al. [4] have proposed that the efflux velocity which is the maximum velocity at the face of the propeller jet tends to decrease along the longitudinal axis (Figure 3.5).

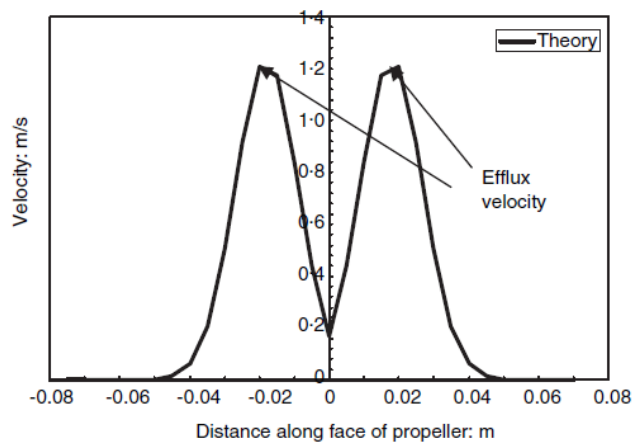


Figure 3.5 Velocity distribution of 76 mm diameter propeller at 100 rpm (Hamill et al. [3])

PIANC [28] defined the tip vortex of a propeller jet (as seen in Figure 3.6) in a higher turbulence level and a shorter length of the ZFE with a wider radial spread compared to free jet.

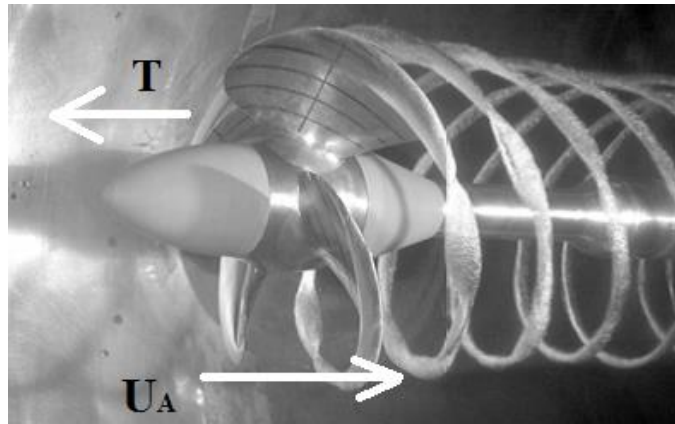


Figure 3.6 Tip vortex sheet cavitation of a four-bladed propeller (Faltinsen [39])

Petersson et al. [40] also defined some dimensionless numbers, such as Froude number, Reynolds number, Weber number, tip vortex number which are the ratio of axial flux of linear momentum and angular momentum for the characteristics of a vortex jet produced by the propeller (Situ et al. [37]).

A propeller jet can be analyzed globally and locally using the axial momentum theory and blade element method (BEM), respectively (Lam et al. [41]).

The axial momentum theory is widely accepted by researchers to describe the characteristics of the propeller jet with neglecting the vortex jet flow behind the propeller.

Lam et. al. [4] used axial momentum theory with the general assumptions given below;

- propeller is considered as an ideal actuator disc of equivalent diameter,
- One-dimensional analysis,
- the disc has an infinite number of blades rotating at an infinite speed,
- the thickness of the disc is negligible,
- the fluid is considered ideal fluid and there is no rotation in the fluid,
- there is an unlimited inflow of fluid to the disc.

The propeller is regarded as an ideal actuator disc that generates the thrust (T) as schematized in Figure 3.7.

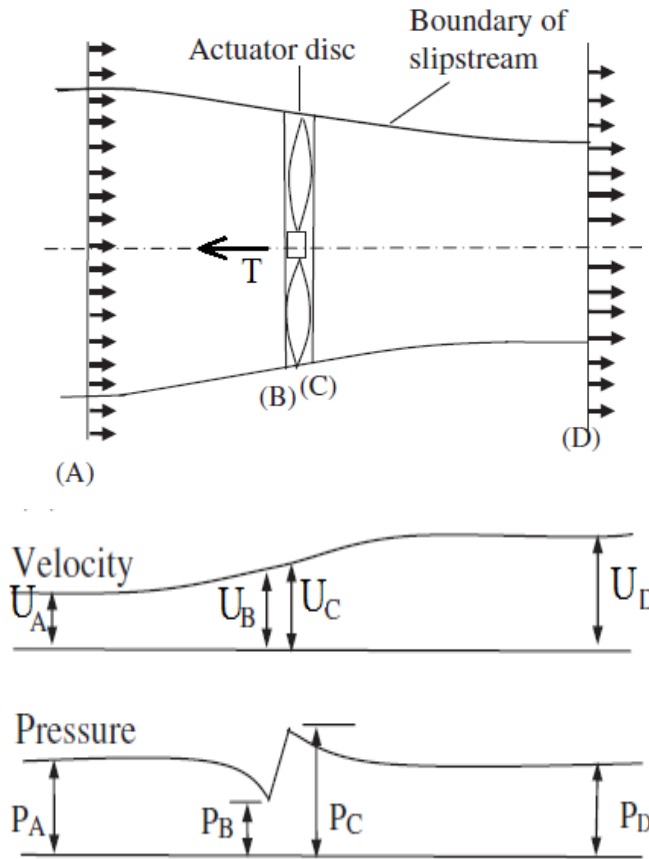


Figure 3.7 Propeller's slip stream by an actuator disc model (Lam et. al. [4])

In the figure, U_A is the inflow flow velocity (advance velocity) far upstream at point A is assumed equal to ship velocity, U_B is the inflow flow velocity at the actuator disc, U_C is through-flow at the actuator disc, U_D is through-flow velocity far downstream at point D.

The propeller depicted in Figure 3.7 is an ideal actuator disc and the fluid is passing through the disc. From point A to B; pressure drops gradually from (P_A) hydrostatic pressure to the P_B . The pressure increases (P_C) suddenly at the actuator disc and then gradually decreases again until the pressure reaches the (P_D) hydrostatic pressure at point D which is far from the disc (Lam et. al. [4]).

The actuator disc depicted in the Figure 3.5 imparts pressure increase considered as an energy supplier to the system and as a result of this, Bernoulli's equation does not apply between point B and C. If the total power supplied from the propeller (actuator disc) is written as the kinetic energy (KE) increase of the fluid per unit time;

$$KE = m \cdot \frac{(U_D^2 - U_A^2)}{2} \quad (3.1)$$

By applying to the Bernoulli equation just from the near of the disc at point C too far from the disc at point D and from point A to B (for the same hydrostatic pressure at point D and A; $P_D = P_A$);

$$P_C + \frac{1}{2} \cdot \rho \cdot U_{disc}^2 = P_D + \frac{1}{2} \cdot \rho \cdot U_D^2 \quad (3.2)$$

$$P_B + \frac{1}{2} \cdot \rho \cdot U_{disc}^2 = P_D + \frac{1}{2} \cdot \rho \cdot U_A^2 \quad (3.3)$$

Equation (3.2) and Equation (3.3) considered together is as follows:

$$P_C - P_B = \frac{1}{2} \cdot \rho \cdot (U_D^2 - U_A^2) \quad (3.4)$$

The propeller thrust defined is given as;

$$\begin{aligned} T &= A_{disc} \cdot (P_C - P_B) \\ T &= \frac{1}{2} \rho A_{disc} (U_D^2 - U_A^2) \end{aligned} \quad (3.5)$$

where T is the propeller thrust, $(P_C - P_B)$ is the pressure rise across the actuator disc representing the propeller, ρ is density of the fluid, A_{disc} is the area of actuator disc, U_D , U_A are the velocities at sections A and D.

The forces and moments produced by the propellers are expressed by Carlton [42] in their most fundamental form in terms of a series of a non-dimensional characteristics. The non-dimensional terms used to express the general performance characteristics are given as follows.

$$\begin{aligned} C_T &= \frac{T}{\rho n^2 D_p^4} \\ K_Q &= \frac{T}{\rho n^2 D_p^5} \\ J &= \frac{U_A}{n D_p} \\ \sigma_0 &= \frac{P_a + \rho g h - p_v}{0.5 \rho U_A^2} \end{aligned} \quad (3.6)$$

where C_T is thrust coefficient, K_Q is torque coefficient, J is advance coefficient, U_A is the speed of the ship (advance speed), σ_0 is cavitation number, n is rotational speed (rpm), D_p is the propeller diameter, ρ is density of the fluid, p_v is the vapor pressure

somewhere on the propeller surface, p_a is the atmospheric pressure and hydrostatic pressure at a given instantaneous position on the propeller.

Hence, Tsinker [34] proposed the thrust (T) proportional to; ρ , D_p , U_A , n , μ , $P_a + \rho gh - p_v$,

$$T = \rho n^2 D_p^4 \cdot \left(\frac{U_A}{n D_p} \right) \cdot \left(\frac{\mu}{\rho n D_p^2} \right) \cdot \left(\frac{P_a + \rho gh - p_v}{\rho n^2 D_p^4} \right) \quad (3.7)$$

the non-dimensional groups given in Equation (3.7) are written as;

$$\begin{aligned} C_T &= \frac{T}{\rho n^2 D_p^4} \\ J &= \frac{U_A}{n D_p} \\ Re &= \frac{\rho n D_p^2}{\mu} \\ \sigma_0 &= \frac{P_a + \rho gh - p_v}{0.5 \rho n^2 D_p^2} \end{aligned} \quad (3.8)$$

where Re is Reynolds number, μ is dynamic viscosity of fluid, C_T is proportional to dimensional parameters and expressed as a function of J, Re and σ_0 . Propeller thrusts are defined in Equation (3.5) are also written as;

$$T = C_T \rho n^2 D_p^4 \quad (3.9)$$

According to Verhey [23], using the momentum change caused by the propeller and the condition of mass conservation, total unit thrust can be expressed as:

For a free propeller;

$$T = \frac{\pi}{8} \rho D_p^2 U_D^2 \quad (3.10)$$

For a ducted propeller;

$$T = \frac{\pi}{4} \rho D_p^2 U_D^2 \quad (3.11)$$

In the case, during maneuvers of ship, the speed of the ship is very low, the influence of the ship on the propeller slipstream is very small, that is why the ship is assumed to

have zero speed of advance (Blaauw and Van de Kaa [1]) since Equation (3.6), Equation (3.9) and $\pi D^2 / 4 = A_{\text{disc}}$ result in;

$$C_T \rho n^2 D_p^4 = \frac{1}{2} \rho A_{\text{disc}} (U_D^2 - U_A^2)$$

$$U_D^2 = \frac{8}{\pi} C_T n^2 D_p^2$$

$$U_D = 1.59 n D_p \sqrt{C_T}$$
(3.12)

The exit plane of a propeller flow (U_D) is called the efflux velocity (U_0) seen in Figure 3.8. This initial plane in front of the propeller is where the velocities within the jet are at a maximum (Lam et al. [41]). The predictions of the velocity can be done by using several semi-empirical equations. Knowing the efflux velocity is the pre-requisite to predict the downstream diffusion through these semi-empirical equations. Theoretical development of equations used to predict the efflux velocity of a propeller wash is based on the axial momentum theory shown in Equation (3.12) and has widely been investigated by several researchers such as PIANC [28], Hamill [7], Hashmi [13], Lam et. al. [4].

Equation (3.13) is the theoretical equation used to predict the efflux velocity of a ship's propeller. This equation is derived from axial momentum theory with the assumption of zero advance speed for the case of a ship as maneuvers (Fuehrer and Römish [22]).

$$U_0 = 1.59 n D_p \sqrt{C_T}$$
(3.13)

However, Hamill et al. [3] found the core assumption of axial momentum theory inadequate for describing the process involved in the formation of a propeller jet. Equation (3.13) was developed for the maneuvering conditions of a ship by several researchers taking the geometric characteristics of the propellers into consideration.

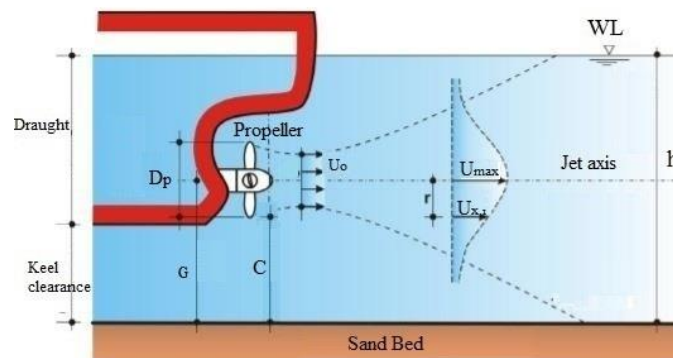


Figure 3.8 Velocity distribution induced by a ship's propeller (PIANC [28])

Blaauw and Van de Kaa [1] presented an empirical equation for the case with no values are available for the number of revolutions and / or the thrust coefficient C_T as,

$$U_0 = C_3 \left(\frac{f_p P}{\rho D_p^2} \right) \quad (3.14)$$

where; C_3 is coefficient, f_p is percentage of installed engine power, P is maximum installed engine power. C_3 is 1.17 for ducted propeller and 1.48 for free propeller.

Hamill [7] proposed an equation vis-à-vis efflux velocity with a lower coefficient for experimental investigation conducted with plain water jet (Lam et al. [24]).

$$U_0 = 1.33nD_p \sqrt{C_T} \quad (3.15)$$

Stewart [12] suggested this equation in a more general form as;

$$U_0 = \zeta n D_p \sqrt{C_T} \quad (3.16)$$

where the efflux coefficient defined as ζ is expressed as;

$$\zeta = D_p^{-0.0686} \cdot \left(\frac{P}{D_p} \right)^{1.519} \cdot \beta^{0.323} \quad (3.17)$$

where β is blade area ratio and (P/D_p) is the pitch propeller diameter ratio.

Hashmi [13] refined the efflux velocity equation by non-dimensioning the propeller diameter (D_p), dividing by the hub diameter (D_h);

$$U_0 = E_0 n D_p \sqrt{C_T} \quad (3.18)$$

where,

$$E_0 = \left[\frac{D_p}{D_h} \right]^{-0.403} \cdot C_T^{-1.79} \cdot \beta^{0.744} \quad (3.19)$$

Tsinker [34] also derived this equation for an open and ducted propeller as;

For a free propeller;

$$U_0 = 1.6 n D_p \sqrt{C_T} \quad (3.20)$$

For a ducted propeller;

$$U_0 = 1.1 n D_p \sqrt{C_T} \quad (3.21)$$

PIANC [28] also suggested efflux velocity equation derived as;

$$U_0 = \alpha n D_p \sqrt{C_T} \quad (3.22)$$

where α is coefficient and general value of α is defined as 1.6 whereas values for C_T can be derived from the Wageningen B- and K- series for propellers which are ship specific.

Table 3.1 Lists proposed efflux velocity equations by researchers in the literature.

Table 3.1 Equations used for the calculation of efflux velocity

Researchers	Equations
Fuehrer and Römisch [22]	$U_0 = 1.59 n D_p \sqrt{C_T}$
Blaauw and Van de Kaa [1]	for a ducted propeller; $U_0 = 1.17 \left(\frac{f_p P}{\rho D_p^2} \right)$ for a free propeller; $U_0 = 1.48 \left(\frac{f_p P}{\rho D_p^2} \right)$
Hamill [7]	$U_0 = 1.33 n D_p \sqrt{C_T}$
Stewart [12]	$U_0 = \zeta n D_p \sqrt{C_T} \quad \zeta = D_p^{-0.0686} \cdot \left(\frac{P}{D_p} \right)^{1.519} \cdot \beta^{0.323}$
Hashmi [13]	$U_0 = E_0 n D_p \sqrt{C_T}$ $E_0 = \left[\frac{D_p}{D_h} \right]^{-0.403} \cdot C_T^{-1.79} \cdot \beta^{0.744}$
Tsinker [34]	for a free propeller; $U_0 = 1.6 n D_p \sqrt{C_T}$
	for a ducted propeller; $U_0 = 1.1 n D_p \sqrt{C_T}$

Table 3.1 Equations used for the calculation of efflux velocity (cont'd)

Hamill et al. [3]	$\frac{U_0}{Nnr} = 1.261 - 0.974 \left[\frac{P}{r} \right] + 0.733 \left[\frac{G}{r} \right] + 18.53 \left[\frac{t_{\text{section}}}{r} \right] + 5.028 \left[\frac{h_d}{r} \right]$ $+ 0.106 \left[\frac{P}{r} \right]^2 - 7.277 \left[\frac{h_d}{r} \right]^2 - 4.093 \left[\frac{h_t}{G} \right]^2$
Lam et al. [24]	$U_0 = E_0 n D_p \sqrt{C_t}$ <p>E_0 varies between range 0.89-1.71 as defined in detailed (Table 1.17) based on propeller dimensions and characteristics of propellers.</p>
Hamill et al. [38]	$U_0 = 1.22 n^{1.01} D_p^{0.84} C_T^{0.62}$
PIANC [28]	$U_0 = \alpha n D \sqrt{C_T}$ <p>for Wageningen B- and K- series for propellers $\alpha = 1.6$.</p>

In the table, h_t is helical distance from the blade's leading edge to the position of maximum thickness, h_d is helical distance from the blade's leading edge to rake datum line, P is pitch of propeller blade, t_{section} thickness of the section, r is radial distance from the propeller axis.

SCOUR MECHANISM

Scour that is formed by the impact of the hydraulic structure on the flow and just around the structure is called local scour (Balachandar and Prashanth [43]). In this chapter local scour mechanism induced by propeller jet around a vertical pile - as a hydraulic structure - is described.

4.1 Scour Mechanism

The type of local scour is classified according to the mode of sediment transport in the approaching flow as (Sumer and Fredsøe [44]);

- clear water scour: occurs when sediment is removed from the scour hole but not supplied by the approaching flow,
- live (mobile) bed scour: occurs when there is a general sediment transport by the approaching flow.

Different parameters such as; water depth, flow velocity, time, sand grain size, obstruction size and shape etc. are effective on the local scour mechanism.

4.1.1 Scour Mechanism Induced by Jet Diffusion

The scour hole formation by various forms of jets can destabilize a hydraulic structure in the immediate vicinity of the jet. Balachandar and Prashanth [43] gave the definition sketch of the scour hole geometry owing to two-dimensional jet diffusion jet as shown in Figure 4.1.

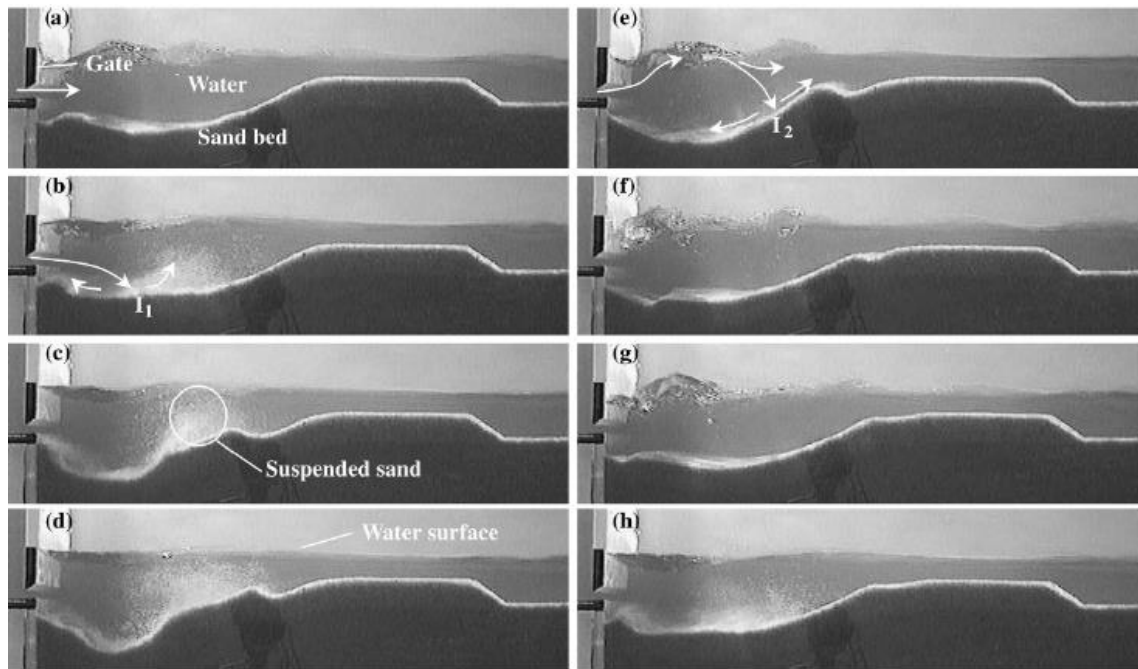


Figure 4.1 Demonstration of a local scour cycle a) scour begins b) digging stage c) digging continues d) maximum digging e) filling phase g) maximum fill h) recurrence of a digging stage (Balachandar and Prashanth [43])

The jet exits the nozzle or the sluice gate, interacts with the bed and the scouring action takes place. This is usually called the digging stage. During digging stage, the jet is directed towards the bed and a hole is formed with a deposition mound just downstream of the scour hole. The scouring process is very rapid in this phase. The surface jet impinges on the mound region and some of the sediment deposited on the mound falls back and refills the scour hole. The jet suddenly flips back towards the bed and once again causes rapid digging of the bed with lifting of the bed material into suspension. The free surface is not wavy during the rapid digging process. An intermediate hump is formed in the scour hole. In time, the jet is once again directed towards the free surface and refilling occurs. The alternate digging and refilling occurs only at low tailwater depths (Balachandar and Prashanth [43]).

4.1.2 Propeller Jet Induced Scour Mechanism

The mechanism of scour induced by an offset jet or a propeller jet, particularly the latter, is highly complex. The schematic diagrams of the flow field caused by an offset and a propeller jet are illustrated in Figure 4.2 (a) and Figure 4.2 (b), respectively. Because of the structural difference between these two types of jet, the velocity distributions of the resulting flow fields also are different as mentioned in Chapter 3.

For an offset jet flow, only single - peak exists in a given vertical velocity profile. Both the magnitude of the maximum velocity and the vertical position decrease with increasing distance from the jet.

In contrast to an offset jet, a propeller jet induces a double - peak velocity profile immediately downstream of the propeller. The double - peak velocity profile changes to a single - peak profile as one moves away from the propeller, as illustrated in Figure 4.2 (b). Similar to that found in an offset jet flow, the value of the maximum velocity and the vertical position also decrease with distance from the propeller.

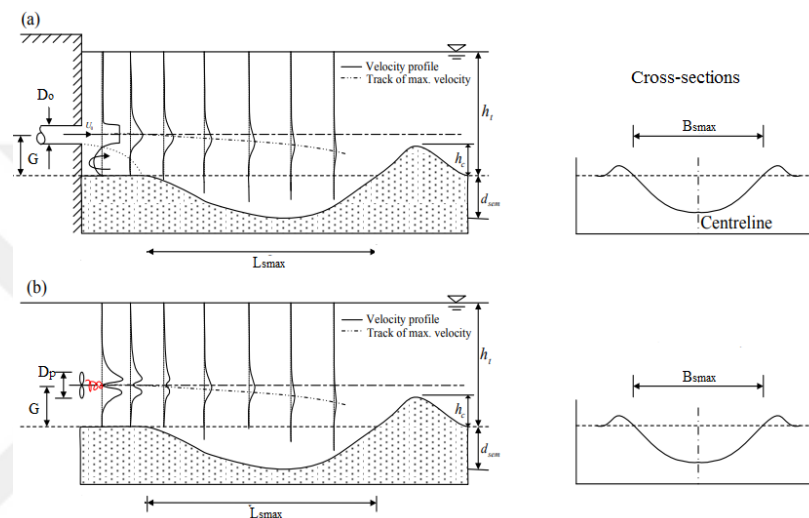


Figure 4.2 Definition sketch of the scour by a) an offset jet b) a propeller jet (Chiew et al. [45])

In the figure, S_{smax} is the maximum equilibrium scour depth, L_{smax} is maximum equilibrium scour length; B_{smax} is the maximum equilibrium scour width; U_0 is the efflux velocity, D_o is the diameter of the jet, D_p is the diameter of propeller, G is the gap of the propeller, h is the water depth.

4.1.3 Scour Mechanism Around a Circular Pile


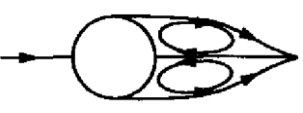


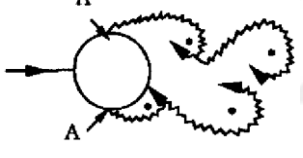
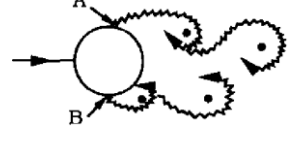
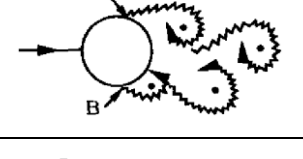
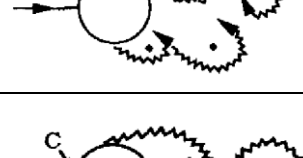

Sumer and Fredsøe [44] suggested that the nondimensional Reynolds number given in Equation (4.1) be used for the description of a flow around a smooth circular cylinder. Some flow regimes are summarized in Table 4.1.

The non - dimensional quantities describing the flow around a smooth circular cylindrical pile depend on the cylinder Reynolds number that is given below.

$$Re_{pile} = \frac{Ud_o}{\nu} \quad (4.1)$$

where U is the flow velocity, d_0 is the diameter of the cylinder and ν is the kinematic viscosity.

Table 4.1 Flow around a cylinder in steady current (Sumer and Fredsøe [44])

	No Separation Flow Creeping Flow	$Re_p < 5$
	A Fixed Pair of Symmetric Vortices	$5 < Re_p < 40$
	Laminar Vortex Street	$40 < Re_p < 200$
	Transition to Turbulence in the Wake	$200 < Re_p < 300$
	Wake Completely Turbulent. A:Laminar Boundary Layer Separation	$300 < Re_p < 3 \cdot 10^5$ Subcritical
	A:Laminar Boundary Layer Separation B:Turbulent Boundary Layer Separation; but Boundary Layer Laminar	$3 \cdot 10^5 < Re_p < 3.5 \cdot 10^5$ Critical (Lower Transition)
	B: Turbulent Boundary Layer Separation; the Boundary Layer Partly Laminar Partly Turbulent	$3.5 \cdot 10^5 < Re_p < 1.5 \cdot 10^6$ Supercritical
	C: Boundary Layer Completely Turbulent at one Side	$1.5 \cdot 10^6 < Re_p < 4 \cdot 10^6$ Upper Transition
	C: Boundary Layer Completely Turbulent at two Sides	$4 \cdot 10^6 < Re_p$ Transcritical

The flow pattern around a cylindrical pile is characterized (Van Rijn [46]) as follows:

- water surface roller in front of the pile;
- downflow in front of the pile;
- vortex - shedding in separation zone;
- wake flow downstream of the pile;
- generation of horseshoe - vortices in the scour hole.

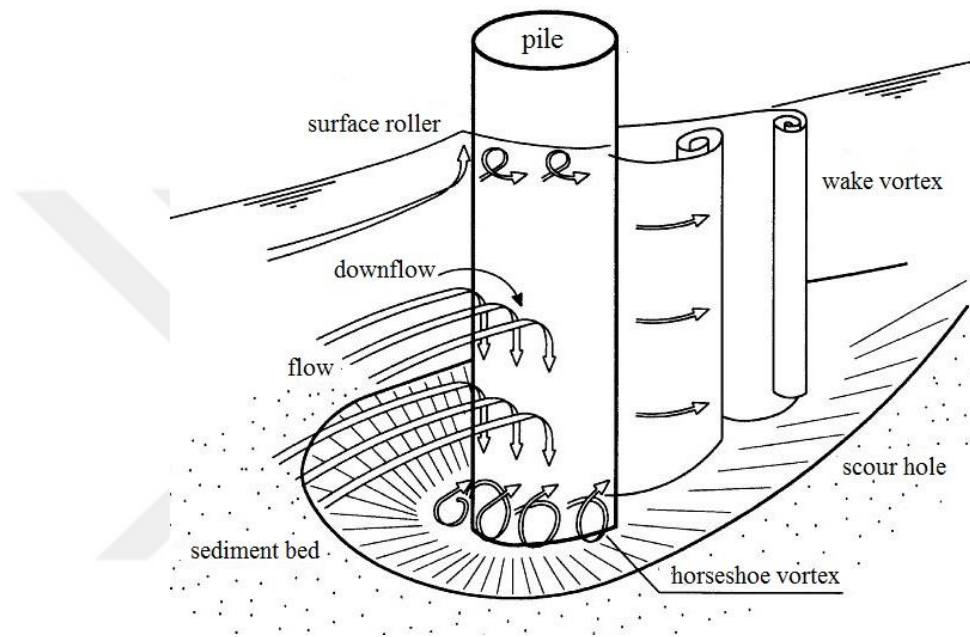


Figure 4.3 Flow pattern and scour around a pile (Van Rijn [46])

The pile structure causes local flow accelerations and vertical downflow at the face of the pile due to the jet flow's impinging onto the pile.

The flow pattern (see Figure 4.3) and mechanism of scouring are very complicated, and the complexity of flow increases with the development of the scour hole. The basic mechanism causing local scour around the pile is the down - flow at the upstream face of the pile and the formation of the horseshoe vortex at the base of the pile. The down - flow is believed to be the primary cause of scour. The horseshoe vortex that develops due to the separation of flow at the edge of the scour hole upstream rolls to form a helical flow. Separation of the flow at the sides of the pile also creates so-called wake vortices (Akib et al. [47]).

Sumer and Fredsøe [44] investigated the regimes of flow around smooth, circular cylinder in steady current. They classified the flow regimes in Table 4.1 by using

nondimensional Reynolds pile number with Equation (4.1). In this study Re_{pile} , Re_p and Re_f range from $2.84 \cdot 10^4$ to $25.06 \cdot 10^4$, $1.10 \cdot 10^4$ to $6.46 \cdot 10^4$ and $4.65 \cdot 10^4$ to $23.24 \cdot 10^4$, respectively. As seen in Table 4.1, experimental tests with the existence of pile have laminar and turbulent boundary layer separations for critical and supercritical regimes of flow (Figure 4.4).

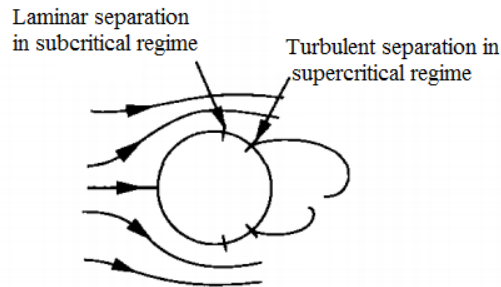


Figure 4.4 Positions of separation points at critical and supercritical regimes (Sumer and Fredsøe [44])

Separation of the flow at the sides of the pile also creates so - called wake vortices. Sumer and Fredsøe [44] stated that two unstable pairs of vortices were formed when exposed to the small disturbances for Reynolds numbers $Re_{pile} > 40$. Figure 4.5 (a) shows that the larger vortex A becomes strong enough to draw opposing vortex B. The approach of vorticity of the opposite sign will cut off vortex A from its boundary layer. Thus being a free vortex, Vortex A is the convected downstream by the flow. Then in Figure 4.5 (b) a new vortex is formed as Vortex C. Vortex B now plays the same role as Vortex A. This process continues each time a new vortex is shed at one side of the cylinder.

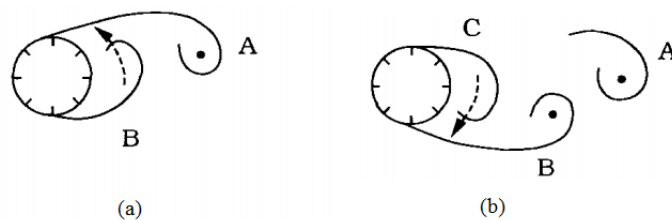


Figure 4.5 (a) Prior to shedding Vortex A, Vortex B is being drawn across the wake (b) Prior to shedding vortex B, vortex C is being drawn across the wake (Sumer and Fredsøe [44])

These vortices are formed as unstable and shed disorderly from each side of the pile. As a result they act as small tornadoes lifting the sediment from the bed to form a scour hole downstream of the pile and cause scouring downstream section of the cylindrical pile.

EXPERIMENTAL STUDY

When designing and building hydraulic structures, the dimensions of a local scour hole must be known very well because these structures could collapse and fall into their own scour holes. To understand the local scour damage on cohesionless sediment bed induced by propeller jet conditions is an important challenge due to the highly turbulent flow area. The main characteristics of bed material such as particle size, shape and flow velocity, water depth etc. have an affective role on transportation and deposition of bed material. The aim of this chapter is to understand these scour characteristics with scour profile measurements under changing conditions such as different bed material sizes and heights of the propellers etc. For this aim, a laboratory flume was built and the detailed descriptions are given below.

5.1 Experimental Setup / Flume

The experiments were carried out in a rectangular laboratory flume, in which all the sides were made of glass with a total length of 6.02 m, width of 1.42 m, and a height of 1.1 m, at the Hydraulic and Coastal Engineering Laboratory of the Civil Engineering Department at Yıldız Technical University (Figure 5.1).

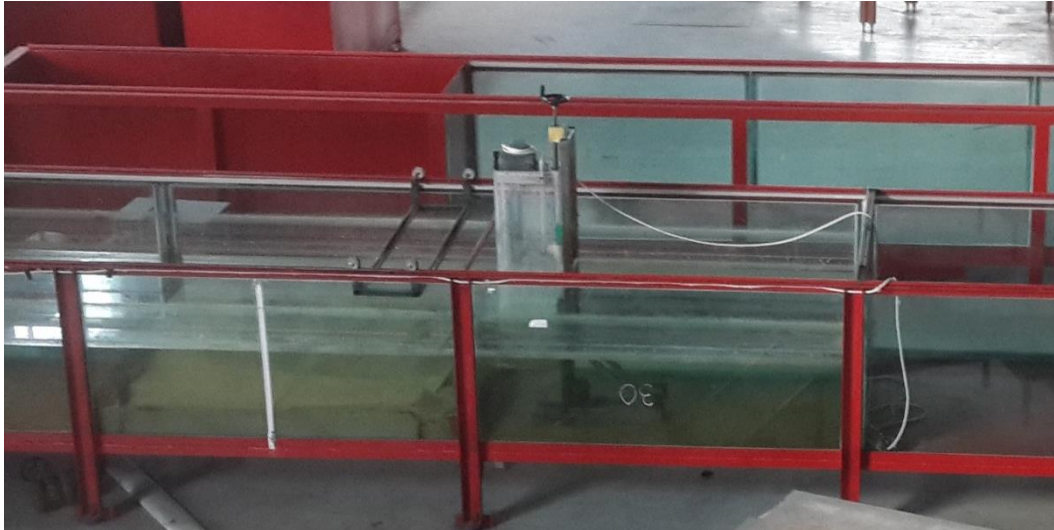


Figure 5.1 View of the experimental setup

A 0.2 – m - deep, 1.56 – m - long, and 1.42 – m - wide sand bed was laid at the bottom of the working section. The sand bed was held in place with false floors on either side ensuring the sand bed was leveled. A cylindrical pile was placed at the working section of the flume. The flume was slowly filled to a height (h) of 0.50 m water above the bed in two hours with a three cm diameter water pipe. Water was filled to a depth 0.5 m, and a sand bed with a thickness (t) of 0.2 m was laid at the bottom of the flume. In addition, two by-passes consisting of rectangular pipe lines of 10 – cm - wide and 1 – cm - high, were constructed under the sediment bed on both sides of the flume. Thus, water piled up at the end of the flume due to continuous flow of propeller jet was returned back through these pipes without disturbing the scouring area. Figure 5.2 and Figure 5.3 show the longitudinal cross - section and plan view of the experimental setup, respectively.

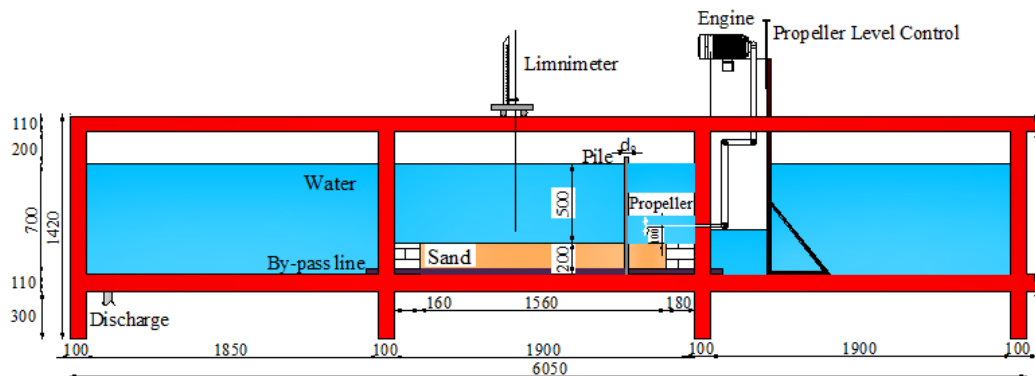


Figure 5.2 Experimental setup in mm (Longitudinal - section)

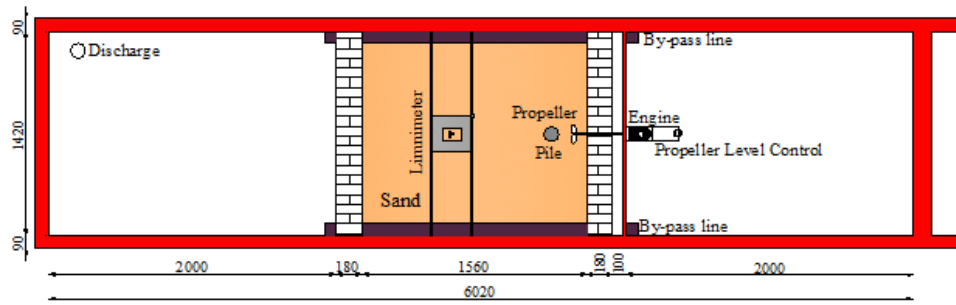


Figure 5.3 Experimental setup in mm (Plan view)

All tests were conducted by using different parameters and other operational variables (shown in Figure 5.4) considering the previous literature (Chin et al. [27], Lam et al. [4], Chiew and Lim [2], Lam et al. [41], Yüksel et al. [33]) as follows:

- Gap of the propeller (G):
Centerline of the propeller adjusted with the controller 10, 15 and 20 cm above the undisturbed bed,
- Propeller diameter (D_p):
Three different submerged Wageningen - B series propellers with diameters (D_p) 6.5, 10 and 13 cm were used,
- Speeds of propeller rotations in terms of revolutions per minute (rpm):
40, 45 and 50 Hertz propeller (approximately 590, 670 and 745 rpm) were tested,
- Pile diameter (d_o):
Three different piles with diameters (d_o) of 4, 10 and 13 cm were used,
- Horizontal distance from the face of propeller to the pile (X):
Pile was located 10, 20, 30 and 40 cm away from the propeller,
- Sediment bed material size (d_{50}):
Four different sediment bed material sizes of $d_{50}=0.52, 1.28, 4.00$ and 8.30 mm were used.

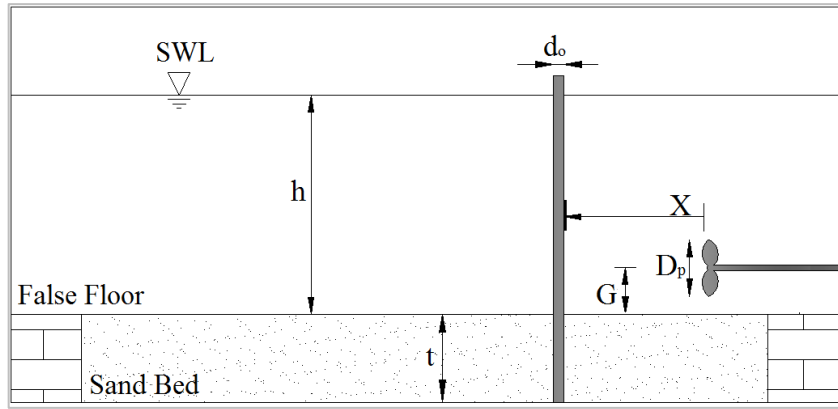


Figure 5.4 Schematic view of the experimental setup

The propeller shaft was placed onto a plexiglass box system as shown in Figure 5.5, and this setup allowed the variation of the impingement distance between the propeller and the pile location (X). The level controller was also added to this plexiglass box system to adjust the distance between the propeller shaft and the sand bed (G).

AGM 80 - 8b series motor designed at a rate of 0.29 kW produced by GAMAK company was fitted at the upper part of the plexiglass box system to rotate the propellers with a belt system. The propeller's operation speed (in rpm) was controlled by a frequency regulator and it was set to 40 Hertz, 45 Hertz and 50 Hertz to obtain 590 rpm, 670 rpm and 745 rpm propeller speeds. Rotational speeds were controlled by measurements of speed meter during the experiments of each test. Measurements had ± 10 rpm differences in the propeller's speed. Thus, speed meter measurements were taken into consideration for the propeller speeds that were nearly 590 rpm, 670 rpm, and 745 rpm. Belts were used to rotate the propeller between the motor and the propeller shaft. Once the motor was switched on, it transferred the torque force with belt system in the box to rotate the propeller. (Figure 5.5).

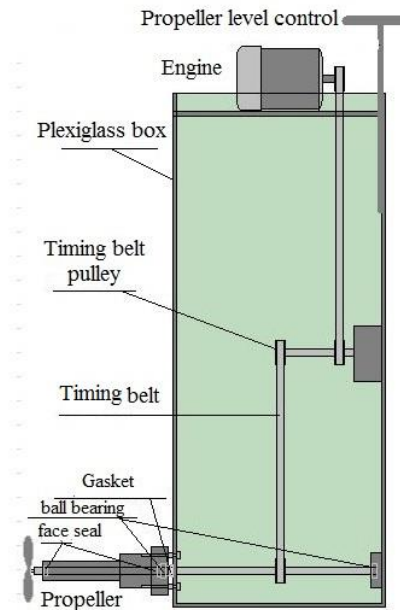


Figure 5.5 Schematic view of the plexiglass box system

5.1.1 Propeller Characteristics

Converting the torque of a shaft to produce axial thrust is the main principle of a propeller's working system. A propeller can be defined as a mechanical device formed by two or more blades that spin around a shaft and produces a propelling force as seen in Figure 5.6. There are several technical terms to define the propeller's characteristics such as; diameter, pitch, disc area relation, hub, blade area ratio etc. All these characteristics are calculated to design the optimal propeller accordingly, to meet the specific needs.

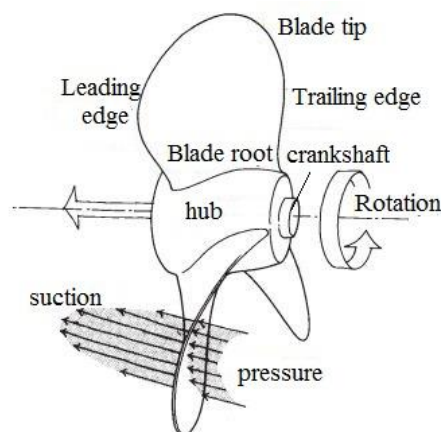


Figure 5.6 General view of a propeller (Faltinsen [39])

Propeller blades attached directly to the shaft with a central hub are seen in Figure 5.7 where; r_h is the radius of hub and D_p is the diameter of the propeller.

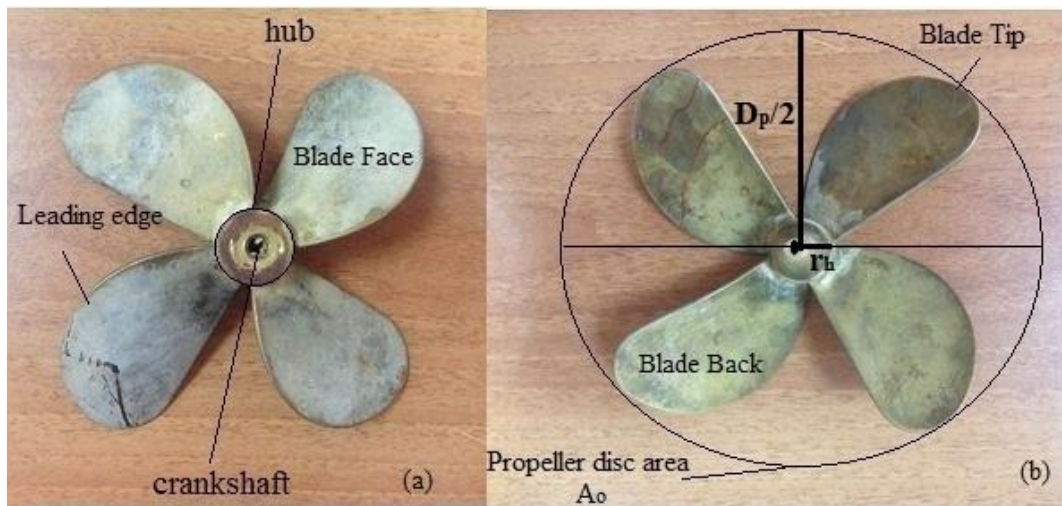


Figure 5.7 View of the propeller a) back view b) face view (aft side)

Pitch is one of the important characteristics of a propeller defined as displacement of a propeller in a complete spin of 360 degrees assuming there is no 'slippage' between the propeller blades and the water as seen in Figure 5.8.

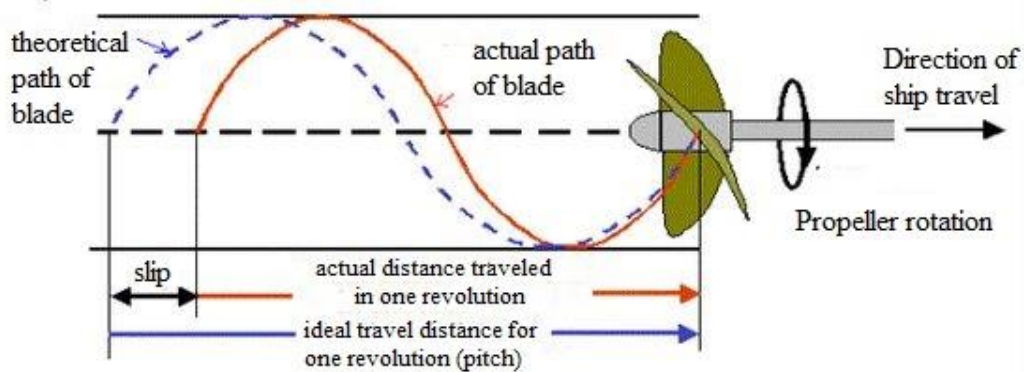


Figure 5.8 Travel path of a propeller's blade in one revolution [48]

Pitch angle of a propeller blade, also defined as the relative direction of water flow across the blade, and the angle of attack between the propeller chord line and the water flow vector are as shown in Figure 5.9.

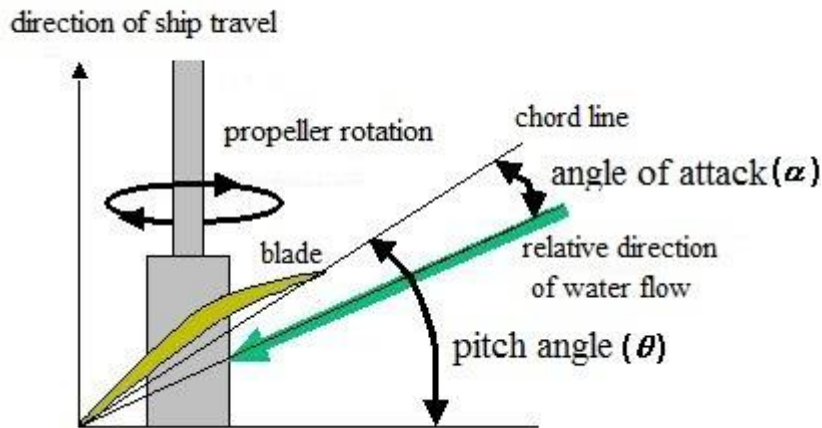


Figure 5.9 Propeller's pitch angle and angle of attack [48]

Fixed - pitch propellers (FPP) are permanently attached to the hub. Thus the position of the blades the position of the pitch are permanently fixed and cannot be changed. However, some propeller have adjustable blades and it is possible to alter the pitch by rotating the blade on its vertical axis and this is called controllable - pitch propellers (CPP). Another type is contra rotating propeller (CRP) referred to an installation in which two propellers are attached to the same motor with one mounted just behind the other.

Blade shape is one of the most important characteristics of the propellers. Four basic areas describe the propeller blade shapes. These are the projected area, the developed area, the expanded area and the swept area. The projected area of the propeller is the area seen at the front side of the shaft axis as shown in Figure 5.10 as A_p (Carlton [42]).

The area from tip to tip blade is called the propeller disc area (A_{disc}). The expanded area (A_E) of the propeller is obtained by considering different circular cylinders with axis coinciding with the propeller shaft axis. The developed area (A_D) is related to the projected area in so far as it is a helically based view, but the pitch of each section is reduced to zero as seen in Figure 5.10 (AB Volvo Penta [49]).

In general, the expanded and developed areas are approximately equal and the developed area is greater than the projected area. However, the developed area is slightly smaller in size than the expanded area (AB Volvo Penta [49]).

Blade area ratio (BAR) is simply calculated with the projected, developed or expanded blade area divided by the propeller disc area A_o .

$$\left. \begin{aligned} \frac{A_P}{A_{disc}} &= \frac{4 \cdot A_P}{\pi \cdot D_p^2} \\ \frac{A_D}{A_{disc}} &= \frac{4 \cdot A_D}{\pi \cdot D_p^2} \\ \frac{A_E}{A_{disc}} &= \frac{4 \cdot A_E}{\pi \cdot D_p^2} \end{aligned} \right\} \text{BAR} \quad (5.1)$$

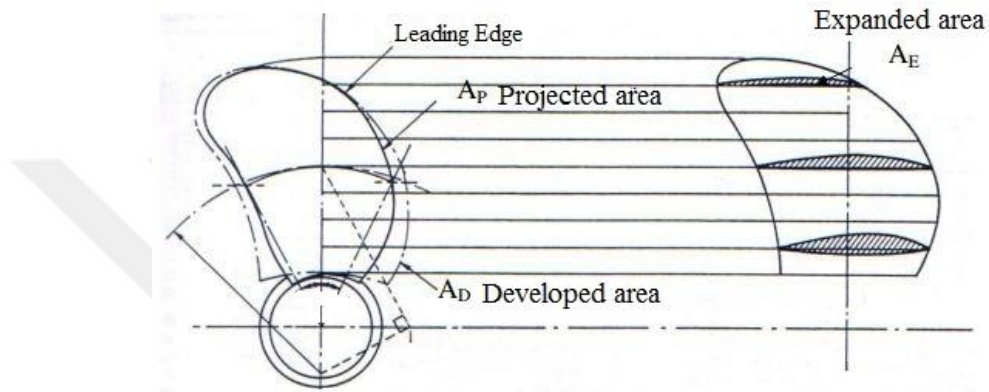


Figure 5.10 Characteristic propeller areas (Carlton [42])

5.1.2 Propellers Used in the Experiments

The present study was conducted by using three different Wageningen - B series propellers. The three fixed pitch propellers (FPP) used in the experiments are referred to as Propeller -130 mm, Propeller - 100 mm, and Propeller - 65 mm according to their diameters (D_p) as in Figure 5.11.

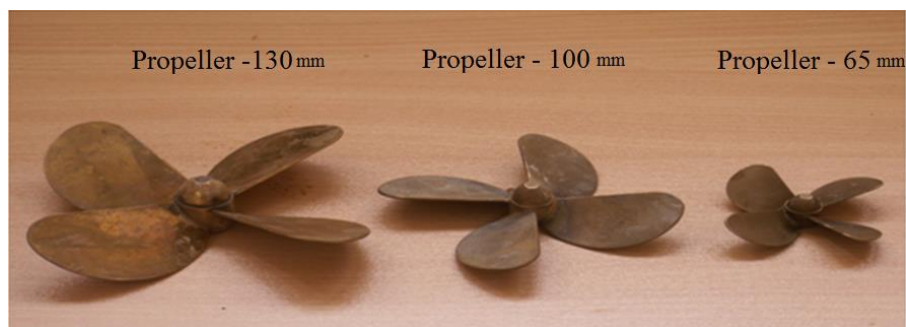


Figure 5.11 Geometry of four bladed propellers used in the experiments

The propeller hub was fitted to a stainless steel shaft to allow the rotation at bollard pull condition ($U_A=0$) as presented in Chapter 3.

A propeller in a ship rotates in ‘clockwise’ direction. In this study, two of the propeller (Propeller - 65 mm and Propeller - 130 mm) viewed from the aft (of the the propellers) rotate in the clockwise and the third propeller (Propeller - 100 mm) rotates in the counterclockwise direction.

The propeller computational geometry was designed by using HydroComp 2005 (3D) as seen in Figure 5.12.

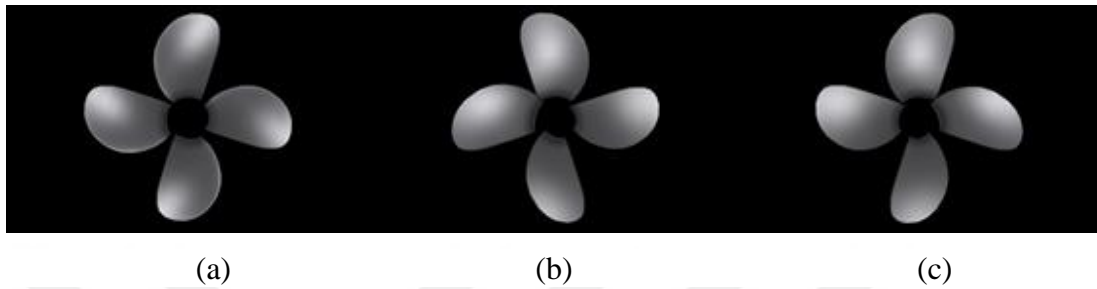


Figure 5.12 Propeller’s computational geometry a) Propeller - 65 mm b) Propeller - 100 mm c) Propeller - 130 mm

Expanded areas were calculated for each propeller and design drawings - profile view, pitch distribution, transverse view, expanded view - were given in Figure 5.13, Figure 5.14, Figure 5.15, respectively.

Table 5.1 lists the detailed characteristics of the propellers used in this study.

Table 5.1 Characteristics of the propellers used in the present study

	Propeller- 65 mm	Propeller-100 mm	Propeller-130 mm
Propeller’s type	Wageningen B Series	Wageningen B Series	Wageningen B Series
Material	Brass	Brass	Brass
Pitch Type of the Blade	FPP	FPP	FPP
Propeller Diameter (D_p)	65 mm	100 mm	130 mm
Propeller Hub Diameter (D_h)	7 mm	10 mm	14 mm
Direction of Rotation	Right-handed	Left-handed	Right-handed
Blade Number (N)	4	4	4
Section Pitch (P)	91 mm	140 mm	180 mm
Pitch Diameter Ratio (P/D_p)	1.4	1.4	1.4
Expanded Area (A_E)	23.12 cm ²	52 cm ²	89 cm ²
Propeller Disc Area (A_{disc})	33.18 cm ²	78.54 cm ²	132.73 cm ²
Blade Area Ratio (BAR)	0.7	0.7	0.7
Thrust Coefficient (C_T)	0.61	0.61	0.61

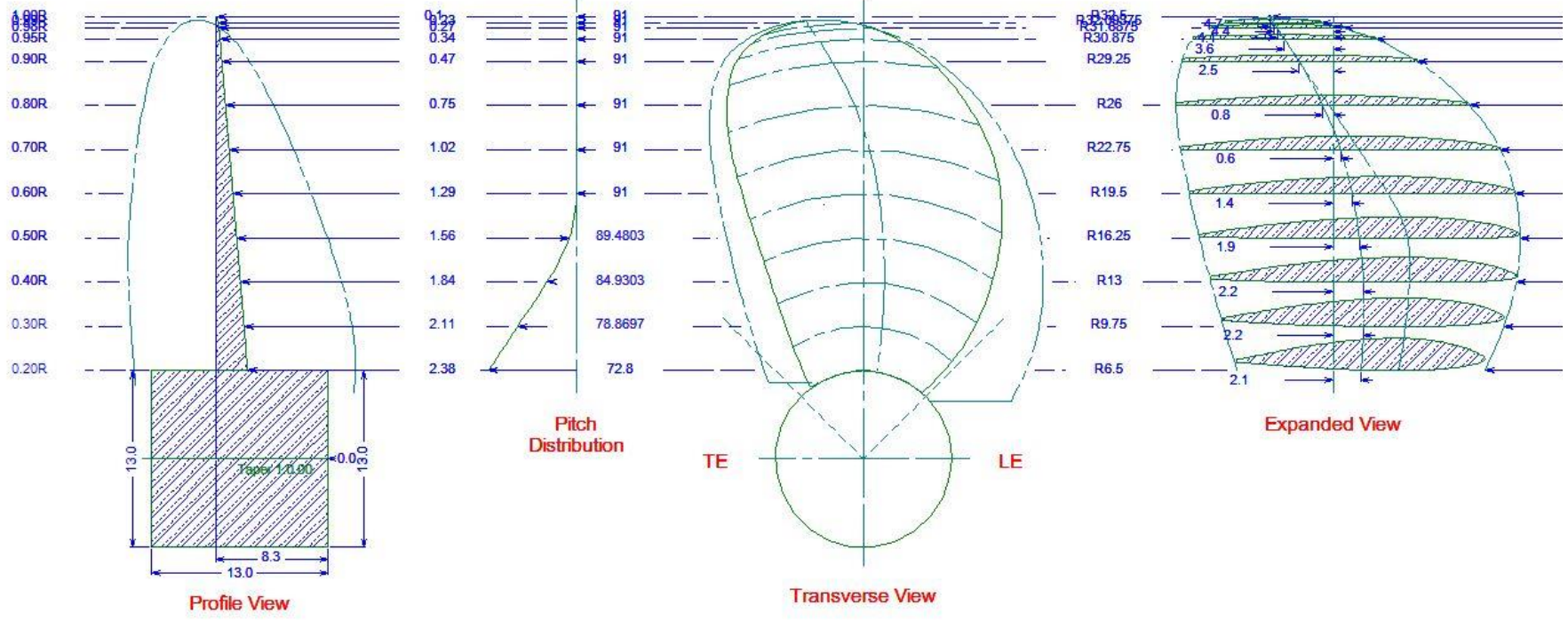
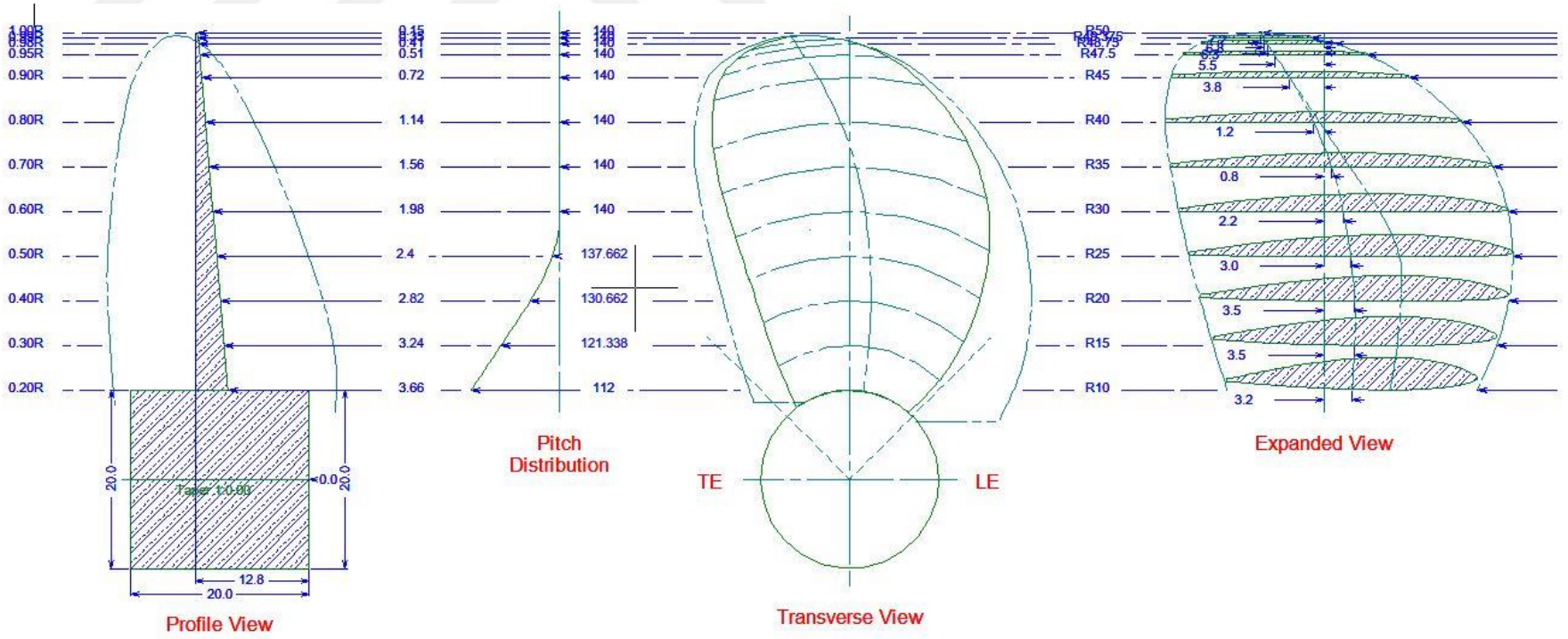


Figure 5.13 Design drawing for the Propeller - 65 mm



Figure 5.14 Design drawing for the Propeller - 100 mm



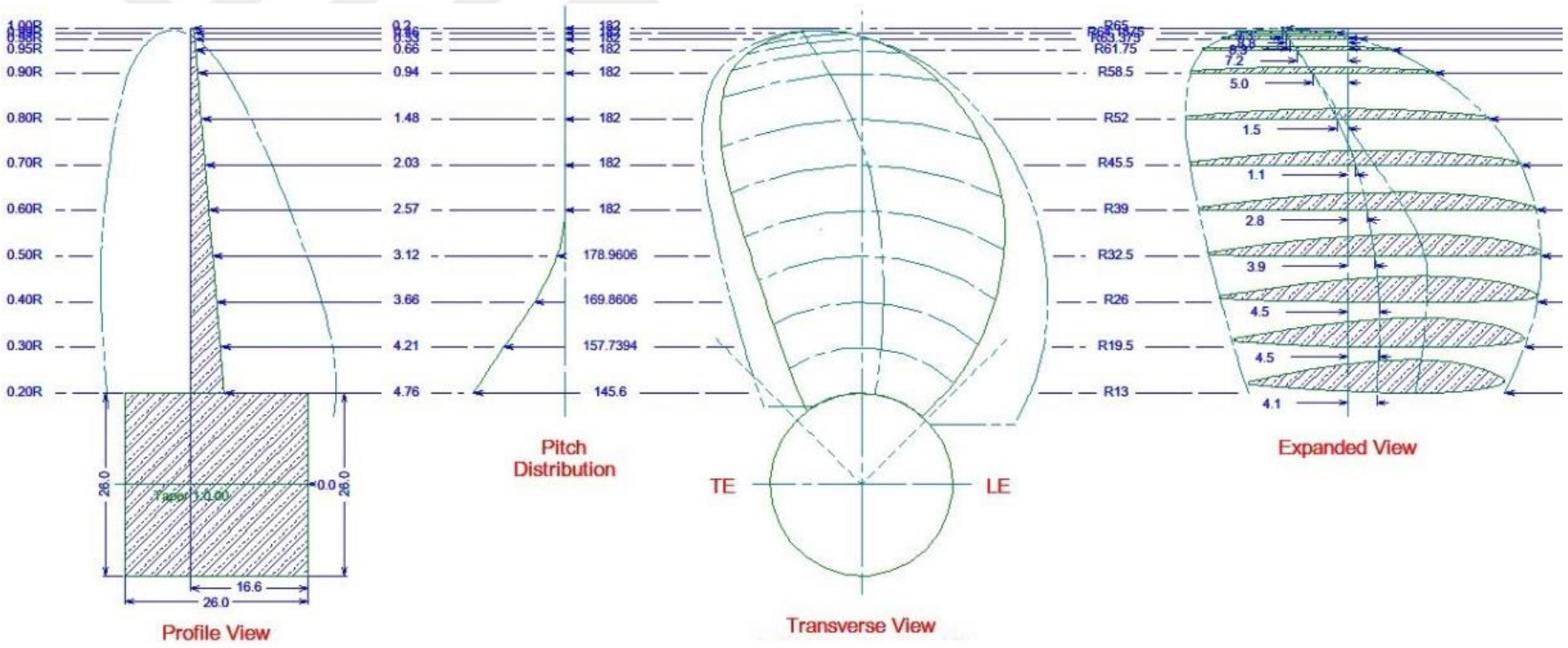


Figure 5.15 Design drawing for the Propeller - 130 mm

Thrust coefficients (C_T) are also given in Table 5.1 for each propeller (Propeller - 65 mm, Propeller - 100 mm and Propeller - 130 mm). C_T is defined from typical open water diagram for a set of fixed pitch propellers working in a non cavitating environment as shown in Figure 5.16. This figure defines, for the particular propeller, the complete set of operating conditions at positive advance and rotational speed, since the propeller under steady conditions can only operate along the characteristic line defined by its pitch propeller diameter ratio P/D_p . C_T values for the propellers taken from the diagram for the smallest value of advance coefficient (J) according to assumption of bullard pull conditions ($U_A=0$) and the value of 1.4 of pitch diameter ratio (P/D_p). Prosser [34] recommended that at zero speed of advance the values of C_T is equal to the function of $f(P/D_p)$ as given in Table 5.2.

Table 5.2 Thrust coefficient (C_T) as function of propeller pitch/diameter ratio (Carlton [42])

P/D_p	0.6	0.8	1	1.2	1.4
C_T (Opened)	0.26	0.37	0.48	0.57	0.54
C_T (Ducted)	0.24	0.37	0.51	0.67	0.82

Propeller pitch / diameter ratio for 1.4 gives 0.54 thrust coefficient according to Table 5.2. In the present study, thrust coefficient was found as 0.61 by using Figure 5.16 for the propellers with P / D_p with 1.4 that have similar values as given in Table 5.2.

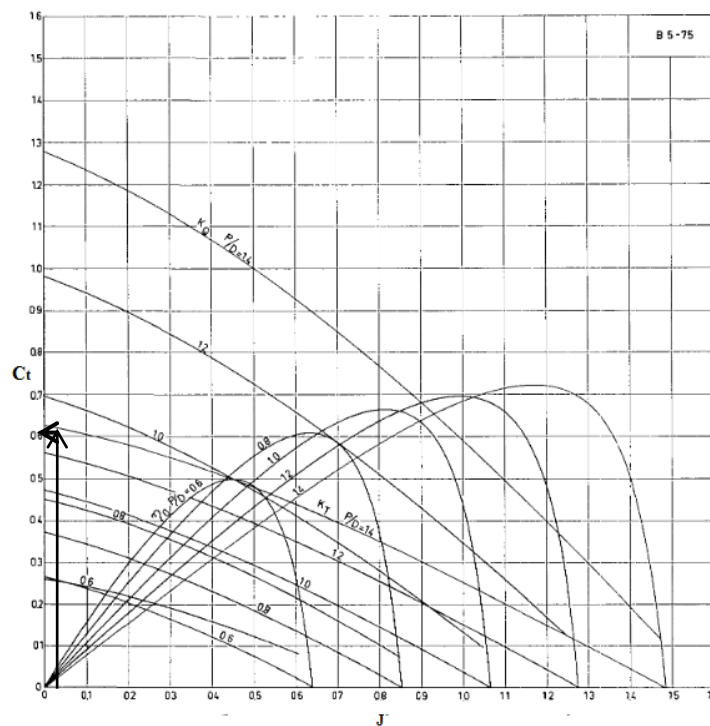


Figure 5.16 Open water diagram for Wageningen B5 - 75 screw series (Carlton [42])

5.1.3 Sand Bed Characteristics Used in the Experiments

Different types of sediment bed materials were used to test the evaluation of scouring processes under propeller jet mechanism in this experimental study. All the tests were conducted by using four uniformly distributed sediment beds as Material 1, Material 2, Material 3, and Material 4 with median grain sizes of $d_{50} = 0.52$ mm, 1.28 mm, 4.00 mm, and 8.30 mm, respectively (Figure 5.17).

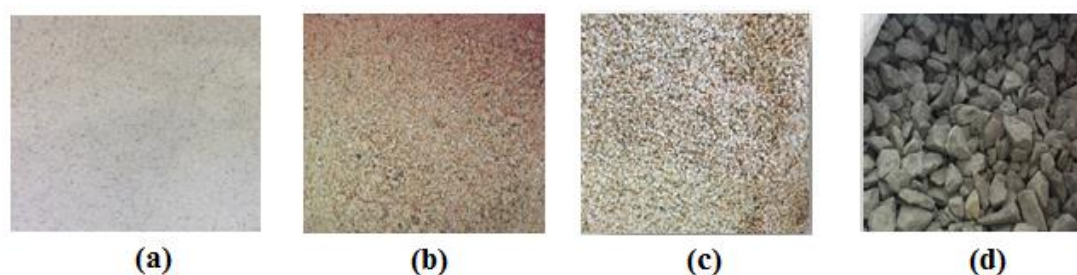


Figure 5.17 Sediment beds (a) Material 1 (b) Material 2 (c) Material 3 (d) Material 4

It is practically impossible to take ‘undisturbed’ samples from the sediment bed, a problem similar to that experienced by Sumer and Fredsøe [44] so, it was assumed that the sediment was as the dense sand with properties shown in Table 5.3. Determination of the characteristic properties of the materials were conducted in the Geotechnical Laboratory of Civil Engineering Department, at Yıldız Technical University. Summarized characteristics of bed materials are given in Table 5.3.

The relative density of compaction (D_r) of sediments was calculated from Equation (5.2) with the determination of maximum and minimum voids as listed in Table 5.3, with γ_d ; dry specific weight of sediment, $\sigma_g = \sqrt{d_{84}/d_{16}}$; geometric standard deviation of the sediments, and d_{84} and d_{16} are the effective grain sizes with 84% and 16% passing on the cumulative particle size, respectively. These values were obtained through the same method as obtained by Sumer et al. [50]. The void ratio of the sediment was obtained by filling the sand in a mound of known volume in the same way as in the working section (the sediment depth in the mound was exactly the same as in the actual experiments, i.e., 20 cm). Then, the sand was left for a duration equal to the duration to fill the entire working section and subsequently the void ratio was determined.

$$D_r = \frac{e_{\max} - e}{e_{\max} - e_{\min}} \quad (5.2)$$

where D_r is the relative density of compaction, e is the void ratio, and e_{\max} and e_{\min} are the maximum and minimum void ratios, respectively.

Table 5.3 Sediment bed characteristics used in the present study

Parameter	Material 1	Material 2	Material 3	Material 4
d_{50} (mm)	0.52	1.28	4.00	8.30
d_{90} (mm)	0.68	1.68	4.30	12.7
σ_g (-)	1.22	1.46	1.12	1.36
e_{\max} (-)	0.91	0.83	0.75	0.73
e (-)	0.54	0.46	0.55	0.55
e_{\min} (-)	0.46	0.44	0.48	0.47
γ_d (g/cm ³)	1.38	1.42	1.50	1.57
D_r (-)	0.82	0.77	0.74	0.69

Particle size distribution of the materials was given in detail with sieve analysis in Figure 5.18, Figure 5.19, Figure 5.20, Figure 5.21. The materials can be classified as ‘well - graded’ according to Unified Soil Classification System (USCS) and the values of C_u are under ≤ 1.5 , which indicate that the four sand materials can be considered uniform where $C_u = d_{60}/d_{10}$ is uniformity coefficient.

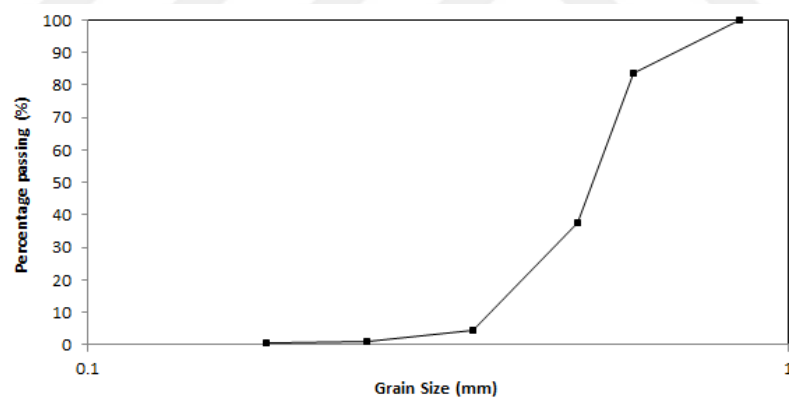


Figure 5.18 Sieve analysis of Material 1

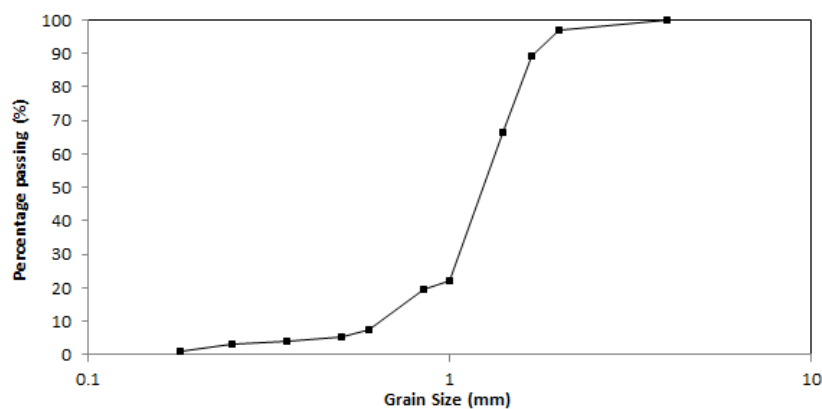


Figure 5.19 Sieve analysis of Material 2

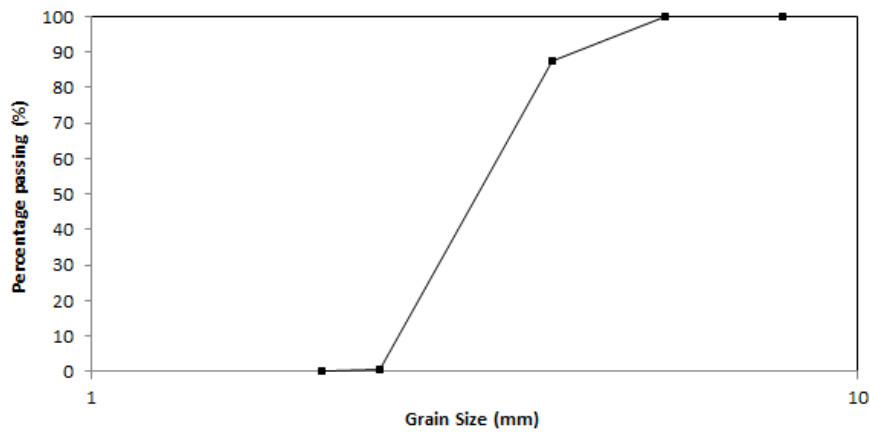


Figure 5.20 Sieve analysis of Material 3

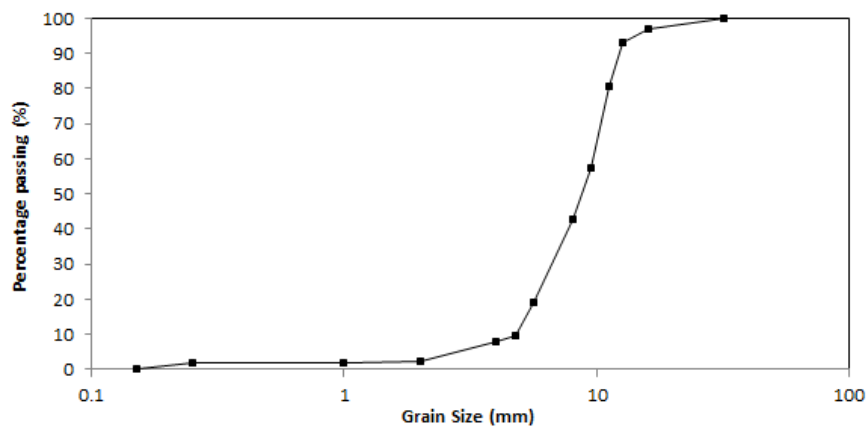


Figure 5.21 Sieve analysis of Material 4

5.1.4 Distribution of the Propeller Jet Velocity

Magnitude of the velocities were measured for the determination of flow characteristics for the evolution of scour. Nortec Doppler Current Velocimeter (NDCV) was used in the experimental study without disturbing the flow during the measurements to get the most accurate results.

Three - dimensional velocity components for the propeller jet (see Figure 3.3 in Chapter 3) were recorded with acoustic Doppler velocimeter (ADV) at an acoustic frequency of 10 MHz. Three main modules - measurement probe, signal conditioning module and signal processing module - for ADV system used in these laboratory tests are given in Figure 5.22, Figure 5.23 and technical specifications in Table 5.4.

Table 5.4 Technical Specifications of ADV (NDV Operations Manual [51])

Acoustic Frequency	10 MHz
Velocity Range	$\pm 0.03, 0.1, 0.3, 1.0,$ or ± 2.5 m/sec
Velocity Resolution	0.1 mm/sec
Velocity Bias	± 1 %, No Measurable Zero Offset in the Horizontal Direction
Sampling Rate	Programmable from 0.1 to 25 Hz
Sampling Volume	Less than 0.25 cm ³
Minimum Water Depth	20 mm for Side - Looking two – dimensional Probe, 60 mm

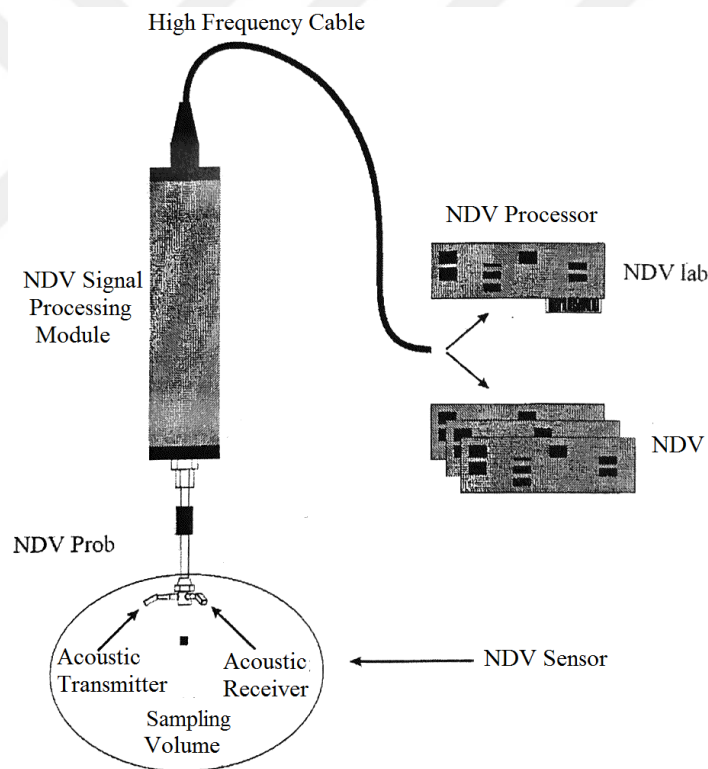


Figure 5.22 ADV modules (NDV Operations Manual [51])

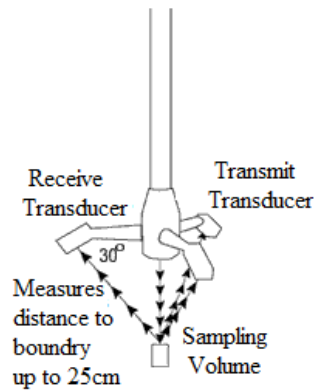


Figure 5.23 Three – dimensional down - looking probes of ADV (NDV Operations Manual [51])

Axial, radial and rotational velocity components were measured by using ADV for the Propeller - 130 mm, Propeller - 100 mm and Propeller - 65 mm located at 15 cm (G) above the rigid bed at three different speeds of rotation values as 40, 45 and 50 Hertz. The axial components of velocity were determined as the largest contributor to the resultant velocity by Brewster [17]. Hamill et al. [38] also measured axial velocity as about 90% of resultant velocity. Thus the axial velocity was taken into consideration for the following calculations. Measurements of the axial velocity distributions with respect to water depth propeller diameter ratio (Z/D_p) are given in the following Figures (Figure 5.20 – Figure 5.28).

Axial velocities were also measured by a flowmeter (streamflow velocity meter V1.3) for the Propeller - 130 mm and compared with the results obtained from ADV. Specifications of the flowmeter used in this study are summarized in Table 5.5.

Table 5.5 Technial specifications of flowmeter (Nixon Operations Manual [52])

403 Low Speed Probe	
Range	5-150
Accuracy	±2 % of True Velocity
Immersion Length Max	420mm
Connector	UNC Co - Axial Socket
Steam Material	316 Stainless Steel
Rotor	Delrin

Flowmeter velocity measurements were plotted in Figure 5.24, Figure 5.25 and Figure 5.26 for different propeller speeds; 590 rpm, 670 rpm and 745 rpm. It is seen that both measurements recorded by ADV and flowmeter have a good agreement for the Propeller-130 mm.

Lam et. al. [4] defined velocity distributions with two peak ridges as defined in the previous literature studies by Hamill et al. [3], Lam et al. [24], Hamill et al. [38]. The axial velocity distribution of propeller jets has low velocity core due the hub at the centerline of the propeller while two peak ridges are observed with increasing radial distance from the centerline as given in detail in Figure 3.3. The velocities measured $X=0.5D_p$ far away from the propeller's face. ADV measurements also showed similar velocity distributions for all the propeller diameters with different speeds as seen in Figure 5.24, Figure 5.25, Figure 5.26, Figure 5.27, Figure 5.28, Figure 5.29, Figure 5.30, Figure 5.31, and Figure 5.32.

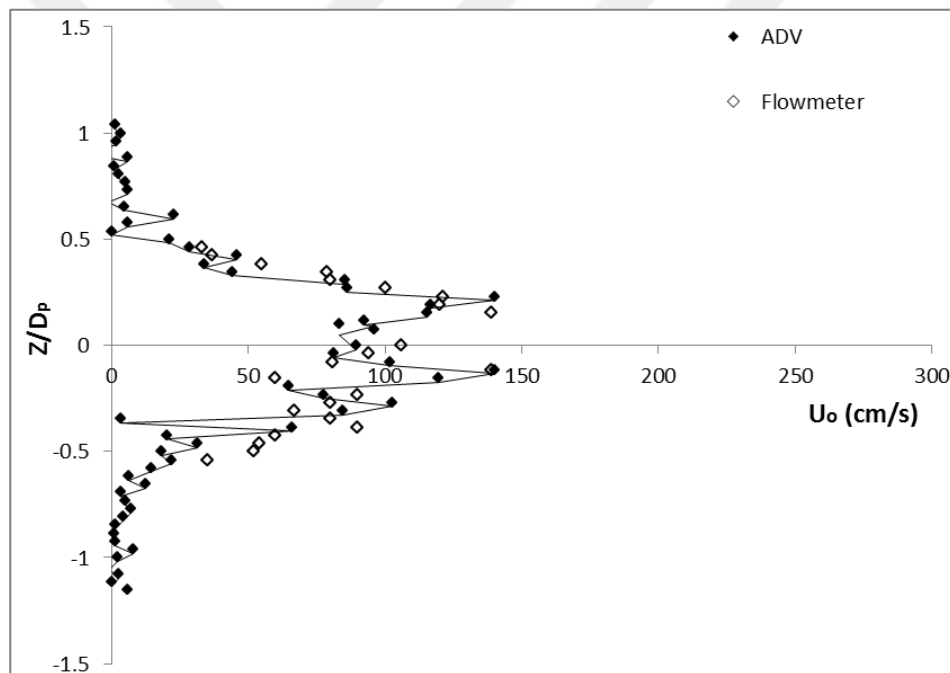


Figure 5.24 Distribution of the axial velocity at the face of the Propeller - 130 mm at 590 rpm

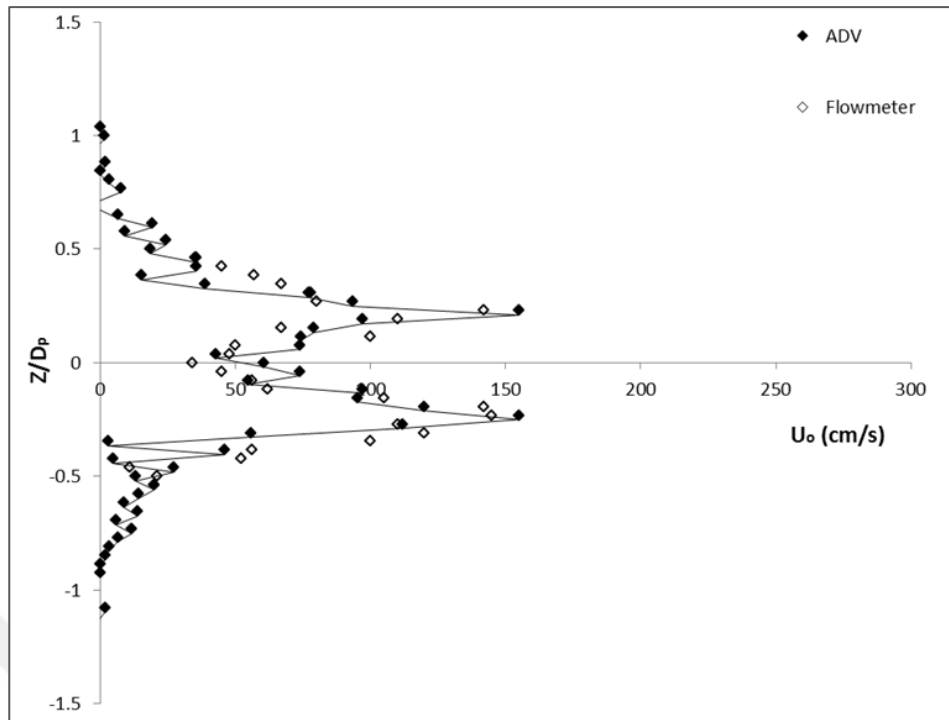


Figure 5.25 Distribution of the axial velocity at the face of the Propeller - 130 mm at 670 rpm

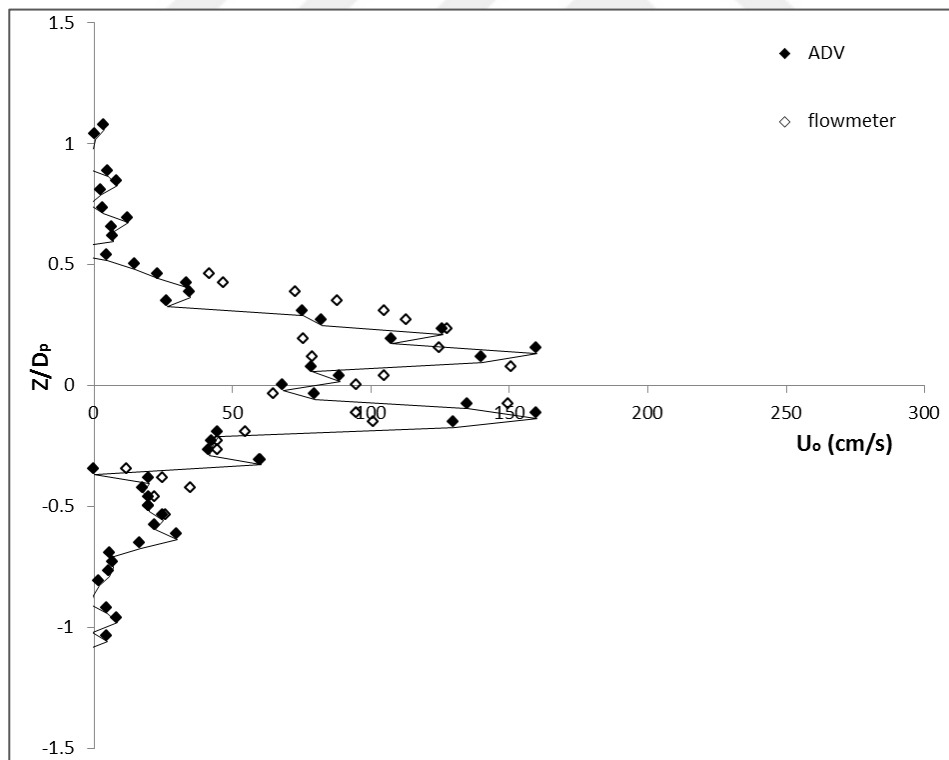


Figure 5.26 Distribution of the axial velocity at the face of the Propeller - 130 mm at 745 rpm

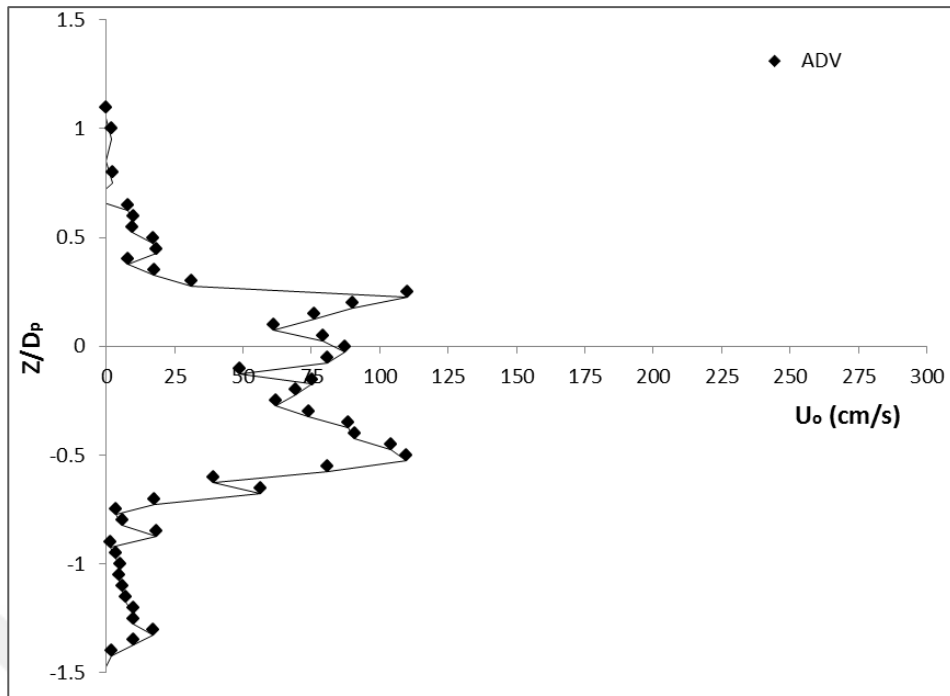


Figure 5.27 Distribution of the axial velocity at the face of the Propeller - 100 mm at 590 rpm

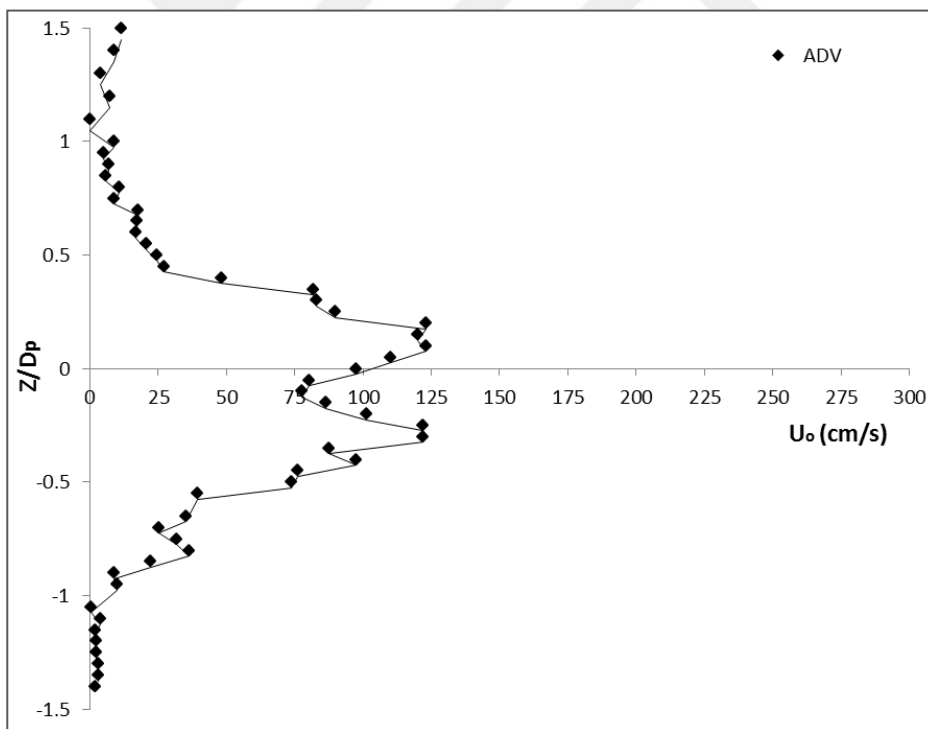


Figure 5.28 Distribution of the axial velocity at the face of the Propeller - 100 mm at 670 rpm

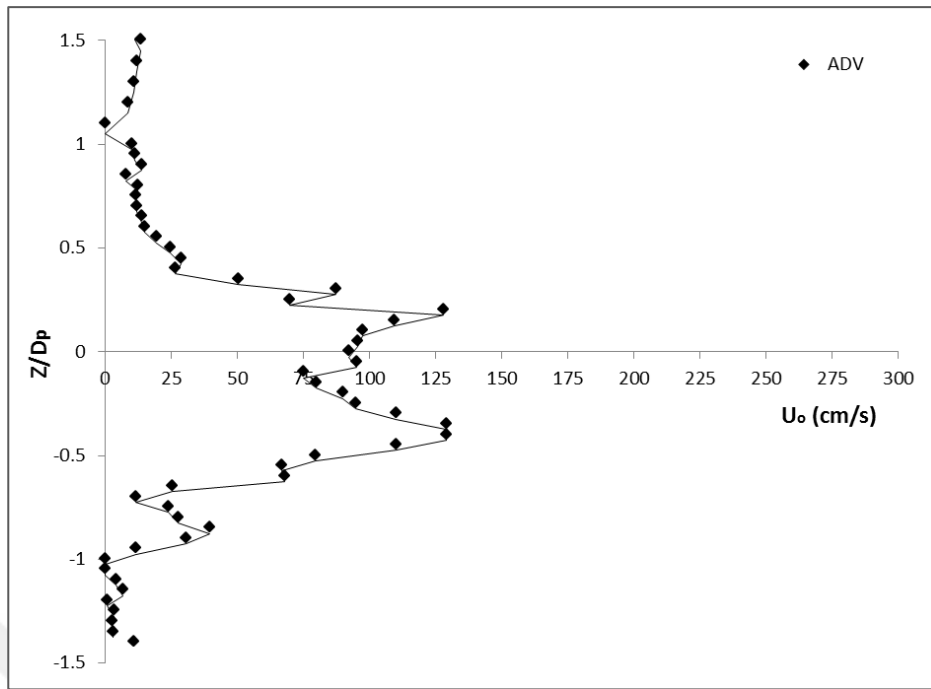


Figure 5.29 Distribution of the axial velocity at the face of the Propeller - 100 mm at 745 rpm

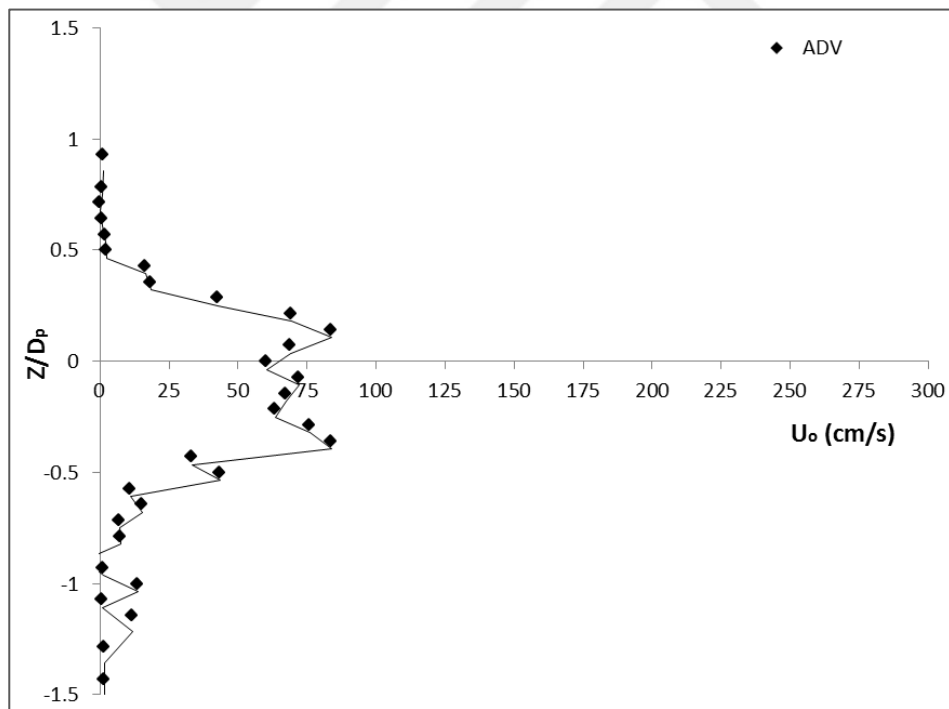


Figure 5.30 Distribution of the axial velocity at the face of the Propeller - 65 mm at 670 rpm

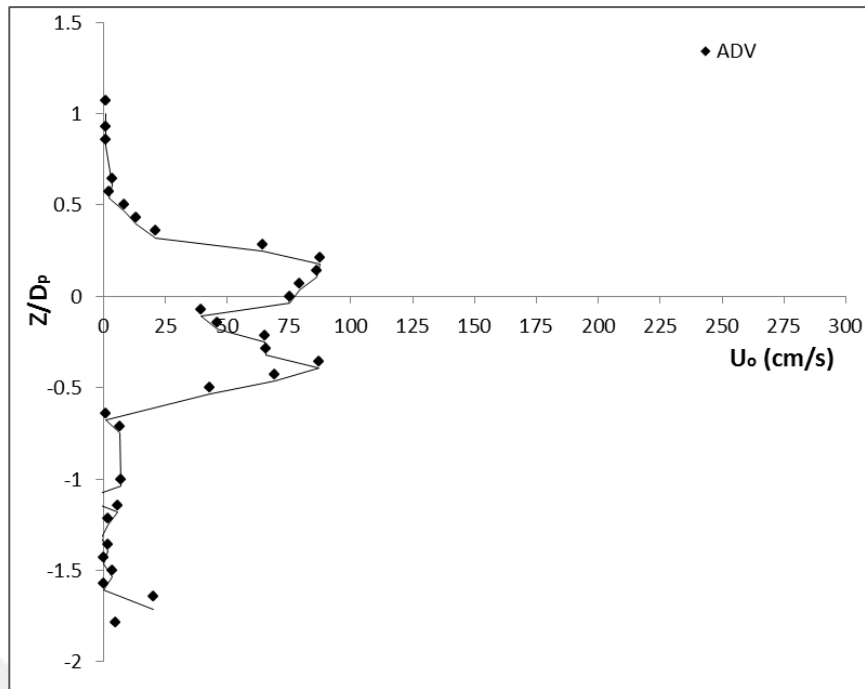


Figure 5.31 Distribution of the axial velocity at the face of the Propeller - 65 mm at 670 rpm

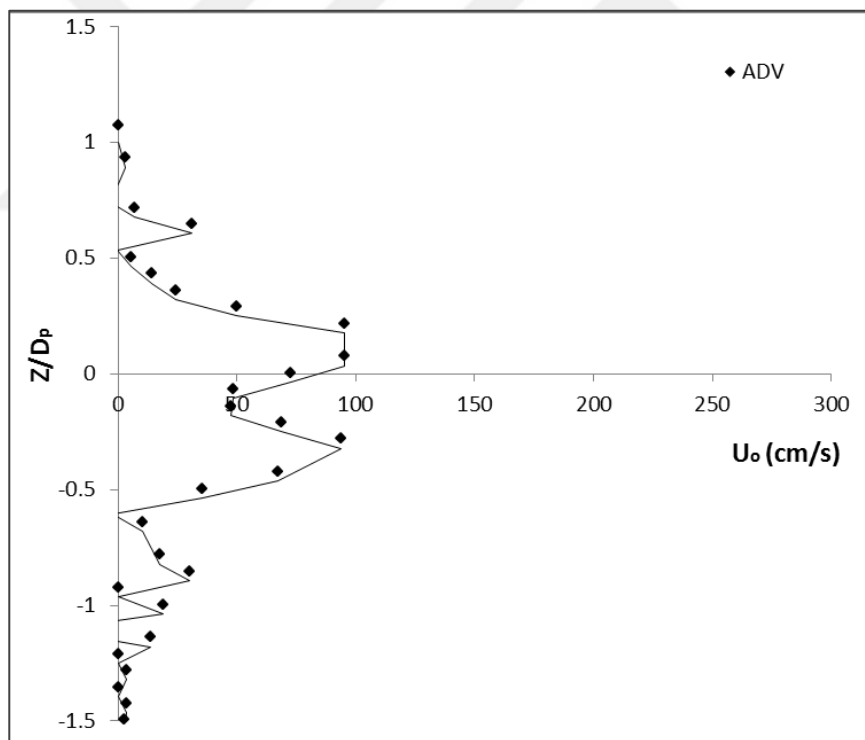


Figure 5.32 Distribution of the axial velocity at the face of the Propeller - 65 mm at 745 rpm

Determination of the velocity caused by the propeller jet has is difficult due to the complexity of the rotating propeller mechanism. Thus 'efflux' velocity which is defined as the maximum velocity along the propeller face is used for the engineering calculations.

Efflux velocity (U_0) values are taken as the average of two maximum peak velocity obtained from the velocity distribution profiles for three different types of propellers seen in Table 5.6.

Table 5.6 Measured efflux velocity values at different speeds

	Propeller Speed		Measured Velocities	
	Hertz	Rpm	U_{ADV} (m/sec)	$U_{Flowmeter}$ (m/sec)
Propeller - 6.5	40	590	0.84	
Propeller - 6.5	45	670	0.88	
Propeller - 6.5	50	745	0.94	
Propeller - 10	40	590	1.10	
Propeller - 10	45	670	1.23	
Propeller - 10	50	745	1.32	
Propeller - 13	40	590	1.40	1.39
Propeller - 13	45	670	1.55	1.49
Propeller - 13	50	745	1.60	1.57

The exit plane of the propeller flow, called the efflux velocity (U_0) of the propeller wash, has widely been investigated by several researchers, leading to modified equations of U_0 as shown in Table 3.1 (in Chapter 3). Predicted efflux velocities have been calculated by using each investigator's equations and compared with measured velocities in the present study (Figure 5.33, Figure 5.34, Figure 5.35).

Increasing values of the efflux velocity versus the rotation speed have the same linear tendency for each equation. Measured velocities for the Propeller - 65 mm in the present study, have approximate values with the equation suggested by PIANC [28], having a greater efflux coefficient of 1.6.

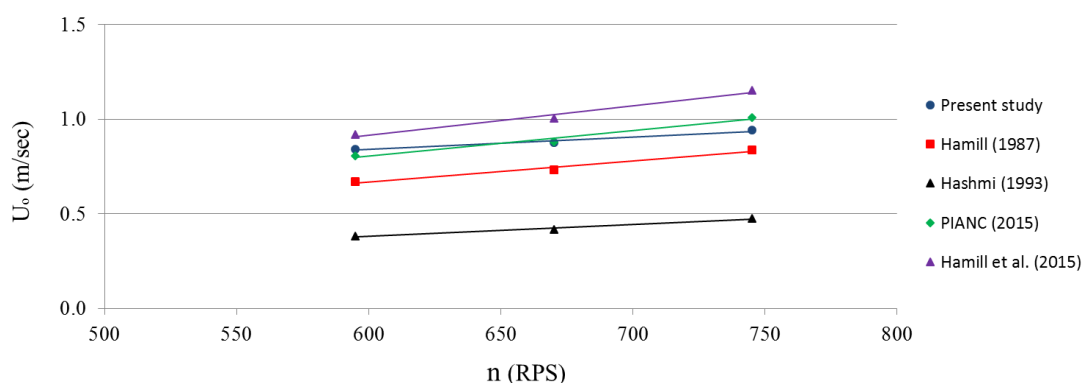


Figure 5.33 Measured and predicted efflux velocity comparisons for the Propeller - 65 mm. The values for the Propeller - 100 mm are somewhere between the results obtained from PIANC [28] and Hamill [7] (Figure 5.34). However, efflux velocities (U_0) of the Propeller -

130 mm have similar values with the equation defined by Hamill [7], having efflux coefficient of 1.33 (Figure 5.35).

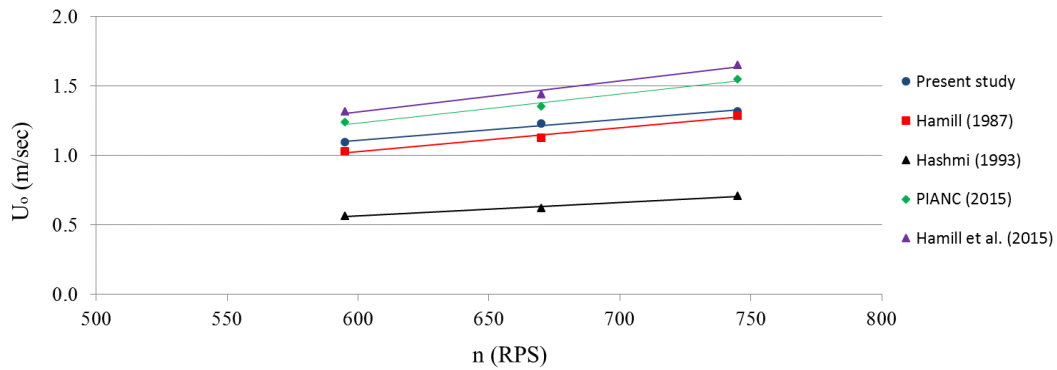


Figure 5.34 Measured and predicted efflux velocity comparisons for the Propeller - 100 mm

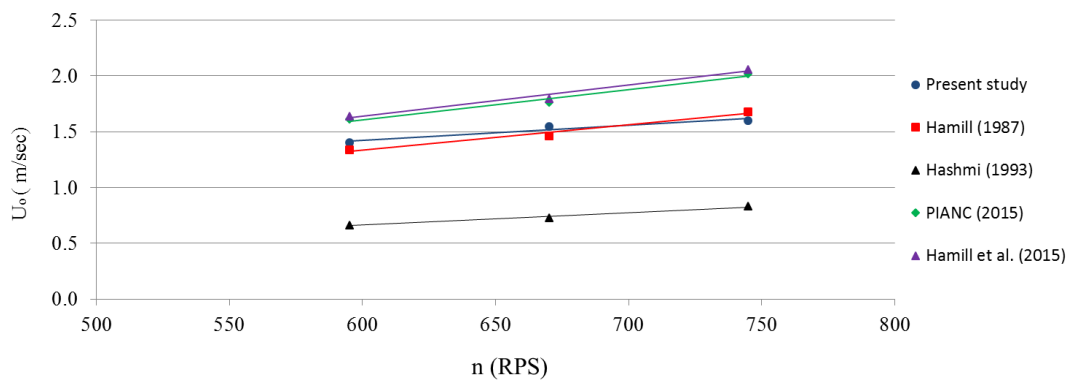


Figure 5.35 Measured and predicted efflux velocity comparisons for the Propeller - 130 mm

Hamill [7] suggested that the efflux coefficient defined in the equation can be changeable based on the propeller characteristics such as blade area ratio and hub diameter. This value is also somewhere between the values proposed by PIANC [28] and Hamill [8]. PIANC [28] defined this coefficient as 1.6 for the Wageningen B- and K- series propellers whereas Hamill [7]'s proposed these values as 1.33. The efflux coefficient chosen as 1.42 is also very similar to Lam et al. [10]'s coefficient as 1.48 obtained by using CFD model results modified for four bladed propellers (see Table 1.12 in Chapter 1).

Equation (5.3) was developed for the maneuvering conditions of a ship by considering the geometrical characteristics of the propellers used in this study. This equation was derived from four bladed Wageningen B- series propellers's values of $D_p=6.5$ cm, 10 cm and 13 cm with a blade area ratio of 0.7.

$$U_0 = 1.42nD_p\sqrt{C_T} \quad (5.3)$$

The experimental measurements were compared with the equations proposed by Hashmi [13], Hamill [7] and PIANC [28] as seen in Figure 5.36 . Equation (5.3) gave the estimation of the efflux velocity with $R^2 = 0.953$ for the Propeller - 130 mm, Propeller - 100 mm, and Propeller - 65 mm similar to Hashmi [13]’s, Hamill [7]’s and PIANC [28]’s equations. The measured data also have a linear component that can be described by a best fit line (reference line) with a 1:1 slope for Equation (5.3). Linearized plots of Equation (5.3) for the prediction of efflux velocity (U_0) versus measured data provide the lower value of the root-mean-squared error with $RMSE = 0.020$ (Table 5.7).

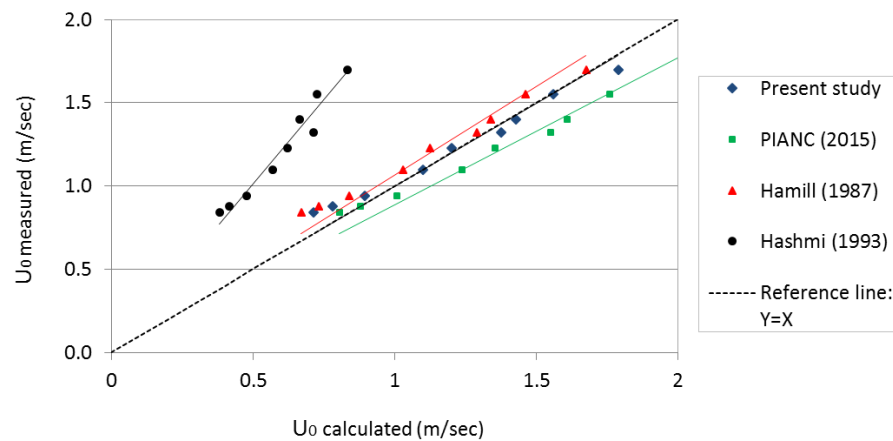


Figure 5.36 Comparisons of measured and calculated efflux velocities

Hashmi [13]’s, Hamill [7]’s, PIANC [28]’s and the Equation (5.3)’s calculated efflux velocities near the propeller overestimate the predicted values when compared with measurements for $U_0 < 1\text{m/sec}$. Hamill and Kee [53] stated similar conditions and attempted to provide corrections to the limiting assumptions used in axial disc theory which tend to overestimate the U_0 value. They also stated that this deviation in the predicted values of U_0 is clearer for larger propellers.

Table 5.7 Descriptive statistical performance indices for datasets

Performance Indicators	Hamill [7]	Hashmi [13]	PIANC [28]	Present Study
Linearized Plots of Equations	$Y=1.063X$	$Y=2.023X$	$Y=0.883X$	$Y=0.995X$
Determination Coefficient (R^2)	0.946	0.946	0.946	0.953
Root-Mean- Squared-Error (RMSE)	0.033	0.08	0.059	0.02

5.1.5 Scaling of the Experimental Model

Dimension analysis for the determination of scour dimensions such as (S_{max} , B_{max} , L_{max}) is a useful tool in such a complex physical system including specific independent variables. These variables are defined for this model in Table 5.8.

The maximum scour depth (S_{max}) is one of the main dimensions of the scouring formation owing to propeller action, and can be described using independent parameters involved in the dimensional analysis by using Langhaar Method as follows:

$$S_{max} = f(U_0, D_p, n, d_{50}, G, \rho, \mu, g, v, \rho_s, d_o, X, L_m, h) \quad (5.4)$$

These variables were substituted for dimensionless parameter of Π ;

$$\Pi = D_p^{k_1} X^{k_2} g^{k_3} S_{max}^{k_4} \mu^{k_5} d_{50}^{k_6} h^{k_7} G^{k_8} \rho_s^{k_9} \rho^{k_{10}} d_o^{k_{11}} U_0^{k_{12}} n^{k_{13}} L_m^{k_{14}} \quad (5.5)$$

where $k_1, k_2, k_3, \dots, k_{14}$ are defined as the exponents.

Defined $k_1, k_2, k_3, \dots, k_{14}$ exponents are given in Table 5.9 when all variables are expressed in terms of basic dimensions (M, L, and T) into dimensionless pi term.

Table 5.8 Dimensions of defined physical quantities

	Quantity	Symbol	SI Unit	Dimension
Fluid Characteristics	Density	ρ	kg/m ³	ML ⁻³
	Dynamic Coefficient Viscosity	μ	Ns/m ²	ML ⁻¹ T ⁻¹
Flow Characteristics	Efflux Velocity	U_0	m/sec	MT ⁻¹
	Water Depth	h	m	L
Ship Properties	Propeller Diameter	D_p	m	L
	Propeller Speed	n	r/s	T ⁻¹
	Characteristics Length of the Propeller	L_m	m	L
Geometric Parameters	Pile Diameter	d_o	m	L
	Gap between Propeller Axis and Sediment Bed	G	m	L
	Distance between Propeller Face and Pile	X	m	L
Sediment Bed Properties	Median Grain Size	d_{50}	M	L
	Mass Density	ρ_s	kg/m ³	ML ⁻³
Other Parameters	Acceleration of Gravity	g	m/sec ²	LT ⁻²

Table 5.9 Exponents for each basic dimension

	k ₁	k ₂	k ₃	k ₄	k ₅	k ₆	k ₇	k ₈	k ₉	k ₁₀	k ₁₁	k ₁₂	k ₁₃	k ₁₄
Symbol	D _p	X	g	S _{max}	μ	d ₅₀	h	G	ρ _s	ρ	d _o	U ₀	n	L _m
M	0	0	0	0	1	0	0	0	1	1	0	0	0	0
L	1	1	1	1	-1	1	1	1	-3	-3	1	1	0	1
T	0	0	-2	0	-1	0	0	0	0	0	0	-1	-1	0

The exponents k₁, k₂, k₃... k₁₄ are determined by the following equations for each of M, L, and T for $\Pi = M^0 L^0 T^0$;

$$\text{For M; } k_9 + k_{10} + k_5 = 0 \quad (5.6)$$

$$\text{For L; } k_1 + k_2 + k_3 + k_4 - k_5 + k_6 + k_7 + k_8 - 3k_9 - 3k_{10} + k_{11} + k_{12} + k_{14} = 0 \quad (5.7)$$

$$\text{For T; } -2k_3 - k_5 - k_{12} - k_{13} = 0 \quad (5.8)$$

Equation (5.6), (5.7) and (5.8) are rearranged as follows:

$$k_{10} = -(k_9 + k_5) \quad (5.9)$$

$$k_1 = -(k_2 + k_3 + k_4 - k_5 + k_6 + k_7 + k_8 - 3k_9 - 3k_{10} + k_{11} + k_{12} + k_{14}) \quad (5.10)$$

$$k_{12} = -2k_3 - k_5 - k_{13} \quad (5.11)$$

Dimensionless Π groups are determined by using the Equation (5.9), (5.10) and (5.11) are given in Table 5.10.

Table 5.10 Dimensionless Π groups with defined exponents for each dimension

	k ₁	k ₂	k ₃	k ₄	k ₅	k ₆	k ₇	k ₈	k ₉	k ₁₀	k ₁₁	k ₁₂	k ₁₃	k ₁₄
Π ₁	-1	0	0	0	1	0	0	0	0	-1	0	-1	0	0
Π ₂	-1	0	0	0	0	0	1	0	0	0	0	0	0	0
Π ₃	-1	1	0	0	0	0	0	0	0	0	0	0	0	0

Table 5.10 Dimensionless Π groups with defined exponents for each dimension (cont'd)

Π_4	-1	0	0	0	0	0	0	1	0	0	0	0	0	0
Π_5	-1	0	0	1	0	0	0	0	0	0	0	0	0	0
Π_6	1	0	0	0	0	-1	0	0	0	0	0	0	0	0
Π_7	0	0	1	0	0	1	0	0	0	0	0	-2	0	0
Π_8	0	0	0	-1	0	0	0	0	0	0	1	0	0	0
Π_9	0	0	0	0	0	-1	0	1	0	0	0	0	0	0
Π_{10}	-1	0	0	0	1	0	0	0	0	-1	0	0	1	-1
Π_{11}	-1	0	0	0	0	1	0	0	0	0	0	0	0	0

$$\left. \begin{aligned}
 \Pi_1 &= D_p^{-1} \rho^{-1} \mu U_0^{-1} \\
 \Pi_2 &= h D_p^{-1} \\
 \Pi_3 &= X d_o^{-1} \\
 \Pi_4 &= G D_p^{-1} \\
 \Pi_5 &= S_{\max} D_p^{-1} \\
 \Pi_6 &= G d_o^{-1} \\
 \Pi_7 &= U_0^{-2} d_{50} g \\
 \Pi_8 &= S_{\max}^{-1} d_o \\
 \Pi_9 &= G d_{50}^{-1} \\
 \Pi_{10} &= D_p^{-1} \mu \rho^{-1} n^{-1} L_m^{-1} \\
 \Pi_{11} &= D_p d_{50}^{-1}
 \end{aligned} \right\} \quad (5.12)$$

Thus, dimensionless scour depths can be expressed as;

$$\frac{S_{\max}}{D_p}, \frac{S_{\max}}{d_o} = f \left[\frac{U_0}{\sqrt{g d_{50} \Delta}}, \frac{U_0 D_p}{\nu}, \frac{G}{D_p}, \frac{D_p}{d_{50}}, \frac{n D_p L_m}{\nu}, \frac{G}{d_o}, \frac{X}{d_o}, \frac{G}{d_{50}}, \frac{h}{D_p} \right] \quad (5.13)$$

where $Fr_d = U_0 / \sqrt{g d_{50} \Delta}$ is the densimetric Froude number and $Re_f = U_0 D_p / \nu$ is Reynolds flow number, and $Re_p = n D_p L_m / \nu$ is Reynolds propeller number. L_m is calculated with the formula given by Blaauw and van de Kaa (1978);

$$L_m = \beta D_p \pi \left(2N \left(1 - \frac{D_h}{D_p} \right) \right)^{-1} \quad (5.14)$$

where D_h is the diameter of the hub of propeller, L_m is the characteristic length of the propeller.

Quarrin [11] found that typical propeller speeds and diameters that caused seabed scouring were 200 – 400 rpm and 1.5 – 3.0 m, respectively. Lam et al. [10] selected a propeller with a diameter of 2.5 m at a rotation speed of 200 rpm, and with a thrust coefficient $C_T = 0.35$ as the prototype in their study. The propeller diameter was scaled by 1:33 by using a 76 – mm - propeller with $C_T = 0.35$ in their model. In the present study, prototype ships that may cause a scouring effect are assumed to have propeller diameters of 1.0 m, 1.5 m, and 2 m and an operating speed of 200–255 rpm with $C_T = 0.35$, similar to the typical ship dimensions provided by Quarrin [11]. They calculated the initial efflux velocity with Equation (3.13) as 7.84 m/sec for the prototype and determined the $U_{0(model)} = 1.37$ m/sec by considering the Froudian scaling law expressed in Equation (5.15). The operation speed was determined as 1000 rpm by using Equation (3.13) corresponding to 1.37 m/sec for model's efflux velocity in their study.

$$U_{0(model)} = U_{0(prototype)} \sqrt{\frac{D_{p(model)}}{D_{p(prototype)}}} \quad (5.15)$$

Yew et al. [25] scaled propeller diameter to 1:11 with using 22 cm twin-propellers ($C_T=0.35$) for the same prototype as Lam et al.[10]'s. By using similar calculations, they determined propeller speed as 500 rpm with corresponding to $U_{0(model)}$ of 2.33 m/sec.

In the present study the prototype ship was considered as a ro-ro vessel and the scouring mechanism during berthing and unberthing conditions was investigated. Modern ro-ro conventional vessels are equipped with two or three bow thrusters and each thruster has 1,500 kW power according to PIANC [28]. In Figure 5.37, the diameter of the bow thruster is about 2.0 m, propeller diameter with corresponding power of 1,500 kW which is in the range for typical propeller diameter given by Quarrin [11]. In the present study, the prototype ship which may cause the scouring effect is assumed to have a propeller diameter of 1.0 m, 1.5 m and 2.0 m and an operating speed at 200 - 255 rpm with $C_T = 0.35$ as in the similar range for typical ship dimensions given by Quarrin [11]. Also, PIANC [28] recommended that the speed of the propeller (rpm) decreases about 50% during the ship's maneuver. Thus the propeller's speed was considered as 200 - 255 rpm for the prototype.

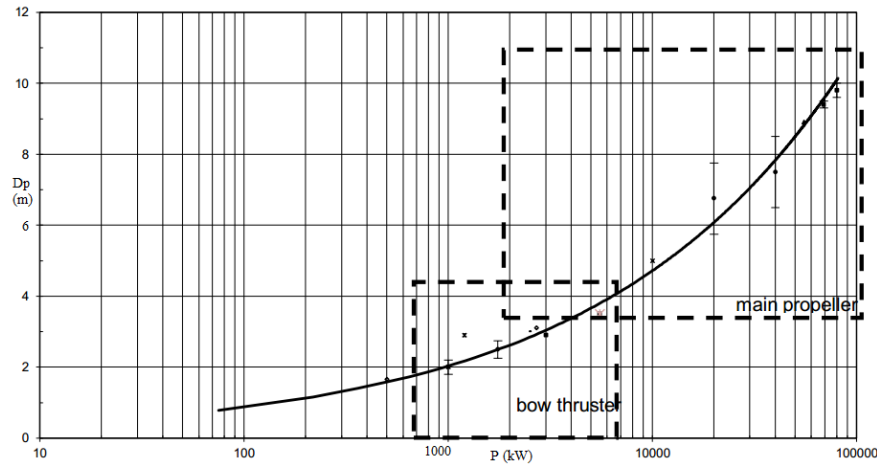


Figure 5.37 Relationship between power and diameter of the main and bow thruster (PIANC [28])

The scale for the propeller diameters was considered as 1:15, similar to the one given in the previous studies. Thus, Wageningen - B series propellers with diameters of 6.5 cm, 10 cm, and 13 cm (Figure 5.11) were used in the model corresponding to 1.0 m, 1.5 m, and 2.0 m propellers set to rotation speeds of 590, 670, and 745 rpm, respectively.

As an example; the efflux velocity for the 10 – cm - diameter model propeller was chosen in the model to be 1.2 m/sec (2.33 kn) using Equation (5.3) to achieve the field speed of 4.8 m/sec (9.3 kn). Furthermore, the efflux velocity for the model was converted with Equation (5.3) to an optimal speed of 670 rpm for the propeller speed of 1.2 m/sec. A typical vessel having dimensions similar to that of the typical ship’s dimensions given by Quarrin [11] was chosen for the study with characteristics for the model propellers of 6.5 cm, 10 cm, and 13 cm as listed in Table 5.11. Consequently, the rotation speeds were found (and calculated) to be 590 rpm, 670 rpm, and 745 rpm for each propeller in the experimental tests. Thus it was intended to conduct tests over a wide practical range of typical prototype ship speeds U_0 (prototype) = 3.5 m/sec to 5.5 m/sec (6.8 kn to 10.7 kn).

Table 5.11 Summarized parameters for the prototype and model propellers

Prototype				Model				
Propeller Diameter D_p (m)	Propeller Speed rpm	Efflux Velocity U_0 (m/sec)	Thrust Coefficient	Propeller Diameter D_p (m)	Calculated Propeller Speed, rpm	Efflux Velocity U_0 (m/sec)		Thrust Coefficient
						Measured	Calculated	
2.0	200	5.5	0.35	0.13	590	1.40	1.4	0.61
2.0	230	6.2	0.35	0.13	670	1.55	1.6	0.61
2.0	255	6.9	0.35	0.13	745	1.60	1.8	0.61

Table 5.11 Summarized parameters for prototype and model propellers (cont'd)

1.5	200	4.2	0.35	0.1	590	1.10	1.1	0.61
1.5	230	4.8	0.35	0.1	670	1.23	1.2	0.61
1.5	255	5.3	0.35	0.1	745	1.32	1.4	0.61
1.0	200	2.7	0.35	0.065	590	0.84	0.7	0.61
1.0	230	3.1	0.35	0.065	670	0.88	0.8	0.61
1.0	255	3.5	0.35	0.065	745	0.90	0.9	0.61

In the present study, the Reynolds numbers are calculated for the three propellers at the operating speeds considered herein. Re_p and Re_f range from $1.28 \cdot 10^4$ to $6.46 \cdot 10^4$ and $4.61 \cdot 10^4$ to $23.27 \cdot 10^4$, respectively (Table 5.12).

Table 5.12 Propeller speeds of rotation and corresponding Reynolds numbers

Propeller Diameter (D_p , cm)	Propeller Speed	Re_f	Re_p
	Rpm		
6.5	590	$1.28 \cdot 10^4$	$4.61 \cdot 10^4$
	670	$1.44 \cdot 10^4$	$5.19 \cdot 10^4$
	745	$1.62 \cdot 10^4$	$5.82 \cdot 10^4$
10	590	$3.00 \cdot 10^4$	$10.91 \cdot 10^4$
	670	$3.41 \cdot 10^4$	$12.29 \cdot 10^4$
	745	$3.79 \cdot 10^4$	$13.77 \cdot 10^4$
13	590	$5.12 \cdot 10^4$	$18.43 \cdot 10^4$
	670	$5.81 \cdot 10^4$	$20.93 \cdot 10^4$
	745	$6.46 \cdot 10^4$	$23.27 \cdot 10^4$

Rajatratham [54] stated that scale effects due to viscosity could be ignored if the Reynolds numbers exceeded 10^4 . Blaauw and Van de Kaa [1] calculated Re_p between the ranges of $3 \cdot 10^4$ to $6 \cdot 10^4$ for non-ducted propeller and $3 \cdot 10^4$ to $5 \cdot 10^4$ for the ducted propellers. They stated that the scaling effects due to the viscosity could be neglected if Re_f and Re_p numbers are greater than $3 \cdot 10^3$ and $7 \cdot 10^4$, respectively.

For the propeller jet properties used by Hamill [7] the value of Re_f was found to be between $1.2 \cdot 10^5$ and $2.3 \cdot 10^5$, and therefore, the effect of viscosity could be neglected. Based on the studies done by Blaauw and Van de Kaa [1] and Verhey [23], the scale effects in these experiments were insignificant between these ranges when the experiments satisfied the Froude scale.

In the present study, the Reynold numbers are compared with the ones used in the previous research calculations. All the Reynolds flow numbers exceeded $3 \cdot 10^3$ for the determined speeds of rotation, satisfying the criteria for the Froude pile . The Reynolds numbers for the

propellers were found to be slightly smaller than $7 \cdot 10^4$ so the scaling effects due to the viscosity were neglected.

In addition, Hong et al. [45] stated that the effect of h/D_p on the scouring formation could be neglected. If the water depth (h) is higher six times than the diameter jet (D_o), this effect may be ignored as suggested by Faruque et al. [55] and Sarathi [56] for the submerged jets. Hence, the effect of h/D_p was neglected in the present study as the water level (h) was defined high enough compared with D_p .

The effect of the sediment fall velocity was neglected since the grain sizes were rather large in the present study as stated in Sumer and Fredsøe [57]'s. Thus, the relative scour depths (S_{\max}/D_p and S_{\max}/d_o) can be simplified as follows

$$\frac{S_{\max}}{D_p}, \frac{S_{\max}}{d_o} = f \left[\frac{U_o}{\sqrt{g d_{50} \Delta}}, \frac{D_p}{d_o}, \frac{G}{D_p}, \frac{G}{d_o}, \frac{X}{d_o}, \frac{G}{d_{50}} \right] \quad (5.16)$$

The dimensionless parameters in the right hand side of Equation (5.16) were examined to assess the evolution of the scouring process after all experiments had been conducted as mentioned in the following chapters.

SCOUR FORMATIONS INDUCED BY PROPELLER JET MECHANISM

In this chapter, the experimental results of local scour formation due to three-dimensional submerged propeller jet mechanism are summarized. In addition, since the goal of this thesis is to find a suitable scour formula, this chapter will focus on the scouring mechanism with the absence and presence of a vertical pile structure. Furthermore two-pile tandem arrangements and application of rock protection around a pile have been investigated.

6.1 Scouring Formations without Pile Cases

Totally 63 experimental tests were carried out without considering the berth structure near propeller jet in the flume (see Figure 5.1). In each test, one variable was changed. For example, the propeller diameter ($D_p = 6.5$ cm, 10 cm, and 13 cm) and speed (590 rpm, 670 rpm, and 745 rpm) over four sediment bed sizes ranging from $d_{50} = 0.52$ mm to $d_{50} = 8.3$ mm for a propeller gap which is the horizontal distance between the propeller axis and sediment bed at $G = 10$ cm. In addition, higher propeller gaps of $G = 15$ and 20 cm were tested on finer and coarser sediment beds of $d_{50} = 0.52$ mm and $d_{50} = 8.3$ mm. All tests were conducted within the range of $Fr_d: 1.89 \leq Fr_d \leq 15.01$ and are given in Table 6.1.

Table 6.1 Test conditions with the absence of structure

Sediment Size	Gap Height	Propeller Speed	Propeller Diameter	Densimetric Froude Number	Reynolds Flow Number	Reynolds Jet Number
(d_{50} , mm)	(G, cm)	rpm	(D_p , cm)	(Fr_d)	($Re_f \times 10^4$)	($Re_p \times 10^4$)
0.52	10 / 15 / 20	590 / 670 / 745	6.5 / 10*	7.73–15.01	4.61–13.77	1.28–3.79
1.28	10	590 / 670 / 745	6.5 / 10 / 13	4.99–12.59	4.61–23.27	1.28–6.46
4.00	10	590 / 670 / 745	6.5 / 10 / 13	2.79–7.06	4.61–23.27	1.28–6.46
8.30	10 / 15 / 20	590 / 670 / 745	6.5 / 10 / 13	1.89–4.87	4.61–23.27	1.28–6.46

*Tests for $D_p = 13$ cm conducted were not included because the scour depth reached the bottom of the flume.

The evolution of a typical scouring profile attains the equilibrium conditions after a specific time. Beyond this time, the dimensions of the scour hole remain unchanged. Chin et al. [8] explained this time with experiments for a water jet flow. They concluded that the flow pushes the sediment particles up to the upstream slope of the deposition mound, but the particles slide back and settle into a stable location under the equilibrium condition because the particles do not have sufficient momentum to cross the deposition mound. Thus, it can be stated that at the equilibrium state the scour hole is formed even if this dynamic process repeats itself.

In the present study, the time-dependent variation of the maximum scour depth was measured to consider the duration till the scour hole attained its equilibrium state during each test. Figure 6.1 shows the time development of the maximum scour depth for different propeller diameters and speeds on fine sand bed material of $d_{50}=0.52$ mm.

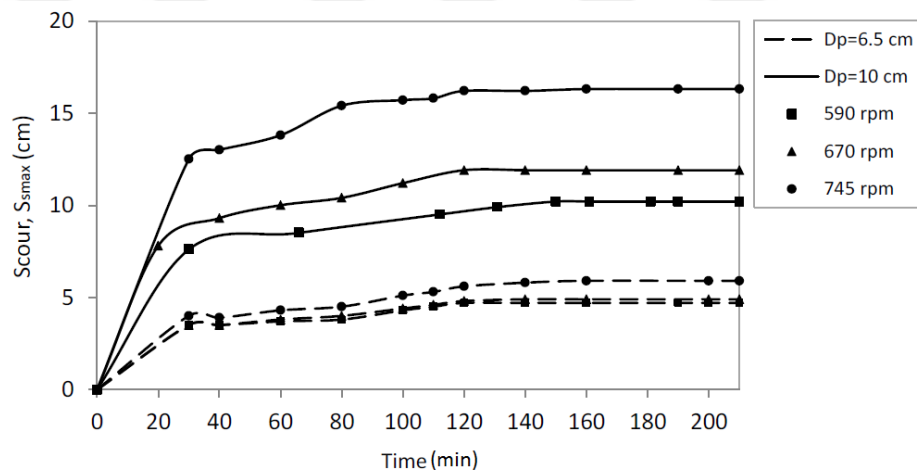


Figure 6.1 Time development of maximum scour depth with $D_p = 6.5$ cm and 10 cm for $G = 10$ cm on sand bed, with $d_{50} = 0.52$ mm

Figure 6.1 shows that the scour formations reached their equilibrium conditions at a specific time after the propeller started to rotate. Hence, by considering all the experimental tests, the duration was chosen to be 160 minutes, after which all of the tests had reached their equilibrium states. This unchanged maximum scour depth is called as the maximum equilibrium scour depth (S_{smax}). S_{smax} were measured as 10.2 cm for 590 rpm propeller speed and $D_p=10$ cm at $G=10$ cm. Similarly, scour depths remained unchanged after 140 minutes at 11.9 cm and 16.3 cm for 670 rpm and 745 rpm propeller speeds, respectively (Figure 6.1). Hence, by considering all the unconfined experimental tests; it was decided that 160 minutes was the duration of time needed for the scour formations to reach the equilibrium states.

Measurements also showed that the scour depths reached more than 70% of S_{smax} during the time of 30% of the total duration. It can also be stated that the greater part of the scouring formation occurs in a very short time when the total test duration is considered. Comparatively, little variation of the scour depth occurs after the first 100 minutes.

Hong et al. [5] called the equilibrium state of the scouring formation as the asymptotic stage in their study. They also defined three more stages before this equilibrium state as initial, developing and stabilization stages (see Figure 1.6 in Chapter 1). These four stages were observed similarly in the experimental tests of the present study as seen in Figure 6.2. According to this, first in the initial stage, primary scour hole is formed very quickly at about 5 minutes with small ripples behind it. Then a small scour hole formed beneath the propeller after 10 minutes of the propeller rotation while the primary hole deepens. During stabilization stage the small and primary scour increase and the distance between them decrease. During the tests, after approximately 140 minutes in the last stage which is called the asymptotic stage, both the small and the primary scour holes merge and remain still.

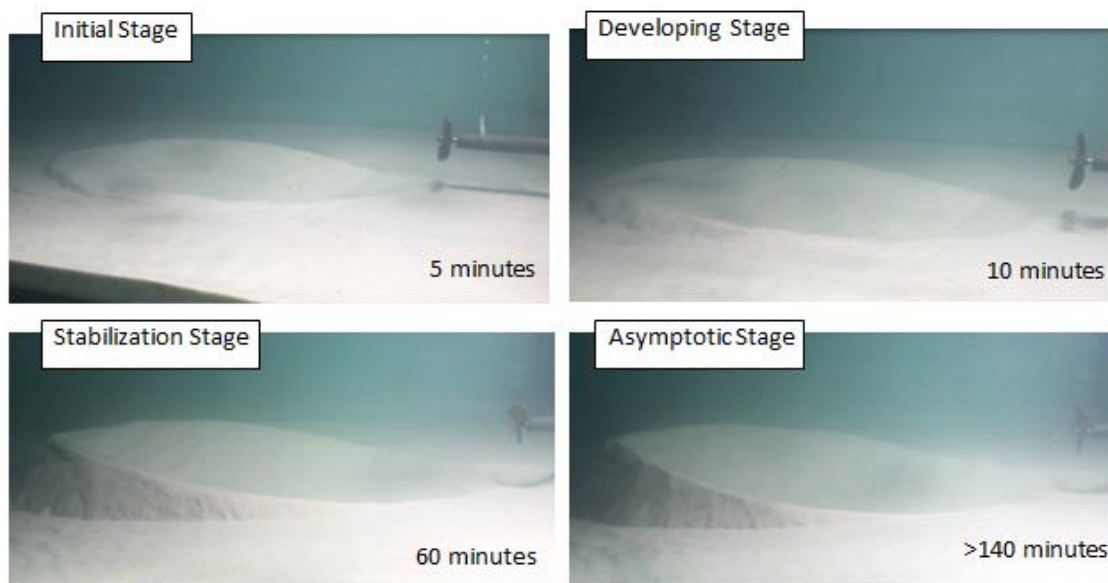


Figure 6.2 Time dependent evolution of scour profile without structure over sediment bed sizes of $d_{50}=0.52$ mm with $D_p=10$ cm, $G=10$ cm at 745 rpm

Densimetric Froude number as a ratio between inertia force and the gravitational force, Fr_d may be considered as the driving force on the sand bed. All test conditions shown in Table 6.1 were given in detail with Fr_d and efflux velocity (U_0) values calculated by using Equation (5.3) in Table 6.2.

Table 6.2 Summarized test conditions

Propeller Diameter	Propeller Speed		Sediment Bed Size	Gap Height	Efflux Velocity	Densimetric Froude Number
	D _p (cm)	Hertz				
6.5	40	597	0.52	10	0.72	7.82
6.5	45	671	0.52	10	0.81	8.79
6.5	50	744	0.52	10	0.89	9.74
10	40	595	0.52	10	1.10	11.99
10	45	665	0.52	10	1.23	13.40
10	50	774	0.52	10	1.43	15.59
6.5	40	597	0.52	15	0.72	7.82 *
6.5	45	670	0.52	15	0.80	8.77 *
6.5	50	745	0.52	15	0.90	9.76 *
10	40	596	0.52	15	1.10	12.01
10	45	670	0.52	15	1.24	13.50
10	50	745	0.52	15	1.38	15.01
6.5	40	597	0.52	20	0.72	7.82 *
6.5	45	672	0.52	20	0.81	8.80 *
6.5	50	746	0.52	20	0.90	9.77 *
10	40	597	0.52	20	1.10	12.03
10	45	670	0.52	20	1.24	13.50
10	50	745	0.52	20	1.38	15.01
6.5	40	595	1.28	10	0.71	5.03
6.5	45	670	1.28	10	0.80	5.66
6.5	50	744	1.28	10	0.89	6.29
10	40	596	1.28	10	1.10	7.75
10	45	673	1.28	10	1.24	8.75
10	50	746	1.28	10	1.38	9.70
13	40	591	1.28	10	1.42	9.99
13	45	666	1.28	10	1.60	11.26
13	50	743	1.28	10	1.79	12.56
6.5	40	596	4.00	10	0.72	2.82
6.5	45	673	4.00	10	0.81	3.19
6.5	50	746	4.00	10	0.90	3.53
10	40	596	4.00	10	1.10	4.34
10	45	670	4.00	10	1.24	4.88
10	50	744	4.00	10	1.38	5.42
13	40	591	4.00	10	1.42	5.60
13	45	665	4.00	10	1.60	6.30
13	50	738	4.00	10	1.77	6.99
6.5	40	595	8.30	10	0.72	1.91 *
6.5	45	665	8.30	10	0.81	2.17 *
6.5	50	745	8.30	10	0.90	2.44 *
10	40	595	8.30	10	1.10	2.99
10	45	670	8.30	10	1.24	3.37

Table 6.2 Summarized test conditions (cont'd)

10	50	744	8.30	10	1.38	3.74
13	40	593	8.30	10	1.42	3.88
13	45	665	8.30	10	1.60	4.35
13	50	744	8.30	10	1.77	4.87
6.5	40	595	8.30	15	0.71	1.95 *
6.5	45	665	8.30	15	0.80	2.17 *
6.5	50	745	8.30	15	0.90	2.44 *
10	40	595	8.30	15	1.10	2.99 *
10	45	664	8.30	15	1.23	3.34
10	50	745	8.30	15	1.38	3.75
13	40	592	8.30	15	1.42	3.87
13	45	665	8.30	15	1.60	4.35
13	50	739	8.30	15	1.78	4.83
6.5	40	595	8.30	20	0.71	1.95 *
6.5	45	665	8.30	20	0.80	2.17 *
6.5	50	745	8.30	20	0.90	2.44 *
10	40	595	8.30	20	1.10	2.99 *
10	45	665	8.30	20	1.23	3.35 *
10	50	745	8.30	20	1.38	3.75 *
13	40	591	8.30	20	1.42	3.87
13	45	664	8.30	20	1.60	4.34
13	50	738	8.30	20	1.77	4.83
*No scour was formed						

Fr_d between 1.95 to 9.77, no scour hole was formed for higher propeller gaps, such as $G = 15$ cm and 20 cm above the sediment bed, whereas scour hole was observed at a lower propeller gap such as at $G = 10$ cm. Since the propeller gap plays an important role in the scour formation, initiation of the scour formation was determined by considering both the gap ratio (G/D_p) and Fr_d .

Hong et al. [5] investigated critical conditions for initiation of scouring and they defined an empirical Equation (1.10) related to Fr_d and G/D_o . Hong et al. [5] performed their experiments in the test ranges of $5.55 \leq Fr_d \leq 11.1$ to define the critical densimetric Froude number (Fr_{dc}) shown as follows:

$$Fr_{dc} = 4.114 \frac{G}{D_o} \quad \text{for} \quad 2.87 > \frac{G}{D_o} \geq 0.5 \quad (6.1)$$

In the present study, Figure 6.3 shows critical conditions for the initiation of scouring by considering all test results for $1.95 \leq Fr_d \leq 15.01$ as listed in Table 6.2.

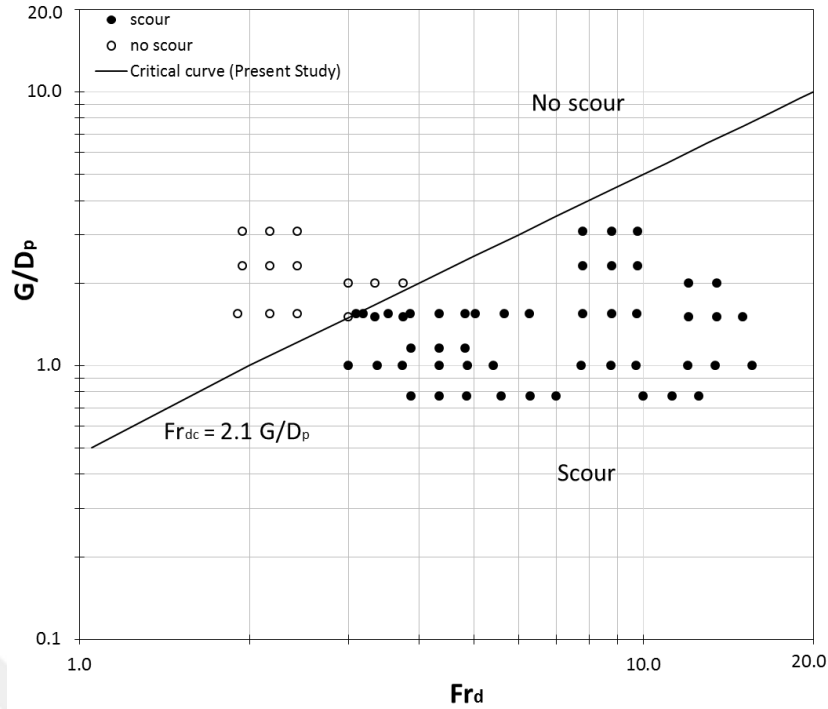


Figure 6.3 Critical conditions for the initiation of scour caused by the propeller jet flow

The left - hand side of the line represents no scour conditions, whereas scour hole formation conditions are shown on the right-hand side in the Figure 6.3. According to this representation, critical densimetric Froude number for the initiation of the propeller jet scouring can be obtained by considering G/D_p which is similar to Hong et al. [5]'s definition as follow,

$$Fr_{dc} = 2.1 \frac{G}{D_p} \quad \text{for} \quad 3.08 \geq \frac{G}{D_p} \geq 0.77 \quad (6.2)$$

Equation (6.1) has the compatibility with the data obtained from the previous studies that were conducted with circular wall jet and square jet (see Figure 1.9 in Chapter 1). Experimental conditions for the data set defined by Hong et al. [5] under propeller jet mechanism are given in Table 1.5. They tested two different propeller diameters of 10 cm and 21 cm over two uniformly distributed sediment bed materials of $d_{50}=0.024$ cm and 0.034 cm. Equation (6.1) gives higher critical Fr_d the same with G/D_p for the initiation of scouring when compared with Equation (6.2). Equation (6.2) includes a wider range of data set than Hong et al. [5]'s with coarser bed material sizes of $d_{50}=0.052$ cm, 0.128 cm, 0.4 cm and 0.83 cm and smaller propeller diameter of 6.5 cm while other parameters such as; water depth, gap height and propeller speeds are similar. When the test results of this study were added to

Hong et al. [5]'s, it was observed that the critical curve for the initiation of the scouring shifted to the left within the range of $1.95 \leq Fr_d \leq 15.01$ (Figure 6.4).

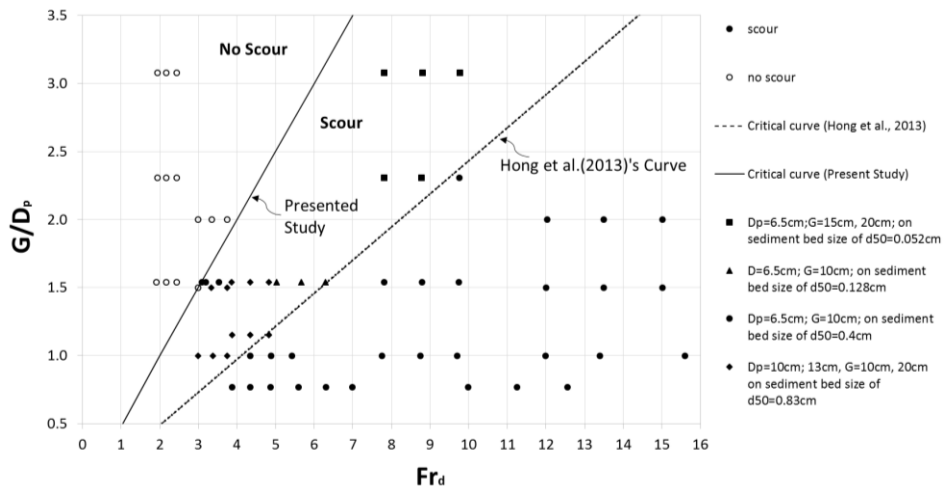


Figure 6.4 Critical curve for the initiation of scour

The critical scour initiation conditions defined by Hong et al. [5] agreed with the experimental data sets of Chiew and Lim [2] and Karki et al. [6] whose experiments were conducted with submerged circular and square jets, according to the relationship between Fr_d , the ratio of propeller gap, and circular jet diameter (G/D_o) (Figure 6.7). Hong et al. [5] carried out their experiments by using very limited test conditions. Their test range is $5.55 < Fr_d < 11.1$ and $0.5 < G/D_p < 1.5$ whereas the range in the present study is $1.89 \leq Fr_d \leq 15.01$ and $0.77 \leq G/D_p \leq 3.08$ (Figure 6.5).

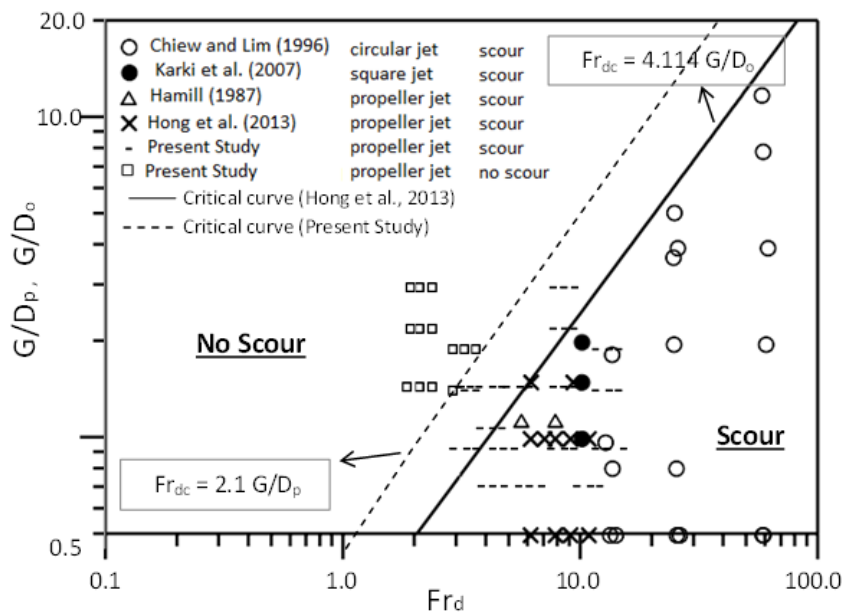


Figure 6.5 Comparisons of critical curves for the initiation of scouring

The scouring formation of a bed, which consists of cohesionless sediments by a propeller jet without considering its structure was characterized by Hong et al. [5] for small and primary scour holes and a deposition mound behind these holes (Figure 1.5 in Chapter 1). A similar formation was observed in the present study as seen in Figure 6.6 and Figure 6.7. All measured scour profiles in the present study are given in Figures A.1 - A.50.

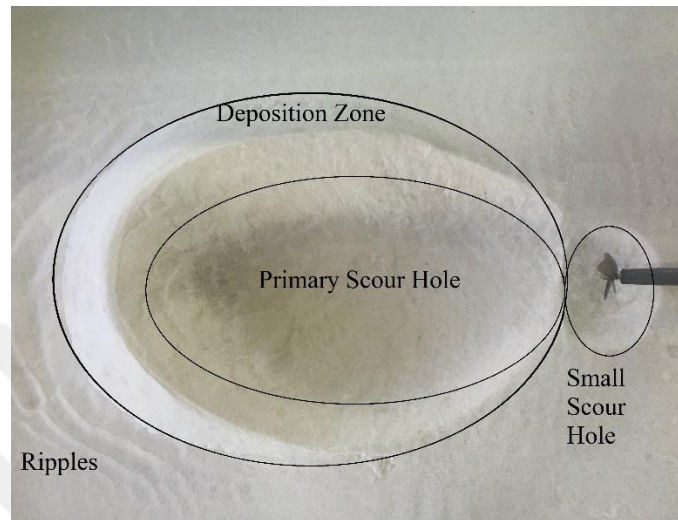


Figure 6.6 Plan view of the scour formation with $D_p=10$ cm, at 590 rpm and $G=10$ cm, on $d_{50}=0.52$ mm sediment bed

Figure 6.8 shows the shape of the unconfined scour formation with two different eroded areas and a deposition zone around the primary hole. Figure 6.7 shows scour profile formations with eroded scour holes and a deposition zone at the equilibrium state with respect to the original bed level (OBL) at zero.

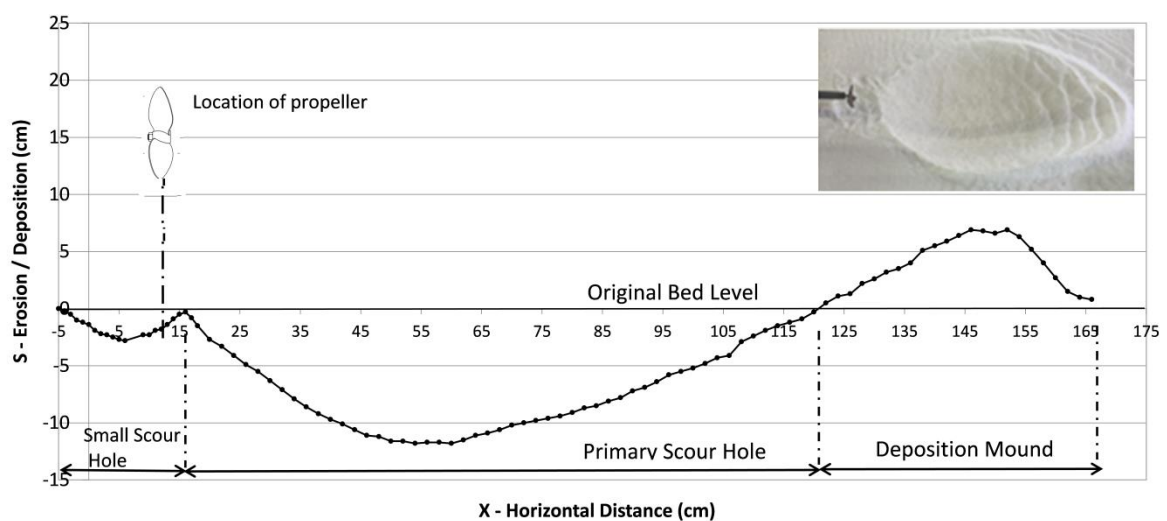


Figure 6.7 Scour profile with $D_p=10$ cm, at 745 rpm and $G=15$ cm, on sediment bed of $d_{50}=0.52$ mm

The shape of the unconfined scour profile may differ with its wide, length and presence of small scour formations under the propeller for changing test conditions such as; the propeller diameter, speed and gap. Typical scour formations with two scour holes werenot distinctly observed for smaller propeller diameter of 6.5 cm at 15 cm above the undisturbed bed as seen in Figure 6.10.

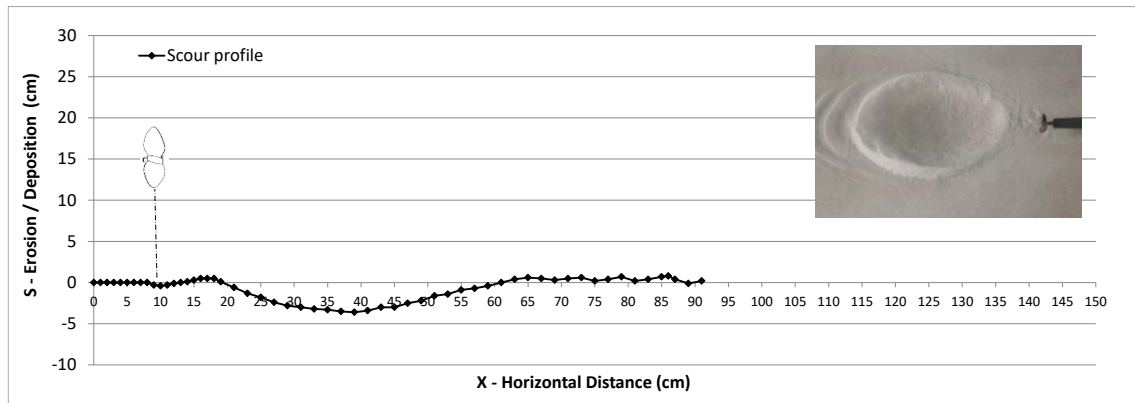


Figure 6.8 Scour profile with $D_p=6.5$ cm, at 745 rpm and $G=15$ cm, on sediment bed of $d_{50}=0.52$ mm

Figure 6.9 shows an isometric three – dimensional view of unobstructed scour formation measured by using General Acoustics Ultralab (UWS Ultralab ULS 80 D). This illustration shows the general view of the unconfined profile that is reasonably symmetrical about the propeller centerline. Also, no distinct small scour formation was observed while primary scour hole was being formed.

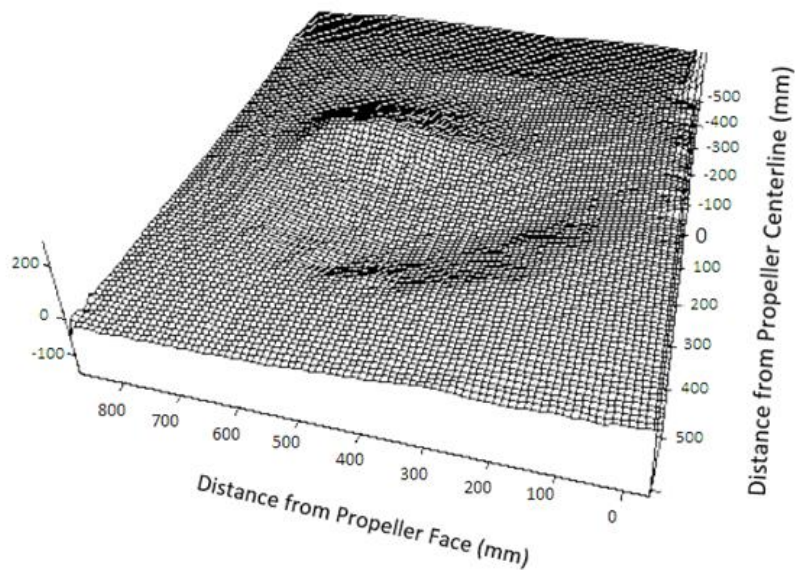


Figure 6.9 Isometric view of the scour hole with $D_p=6.5$ cm, at 745 rpm $G=15$ cm, on sediment bed of $d_{50}=0.52$ mm

The small scour hole had a very weak formation or it was not observed in the tests conducted with smaller propeller diameter of 6.5 cm over four different sediment bed materials at different propeller gaps of 15 and 20 cm. In addition, the small scour formation was not observed on coarse sediment bed material of $d_{50}=8.3$ mm for greater diameters of propeller as 10 and 13 cm (Figures A.37- 50). All the test observations with or without the small scour formation are summarized in Table 6.3.

Table 6.3 Observations of small scour formation according to different test conditions

(cm)	Material 1 ($d_{50}=0.52$ mm)		Material 2 ($d_{50}=1.28$ mm)			Material 3 ($d_{50}=4$ mm)			Material 4 ($d_{50}=8.3$ mm)		
	D_p										
G	6.5	10	6.5	10	13	6.5	10	13	6.5	10	13
10	W	✓	X	✓	✓	X	✓	✓	N.S	X	X
15	X	✓	-	-	-	-	-	-	N.S	X	X
20	X	✓	-	-	-	-	-	-	N.S	N.S	X
- : There are not any tests conducted, N.S : No scour occurred, W : Weak, Scour hole was not observed significantly, X : Small scour hole was not observed, ✓ : Small scour hole was observed.											

As an example, Figure 6.10 shows the typical scour formation with two scour holes observed with larger densimetric Froude numbers ($Fr_d = 7.90$ and 15.01). However, the small scour hole beneath the propeller was not distinctly observed with smaller densimetric Froude numbers ($Fr_d = 3.75$ and 5.43). Similarly with larger propeller diameters of 10 and 13 cm, the small scour formation was not observed on the coarser sediment bed material with $d_{50} = 8.3$ mm for smaller densimetric Froude numbers ($Fr_d = 3.00$ and 6.46). G is also a significant parameter for the formation of typical scour holes. As an example; at higher propeller gaps of 15 and 20 cm the small scour hole had a very weak formation or it was not observable in the tests conducted with a smaller D_p of 6.5 cm on all the four different sediment bed materials, even with larger densimetric Froude numbers ($Fr_d = 8.77$ and 9.76).

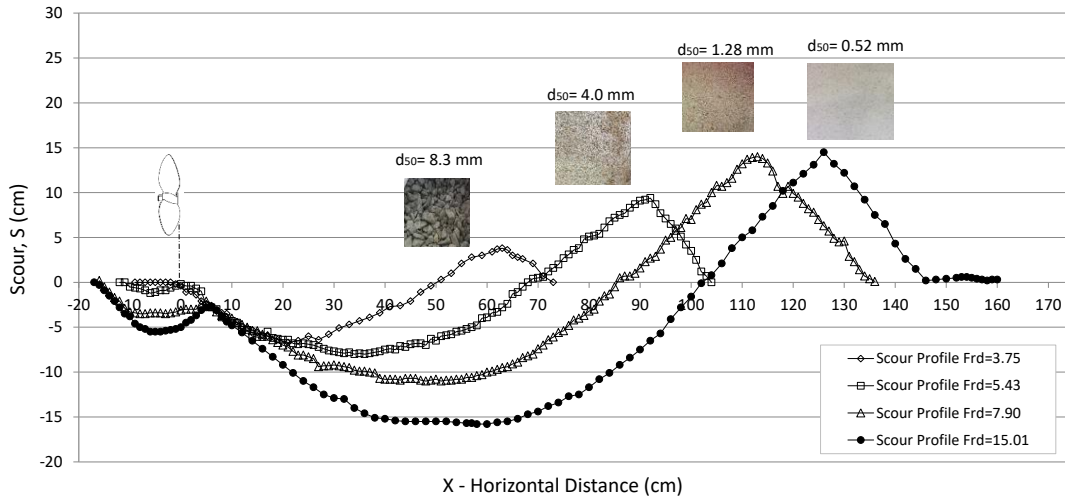


Figure 6.10 Scour profiles with $D_p = 10$ cm and $G = 10$ cm at 670 rpm propeller speed for different sediment bed materials

The functional relationship between G/D_p and Fr_d can also be used to determine the small scour formation. A small scour hole was formed under the propeller for values of Fr_d less than $5.3G/D_p$, as expressed in Equation (6.3), when considering all the test results in which scour initiated (Figure 6.11).

$$Fr_d < 5.3G/D_p \quad (6.3)$$

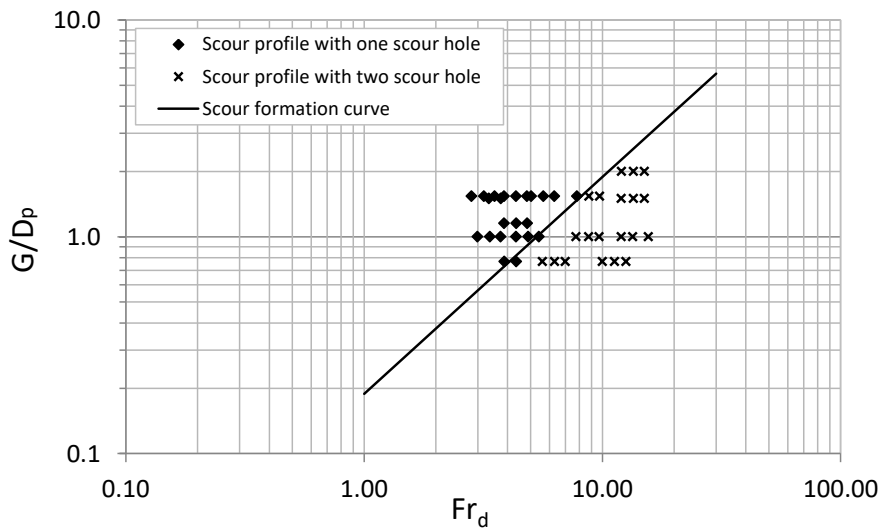


Figure 6.11 Scour profiles with or without small scour formation under the propeller in terms of Fr_d and G/D_p

Scour profile formations induced by the propeller jet were investigated by measuring the geometrical parameters of the scour hole such as; the maximum scour width (B_{smax}),

maximum scour length (L_{smax}), maximum scour depth (S_{smax}), at the end of a specific time period for each test (Figure 6.12).

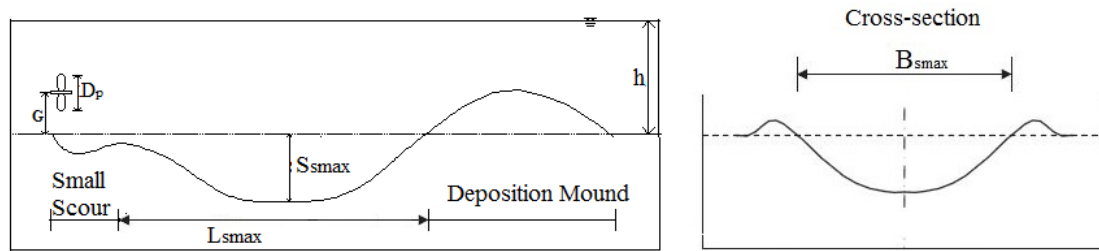


Figure 6.12 Dimensions of scour hole

Schematic diagram of scour profile without considering any structure, is given in Figure 6.13. Where; L_{smax} is the maximum length of the primary hole, X_c is the horizontal distance of deposition crest from propeller face, S_{smax} is the maximum scour depth, L_{tsmax} is the total length of scour holes both including small and primary holes, X_{mu} is the distance from the face of propeller to the maximum scour hole.

The main characteristics of the dimensions of a scour hole may change depending on D_p , G , sediment bed material and rotation speed (rpm).

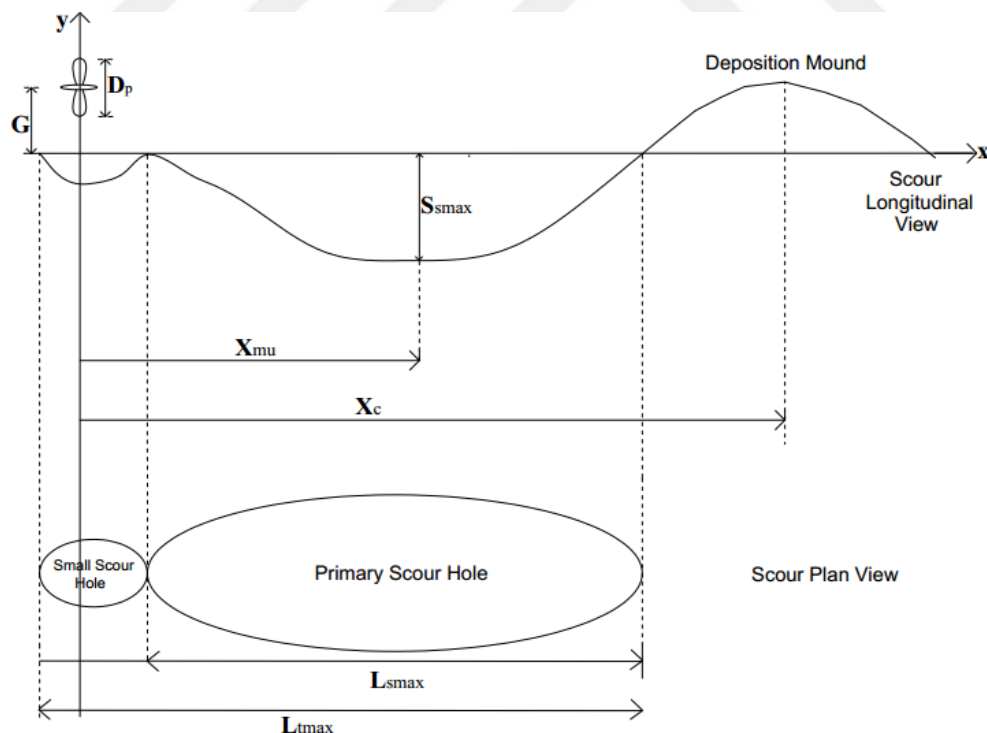


Figure 6.13 Schematic diagram of scour formations due to the propeller jet

Figure 6.14 shows the comparison of scour profiles over different sediment beds. As the materials used on the sediment beds go from finer to coarser material sizes increase whereas

the length (L_{smax}) and the depth of the primary scour hole decrease under the same test conditions such as the propeller gap, speed and diameter.

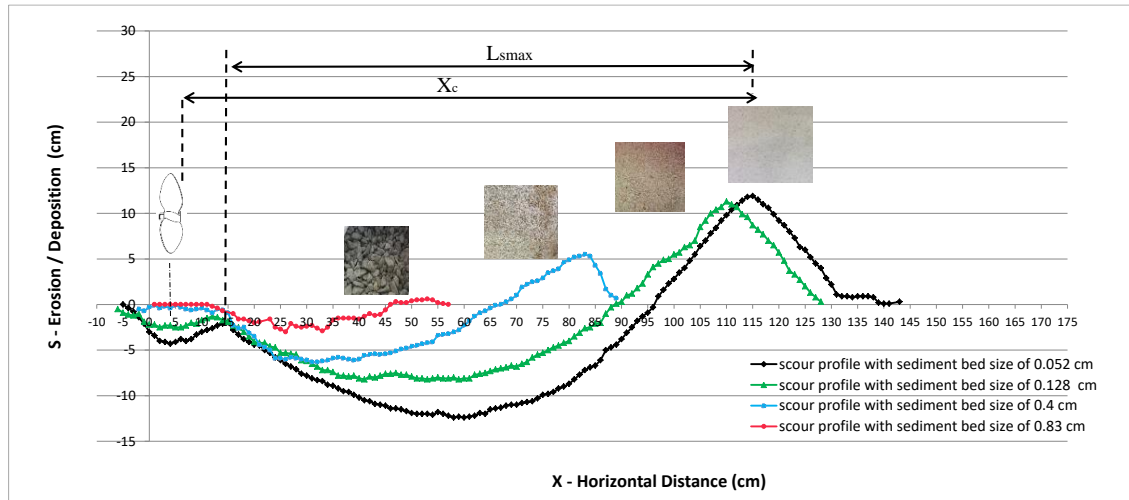


Figure 6.14 Scour profiles with $D_p=10$ cm, $G=10$ cm at 590 rpm for different sediment beds. The sediment bed plays an important role in the scour formation. As an example, no scour was formed with the smallest propeller diameter of 6.5 cm over the coarser sediment bed of $d_{50}=8.3$ mm whereas scour holes deepened on finer beds of 0.52 mm and 1.28 mm (Figure 6.15). The lengths (L_{smax}) of scour profiles over sediment beds of 0.52 mm and 1.28 mm were similar.

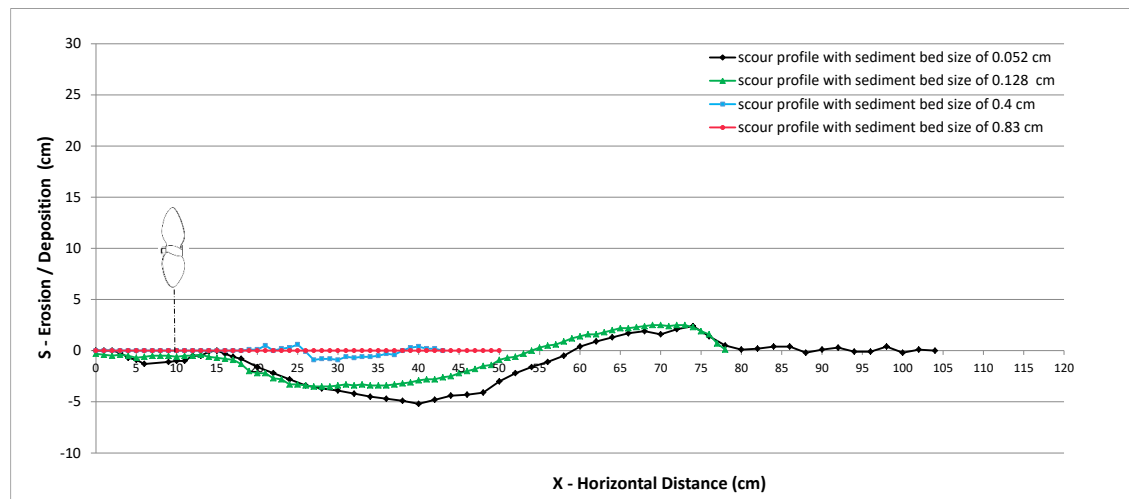


Figure 6.15 Scour profiles with $D_p=6.5$ cm, $G=10$ cm at 590 rpm over different sediment beds

However, the change in the primary scour hole length became significant over different sediment beds for the greater diameter of propeller of 10 cm (Figure 6.16). The length of the primary (main) scour hole (L_{smax}), decreased with increasing sediment bed material sizes. L_{smax} was approximately 60 cm less on finer sediment bed ($d_{50}=0.052$ cm) when

compared with coarser bed ($d_{50}=0.83$ cm) for $D_p=10$ cm at different rotation speeds of 590 rpm, 670 rpm and 745 rpm (Figure 6.16, Figure A.55, Figure A.56).

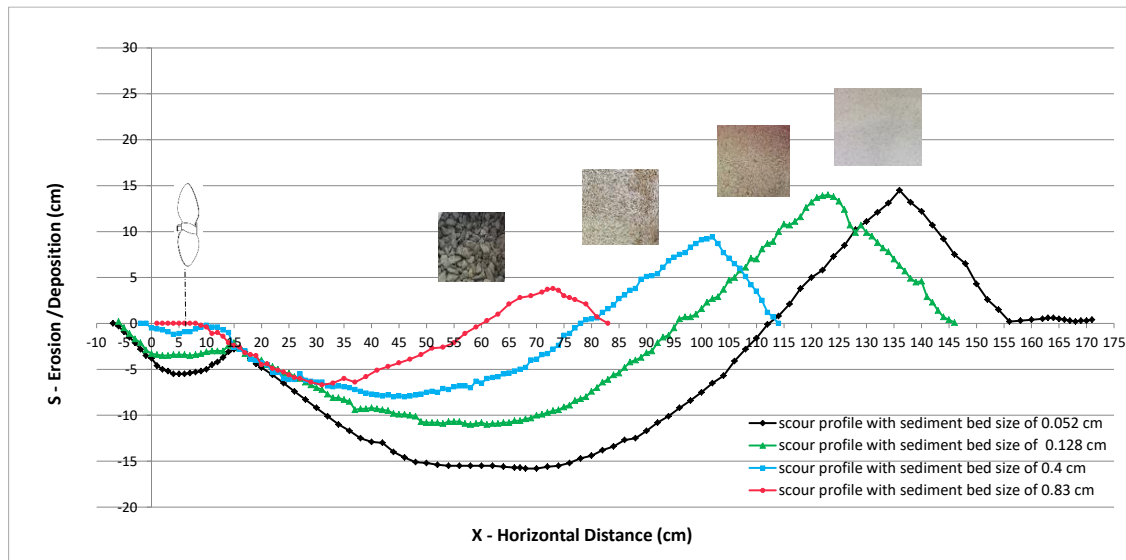


Figure 6.16 Scour profiles with $D_p=10$ cm, $G=10$ cm at 745 rpm over different sediment beds

The length of the primary scour hole (L_{smax}) for the coarse sediment bed material ($d_{50}=4$ cm) was measured approximately 40 cm shorter than the the scour measured in tests conducted with fine bed materials ($d_{50}=1.28$ mm and 0.52 mm) at different speeds for the 13 cm propeller diameter (Figure 6.17, Figure A.58, Figure A.59). Thus, it is stated that the sediment bed and propeller diameter have significant effects on scour formation and the location for the depositon crest.

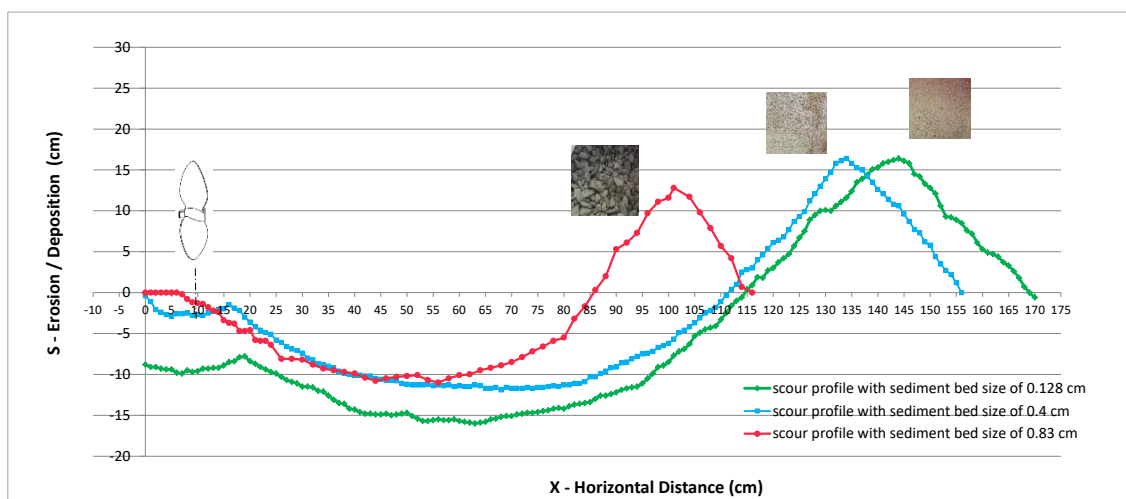


Figure 6.17 Scour profiles with $D_p=13$ cm, $G=10$ cm at 745 rpm over different sediment beds

According to scour profile evolutions, the distance of the deposition crest from the propeller's face (X_c) is always less over coarser bed materials when other parameters such as propeller gap, diameter and speed were kept constant (Figure 6.18).

Tests results indicated that similar scour profiles were observed over relatively finer sediment beds ($d_{50}=1.28$ mm and 0.52 mm) with the same propeller diameter, speed and gap. In addition, the deposition crests were formed at about same distance from the propeller's face (Figure 6.18). Figure 6.18 also shows that the length (X_c) is almost the same for both bed materials of $d_{50}=1.28$ mm and 4 mm for 13 cm propeller.

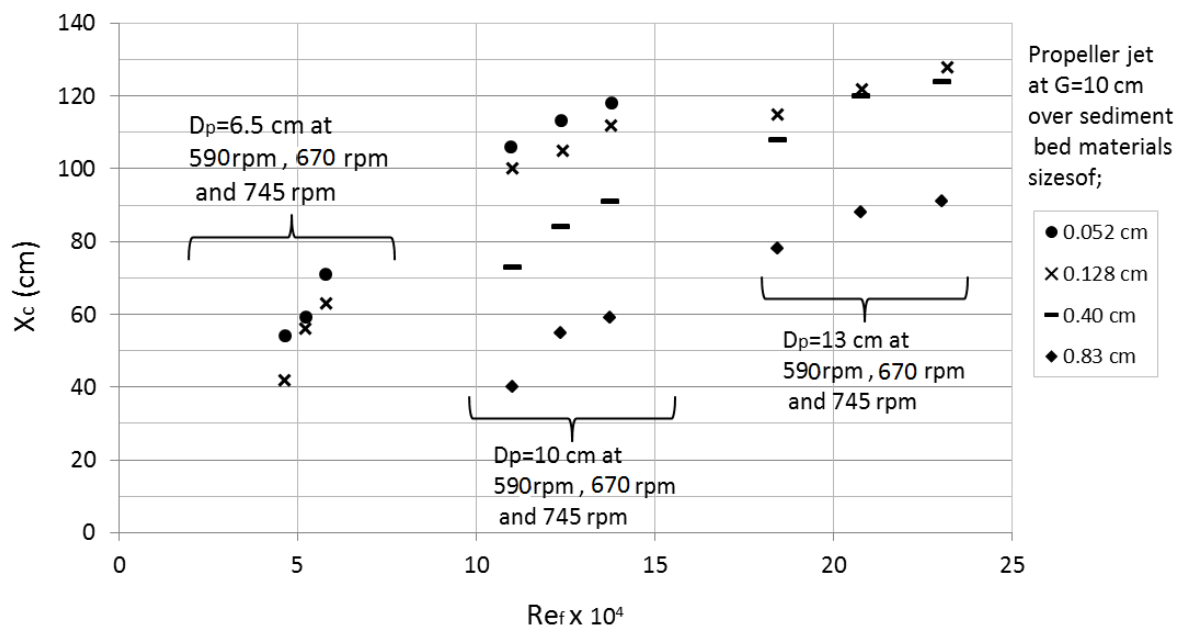


Figure 6.18 X_c versus Re_f of the propellers over different sand bed materials at constant gap Chiew and Lim [2] and Hong et al. [5] found that the deeper the scour hole (S_{smax}) was, it associated with a lower G/D_p under the same test conditions. Different gaps of the propeller have effective roles on the scour formation. Increasing gap of the propeller causes a lower S_{smax} with a decreasing distance between the propeller face and deposition crest (X_c).

In Figure 6.19 and Figure 6.20, scour profiles are given with different gaps (as $G=10$ cm, 15 cm and 20 cm) over finer and coarser sediment bed materials, respectively.

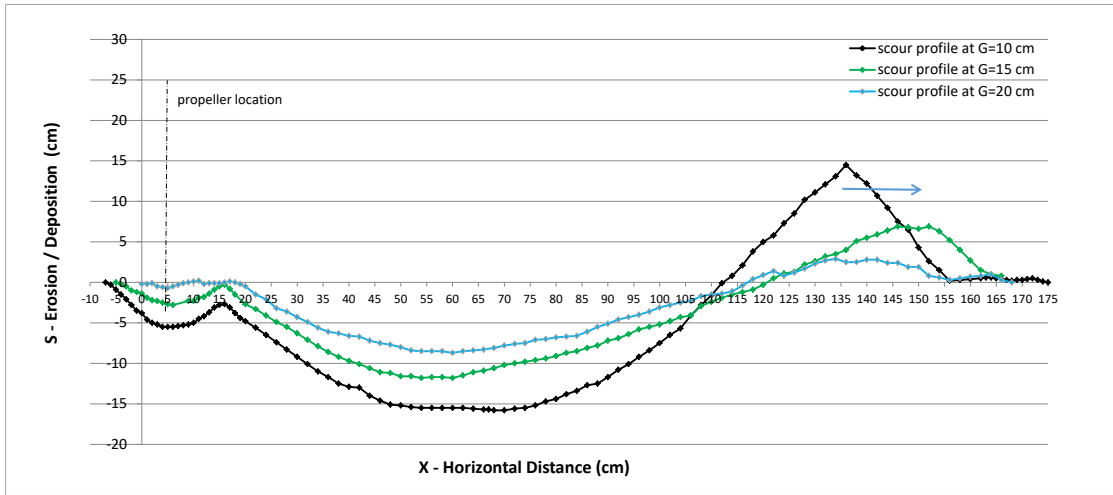


Figure 6.19 Scour profiles for different gaps of the propeller on $d_{50}=0.52$ mm beds ($D_p=10$ cm at 745 rpm)

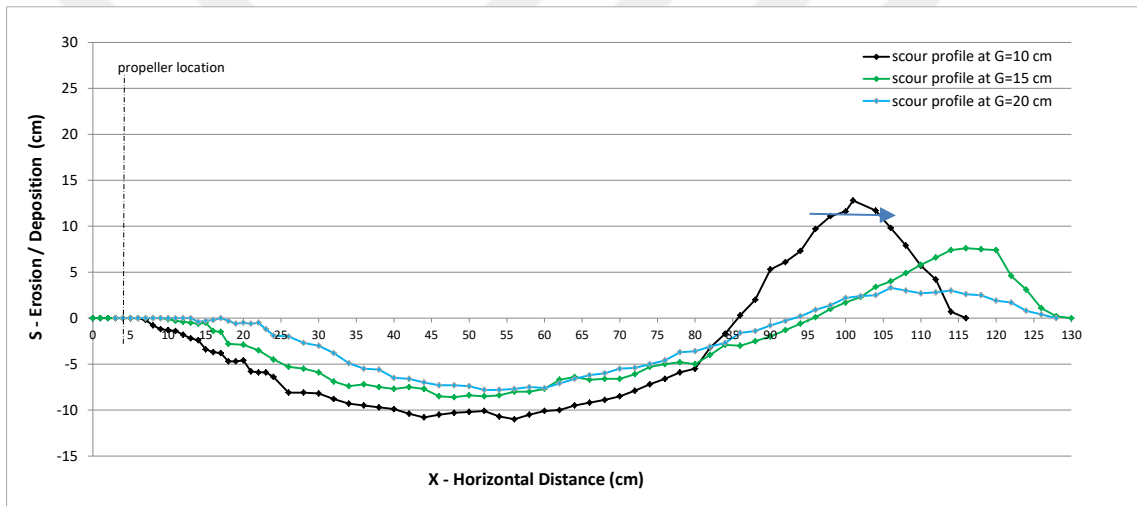


Figure 6.20 Scour profiles for different gaps of the propeller on $d_{50}=8.30$ mm beds ($D_p=13$ cm at 745 rpm)

Increasing the propeller gap from 10 cm to $G=15$ cm and $G=20$ cm, also cause an increase in the width of the scour hole. Deposition crest almost disappears for the smaller propeller diameter ($D_p=6.5$ cm) with increasing gap of the propeller as seen in Figure 6.21.

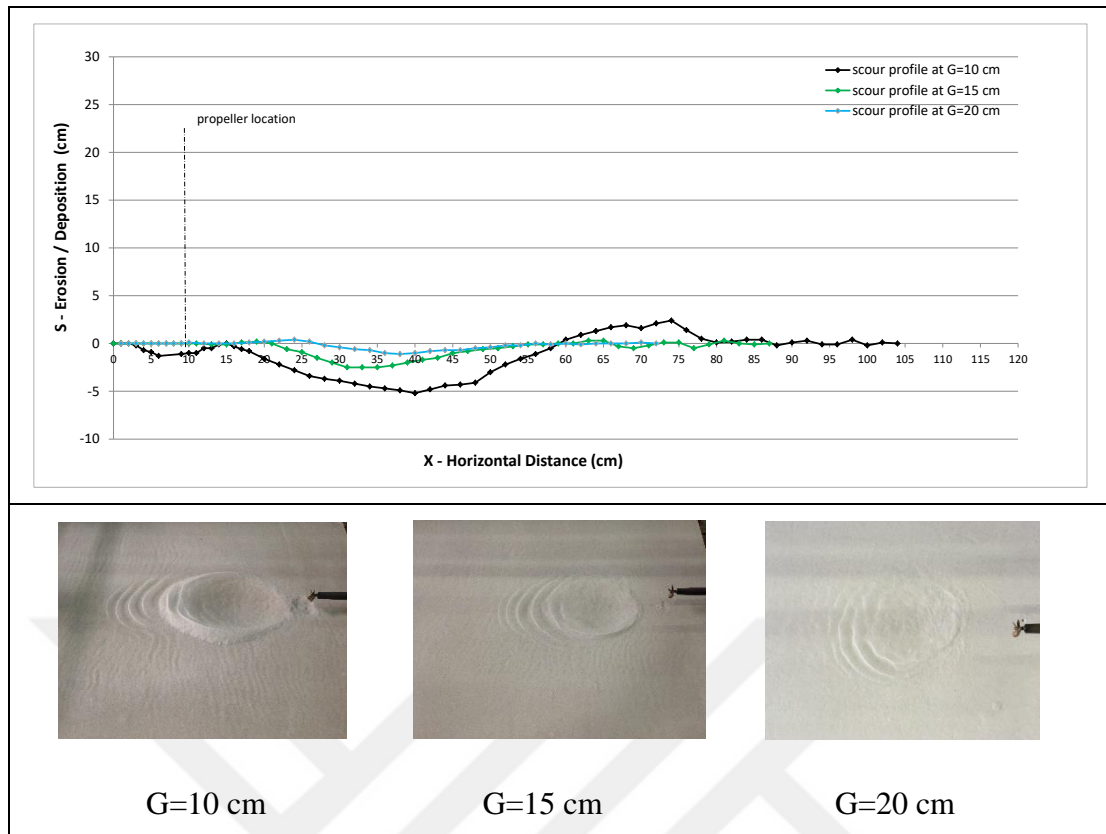


Figure 6.21 Scour profiles with different gaps of the propeller with $D_p=6.5$ cm, at 670 rpm on the sediment bed of $d_{50}=0.52$ mm

When different bed materials were tested, the scour profiles and the locations of the deposition crests of finer material intersected with the coarser material's at different gaps for the same propeller diameters. The positions of the deposition crest were similar with $G=10$ cm over bed material size with 0.52 mm at the same gap of the propeller ($G=10$ cm) on $d_{50}=1.28$ mm bed, while it intersected with profiles on coarser beds of $d_{50}=4$ mm and 8.3 mm at higher gap of $G=15$ cm, and 20 cm, respectively (Figure 6.22). As a result, deposition crests for higher gaps over fine bed material and deposition crests for lower gaps over coarse bed material accumulated approximately at the same distance from the propeller face. All scour profiles with different propeller gap were given in Figures A.60 – A.68).

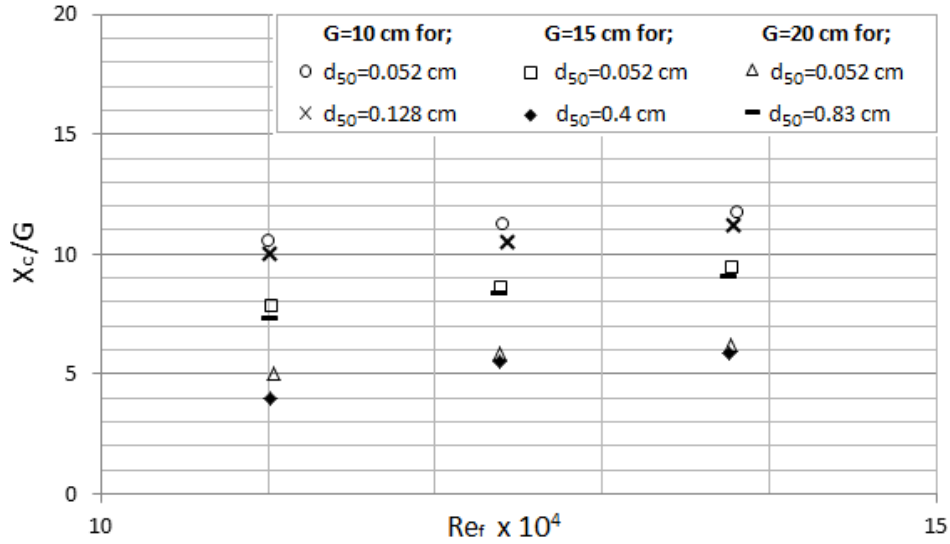


Figure 6.22 X_c/G versus Re_f for $D_p=10$ cm over different sand beds

Dimensions of a scour hole (L_{smax} , S_{smax} , and B_{smax}) formed by a circular jet related to the Fr_d were investigated by Chiew and Lim [2]. They proposed a relationship between Fr_d and the dimensionless scour length as a ratio of L_{smax}/D_o with a circular wall jet for $4.8 < Fr_d < 85.3$ as follows:

$$\frac{L_{smax}}{D_o} = 4.41 Fr_d^{0.75} \quad (6.4)$$

They also defined the relationship between Fr_d with dimensionless scour width B_{smax}/D_o and S_{smax}/D_o (Equation (6.5) – Equation (6.6)).

$$\frac{B_{smax}}{D_o} = 1.9 Fr_d^{0.75} \quad (6.5)$$

$$\frac{S_{smax}}{D_o} = 0.21 Fr_d \quad (6.6)$$

Experimental data conducted by the propeller jet by Hamill [7] and Chiew and Lim [2]'s data set associated with circular wall jet are given in Figure 6.23. Hamill [7]'s study was conducted with two different propellers (diameters of 6.1 cm and 15.4 cm) on different sediment bed material sizes of 0.76 cm and 1.46 cm at $G=12.5$ cm and 17.5 cm for $8.3 < Fr_d < 11$. In the present study, data range was increased for propeller jet as $2.99 < Fr_d < 15.01$ with given test conditions in Table 6.4.

Figure 6.23 reveals that the data associated with the circular jet mostly have a larger Fr_d than the data associated with the propeller jet. In addition, the solid line in this figure represents

the formula proposed by Chiew and Lim [2] which was for a circular wall jet, and it does not fit the test data obtained with the propeller jet for $2.99 < Fr_d < 15.01$. Thus, the Equation (6.6) was rewritten using S_{smax}/D_p versus Fr_d for the propeller jet with a determination coefficient (R^2) of 0.71 as follows:

$$\frac{S_{smax}}{D_p} = 0.09 Fr_d \quad (6.7)$$

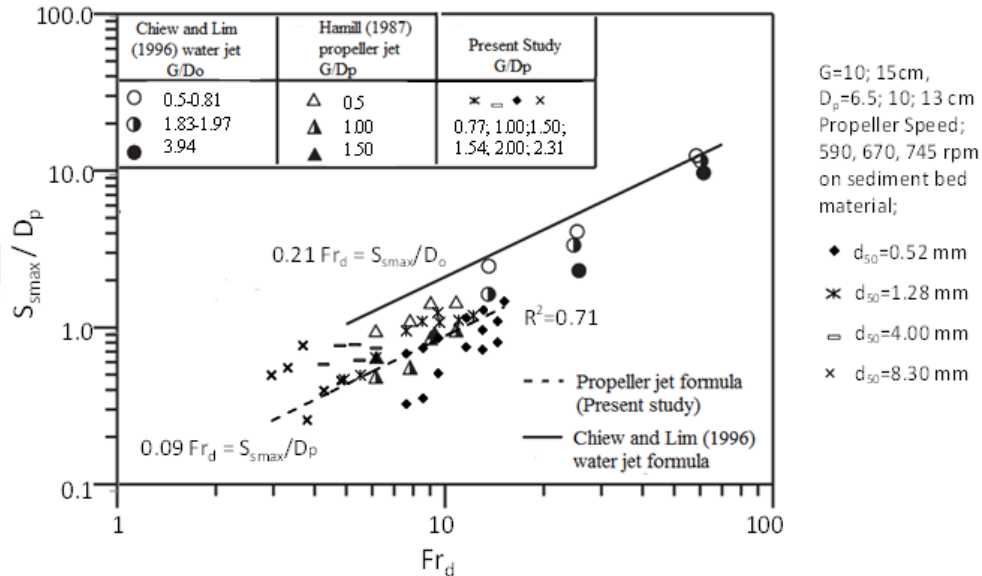


Figure 6.23 Relationship between S_{smax}/D_p and Fr_d for propeller and circular wall jet conditions

The slopes of the formulas for the propeller and circular jets are significantly different, and the scour depth has a smaller value for the propeller jet at the same Fr_d when compared with the circular jet. This is in agreement with the study conducted by Hawkswood et al. [58] explaining that a circular jet causes more effective erosion than a propeller jet of a similar velocity owing to the angle of incidence of the water jet with the bed.

Figure 6.24 and Figure 6.25 display the relationship between Fr_d and the dimensionless scour width B_{smax}/D_p and length L_{smax}/D_p , respectively. These relationships are defined under the propeller jet mechanism in Equations (6.8) and (6.9).

$$\frac{B_{smax}}{D_p} = 0.89 Fr_d^{0.8} \quad (6.8)$$

$$\frac{L_{smax}}{D_p} = 0.52 Fr_d^{1.59} \quad (6.9)$$

The solid lines in Figure 6.24 and Figure 6.25 are the formulas proposed by Chiew and Lim [2] for a circular wall jet and the dashed lines are determined for the propeller jet using the dataset in the present study.

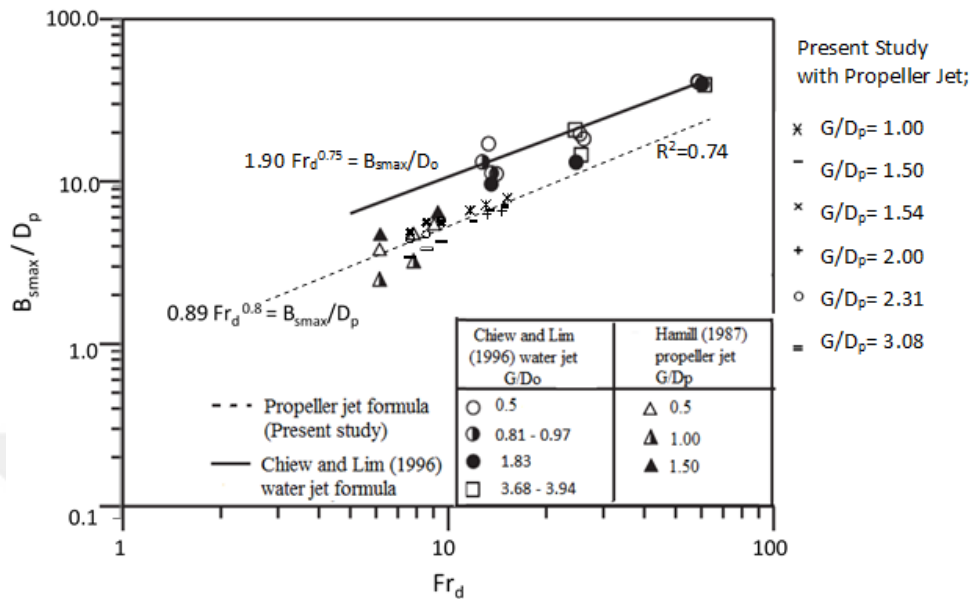


Figure 6.24 Relationship between B_{smax}/D_p and Fr_d for the propeller and circular wall jets

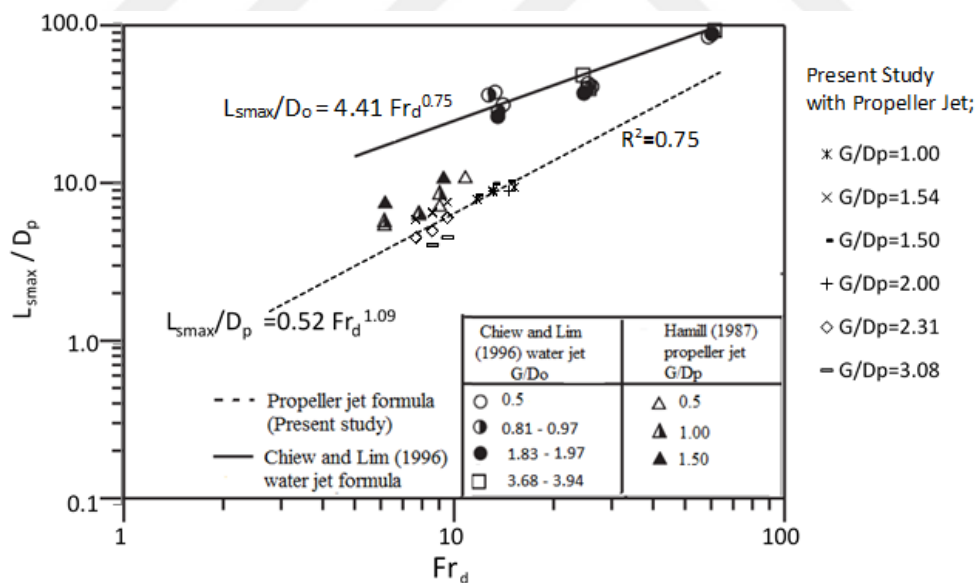


Figure 6.25 Relationship between L_{smax}/D_p and Fr_d for the propeller and circular wall jets

Previous researchers proposed different equations to estimate the maximum scour (S_{max}) depth for the time history of scouring process in the literature. Hamill et al. [9] and Hong et al. [5] studied a propeller jet and took the time required for the determination of S_{max} into consideration. Hong et al. [5] defined an equation valid between $0.5 < G/D_p < 2.87$ and $5.55 \leq Fr_d \leq 11.1$ while considering D_p , G , d_{50} , Fr_d to estimate the time-dependent scour depth in

Equation (1.4). This is presented in Chapter 1. Hamill et al. [9] also defined another equation for estimating the scour depth as a logarithmic function of time valid for the ratio clearance versus propeller diameter, i.e., $0.5 < C/D_p < 2.5$ and $5.55 \leq Fr_d \leq 18.53$ and this is presented in Equation (1.18).

The maximum scour depths at the equilibrium state were calculated by using the equations defined by Hamill et al. [9] and Hong et al. [5]. The computed results were compared with the measured S_{smax} at the end of each test after the scour formations reached their equilibrium states under summarized conditions. They are listed in Table 6.2.

Comparison(s) of the measured and predicted values of S_{smax} is presented in Figure 6.26 and Figure 6.27 . using equations proposed by Hong et al. [5] and Hamill et al. [9], respectively. Both the predicted scour depths with Equation (1.4) and Equation (1.18) underestimated the measured depths with $R^2=0.68$ and 0.78 , respectively.

The equation by Hong et al. [5] underestimated the scour depths approximately 60% less than the measured scour depths. Their equation was rearranged in the form in Equation (1.4) to achieve a better consistency between the measured and predicted values (Figure 6.26) as follows:

$$\begin{aligned} \frac{S_{max}}{D_p} &= k_1 \left[\log_{10} \left(\frac{U_o t}{D_p} \right) - k_2 \right]^{k_3} \\ k_1 &= 0.042 \cdot Fr_d^{1.12} \cdot \left(\frac{G}{D_p} \right)^{-0.40} \cdot \left(\frac{G}{d_{50}} \right)^{-0.17} \\ k_2 &= 1.882 \cdot Fr_d^{-0.009} \cdot \left(\frac{G}{D_p} \right)^{2.302} \cdot \left(\frac{G}{d_{50}} \right)^{-0.441} \\ k_3 &= 2.477 \cdot Fr_d^{-0.073} \cdot \left(\frac{G}{D_p} \right)^{0.53} \cdot \left(\frac{G}{d_{50}} \right)^{-0.045} \end{aligned} \quad (6.10)$$

A comparison of the measured and predicted scour depths with the modified equation of Hong et al. [5] is shown in Figure 6.26. The modified equation was applied to all the test results of the present study for $0.77 < G/D_p < 3.08$ and $2.17 < Fr_d < 15.01$. The experimental data set in the present study has a wider range than previous studies because of the inclusion of tests conducted on coarser sediment bed materials. Therefore, the modified equation has been rewritten with larger dataset, and the new equation has yielded a better estimation of the scour depths with a higher determination coefficient of $R^2 = 0.84$.

Hong et al. [5] governed their equation by using sediment bed material sizes of $d_{50} = 0.024$ cm and 0.034 cm. However, the modified equation formulated in Equation (6.10) was fitted by using the dataset of the present study. This dataset included the coarser sediment bed materials of $d_{50} = 0.052$ cm, 0.128 cm, 0.4 cm, and 0.83 cm with a smaller propeller diameter of $D_p = 6.5$ cm than the one used by Hong et al. [5].

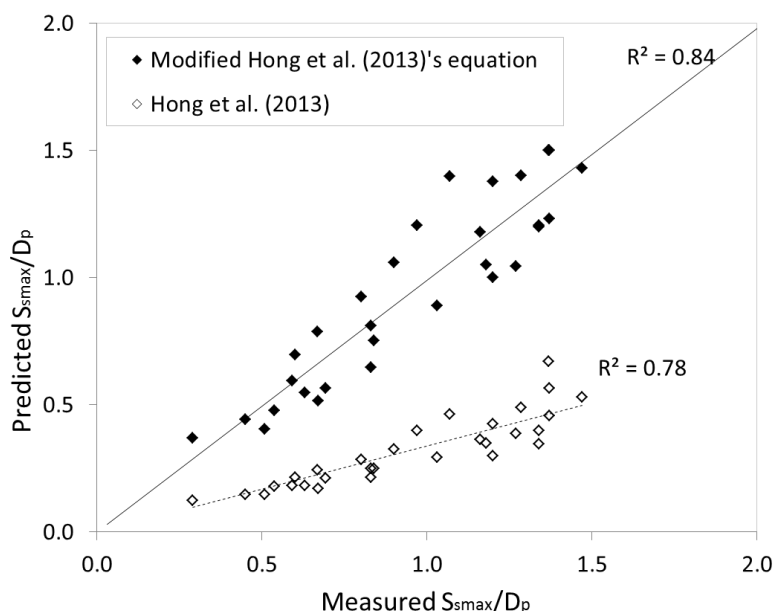


Figure 6.26 Comparison between the observed and calculated scour depths using equations proposed by Hong et al. [5]

Therefore, the propeller speeds were varied over a wider range of the dataset in this study from 0.0081 cm/sec to 0.0201 cm/sec that corresponds to an approximately 60% higher efflux velocity than in the study by Hong et al. [5], where the range was 0.0038–0.0068 cm/sec (Table 6.4). Thus, the modified equation defined in Equation (6.10) was governed by including a wider range of sediment bed materials with smaller propeller diameters at higher speeds.

The other estimation for the time-dependent maximum scour depth provided by Hamill et al. [9], was also rearranged to the form in Equation (6.11).

$$S_{max} = \Omega [1n(t)]^\Gamma$$

$$\Omega = 6.9 \cdot 10^{-4} \left(\frac{G}{d_{50}} \right)^{-4.63} \left(\frac{D_p}{d_{50}} \right)^{3.58} Fr_d^{4.535} \quad (6.11)$$

$$\Gamma = 3.8 \left(\frac{G}{d_{50}} \right)^{0.742} \left(\frac{D_p}{d_{50}} \right)^{-0.52} Fr_d^{-0.682}$$

Equation (6.11) is valid within the ranges of $0.77 < G/D_p < 3.08$ and $2.17 < Fr_d < 15.01$. The equation by Hamill et al. [9] underestimated the measured scour depths, whereas the Equation (6.11) yields a better estimation, as can be seen in Figure 6.27.

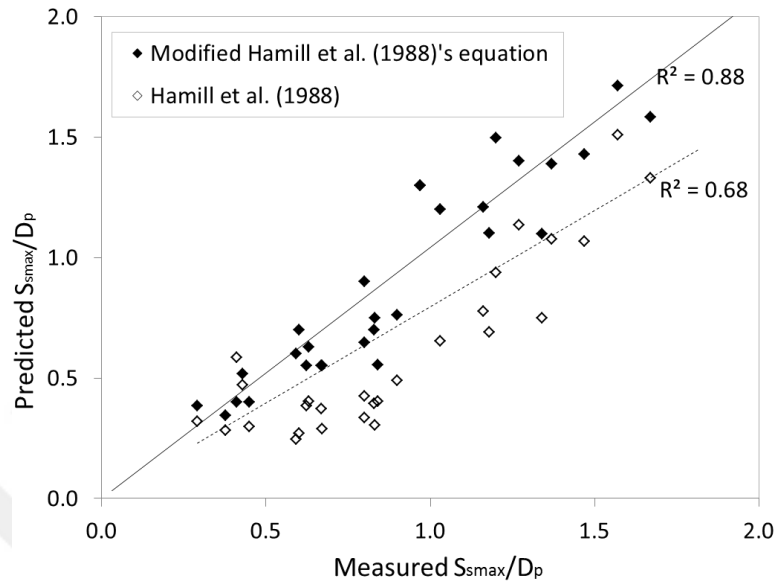


Figure 6.27 Comparison between the observed and calculated scour depths using equations proposed by Hamill et al. [9]

Even though the equation by Hamill et al. [9] provided better estimations than the equation by Hong et al. [5], both equations underestimated the maximum scour depths when compared with the results of the present study.

The ranges of the sediment bed material sizes and efflux velocities used in Hamill et al. [9] and Hong et al. [5]'s studies were limited to similar propeller gaps. It was therefore decided to extend the test conditions by considering finer and coarser sediment bed material sizes of $d_{50} = 0.052$ cm to 0.83 cm and efflux velocities of the propeller of 0.081 to 0.0201 cm/sec in the present study. An increased range of efflux velocities of 60% more than the ones in the previous studies led to the observations of deeper scouring formations. That is why both Hamill et al. [9]'s and Hong et al. [5]'s equations underestimated the scour depths while the modified equations (Equations (6.10) and (6.11)) that used a data set with a wider range of greater scour depths, were able to estimate the scour depth more accurately. Thus, the modified equations had increasing coefficients of Fr_d and propeller diameters and were able to predict deeper scours for higher efflux velocities with larger propeller diameters.

Table 6.4 Range of the data collected for the scours caused by a propeller jet in different studies

Researchers	G (=C+D _p /2, cm)	N	D _p (cm)	d ₅₀ (cm)	Fr _d	U ₀ (m/sec)
Hamill et al. [7]	*7.5, 12.5, 17.5	3, 4, 6	6.1, 7.6, 13.1, 15.4	0.076, 0.146, 0.3	5.55-18.53	0.00853, 0.01219
Hong et al. [5]	10.5, 15, 21		10, 21	0.024, 0.034	6.08-10.69	0.0038-0.0068
Present Study	10, 15, 20	4	6.5, 10, 13	0.052, 0.128, 0.4, 0.83	2.17-15.01	0.0081-0.0201

*These values were given as the distance from the propeller tip to sediment bed (C) by Hamill [9] while gap (G) is defined as the distance from the centerline of the propeller to the sediment bed.

Estimation of the maximum scour depth (S_{max}) without berth structure was investigated by previous researchers for circular jet and propeller jet as one of the important scour dimensions. Hamill et al. [9] and Hong et al. [5] studied the propeller jet and took the time for the determination of S_{max} into consideration. Also, Hong et al. [5] gave a definition of S_{max} both for the circular wall jet and propeller jet by considering Fr_{dc} given as follows:

$$Fr_{dc} = 4.114 \cdot \frac{G}{D_p} \quad (6.12)$$

$$13 \cdot \frac{S_{max}}{D_p} = 0.265 \cdot (Fr_d - Fr_{dc})^{0.955} \cdot \left(\frac{G}{D_p} \right)^{-0.022}$$

Figure 6.28 shows the change in S_{max}/D_p versus G/D_p associated data with circular wall and square jet. In this Figure, simulations of Equation (6.12) for different Fr_d values were in good agreement with data for circular and square wall jet. However, it included very limited data set for the propeller jet with $6.08 < Fr_d < 9.19$ for finer sediment bed materials of $d_{50} = 0.024$ and 0.034 cm. It was therefore decided to extend the data set for only the propeller jet, and Equation (6.12) was rearranged by using the data in this study.

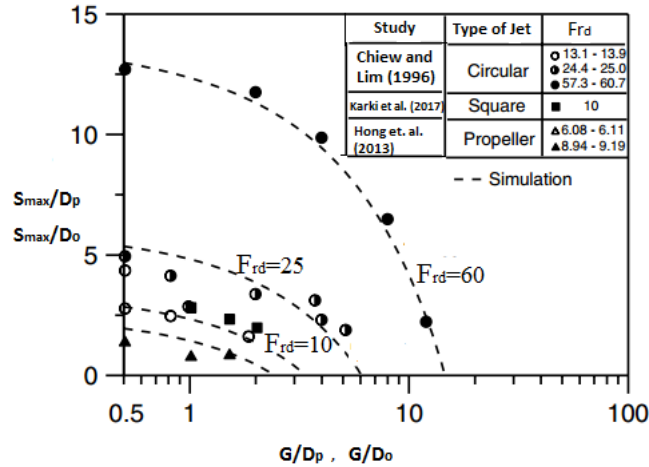


Figure 6.28 Relationship between S_{\max}/D_p and G/D_p for the circular and square wall jet with included propeller jet data (Hong et al. [5])

In the present study, their equation has been rewritten as Equation (6.13) with a wider range of $7.75 < Fr_d < 15.01$ for coarser sediment bed material sizes of $d_{50} = 0.52$ to 8.33 mm than in the study by Hong et al. [5]. This equation was expressed by considering Fr_{dc} as $2.1 G/D_p$ as previously defined in Equation (6.2) for the initiation of scouring. The estimation of the dimensionless maximum scour depth, in terms of S_{\max}/D_p , is as follows:

$$Fr_{dc} = 2.1 \frac{G}{D_p}$$

$$\frac{S_{\max}}{D_p} = 0.57 (Fr_d - Fr_{dc})^{0.33} \cdot \left(\frac{G}{D_p} \right)^{-1.1} \quad \text{for} \quad 2.82 \leq Fr_d \leq 15.01 \quad (6.13)$$

Figure 6.29 shows the relationship between S_{\max}/D_p and G/D_p for the propeller jet only. Based on the bed material sizes, Fr_d had different values between $2.82 \leq Fr_d \leq 15.01$, for the fine and coarse bed materials with $d_{50} = 0.52$ mm, 1.28 mm, 4.0 mm and 8.3 mm. Thus, the Equation (6.13) has been written to determine the S_{\max} with different propeller speeds within $590 - 745$ rpm valid for $0.77 < G/D_p < 3.08$. This equation agrees with the data of 0.87 as shown in Figure 6.29. This figure also shows that S_{\max}/D_p decreases with increasing G/D_p , and it is similar to the results in the study done by Chiew and Lim [2] for a circular jet that attributes this trend to jet diffusion.

S_{\max} for coarser bed material had smaller values than the values for finer bed materials. Thus, S_{\max}/D_p for coarser bed materials ($d_{50} = 8.30$ mm and 4.00 mm) had values below the

linearized plots of Equation (6.13) while S_{smax}/D_p for finer bed materials ($d_{50}= 1.28$ mm and 0.52 mm) was above this line.

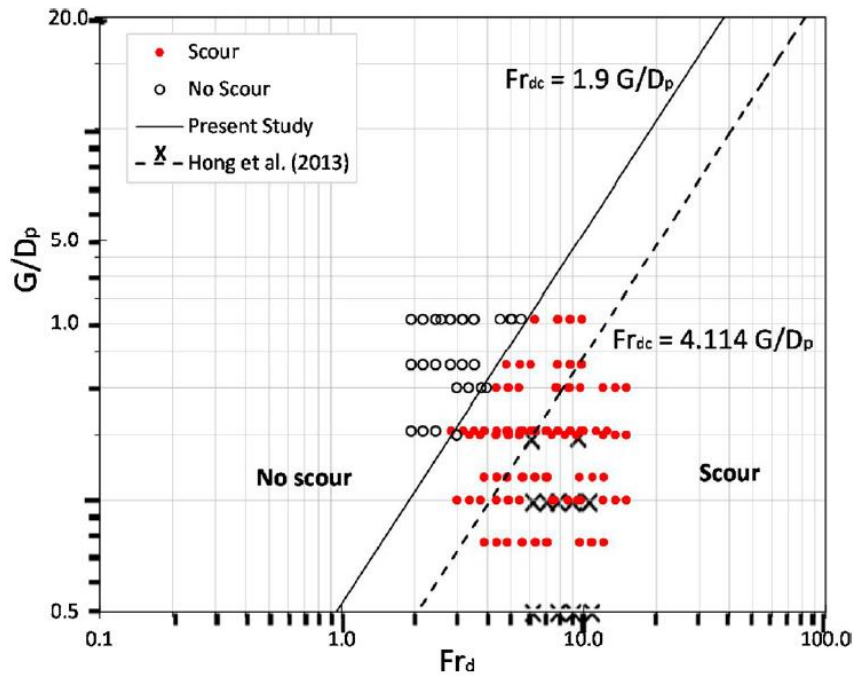


Figure 6.29 Relationship between S_{smax}/D_p and G/D_p for the propeller jet mechanism

Hamill et al. [9] also provided an expression for the estimation of the maximum scour depth location (X_{mu}) for the unconfined cases as illustrated in Figure 6.13 with Equation (6.14) as follows:

$$X_{mu} = Fr_d^{0.94} C \quad (6.14)$$

$$C = G - D_p / 2$$

where C is the clearance of the propeller, D_p is the diameter of the propeller, and Fr_d is the densimetric Froude number.

In the present study, Equation (6.15) is proposed to obtain the X_{mu} by using the relationship between the rotation speeds and the gaps of the propeller. Equation (6.15) is suggested based on a higher correlation agreement of $R^2 = 0.90$ (Figure 6.30) in comparison with Hamill et al. [9]'s Equations.

$$\frac{X_{mu}}{G^{0.09} D_p^{0.91}} = Fr_d^{0.724} \quad (6.15)$$

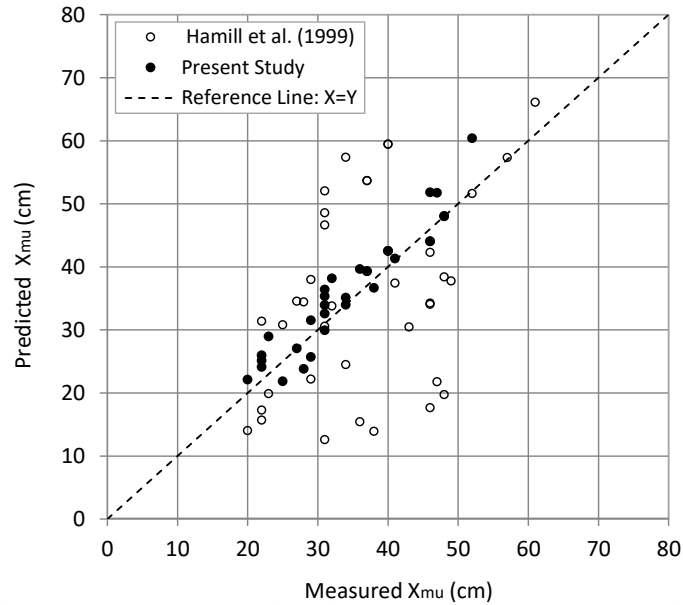


Figure 6.30 Comparison between the observed and calculated maximum scour depth location (X_{mu}) using the equation proposed by Hamill et al. [9]

6.2 Scour Formation Around Pier Piles

Container vessels, ro-ro vessels, and ferries, are known to be the major contributors to the erosion problem encountered near berth structures. PIANC [28] reported that the scouring damage incurred by propellers and transverse thrusters during berthing and/or unberthing conditions, without the use of tugs, was first discovered at ro-ro and ferry berths. Investigations of scouring problems have been studied upon consideration of different types of berths. For example, Sumer and Fredsøe [57] have defined the closed - type and open - type structures. However, there have been very limited studies on the scouring due to propeller jets for piled berths as open-type structures. This is because the scour formed near pile - supported structures is a more complex problem owing to pile obstruction and jet diffusion mechanisms, as reported by Chin et al. [8]. Among the earlier researchers study who conducted experiments either with or without confined jets are such as; Blaauw and Van der Kaa [1], Verhey [23], Hamill [7], Stewart [12], Hashmi [13], Hong et al. [5], and who conducted experiments on scouring processes are such as Wei and Chiew [26]. They proposed equations for the estimation of the scour depth both for the unconfined and confined cases with quay walls. Scour, piled near the supported structures is more complex including; (1) scour around the piles, in particular those near the berthing face and (2) scour of the slopes underneath the quay, as PIANC [28] reported. Chin et al. [8] and Yuksel-Ozan and Yuksel [59] investigated the scour around a vertical pile with a physical model under circular wall jet effect.

In addition, Hoffmans [60] stated that the dimensions of the scour hole should be known for the hydraulic structures since these structures could collapse into their scour holes owing to erosion. In accordance with this aim, scour depths should be investigated at the toe of piles (S_o) as one of the primary scour dimensions. Hamill et al. [9] gave an estimation of the scour induced by propeller jets for the unconfined and confined conditions with closed-type quay walls. Hong et al. [5] also examined the scouring process induced by a single propeller jet without considering any structures, and defined equations used to estimate the scour. Yew et al. [25] investigated scouring process with the absence of berth structure and proposed equations for prediction of the scour induced by twin-propeller wash. Mujal-Colilles et al. [61] studied the scouring process due to a single propeller jet and they used the data set at a particular basin's bathymetries during a specific period. They also evaluated the proposed equations for the estimation of the scour depth with considering the data obtained from the basin field.

Wei and Chiew [26] investigated the scouring action induced by a ship propeller jet in an open type quay with an armored slope and vertical skirting. Wei and Chiew [26] examined three dimensional flow fields and turbulence characteristics of propeller jets in the presence of a plane bed boundary using the particle image velocimetry (PIV). Wei and Chiew [62] extended their study for a better understanding of scouring action in an open type quay by considering velocity and turbulence data by using the PIV technique.

This chapter of the present study aims to extend laboratory tests on the scouring induced by a ship propeller jet during berthing and / or unberthing for pile -supported, pier type berth structures. The tests already undertaken in the experimental flume without obstruction was extended with the effect of the confinement of the propeller wash by a pile obstruction. The effect of different sand bed material, pile diameter with different propeller speeds and diameters on scour formation around pile were investigated.

Model tests were performed with the same experimental conditions as defined for no pile cases. Tsinker [34] also stated that one of the main factors which affects the propeller-induced scour in design is the position of the propeller in relation to underkeel clearance. The gap between the propeller axis and the sand bed (G) was chosen by considering the recommended minimum of 1.5 m of the underkeel clearance in fairways and maneuvering areas. Thus, the model propeller's dimensions were adjusted to 10 cm, 15 cm and 30 cm for 1.50 m, 2.25 m and 3.00 m prototype gap heights, respectively.

In the experimental model, pile obstructed tests were conducted using plexiglass pile diameter of 4 cm, and two steel piles that had diameters of 9 cm and 14 cm with corresponding to the prototype pile diameters of 0.6 m, 1.35 m, and 2.1 m, respectively, for the same geometrical scale factors used for the propeller diameters at a scale of 1:15 presented in Chapter 5.

Totally 381 tests were conducted by changing variables such as; propeller diameters (6.5 cm, 10 cm, 13 cm), propeller speeds (745, 670 and 590 rpm when frequency regulator was adjusted at 40, 45 and 50 Hz) gap of the propeller (G=10, 15 and 20 cm) on four different sediment bed material sizes ($d_{50}=0.52$ mm, $d_{50}=1.28$ mm, $d_{50}=4$ mm and $d_{50}=8.3$ mm).

Each test was repeated by changing one variable at a time, and keeping all other parameters constant in the instance when the pile was fixed at a location of X=10 cm apart from the propeller's face. In addition, this distance was subsequently tested at different pile locations (X=10, 20, 30, 40 cm) with 4 cm pile on finer sediment bed size of 1.28 mm. All test conditions are listed in Table 6.5.

Table 6.5 Experimental conditions for tests with piles

Defined Parameters of the Experimental Tests with Piles					
Pile	Sediment Bed Size	Gap	Propeller Diameter	Propeller Speed	Distance between propeller and pile
(d_o , cm)	(d_{50} , mm)	(G, cm)	(D_p , cm)	(rpm)	(X, cm)
4	0.52	10 / 15 / 20	6.5 / 10*	590 / 670 / 745	10
	1.28	10 / 15 / 20	6.5 / 10 / 13	590 / 670 / 745	10, 20, 30, 40
	4.00	10 / 15 / 20	6.5 / 10 / 13	590 / 670 / 745	10
	8.30	10 / 15 / 20	6.5 / 10 / 13	590 / 670 / 745	10
9	0.52	10 / 15 / 20	6.5 / 10*	590 / 670 / 745	10
	1.28	10 / 15 / 20	6.5 / 10 / 13	590 / 670 / 745	10
	4.00	10 / 15 / 20	6.5 / 10 / 13	590 / 670 / 745	10
	8.30	10 / 15 / 20	6.5 / 10 / 13	590 / 670 / 745	10
14	0.52	10 / 15 / 20	6.5 / 10*	590 / 670 / 745	10
	1.28	10 / 15 / 20	6.5 / 10 / 13	590 / 670 / 745	10
	4.00	10 / 15 / 20	6.5 / 10 / 13	590 / 670 / 745	10
	8.30	10 / 15 / 20	6.5 / 10 / 13	590 / 670 / 745	10

*Tests for $D_p=13$ cm on the sediment bed of $d_{50}=0.52$ mm, are not included because during the tests the scour depth reached the bottom of the flume.

At the end of each test, scour profile formations were measured by using a limnimeter (Figure 6.31) when they reached at the equilibrium stage. This final scour profile termed as scour profile, varied within a range of ± 1 mm during the experiments. After the propeller

rotation started scour profiles reached their asymptotic stages after 160 minutes later. This duration is also the same duration for the initiation of scour without pile cases.



Figure 6.31 Scour profile measurements by using a limnimeter

The critical conditions necessary for the initiation of scour formation due to propeller jet flow around a pile type berth structure were investigated by executing all the tests listed in Table 6.5 with $1.91 \leq Fr_d \leq 15.01$. Figure 6.32 shows the cases without scour and with scour conditions.

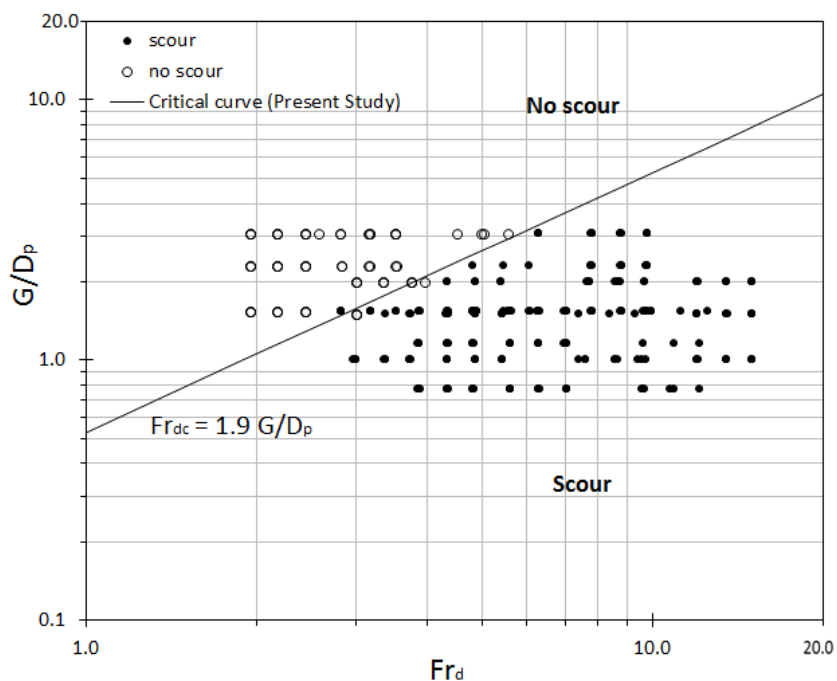


Figure 6.32 Critical curve for initiation of scour with the presence of a pile type structure

In Figure 6.32 the left hand side of the line represents the conditions without scours, whereas scour hole formations at the toe of the pile, are shown on the right hand side. The critical densimetric Froude number (Fr_{dc}) for the initiation of the scour hole around the pile was obtained with respect to G/D_p given as follows:

$$Fr_{dc} = 1.9 \frac{G}{D_p} \quad \text{for} \quad 3.08 \geq \frac{G}{D_p} \geq 0.77 \quad (6.16)$$

Equation (6.16) has given similar Fr_{dc} as Equation (6.2) with coefficient 2.1 in the absence of pile. This is because the scour forms in an easier manner around a pile than no pile conditions, due to downflows and vortex flow field at the toe of pile which initiates scouring on sand bed.

In the existence of pile various scour profiles are formed when compared with the absence of pile case conditions. Hamill [7] reported that the scour profile induced by an unconfined propeller jet is nearly symmetrical along the jet centerline. The same situation is observed for scour profiles with the absence of pile cases as seen in Figure 6.33.

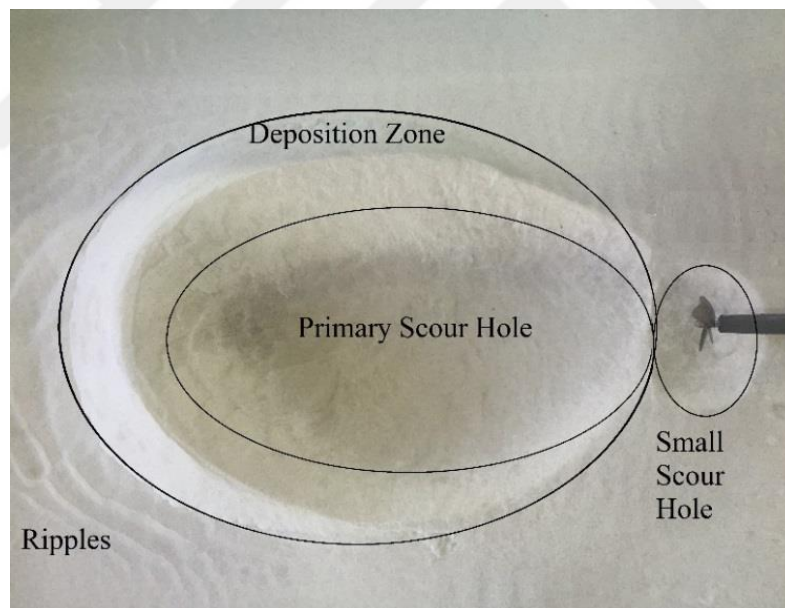
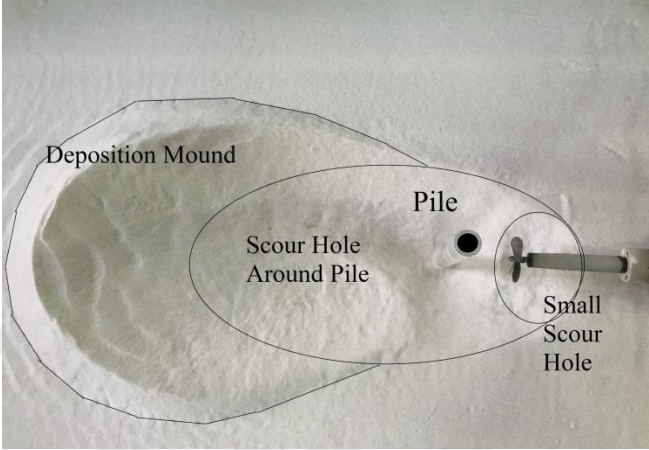
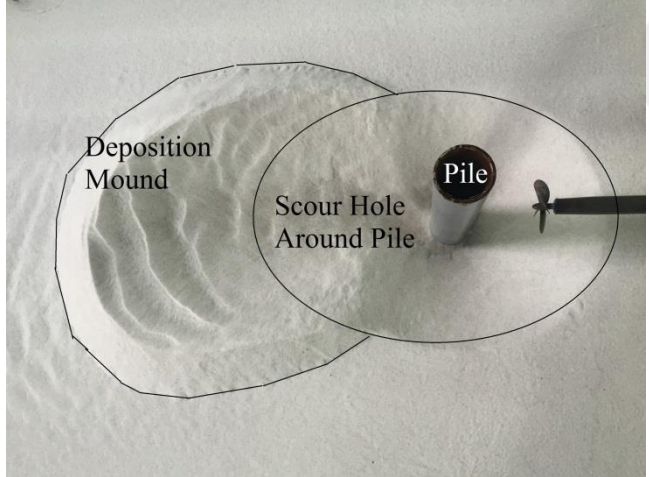
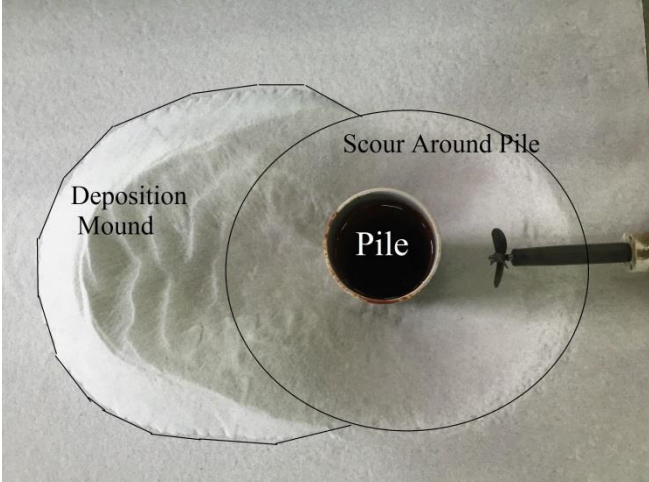


Figure 6.33 Typical plan view of a scour profile without pile for sediment bed of $d_{50}=0.52$ mm ($D_p=10$ cm at 590 rpm)

However, scour profiles with pile at the asymptotic state were observed as slight asymmetrical deposition on its transverse side. As an example; scour profiles with left hand propeller ($D_p=10$ cm) when looking upstream toward the propeller which rotates in the counterclockwise direction are given in Table 6.6 (b). It is seen that the profiles have higher deposition mounds on their right. Wei et al. [63] also explained that the asymmetrical

formation may be produced due to the propeller jet is inherently a swirling jet, which is axisymmetric when looking upstream toward the propeller.

Table 6.6 Scour formations with pile conditions

Photographs of the Scour Formations with Pile Obstructions	Test Conditions
	<p>(a) $D_p=10$ cm, at 590 rpm $G=10$ cm, $d_{50}=0.52$ mm $d_o=4$ cm pile</p>
	<p>(b) $D_p=10$ cm, at 590 rpm $G=10$ cm, $d_{50}=0.52$ mm $d_o=9$ cm pile</p>
	<p>(c) $D_p=10$ cm, at 590 rpm $G=10$ cm, $d_{50}=0.52$ mm $d_o=14$ cm pile</p>

The flow pattern with the existence of a cylindrical pile changes and it is characterized with water surface roller and downflow in front of the pile, vortex-shedding in separation zone, wake flow downstream of pile, generation of horseshoe-vortices in the scour hole as given in Figure 4.3 (Qi and Gao [64]).

Maximum scour depth always occurred at the toe of the pile as Type 3 profiles showed for the larger pile diameters of 9 cm and 14 cm. However, downstream scour (S_d) may be greater than S_o with relatively smaller pile diameters for $d_o = 4$ cm. This is because an increase in the pile diameter will cause more severe downflows and vortex mechanisms at the front-end of the pile. Thus, for relatively smaller pile diameters, i.e., $G/d_o > 2.3$, maximum scour depth forms downstream of the pile. This scour may either be equal to the scour formed at the upstream section of the pile or smaller than that. However, for larger pile diameters, i.e., $G/d_o < 2.3$, local maximum scour was formed only at the upstream toe of the pile because at a larger pile diameter $G/d_o (< 2.3)$, the pile acts as a blockade and alters the jet flow pattern, causing lower flow at the downstream section of the pile while more severe downflows occur at the upstream of the pile. Examples are given in Figure 6.64 for the scour formation in two different test conditions for $Fr_d = 7.73$. Vortices formed at the upstream of the pile create bigger scour formation in the case where $G/d_o = 2.22$, as depicted in Figure 6.64 (a) when compared with smaller pile diameters of $G/d_o = 5.0$, as depicted in Figure 6.64 (b) under the same flow conditions. These figures show that the diameter of the pile is a very effective parameter on scouring formation.

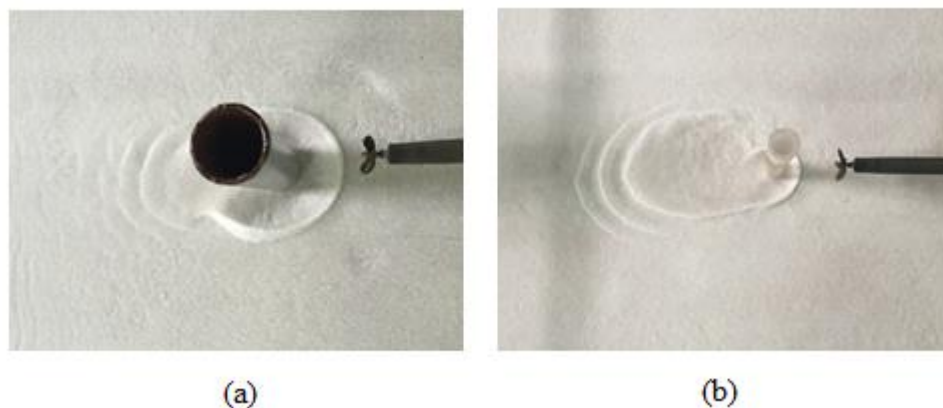
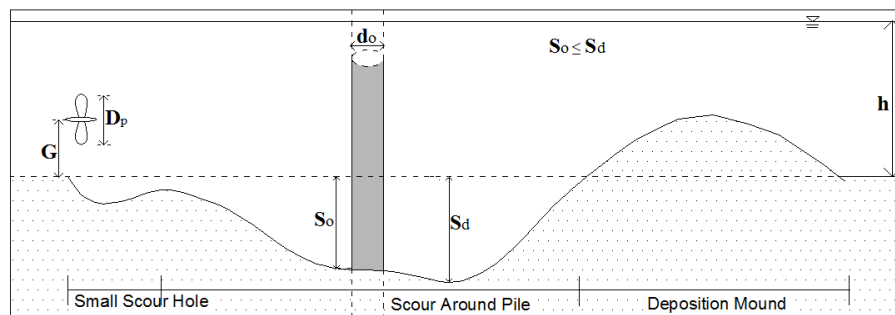


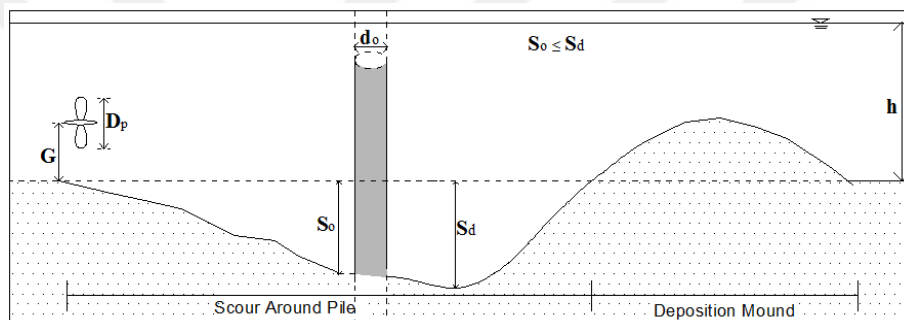
Figure 6.34 Scour formations on the sediment bed of $d_{50} = 0.52$ mm for $D_p = 6.5$ cm propeller speed 590 rpm, $X = 10$ cm and $G = 20$ cm with (a) $d_o = 9$ cm and (b) $d_o = 4$ cm

The three different scour profiles were observed, when the cylindrical pile was located at $X = 10$ cm apart from the propeller face, for tested conditions with different pile diameters, propeller speeds and gaps on four different sediment beds. These scour profiles were

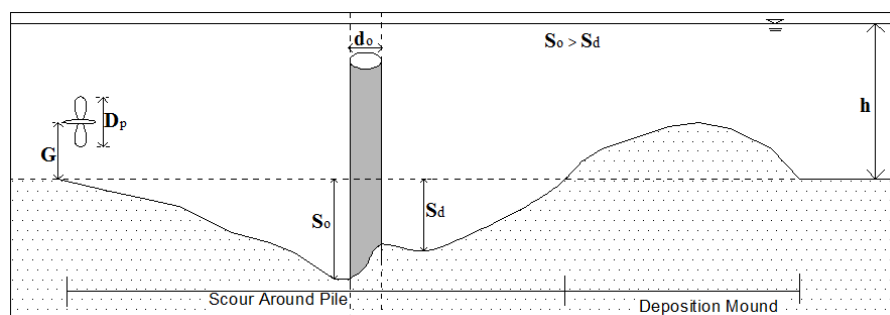
characterized by considering all scour profiles obtained at the equilibrium state at given test conditions for pile obstructed cases. These scour profiles were schematized in Figure 6.35. This figure shows equilibrium scour depth at the toe of pile (S_o) and at the downstream of the pile (S_d) defined as significant scour depths for the description of scour profiles.



(a) Type 1; $S_o \leq S_d$ with small scour hole



(a) Type 2; $S_o \leq S_d$ without small scour hole (transition)



(c) Type 3; $S_o > S_d$ without small scour hole

Figure 6.35 Characteristic scour profiles induced by propeller jet flow around a pile structure

Maximum equilibrium scour depth (S_{smax}), scour depth at the toe of pile (S_o) and at the downstream of the pile (S_d) defined in Figure 6.35 are significant parameters for the description of scour profiles. S_d were measured between D_p and $4.5D_p$ distance away from pile face at the downstream section.

At equilibrium states, Type 1 and Type 2 scour formations were observed when the scour depths at the upstream toe of pile were equal to the scour depth or smaller than that at the downstream section (S_d). The profile for Type 1 has a distinct formation of a small scour hole beneath the propeller which differs from the profile for Type 2. Type 3 scour formation was observed when the maximum equilibrium scour depth was formed at the toe of the pile (S_o).

Type 1 and Type 2 profiles were observed for only 4 cm pile diameter at different test conditions such as; gaps of 10, 15, or 20 cm, propeller diameters of 6.5, 10, or 13 cm and propeller speeds of 590, 670, or 745 rpm on different types of sediment beds defined for $d_{50} = 0.52$ mm, 1.28 mm, 4 mm and 8.3 mm. Type 1 and Type 2 scour formations were defined for a pile diameter of $d_o = 4$ cm as seen in Table 6.7 (a) and (b) while Type 3 scour profiles were formed with larger pile diameter sizes of $d_o = 9$ cm and 14 cm (Table 6.7 (c), Table 6.7 (d)) for the same propeller diameter, speed, bed material and pile location.

Table 6.7 Measured scour profiles for different pile diameters (d_o)


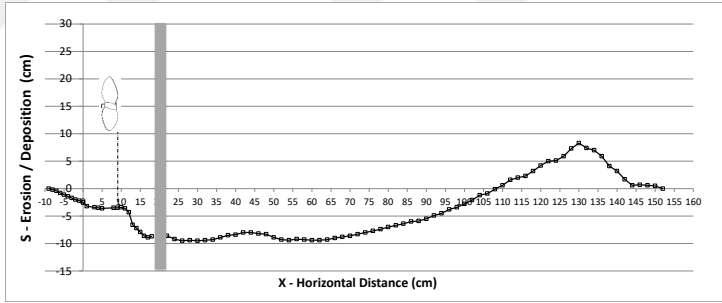

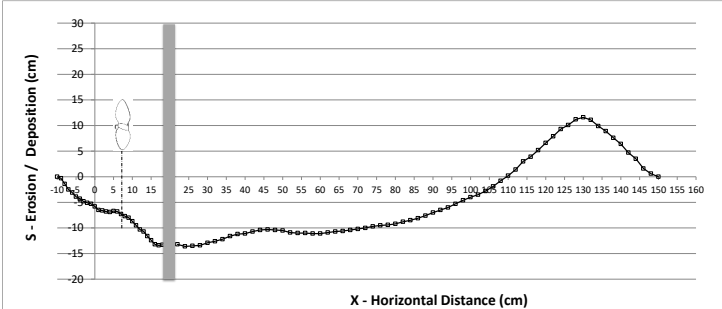

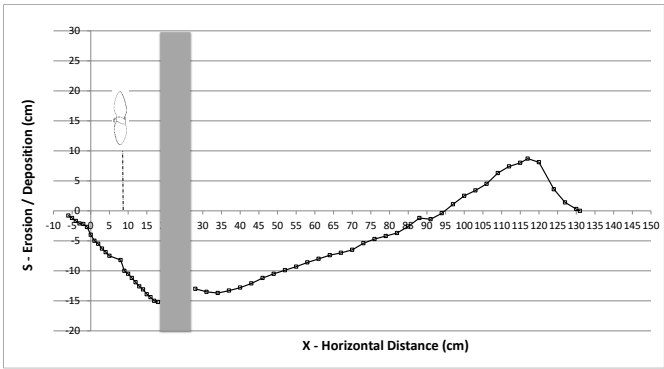

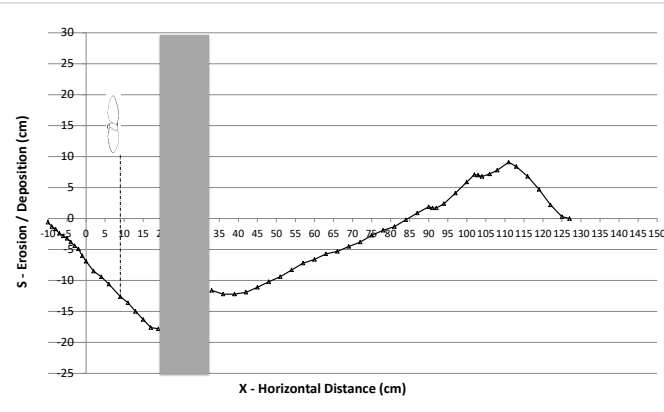
Test conditions	Photograph of Scour Formation	Scour Profile
$D_p = 10$ cm $G = 15$ cm $R_{pm} = 745$ $d_{50} = 0.52$ mm $X = 10$ cm $d_o = 4$ cm	 <p style="text-align: center;">Type 1</p>	 <p style="text-align: center;">(a)</p>
$D_p = 10$ cm $G = 10$ cm $R_{pm} = 745$ $d_{50} = 0.52$ mm $X = 10$ cm $d_o = 4$ cm	 <p style="text-align: center;">Type 2</p>	 <p style="text-align: center;">(b)</p>

Table 6.7 Measured scour profiles for different pile diameters (cont'd)

<p> $D_p=10$ cm $G=15$ cm $R_{pm}=745$ $d_{50}=0.52$ mm $X=10$ cm $d_o=9$ cm </p>	 <p style="text-align: center;">Type 3</p>	 <p style="text-align: center;">(c)</p>
<p> $D_p=10$ cm $G=15$ cm $R_{pm}=745$ $d_{50}=0.52$ mm $X=10$ cm $d_o=14$ cm </p>	 <p style="text-align: center;">Type 3</p>	 <p style="text-align: center;">(d)</p>

The pile diameter is a dominant parameter for the growth of scour Type 3. Thus, the distinction between Type 3 and Types 1-2 may be defined based on the gap ratio (G/d_o) that is related to the pile diameter (d_o) for all the tested experimental conditions. Figure 6.36 shows the distinction of the scour observed with smaller pile diameters ($G/d_o > 2.3$) and Type 3 scour was formed when $G/d_o < 2.3$ in the experiments.

Specified limit may not be defined between Type 1 and 2 scour profiles which is identified with the existence of the small scour hole beneath the propeller for pile cases in Table 6.7 (a) and (b). However, Type 2 may be classified as a transition profile type, but there is a limit for existence of the small scour hole with respect to dimensionless parameter of G/D_p versus Fr_a (Equation (6.3)) for no pile case in Figure 6.11.

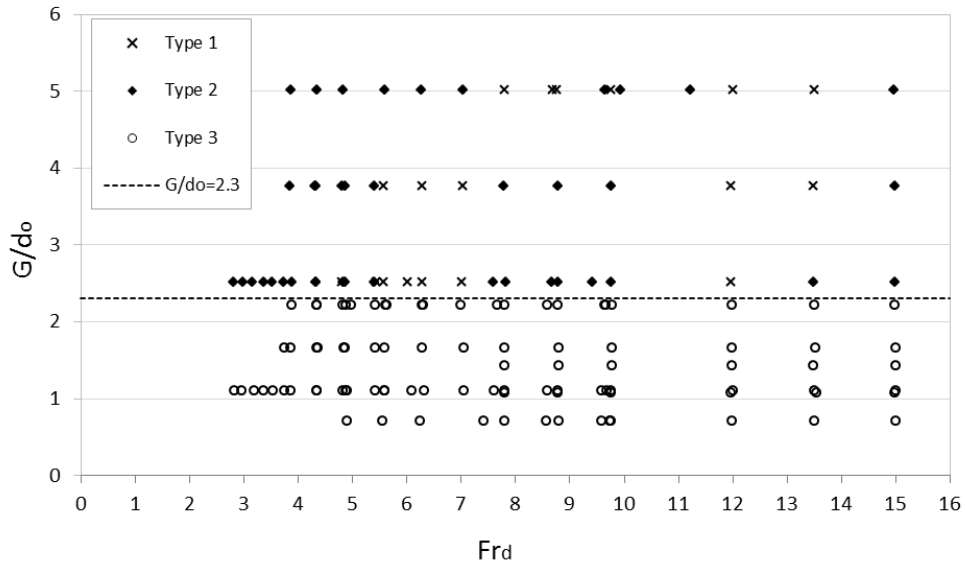


Figure 6.36 Type 1, 2 and 3 scour formations with respect to the G/d_o versus Fr_d

Small scour formations induced by propeller jet for Type 1 and 2 depend not only propeller gaps but also the propeller sizes and speeds. Increasing propeller speeds and sizes cause stronger horseshoe vortices and increase the reversed flows at the upstream face of the pile. So, small scours disappear under the propeller and large scour holes form around the pile as seen in Figure 6.37.

Chin et al. [8] investigated the formation of the scour hole mechanism due to circular jet around a vertical pile. They stated that scouring around pile occurred due to 'Pile obstruction mechanism' or 'Jet mechanism' according to the distance between the pile and the jet as impinging distance. Pile obstruction mechanism occurs due to the small impinging distance of jet flow onto the pile. Thus, the downflow due to the deceleration in front of the pile and the latter horseshoe vortex with the deflected flow into scour hole cause scouring at the toe of pile and maximum scour depth is observed at the toe of pile. However, the jet mechanism is effective with the large impinging distance because scouring formation cause predominantly due to the jet diffusion instead of obstruction.

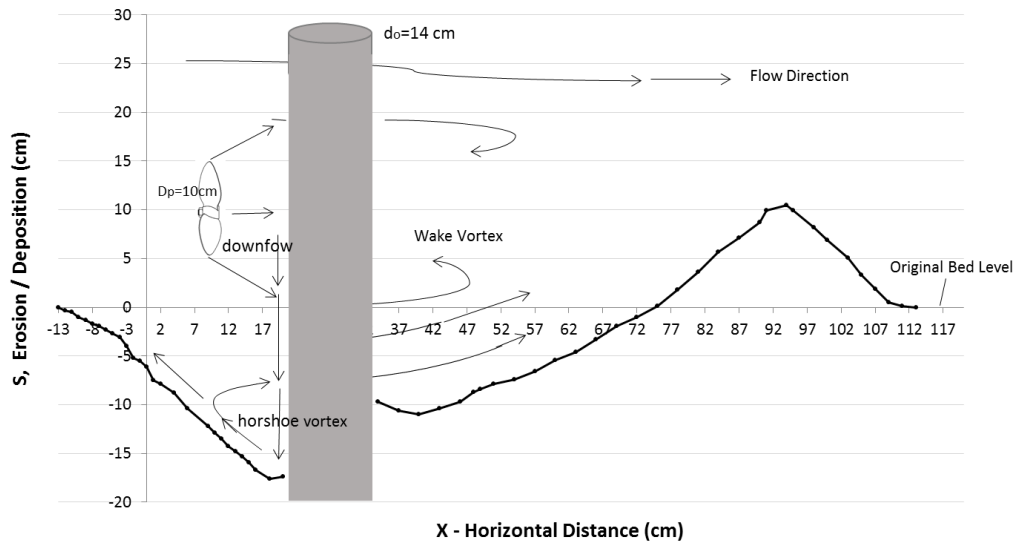


Figure 6.37 Schematic view of the flow pattern around the vertical pile

Although Chin et al. [8] investigated scour formations around a pile under a wall jet mechanism, the presented observations of this study were discussed with their results. They defined four different scour profile formations by changing location of the pile on the sediment bed without considering the gap of the jet. Chin et al. [8] classified scour profiles based on impingement distance which is the distance between the pile and orifice face for circular wall jets. They defined scour profile types with respect to the ratio of impingement distance to the jet diameter (X/D_o) (Figure 1.13 in Chapter 1). In accordance to this impingement distance, they determined the predominant effective mechanism on scouring formation. They stated that scouring formation was caused by two combined effects's obstruction and jet mechanism. In the present study, predominant mechanism on scour profiles were evaluated by taking pile diameters into consideration since the location of pile was kept constant at $X=10$ cm. As an example, Type 3 scour formation was observed when the pile diameter was increased to 9 cm and 14 cm. Thus, increasing the diameters of piles cause more intensive downflows at the face of pile and they deepen the scour hole at the toe. In addition, small scour formation beneath the propeller disappears with stronger reverse flow. Thus, effective mechanism on scouring formation for Type 3 occurs mainly due to the pile obstruction which is more effective than on Type 1 or 2 scour profiles. However, Type 1 and Type 2 scour formations have weaker downflows for smaller pile diameters ($d_o=4$ cm). Also, more erosion takes place at the downstream section of the pile as a result of separation of the flow from the side edges of pile due to the wake vortex for Type 1 and 2 formations. However, the separation at the sides decreases, so the wake vortex does not

produce erosion at the downstream section of the pile as much as it occurs with Type 1 and 2 than Type 3 profile. Instead, the flow creates more horseshoe vortex with increasing downflows at the upstream section of pile and maximum scour always occurs at the upstream toe of pile.

6.2.1 Effects of Pile Diameters, Bed Material Sizes, Propeller Diameters and Speeds

An extensive series of tests were carried out with various sizes of circular cross-section piles that had the ranges of 4 cm, 9 cm and 13 cm. Four different sediment bed materials, three different propellers with different speeds and specified gaps were also taken into consideration as effective parameters to define the scour dimensions. In the present study, test conditions were limited to circular piles of $0.77 \leq G/D_p \leq 3.08$ and $1.92 \leq Fr_d \leq 15.01$. The following sections of the study define the equilibrium scour depth around the piles with nondimensional parameters.

A flow pattern changes substantially when a vertical circular pile is placed on the sediment bed (Figure 6.37). Scour formation changes significantly with the existence of a vertical pile when compared with the absence of pile cases. Sumer and Fredsoe [44] indicated that scour depth around a pile in steady current, was influenced by various factors such as shields parameter, sediment material sizes, sediment size to the pile size ratio and the shape factor of the bed material.

In the present study, in addition to the effects of bed material and effects of pile diameter sizes in accordance to the developing of scour around piles, propeller speeds and gaps are also taken into consideration individually under propeller jet flows.

Scour depth over propeller diameter (S_o/D_p) with and without pile conditions are defined by dimensionless parameters of Fr_d , Re_p and Re_f in Figure 6.38, Figure 6.39 and Figure 6.40, respectively.

S_o/D_p are shown for propeller diameter of 6.5 cm and 10 cm with three different speeds of 590 rpm, 670 rpm, and 745 rpm on the finest sediment bed ($d_{50}=0.52$ mm) for constant gap $G=10$ cm in Figure 6.38. In this figure the scour depth which is $X=10$ cm away from the propeller face is defined as S_{10} for no pile cases.

Relative scour depth at the toe of pile (S_o/d_o) increases with increasing Fr_d (Figure 6.38). Scour depths (S_o) with pile cases are always greater than the cases with the absence of piles (S_{10}) which are measured at the same location from the propeller face.

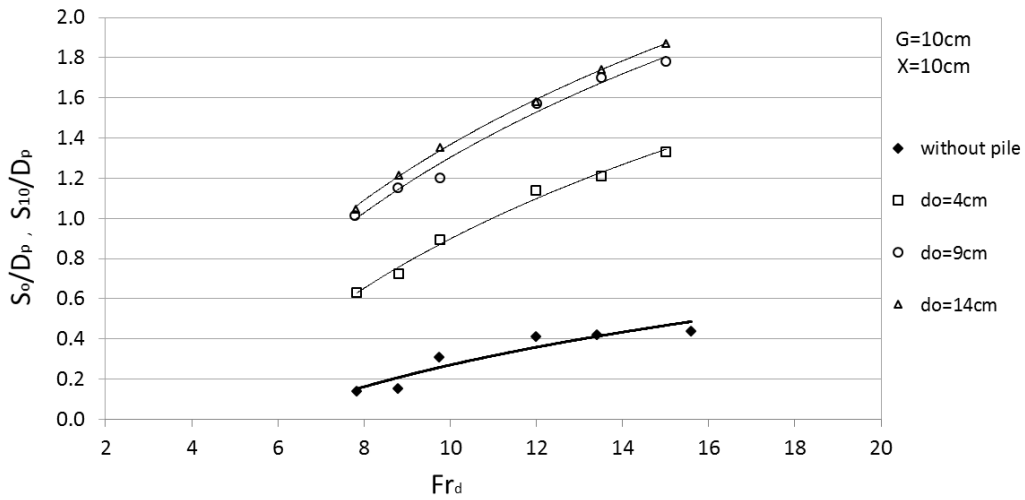


Figure 6.38 Variation of S_o/D_p and S_{10}/D_p with Fr_d over bed of $d_{50}=0.52$ mm ($D_p=6.5$ cm and 10 cm at propeller speeds of 590 rpm, 670 rpm and 745 rpm)

Similarly, relative scour depth (S_o/D_p) increases with increasing Re_p and Re_f in Figure 6.39 and Figure 6.40. Figure 6.38 also shows that scour depth (S_o) increases at the toe of pile with increasing pile diameter, and the same increment was obtained for S_o/D_p versus Re_f and Re_p numbers as seen in Figure 6.39 and Figure 6.40.

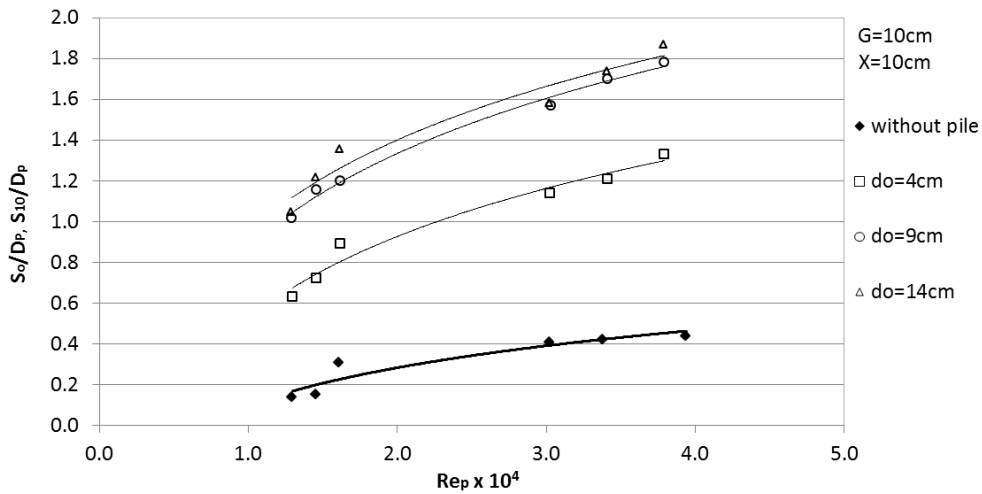


Figure 6.39 Variation of S_o/D_p and S_{10}/D_p with Re_p over bed of $d_{50}=0.52$ mm ($D_p=6.5$ cm and 10 cm at propeller speeds of 590 rpm, 670 rpm and 745 rpm)

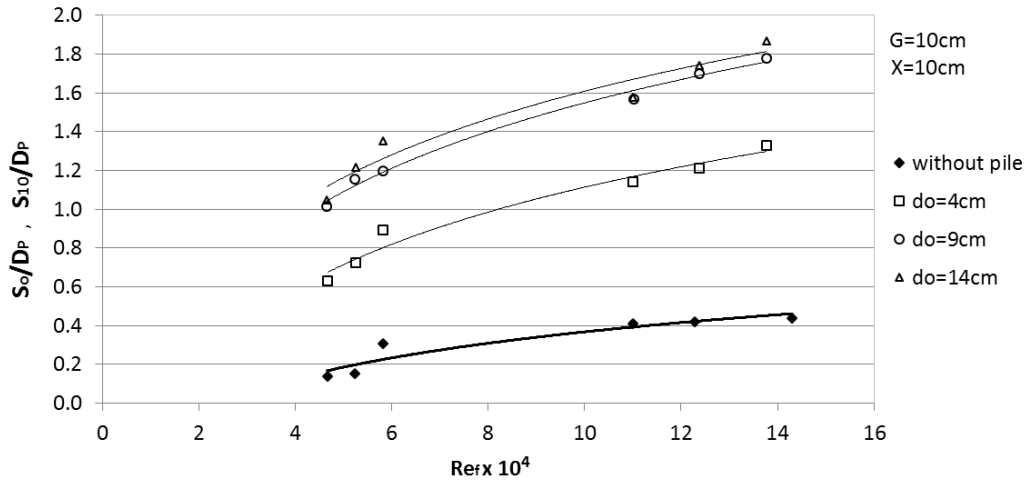


Figure 6.40 Variation of S_o/D_p and S_{10}/D_p with Re_f over bed of $d_{50}=0.52$ mm ($D_p=6.5$ cm and 10 cm at propeller speeds of 590 rpm, 670 rpm and 745 rpm)

S_o/D_p versus Fr_d were depicted in Figure 6.41, Figure 6.42 and Figure 6.43 for sediment beds of $d_{50}=1.28$ mm, 4.0 mm and 8.3 mm, respectively. In these figures relative scour depth (S_o/D_p) variations versus Fr_d have the same tendency as on fine bed material of $d_{50}=0.52$ mm (Figure 6.38).

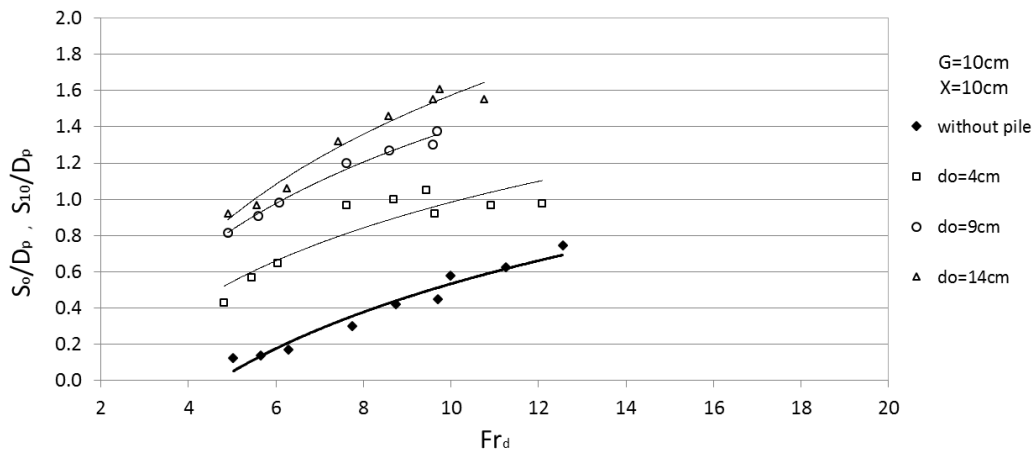


Figure 6.41 Variation of S_o/D_p and S_{10}/D_p with Fr_d over bed of $d_{50}=1.28$ mm ($D_p=6.5$ cm, 10 cm and 13 cm at propeller speeds of 590 rpm, 670 rpm and 745 rpm)

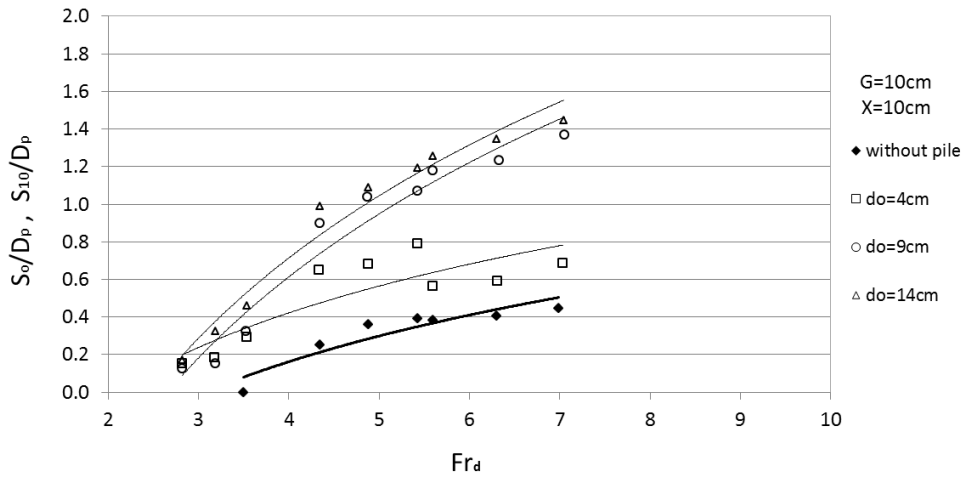


Figure 6.42 Variation of S_0/D_p and S_{10}/D_p with Fr_d over bed of $d_{50}=4$ mm ($D_p=6.5$ cm, 10 cm and 13 cm at propeller speeds of 590 rpm, 670 rpm and 745 rpm)

Trendlines for S_0/D_p versus Fr_d show that with increasing bed material sizes, trendlines for the scours at the toe of pile come closer without pile conditions on the sediment beds of $d_{50}=0.52$ cm, 1.28 cm, 4.0 mm and 8.3 mm in Figure 6.38, Figure 6.41, Figure 6.42, Figure 6.43, respectively. Also, scour depth (S_{10}) without pile cases are always smaller than pile cases as seen in these figures.

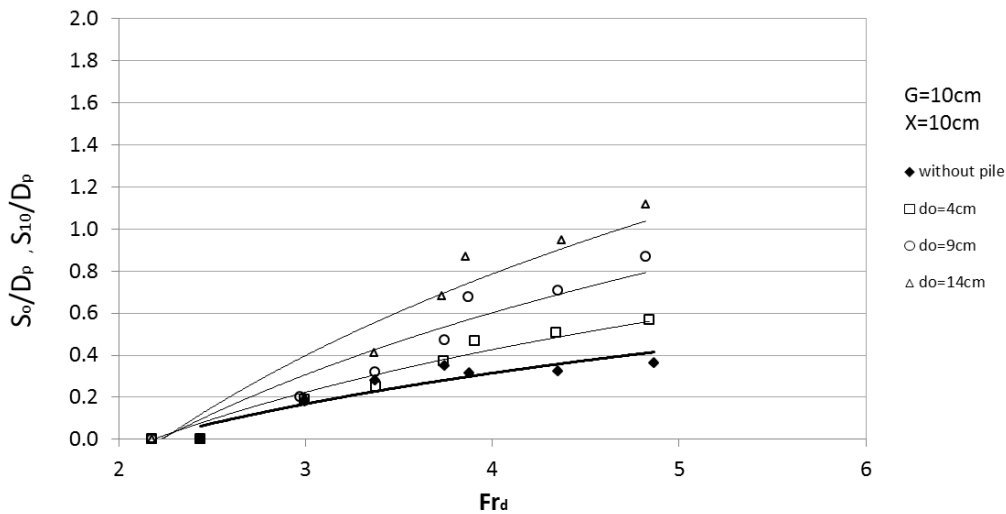


Figure 6.43 Variation of S_0/D_p and S_{10}/D_p with Fr_d over bed of $d_{50}=8.3$ mm ($D_p=6.5$ cm, 10 cm and 13 cm at propeller speeds of 590 rpm, 670 rpm and 745 rpm)

Another dimensionless parameter of S_0/d_o was depicted versus Re_f , Re_p and Fr_d in Figure 6.44, Figure 6.45 and Figure 6.46, respectively. These figures indicate S_0/d_o increase with increasing Re_f , Re_p and Fr_d on the sand beds ($d_{50}=0.52$ mm) for the test conditions of $D_p=6.5$ cm and 10 cm at 590 rpm, 670 rpm, 745 rpm. Similar tendency was obtained for the

other sand bed materials of $d_{50}=1.28$ mm, 4.0 mm and 8.3 mm as seen in Figures A.69 - A74.

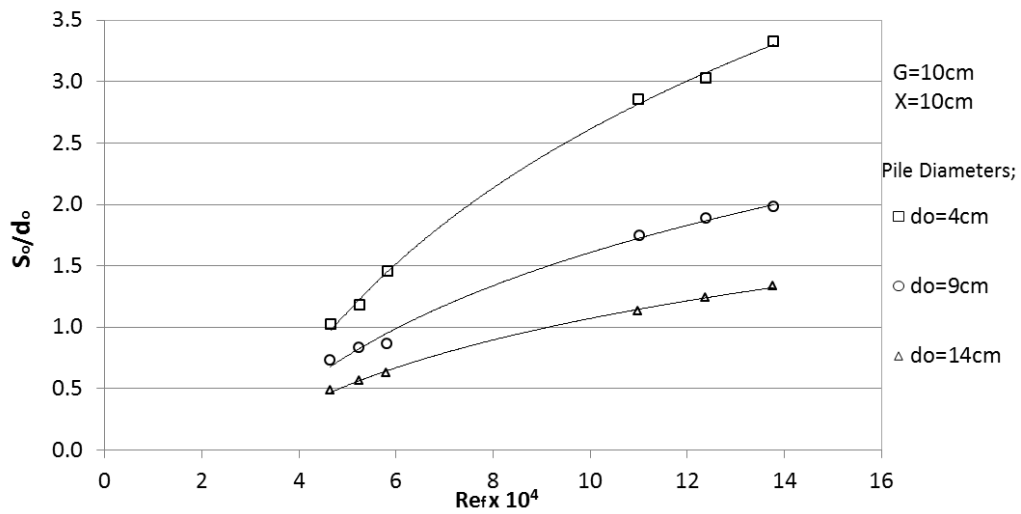


Figure 6.44 Variation of S_0/d_0 with Re_f on sediment bed of $d_{50}=0.52$ mm ($D_p=6.5$ cm and 13 cm at propeller speeds of 590 rpm, 670 rpm and 745 rpm)

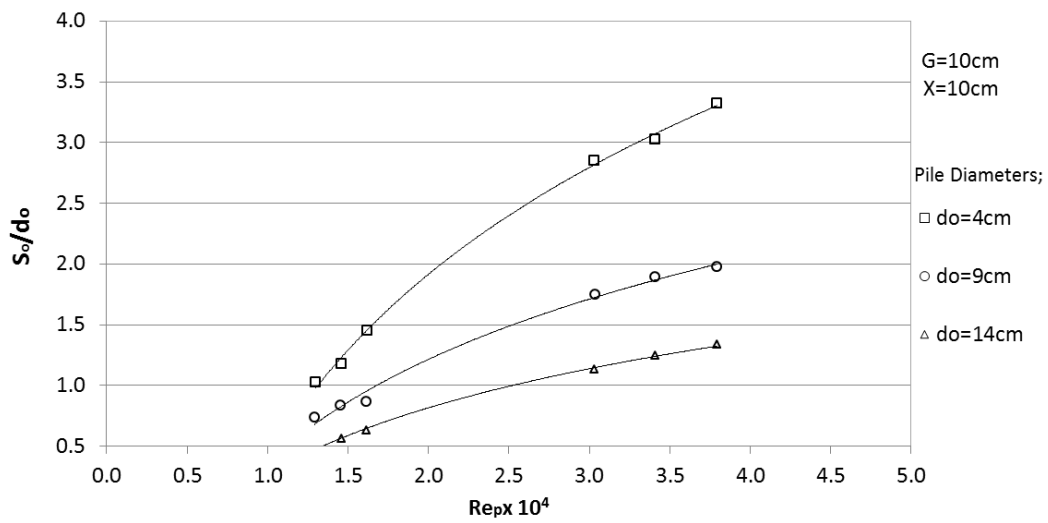


Figure 6.45 Variation of S_0/d_0 with Re_p on sediment bed of $d_{50}=0.52$ mm ($D_p=6.5$ cm and 13 cm at propeller speeds of 590 rpm, 670 rpm and 745 rpm)

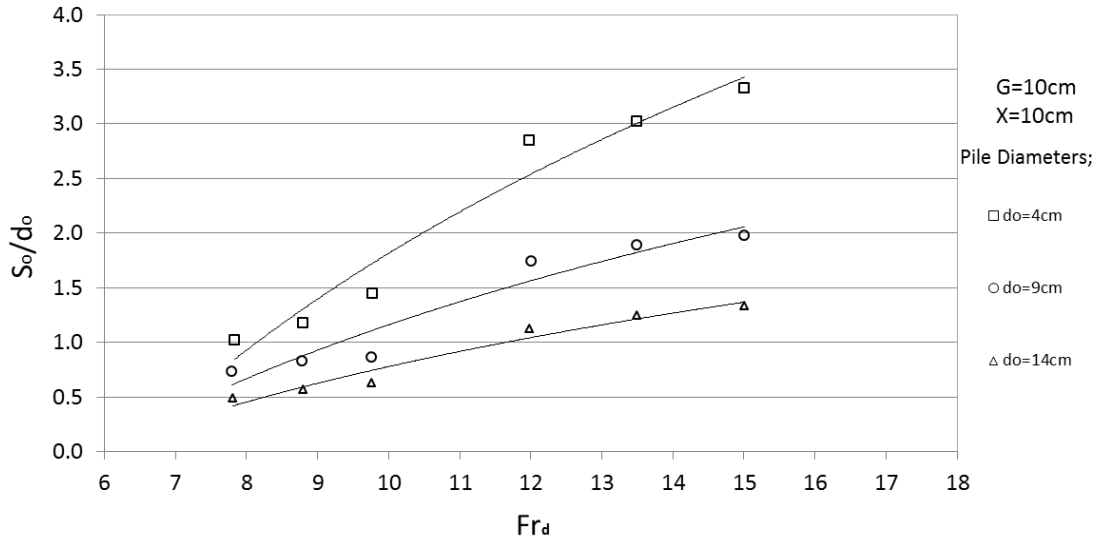


Figure 6.46 Variation of S_o/d_o with Fr_d on sediment bed of $d_{50}=0.52$ mm ($D_p=6.5$ cm and 10 cm at propeller speeds of 590 rpm, 670 rpm and 745 rpm)

Variation of S_o/d_o versus Fr_d for the other sediment bed material sizes of $d_{50} = 1.28$ mm, 4 mm and 8.3 mm are given in Figure 6.47, Figure 6.48 and Figure 6.49, respectively. These figures indicate that the values of S_o/d_o have lower limits for the smaller pile diameter ($d_o=4$ cm) while they have higher limits for the greater pile diameter of $d_o=14$ cm.

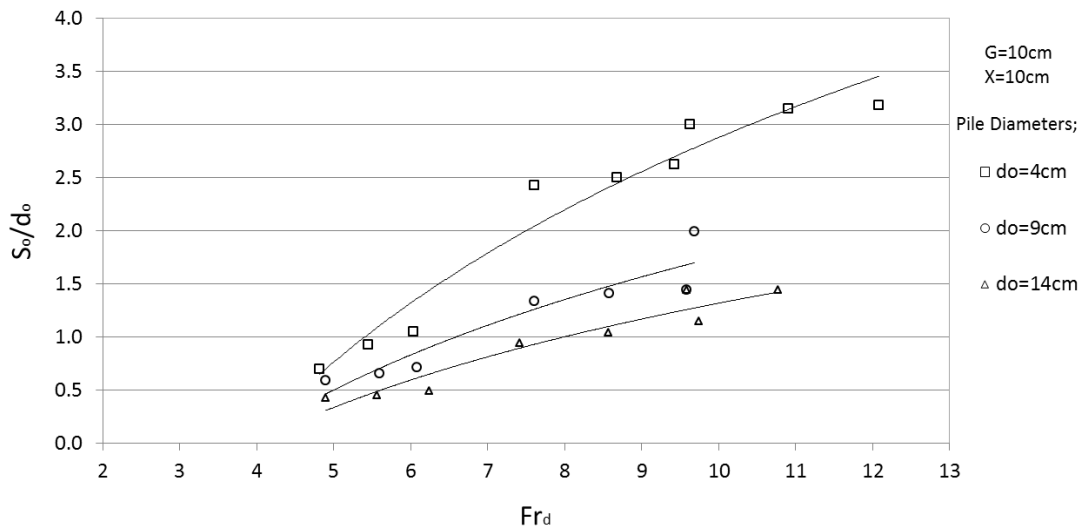


Figure 6.47 Variation of S_o/d_o with Fr_d on sediment bed of $d_{50}=1.28$ mm ($D_p=6.5$ cm, 10 cm and 13 cm at propeller speeds of 590 rpm, 670 rpm and 745 rpm)

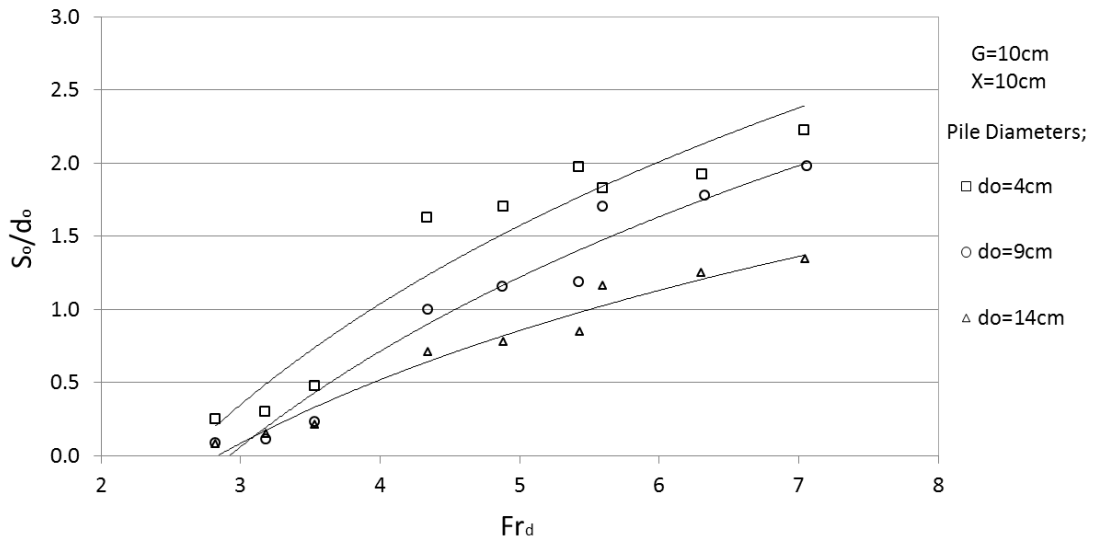


Figure 6.48 Variation of S_o/d_o with Fr_d on sediment bed of $d_{50}=4$ mm ($D_p=6.5$ cm, 10 cm and 13 cm at propeller speeds of 590 rpm, 670 rpm and 745 rpm)

Scour (S_o) was observed for the test conditions of $D_p=6.5$ cm, 10 cm and 13 cm propellers with rotation speeds of 590 rpm, 670 rpm and 745 rpm on the sediment beds of $d_{50}=1.28$ mm and 4.0 mm as shown in Figure 6.47 and Figure 6.48, respectively. There were no scours formed for $D_p=6.5$ cm propeller at 590 rpm, 670 rpm and 745 rpm on coarser sediment bed of $d_{50}=8.3$ mm for small Fr_d numbers ($Fr_d \leq 2.44$) (Figure 6.49).

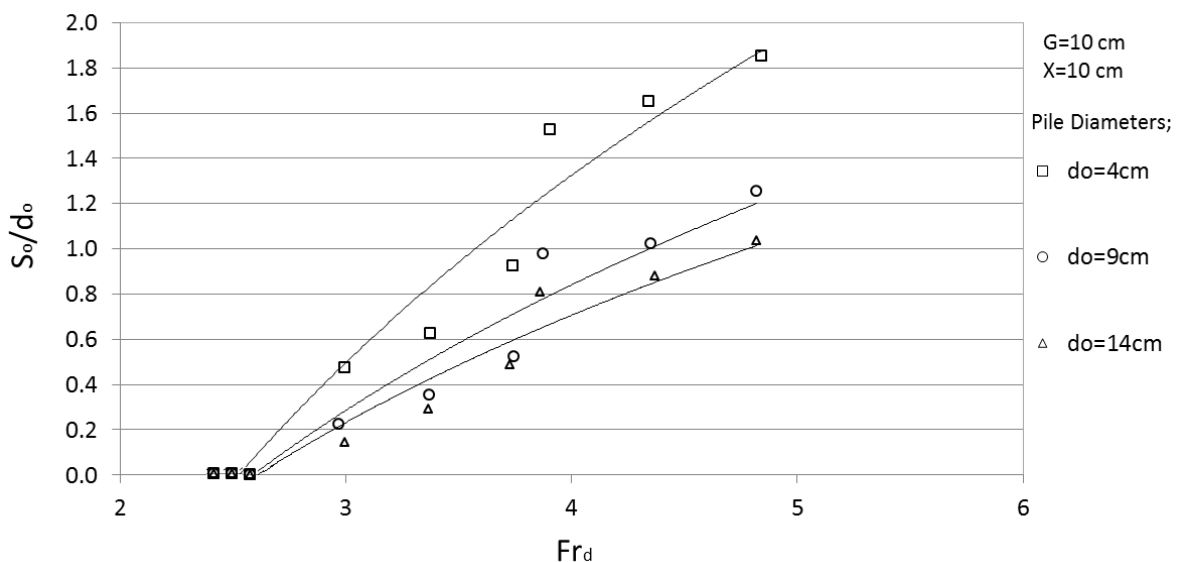


Figure 6.49 Variation of S_o/d_o with Fr_d on sediment bed of $d_{50}=8.3$ mm ($D_p=6.5$ cm, 10 cm and 13 cm at propeller speeds of 590 rpm, 670 rpm and 745 rpm)

As the bed material size increases, S_o/d_o decreases as shown in Figure 6.47, Figure 6.48 and Figure 6.49. Increasing S_o/d_o values versus Fr_d on each sediment bed were indicated for

each propeller diameter ($D_p=6.5$ cm, 10 cm and 13 cm) in Figure 6.50, Figure 6.51 and Figure 6.52, respectively.

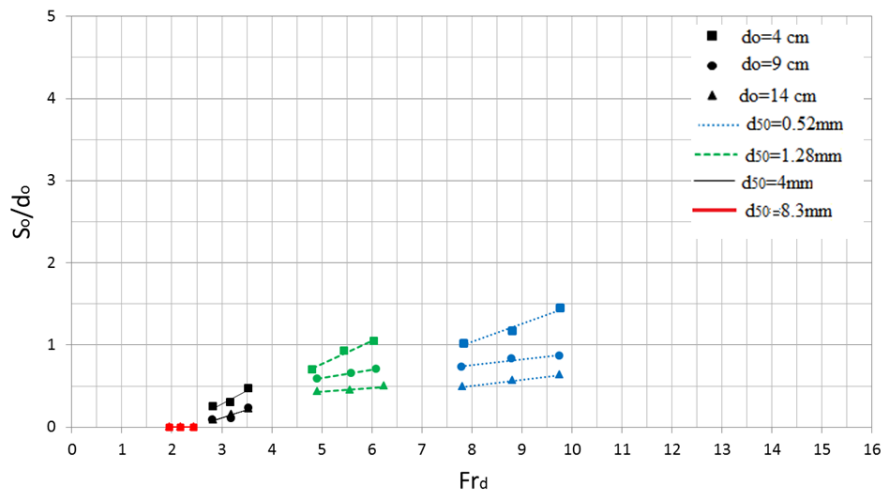


Figure 6.50 Relationship between S_o/d_o with Fr_d on different sand beds for different speeds (590 rpm, 670 rpm, 745 rpm) of Propeller - 65 mm at $X=10$ cm, $G=10$ cm

These figures indicate that, S_o/d_o increases with increasing Fr_d related to the propeller speeds of 590 rpm, 670 rpm and 745 rpm. S_o has the maximum value of $S_o=3.3d_o$ for the fine bed material of $d_{50}=0.52$ mm, $D_p=10$ cm at 745 rpm for the pile diameter of $d_o=4$ cm while minimum value is $0.14d_o$ for the coarse bed material of $d_{50}=8.3$ mm for $D_p=10$ cm at 745 rpm for $d_o=14$ cm (Figure 6.51). S_o/d_o varies within the range of 0.14 – 3.3 by considering all scour formations for $2.44 < Fr_d \leq 15.01$ on the sediment bed sizes from $d_{50}=0.52$ mm to 8.3 mm.

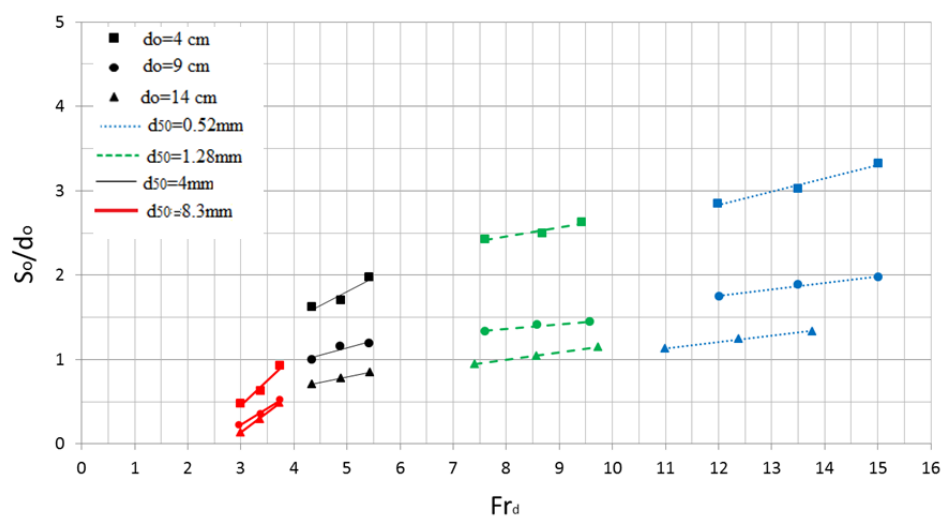


Figure 6.51 Relationship between S_o/d_o with Fr_d on different sand beds for different speeds (590 rpm, 670 rpm, 745 rpm) of Propeller - 100 mm at $X=10$ cm, $G=10$ cm

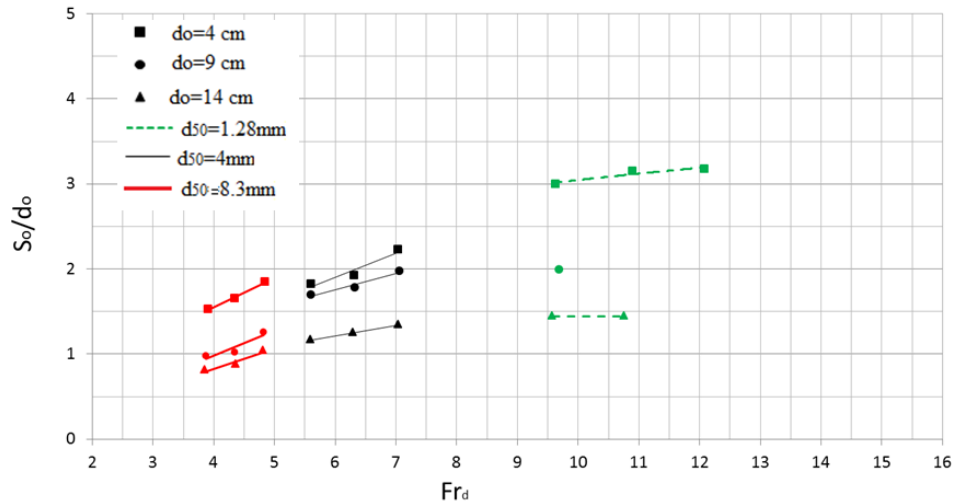


Figure 6.52 Relationship between S_o/d_o with Fr_d on different sand beds for different speeds (590 rpm, 670 rpm, 745 rpm) of Propeller - 130 mm at $X=10$ cm, $G=10$ cm

Scour profiles were defined by X_c , X_{pc} , L_{pt} and L_{pmax} are shown in Figure 6.53, where, X_c is the horizontal distance from the propeller's face to the deposition crest, X_{pc} is the horizontal distance from the pile face to the deposition crest, L_{pmax} is the maximum length of the scour hole around the pile at the equilibrium state for pile cases and L_{pt} is the total length of the scour hole at the equilibrium state, B_{smax} is the width of the scour hole for pile cases.

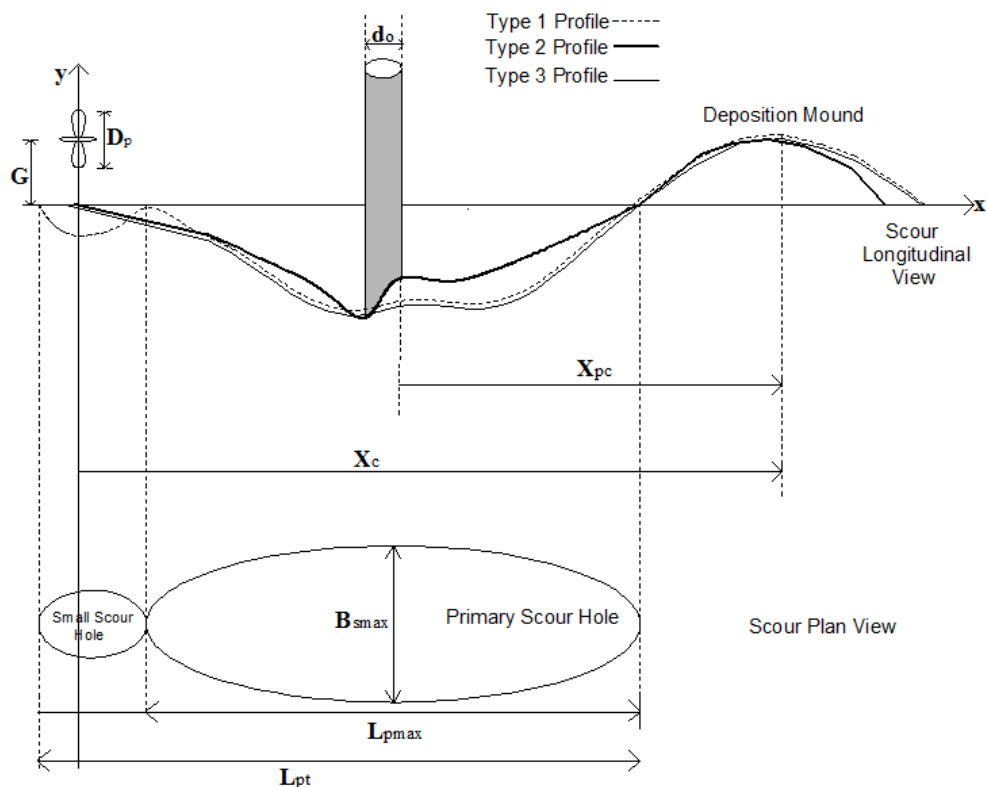


Figure 6.53 Schematic of scour profile with a pile at the equilibrium state induced by the propeller jet

Scour profiles changed significantly for different sand beds of $d_{50}=0.52$ mm, 1.28 mm, 4.0 mm and 8.3 mm, even though the propeller speed and diameter were kept constant. Scour depths (S_o) at the toe of the 4 cm pile decrease and the deposition crests are formed closer to the pile for coarser sediment beds as seen in Figure 6.54. Similar conditions were observed for relatively larger pile diameters of $d_o=9$ cm and 14 cm as seen in Figure 6.55 and Figure 6.56, respectively.

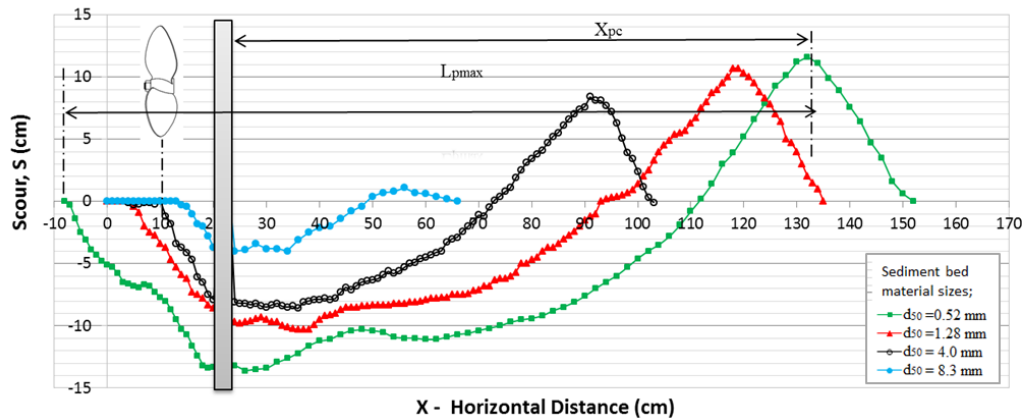


Figure 6.54 Scour profiles around the 4 cm pile on different beds with $D_p=10$ cm, at 745 rpm, and at $G=10$ cm

Scour profiles over sediment beds of $d_{50}=0.52$ mm to 8.3 mm for all defined propeller diameters and speeds are given in Figure A.75 - Figure A.101.

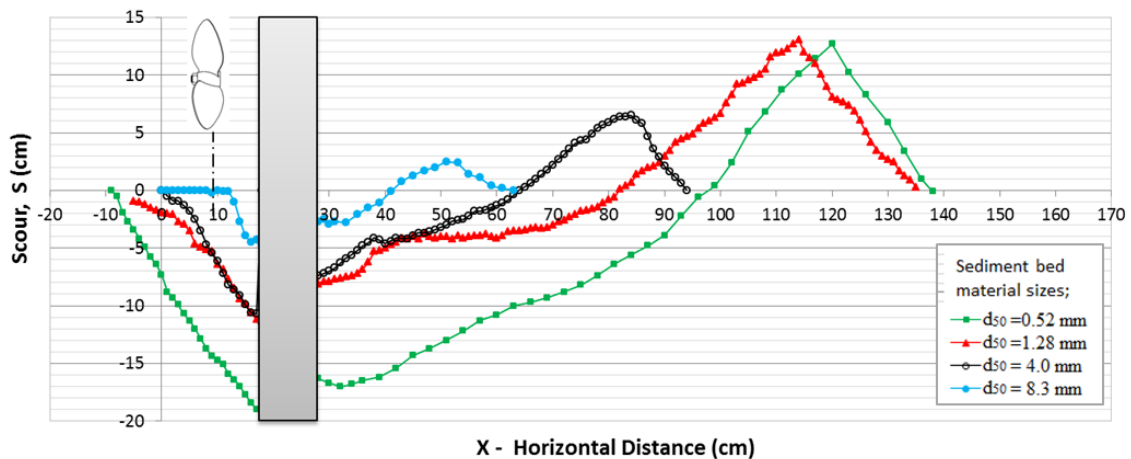


Figure 6.55 Scour profiles around the 9 cm pile on different beds with $D_p=10$ cm, at 745 rpm, and at $G=10$ cm

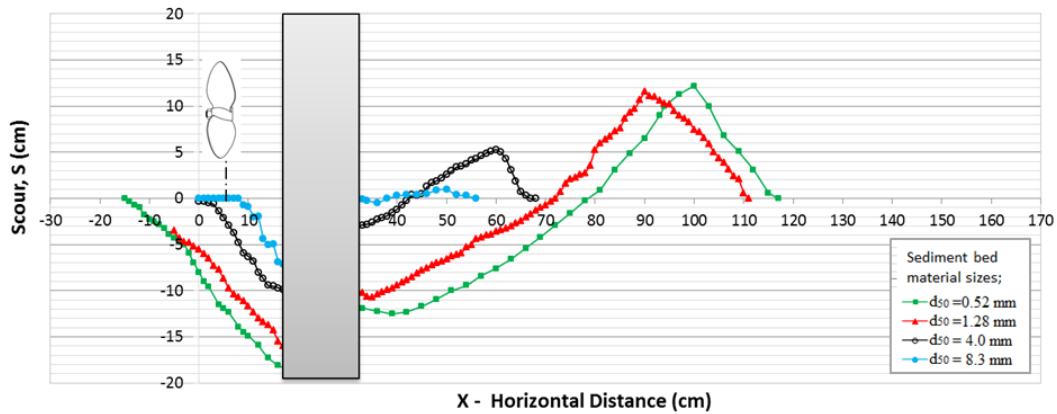


Figure 6.56 Scour profiles around the 14 cm pile on different beds with $D_p=10$ cm, at 745 rpm, and at $G=10$ cm

Overall length of the scour hole (L_{pt}) and the length between the propeller face and deposition crest (X_{pc}) decrease with increasing pile diameters for all the sand bed materials with the same test conditions. Scour profiles with pile ($d_o=4$ cm) cases for the same propeller diameter and speed ($D_p=10$ cm with 745 rpm) are given in Figure 6.54. Other conditions (propeller diameters of $D_p=13$ cm and 6.5 cm tested with propeller speeds of 590 rpm, 670 rpm and 745 rpm) of all tested sand beds are given in Figure A.75 – Figure A.101.

Similarly, Figure 6.57 indicates scour profiles with and without pile conditions on the same sediment bed of $d_{50}=0.52$ mm. Pile diameter (d_o) has significant effects on scour formations. If the pile diameter increases on the same sediment bed from $d_o=4$ cm to 9 and 14 cm, also the scour depth (S_o) increases for the same propeller diameter and speed as seen in Figure 6.57, Figure 6.58, Figure 6.59 and Figure 6.60. However, the distance between deposition crest and the pile (X_{pc}) decreases with increasing pile diameter on the same sediment bed material. Figure 6.57 also, reveals that the overall length of the scour hole (L_{pt}) with pile cases is shorter than the scour length for no pile conditions. Similar conditions were observed for different sediment bed materials as seen in, Figure 6.58, Figure 6.59 and Figure 6.60.

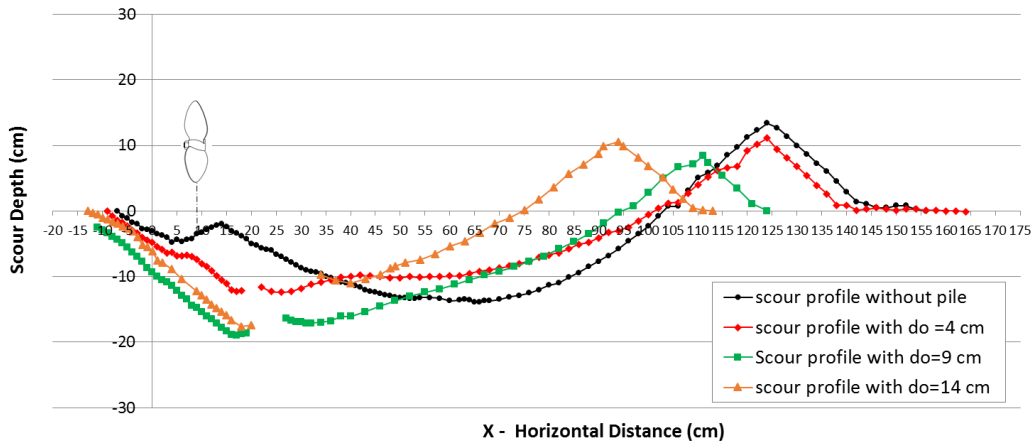


Figure 6.57 Scour profiles with and without pile cases on $d_{50}=0.52$ mm sediment bed ($D_p=10$ cm, $G=10$ cm, at 670 rpm)

The deposition crest was formed closer to the piles with increasing pile diameters on the same sediment bed when the experimental conditions such as; the gap, propeller diameter and speed were kept constant as seen in Figure 6.57, Figure 6.58, Figure 6.59, and Figure 6.60. Other conditions (propeller diameters of $D_p=13$ cm and 6.5 cm at all tested speeds at 590 rpm, 670 rpm and 745 rpm) are given in Figures A.102- A.119 and Figures A.128- A.176.

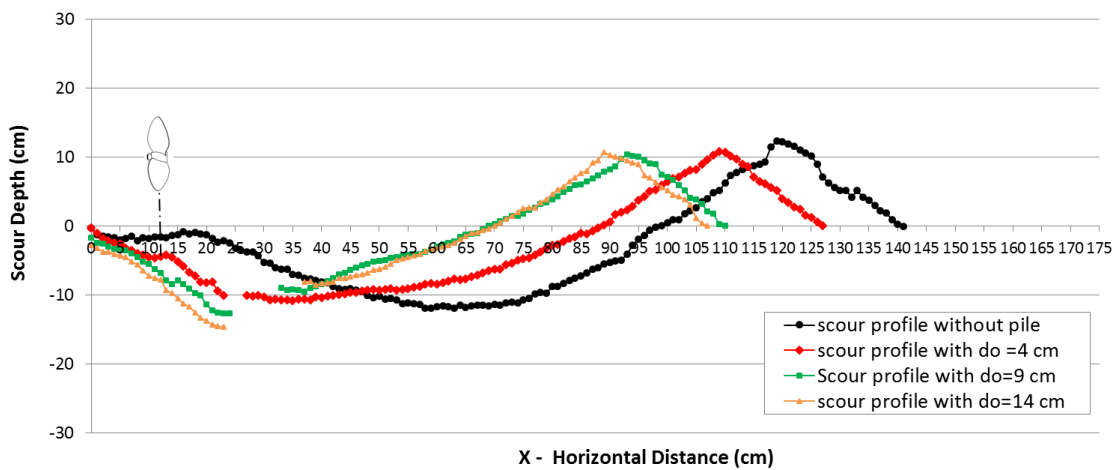


Figure 6.58 Scour profiles with and without pile cases on $d_{50}=1.28$ cm sediment bed ($D_p=10$ cm, $G=10$ cm, at 670 rpm)

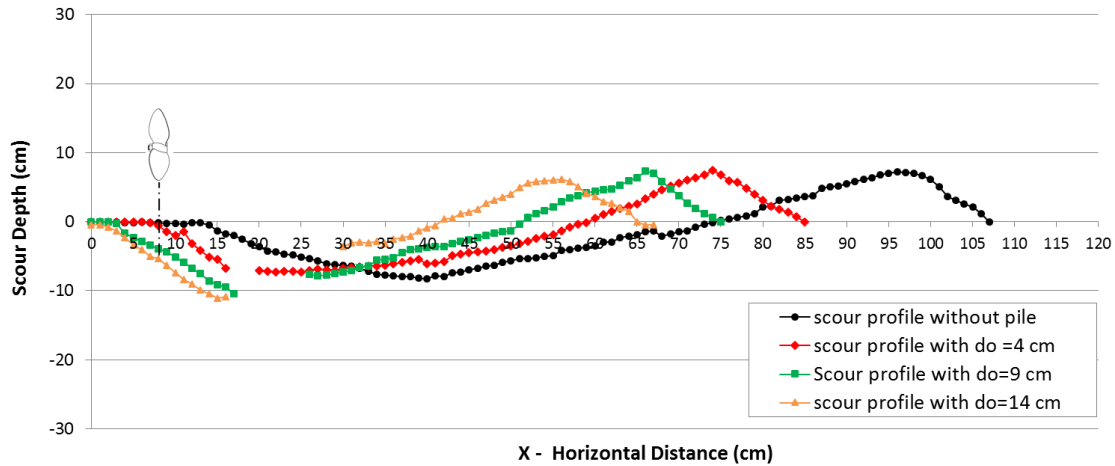


Figure 6.59 Scour profiles with and without pile cases on $d_{50}=4$ mm sediment bed ($D_p=10$ cm, $G=10$ cm, at 670 rpm)

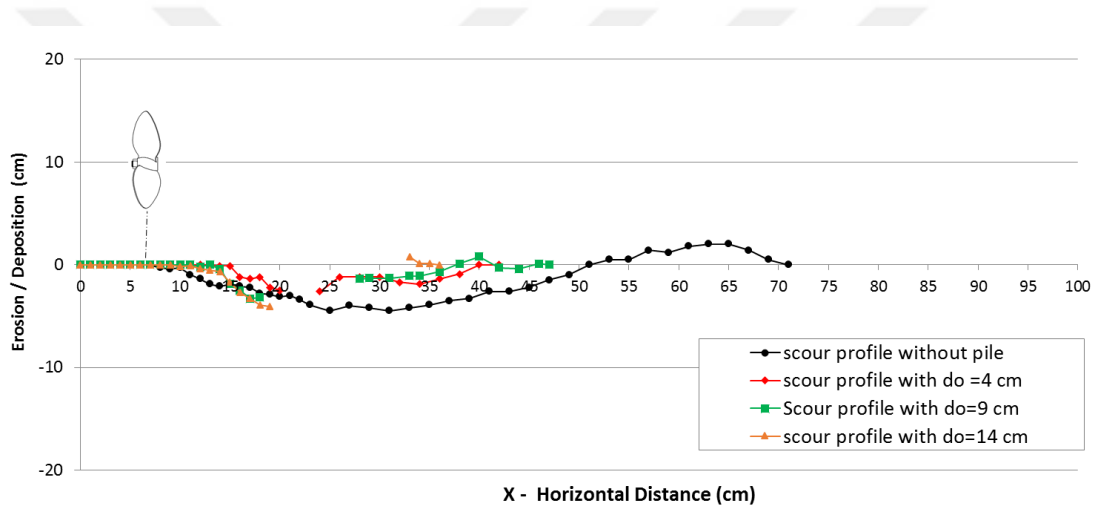


Figure 6.60 Scour profiles with and without pile cases on $d_{50}=8.3$ mm sediment bed ($D_p=10$ cm, $G=10$ cm, at 670 rpm)

The length of the scour hole (L_{pmax}) and the maximum scour depth (S_{max}) around a pile located at $X=10$ cm away from the propeller were measured at different gaps and speed settings of the three propellers, on four uniform sand beds. The width of the scour hole (B_{smax}) was only measured on the finer sediment bed material of $d_{50}=0.52$ mm. The width of the scour hole (B_{smax}) was measured under test conditions of $D_p=6.5$ cm and 10 cm propeller speeds of 590 rpm, 670 rpm and 745 rpm; $G=10$ cm, 15 cm and 20 cm for $7.83 \leq Fr_d \leq 15.01$ and $1.00 \leq G/D_p \leq 3.08$. B_{smax}/D_p versus Fr_d in the presence and absence of piles are given in Figure 6.61.

The linear response of B_{smax}/D_p associated with the data in cases where piles are absent tends to elicit values that are higher compared to the responses elicited when piles are present for greater densimetric Froude numbers ($Fr_d \geq 10$), as seen in Figure 6.61. The

Figure also reveals that the widths of scour holes induced by the propeller jet are different for tests conducted with circular jets. Equation (6.17) is defined as the relationship between Fr_d and the relative width of the scour hole (B_{smax}/D_p) caused by the propeller jet as follows,

$$\frac{B_{smax}}{D_p} = 1.19 Fr_d^{0.62} \quad (6.17)$$

Trend lines of B_{smax}/D_p for both pile and no pile conditions are practically the same in (6.17) However, the flow may be dominated by pile obstruction for pile cases while the jet mechanism dominates on flow conditions for no pile cases.

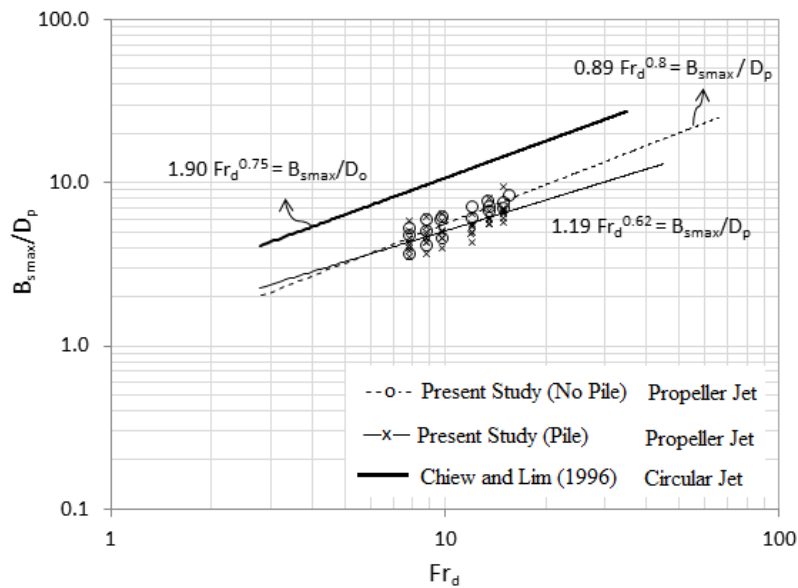


Figure 6.61 Relationship between B_{smax}/D_p and Fr_d with $d_o = 4$ cm, 9 cm, and 14 cm, with and without piles, based on propeller jet mechanisms on a sand bed with $d_{50} = 0.52$ mm

Other characteristic dimensions of relative length and scour (L_{pmax}/D_p and S_{max}/D_p) for pile conditions ($d_o = 4$ cm, 9 cm and 14 cm) are also plotted as a function of Fr_d , and they are compared with the values obtained from the cases without pile conditions. The L_{pmax}/D_p and S_{max}/D_p data collected in the presence of piles are shown to be scattered around the data elicited in the case when piles are absent (Figure 6.62 and Figure 6.63). Thus, the relations of L_{pmax}/D_p and S_{max}/D_p versus Fr_d do not elicit a good correlation, as shown in without pile condition.

Comparisons of B_{smax}/D_p , L_{smax}/D_p , S_{smax}/D_p versus Fr_d for the lack of pile and pile data, are given in Figure 6.61, Figure 6.62 and Figure 6.63, respectively. As seen in these figures, the lack of pile and pile data are mostly scattered in areas below the predicted values based on the formula proposed by Chiew and Lim [2]. This is because the propeller jet has more

turbulent flow type than the flow jet. Highly turbulent propeller jet decays more rapidly than the flow jet. Hence, scour dimensions of propeller jet flows are smaller.

Therefore, the reason for this decay is mostly caused due to the nature of unducted propeller. Propeller jets have a rotational flow velocity in the jet and swirl at the tip of the propeller blades as stated in PIANC [28] report. The results of unducted propellers when compared with the results of circular jets, have higher turbulence level, a shorter length of the flow establishment zone and a wider radial spread.

L_{psmax}/D_p values are also below the Chiew and Lim [2]’s water jet formula and scattered around the line associated with no pile cases (Figure 6.62). However, most S_{smax}/D_p values for pile cases lay between the lines corresponding to propeller jet (with no pile) and water jet (Figure 6.63).

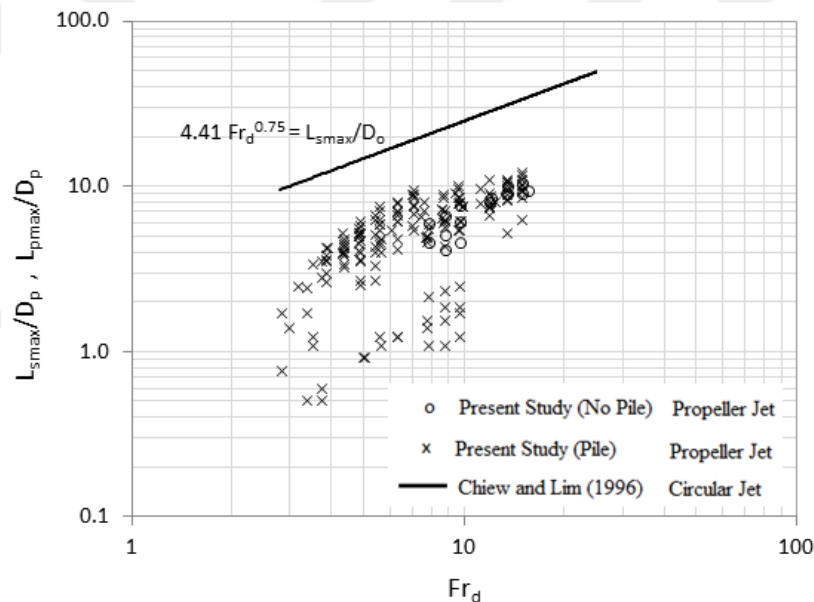


Figure 6.62 Relationship between L_{smax}/D_p and Fr_d with $d_o = 4$ cm, 9 cm, and 14 cm, with and without piles, based on propeller jet mechanisms on sand beds with $d_{50} = 0.52$ mm, 1.28 mm, 4.0 mm, and 8.3 mm

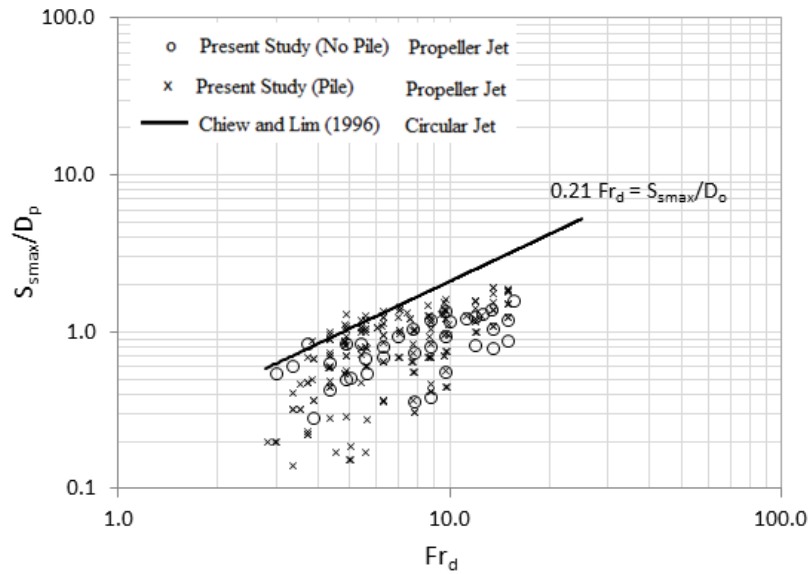


Figure 6.63 Relationship between S_{\max}/D_p and Fr_d with $d_o = 4$ cm, 9 cm, and 14 cm, with and without piles, based on propeller jet mechanisms on sand beds with $d_{50} = 0.52$ mm, 1.28 mm, 4.0 mm, and 8.3 mm

6.2.2 Effects of the Propeller Gap

Vessels like ro-ro ships have different propeller gaps fitted on the stern or bow. Thus, scour profiles for changing vertical distance of propellers from the sea bed (gap) were investigated while other parameters were kept constant. In the present study, the gap of the propeller (G) was adjusted 10 cm above from the sand bed and all tests were repeated for $G=15$ cm and 20 cm.

Variations of S_o/D_p with Fr_d given for $G=10$ cm and 15 cm and $G=20$ cm on a sediment bed of $d_{50}=0.52$ mm are given in Figure 6.64, Figure 6.65 and Figure 6.66, respectively. These figures indicate that S_o/D_p increases with increasing Fr_d and trendlines indicate the same tendency for different gaps of the propeller with $G=10$ cm, 15 cm and 20 cm. Similar results were obtained for coarser bed materials of $d_{50}=1.28$ mm, 4.0 mm and 8.3 mm as seen in Figure A.120 - Figure A.127.

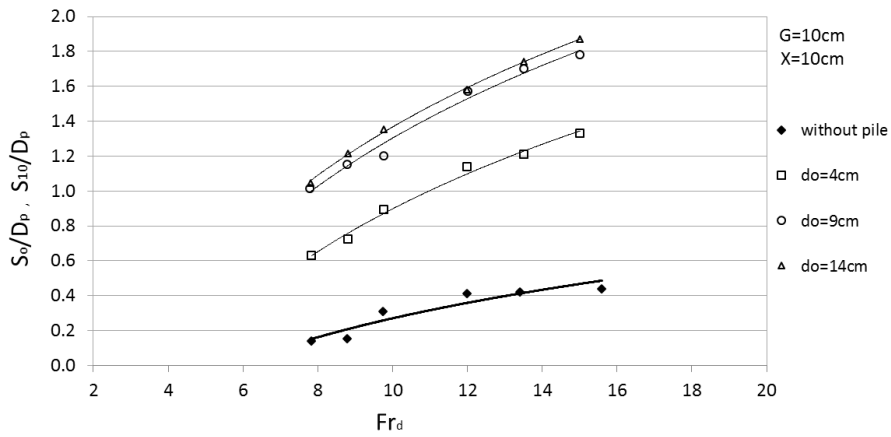


Figure 6.64 Variation of S_o/D_p with Fr_d on sediment bed of $d_{50}=0.52$ mm ($G=10$ cm)

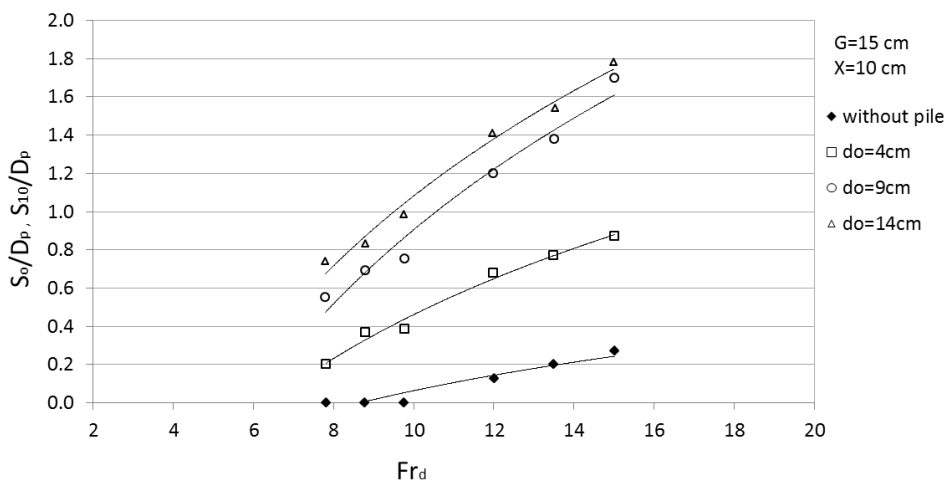


Figure 6.65 Variation of S_o/D_p with Fr_d on sediment bed of $d_{50}=0.52$ mm ($G=15$ cm)

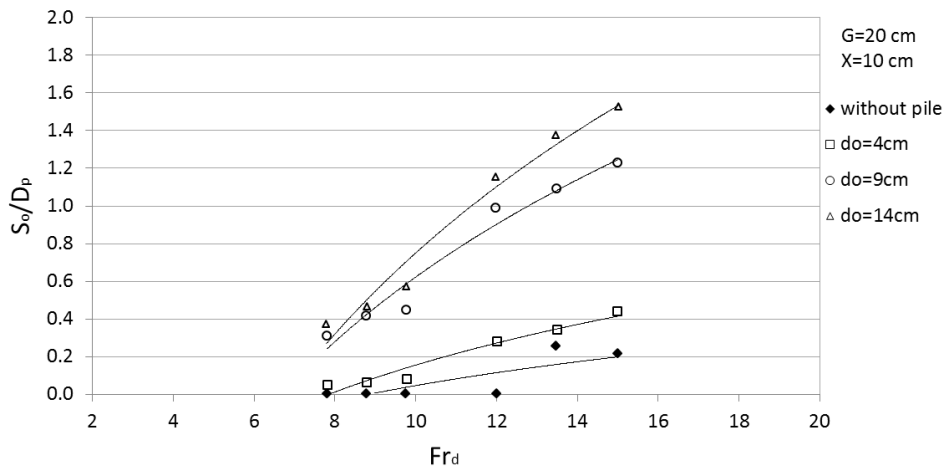


Figure 6.66 Variation of S_o/D_p with Fr_d on sediment bed of $d_{50}=0.52$ mm ($G=20$ cm)

Increasing gap causes lower S_o/D_p values with respect to Fr_d as seen in Figure 6.67, Figure 6.68 and Figure 6.69.

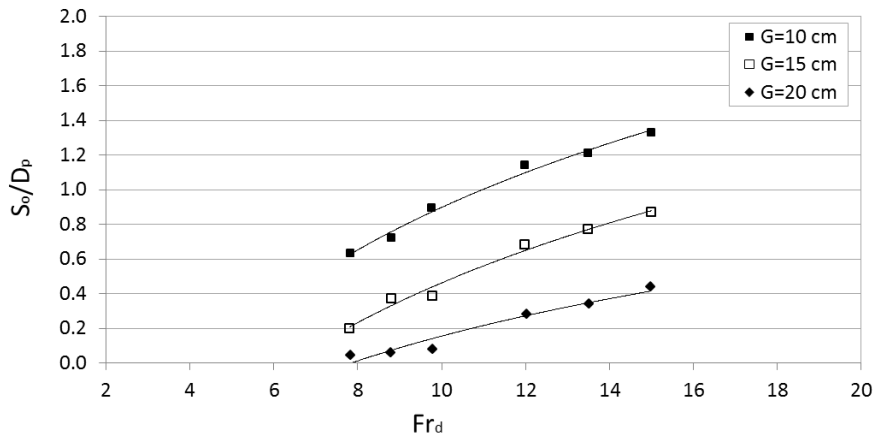


Figure 6.67 Variation of S_o/D_p with Fr_d with $d_o=4$ cm pile on sediment bed of $d_{50}=0.52$ mm for different gaps of the propeller

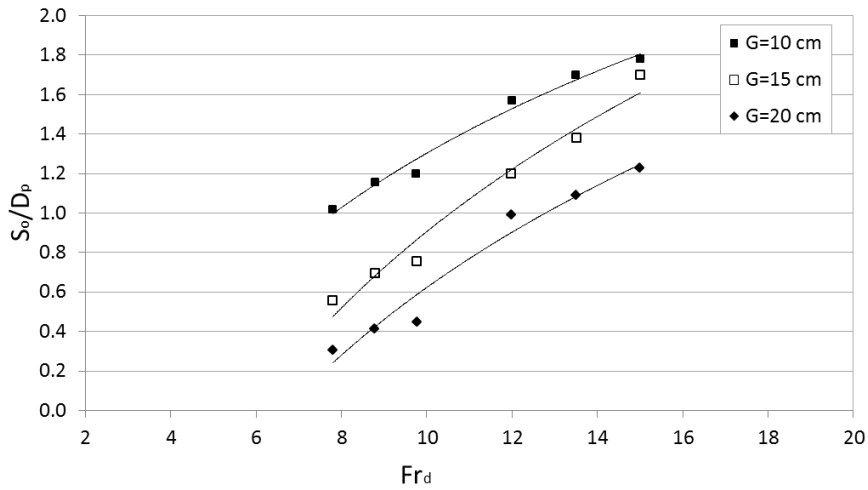


Figure 6.68 Variation of S_o/D_p with Fr_d with $d_o=9$ cm pile sediment bed of $d_{50}=0.52$ mm for different gaps of the propeller

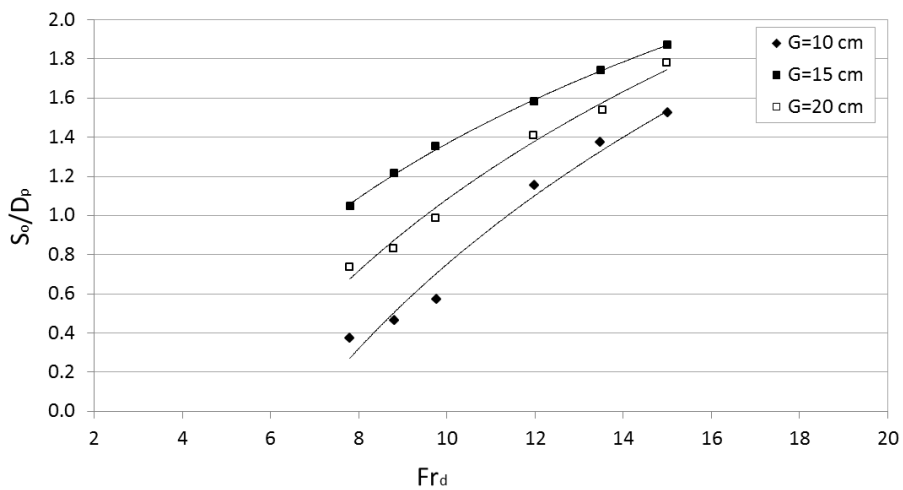


Figure 6.69 Variation of S_o/D_p with Fr_d with $d_o=14$ cm pile sediment bed of $d_{50}=0.52$ mm for different gaps of the propeller

Scour profiles are given in Table 6.8 for different gaps of the propeller for the same experimental conditions ($D_p=10$ cm, and the propeller speed was 745 rpm). As seen in Table 6.8 the height of the deposition crest (h_r) and scour depth at the toe of pile (S_o) decrease with an increase in the gap of the propeller from 10 cm to 20 cm for the sand bed size of $d_{50}=0.52$ mm. As the gap increased, the intensity of the propeller jet became too weak to entrain the sediment bed. Similar profile developments were observed on different sediment bed material sizes of $d_{50}=1.28$ mm, 4.0 mm and 8.3 mm given in Table 6.9, Table 6.10, and Table 6.11, respectively.

Table 6.8 Scour profiles with different gaps of the propeller over the sediment bed of $d_{50}=0.52$ mm

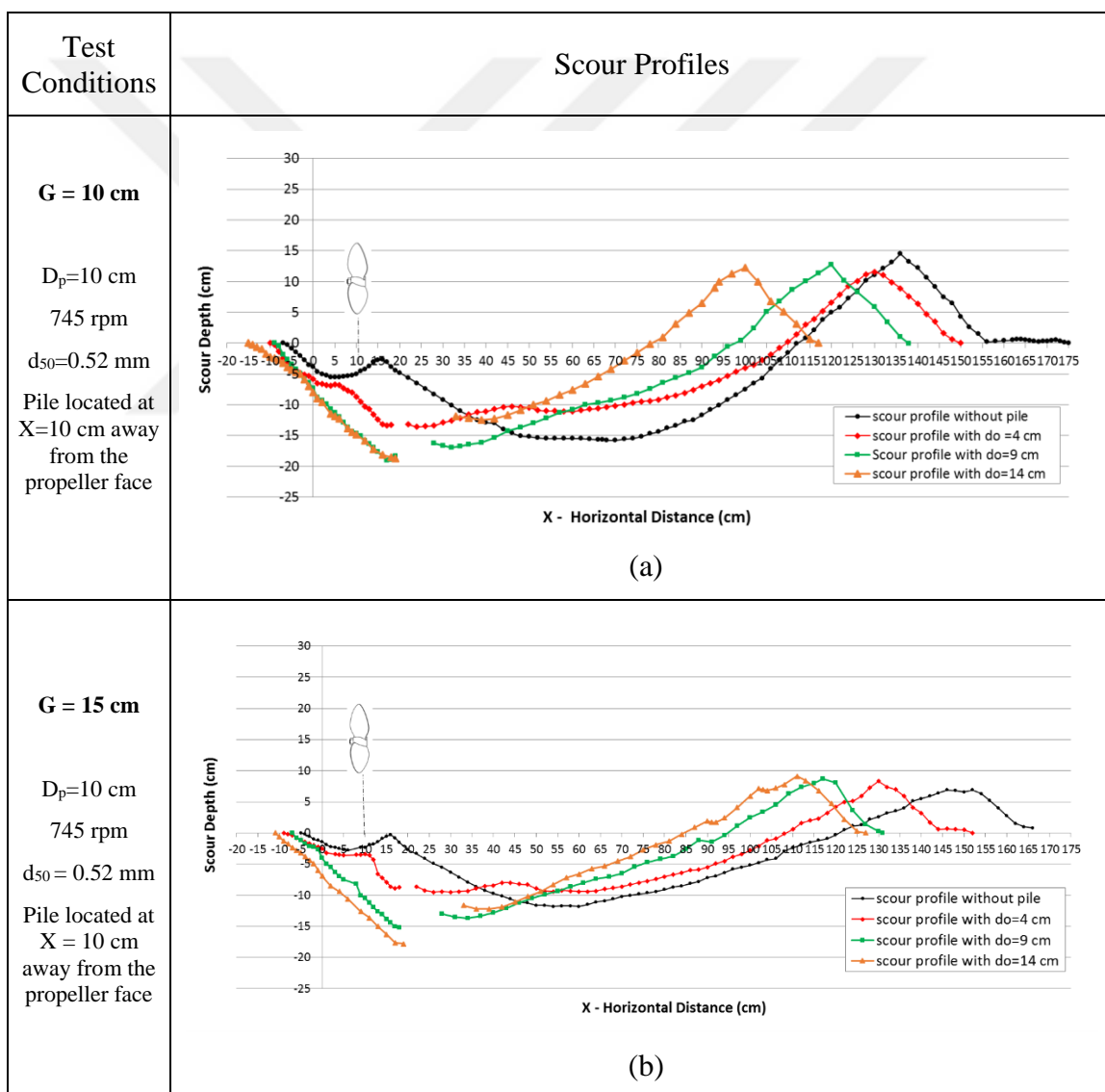


Table 6.8 Scour profiles with different gaps of the propeller over the sediment bed of $d_{50}=0.52$ mm (cont'd)

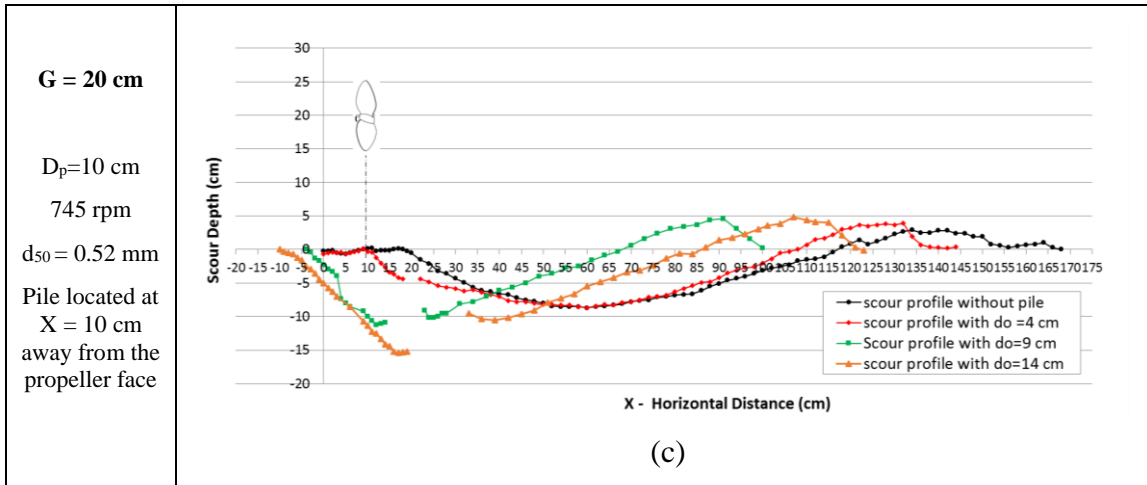


Table 6.9 Scour profiles with different gaps of the propeller over the sediment bed of $d_{50}=1.28$ mm

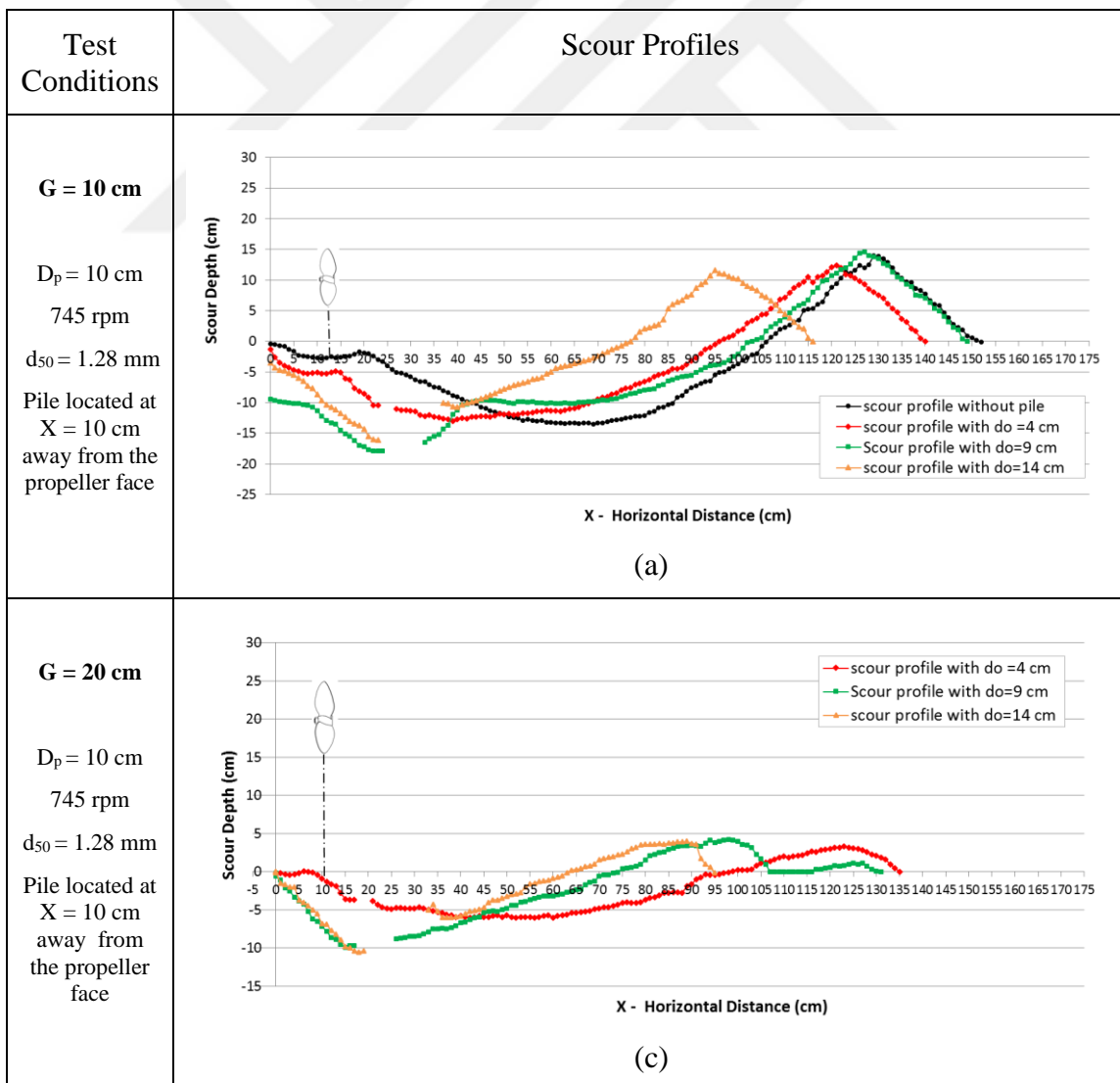


Table 6.10 Scour profiles with different gaps of the propeller over the sediment bed of $d_{50}=4.00$ mm

Test Conditions	Scour Profiles
<p>G = 10 cm</p> <p>$D_p = 10$ cm</p> <p>745 rpm</p> <p>$d_{50} = 4$ mm</p> <p>Pile located at X = 10 cm away from propeller the face</p>	<p>(a)</p>
<p>G=15 cm</p> <p>$D_p = 10$ cm</p> <p>745 rpm</p> <p>$d_{50} = 4$ mm</p> <p>Pile located at X = 10 cm away from the propeller face</p>	<p>(b)</p>
<p>G=20 cm</p> <p>$D_p = 10$ cm</p> <p>745 rpm</p> <p>$d_{50} = 4$ mm</p> <p>Pile located at X = 10 cm away from the propeller face</p>	<p>*No scours were formed with $d_o = 4$ cm pile.</p> <p>(c)</p>

Table 6.11 Scour profiles with different gaps of the propeller over the sediment bed of $d_{50}=8.30$ mm

Test Conditions	Scour Profiles
<p>G = 10 cm</p> <p>$D_p = 13$ cm</p> <p>745 rpm</p> <p>$d_{50} = 8.3$ mm</p> <p>Pile located at X=10 cm away from the propeller face</p>	<p>(a)</p>
<p>G = 15 cm</p> <p>$D_p = 13$ cm</p> <p>745 rpm</p> <p>$d_{50} = 8.3$ mm</p> <p>Pile located at X = 10 cm away from the propeller face</p>	<p>(b)</p>
<p>G = 20 cm</p> <p>$D_p = 13$ cm</p> <p>745 rpm</p> <p>$d_{50} = 8.3$ mm</p> <p>Pile located at X = 10 cm away from the propeller face</p>	<p>(c)</p>

No scour holes were formed for G=15 cm and G=20 cm gap height for $D_p=10$ cm. So, scour formation comparisons with different gap height, are given for only the 13 cm propeller in this table.

6.2.3 Effects of the Pile Location

The scour depth at the toe of the pile (S_o) at different pile locations from the propeller's face were also investigated for sand bed material sizes $d_{50} = 1.28$ mm. Chin et al. [8] studied a wall jet around a vertical pile and classified the predominant effective mechanism with the ratio between impingement distance to jet diameter (X_i/D_o). In the present study, effect of impingement distance was investigated and effective pile locations were considered for the propeller jet flow.

The variation of the relative scour depth (S_o/D_p) was given for different pile locations at $X = 10$ cm, 20 cm, 30 cm and 40 cm, away from the propeller's face as seen in Figure 6.70, Figure 6.71, Figure 6.72 and Figure 6.73, respectively. These figures include the rotation speeds of 590 rpm, 670 rpm, and 745 rpm for each propeller ($D_p=6.5$ cm, 10 cm and 13 cm) for only pile diameter of $d_o=4$ cm for $5.03 \leq Fr_d \leq 12.59$. Therefore, relative scour depths for no pile conditions (S_{10}/D_p , S_{20}/D_p , S_{30}/D_p , S_{40}/D_p) are illustrated as filled symbols in the figures. Scour depths were measured at $X=10$ cm, 20 cm, 30 cm and 40 cm ($X/d_o=2.5$, $X/d_o=5$, $X/d_o=7.5$, $X/d_o=10$) away from the propeller's face with no pile conditions as defined with S_{10} , S_{20} , S_{30} and S_{40} , respectively. These scours were compared with the scour depths occurred at the toe of pile (S_o) at the same location.

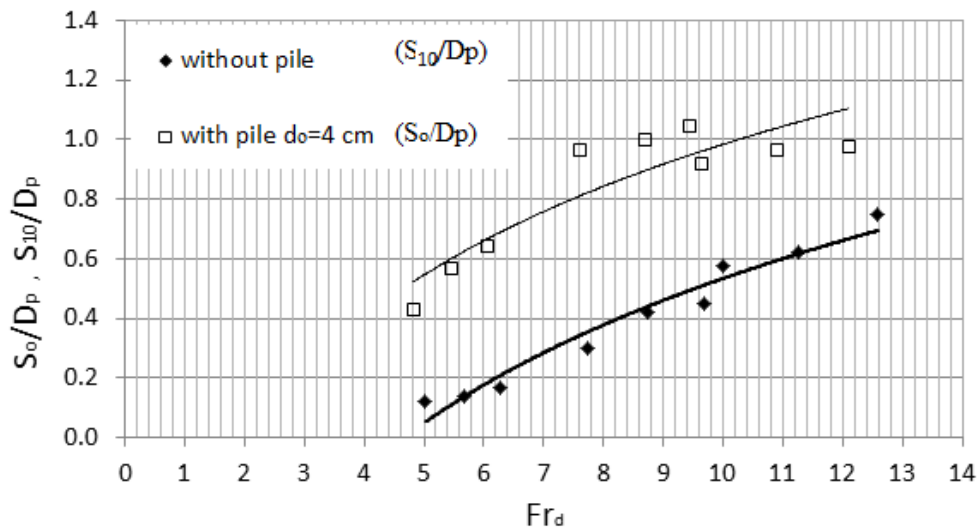


Figure 6.70 Variation of S_o/D_p with Fr_d based on the propeller jet mechanism with and without pile cases for $G=10$ cm and $X/d_o=2.5$

Relative scour depths (S_{10}/D_p) in the cases where piles are absent are always smaller than scours occurring at the toe of pile (S_o/D_p) when the pile is located at $X=10$ cm away from the propeller for $5.03 \leq Fr_d \leq 12.59$ (Figure 6.70). This is because pile obstruction is highly

effective in promoting the scouring formation at distances 10 cm away from the propeller. However, the trend lines (without and with piles) come closer to each other when the distances between the pile and the propeller face are increased to $X = 20$ cm, 30 cm, and 40 cm, as seen in Figure 6.71, Figure 6.72 and Figure 6.73, respectively. This is because an increasing pile distance leads to diminished pile obstructions.

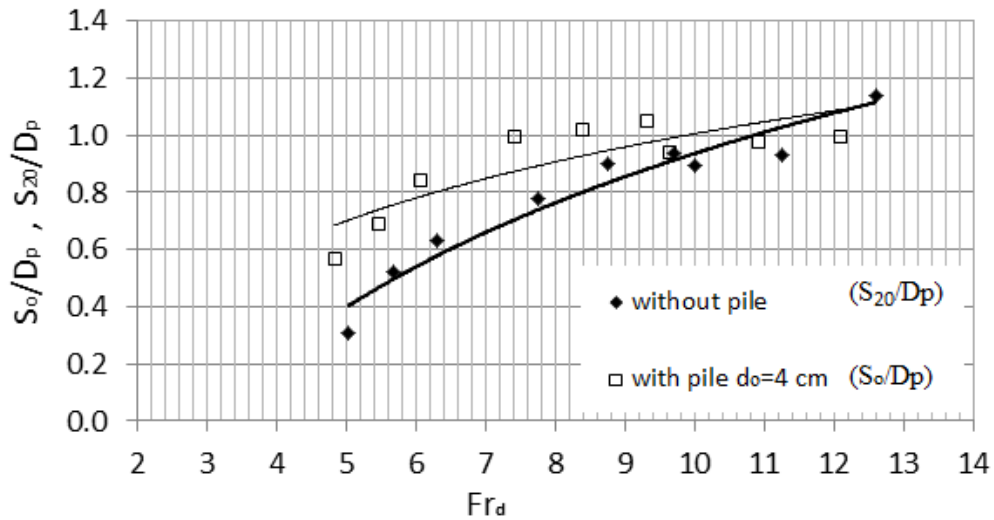


Figure 6.71 Variation of S_o/D_p with Fr_d based on the propeller jet mechanism with and without pile cases for $G=10$ cm and $X/d_o=5.0$

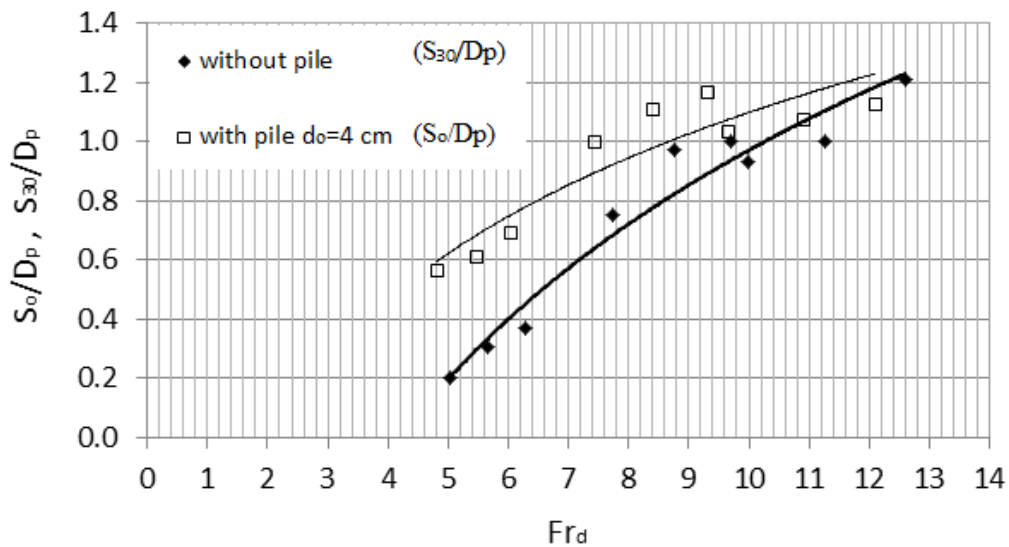


Figure 6.72 Variation of S_o/D_p with Fr_d based on the propeller jet mechanism with and without pile cases for $G=10$ cm and $X/d_o=7.5$

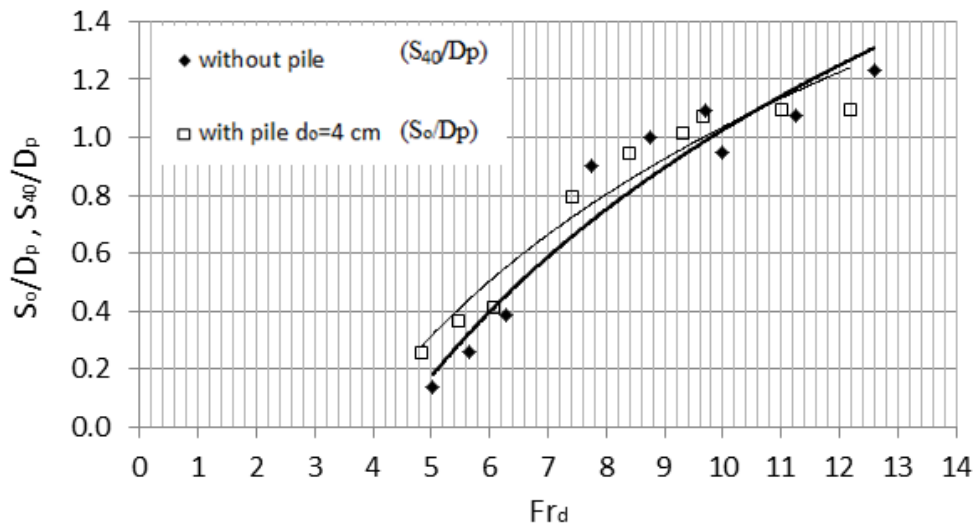


Figure 6.73 Variation of S_o/D_p with Fr_d based on the propeller jet mechanism with and without pile cases for $G=10$ cm and $X/d_o=10$

Chin et al. [8] classified different scour profile types due to predominant effective mechanism defined as water jet and / or obstruction mechanism on scouring formation. They stated that obstruction mechanism is predominantly effective for relatively small impingement distance (X_i/D_p) for Type 1 profiles while jet mechanism becomes the dominant mechanism for relatively large distances for Type 2. Both mechanisms are effective on Type 3 scour profiles. In the first region, the jet exit extends from the jet exit to some distance where scouring formation is characterized by the jet diffusion similar to Type 1. In the second region, erosion around the pile is mainly caused by the obstruction mechanism as Type 2. Illustrations of these two regions are given in Figure 1.14 (a) for the boundary condition between Type 1 and 3.

In the present study, the predominant effective mechanism was investigated for different pile locations from the propeller face by considering the jet diffusion area.

Johnston et al. [19] introduced the definition of the boundary layer development for the propeller jet, as seen in Figure 6.74.

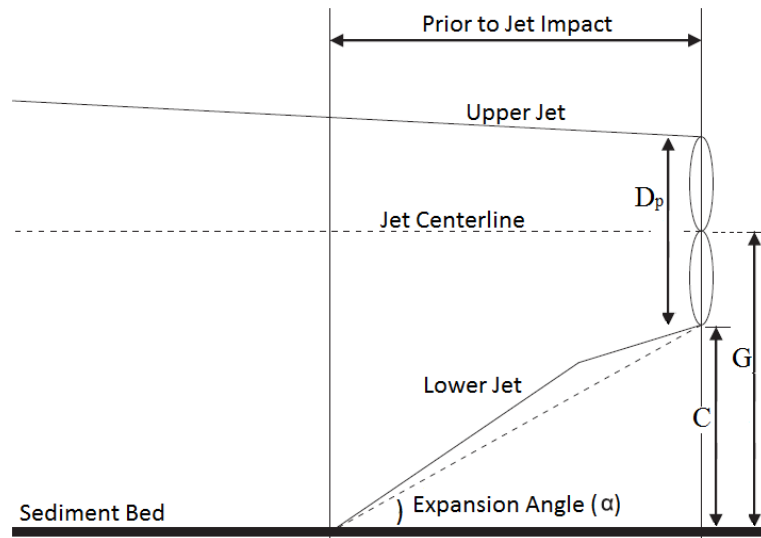


Figure 6.74 Schematic view of boundary layer development (Johnston et al. [19])

This figure shows that boundary layer of the propeller jet diffusion is not expanding symmetrically with respect to the jet's centerline. Johnston et al. [19] explained that the stream of the propeller jet expands at a faster rate owing to the reduction in pressure beneath the jet for the confined cases with the use of sand beds. Hence, Johnston et al. [19] defined the expansion angle for a lower jet boundary layer, as indicated in Equation (6.18).

$$\alpha = 66 \cdot 10^{-3} C + 8.3 \quad (6.18)$$

where, α is the expansion angle of a propeller jet, C is the clearance height in millimeters.

In the present study, calculated expansion angles with the clearance heights and gaps for each propeller are given in Table 6.12.

Table 6.12 Propeller jet expansion angles for propeller gaps of 10 cm, 20 cm and 30 cm

Propeller	Propeller Diameter (D_p , cm)	Gap (G, cm)	Clearance (C, cm) $C = G - (D_p / 2)$	Expansion angle (α , °)
Propeller - 6.5	6.5	10	6.75	12.8
Propeller - 6.5	6.5	15	11.75	16.1
Propeller - 6.5	6.5	20	16.75	19.4
Propeller - 10	10	10	5.00	11.6
Propeller - 10	10	15	10.00	14.9
Propeller - 10	10	20	15.00	18.2
Propeller - 13	13	10	3.50	10.6
Propeller - 13	13	15	8.50	13.9
Propeller - 13	13	20	13.50	17.2

Scour depths (S_o) are shown in Figures 6.78 - Figure 6.83 with scour profiles for the instances where piles were absent. The square symbols in this figure show the measured scour depths at the upstream toe of piles located at different distances ($X = 10, 20, 30$ and 40 cm) from the propeller's face. The developments of lower boundary layer at different expansion angles of propeller jets are also included. Increasing distances between the propeller and the pile, cause decreasing scour depths (S_o). X_{int} is defined as the distance from the location of the propeller's face to the location where the jet boundary layer intersected the original (horizontal) bed level. This intersection point represents the transition location where the predominant effect on scouring process changed from a pile vortex mechanism (obstruction mechanism) to a jet mechanism.

Scour depths at the toe of pile (S_o) are given for different pile locations ($X=10$ cm, 20 cm, 30 cm and 40 cm) for 10 cm propeller at 590 rpm, 670 rpm, and 745 rpm as seen in Figure 6.75, Figure 6.76 and Figure 6.77, respectively.

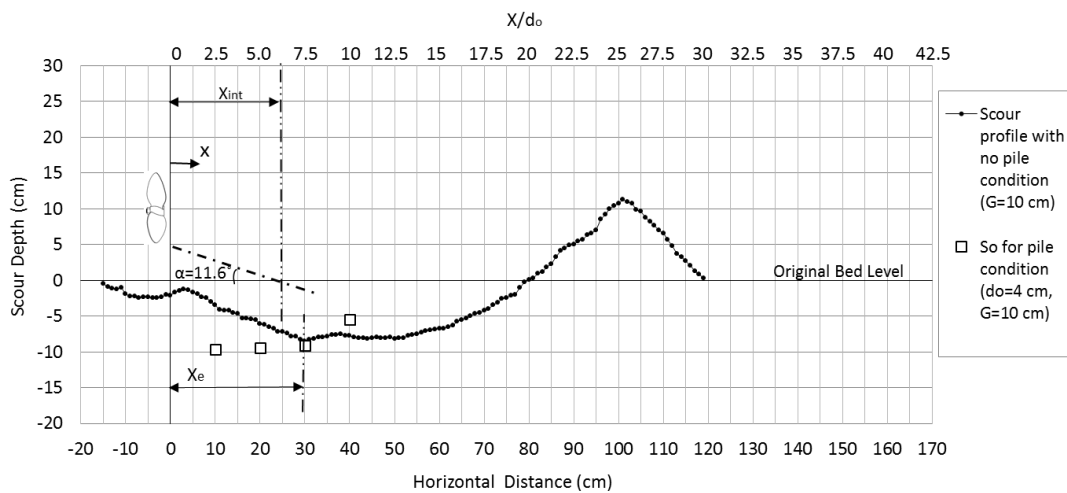


Figure 6.75 Scour profile without piles and scour depths at the toe of pile (S_o) for different locations at $X/d_o=2.5, 5, 7.5, 10, D_p=10$ cm, speed = 590 rpm, and $G=10$ cm

The scour depth at the toe of each pile (S_o) was bigger than the scour depth without a pile condition when the pile was located at $X = 10$ cm and 20 cm ($X/d_o = 2.5$ and 5) away from the propeller whereas it was smaller at $X = 40$ cm ($X/d_o=10$) as seen in Figure 6.75. The propeller jet extended from the propeller's face to the locus where the lower jet layer intersected the original bed level (X_{int}). On the other hand, at $X_{int} = 24.4$ cm ($X_{int}/d_o = 6.0$) propeller jet flow was diffusion mainly effective on scouring process with pile vortex mechanism when the pile was located before this distance ($X_{int}/d_o < 6.0$) the scour at the toe of the pile was caused mostly due to the pile vortex mechanism. At the distance of $X_{int}/d_o =$

6.0, the propeller jet mechanism fully expanded and established contact with the original sediment bed. Beyond this distance ($X_{int}/d_o > 6.0$), the propeller jet flow became effective, and scour depths (S_o) were closer or/and smaller in values than those elicited in the no-pile case (Figure 6.75). The same situation was observed for the increasing propeller speeds of 670 rpm and 745 rpm for the same conditions ($D_p=10$ cm, $C=5.0$, $\alpha = 11.6^\circ$) as seen in Figure 6.76 and Figure 6.77.

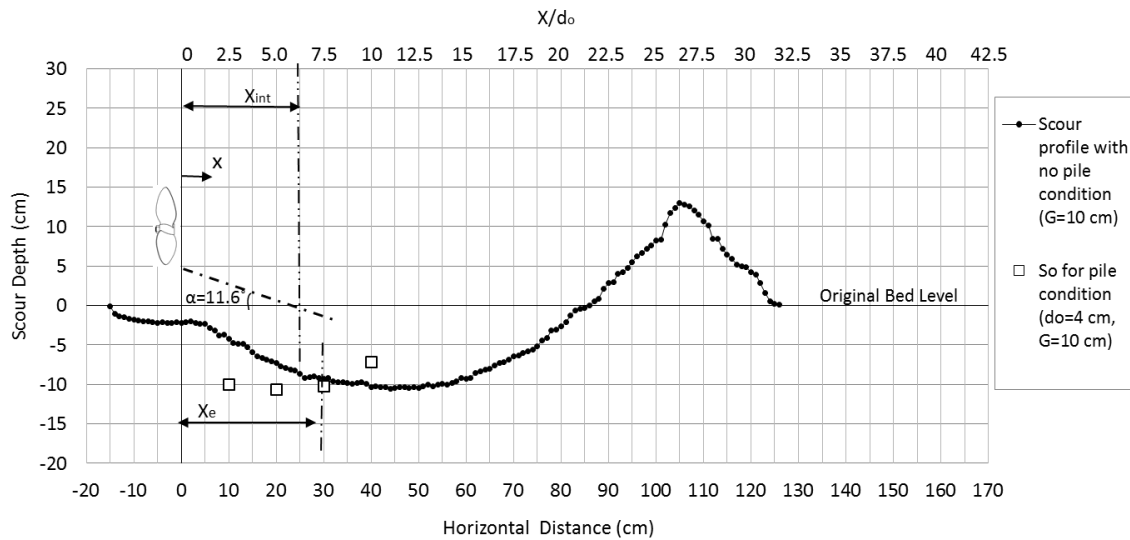


Figure 6.76 Scour profile without piles and scour depths at the toe of pile (S_o) for different locations at $X/d_o=2.5, 5, 7.5, 10$, $D_p=10$ cm, speed = 670 rpm, and $G=10$ cm

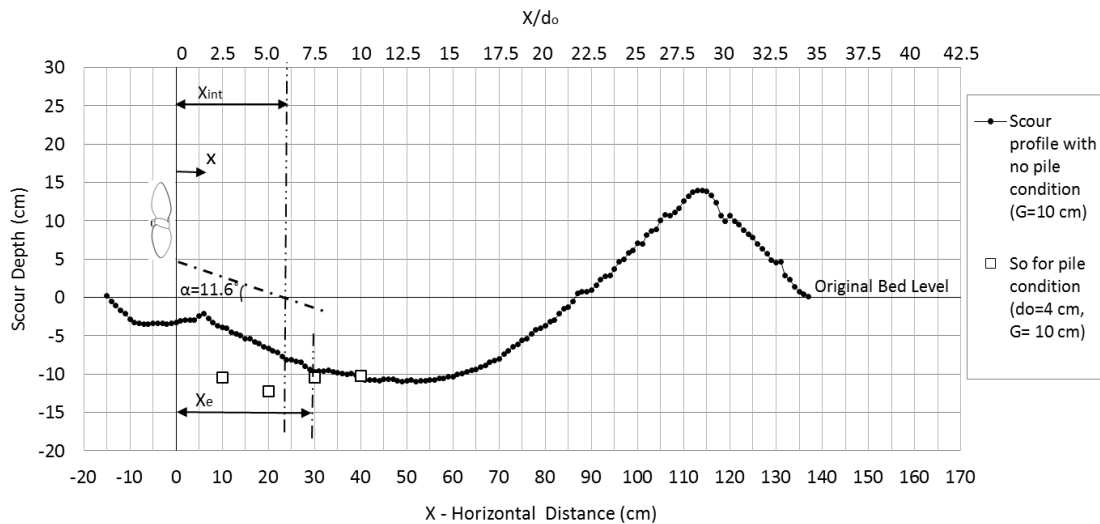


Figure 6.77 Scour profile without piles and scour depths at the toe of pile (S_o) for different locations at $X/d_o=2.5, 5, 7.5, 10$, $D_p=10$ cm, speed = 745 rpm, and $G=10$ cm

Scour depth at the toe of each pile (S_o) at different locations are marked with square symbols on the scour profiles without pile conditions at propeller speeds of 590 rpm, 670 rpm and

745 rpm in Figure 6.75, Figure 6.76 and Figure 6.77, respectively. Figures indicate that the scour depths around piles are always bigger than scour profiles before point X_{int} .

The effective pile location (X_e) defined as the distance between the propeller's face and the point where the scour depth at the toe of the pile (S_o) is almost equal to the scour profile in the case where piles were absent. This point always occurs downstream of the intersection point of the lower jet boundary layer and on the original bed level (X_{int}). As an example, scour profile without pile was intersected with S_o at about $X_e=30$ cm ($X_e/d_o=7.5$) for the clearance of the propeller at 5 cm as seen in Figure 6.77 while lower layer intersected original bed at $X_{int}=24.4$ cm ($X_{int}/d_o=6.0$). Beyond the distance of X_e scour depth around pile (S_o) decreases. Thus, predominant effective scouring mechanism may be changed from pile vortex mechanism to jet mechanism after propeller jet is fully expanded and touched the sediment bed at $X_{int}/d_o > 6.0$.

Scour profiles with the absence of piles and scour depths (S_o) for different pile locations are also shown for other propellers of $D_p=6.5$ cm and 13 cm in Figures 6.79, 6.80, 6.81, and Figures 6.82, 6.83, 6.84, respectively. Effective pile location (X_e) that coincided with the point X_{int} for smaller propeller diameters is seen in Figure 6.78. Effective pile location is found at $X_e/d_o = 7.5$ for $0.77 \leq G/D_p \leq 1.54$ with considering all tests results for different propeller speeds of 590 rpm, 670 rpm and 745 rpm. Beyond this distance (X_e) predominant effective mechanism of the pile vortex starts to decrease and the propeller jet mechanism predominantly starts to be effective on the scouring formation. In other words, beyond the distance of $X_e/d_o=7.5$, predominant effective mechanism due to the pile decreases and jet mechanism becomes more effective on the scouring formation. This distance is also found downstream of the point where lower jet layer intersects with original bed level (X_{int}) but these two distances are almost the same ($X_{int}=X_e$) for only the smaller propeller diameter of $D_p=6.5$ cm. Effective pile location may be defined between $2.3 \leq X_e/D_p \leq 4.61$ for $0.77 \leq G/D_p \leq 1.54$.

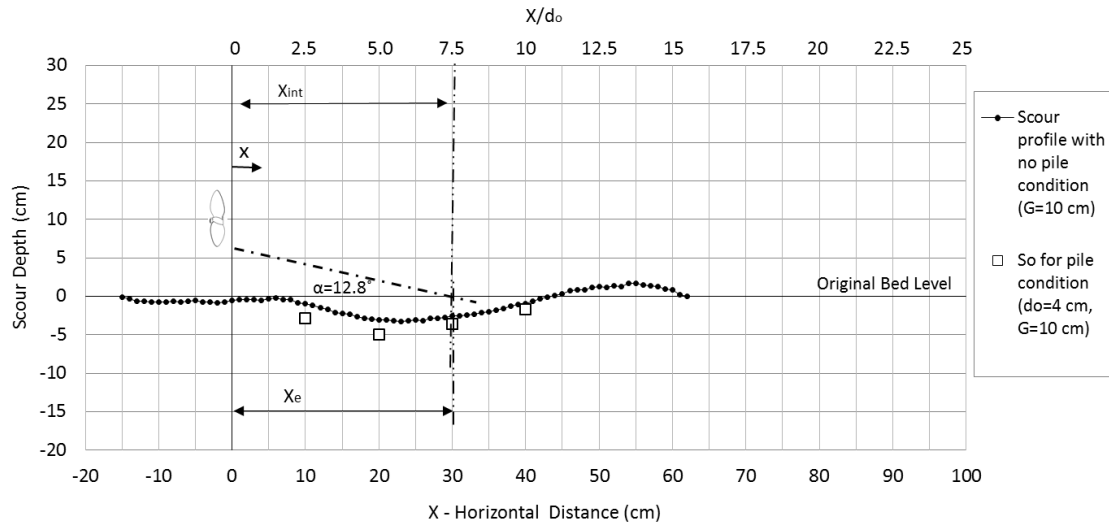


Figure 6.78 Scour profile without piles and scour depths at the toe of pile (S_o) for different locations at $X/d_o = 2.5, 5, 7.5, 10$, $D_p = 6.5$ cm, speed = 590 rpm, and $G=10$ cm

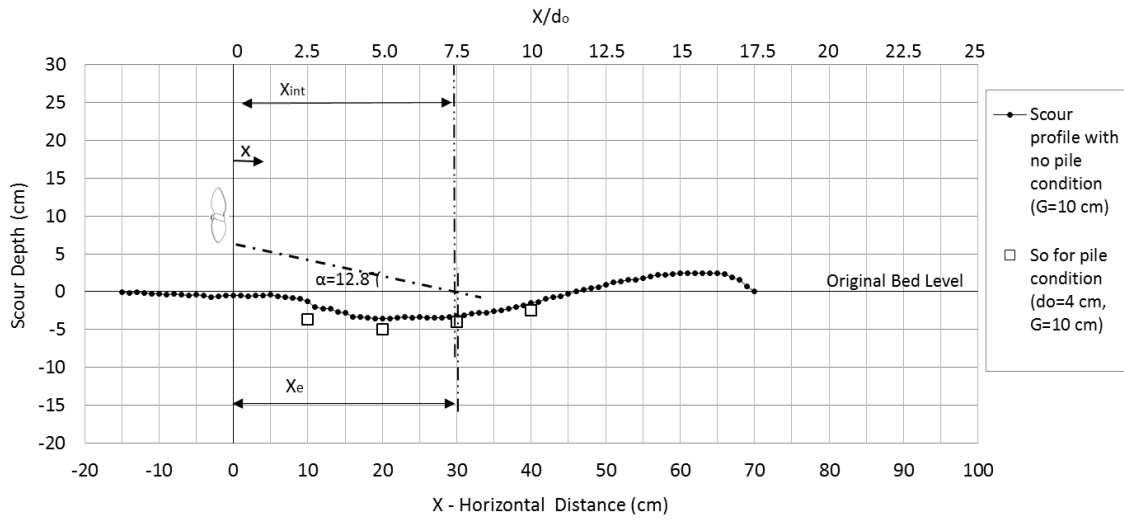


Figure 6.79 Scour profile without piles and scour depths at the toe of pile (S_o) for different locations at $X/d_o = 2.5, 5, 7.5, 10$, $D_p=6.5$ cm, speed = 670 rpm, and $G=10$ cm

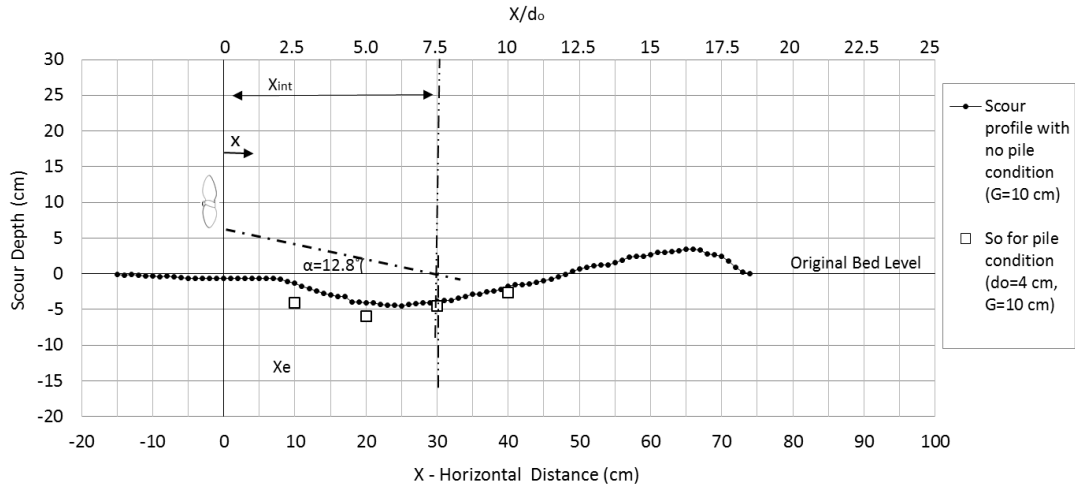


Figure 6.80 Scour profile without piles and scour depths at the toe of pile (S_o) for different locations at $X/d_o = 2.5, 5, 7.5, 10$, $D_p=6.5$ cm, speed = 745 rpm, and $G=10$ cm

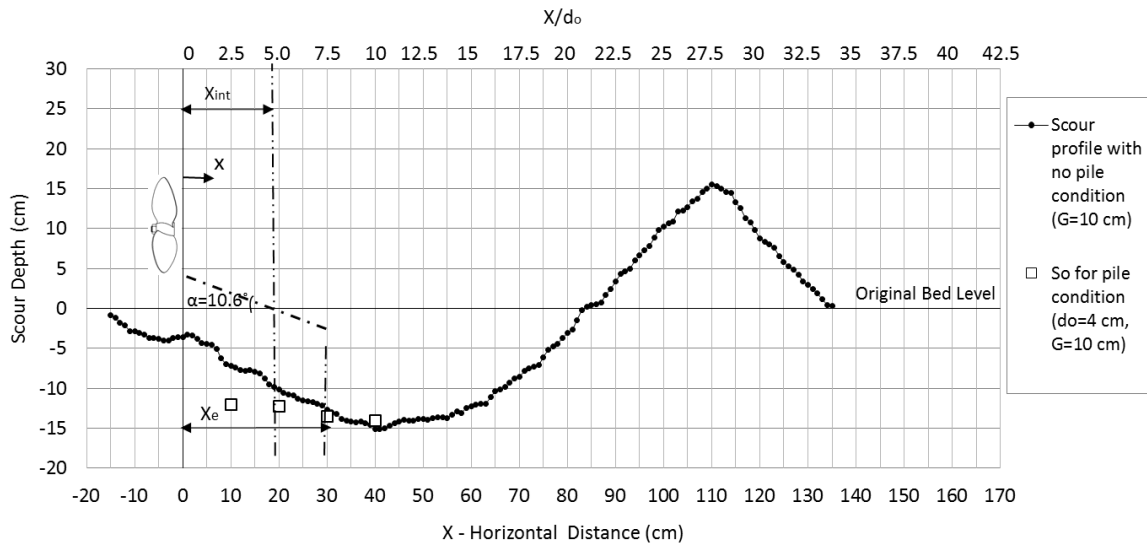


Figure 6.81 Scour profile without piles and scour depths at the toe of pile (S_o) for different locations at $X/d_o = 2.5, 5, 7.5, 10$, $D_p=13$ cm, speed = 590 rpm, and $G=10$ cm

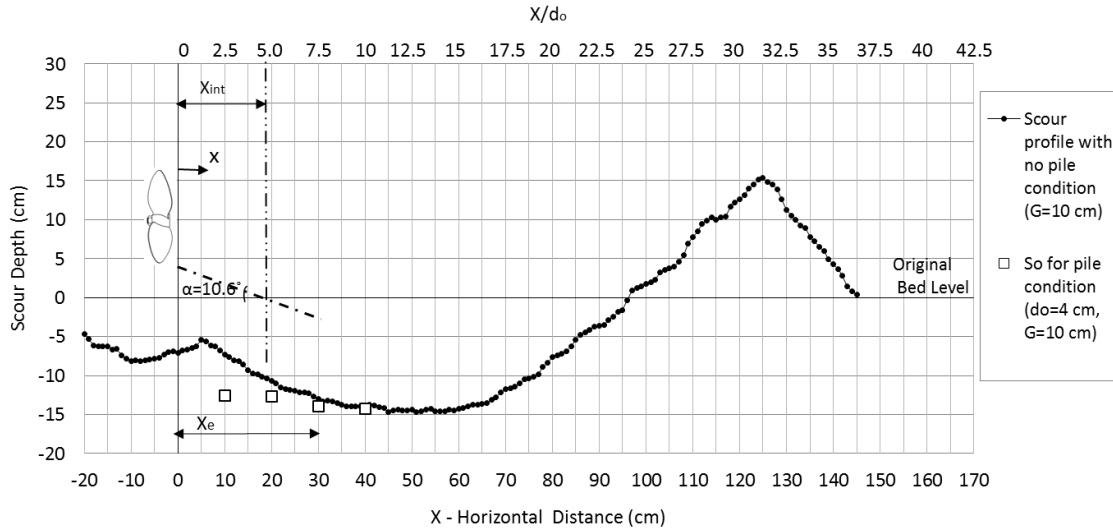


Figure 6.82 Scour profile without piles and scour depths at the toe of pile (S_o) for different locations at $X/d_o = 2.5, 5, 7.5, 10$, $D_p=13$ cm, speed = 670 rpm, and $G=10$ cm

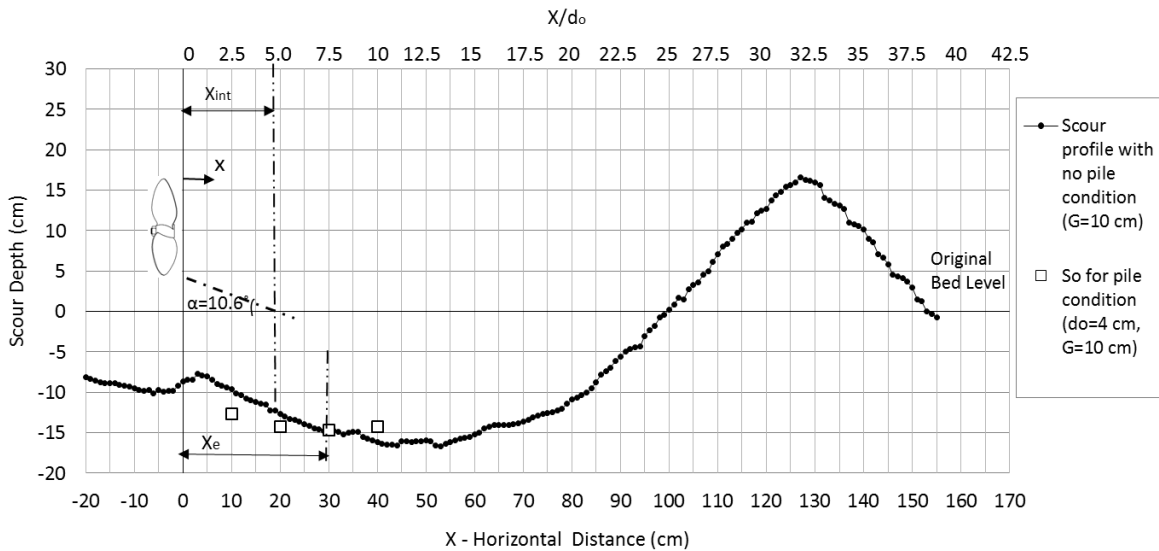


Figure 6.83 Scour profile without piles and scour depths at the toe of pile (S_o) for different locations at $X/d_o = 2.5, 5, 7.5, 10$, $D_p=13$ cm, speed = 745 rpm, and $G=10$ cm

If the gap is increased to $G=15$ cm and 20 cm, expansion angle increases significantly (Table 6.12). If the gap of the propeller is increased from $G=10$ cm to 20 cm, expansion angle for each propeller increases with increasing clearance up to 6.6° . So, the scour depth at the toe of the pile (S_o) changes at different pile locations and propeller's gap of $G=10$ cm, 15 cm and 20 cm due to the impact area of the jet diffusion mechanism.

The scour (S_o) for higher gaps of the propeller ($G=15$ cm and 20 cm) increase with increasing distance of the propeller at $X=10$ cm, 20 cm, 30 cm and 40 cm away from the propeller face with $D_p=10$ cm for propeller speeds of 590 rpm, 670 rpm and 745 rpm as seen

in Figure 6.84, Figure 6.85 and Figure 6.86, respectively. The scour depths (S_o) at $G=10$ cm are significantly bigger than the scours when the propeller gap is at $G=15$ cm and 20 cm if pile is located at $X=10$ cm, 20 cm. However, the scour (S_o) is smaller at $G=10$ cm than it is at 15 cm and 20 cm for the pile location at $X=40$ cm because at that distance ($X = 40$ cm) jet diffusion at $G=10$ cm extends sufficiently while the lower jet boundary is still expanding at $G=15$ cm and 20 cm. Similar conditions are observed for the propeller diameters of 6.5 cm and 13 cm as seen in Figure A.177 - Figure A.182. However, scours around pile are always bigger at $G=10$ cm than at the gaps of 15 cm and 20 cm. For bigger gaps $G=20$ cm, the scours around the pile (S_o) are smaller than the scours without pile condition because pile vortex mechanism may not become effective enough for the scour development when compared with smaller gaps.

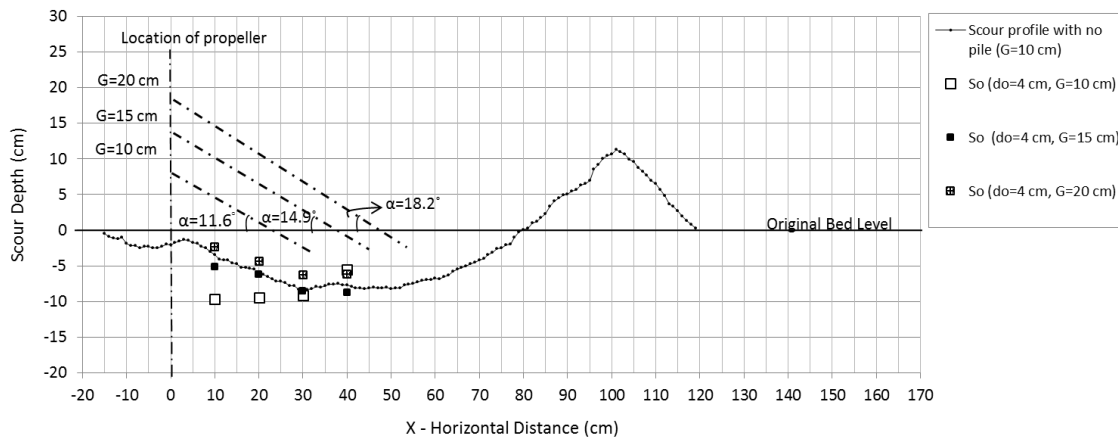


Figure 6.84 Scour profile without piles and scour depths at the toe of pile (S_o) for different locations at $X/d_0=2.5, 5, 7.5, 10$, and different gaps of the propeller ($D_p=10$ cm with 590 rpm)

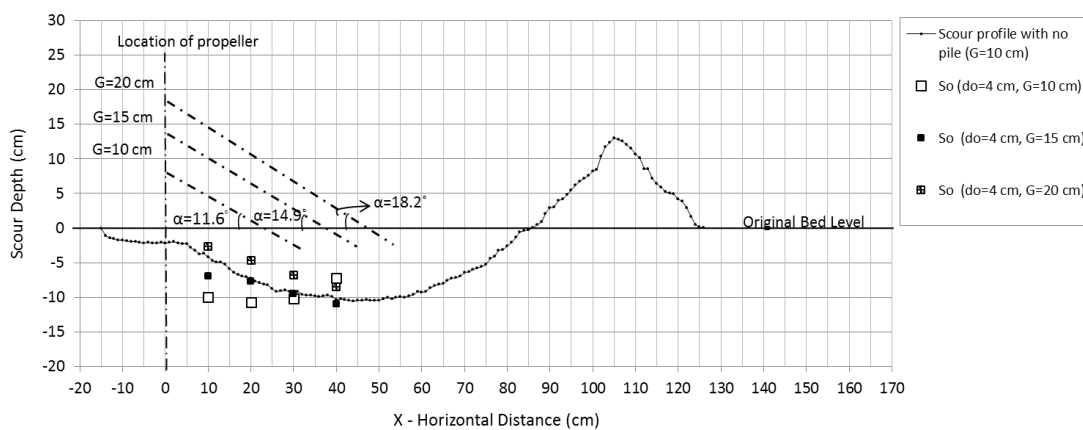


Figure 6.85 Scour profile without piles and scour depths at the toe of pile (S_o) for different locations at $X/d_0=2.5, 5, 7.5, 10$, and different gaps of the propeller ($D_p=10$ cm with 670 rpm)

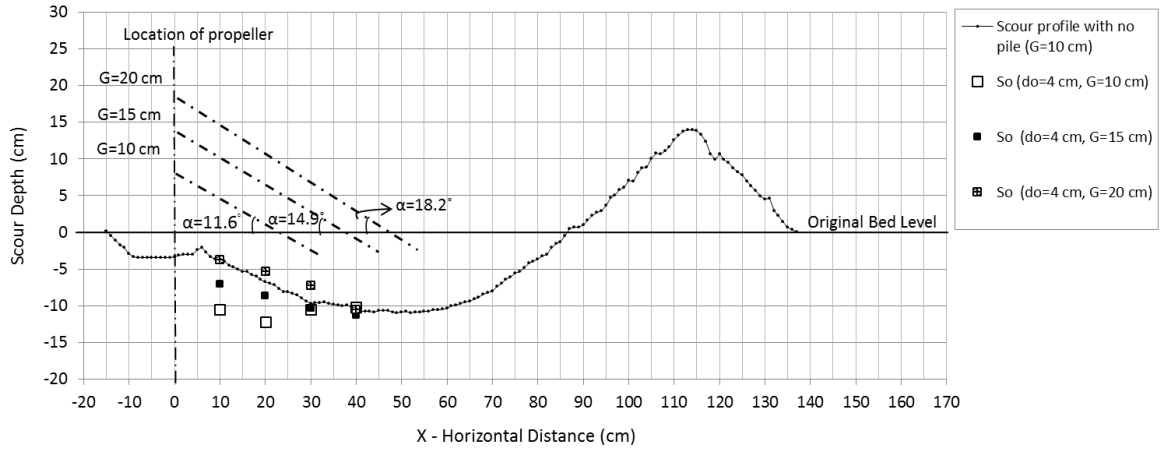


Figure 6.86 Scour profile without piles and scour depths at the toe of pile (S_o) for different locations at $X/d_o=2.5, 5, 7.5, 10$, and different gaps of the propeller ($D_p=10$ cm with 745 rpm)

Relative scour depth (S_o/d_o) versus Fr_d are given for different locations of the pile ($d_o=4$ cm) with propeller gaps of $G=10$ cm, 15 cm and 20 cm ($G/d_o=2.5, 3.75$ and 5.0) as seen in Figure 6.87, Figure 6.89 and Figure 6.89, respectively.

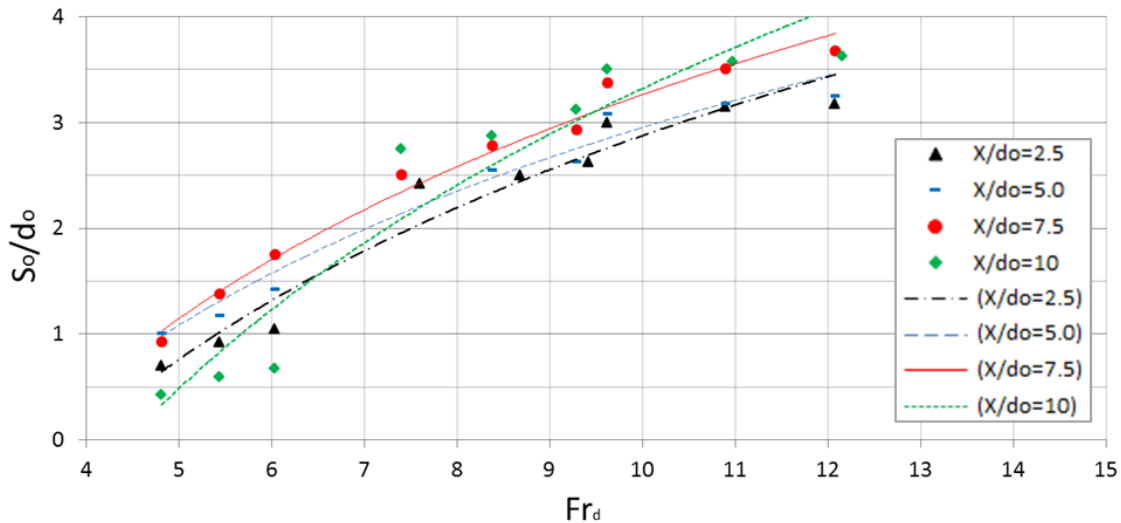


Figure 6.87 Relationship between S_o/d_o and Fr_d on the sediment bed of $d_{50}=1.28$ mm for $G/d_o=2.5$

Maximum S_o/d_o values are obtained when the pile is located at $X=30$ cm ($X/d_o=7.5$) for $G=10$ cm ($G/d_o=2.5$) (Figure 6.87). When the gap is increased to $G=15$ cm and 20 cm ($G/d_o=3.75$ and 5.0), maximum S_o/d_o values are obtained at $X=40$ cm ($X/d_o=10$) as seen in Figure 6.89 and Figure 6.89, respectively. The reason for this is, for the smaller gap and clearance height of the propeller, the intensity of the jet become too strong to entrain the bed sediments nearer the propeller as seen in Figure 6.84.

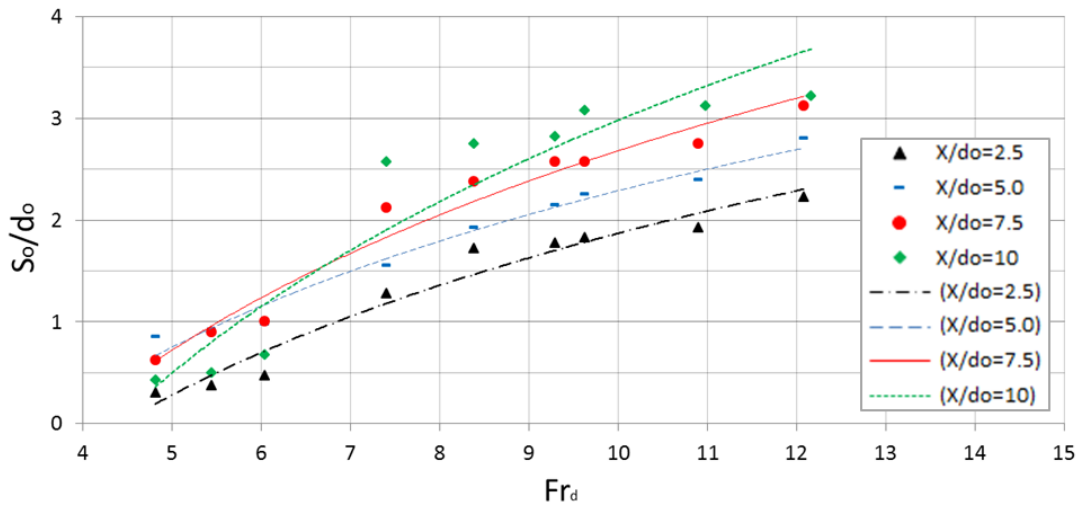


Figure 6.88 Relationship between S_o/d_o and Fr_d on the sediment bed of $d_{50}=1.28$ mm for $G/d_o=3.75$

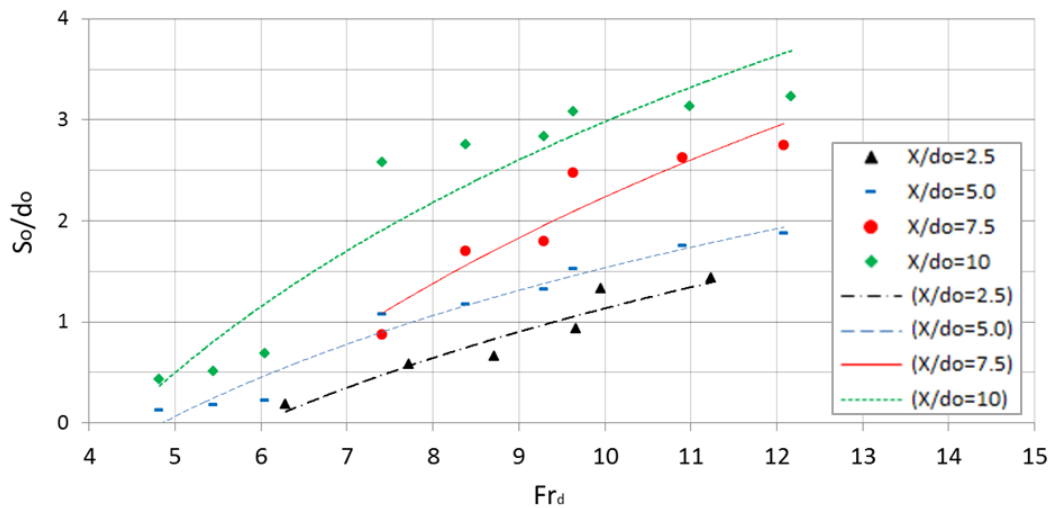


Figure 6.89 Relationship between S_o/d_o and Fr_d on the sediment bed of $d_{50}=1.28$ mm for $G/d_o=5.0$

6.2.4 Estimation of Scour Depth Around a Pile

Erosion problem due to bow or stern thrusters and main propellers of a ship when maneuvering to a berth structure is illustrated by devoting of an entire PIANC [28] report (Figure 2.7).

A number of case studies have been reported, cataloging the problems induced by propeller washes at quay structures. Bergh and Cederwall [31] reported a survey conducted in Swedish harbors and found that 18 quays out of 53 surveyed were damaged as a result of propeller jets. Ryan et al. [65] referred to a similar survey conducted in British ports based

on Quarrin [11]’s findings indicating that 42% of major ports were affected by propeller-induced bed scour. Thus, an improved understanding of scour due to propeller jet near quay structure should be imperative.

To this end, Hamill et al. [9] gave an estimation of scour both for the unconfined and confined quay wall conditions induced by propeller jets. Chin et al. [8] investigated scouring process around the vertical pile by using a simplified circular jet. Hong et al. [5] also examined the scouring process induced by propeller jets without considering any structure and they defined an equation estimating the scour. Despite all the case studies, no literature could be found that adequately considers the scour depth induced by propeller jets at the toe of pile for an open type berth structure. The main aim of this study is to define an empirical equation for the prediction of scour at the toe of pile (S_o) at the equilibrium state.

Chin et al. [8] gave the relationship in between Fr_d and dimensionless scour depth S_{smax}/D_o as defined in Equation (6.6) for a circular wall jet. In the present study, this equation has been re-written by considering the propeller jet flow for no pile conditions as given in Equation (6.7). However, in the literature, reserarchers did not propose any suitable/satisfying equation for the scour depth estimation around pile under propeller jet flow.

In the present study, a nonlinear regression analysis leads to the estimation of scour at the toe of the pile (S_o/D_p) using predominantly dimensionless parameters for a fixed pile location at $X = 10$ cm, and this is defined in Equation (5.13) for the fixed pile location at $X = 10$ as follows:

$$\frac{S_o}{d_o} = 0.232 \cdot Fr_d^{2.046} \cdot \left(\frac{G}{d_{50}} \right)^{-0.631} \cdot \left(\frac{D_p}{d_o} \right)^{0.428} \quad (6.19)$$

where S_o is the maximum scour at the toe of pile, G is the gap of the propeller, d_{50} is the median sand size, D_p is the propeller diameter, and d_o is the pile diameter.

This equation was taken into consideration when the pile was located at a constant distance from the propeller’s face for $0.72 \leq X/d_o \leq 2.5$ and is only valid for $1.89 \leq Fr_d \leq 15.01$.

The DataFit[®] software package (V8.1.69, Oakdale Engineering, PA, US) was used for the implementation of multiple regression-based analysis of the emprical Equations (6.19), (6.22) and (6.23). The Richardson’s Extrapolation method and Levenberg-Marquardt method with double precision were used for the estimation of the performing nonlinear regression with the following values of the solution preferences: (a) regression

tolerance= 1×10^{-10} , maximum number of iterations=250, and (b) diverging nonlinear iteration limit=10.

Linearized plots of Equation (6.19) for the prediction of scour at the toe of pile (S_o/d_o) versus measured data of S_o/d_o are in good agreement considering that the means of the determination coefficient was 0.80 (Figure 6.90) and that the data evaluated at a 95% certainty level ($p=0.05$) lie within the upper and lower predicted limits as seen in Figure 6.90.

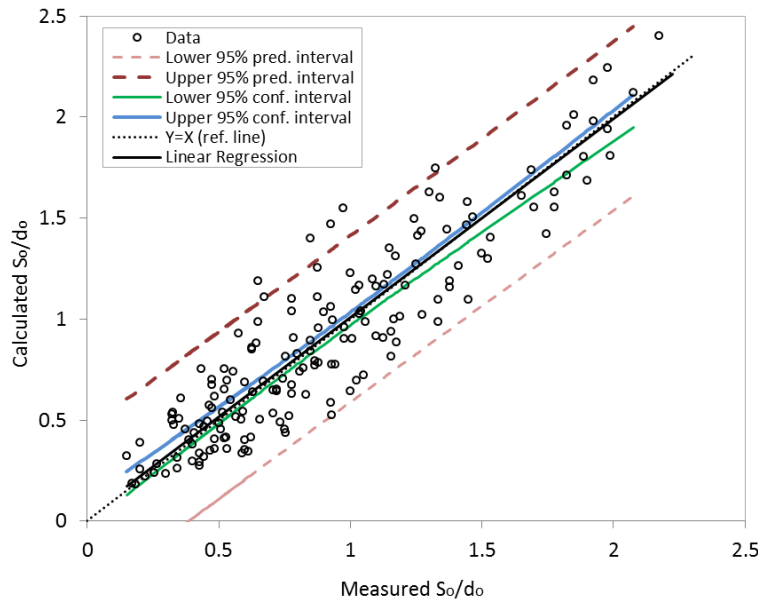


Figure 6.90 Comparison between measured and calculated relative scour at the toe of pile (S_o/d_o) with 95% confidence interval

Confidence and prediction intervals drawn in Figure 6.90 were calculated within the scope of analysis of variance (ANOVA) for a single value by using Equation (6.20) and (6.21), respectively.

$$= Y \pm t_{\alpha} \cdot \sigma \cdot \sqrt{\frac{1}{n_d} + \frac{(X - X_m)^2}{\sum_{i=1}^{n_d} X_i^2 - \frac{1}{n_d} \left(\sum_{i=1}^{n_d} X_i \right)^2}} \quad (6.20)$$

$$= Y \pm t_{\alpha} \cdot \sigma \cdot \sqrt{1 + \frac{1}{n_d} + \frac{(X - X_m)^2}{\sum_{i=1}^{n_d} X_i^2 - \frac{1}{n_d} \left(\sum_{i=1}^{n_d} X_i \right)^2}} \quad (6.21)$$

where σ is the standard residual error $\sigma = \sqrt{SS_{res}/n-2}$, SS_{res} is the sum of squares of residuals (also referred as the residual sum of squares), X is the measured relative scour depths, Y is

the calculated relative scour depths with defined equation, m is the mean values, n_d is the number of data, t_α is the Student's t-distribution, α is the confidence level.

Equation (6.19) was also written in terms of the propeller diameter (D_p). Relative scour depth (S_o/D_p) that was defined in Equation (6.22) is as follows:

$$\frac{S_o}{D_p} = 0.232 \cdot Fr_d^{1.911} \cdot \left(\frac{G}{d_{50}} \right)^{-0.577} \cdot \left(\frac{D_p}{d_o} \right)^{-0.914} \quad (6.22)$$

where S_o is the scour at the toe of pile, G is the gap of the propeller, d_{50} is the median sand size, D_p is the propeller diameter, d_o is the pile diameter. Equation (6.21) gave a determination coefficient of $R^2 = 0.82$ revealed with 95% certainty (Figure 6.91).

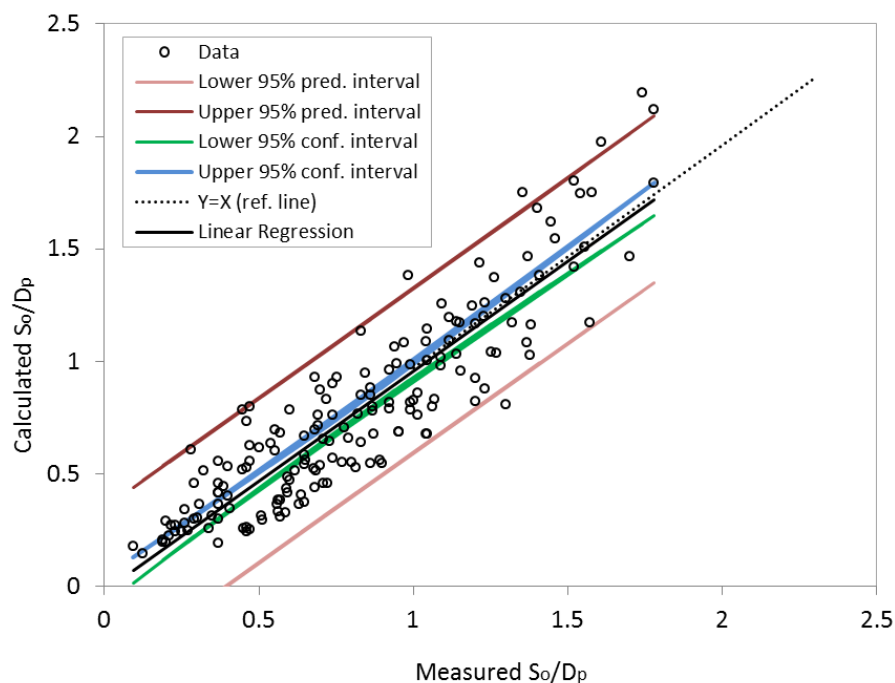


Figure 6.91 Comparison between measured and calculated relative scour at the toe of pile (S_o/D_p) with 95% confidence interval

The difference between Equations (6.19) and (6.22) is that the non-dimensional maximum scour depth parameter is changed from S_o/d_o to S_o/D_p . If S_o/D_p is multiplied by D_p/d_o , the parameter easily changes. Since Equation (6.22) has better performance, Equation (6.22) may be more useful instead of Equation (6.19).

Equation (6.22) was rearranged by considering new data sets obtained under test conditions that used different pile locations from the propeller's face, namely, at $X=10$ cm, 20 cm, 30 cm and 40 cm with all the propellers. These datasets were only tested for a sand bed material with $d_{50}=1.28$ mm and a pile with $d_o=4$ cm at different propeller speeds (590 rpm, 670 rpm,

and 745 rpm). Thus, Equation (6.23) was obtained for the wider range of values of $2.5 \leq X/d_o \leq 10$, and $4.99 \leq Fr_d \leq 12.59$, with an increased number of datasets, and a determination coefficient of $R^2 = 0.87$ (Figure 6.92), as shown below.

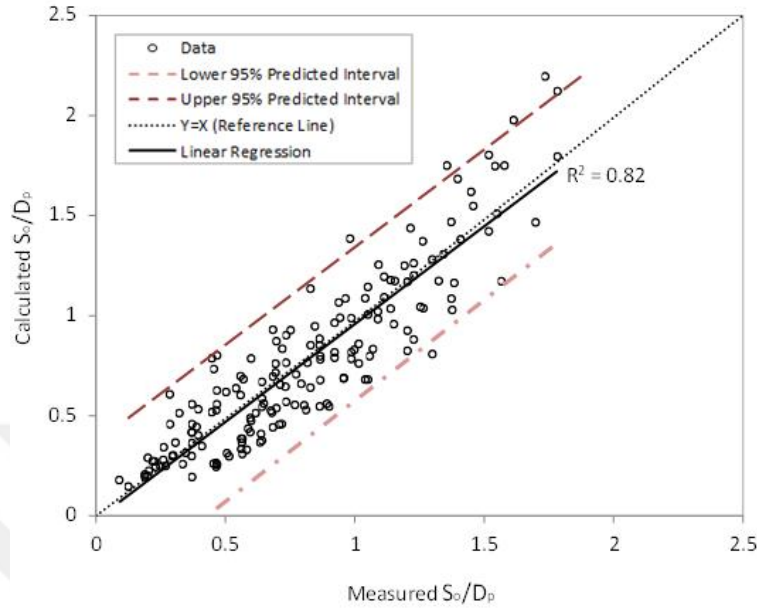


Figure 6.92 Comparison between measured and calculated relative scours at the toe of the pile (S_o/d_o)

$$\frac{S_o}{d_o} = 0.448 \cdot Fr_d^{1.616} \cdot \left(\frac{G}{d_{50}}\right)^{-0.601} \cdot \left(\frac{X}{d_o}\right)^{0.526} \quad (6.23)$$

where S_o is the scour at the toe of pile, G is the gap of the propeller, d_{50} is the median sand size, D_p is the propeller diameter, d_o is the pile diameter, X is the horizontal distance in between pile and propeller face.

In the present study, various descriptive statistics such as; R^2 , MAE, RMSE, IA, FV and DW are given for the validation of the estimation capability of relative scour depths (S_o/D_p and S_o/d_o) with defined Equations (6.19), (6.22) and (6.23) are given in Table 6.13. According to this, X is the measured relative scour depths, Y are the calculated relative scour depths with defined equation, m indicates the mean values, i is the index of each of the n distinct X or Y values, n_d is number of data, $\sigma_x = \sqrt{\sum(X_i - X_m)^2 / n - 1}$ and $\sigma_y = \sqrt{\sum(Y_i - Y_m)^2 / n - 1}$; standart deviations of measured and calculated data X , and Y respectively.

Table 6.13 Descriptive statistical performance indices for data sets

Performance Indicators	Definition	Equation (6.19)	Equation (6.22)	Equation (6.23)
		Data Set for Pile Location at X=10 cm (n _d =172)		Data Set for Different Pile Locations (n _d =108)
Determination Coefficient (R ²)	$R^2 = \frac{\left(\sum_{i=1}^{n_d} (X_i - X_m)(Y_i - Y_m) \right)^2}{\sum_{i=1}^{n_d} (X_i - X_m)^2 \sum_{i=1}^{n_d} (Y_i - Y_m)^2}$	0.80	0.82	0.87
Mean Absolute Error (MAE)	$MAE = \left(\frac{1}{n_d} \sum_{i=1}^{n_d} Y_i - X_i \right)$	0.165	0.150	0.297
Root Mean Squared Error (RMSE)	$RMSE = \left(\frac{1}{n_d} \sum_{i=1}^{n_d} [Y_i - X_i]^2 \right)^{0.5}$	0.207	0.187	0.353
Index of Agreement (IA)	$IA = 1 - \frac{\sum_{i=1}^{n_d} (Y_i - X_i)^2}{\sum_{i=1}^{n_d} (Y_i - X_i + Y_i - Y_m)^2}$	0.877	0.957	0.876
Fractional Variance (FV)	$FV = \frac{2(\sigma_x - \sigma_y)}{(\sigma_x + \sigma_y)}$	-0.069	0.021	0.013
Durbin–Watson (DW) Statistic	$DW = \frac{\sum_{i=2}^{n_d} ((X-Y)_i - (X-Y)_{i-1})^2}{\sum_{i=1}^{n_d} (X-Y)_i^2}$	1.75	1.81	0.92

The quality of regression equations is determined by the coefficient of determination (R²). Moreover, its significance was judged by the adjusted R² value, which is denoted as R_a². The R² and R_a² values should also be in close agreement. In the present analysis, the R² and R_a² values were determined by the following equations:

$$R^2 = 1 - \frac{SS_{res}}{SS_{tot}} = \frac{SS_{tot} - SS_{res}}{SS_{tot}} = \frac{SS_{reg}}{SS_{res} + SS_{reg}} \quad (6.24)$$

$$R^2 = \frac{\sum_{i=1}^{n_d} (Y_i - X_m)^2}{\sum_{i=1}^{n_d} (Y_i - X_i)^2 + \sum_{i=1}^{n_d} (Y_i - X_m)^2} = \frac{\sum_{i=1}^{n_d} (Y_i - X_m)^2}{\sum_{i=1}^{n_d} (Y_i - X_m)^2} \quad (6.25)$$

$$R_a^2 = 1 - \left(\frac{SS_{res}/df_e}{SS_{tot}/df_t} \right) = 1 - \left[(1 - R^2) \left(\frac{n_d - 1}{n_d - p - 1} \right) \right] = R^2 - \left[(1 - R^2) \left(\frac{p}{n_d - p - 1} \right) \right] \quad (6.26)$$

where SS_{tot} is the total sum-of-squares (proportional to the variance of the data), SS_{res} is the sum-of-squares of residuals, SS_{reg} is the regression sum-of-squares (also referred to as the explained sum-of squares), p is the total number of explanatory variables, n_d is the size of

the sample, df_t denotes $(n_d - 1)$ degrees-of-freedom, and df_e denotes $(n_d - p - 1)$ degrees-of-freedom.

According to Equations (6.19), (6.22) and (6.23) the goodness-of-fit-of values of the tested experimental data in accordance to the adjusted determination coefficient (R_a^2) and the determination coefficients (R^2) were 0.80, 0.82 and 0.87, respectively. These equations satisfactorily predicted the expected responses with very small deviations (maximum residuals < 0.05) for the relative scour depth in terms of the propeller diameter (D_p) and pile diameter (d_o) for the constant pile locations ($X= 10$ cm), and different pile locations ($X= 20$ cm, 30 cm, and 40 cm). It is noted that the R_a^2 corrects the R^2 value for the sample size and the number of terms used in these equations. If there are many terms, and the sample size is not very large, the R_a^2 may be noticeably smaller compared to R^2 (Liu et al. [66]). For the present case, the values of the adjusted determination coefficient ($R_a^2 = 0.82, 0.83$ and 0.90 corresponding to Equations (6.19), (6.22) and (6.23), respectively) were also very high, implying increased significance for the derived equations. Finally, the Durbin–Watson (DW) statistics ($DW = 1.75, 1.81$ and 0.94 corresponding to Equations (6.19), (6.22) and (6.23)) were determined to be close to 2, thereby confirming the goodness of fit of the equations, and indicating positive autocorrelations ($DW \leq 2$) as Hewings et al. [67] stated for each of these equations.

In practice, Equations (6.22) and (6.23) may provide an estimation for the scour depths at the toe of a pile as an open type structure due to propeller jet flow for engineering considerations. These equations provide the estimation of scour depths at the toe of a pile (S_o) that will occur for a given ship type (D_p, G etc.) by considering the sediment grain size (d_{50}) and pile location (X) for berthing or unberthing conditions.

As a numerical example for practical applications:

- a) If we consider a vessel with the following characteristics de-berthed from a piled type berth structure: $D_p = 1$ m, $G = 1$ m $U_0 = 1.5$ m/sec. The piles are placed at $X = 5$ m away from the propeller and have a diameter of $d_o = 2$ m. The seabed is sand with $d_{50} = 1.28$ mm and $s = 2.65$ ($\Delta = 1.65$).
- b) The non-dimensional pile distance for this case is $X/d_o = 2.5$ and the densimetric Froude number is calculated as $Fr_d = 10.4$ by Equation (6.27).

$$Fr_d = \frac{U_0}{\sqrt{gd_{50}\Delta}} = \frac{1.5}{\sqrt{9.81 \cdot (1.28 \cdot 10^{-3}) \cdot 1.65}} = 10.4 \quad (6.27)$$

c) Equation (6.22) was obtained for the range of values of $0.72 \leq X/d_o \leq 2.5$ whereas Equation (6.23) was considered for $2.5 \leq X/d_o \leq 10$. Both Equation (6.22) and (6.23) can be used for this example as with ($X/d_o = 2.5$ and $Fr_d = 10.4$) due to the validity range of equations. Therefore, these equations for the estimation of scour depth at the toe of pile (S_o) give comparable values.

d) Employing Equation (6.22):

$$\frac{S_o}{D_p} = 0.232 \cdot 10.4^{1.911} \cdot 781.25^{-0.577} \cdot 0.5^{-0.914} = 0.82 \quad (6.28)$$

which results with a scour depth at the toe of pile approximately $S_o \approx 0.8$ m.

e) Employing Equation (6.23):

$$\frac{S_o}{d_o} = 0.496 \cdot 10.4^{1.586} \cdot 781.25^{-0.687} \cdot 2.5^{0.575} = 0.35 \quad (6.29)$$

This time the scour depth at the toe of pile found as $S_o \approx 0.7$ m.

f) This small numerical example shows that the scour depths (S_o), which yield 0.8 m for Equations (6.22) and 0.7 m for Equation (6.23), ensure the applicability of both equations with comparable values given below.

6.3 Scour Around Two- Pile Tandem Arrangements

Scour around the pile groups were studied in the past (Sumer and Fredsøe [68], Sumer and Fredsøe [69], Yuksel et al. [70], Ataie-Ashtiani and Beheshti [71], Amini et al. [72]).

Sumer and Fredsøe [69] studied wave induced scour around group of piles with different configurations (side by side arrangements of piles, tandem arrangements of piles, three-, two-, and four-, pile groups including the triangular and 4×4 square arrangements) on the sand bed with size of $d_{50} = 0.2$ mm. They also found that the scouring mechanism was dependent on Keulegan-Carpenter number (KC) and the distances between piles.

Sumer and Fredsøe [68] performed an experimental investigation on scour around pile groups with different configurations such as; single, side by side, tandem, (2x2, 3x3, 5x5) square, circular pile groups and exposed to steady current.

Rigid bed tests and actual scour tests were carried out experimentally on $d_{50}=0.2$ mm sand bed. They also defined two different mechanism which cause scour formation for pile groups such as; the local scour at individual piles and the global scour (the general lowering of the bed).

Yuksel et al. [70] investigated the local scour around vertical pile and pile groups. The propeller jet was simplified using a circular water jet on cohesionless sediment bottom in their study. Their study showed that the scouring around the pile groups was a function of densimetric Froude number (Fr_d), the distance between the piles to pile diameter and the relative size of the pile to circular water jet diameter.

Ataie-Ashtiani and Beheshti [71] performed an experimental study on pile groups under steady clear-water scour conditions. They derived a correction coefficient to predict the maximum local scour depth for the pile groups.

Amini et al. [72] carried out an experimental study on clear water scour on submerged and unsubmerged pile groups under steady flows. They found the scour depth changed with respect to the pile diameter, the distance between piles and submergence ratio for different configurations of the pile groups. They also achieved empirical relations to demonstrate the effect of the studied variables and proposed a new method to predict the effect of pile group arrangements, pile spacing and submergence ratio on local scour depth.

In this section, scour mechanism induced by propeller jet around two-pile tandem arrangement as seen in Figure 6.93 is presented. Experiments were performed on sand bed size of $d_{50}=0.52$ mm for $D_p=10$ cm propeller speed of 745 rpm with two different pile diameters ($d_o=4$ cm and 9 cm). In addition, the same propeller diameter and speed were tested on a coarse sand bed size of $d_{50}=1.28$ mm for only pile diameter of $d_o=4$ cm. While the distance between two piles (X_i) was determined to be the pile diameter of the times, the distance of the first pile was kept constant at 10 cm away from the propeller.

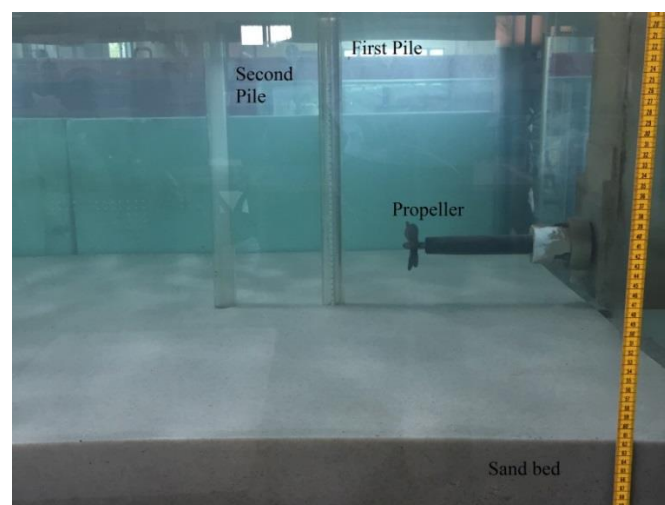


Figure 6.93 View of the flume at the beginning of the tests

14 different configurations were tested as given in Table 6.14. At the end of each test, scour depths at the toe of piles were measured and also compared with the ones of no pile cases. Schematic view of scour profile at the equilibrium state with defined parameters are given in Figure 6.94, where, S_o is the scour at the toe of first pile, S_{o2} is the scour at the toe of second pile, X_t is the distance between the first and second pile, h is the water depth, t is the thickness of sediment bed.

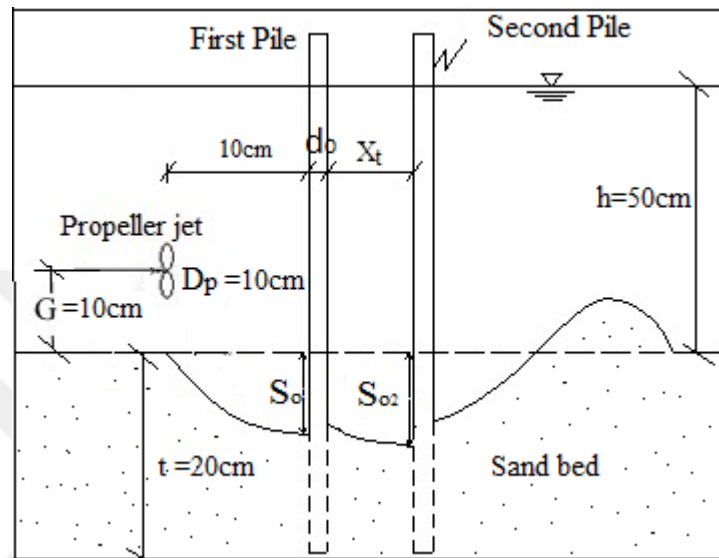


Figure 6.94 Schematic view of the scour formation with two-pile tandem arrangement

The examples of scour profile evolutions with two pile tandem arrangements are given in Figure 6.95, Figure 6.96 and Figure 6.97. These figures show tests results for Set 1 with different pile spacings of $X_t = 2.5d_o, 5d_o, 7.5d_o$.

Table 6.14 Parameters used during experimental tests

Tests	Propeller Gap	Propeller Diameter	Propeller Speed	Pile Diameter	Sediment Bed Size	Distance Between Two Piles
	(G, cm)	(D_p , cm)	(rpm)	(d_o , cm)	(d_{50} , mm)	(X_t , cm)
Set 1	10	10	745	4	0.52	$2.5d_o / 3d_o / 5d_o / 7.5d_o$
Set 2				9		
Set 3				4		

In each test, for different pile spacings (X_t) there is no change occurred for the scour depths at the toe of first pile (S_o) which was located at 10 cm away from the propeller jet. However, scour profile changed and increasing distance between piles ($X_t=7.5d_o$) caused a distinctive ridge between the piles (Figure 6.97).

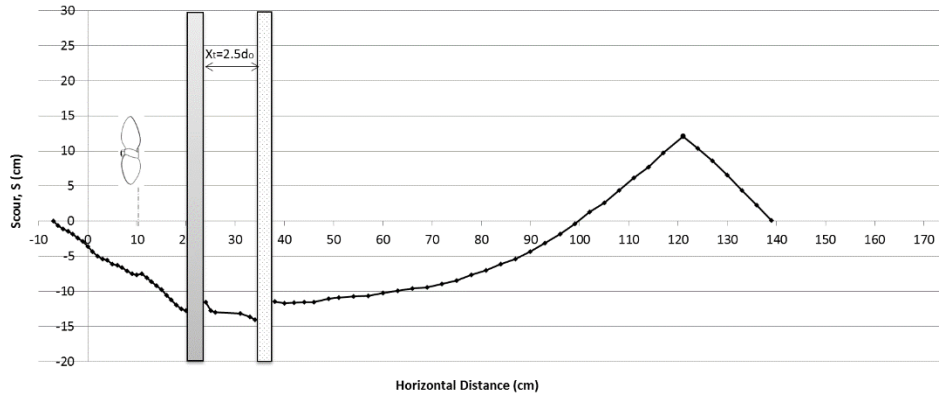


Figure 6.95 Scour profile of two-pile tandem arrangement for $X_t=2.5d_o$ (Set 1)

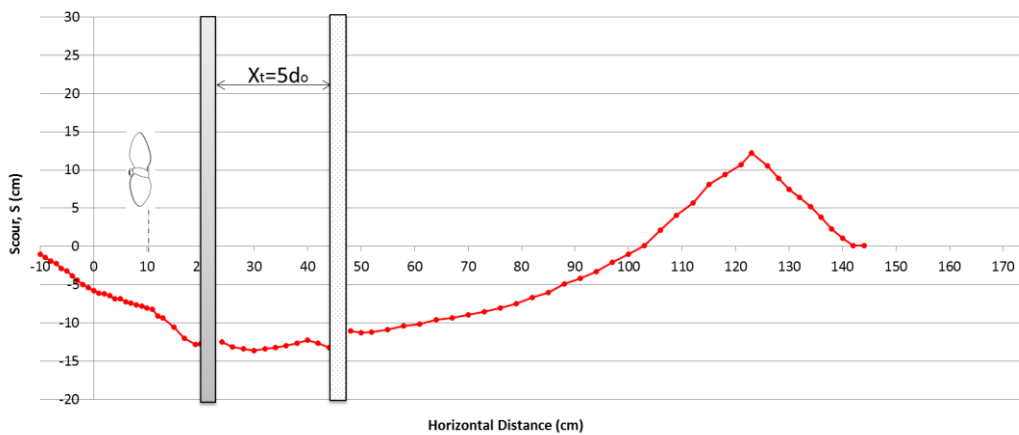


Figure 6.96 Scour profile of two-pile tandem arrangement for $X_t=5d_o$ (Set 1)

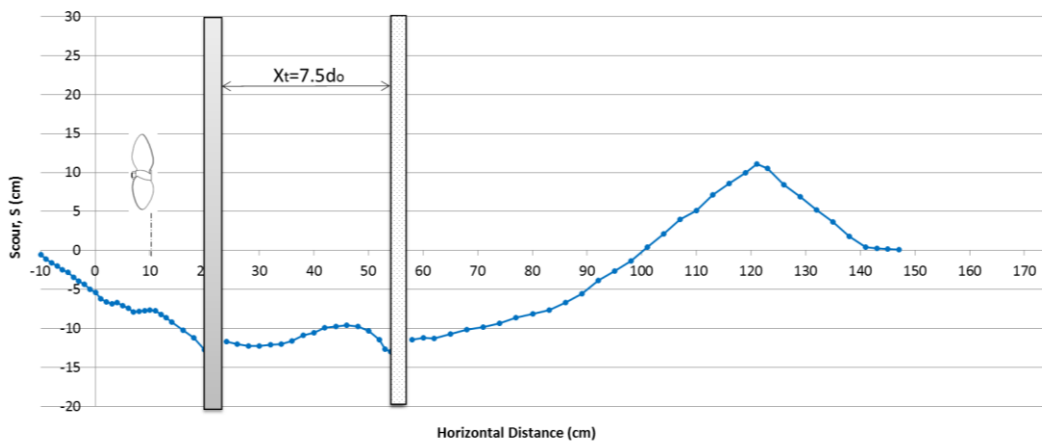


Figure 6.97 Scour profile of two-pile tandem arrangement for $X_t=7.5d_o$ (Set 1)

For each experimental test, the scour depths at the toe of piles for two-pile tandem arrangements were marked on scour profiles with the absence of pile as shown in Figure 6.98, Figure 6.99 and Figure 6.100. Figures show that the scours at the toe of first pile (S_o) for two-pile tandem cases are the same when compared with the scour around a single pile cases at $X=10$ cm from the propeller's face because the second pile has no effect on the

scouring process at the toe of first pile. However, scour depths at the toe of the second pile (S_{o2}) changed, related to the pile location as seen in Figure 6.98, Figure 6.99 and Figure 6.100, respectively.

Different pile spacing for two-pile tandem groups are also descriptive for scour dimensions. Scour at the toe of the second pile (S_{o2}) intersected the scour profile for no pile case beyond $X_t = 3d_o$ for 4 cm pile diameter on sand bed material size of $d_{50}=0.52$ mm and 1.28 mm (Figure 6.98 and Figure 6.99). In other word for the same pile diameter, pile obstruction mechanism decreases beyond the distance between piles and the second pile not effective on scour profile beyond the distance at $X_t = 3d_o$ for sand beds of $d_{50} = 0.52$ mm and 1.28 mm, respectively. This distance also defined as $X_s \geq 5.5d_o$ which is the distance between the propeller and the second pile.

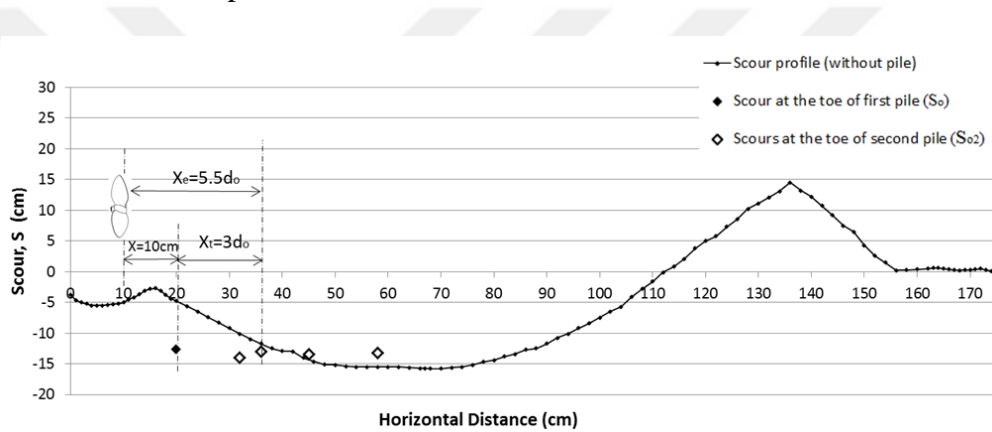


Figure 6.98 Scour profile without pile case and scour depths at the toe of 4 cm piles for two-pile tandem arrangement on sediment bed of $d_{50}=0.52$ mm (Set 1)

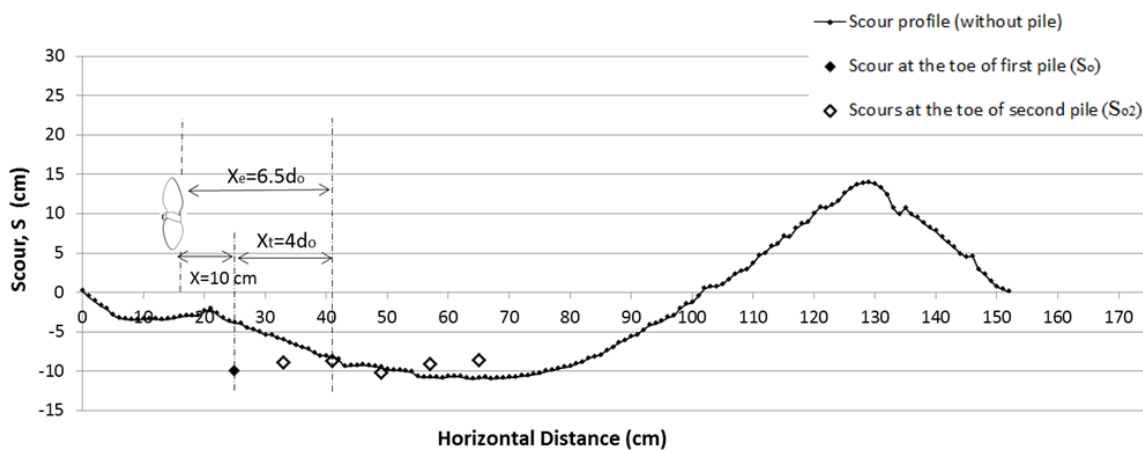


Figure 6.99 Scour profile without pile case and scour depths at the toe of 4 cm piles for two-pile tandem arrangement on sediment bed of $d_{50}=1.28$ mm (Set 3)

Therefore, pile obstruction mechanism begins to decrease at about $X_s=5.5d_o$ and $5.7d_o$ for different pile diameters of 4 cm and 9 cm on the same sand bed ($d_{50}=0.52$ mm) as seen in Figure 6.98 and Figure 6.100.

Scour depths at the toe of the second pile (S_{o2}) also decrease, by increasing the pile spacing ($X_t = d_o/ 2d_o/ 3d_o/ 4d_o/ 5d_o$) with greater pile diameter of $d_o=9$ cm (Figure 6.100). Similarly, scour depths (S_{o2}) decrease beyond the distance between piles at $X_t = 3d_o$ for the smaller pile diameter of $d_o=4$ cm (Figure 6.98). Thus, the evolution of scour profile around pile groups indicated that the scour at the toe of the second pile is always smaller than the first pile ($S_{o2} \leq S_o$) after $X_t = 3d_o$. Yuksel et al. [70] stated that jet diffusion energy decays due to the first pile, in a study conducted by a wall jet.

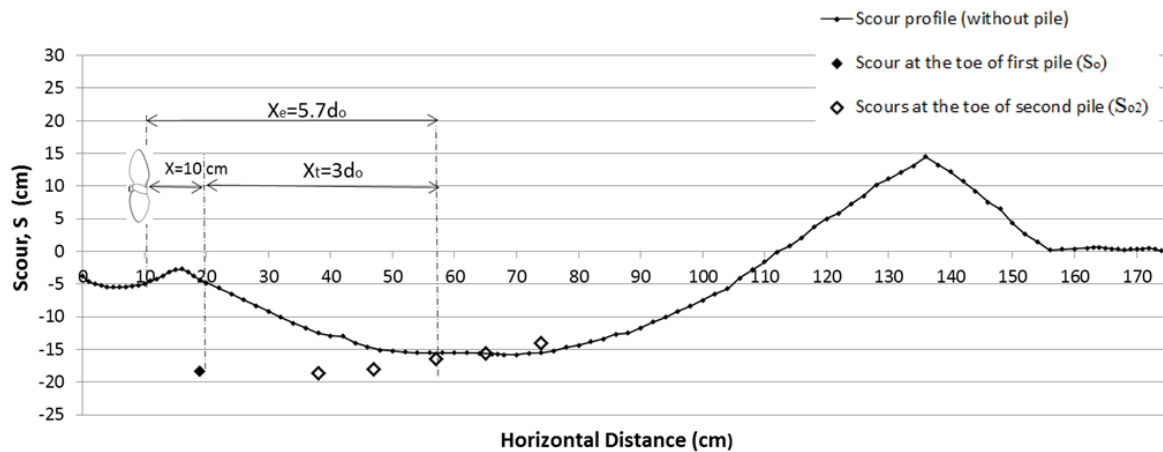


Figure 6.100 Scour profile without pile case and scour depths at the toe of 9 cm piles for two-pile tandem arrangement on sediment bed of $d_{50}=0.52$ mm (Set 2)

6.4 Scour Protection Around a Pile Structure

Established design methods and investigation of scour protection around berth structure induced by propeller jet flow were given by EAU [73], BAW [74] and [75], PIANC [28] and [76], Van Doorn [77], Hawkswood et al. [58] and [78]. Different berth scour protection types and failure mechanisms are summarized by Hawkswood et al. [78] in Table 6.15. They also stated that the rock protection generally fails in rolling and/or sliding particle displacement from the turbulent action due to ship's propeller jet flow.

Table 6.15 Scour protection types and failure mechanisms (Hawkswood et al. [78])

Scour Protection Type	Limiting Failure Mode
Rock	Flow Displacement
Insitu concrete	Suction Uplift
Prefabricated mattress	Various

Up to now, rock protection has been the main type of scour protection used against propeller action as reported by PIANC [76]. Rock protection generally comprises two layers of rip rap or armor stone upon a filter layer which is usually a geotextile filter membrane as illustrated in Figure 6.101.

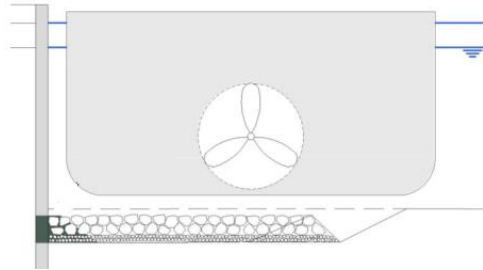


Figure 6.101 Application of rock protection (Hawkswood et al. [78])

In the present study, the design of scour protection around a vertical pile is considered as the rock in two layers as illustrated in Figure 6.102.

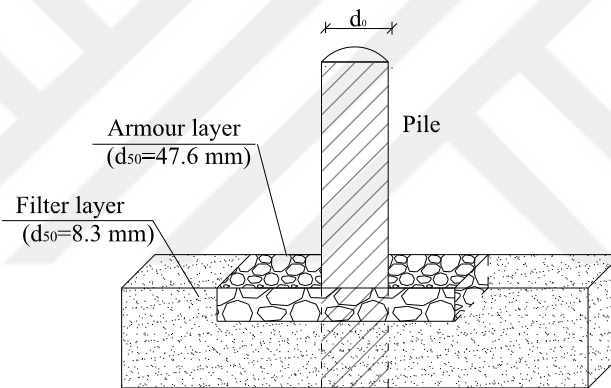


Figure 6.102 Cross-section of application for protection layer

Scour protection layer was constructed in two layers of armor stone of $d_{50}=47.6$ mm upon a filter layer of $d_{50}=8.3$ mm at the same level of sediment bed as illustrated in Figure 6.102 which was used as rough bed material for scour mechanism around piles are presented in the previous section. Particle size distribution of armor layer is given in Figure 6.103.

In the present study, the rock size of armor layer was determined as $d_{15(\text{armor layer})}=40.5$ mm (Figure 6.103) that is about 5 times bigger than $d_{85(\text{filter layer})}=7.9$ mm according to Rock Manual [78] and AYGM [79] because AYGM [79] stated that the relationship between the protection layer and base material should be as follows:

$$\frac{d_{50(\text{armor layer})}}{d_{50(\text{filter layer})}} \leq (2.2-2.5) \quad \text{or} \quad d_{15(\text{armor layer})} \leq 5d_{85(\text{filter layer})} \quad (6.30)$$

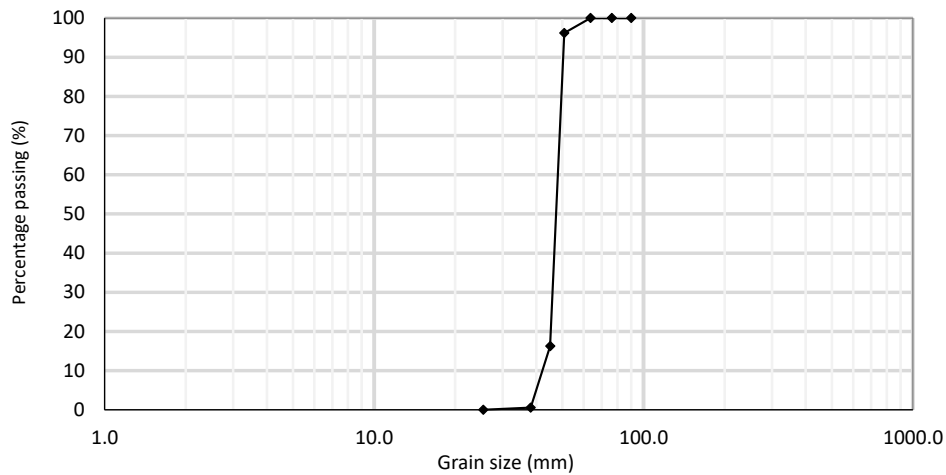


Figure 6.103 Sieve Analysis of rocks used in armor layer

Tests were carried out around two different pile diameters with $d_o=4$ cm and 14 cm as illustrated in Figure 6.104. Size of the rocks used in the armor layer are given in Table 6.18.

Final widths of the scour holes (B_{smax}) for non existing protection layer were also measured as 66 cm and 50 cm for the cases with piles of $d_o=4$ cm and 14 cm, respectively. Thus, rock protection layer was applied as 60×65 cm and 50×60 cm onto the areas around the pile of $d_o = 4$ cm and 14 cm, respectively. The determined application areas were greater than Melville and Coleman [80]’s recommended area that is calculated as 3 - 4 times of pile diameters (d_o) for steady current condition.

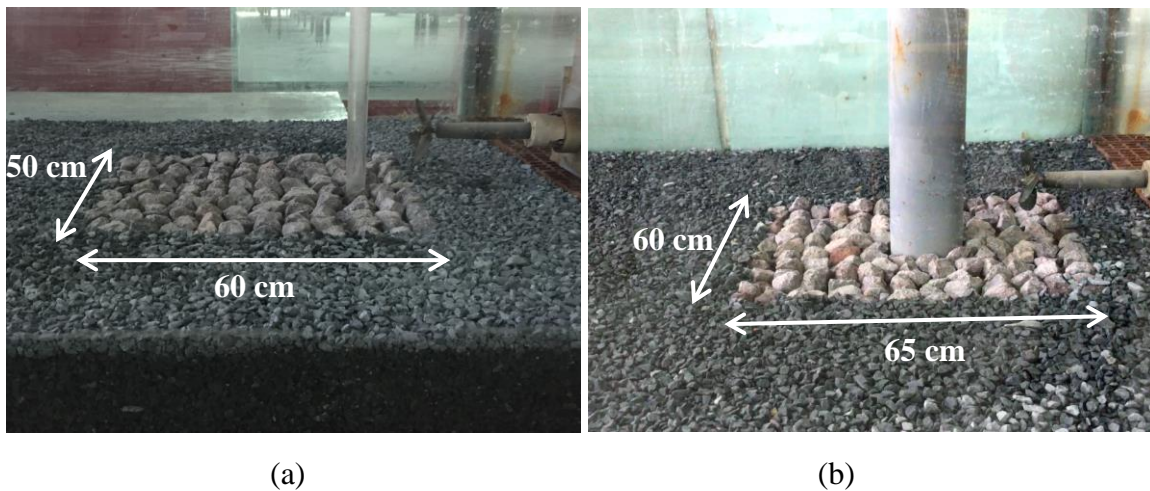


Figure 6.104 Application of armor layer in two layers around a pile diameter of (a) $d_o=4$ cm (b) $d_o=14$ cm

The stability of tested rock size used in armor layer with the effect of propeller jet has been examined around a single pile case in this section. For a better understanding, first of all, maximum velocity near the bed ($U_{b,max}$) that causes scouring on the sediment bed should be calculated with the absence of protection layer. Within this context, most researchers such as

PIANC [76], Fuehrer and Römisch [22], EAU [73] gave definitions for $U_{b,max}$ with the absence of structure.

PIANC [76] idealised propeller jet flow as seen in Figure 6.105 with the absence of structure. Verhey [23] found that the zone of maximum bed velocity is related to the gap of propeller and occurs from a distance of 4 G to 10 G as illustrated in Figure 6.105.

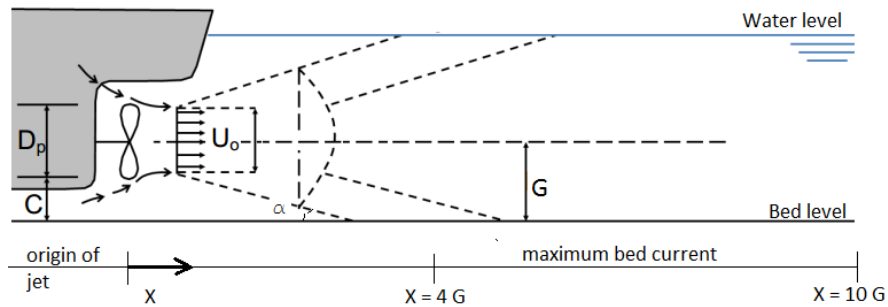


Figure 6.105 Idealised propeller jet flow (modified from Hawkswood et al. [78])

BAW [74] reported that the geometry of propeller jet depends on: (1) rudder configuration of the ship and (2) limitation of the dispersion area due to the quay wall as illustrated in Table 6.16.

Table 6.16 Standard jet dispersion conditions (BAW [74])

<p>a) Without Lateral Limitation Without Splitting of the Jet</p>	<p>b) With Lateral Limitation With Splitting of the Jet</p>
<p>c) Without Lateral Limitation With Splitting of the Jet</p>	<p>d) With Limitation Of Quay Wall Without Splitting of the Jet</p>

Different recommendations are given in the literature to determine the bed velocity via a propeller jets. The maximum near bed velocity ($U_{b,max}$) was given related to the gap ratio (G/D_p) in EAU [73], BAW [74] and PIANC [28] based on Fuehrer and Römisch [22]'s

study. Hawkswood et al. [78] also gave a relationship of relative maximum bed velocity ($U_{b,max}/U_0$), versus G/D_p found by different researchers in one graph (Figure 6.106).

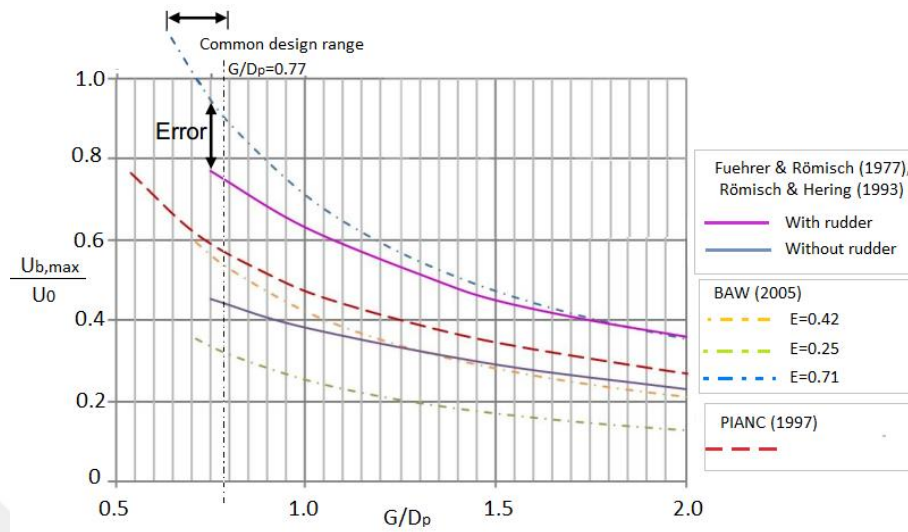


Figure 6.106 Relative bed velocity ($U_{b,max}/U_0$) of the propeller jet as a function of gap ratio (G/D_p) (Modified from Hawkswood et al. [78])

These graphs were expressed by the following equation and coefficients;

$$U_{b,max} = U_0 E \left(\frac{D_p}{G} \right) \quad (6.31)$$

where $E=0.71$ for slender stern with a rudder, $E=0.42$ for slender stern with no rudder behind the propeller, $E=0.25$ for slender stern with twin rudders.

PIANC [76] also gave German and Dutch approaches for the calculation of the $U_{b,max}$. German method uses Equation (6.31) to define $U_{b,max}$ whereas the Dutch method uses Equation (6.32) for the calculation of $U_{b,max}$ as follows:

$$U_{b,max} = (0.2 \text{ to } 0.3) U_0 \frac{D_p}{G} \quad (6.32)$$

where; 0.216 is for non ducted propellers and 0.306 is for ducted propellers.

PIANC [76] and BAW [74] established no scour design curve of rock protection in terms of bed velocity ($U_{b,max}$). Hawkswood et al. [78] gave these relationship as illustrated in Figure 6.107.

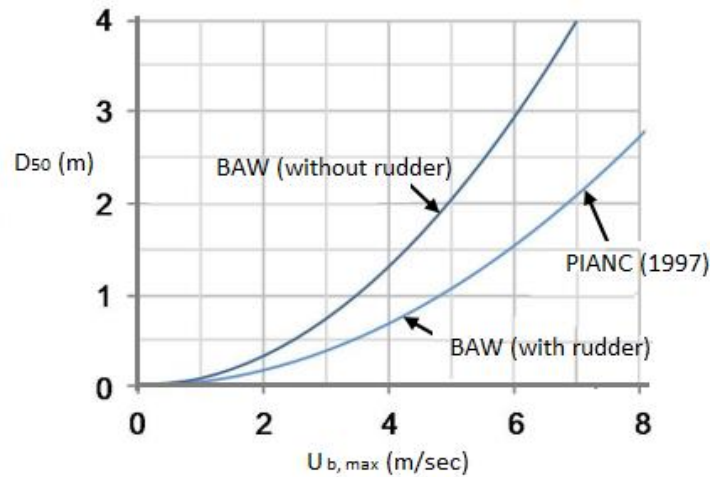


Figure 6.107 Stone sizes related to maximum bed velocities ($U_{b, \max}$) (Hawkswood et al. [78])

German and Dutch methods were also used and movement of rocks were investigated for critical rock sizes for bottom protection. The German method uses formulas particularly suited for propeller jets, while the Dutch method uses general stability formulas such as Izbash and Pilarczyk equation. Pilarczyk equation has not been validated for the propeller jet flow. So, according to calculated $U_{b, \max}$, Equation (6.33) and (6.34) were determined to use. Equation (6.33) is based on comparisons of critical flow velocity (U_{cr}) with $U_{b, \max}$ as the German stability approach (Equation (6.31)). However, Izbash Equation (6.34) used in Dutch method gives rock sizes for $U_{b, \max}$.

$$U_{cr} = B_{cr} \sqrt{d_{85} g \Delta} \quad (6.33)$$

where U_{cr} is the critical flow velocity, B_{cr} is the coefficient, given as 0.9-1.25 for turbulent conditions, d_{85} is the 85% passing median rock diameter, Δ is the relative density.

$$\Delta d_{50} = \frac{1}{B_{cr, lz}} \frac{U_{b, \max}^2}{2g} \quad (6.34)$$

where $U_{b, \max}$ is the maximum velocity near the bed, $B_{cr, lz}$ is the coefficient (for standard situations $(1/B_{cr, lz})^2 = 3.0$ (CIRIA, CUR, CETMEF [81]), d_{50} is the 50% passing median rock diameter.

In the present study, applied protection layer as illustrated in Figure 6.104 was tested with the maximum propeller speed (745 rpm) and diameter ($D_p = 13$ cm) for the worst case scenerio. Thus, the efflux velocity was found as $U_0 = 1.78$ m/sec (calculated with using Equation (5.3)) for $D_p = 13$ cm of 745 rpm.

A propeller is located at the minimum gap of $G=10$ cm and rotated until scour profile reaches its equilibrium state on $d_{50}= 8.3$ mm bed. So, maximum near-bed velocity ($U_{b,max}$) is expected to be found between $X = 40$ cm to 100 cm away from the propeller face with the absence of structure as seen in Figure 6.105. This distance is also away from the intersection point of the lower jet layer with the original bed level at $X_{int} = 18.7$ cm. X_{int} is calculated by using Johnston et al. [19]'s definition in Equation (6.18) for the expansion angle of the propeller. The intersection point of the propeller with scour profile for no pile condition is shown in Figure 6.108. The calculated expansion angle from Equation (6.18) as $\alpha = 10.6^\circ$ is almost similar to the value of $\alpha = 13^\circ$ which is given by BAW [74] in Table 6.16 (a).

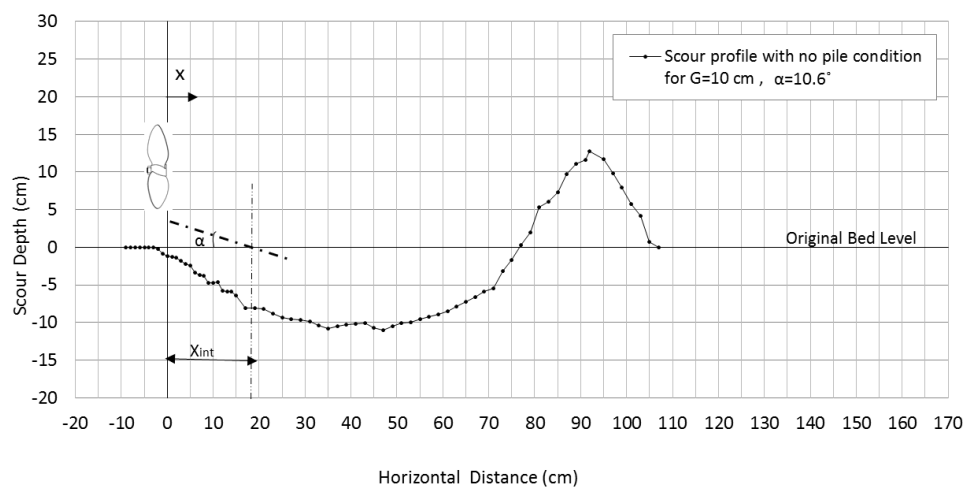


Figure 6.108 Scour profile induced by propeller jet with the absence of pile ($D_p=13$ cm, 745 rpm, $G=10$ cm)

In the tests of the present study, the pile was located at $X=10$ cm before the lower jet layer intersected the original bed level (X_{int}) and the flow conditions changed when the propeller jet flow was confined by a surface (Figure 6.109 and Figure 6.110). Maximum bed velocity ($U_{b,max}$) should be different from the calculated $U_{b,max}$ for no pile conditions (Table 6.17). However, there is not any definition given for the determination of $U_{b,max}$ when the propeller jet flow was confined by a vertical pile. The Dutch and the German methods assume the use of conventional propellers as without ducted propellers and consider jet confinement such as the closed type quay walls. However, the German method uses the Equation (6.31) to define $U_{b,max}$ by not considering the structure conditions.

The maximum flow velocity at the bed ($U_{b,max}$) owing to a propeller jet is calculated with Equation (6.31) reported by BAW [75] $U_{b,max}$ that was found as 0.97 m/sec for $D_p = 13$ cm and $G=10$ cm..

$U_{b,max}$ was also found as 1.01 m/sec and 0.90 m/sec according to Figure 6.106 for the $G/D_p=0.77$ for relative maximum bed velocity defined by PIANC [76] and Fuehrer and Römisch [22], respectively.

PIANC [28] gave the German and the Dutch methods to calculate the $U_{b,max}$. $U_{b,max}$ was found from Equation (6.32) as 0.5 m/sec by using the Dutch method for $D_p=13$ cm propeller at $G=10$ cm. The German method uses the same equation as Equation (6.31) given by BAW [75], so $U_{b,max}$ was found similar as 0.97 m/sec. The calculated $U_{b,max}$ values by using different researchers' formula, are summarized in Table 6.17.

Table 6.17 Maximum flow velocity at the bed ($U_{b,max}$)

Researchers	$U_{b,max}$ (m/sec)	Remarks
PIANC [76]	1.01	Consider without structure conditions for slender sterns with no rudder behind the propeller
BAW [73] and [75]	0.97	
Fuehrer and Römisch [22]	0.90	
Dutch Method (PIANC [76])	0.50	Considers jet confinement such as the closed type quay walls
German Method (PIANC [76])	0.97	Considers without structure conditions and uses BAW [74] and [75]'s equation

According to calculated $U_{b,max}$ (m/sec) required rock size (critical bed material diameter) was found by using the Dutch method by Equation (6.34) as $d_{50}=23$ mm. In the present study, armor layer compromised of $d_{50}=47.6$ mm that is greater than the required rock size of $d_{50}=23$ mm. So, no scour was observed when the armor layer protection was applied as calculated with the Dutch method.

The German method gave the stability of the armor layer with the comparison of critical flow velocity (U_{cr}) and $U_{b,max}$. U_{cr} was determined as 0.32 m/sec and 0.79 m/sec according to the German method in Equation (6.33) for non protected ($d_{50}=8.3$ mm) and protected bed ($d_{50}=47.6$ mm), respectively. The calculated maximum bed velocity ($U_{b,max}$) as 0.97 m/sec (given in Table 6.17) compared with U_{cr} . Comparisons indicated that there would be scour both on non-protected bed of $d_{50}=8.3$ mm ($U_{b,max}=0.97$ m/sec $>$ $U_{cr}=0.32$ m/sec) and armor layer of $d_{50}=47.6$ mm with protected bed ($U_{b,max}=0.97$ m/sec $>$ $U_{cr}=0.79$ m/sec). However, no scour was expected for protected bed when the Dutch method was used. This is because the Dutch method considers jet confinement while the German method assumes without structure conditions for the calculation of $U_{b,max}$. Thus, the Dutch method found more predictable results for the consideration of pile structure.

No scour expectation found by using Dutch method showed same results with the observations of tests with protection layer around piles that have diameters of $d_o=4$ cm and 14 cm. However, with the absence of protection layer (with filter layer only) scour was observed around each pile as seen in Figure 6.109 and Figure 6.110.

Scour profiles with the absence of protection layer around different pile diameters of $d_o=4$ cm and 14 cm have final scour depth at the of pile (S_o) as 7.4 cm and 14.5 cm, respectively (Figure 6.109 and Figure 6.110).

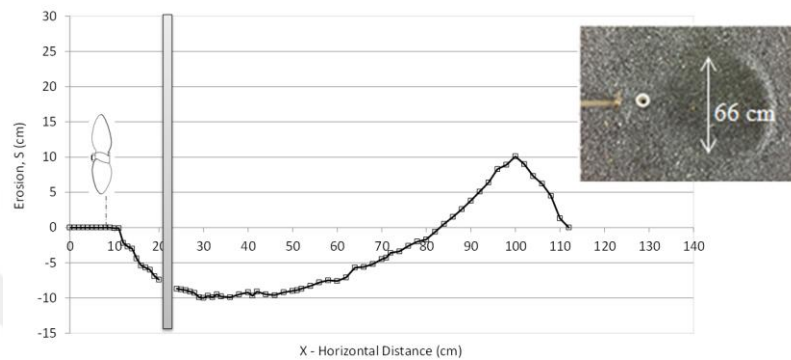


Figure 6.109 Final scour profile without protection layer around pile of $d_o=4$ cm on sediment bed of $d_{50}=8.30$ mm ($D_p=13$ cm, 745 rpm, $G=10$ cm)

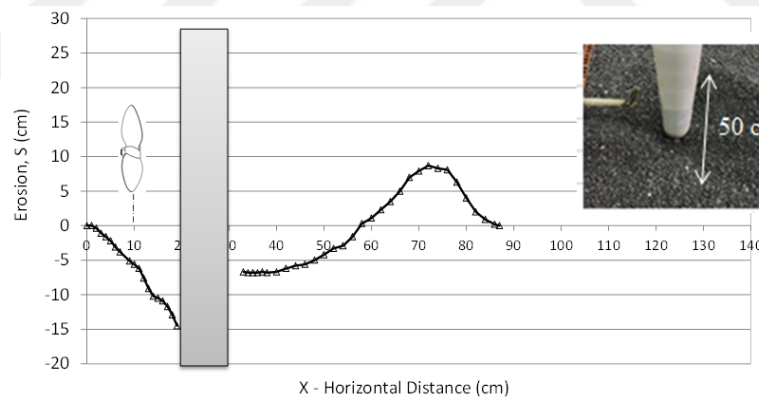


Figure 6.110 Final scour profile without protection layer around pile of $d_o=14$ cm on sediment bed of $d_{50}=8.30$ mm ($D_p=13$ cm, 745 rpm, $G=10$ cm)

Required rock sizes were taken into consideration after the maximum bed velocity ($U_{b,max}$) was calculated as seen in Table 6.17. The calculated maximum bed velocity ($U_{b,max}=0.5$ m/sec) obtained by using the Dutch method with the consideration of jets confinement such as closed type quay walls was smaller than the values calculated by PIANC [76], Fuehrer and Römisch [22] and BAW [74] and [75]'s methods as $U_{b,max}=1.01$ m/sec, 0.97 m/sec and 0.90 m/sec, respectively. Vis a vis this subject, Sumer and Fredsøe [57] stated that the presence of the structure would cause the change in the flow and this local change in the

flow will generally cause an increase in the bed shear stress and in the turbulence level for steady flow. They also added that the bed shear stress underneath the horseshoe vortex at the toe of pile can be larger (or more) than 5 times of the undisturbed bed shear stress. The maximum magnitude of the bed shear stress was found in front of the pile where the shear stress was 3.5 times compared to the jet exit for propeller jet flow around pile structure by Yuksel et al. [33]. So, the bed velocity near the bed ($U_{b,max}$) increases with increasing shear stress when a structure is placed in the flow area.

In the present study, sediment bed materials were used within a wider range of $d_{50}=0.52$ mm, 1.28 mm, 4.00 mm and 8.3 mm. Therefore scour was formed on each sediment bed material with the absence and presence of the pile structure at $D_p=13$ cm at 745 rpm but two layered rocks with greater median sizes than sediment bed material sizes of $d_{50}=47.6$ mm were tested and examined as armor layer around piles but no scour formations were found.

Table 6.18 Rock weights used in the armor layer

Rock	Weight (gr)	Rock	Weight (gr)	Rock	Weight (gr)
1	110.5	43	135.7	85	117.5
2	113.4	44	94	86	91.4
3	129.4	45	109.1	87	141.4
4	161.3	46	100.6	88	145
5	122.7	47	112.2	89	135
6	149	48	149.7	90	121.3
7	105.7	49	137.6	91	120
8	79.9	50	69.6	92	142
9	97.4	51	79.6	93	121
10	133	52	90.6	94	110
11	125.5	53	64	95	116
12	78.8	54	91.8	96	143.4
13	150.7	55	141.2	97	124.5
14	108	56	109	98	143.6
15	102.3	57	110.3	99	147.3
16	113	58	115.1	100	140
17	92.5	59	125.7	101	83.5
18	117.1	60	145.6	102	98.7
19	105.3	61	109.3	103	82.4
20	146	62	125.8	104	125.7

Table 6.18 Rock weights used in the armor layer (cont'd)

21	110.9	63	145.2	105	144.7
22	84	64	120.7	106	134.8
23	120.1	65	130.6	107	139.4
24	112.1	66	122.8	108	106.5
25	99.3	67	113.7	109	161.6
26	95.7	68	141.8	110	95.3
27	104.5	69	145.4	111	81.5
28	118.5	70	111.9	112	141.2
29	106.8	71	131.3	113	102.6
30	76.9	72	111.5	114	128.6
31	89.6	73	147.5	115	89.7
32	101.5	74	131.4	116	139.3
33	92	75	142	117	120.5
34	112.1	76	141	118	147.3
35	100.8	77	100.3	119	128.1
36	104.7	78	67.6	120	110.6
37	81	79	109.3	121	170.2
38	88.2	80	117.8	122	87
39	107.7	81	140	123	127.2
40	126.4	82	105.7	124	130.9
41	186.4	83	142.2	125	121
42	143.9	84	124	126	129.5

RESULTS AND DISCUSSION

The effect of a propeller jet flow on four different sand bed sizes was examined in a flume by varying the propeller gap, propeller diameter, and speed. The experiments simulated (1) a freely expanded propeller jet flow, with no interference from any berth structures, (2) a pile-type berth structure. The scour tests for no structure and the scour around a single pile induced by the propeller's jet flow on four different sand beds ($d_{50} = 0.52$ mm, 1.28 mm, 4.0 mm, and 8.3 mm) at three different gaps, propeller sizes, and speeds, were examined in a laboratory flume. The following results were obtained:

The densimetric Froude number (Fr_d) and gap ratio (G/D_p) are dimensionless parameters that affect the scouring formation, and these parameters may be used for the determination of the scour initiation induced by a propeller jet. However, there are several studies addressing scour initiation by using a wall jet instead of a propeller jet. In addition, studies conducted with a propeller jet flow, such as Hamill [7], Hamill et al. [9] and Hong et al. [5], examined their results with a limited dataset. Thanks to this study an equation using Fr_d has been developed and demonstrated and it has been evaluated that the propeller gap ratio can be used for the consideration of critical conditions within a data set with a wider range of $1.95 \leq Fr_d \leq 15.01$ and $0.77 < G/D_p < 3.08$.

An explanation of the scour formation of cohesionless sediments by a propeller jet without considering its structure has also been given in this study. The shape of scouring formations have been found to be highly related to Fr_d and G/D_p . The scour formation induced by a propeller jet was defined by Hong et al. [5] as: (1) primary scour

hole, (2) small scour hole, and (3) dune or deposition mound. The scour formations in the current experiment are similar to those observed by Hong et al. [5]. However, no defined limitations have been given between these two scour holes in the literature. This study reports that the small scour hole under the propeller is formed only for values of Fr_d smaller than $5.3G/D_p$, as defined in Equation (6.3), by considering all the scours formed by test results $1.95 \leq Fr_d \leq 15.01$.

Parameters affecting the scour dimensions (S_{smax} , B_{smax} , and L_{smax}) such as the propeller speed (rpm), diameter, and propeller gap were tested. Chiew and Lim [2] have provided a correlation between the scour hole dimensions and Fr_d for a submerged circular jet. However, no such correlation is proposed for the propeller jet flow. Only Hong et al. [5] have stated that tests of S_{smax}/D_p conducted with a propeller jet tend to merge into a trend for the jet flow similar to the study conducted by Chiew and Lim [2]. Based on the current experimental data primary scour dimensions, S_{smax}/D_p , B_{smax}/D_p , and L_{smax}/D_p were found to be related to Fr_d for the propeller jet flow as given in Equations (6.7), (6.8) and (6.9), respectively.

In the present study, the relationship between the scour hole dimensions and Fr_d for both a submerged circular jet and a propeller jet show significant differences. In general, for the same Fr_d values, propeller jets induce smaller scour depths, widths, and lengths. This is because a circular jet causes more effective kinds of scour than a propeller jet of similar velocity owing to the angle of incidence of the water jet with the bed as stated by Hawkswood et al. [78].

The distance from the propeller face to the location of maximum scour depth (X_{mu}) has also been defined by Hamill et al. [9] by considering Fr_d and the propeller clearance. In this study, this distance has been found to be highly dependent on the propeller diameter. Thus, Equation (6.15) is proposed for the maximum scour depth location (X_{mu}) based on the relationship between the propeller diameter, propeller gap, and densimetric Froude number (i.e., sediment bed characteristics and efflux velocity) when $1.89 \leq Fr_d \leq 15.01$.

The use of Equation (6.13) presented within this study allows the estimation of the maximum scour depth (S_{smax}) by considering the critical Froude number for the scour initiation. This study also presents a relationship between the S_{smax}/D_p and G/D_p considering the sediment bed size (d_{50}) for the propeller jet flow.

The equations presented within this study now provide the engineer with the ability to estimate the scour dimensions for the propeller jet flow conditions with the assumption of zero advance speeds, simulating the maneuvering operation of a ship.

The critical condition for the scour initiation induced by the propeller jet around a pile was found to be a function of the densimetric Froude number (Fr_d) and of the gap ratio (G/D_p).

During the tests of present study, three different characteristic scour profiles were defined around a pile-type berth structure for fixed locations, at varying pile sizes, for $0.72 \leq X/d_o \leq 2.5$. These profiles varied as a function of the dominant parameters of the pile diameter (d_o). Type 1 and Type 2 scour formations were observed using only smaller pile diameters were used for $G/d_o > 2.3$, while Type 3 scour profiles were formed with $G/d_o < 2.3$. However, the specified limit may not be defined to exist between the Type 1 and Type 2 scour profiles, but was identified by the existence of small scour holes beneath the propeller.

Changing distances between the propeller and the pile, caused changes in the predominant mechanism responsible for the scouring formation from the pile vortex to the propeller jet mechanism. The effective pile location was always found downstream of the point where lower jet layer intersected the original bed level (X_{int}). Test results conducted for different locations of a pile for $2.5 \leq X/d_o \leq 10$ showed that the predominant effective mechanism due to the pile vortex mechanism became less prominent, and that the propeller jet mechanism became more effective on the scouring formation at increasing distances. Beyond this distance, the propeller jet flow mechanism became the dominant mechanism for the formation of scouring at $X_e/d_o \geq 7.5$, which always occurs downstream from the point where the propeller jet flow was fully developed at $X_{int}/d_o \geq 6.0$.

This study also presents the empirical equations developed for the estimation of final scour depths at the toe of the pile (S_o) based on the consideration of fixed and changing pile locations from the propeller's face. Engineers should know the locations of local scour because pile type berth structures could collapse and fall into their own scour hole. However, the presented equations provide the opportunity to estimate scour depths owing to propeller washes at the toe of the pile.

Tests for the investigation of the scour mechanism induced by the propeller jet around the two-pile tandem arrangements showed that different pile spacings ($X_t = 2.5d_o, 5d_o, 7.5d_o$) are also descriptive for scour dimensions. The scour at the toe of second pile is always smaller than the first pile ($S_{o2} \leq S_o$) after $X_t = 3d_o$ because jet diffusion energy decays due to the first pile, which was determined during a test conducted by using a wall jet by Yuksel et al. [70]. In addition, the scour at the toe of the second pile (S_{o2}) intersects with the scour profile for no pile case at $X_s=5.5d_o- 6.5d_o$. In other words, the pile obstruction mechanism is not effective on the scour profile beyond the distance between the propeller and the second pile when $X_s=5.5d_o- 6.5d_o$ valid for $3.1 \leq X_s/d_o \leq 13.5$ and $9.69 \leq Fr_d \leq 15.01$.

Besides the tests and their results so far, in the present study also the design of scour protection around a vertical pile was examined with a sample experiment. The application of rock protection in two layers was tested by using different methods given in the previous studies (PIANC [76], BAW [74] and [75], Fuehrer and Römisch [22]). The Dutch method supplies safer results when compared with the results of the experiments conducted for the rock protection within the context of this study. However, further study is needed to explain the critical bed velocity in order to determine the armor layer for without scour condition around a pile structure.

REFERENCES

- [1] Blaauw, H.G. and Kaa E.J., van de, (1978). Erosion of Bottom and Sloping Banks Caused by the Screw Race of Maneuvering Ships, Report No.202, Delft Hydraulics Laboratory, Delft, Netherlands.
- [2] Chiew, Y.M. and Lim, S.Y., (1996). "Local Scour by a Deeply Submerged Horizontal Circular Jet. *Journal of Hydraulic Engineering*", 122, 529-532.
- [3] Hamill G.A., McGarvey, J.A. and Hughes D.A.B., (2004). "Determination of the Efflux Velocity from Ship's Propeller", *Proceedings of the Institution of Civil Engineers: Maritime Engineering* 157 (2): 83-91.
- [4] Lam, W., Hamill, G.A., Robinson, D.J. and Raghunathan, S., (2011). "A Review of the Equations Used to Predict the Velocity Distribution Within a Ship's Propeller Jet", *Applied Ocean Research*, 38: 1-10.
- [5] Hong, J. H., Chiew, Y. M. and Cheng, N. S., (2013). "Scour caused by a propeller jet", *Journal of Hydraulic Engineering*, 139 (9): 1003-1012.
- [6] Karki, R., Faruque, M.A.A., and Balachandar, R., (2007). "Local scour by submerged offset jets", *Water Management*, 160 (3): 169-179.
- [7] Hamill, G.A., (1987). Characteristics of the Screw Wash of Manoeuvring Ship and the Resulting Bed Scour, Ph.D. Thesis, Queen's University of Belfast, Northern Ireland, UK.
- [8] Chin, C.O., Chiew, Y.M., Lim, S. Y. and Lim, F. H., (1996). "Jet scour Around Vertical Pile", *Journal of Waterway, Port, Coastal, Ocean Engineering*, 122 (2): 59-67.
- [9] Hamill G.A., Johnston H.T. and Stewart D.P., (1999). "Propeller Wash Scour Near Quay Wall", *J. Waterway, Port, Coastal, Ocean Engineering*, 125, 170-175.
- [10] Lam, W., Hamill G.A., Robinson, D.J. and Raghunathan, S., (2010). "Observations of the initial 3D flow from a Ship's Propeller", *Ocean Engineering*, 37, 1380-1388.
- [11] Quarrin, R., (1994). Influence of the sea bed geometry and berth geometry on the hydrodynamics of the wash from a ship propeller, Ph.D. Thesis, Queen

University of Belfast.

- [12] Stewart, D.P.J., (1992). Characteristics of a Ship Screw Wash and the Influence of Quay Wall Proximity, Ph.D. Thesis, Queen's University of Belfast, Northern Ireland, UK.
- [13] Hashmi, H.N., (1993). Erosion of a granular bed at a quay wall by a ship's screw wash, Ph.D. Thesis, Queen's University of Belfast, Northern Ireland, UK.
- [14] Berger, W., FelKel, K., Hager, M., Oebius, H. and Schale, E., (1981). "Courant provoqué par les bateaux protection des berges et solution pour éviter l'érosion du lit du haut rhin", P.I.A.N.C. 25th Congress, Section I-1, Edinburgh.
- [15] Prosser, M., (1986). Propeller induced scour. Technical Report, BHRA Project RP A01415, The Fluid Engineering Centre, Cranfield.
- [16] Mc Garvey, J.A., (1996). The Influence of The Rudder on the Hydrodynamics and the Resulting Bed Scour, of a Ship's Screw Wash, Ph.D. Thesis, Queen's University of Belfast.
- [17] Brewster, P.M., (1997). Modelling the Wash from a Ship's Propeller, Ph.D. Thesis, Queen's University of Belfast.
- [18] Kee, C., Hamill, G.A., Lam, W. and Wilson, P.W., (2006). "Investigation of the Velocity Distributions within a Ship's Propeller Wash", Proceedings of the 16th International Offshore and Polar Engineering Conference, San Francisco, 451-456.
- [19] Johnston, H. T., Hamill, G.A., Wilson, P. R., and Ryan, D., (2013). "Influence of a Boundary On the Development of a Propeller Wash", Ocean Engineering, 61, 50-55.
- [20] Oebius, H. and Schuster, S., (1975). "Modelversuche Zur Frage Der Beschädigung Von Flussohlen Durch Die Schifffahrt Versuchsanstalt Fur Wasserbau Und Schifffbau", Berlin, VWS-Bericht nr. 743/75, 1975.
- [21] Albertson, M.L. Dai, Y. B., Jensen, R. A. and Rouse, H., (1948). "Diffusion of Submerged Jets", ASCE, Transactions, (2409), 639-664.
- [22] Fuehrer, M., and Römisch, K., (1977). "Propeller Jet Erosion and Stability Criteria for Bottom Protection of Various Constructions", In Proceedings of PIANC, Bulletin No.58.
- [23] Verhey, H.J., (1983). "The Stability of Bottom and Banks Subjected to the Velocities in the Propeller Jet Behind Ships", Delft Hydraulics Laboratory, Netherlands.
- [24] Lam W., Hamill G.A., Robinson D.J. and Raghunathan S., (2012). "Semi-Empirical Methods for Determining the Efflux Velocity from a Ship's Propeller", Applied Ocean Research, 35: 14-24.

- [25] Yew, W. T., Hashim, R., Ng, K. C., (2017). “Experimental Investigation of Scour Induced by Twin-Propeller Wash”, *Journal of Waterway, Port, Coastal, and Ocean Engineering*, 143 (4): 04017006.
- [26] Wei, M., and Chiew, Y.M., (2017). “Influence of Toe Clearance on Propeller Scour around an Open-Type Quay”, *Journal of Hydraulic Engineering*, 143 (7).
- [27] Chin, C.O., Chiew, Y.M., Lim, S. Y. and Lim, F. H., (1996). “Jet Scour around Vertical Pile”, *Journal of Waterway, Port, Coastal, Ocean Engineering*, 122 (2): 59-67.
- [28] Permanent International Association of Navigation Congresses (PIANC), (2015). *The World Association for Waterborne Transport Infrastructure, Guidelines for Protecting Berthing Structures from Scour Caused by Ships*, Report No.180, Belgium.
- [29] Thoresen C. A., (2003) *Port Designers Handbook*, Thomas Telford Publishing, Heron Quay, London.
- [30] Ghose J. P., Gokarn R. P., (2004). *Basic Ship Propulsion*, Allied Publishers Ltd., New Delhi.
- [31] Bergh, H., and Cederwall, K., (1981). *Propeller Erosion in Harbors*, Bulletin No, TRITA-VBI-107, Hydraulics Laboratory, Royal Institute of Technology, Stockholm, Sweden.
- [32] Schokking, L.A., (2002). *Bowthruster-Induced Damage*, M.Sc. Thesis, Delft University of Technology.
- [33] Yuksel, Ozan A., Cihan, K. and Yuksel, Y., (2012). “Propeller Induced Scour Around The Pile Type Berth Structures”, *Applied Ocean Research* 38, 16-22.
- [34] Tsinker G.P., (1995). *Marine Structures Engineering: Specialized Applications*, Chapman and Hallan International Thomson Publishing Company, New York.
- [35] Hoffmans G., and Verheij H., (2016) “Jet scour, *Maritime Engineering*”, Vol: 164.
- [36] Van Blaaderen, E.A., (2006). *Modelling bow-thrusters induced flow near a Quay wall*. M.Sc. Thesis, Delft: University of Technology.
- [37] Situ R., Brown R. J. and Loberto A, (2010). “Experimental Study of the Concentration Field of Discharge from a Boat Propeller”, *Environ Fluid Mech.*, 10:657–675.
- [38] Hamill G.A., Kee C. and Ryan D., (2015). “3D Efflux Velocity Characteristics of Marine Propeller Jets”, *Proceedings of the ICE-Maritime Engineering*, 168(2) 62-75.
- [39] Faltinsen O.M., (2005). *“Hydrodynamics of High Speed Marine Vehicles”*, Cambridge University Press the Edinburgh Building, Cambridge, UK.

- [40] Petersson P., Larson M. and Jonsson L., (1996). “Measurements of The Velocity Field Downstream of an Impeller”, *J Fluids Eng Trans ASME* 118: 602–610.
- [41] Lam W., Hamill G.A., Robinson D.J. and Raghunathan S., Submerged Propeller Jet, <http://www.vec.qub.ac.uk/members/weilam/>, 10 April 2015.
- [42] Carlton, J.S., (2007). *Marine Propellers and Propulsion*, Second Edition, Butterworth-Heinemann is an imprint of Elsevier Linacre House, Jordan Hill, Oxford.
- [43] Balachandar R., and H. Prashanth Reddy (2013). *Sediment Transport Processes and Their Modelling Applications*, InTech DTP, Croatia.
- [44] Sumer B. M., and Fredsøe J., (2006). *Hydrodynamics Around Cylindrical Structures*, Revised Edition, World Scientific Publishing Co. Pte. Ltd., Denmark.
- [45] Chiew Y. M., Hong J. H., Susanto I. and Cheng N. S., (2012). “Local scour by offset and propeller jets”, *Sixth International Conference on Scour and Erosion* (148) 949–956.
- [46] Van Rijn L. C., Local Scour Near Structures, www.leovanrijn-sediment.com, 29 March 2015.
- [47] Akib S., Jahangirzadeh A. and Basser H., (2014). “Local scour around complex pier groups and combined piles at semi-integral Bridge”, *J. Hydrol. Hydromech.*, 62, 2014, 2, 108–116.
- [48] Harper S, *Encyclopedia Titanica : Speed and Revolutions*, <https://www.encyclopedia-titanica.org/speed-v-revolutions.html>, 10 June 2016.
- [49] BM Volvo Penta, 1998. *Inboard propellers and speed calculation marine engines 2.1L-16L*. Volvo Penta UK Division, Warwick, UK.
- [50] Sumer, B. M., Hatipoğlu, F., Fredsøe, J., and Sumer S.K., (2006). “The sequence of sediment behavior during wave-induced liquefaction”, *International Association of Sedimentologists*, 53 (3): 611-629.
- [51] Nortek AS., (2000). “Nortek 10 Mhz Velocimeter Operations Manual”, Document N3000 100/Rev.c/01.11.2000.
- [52] Nixon Installation and Operations Manual, (2005). *Streamflo Velocity Meter V1.3*, Nixon Flowmeters Ltd. Leckhampton, Cheltenham.
- [53] Hamill, G. A. and Kee, C., (2016). “Predicting Axial Velocity Profiles within a Diffusing Marine Propeller Jets”, *Ocean Engineering*, 124, 104-112.
- [54] Rajatratham N., (1981). “Erosion by plain turbulent jets”, *J. Hydraul. Res.* (19): 339–358.

- [55] Faruque M.A.A., Sarathi P. and Balanchar R., (2004). “Transient Local Scour by Submerged Three-Dimensional Wall Jets”, Effect Of Tailwater Depth, Singapore, Second International Conference on Scour and Erosion 2, 309–316.
- [56] Sarathi, P., (2005). Scour by Submerged Square Wall Jets at Low Densimetric Froude Number, MSc Thesis, University of Windsor, Oxford.
- [57] Sumer B. M. and Fredsøe J., (2002). “The Mechanics of Scour in The Marine Environment”, Advanced Series on Ocean Engineering (17), World Scientific, Singapore, New Jersey, London.
- [58] Hawkswood, M., Evans, G. and Hawkswood, G., (2013). “Berth Scour Protection for Fest Ferry Jets”, ICE Marine Structure and Breakwaters Conference, Edinburg, England.
- [59] Yuksel, Ozan A. and Yuksel Y., (2010). “Simulation of a 3D submerged flow around a pile”, Ocean Engineering, 37 (8-9), 819-32.
- [60] Hoffsman G., (2012). The Influence of Turbulence on Soil Erosion, Eburon Academic Publishers, Delft.
- [61] Mujal-Colilles A., Gironella X., Sanchez-Arcilla A., Puig Polo C. and Garcia-Leon M., (2017). “Erosion Caused By Propeller Jets In a Low Energy Harbour Basin”, J. Hydraul. Res. 55 (1): 121–128.
- [62] Wei M. and Chiew Y.M, (2018). “Characteristics of Propeller Jet Flow within Developing Scour Holes Around an Open Quay”, J. Hydraul. Eng. 144 (7): 04018040.
- [63] Wei M., Chiew Y.M. and Hsieh S.C., (2017). “Plane Boundary Effects on Characteristics of Propeller Jets”, Exp. Fluids 58 (10): 141.
- [64] Qi W.G., Gao F.P., (2014). “Physical Modeling of Local Scour Development Around a Large Diameter Monopile In Combined Waves And Current”, Coast. Eng. (83): 72–81.
- [65] Ryan D., Hamill G.A. and Hughes D.A.B., (1999). “Designing for Protection Against Propeller Scour in Harbours”, South Africa, Fifth International Conference on Coastal and Port Engineering in Developing Countries, Cape Town 242–253.
- [66] Liu, H.L., Lan, Y.W. and Cheng Y.C., (2004). “Optimal Production of Sulphuric Acid by Thiobacillus Thiooxidans Using Response Surface Methodology”, Process Biochem. 39 (12): 1953–1961.
- [67] Hewings G.J.D., Changnon, S. and Dridi, C., (2002). “Testing for The Significance of Extreme Weather and Climate Event on the State Economies”, Mathews, Urbana, IL, September, The Regional Economics Application Laboratory, REAL 00-T-6, S (2002) 1–16.
- [68] Sumer B. M. and Fredsøe J., (2005). The Mechanics of Scour in the Marine

Environment, Revised Edition, World Scientific Publishing Co. Pte. Ltd., Denmark.

- [69] Sumer B. M. and Fredsøe J., (1998). “Wave Scour around Group of Vertical Piles”, *J. Waterway, Port, Coastal and Ocean Engineering*, ASCE, 124 (5): 248-256.
- [70] Yuksel, Ozan A., Celikoglu Y., Cevik E. and Yuksel Y., (2005). “Jet Scour Around Vertical Piles and Pile Groups”, *Ocean Engineering*, (32): 349-362.
- [71] Ataie-Ashtiani, B., and Beheshti A.A., (2006), “Experimental Investigation of Clear Water Local Scour at Pile Groups”, *Journal of Hydraulic Engineering*, ASCE, 132 (10): 1100-1104.
- [72] Amini, A., Melville, B. W., Ali, T. M., and Ghazli, A. H. (2012). “Clear-water local scour around pile groups in shallow-water flow”, *Journal of Hydraulic Engineering*, ASCE, 138 (2): 177- 185.
- [73] EAU (1996). Recommendations of the Committee for Waterfront Structures-Harbours and Waterways, Ernst und Sohn, 9th German edition Berlin 1997 and 7th English edition Berlin 2000.
- [74] Bundesanstalt für Wasserbau BAW (2005). Principles for the Design of Bank and Bottom Protection for Inland Waterways, Bulletin No. 88 of the Federal Waterways Engineering and Research Institute, Karlsruhe, Germany.
- [75] Bundesanstalt für Wasserbau BAW (2010). Code of Practise-Principles for the Design of Bank and Bottom Protection for Inland Waterways (GBB), Karlsruhe, Germany.
- [76] Permanent International Association of Navigation Congresses (PIANC), (1997). Handling and Treatment of Contaminated Dredged Material from Ports and Inland Waterways, CDM, Supplement TO Bulletin 89, Brussels, Belgium.
- [77] Van Doorn, (2012). Bow Thruster Currents at Open Quay Constructions on Piles, Msc Thesis, Delft University of Technology, Delft, The Netherlands.
- [78] Hawkswood M. G., Lafeber F. H. and Hawkswood G.M., (2014). “Berth Scour Protection for Modern Vessels”, PIANC World Congress San Francisco USA.
- [79] T.C. Ulaştırma, Haberleşme ve Denizcilik Bakanlığı Altyapı Yatırımları Genel Müdürlüğü, AYGM (2016). “Kıyı Yapıları Planlama Ve Tasarım Teknik Esasları”, Turkey.
- [80] Melville, B.W., Coleman, S.E. (2000). “Bridge scour”, Water Resources Pub., LLC, Highlands Ranch, CO, USA.
- [81] CIRIA, CUR, CETMEF, (2007). The Rock Manual, The Use of Rock in Hydraulic Engineering (2nd edition), C683, CIRIA, London.

SCOUR PROFILES

This appendix contains an additional overview of the scour profiles. Scour profiles have been included for different test conditions.

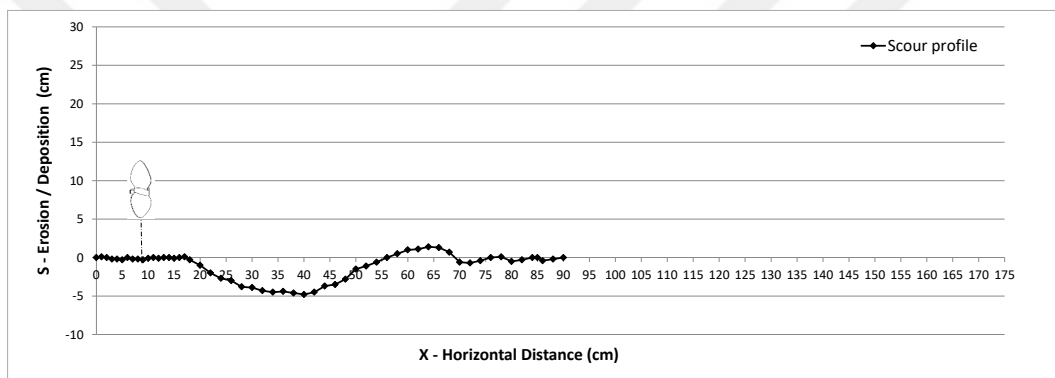


Figure A.1 Scour profile without structure with $D_p=6.5$ cm, at 597 rpm, $G=10$ cm, on sediment bed of $d_{50}=0.052$ cm

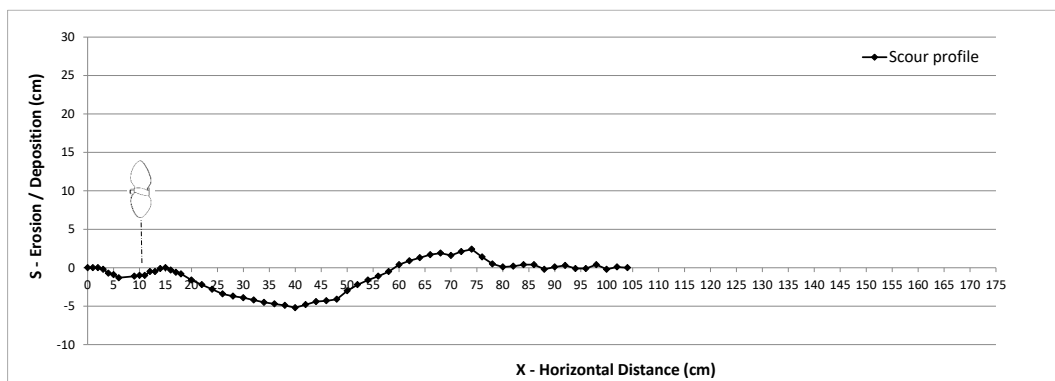


Figure A.2 Scour profile without structure with $D_p=6.5$ cm, at 671 rpm, $G=10$ cm, on sediment bed of $d_{50}=0.052$ cm

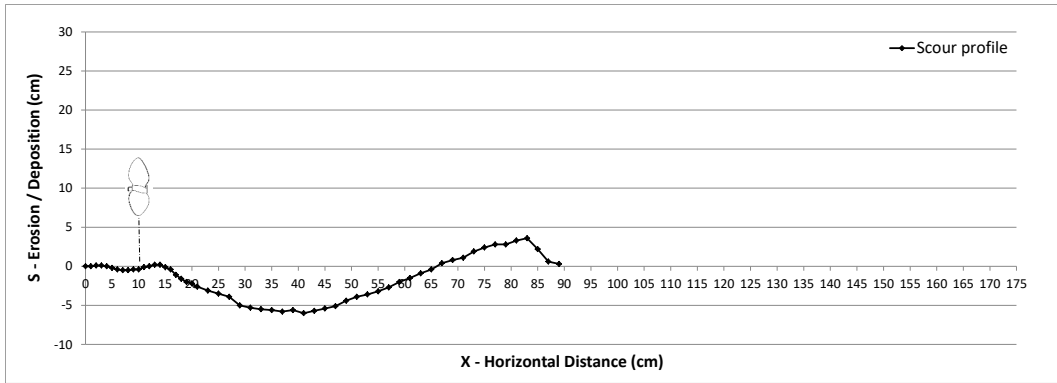


Figure A.3 Scour profile without structure with $D_p=6.5$ cm, at 744 rpm, $G=10$ cm, on sediment bed of $d_{50}=0.052$ cm

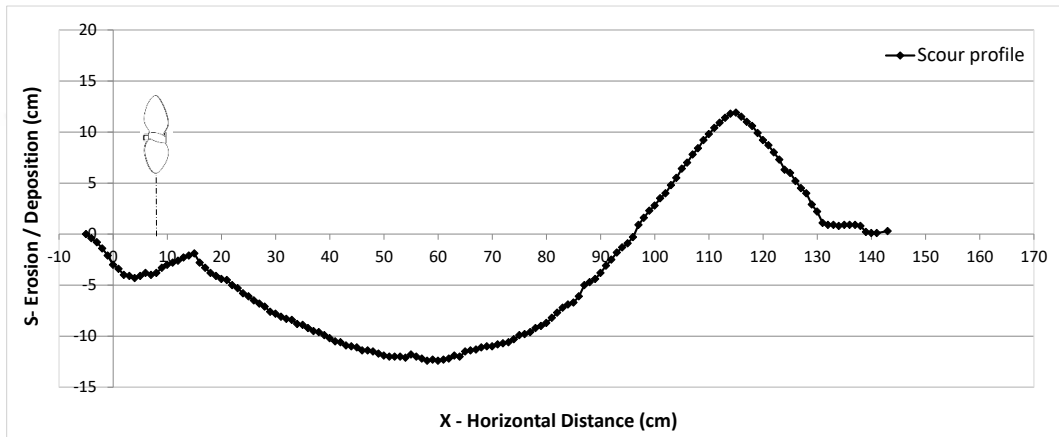


Figure A.4 Scour profile without structure with $D_p=10$ cm, at 595 rpm, $G=10$ cm, on sediment bed of $d_{50}=0.052$ cm

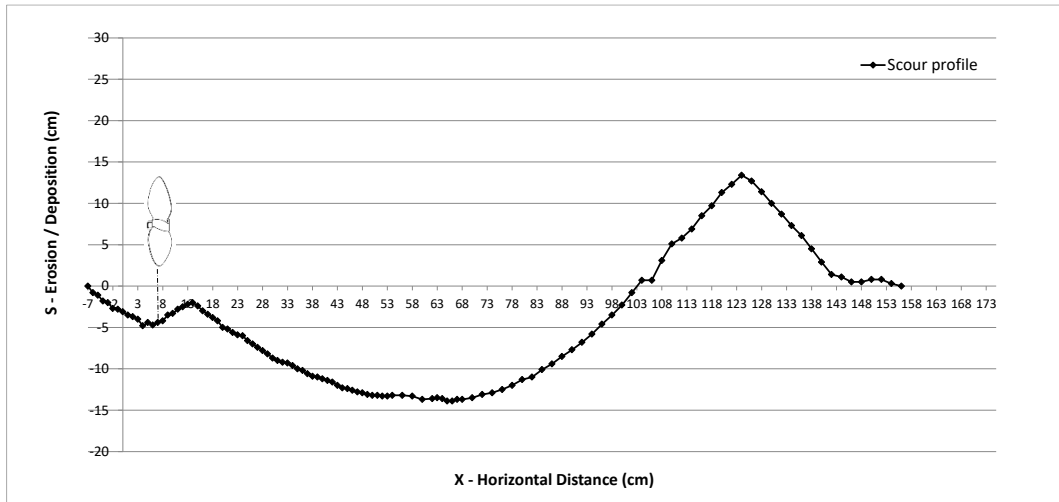


Figure A.5 Scour profile without structure with $D_p=10$ cm, at 665 rpm, $G=10$ cm, on sediment bed of $d_{50}=0.052$ cm

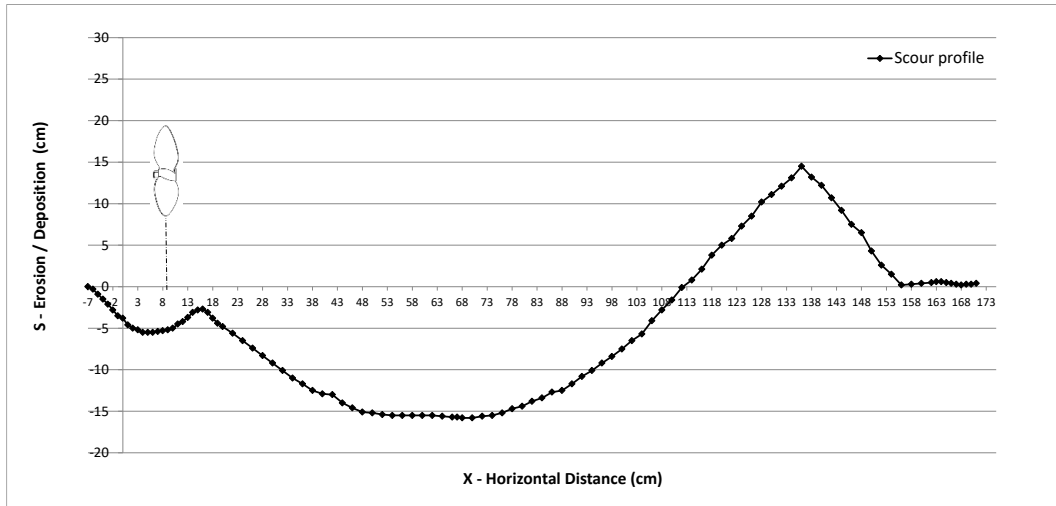


Figure A.6 Scour profile without structure with $D_p=10$ cm, at 774 rpm, $G=10$ cm, on sediment bed of $d_{50}=0.052$ cm

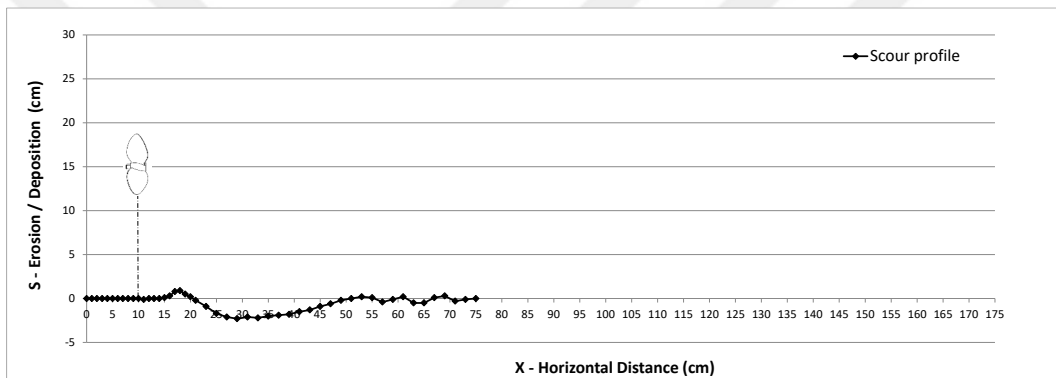


Figure A.7 Scour profile without structure with $D_p=6.5$ cm, at 597 rpm, $G=15$ cm, on sediment bed of $d_{50}=0.052$ cm

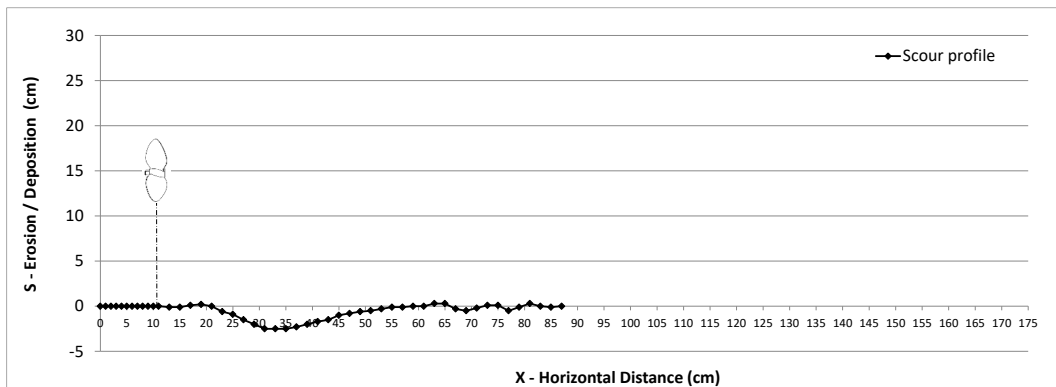


Figure A.8 Scour profile without structure with $D_p=6.5$ cm, at 670 rpm, $G=15$ cm, on sediment bed of $d_{50}=0.052$ cm

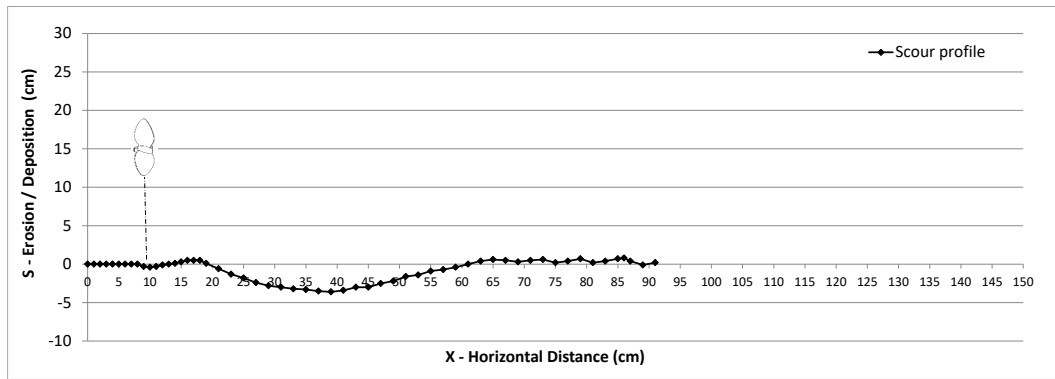


Figure A.9 Scour profile without structure with $D_p=6.5$ cm, at 745 rpm, $G=15$ cm, on sediment bed of $d_{50}=0.052$ cm

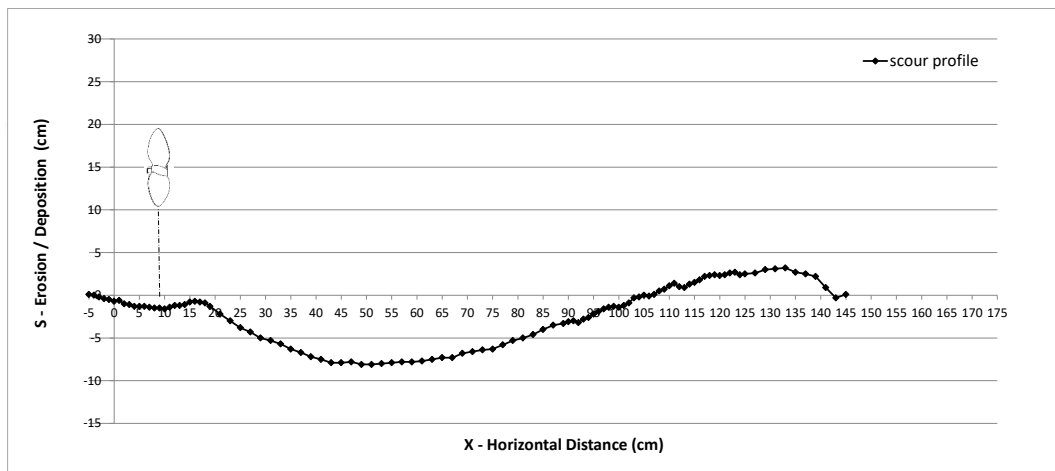


Figure A.10 Scour profile without structure with $D_p=10$ cm, at 596 rpm, $G=15$ cm, on sediment bed of $d_{50}=0.052$ cm

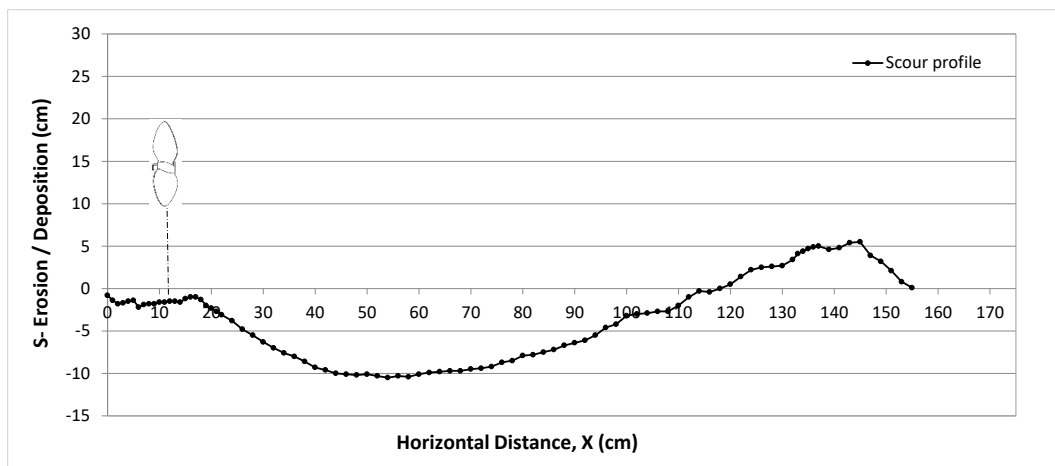


Figure A.11 Scour profile without structure with $D_p=10$ cm, at 670 rpm, $G=15$ cm, on sediment bed of $d_{50}=0.052$ cm

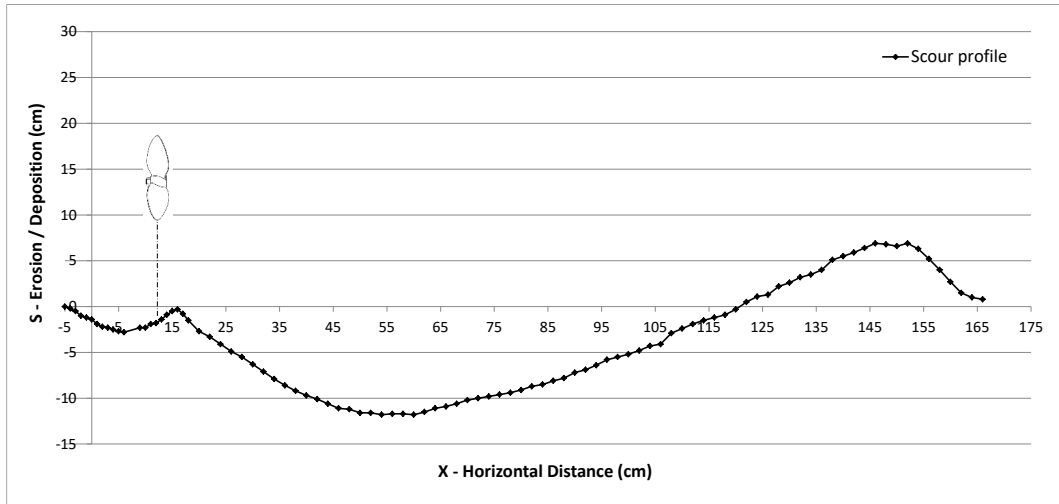


Figure A.12 Scour profile without structure with $D_p=10$ cm, at 745 rpm, $G=15$ cm, on sediment bed of $d_{50}=0.052$ cm

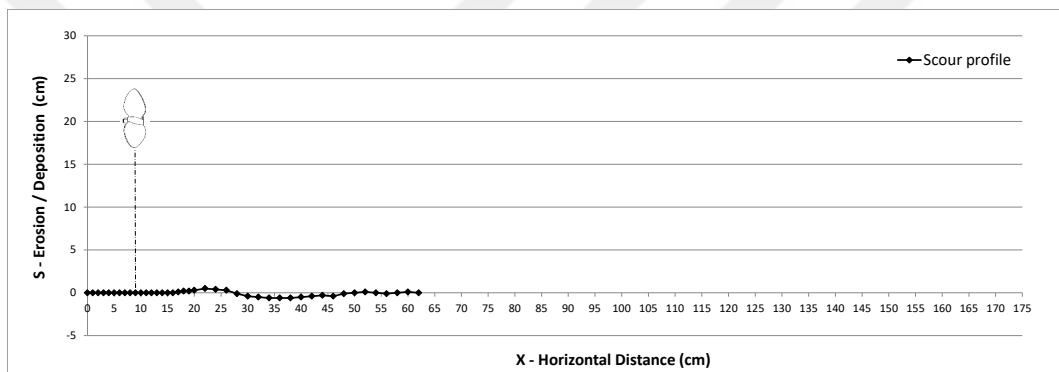


Figure A.13 Scour profile without structure with $D_p=6.5$ cm, at 597 rpm, $G=20$ cm, on sediment bed of $d_{50}=0.052$ cm

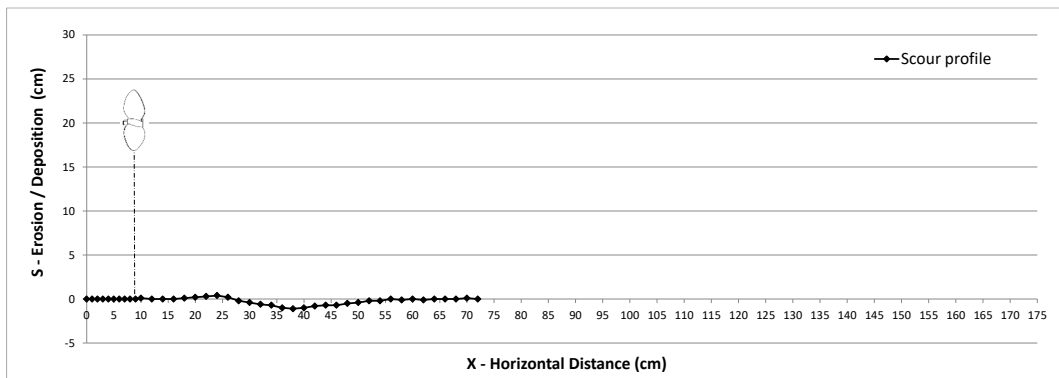


Figure A.14 Scour profile without structure with $D_p=6.5$ cm, at 672 rpm, $G=20$ cm, on sediment bed of $d_{50}=0.052$ cm

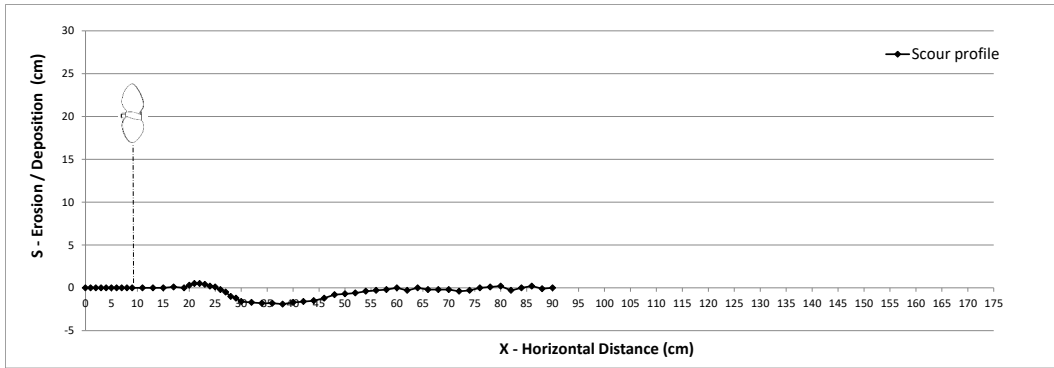


Figure A.15 Scour profile without structure with $D_p=6.5$ cm, at 746 rpm, $G=20$ cm, on sediment bed of $d_{50}=0.052$ cm

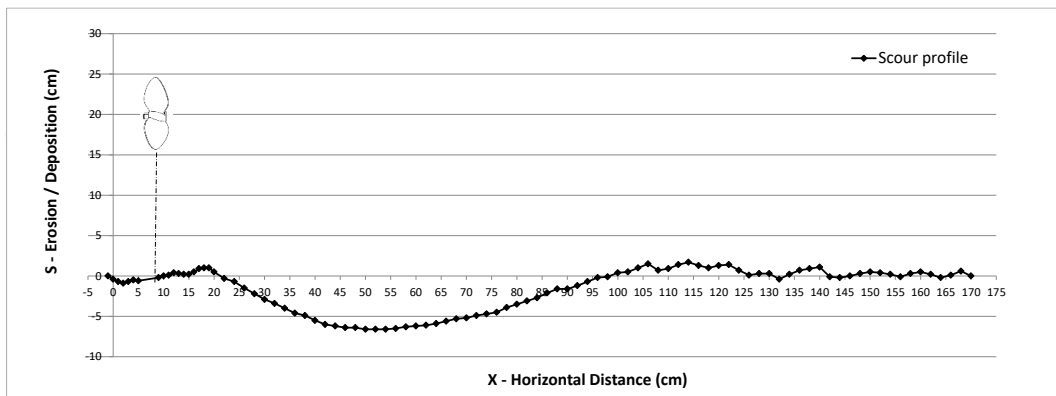


Figure A.16 Scour profile without structure with $D_p=10$ cm, at 597 rpm, $G=20$ cm, on sediment bed of $d_{50}=0.052$ cm

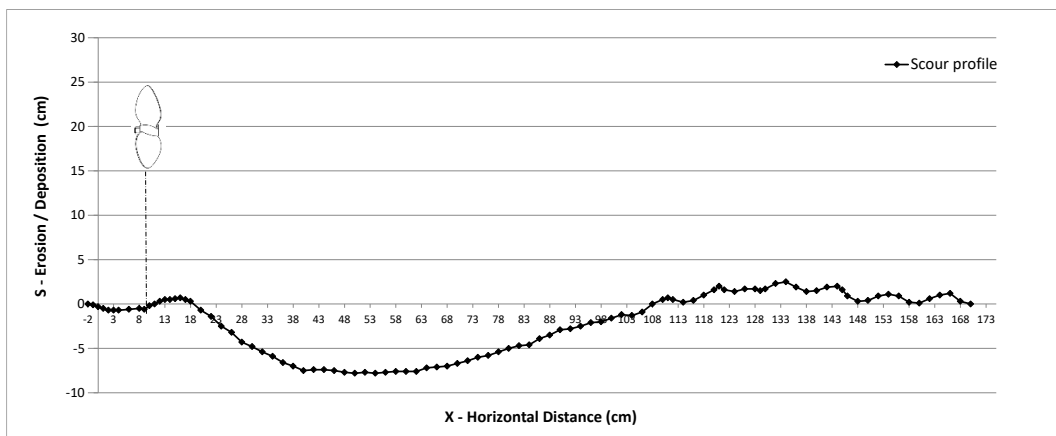


Figure A.17 Scour profile without structure with $D_p=10$ cm, at 670 rpm, $G=20$ cm, on sediment bed of $d_{50}=0.052$ cm

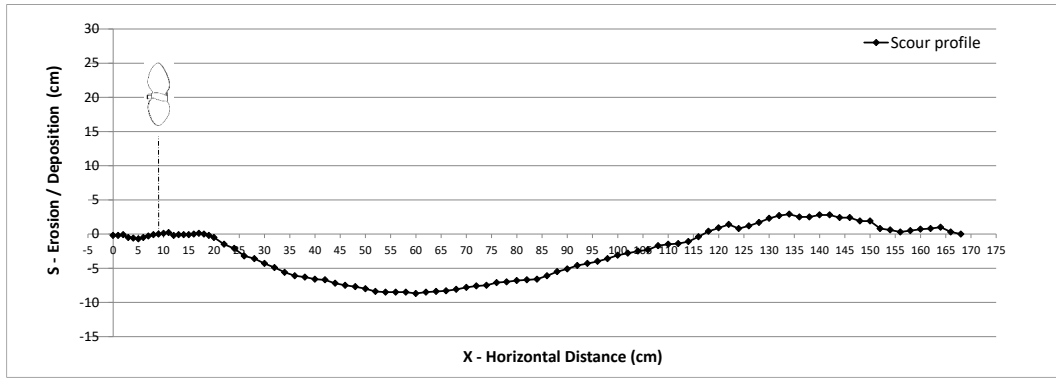


Figure A.18 Scour profile without structure with $D_p=10$ cm, at 745 rpm, $G=20$ cm, on sediment bed of $d_{50}=0.052$ cm

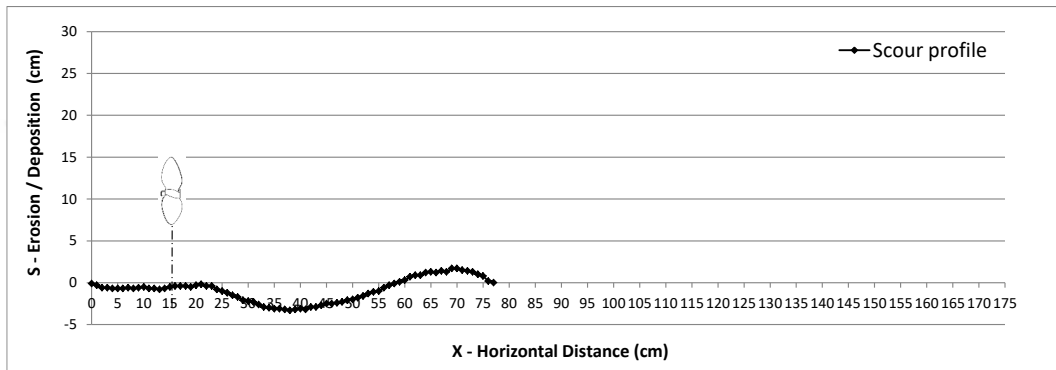


Figure A.19 Scour profile without structure with $D_p=6.5$ cm, at 595 rpm, $G=10$ cm, on sediment bed of $d_{50}=0.128$ cm

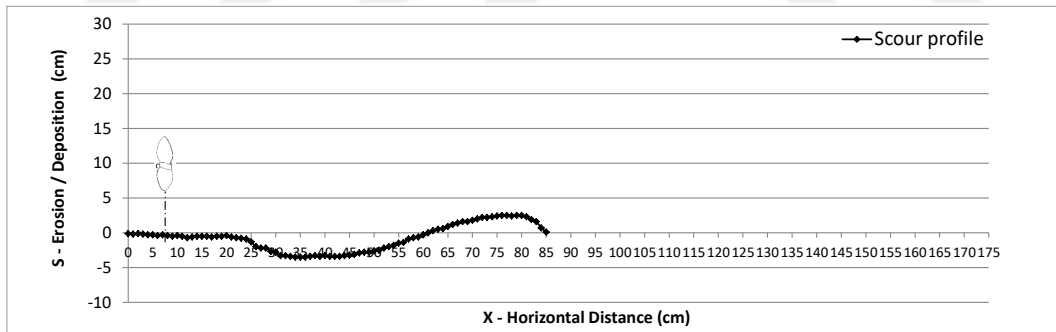


Figure A.20 Scour profile without structure with $D_p=6.5$ cm, at 670 rpm, $G=10$ cm, on sediment bed of $d_{50}=0.128$ cm

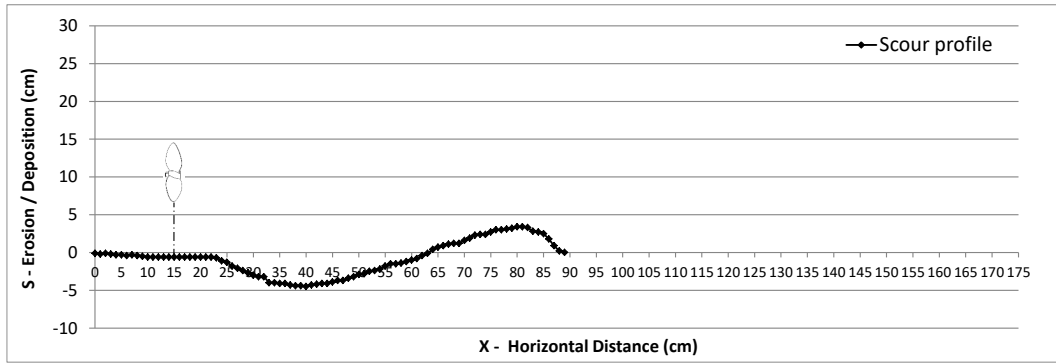


Figure A.21 Scour profile without structure with $D_p=6.5$ cm, at 744 rpm, $G=10$ cm, on sediment bed of $d_{50}=0.128$ cm

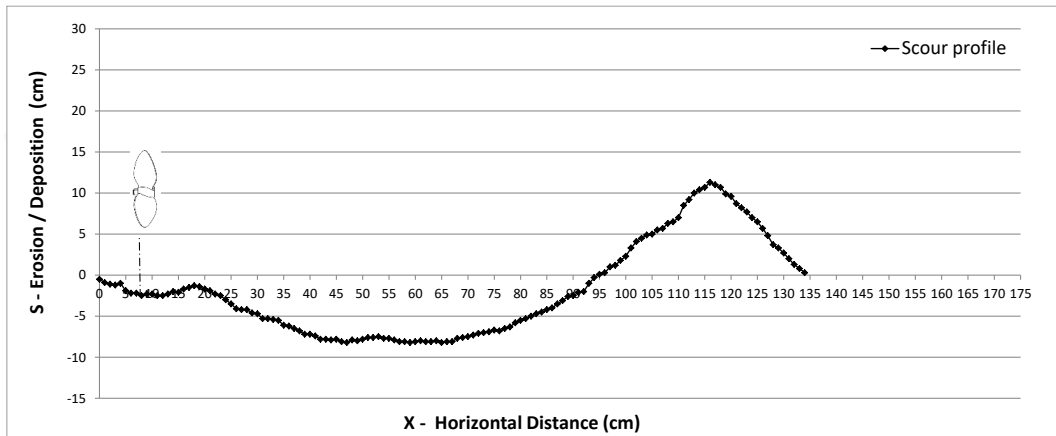


Figure A.22 Scour profile without structure with $D_p=10$ cm, at 596 rpm, $G=10$ cm, on sediment bed of $d_{50}=0.128$ cm

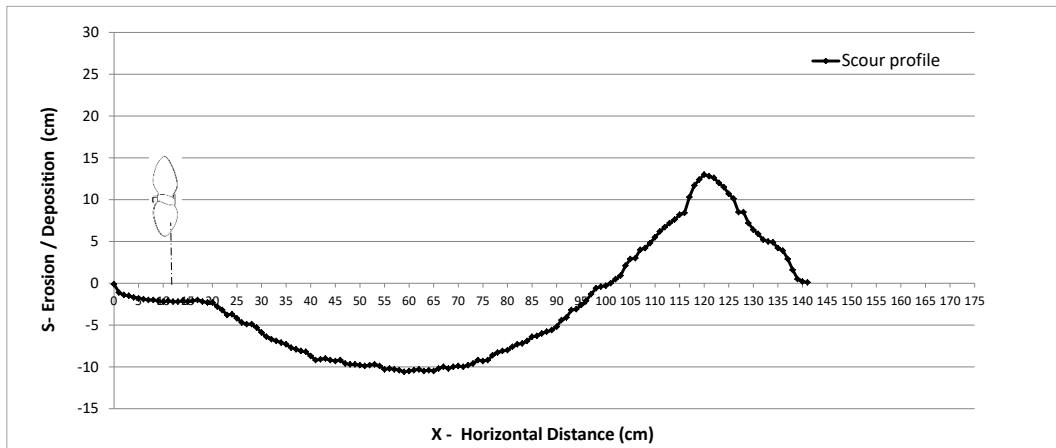


Figure A.23 Scour profile without structure with $D_p=10$ cm, at 673 rpm, $G=10$ cm, on sediment bed of $d_{50}=0.128$ cm

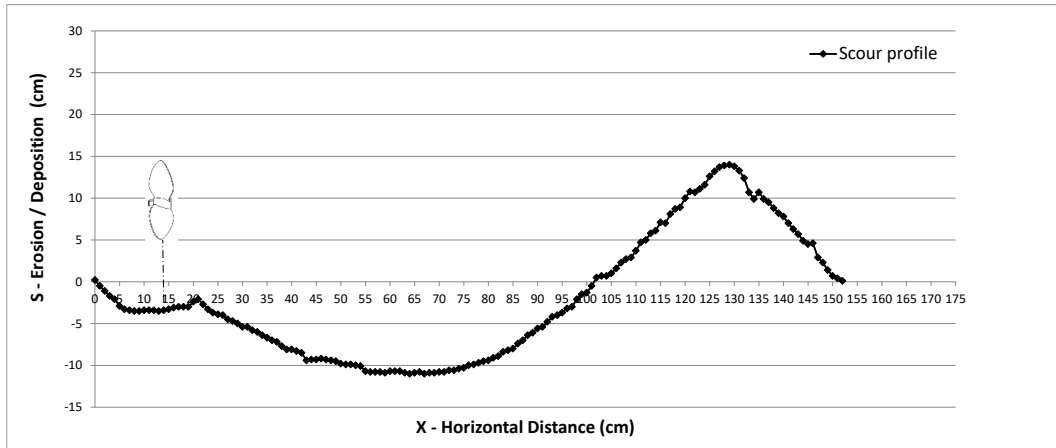


Figure A.24 Scour profile without structure with $D_p=10$ cm, at 746 rpm, $G=10$ cm, on sediment bed of $d_{50}=0.128$ cm

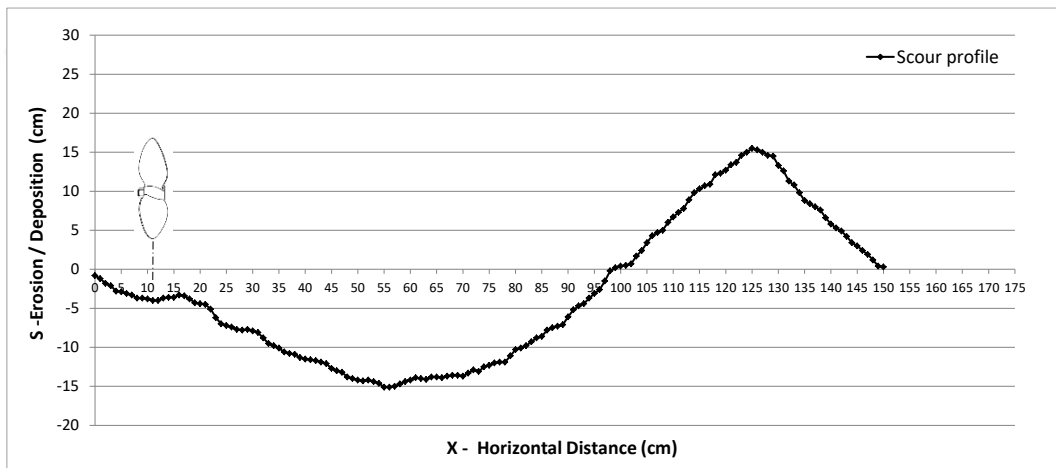


Figure A.25 Scour profile without structure with $D_p=13$ cm, at 591 rpm, $G=10$ cm, on sediment bed of $d_{50}=0.128$ cm

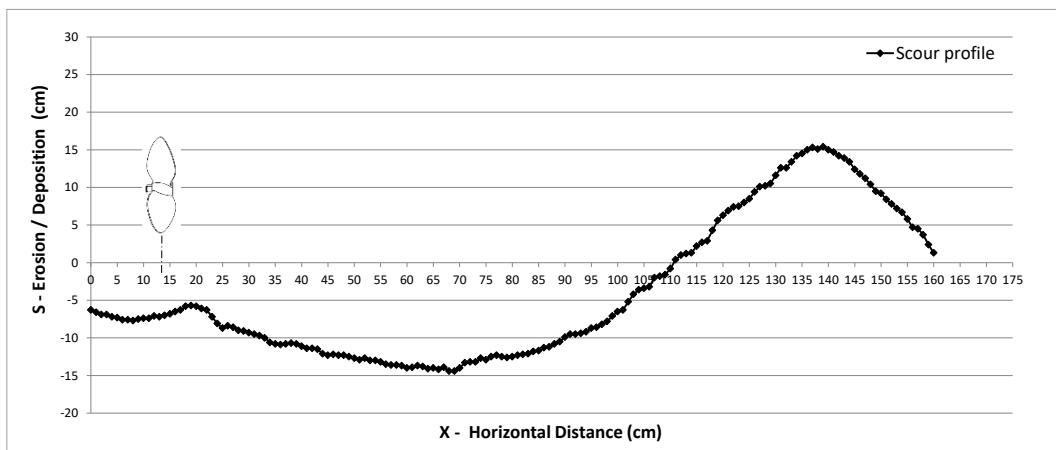


Figure A.26 Scour profile without structure with $D_p=13$ cm, at 666 rpm, $G=10$ cm, on sediment bed of $d_{50}=0.128$ cm

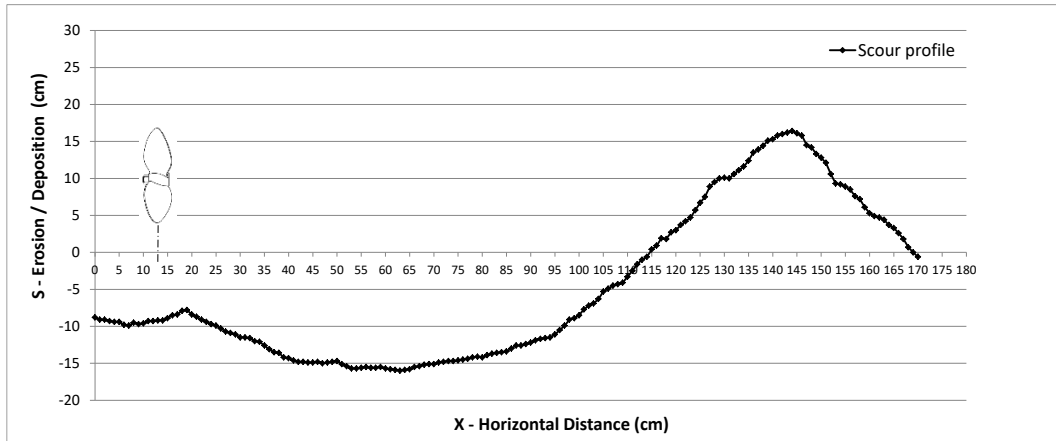


Figure A.27 Scour profile without structure with $D_p=13$ cm, at 743 rpm, $G=10$ cm, on sediment bed of $d_{50}=0.128$ cm

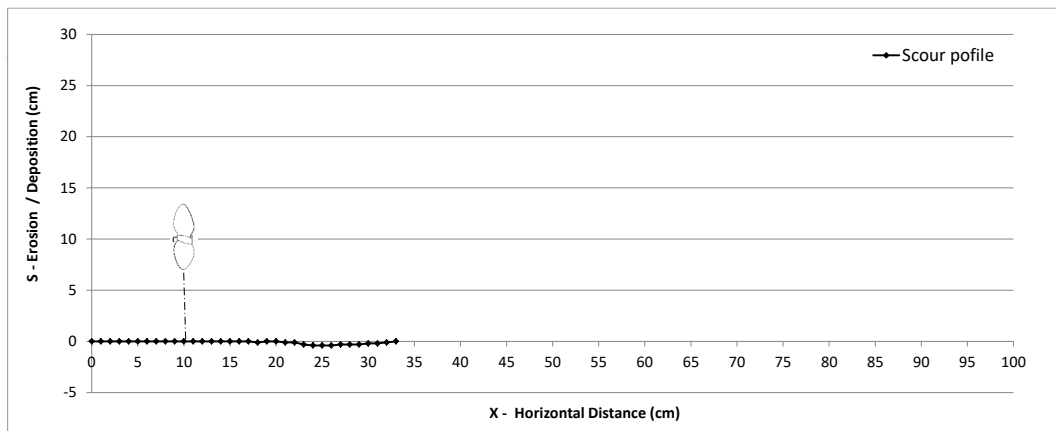


Figure A.28 Scour profile without structure with $D_p=6.5$ cm, at 596 rpm, $G=10$ cm, on sediment bed of $d_{50}=0.4$ cm

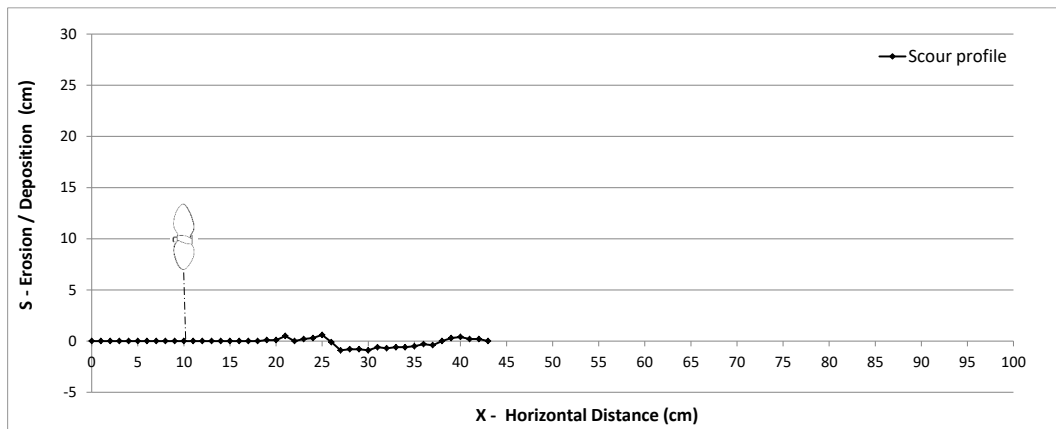


Figure A.29 Scour profile without structure with $D_p=6.5$ cm, at 673 rpm, $G=10$ cm, on sediment bed of $d_{50}=0.4$ cm

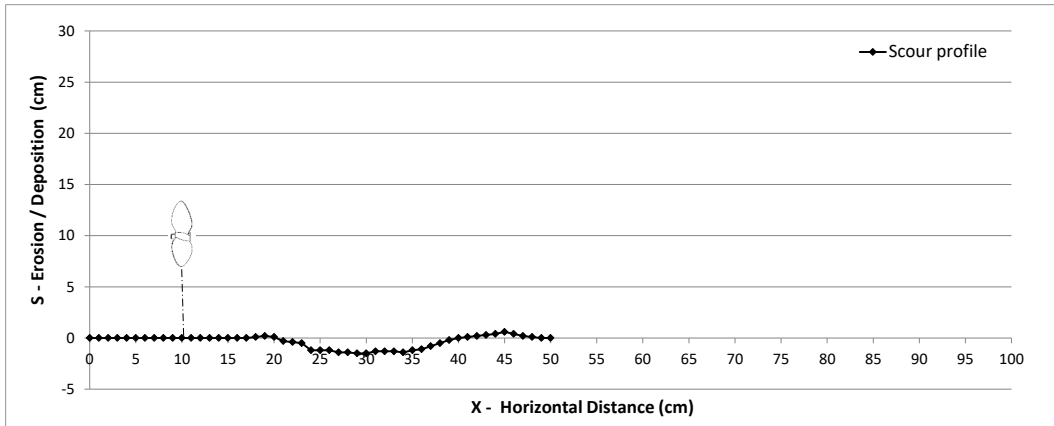


Figure A.30 Scour profile without structure with $D_p=6.5$ cm, at 746 rpm, $G=10$ cm, on sediment bed of $d_{50}=0.4$ cm

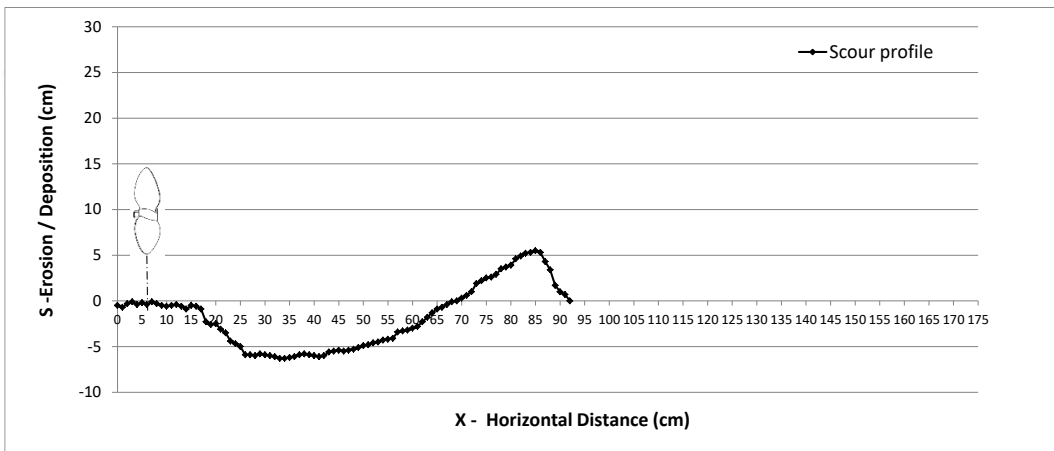


Figure A.31 Scour profile without structure with $D_p=10$ cm, at 596 rpm, $G=10$ cm, on sediment bed of $d_{50}=0.4$ cm

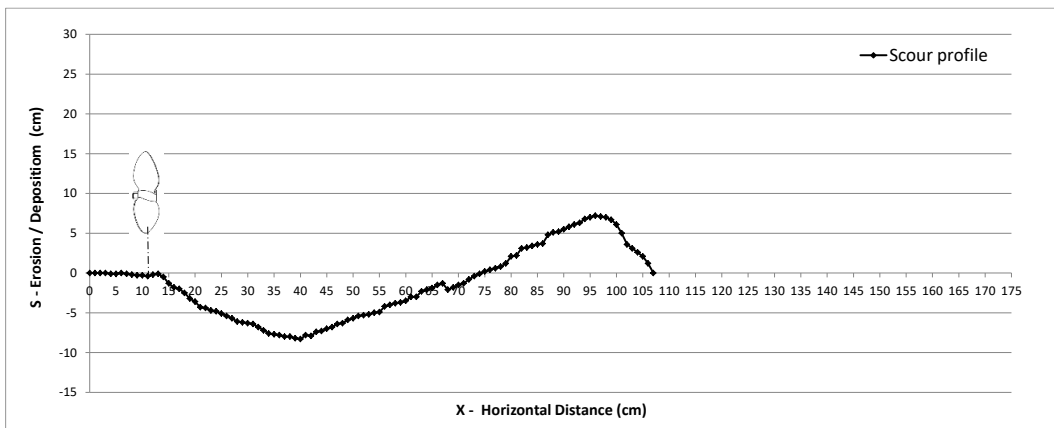


Figure A.32 Scour profile without structure with $D_p=10$ cm, at 670 rpm, $G=10$ cm, on sediment bed of $d_{50}=0.4$ cm

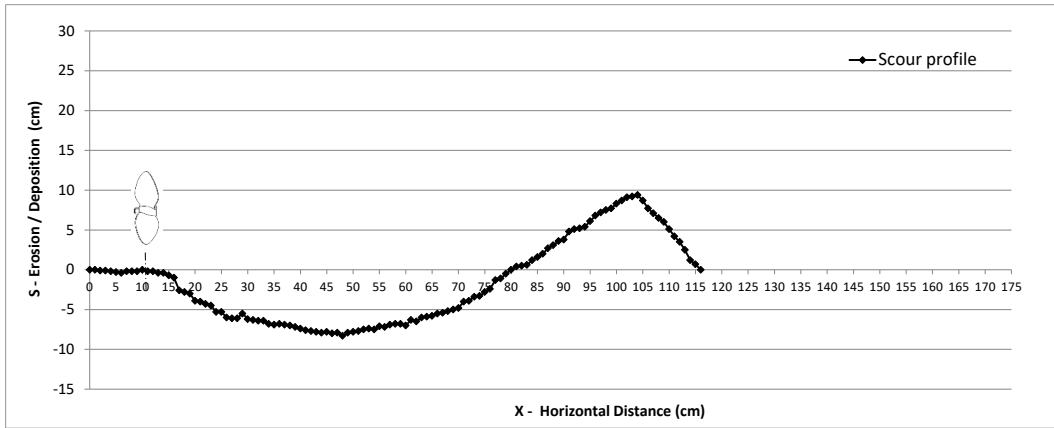


Figure A.33 Scour profile without structure with $D_p=10$ cm, at 744 rpm, $G=10$ cm, on sediment bed of $d_{50}=0.4$ cm

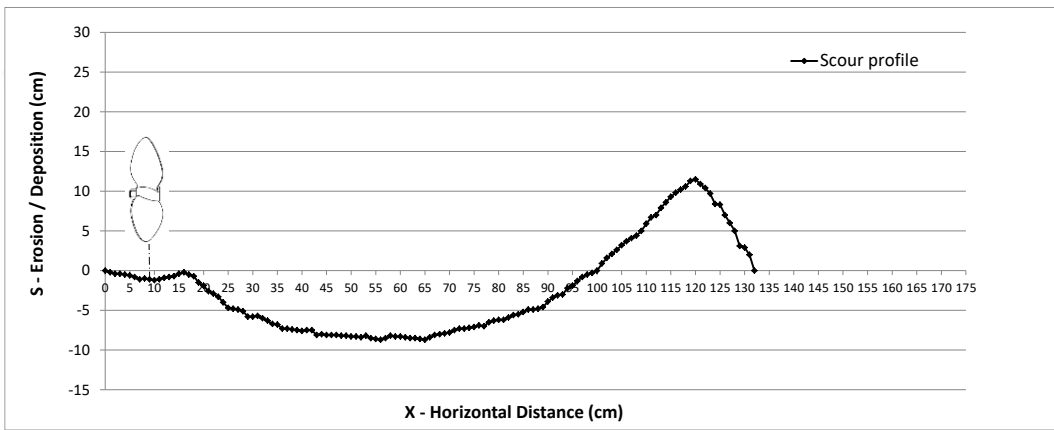


Figure A.34 Scour profile without structure with $D_p=13$ cm, at 591 rpm, $G=10$ cm, on sediment bed of $d_{50}=0.4$ cm

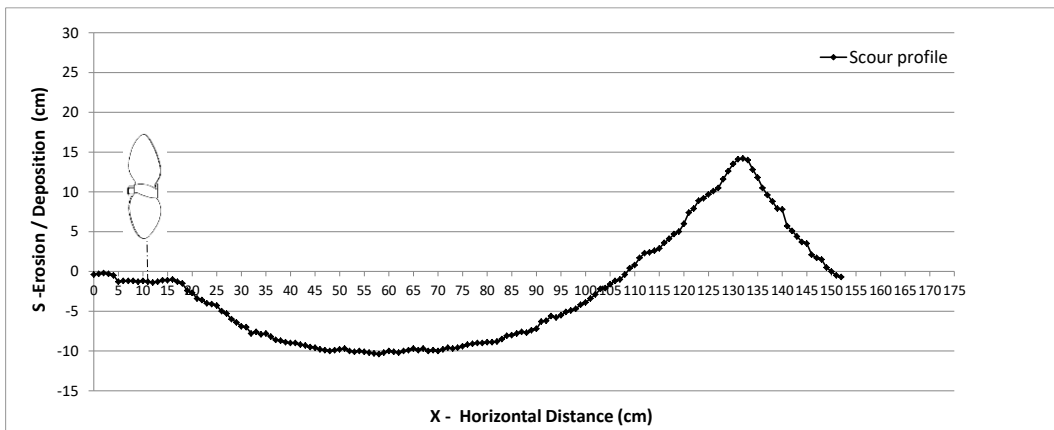


Figure A.35 Scour profile without structure with $D_p=13$ cm, at 665 rpm, $G=10$ cm, on sediment bed of $d_{50}=0.4$ cm

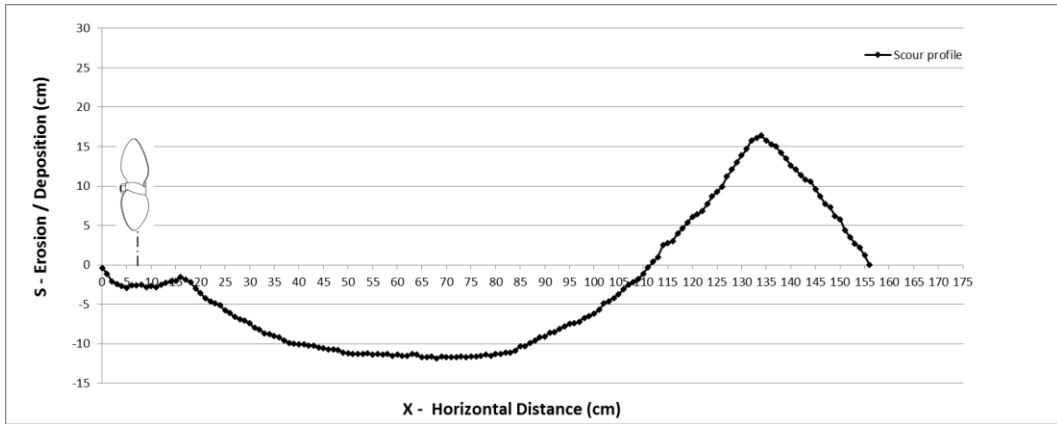


Figure A.36 Scour profile without structure with $D_p=13$ cm, at 738 rpm, $G=10$ cm, on sediment bed of $d_{50}=0.4$ cm

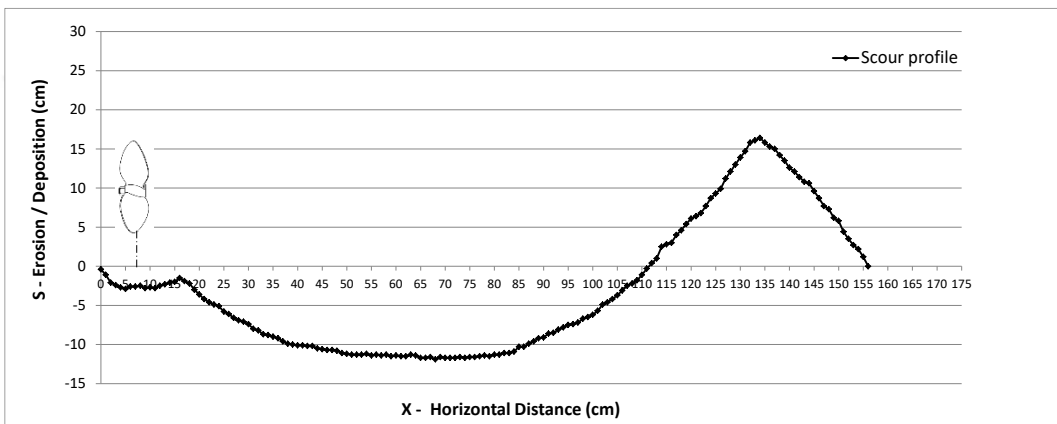


Figure A.37 Scour profile without structure with $D_p=10$ cm, at 595 rpm, $G=10$ cm, on sediment bed of $d_{50}=0.83$ cm

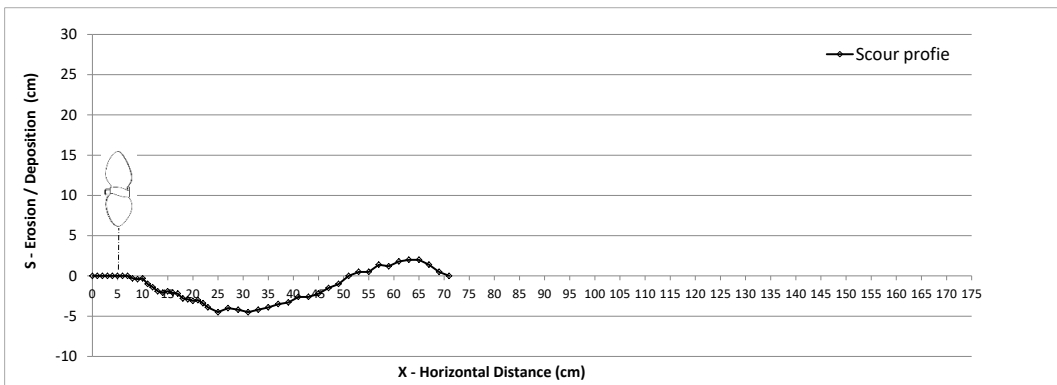


Figure A.38 Scour profile without structure with $D_p=10$ cm, at 670 rpm, $G=10$ cm, on sediment bed of $d_{50}=0.83$ cm

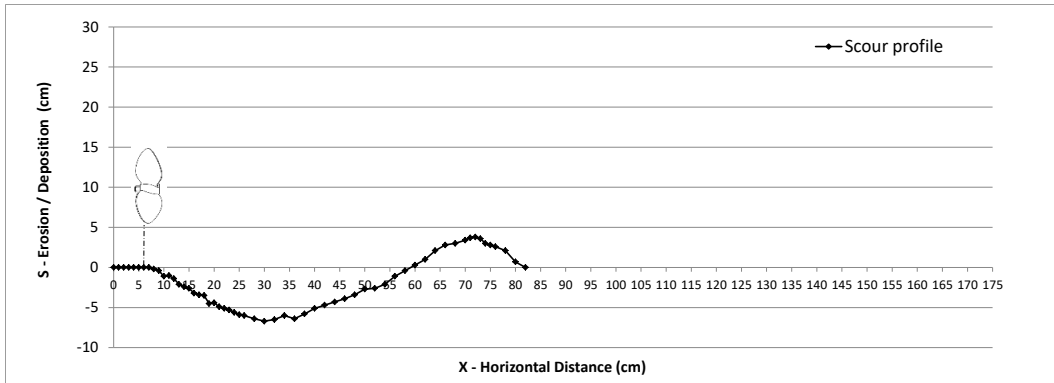


Figure A.39 Scour profile without structure with $D_p=10$ cm, at 744 rpm, $G=10$ cm, on sediment bed of $d_{50}=0.83$ cm

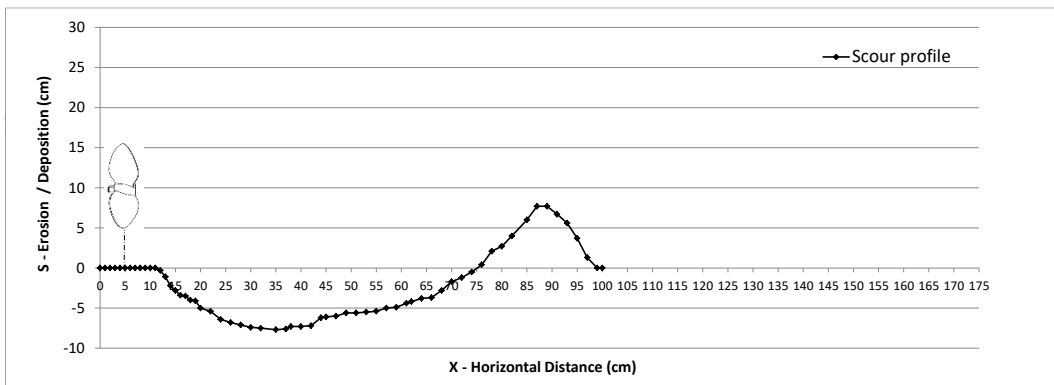


Figure A.40 Scour profile without structure with $D_p=13$ cm, at 593 rpm, $G=10$ cm, on sediment bed of $d_{50}=0.83$ cm

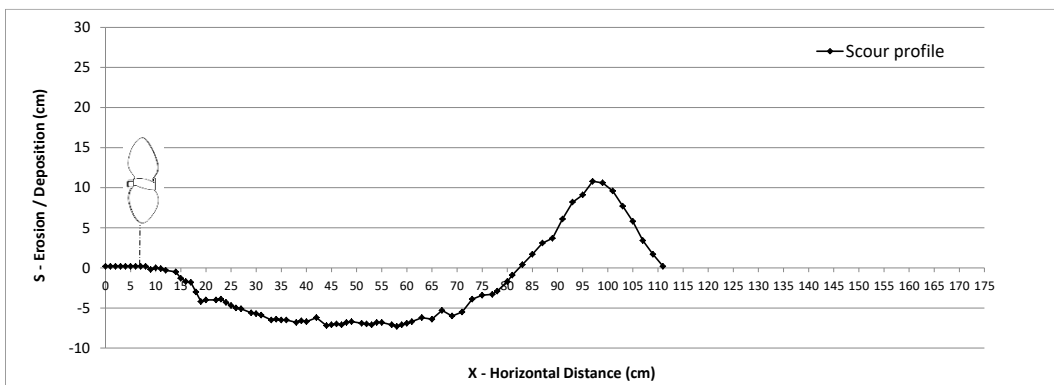


Figure A.41 Scour profile without structure with $D_p=13$ cm, at 665 rpm, $G=10$ cm, on sediment bed of $d_{50}=0.83$ cm

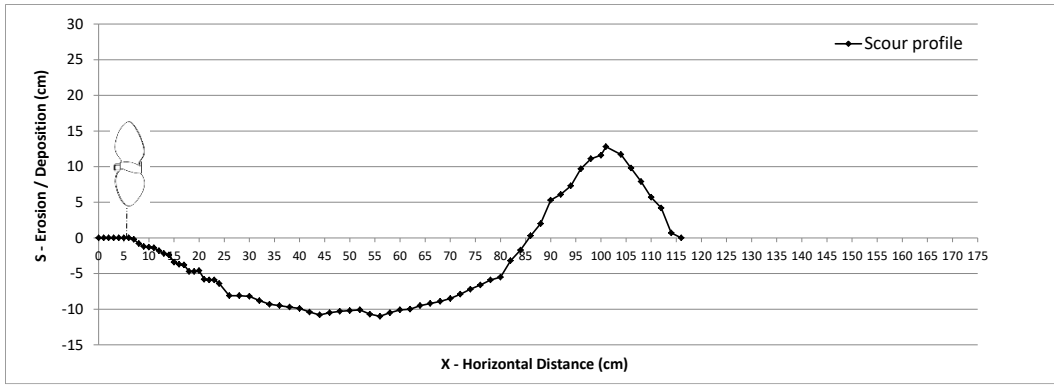


Figure A.42 Scour profile without structure with $D_p=13$ cm, at 744 rpm, $G=10$ cm, on sediment bed of $d_{50}=0.83$ cm

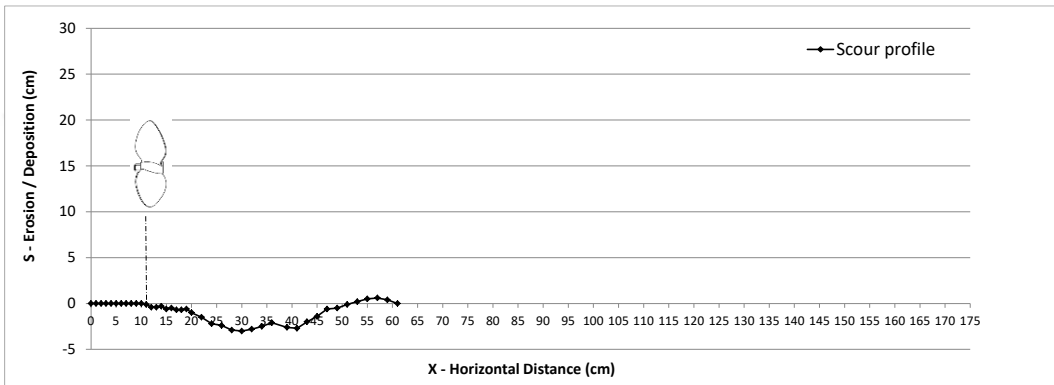


Figure A.43 Scour profile without structure with $D_p=10$ cm, at 664 rpm, $G=15$ cm, on sediment bed of $d_{50}=0.83$ cm

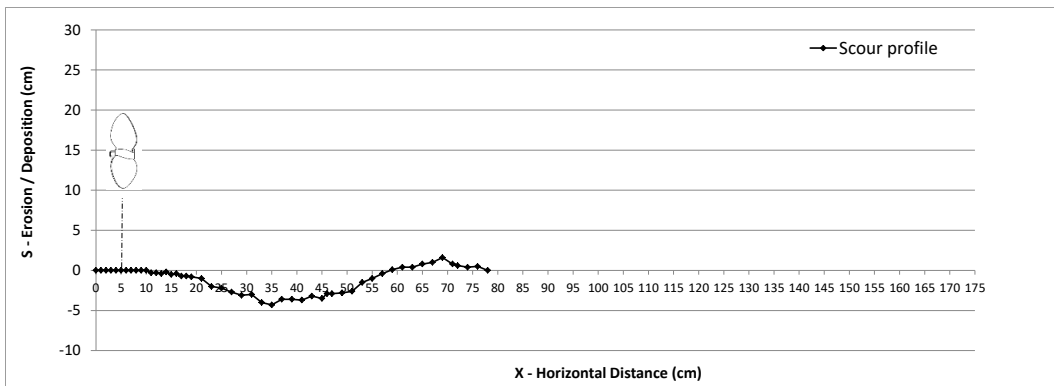


Figure A.44 Scour profile without structure with $D_p=10$ cm, at 745 rpm, $G=15$ cm, on sediment bed of $d_{50}=0.83$ cm

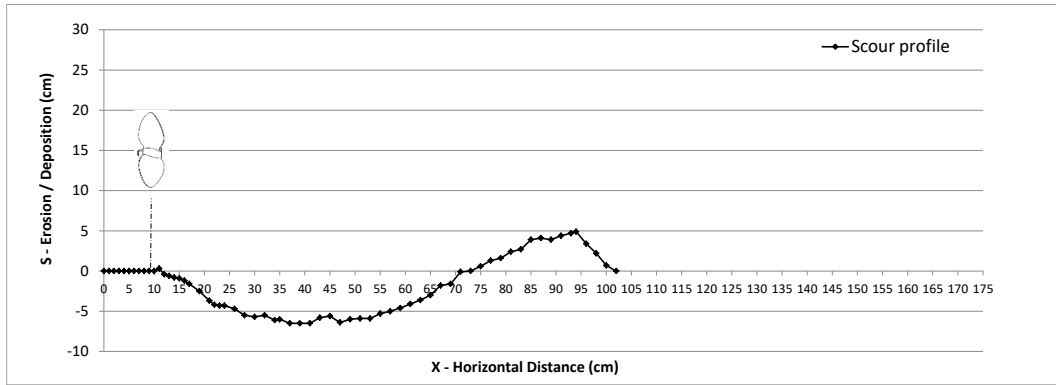


Figure A.45 Scour profile without structure with $D_p=13$ cm, at 592 rpm, $G=15$ cm, on sediment bed of $d_{50}=0.83$ cm

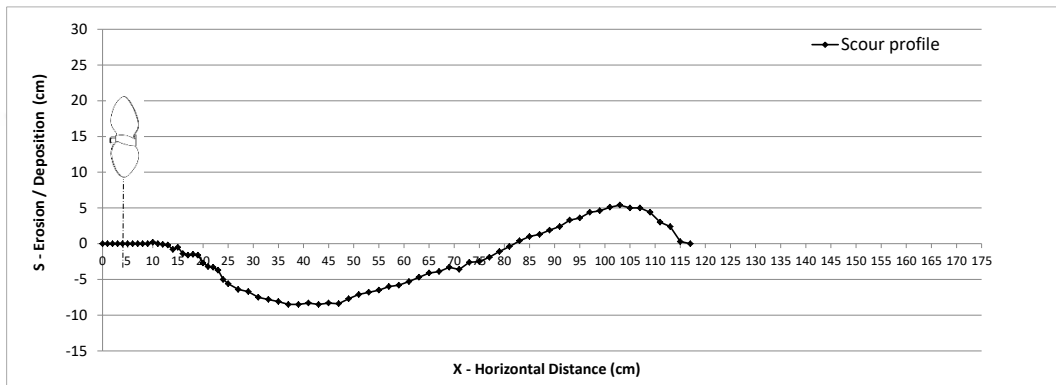


Figure A.46 Scour profile without structure with $D_p=13$ cm, at 665 rpm, $G=15$ cm, on sediment bed of $d_{50}=0.83$ cm

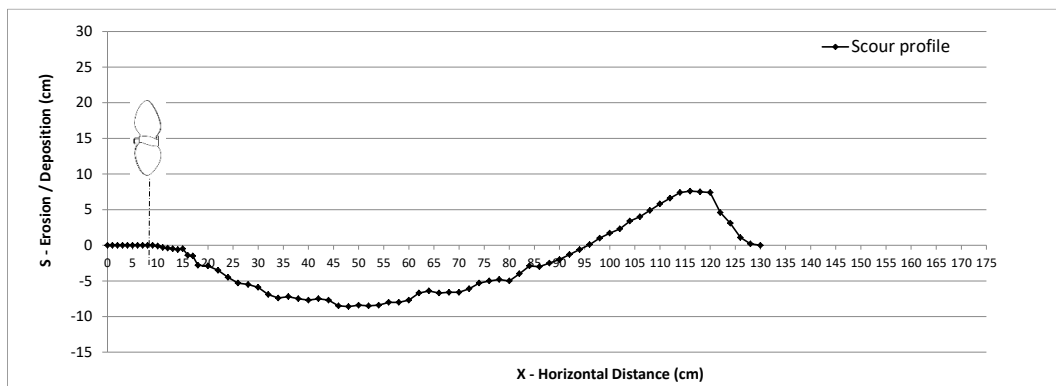


Figure A.47 Scour profile without structure with $D_p=13$ cm, at 739 rpm, $G=15$ cm, on sediment bed of $d_{50}=0.83$ cm

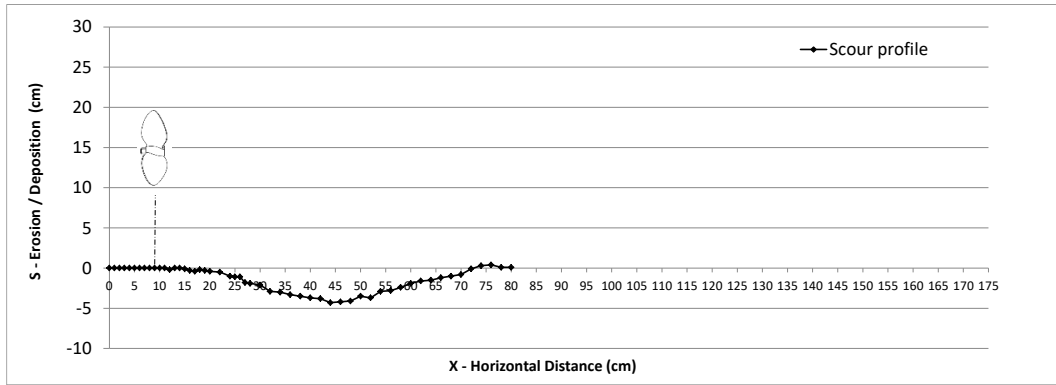


Figure A.48 Scour profile without structure with $D_p=13$ cm, at 591 rpm, $G=20$ cm, on sediment bed of $d_{50}=0.83$ cm

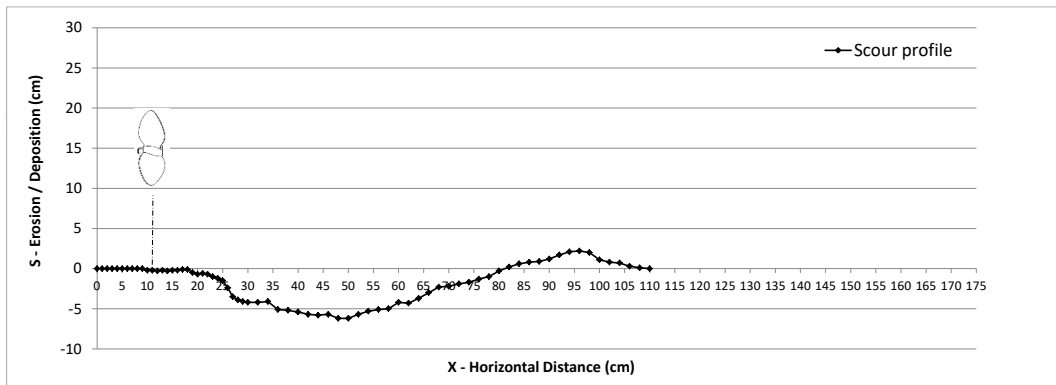


Figure A.49 Scour profile without structure with $D_p=13$ cm, at 664 rpm, $G=20$ cm, on sediment bed of $d_{50}=0.83$ cm

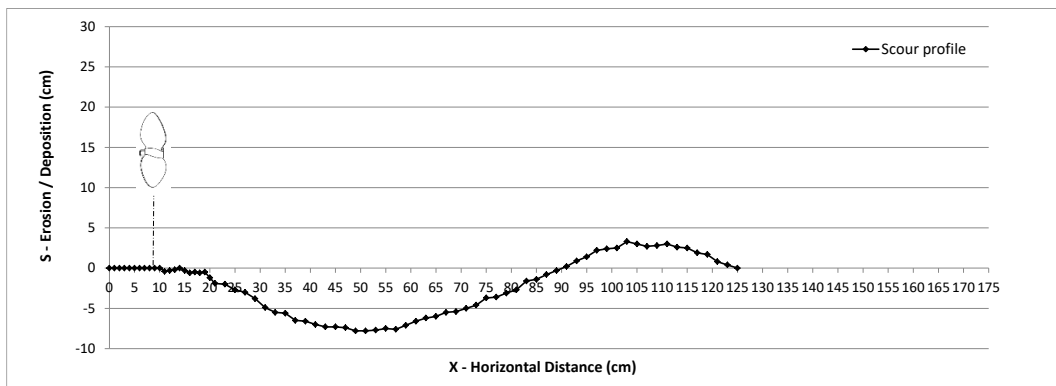


Figure A.50 Scour profile without structure with $D_p=13$ cm, at 738 rpm, $G=20$ cm, on sediment bed of $d_{50}=0.83$ cm

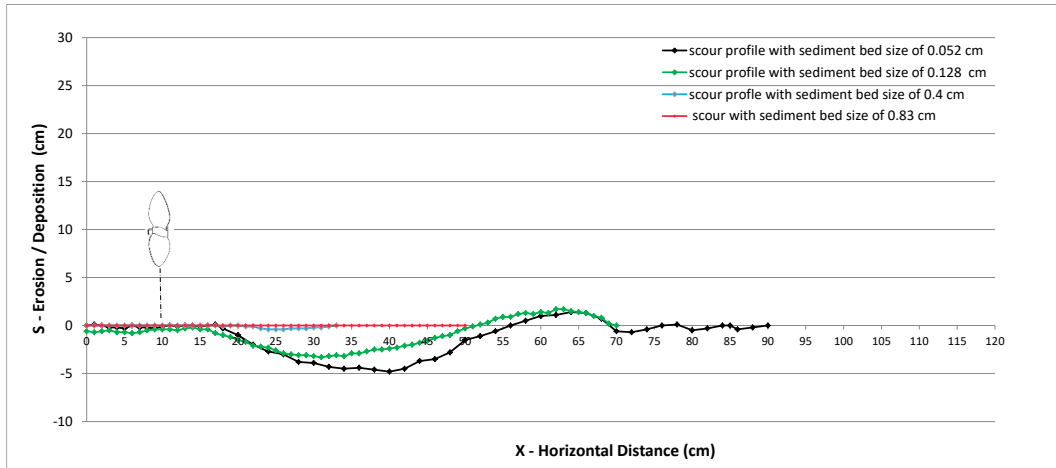


Figure A.51 Scour profiles on different sediment beds with $D_p=6.5$ cm, $G=10$ cm, at 40 Hz

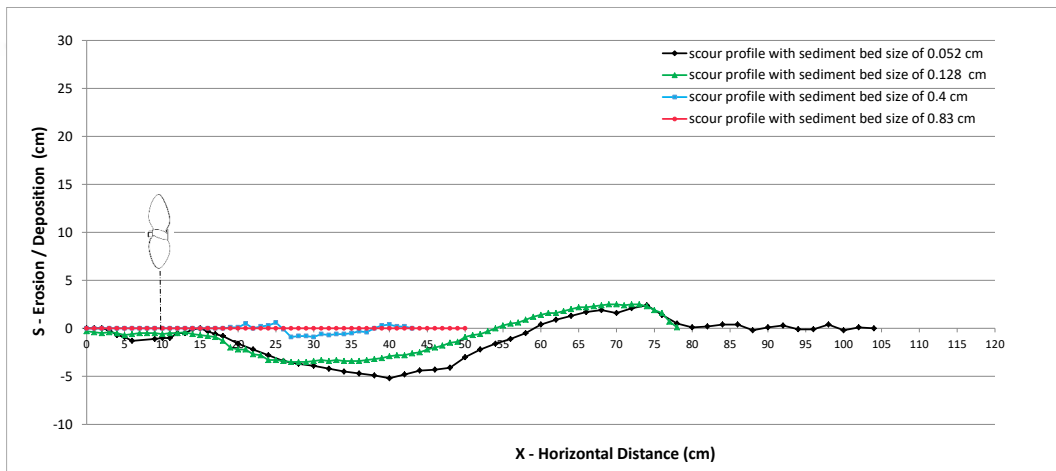


Figure A.52 Scour profiles on different sediment beds with $D_p=6.5$ cm, $G=10$ cm, at 45 Hz

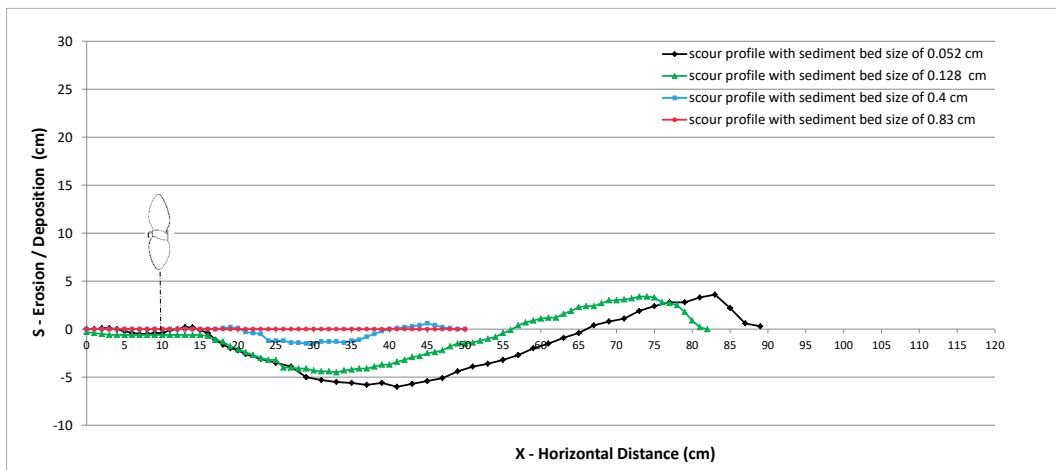


Figure A.53 Scour profiles on different sediment beds with $D_p=6.5$ cm, $G=10$ cm, at 50 Hz

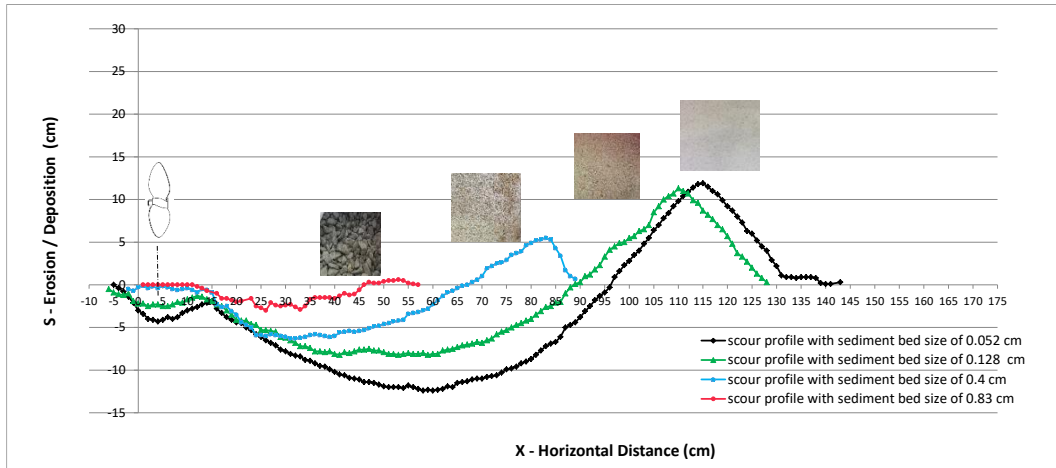


Figure A.54 Scour profiles on different sediment beds with $D_p=10$ cm, $G=10$ cm, at 40 Hz

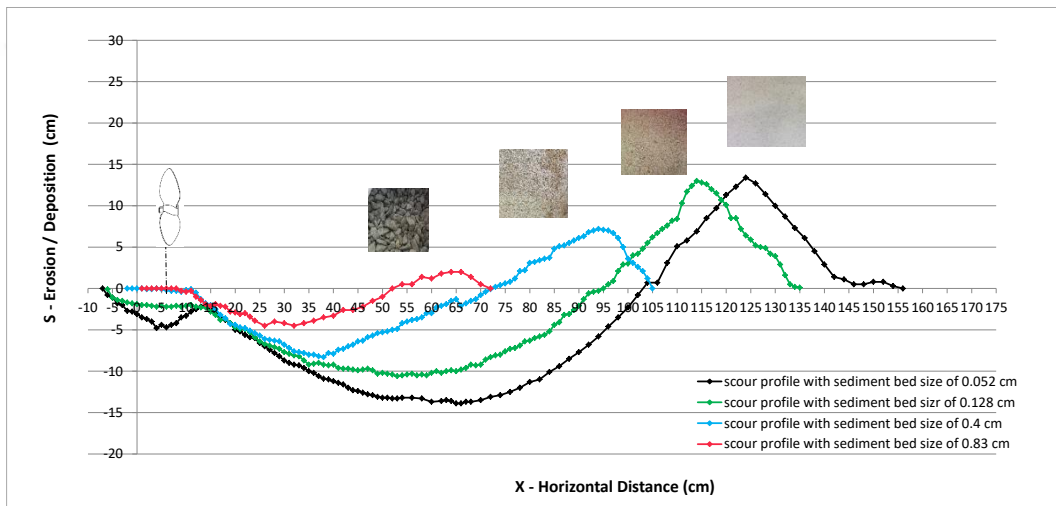


Figure A.55 Scour profiles on different sediment beds with $D_p=10$ cm, $G=10$ cm, 45 Hz

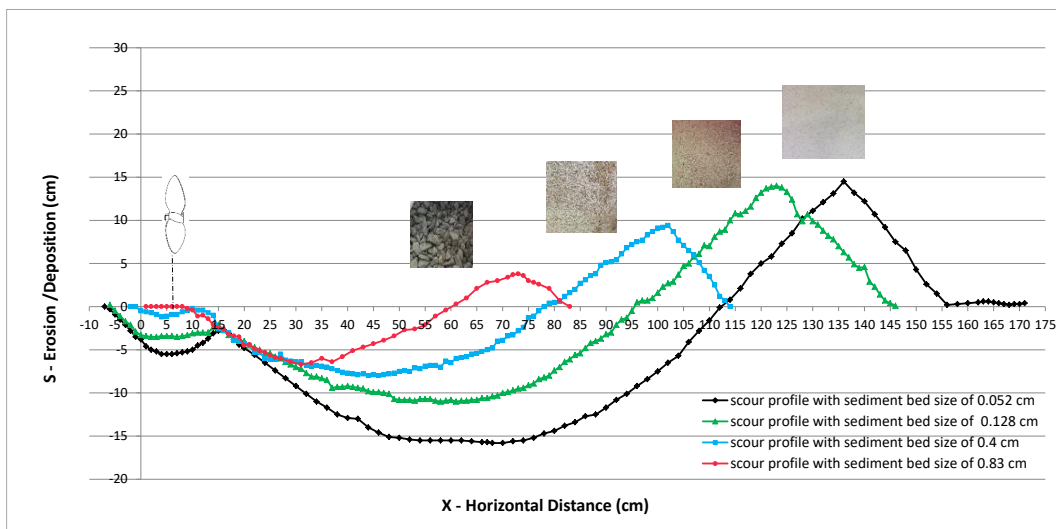


Figure A.56 Scour profiles on different sediment beds with $D_p=10$ cm, $G=10$ cm, 50 Hz

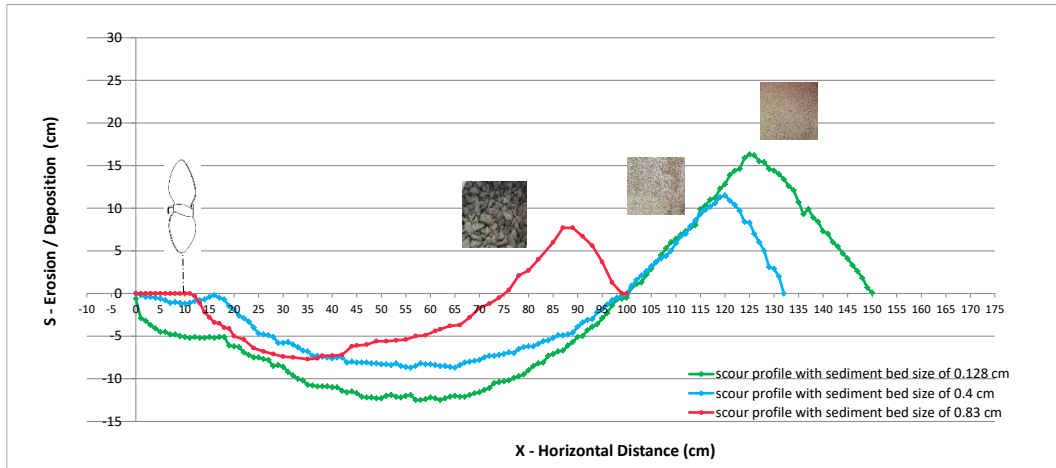


Figure A.57 Scour profiles on different sediment beds with $D_p=13$ cm, $G=10$ cm, 40 Hz

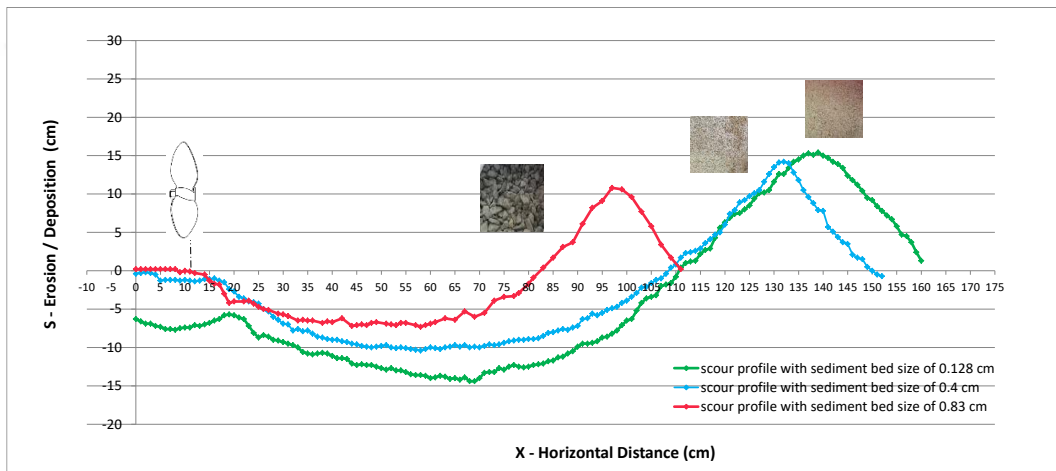


Figure A.58 Scour profiles on different sediment beds with $D_p=13$ cm, $G=10$ cm, 45 Hz

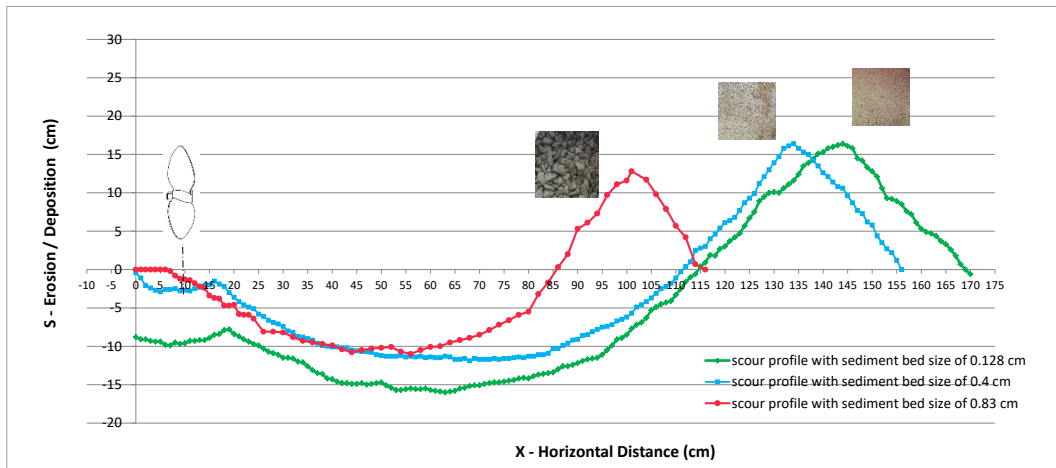


Figure A.59 Scour profiles on different sediment beds with $D_p=13$ cm, $G=10$ cm, 50 Hz

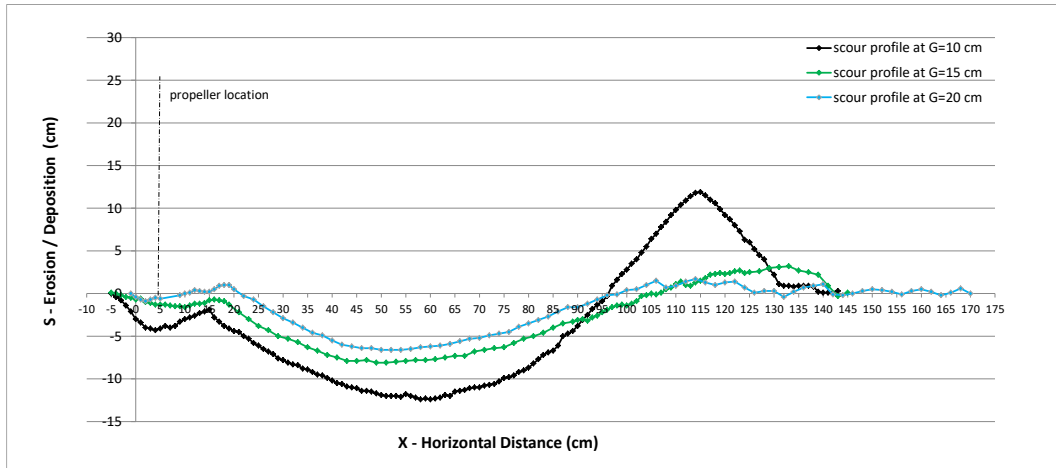


Figure A.60 Scour profiles with different gaps of propeller ($D_p=10\text{ cm}$, at 40 Hz on sediment bed $d_{50}=0.052\text{ cm}$)

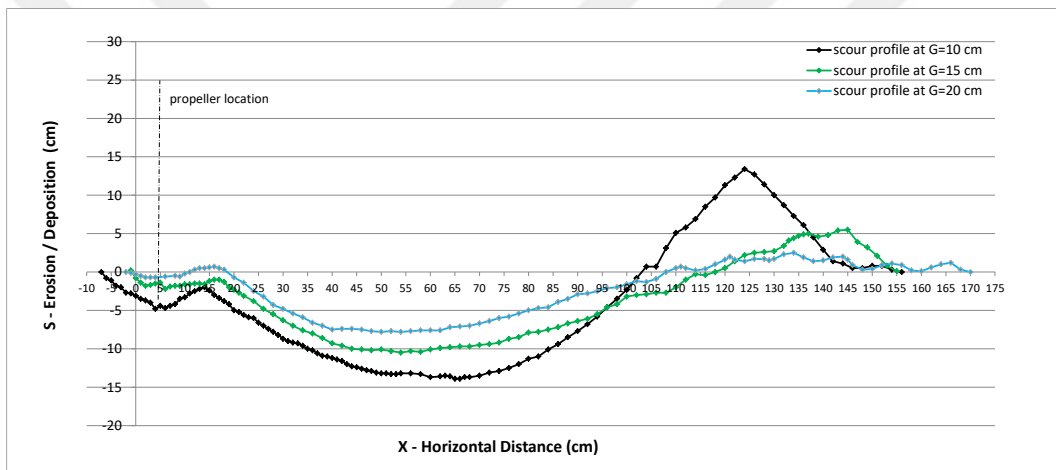


Figure A.61 Scour profiles with different gaps of propeller ($D_p=10\text{ cm}$, at 45 Hz on sediment bed $d_{50}=0.052\text{ cm}$)

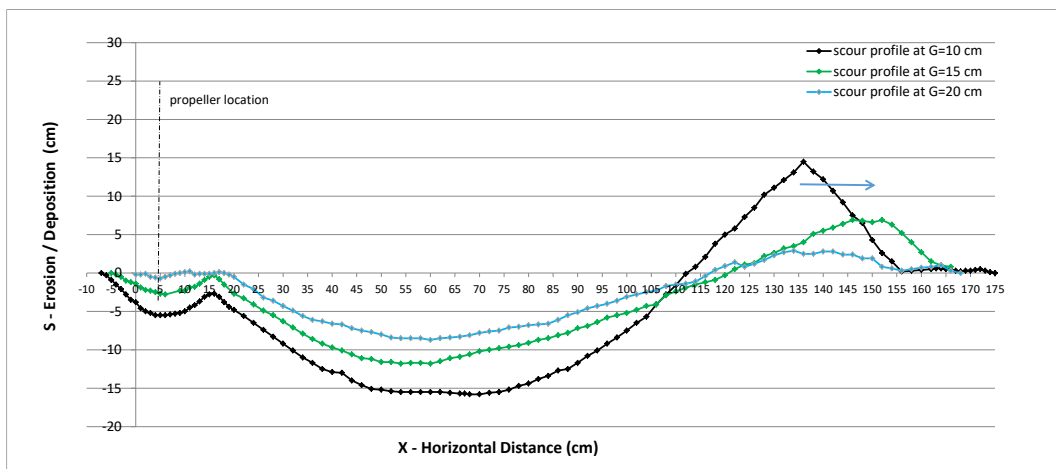


Figure A.62 Scour profiles with different gaps of propeller with ($D_p=10\text{ cm}$, at 50 Hz on sediment bed $d_{50}=0.052\text{ cm}$)

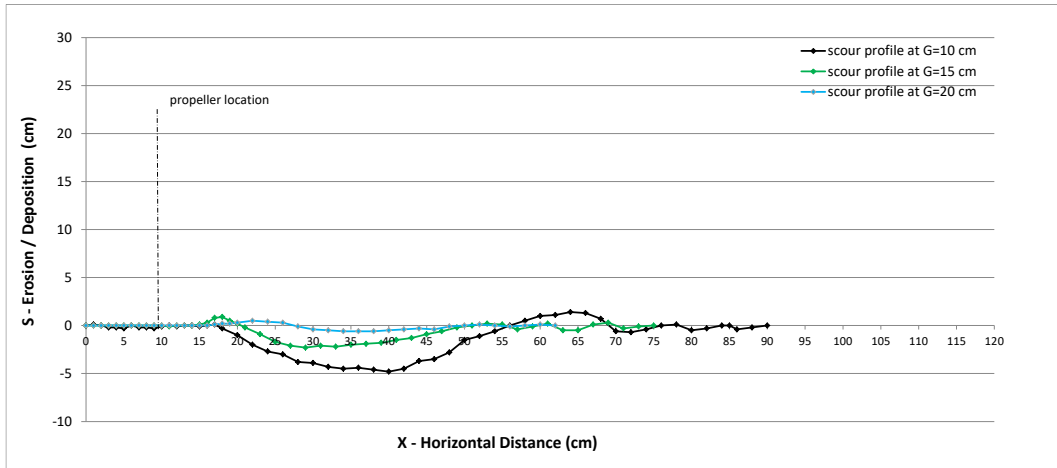


Figure A.63 Scour profiles with different gaps of propeller ($D_p=6.5$ cm, at 40 Hz on sediment bed $d_{50}=0.052$ cm)

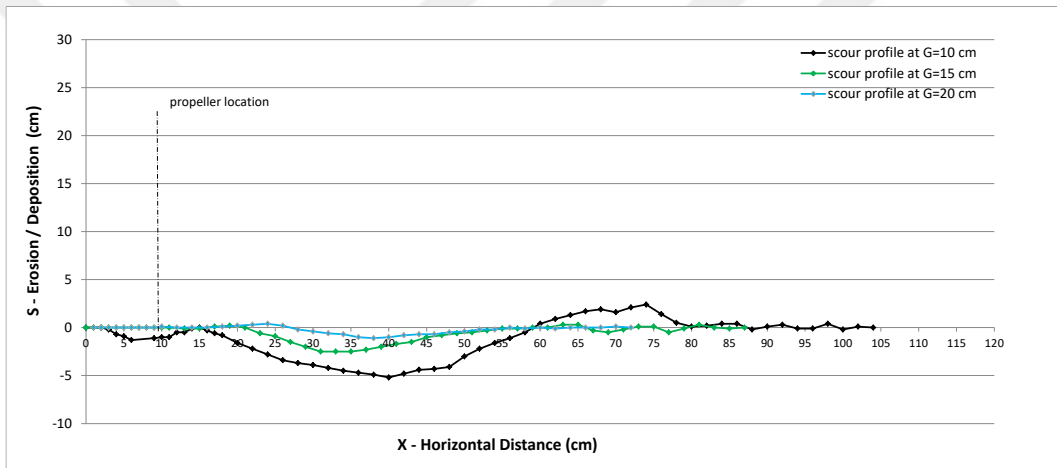


Figure A.64 Scour profiles with different gaps of propeller with ($D_p=6.5$ cm, at 45 Hz on sediment bed $d_{50}=0.052$ cm)

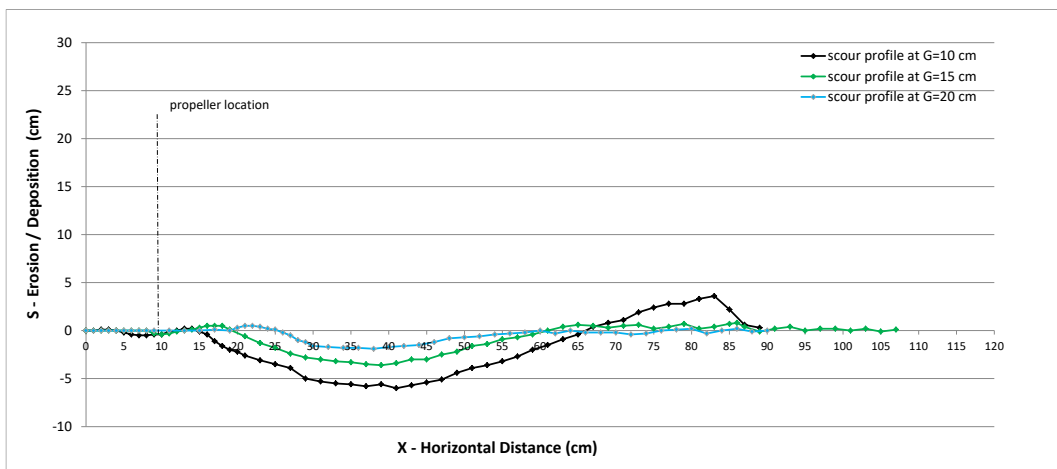


Figure A.65 Scour profiles with different gaps of propeller ($D_p=6.5$ cm, at 50 Hz on sediment bed $d_{50}=0.052$ cm)

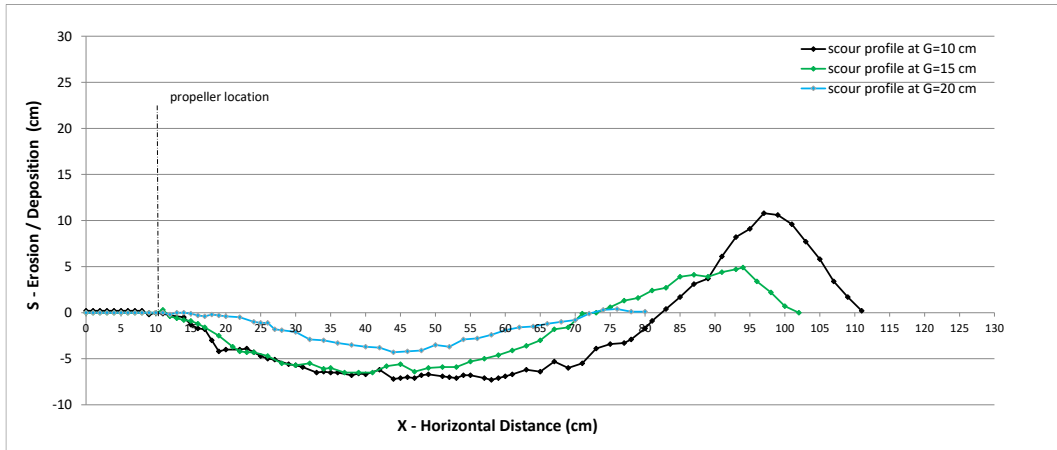


Figure A.66 Scour profiles with different gaps of propeller with ($D_p=13$ cm, at 40 Hz on sediment bed $d_{50}=0.83$ cm)

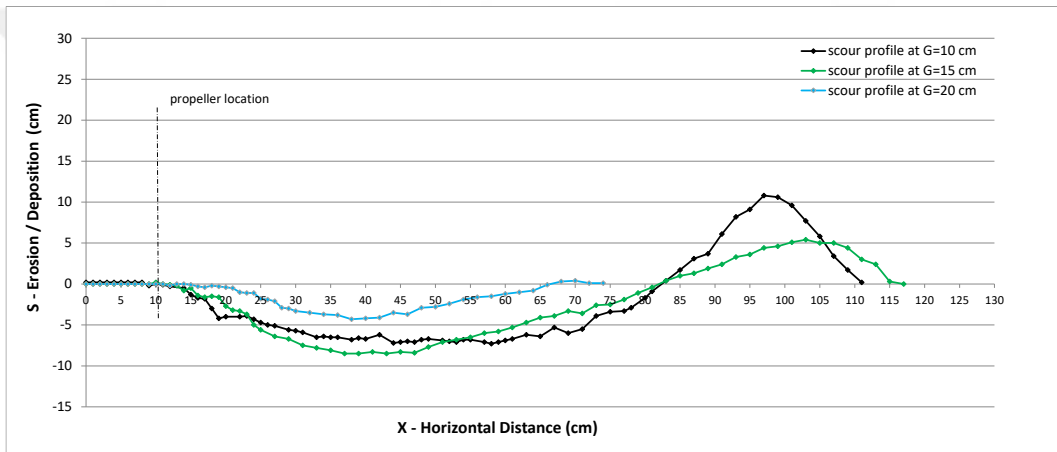


Figure A.67 Scour profiles with different gaps of propeller ($D_p=13$ cm, at 45 Hz on sediment bed $d_{50}=0.83$ cm)

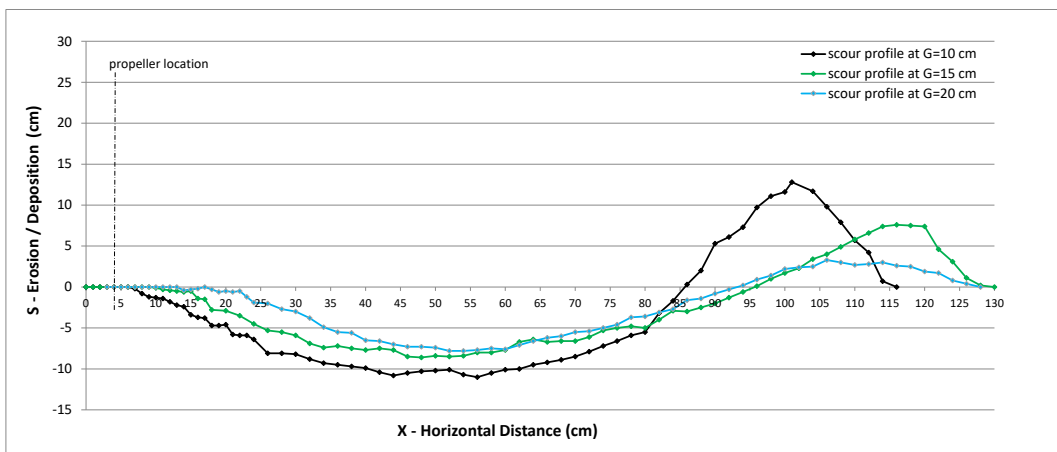


Figure A.68 Scour profiles with different gaps of propeller ($D_p=13$ cm, at 50 Hz on sediment bed $d_{50}=0.83$ cm)

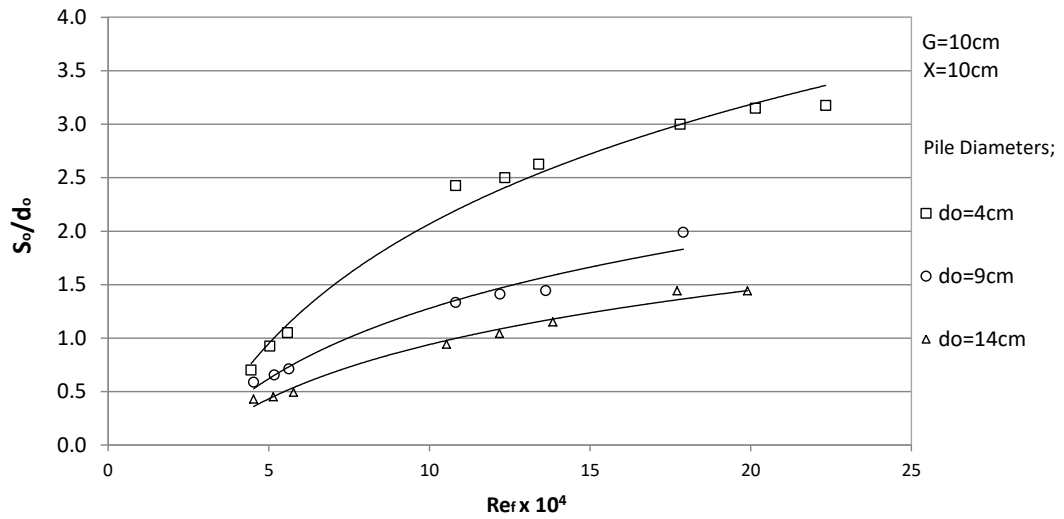


Figure A.69 Variation of S_o/d_o with Re_p on sediment bed of $d_{50}=1.28\text{ mm}$ ($D_p=6.5\text{ cm}$, 10 cm and 13 cm at propeller speed of 590 rpm, 670 rpm and 745 rpm)

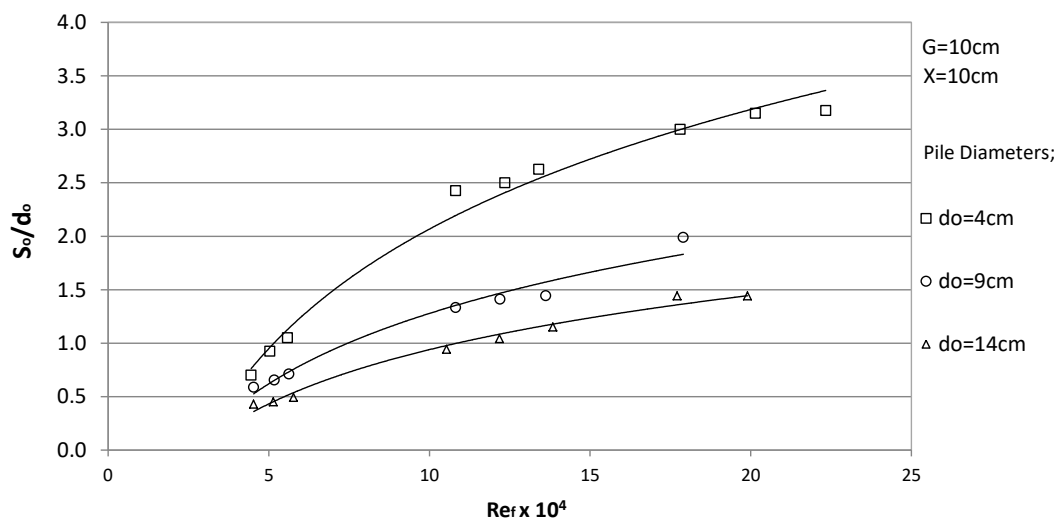


Figure A.70 Variation of S_o/d_o with Re_f on sediment bed of $d_{50}=1.28\text{ mm}$ ($D_p=6.5\text{ cm}$, 10 cm and 13 cm at propeller speed of 590 rpm, 670 rpm and 745 rpm)

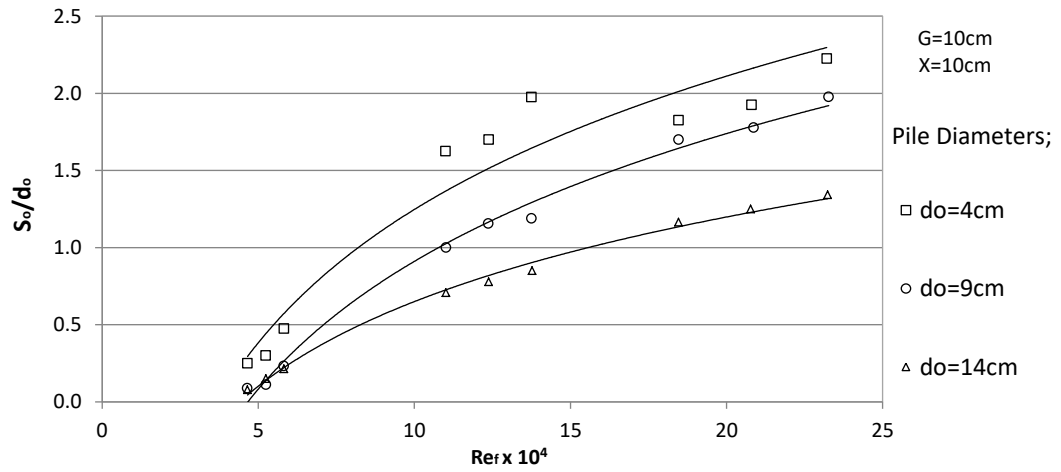


Figure A.71 Variation of S_o/d_o with Re_r on sediment bed of $d_{50}=4.0\text{ mm}$ ($D_p=6.5\text{ cm}$, 10 cm and 13 cm at propeller speed of 590 rpm, 670 rpm and 745 rpm)

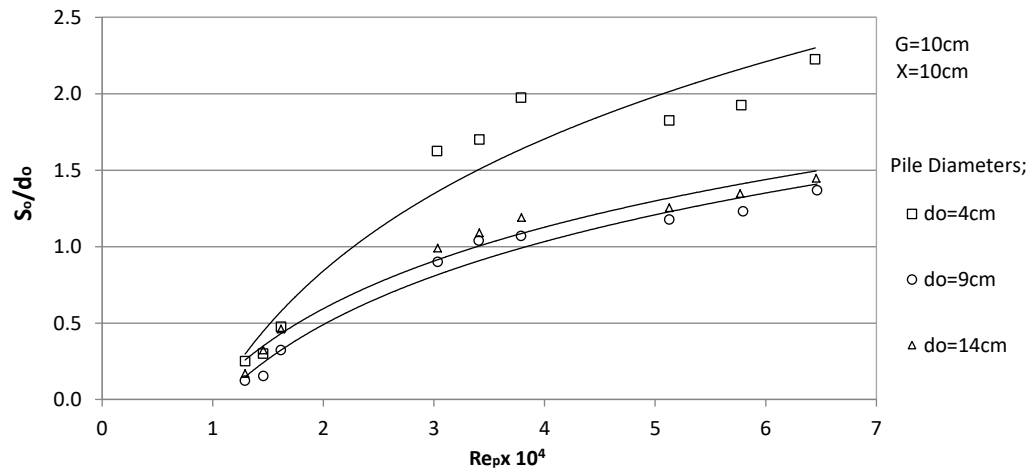


Figure A.72 Variation of S_o/d_o with Re_p on sediment bed of $d_{50}=4.0\text{ mm}$ ($D_p=6.5\text{ cm}$, 10 cm and 13 cm at propeller speed of 590 rpm, 670 rpm and 745 rpm)

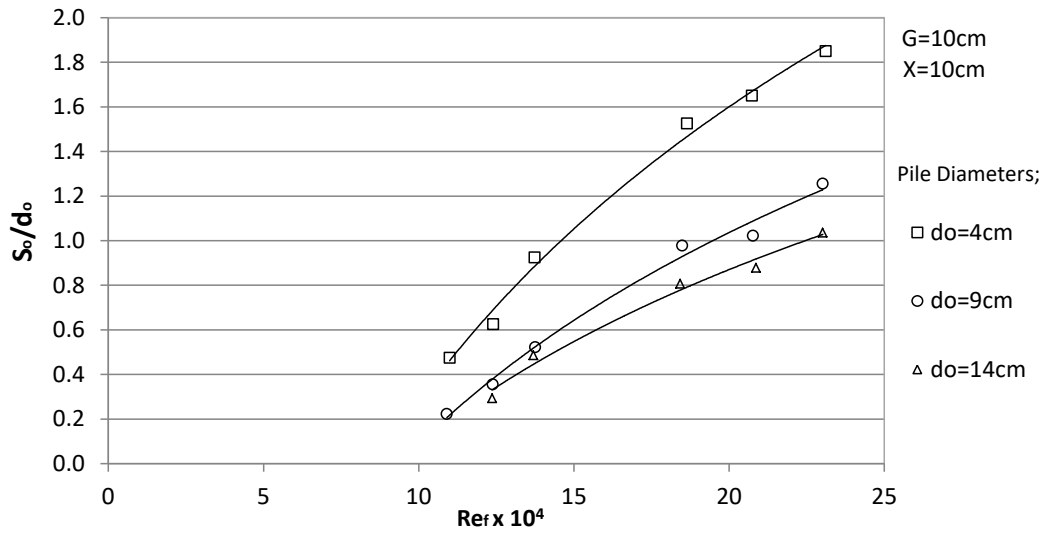


Figure A.73 Variation of S_o/d_o with Re_f on sediment bed of $d_{50}=8.3$ mm ($D_p=6.5$ cm, 10 cm and 13 cm at propeller speed of 590 rpm, 670 rpm and 745 rpm)

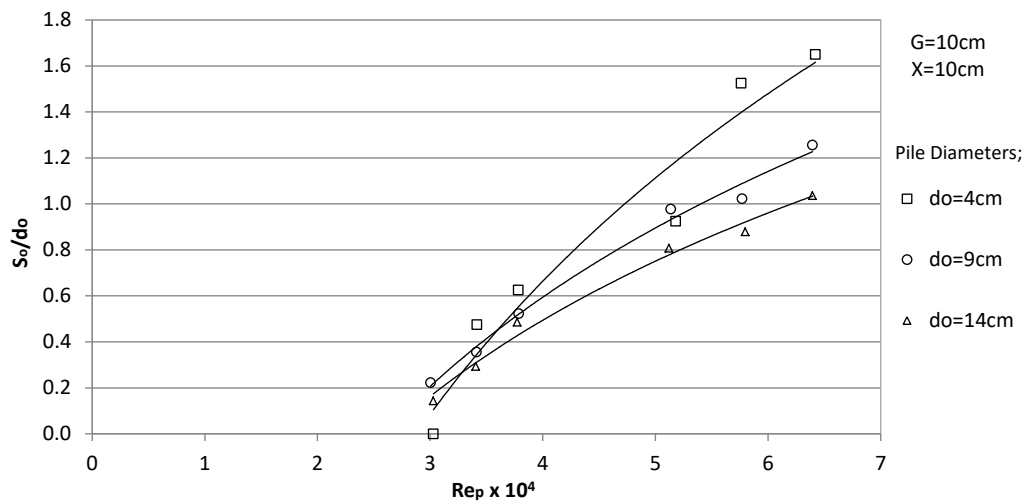


Figure A.74 Variation of S_o/d_o with Re_f on sediment bed of $d_{50}=8.3$ mm ($D_p=6.5$ cm, 10 cm and 13 cm at propeller speed of 590 rpm, 670 rpm and 745 rpm)

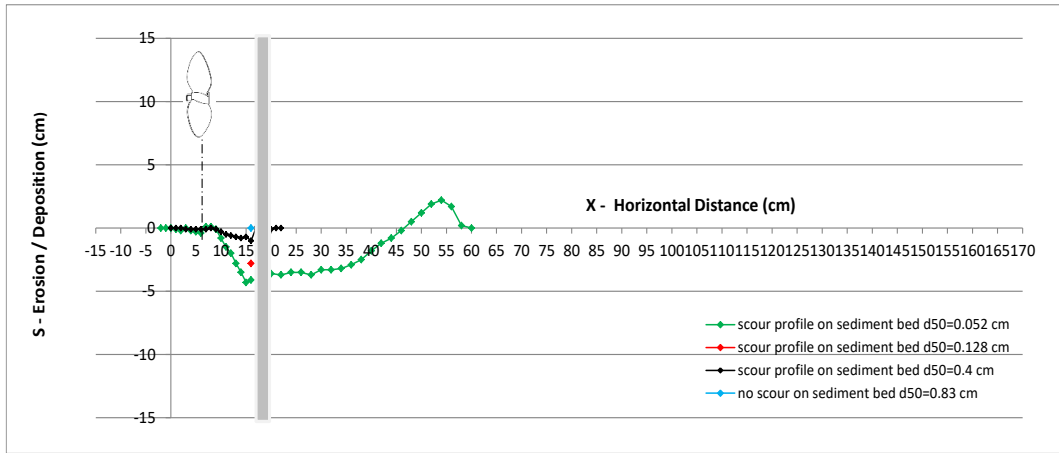


Figure A.75 Scour formations around 4 cm pile on different sediment beds with $D_p=6.5$ cm, 40 Hz, $G=10$ cm

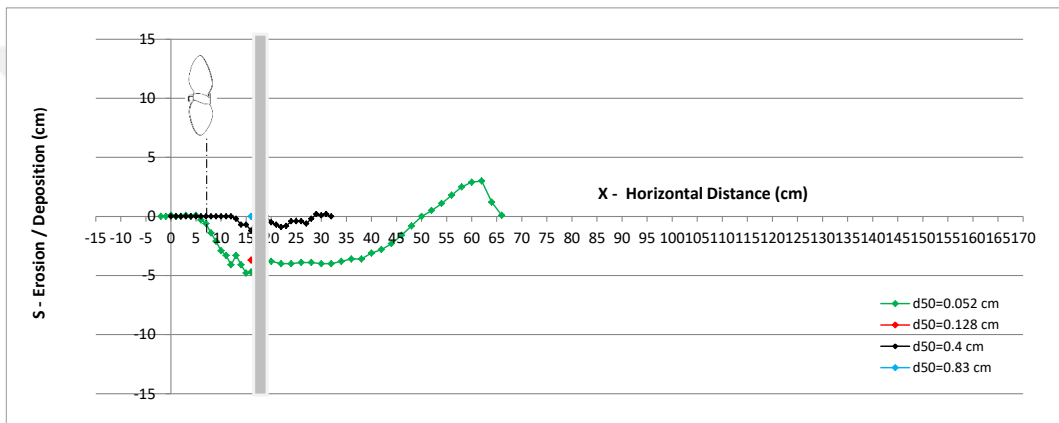


Figure A.76 Scour formations around 4 cm pile on different sediment beds with $D_p=6.5$ cm, 45 Hz, $G=10$ cm

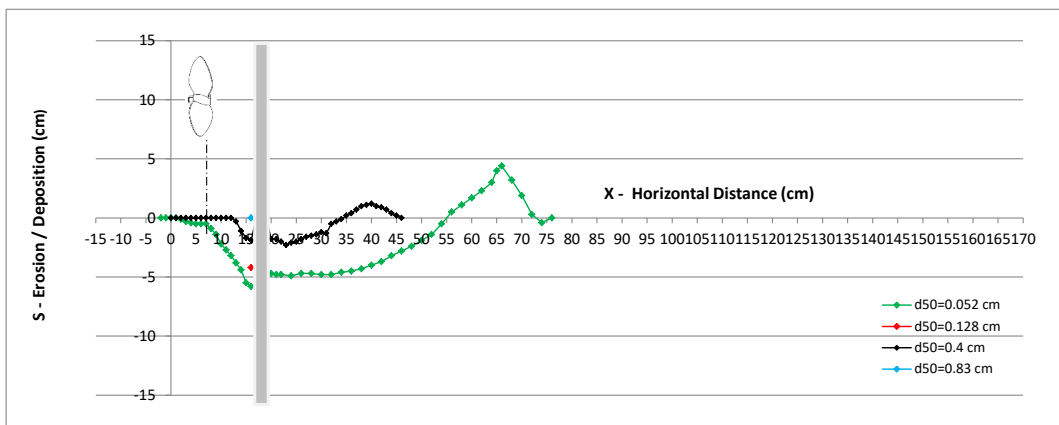


Figure A.77 Scour formations around 4 cm pile on different sediment beds with $D_p=6.5$ cm, 50 Hz, $G=10$ cm

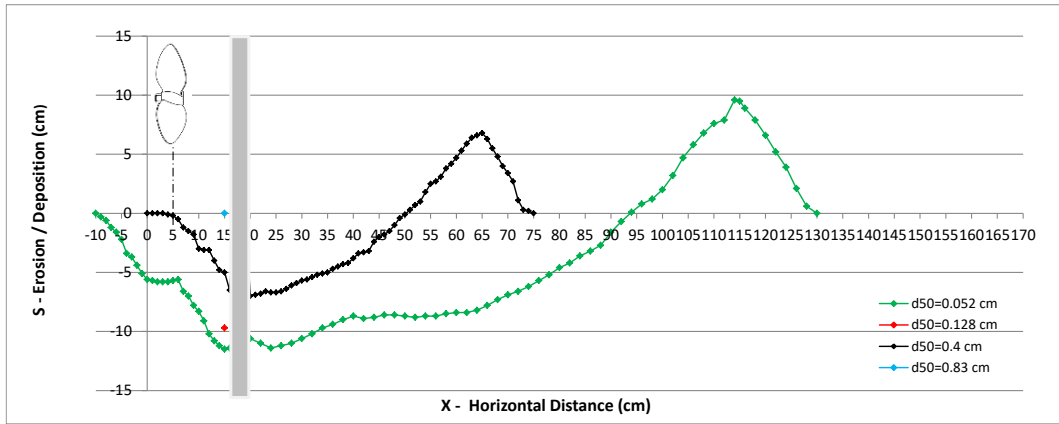


Figure A.78 Scour formations around 4 cm pile on different sediment beds with $D_p=10$ cm, 40 Hz, $G=10$ cm

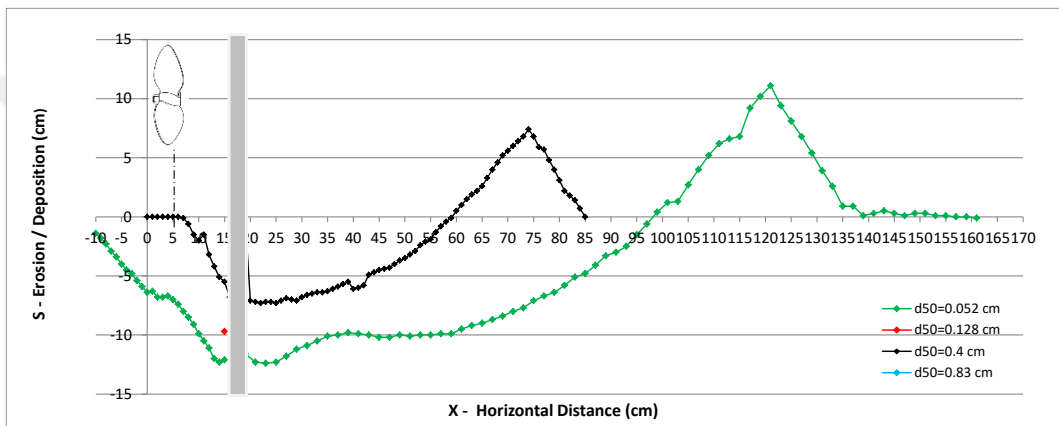


Figure A.79 Scour formations around 4 cm pile on different sediment beds with $D_p=10$ cm and 45 Hz, $G=10$ cm

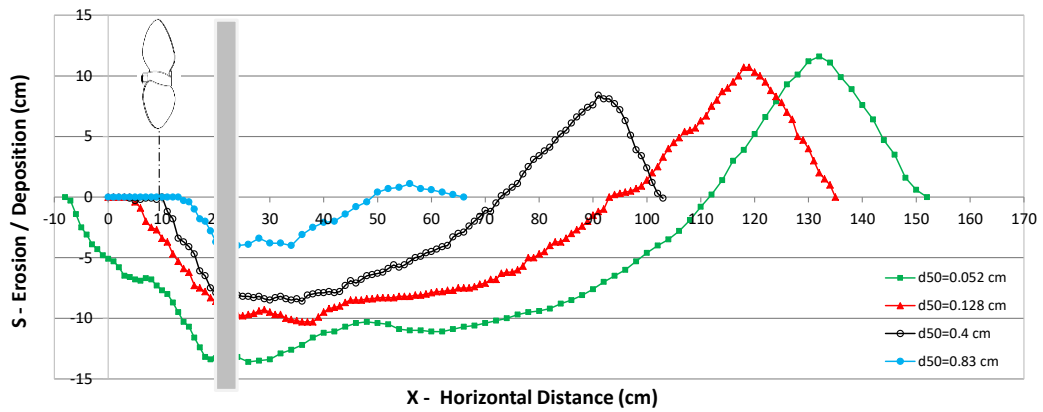


Figure A.80 Scour formations around 4 cm pile on different sediment beds with $D_p=10$ cm, 50 Hz, $G=10$ cm

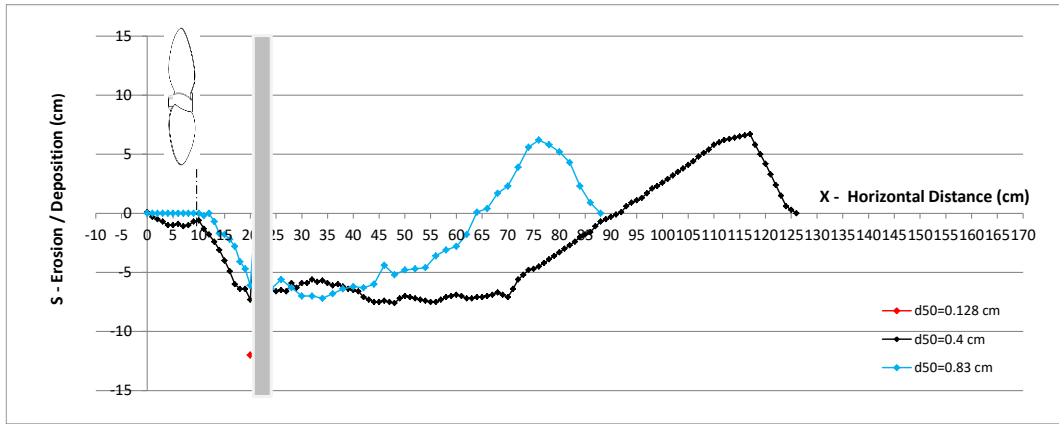


Figure A.81 Scour formations around 4 cm pile on different sediment beds with $D_p=13$ cm, 40 Hz, $G=10$ cm

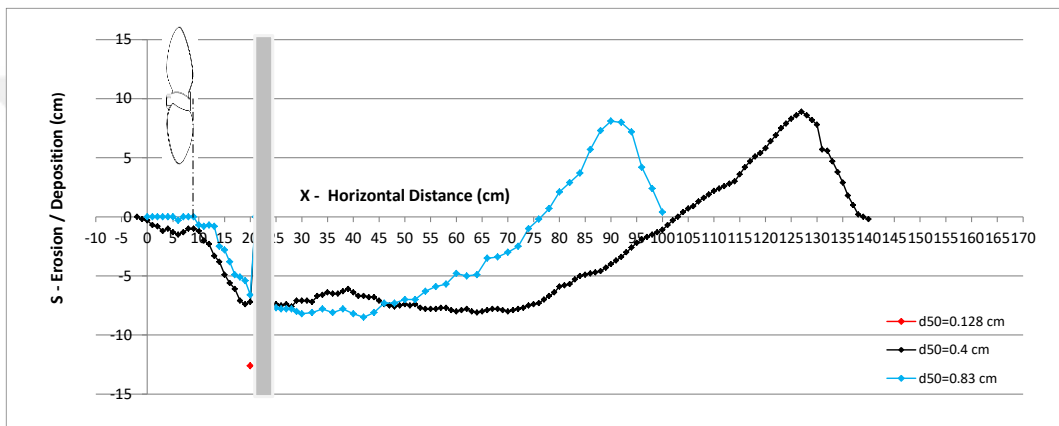


Figure A.82 Scour formations around 4 cm pile on different sediment beds with $D_p=13$ cm, 45 Hz, $G=10$ cm

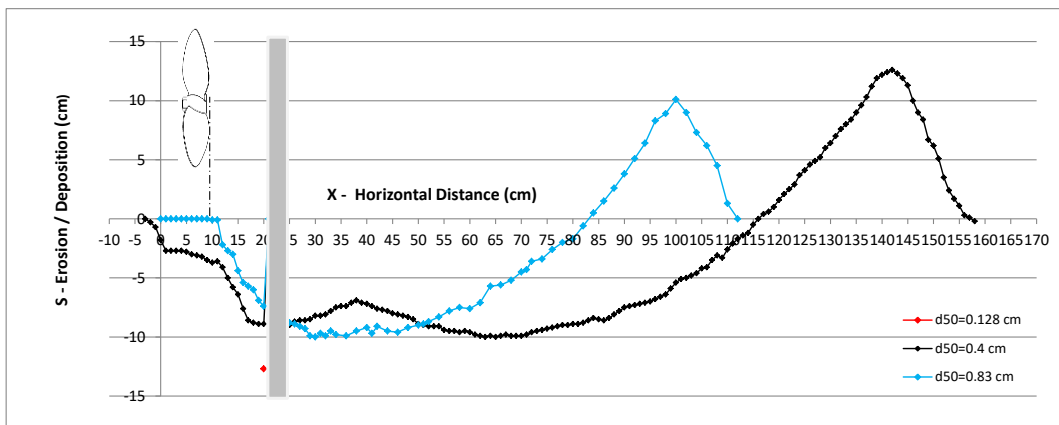


Figure A.83 Scour formations around 4 cm pile on different sediment beds with $D_p=13$ cm, 50 Hz, $G=10$ cm

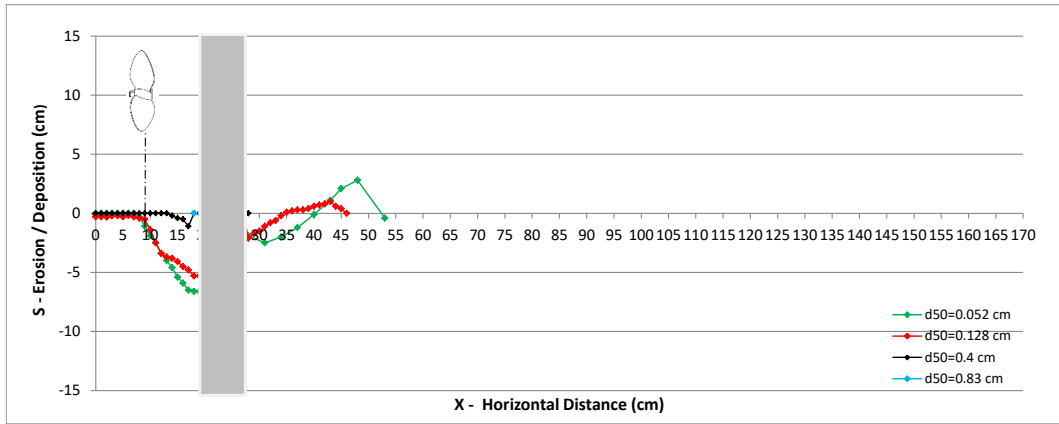


Figure A.84 Scour formations around 9 cm pile on different sediment beds with $D_p=6.5$ cm, 40 Hz, $G=10$ cm

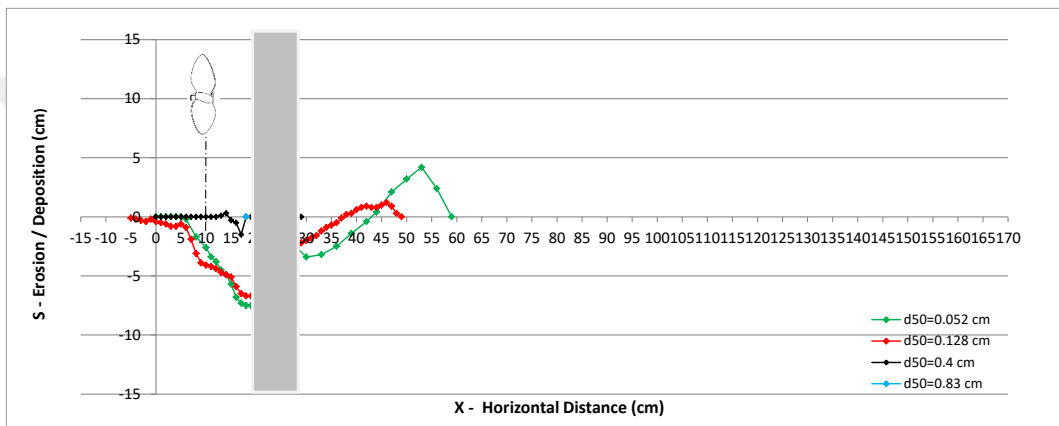


Figure A.85 Scour formations around 9 cm pile on different sediment beds with $D_p=6.5$ cm, 45 Hz, $G=10$ cm

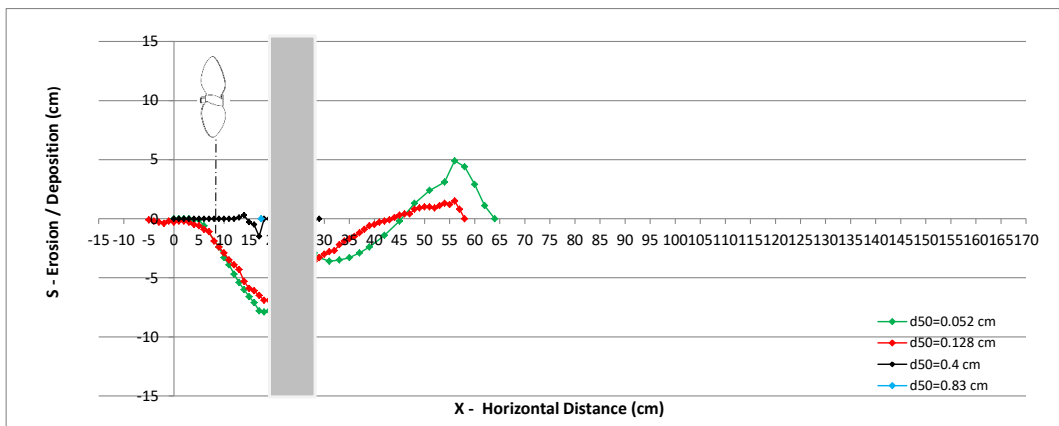


Figure A.86 Scour formations around 9 cm pile on different sediment beds with $D_p=6.5$ cm, 50 Hz, $G=10$ cm

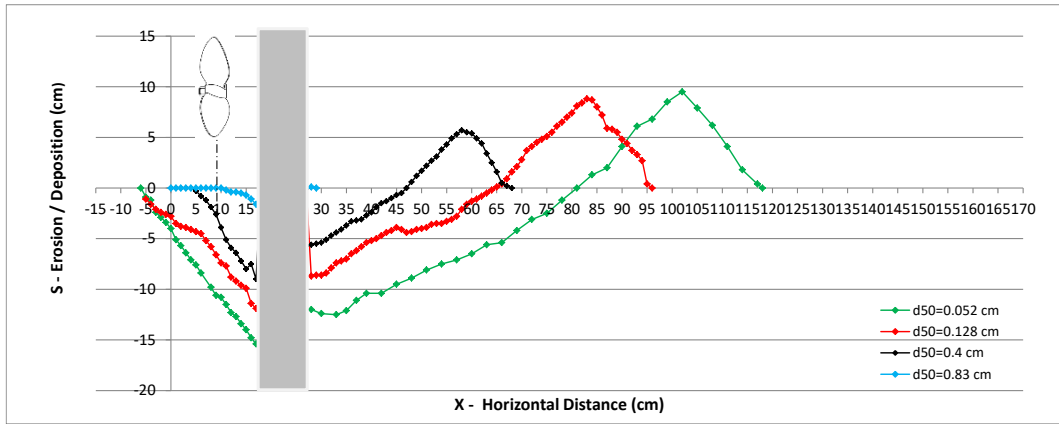


Figure A.87 Scour formations around 9 cm pile on different sediment beds with $D_p=10$ cm, 40 Hz, $G=10$ cm

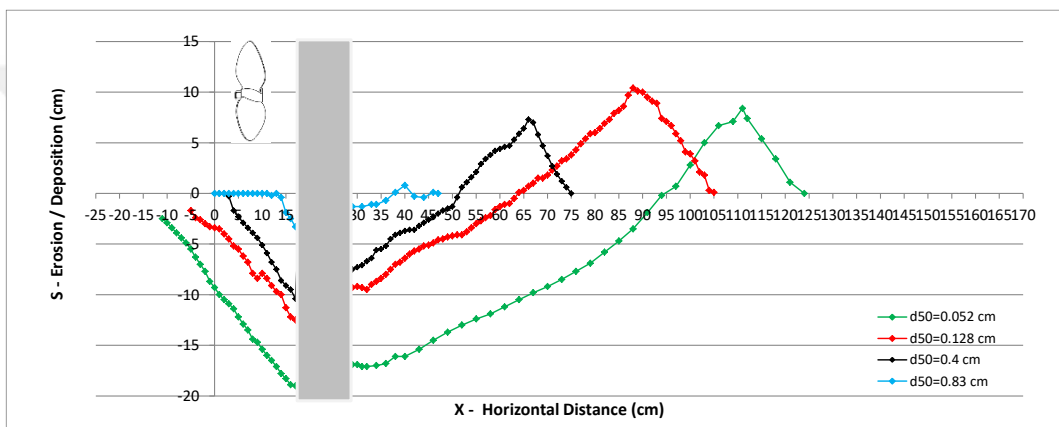


Figure A.88 Scour formations around 9 cm pile on different sediment beds with $D_p=10$ cm, 45 Hz, $G=10$ cm

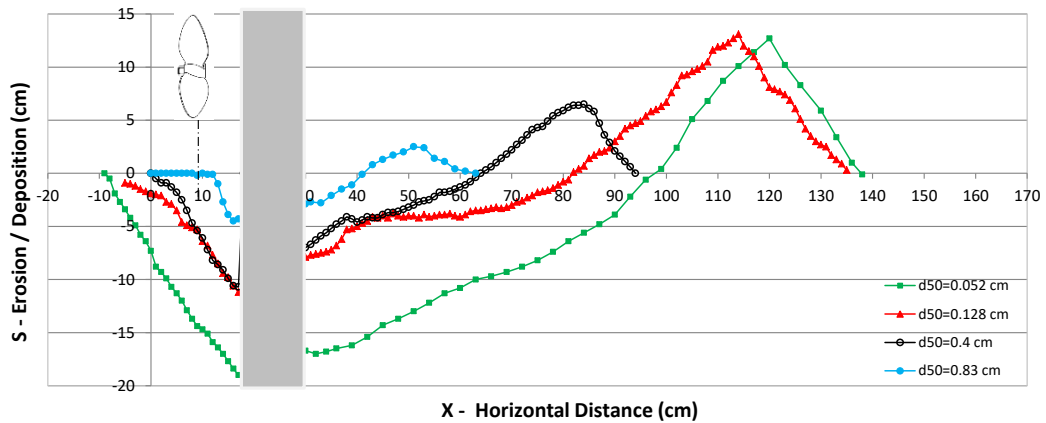


Figure A.89 Scour formations around 9 cm pile on different sediment beds with $D_p=10$ cm, 50 Hz, $G=10$ cm

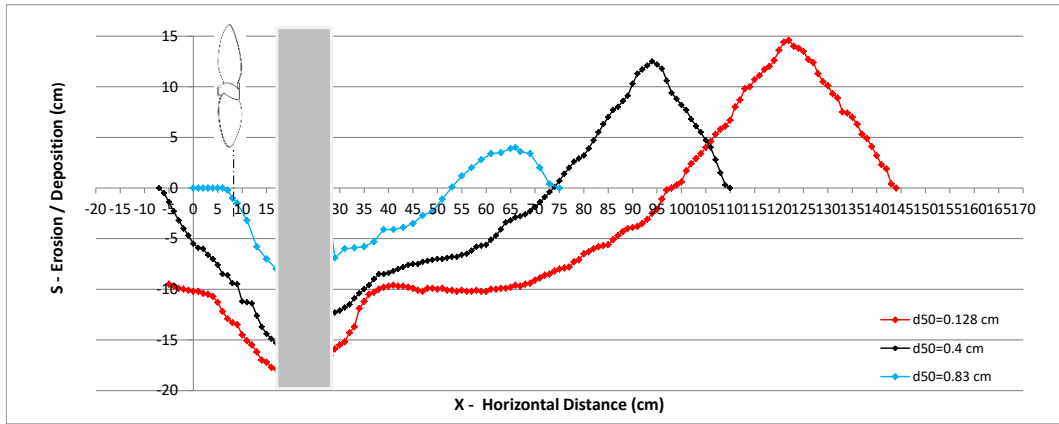


Figure A.90 Scour formations around 9 cm pile on different sediment beds with $D_p=13$ cm, 40 Hz, $G=10$ cm

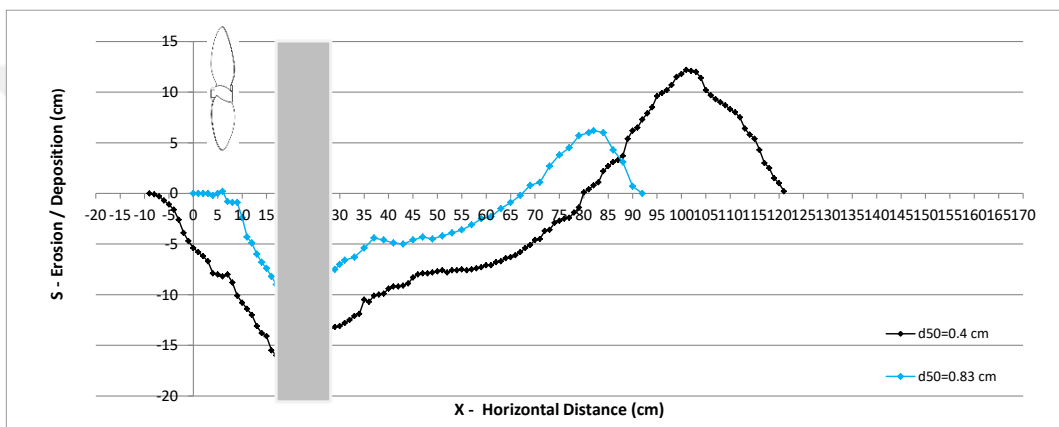


Figure A.91 Scour formations around 9 cm pile on different sediment beds with $D_p=13$ cm, 45 Hz, $G=10$ cm

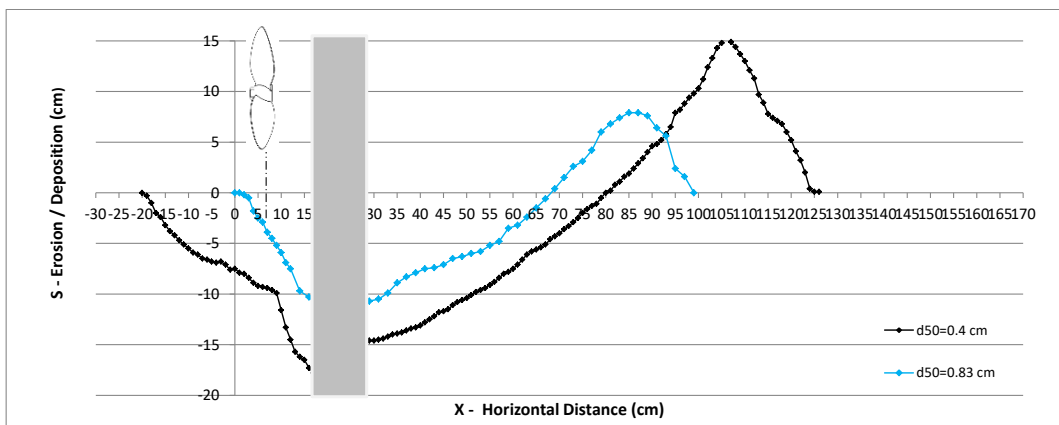


Figure A.92 Scour formations around 9 cm pile on different sediment beds with $D_p=13$ cm, 50 Hz, $G=10$ cm

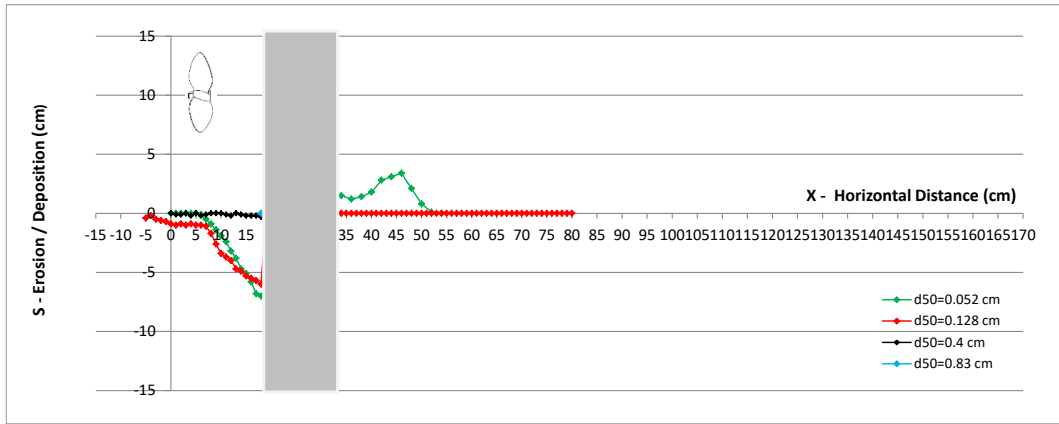


Figure A.93 Scour formations around 14 cm pile on different sediment beds with $D_p=6.5$ cm, 40 Hz, $G=10$ cm

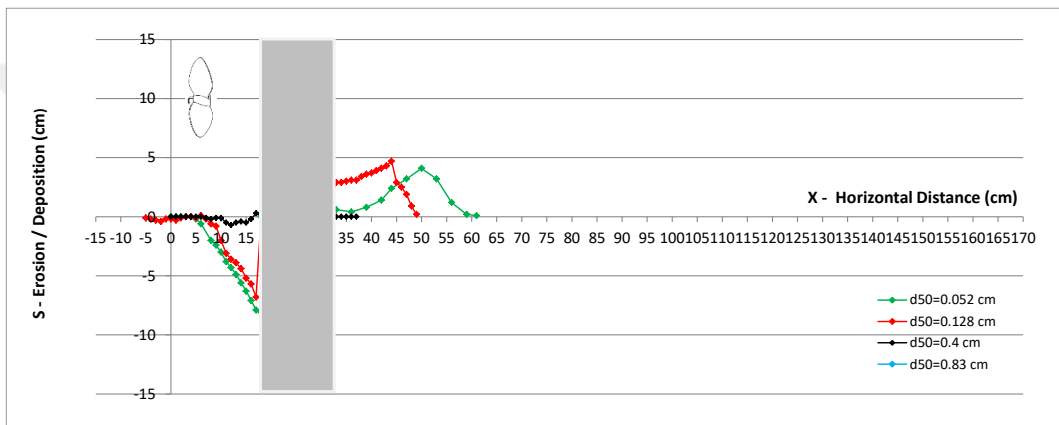


Figure A.94 Scour formations around 14 cm pile on different sediment beds with $D_p=6.5$ cm, 45 Hz, $G=10$ cm

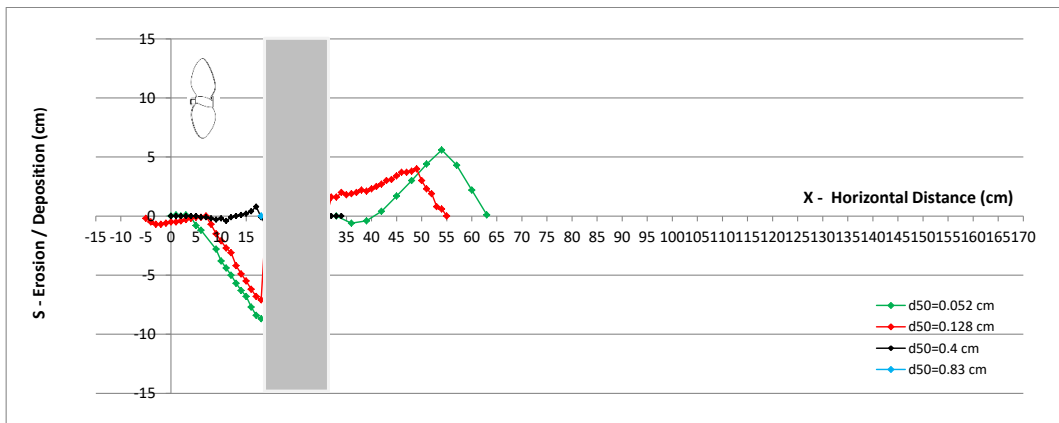


Figure A.95 Scour formations around 14 cm pile on different sediment beds with $D_p=6.5$ cm 50 Hz, $G=10$ cm

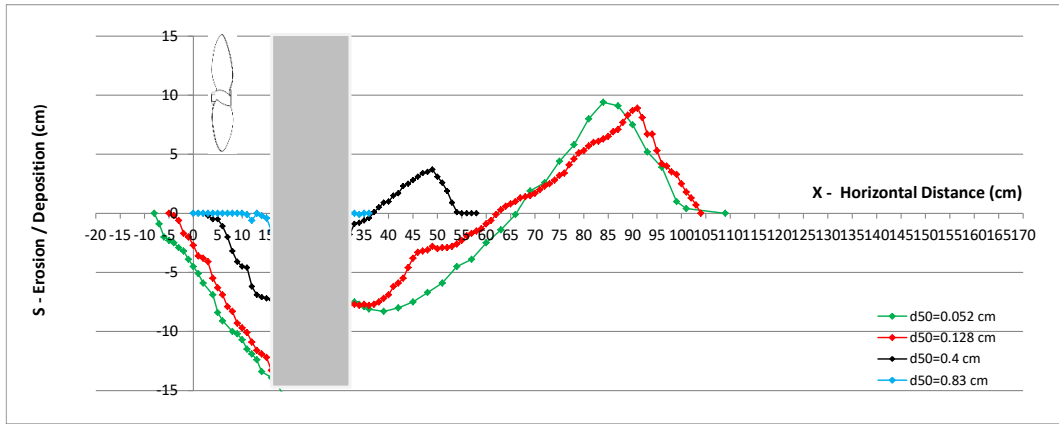


Figure A.96 Scour formations around 14 cm pile on different sediment beds with $D_p=10$ cm, 40 Hz, $G=10$ cm

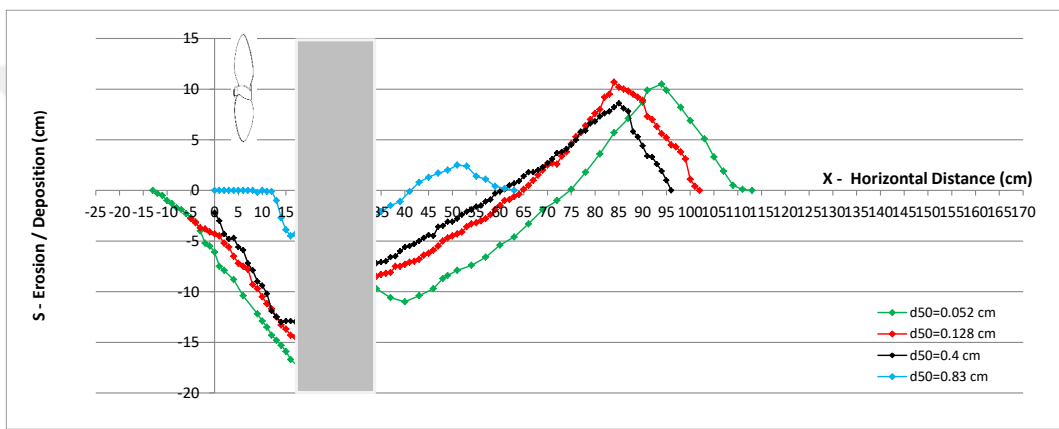


Figure A.97 Scour formations around 14 cm pile on different sediment beds with $D_p=10$ cm, 45 Hz, $G=10$ cm

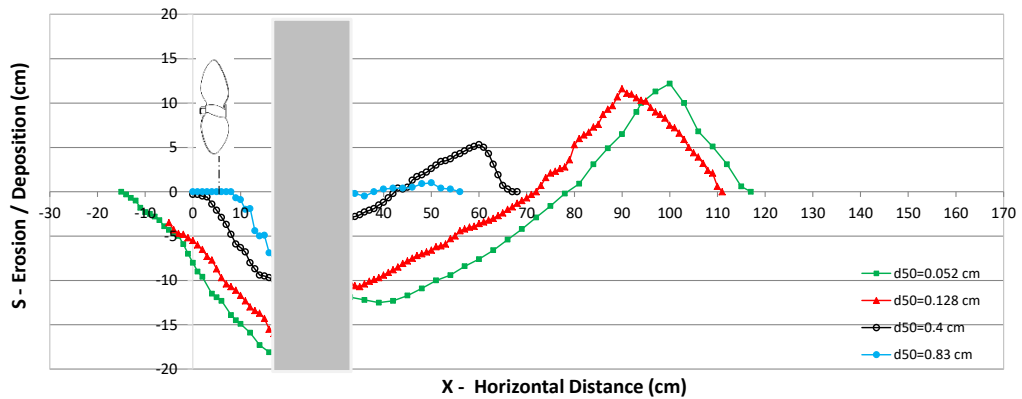


Figure A.98 Scour formations around 14 cm pile on different sediment beds with $D_p=10$ cm, 50 Hz, $G=10$ cm

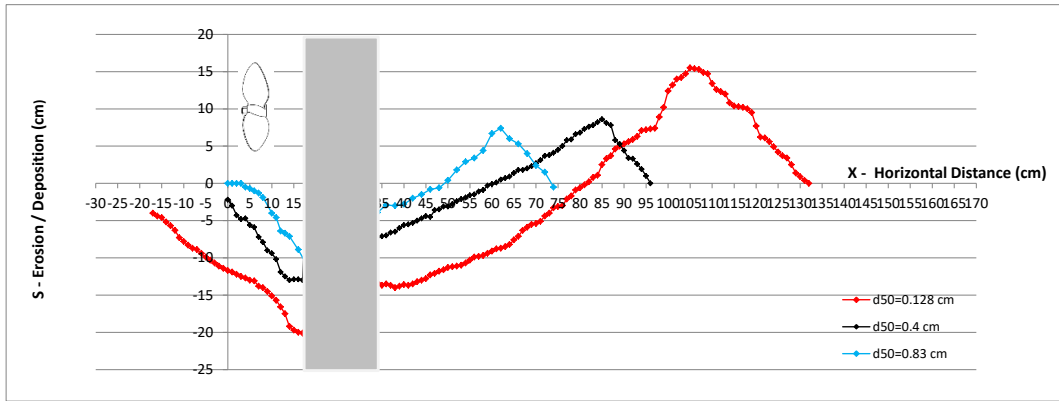


Figure A.99 Scour formations around 14 cm pile on different sediment beds with $D_p=13$ cm, 40 Hz, $G=10$ cm

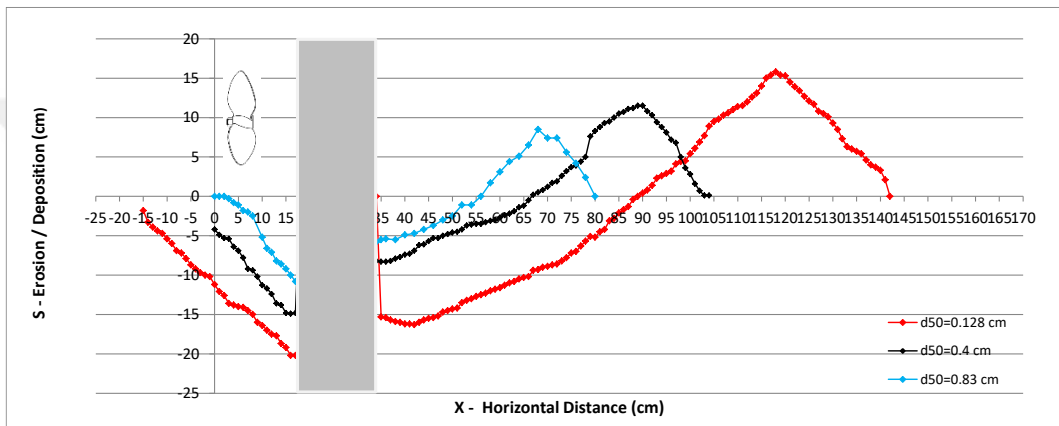


Figure A.100 Scour formations around 14 cm pile on different sediment beds with $D_p=13$ cm, 45 Hz, $G=10$ cm

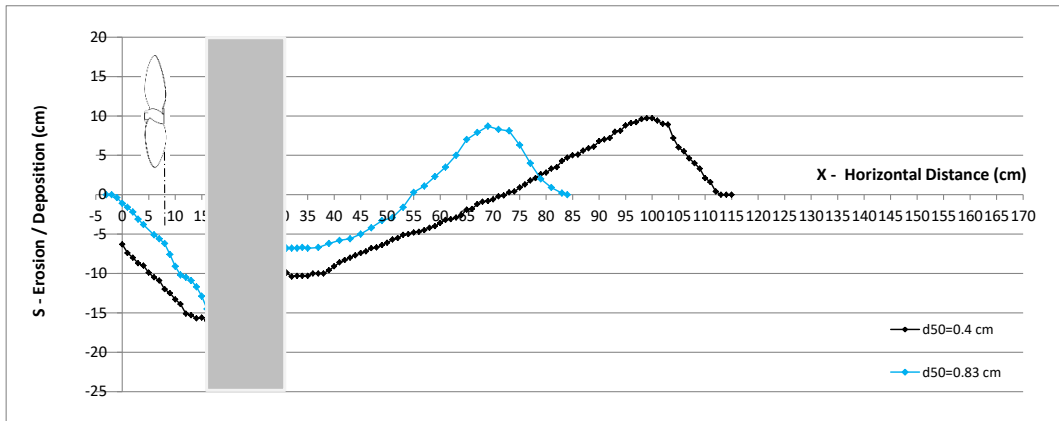


Figure A.101 Scour formations around 14 cm pile on different sediment beds with $D_p=13$ cm, 50 Hz, $G=10$ cm

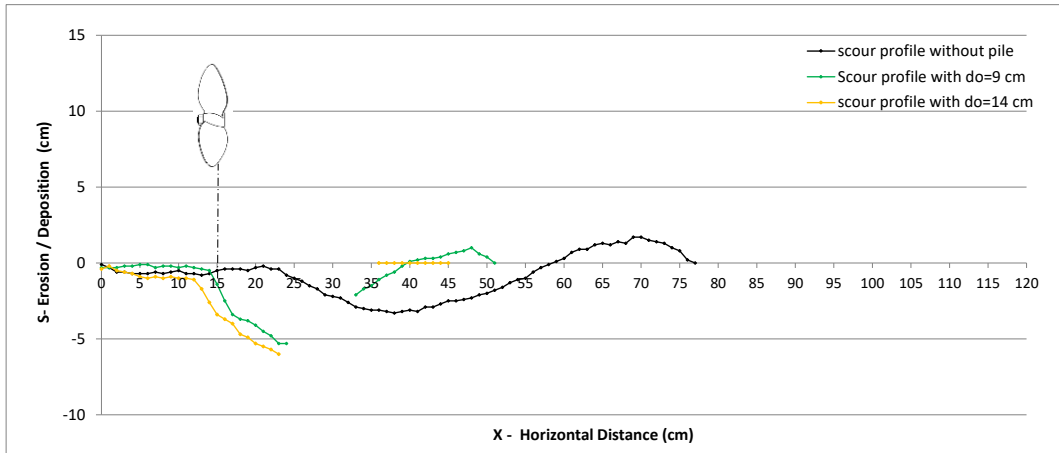


Figure A.102 Scour profiles with pile and without pile conditions ($D_p=6.5$ cm, $G=10$ cm, at 40 Hertz on $d_{50}=0.128$ cm sediment bed)

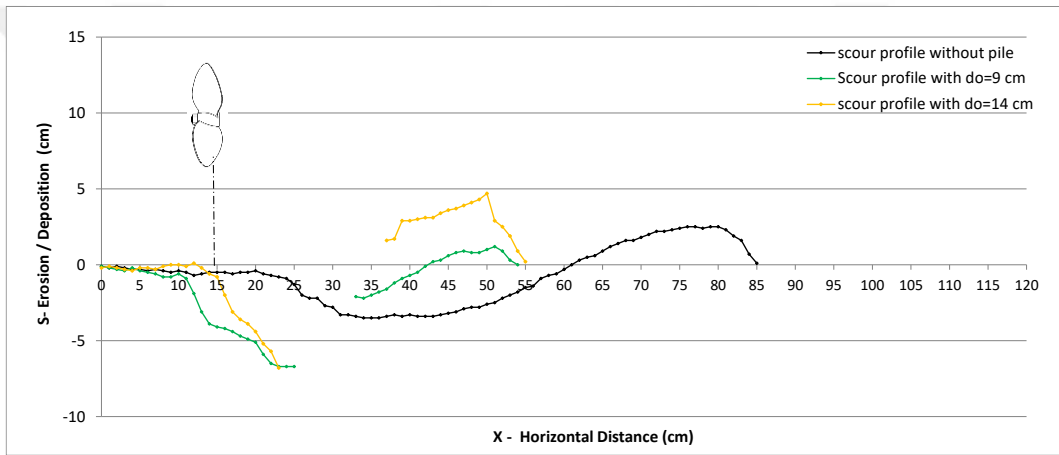


Figure A.103 Scour profiles with pile and without pile conditions ($D_p=6.5$ cm, $G=10$ cm, at 45 Hertz on $d_{50}=0.128$ cm sediment bed)

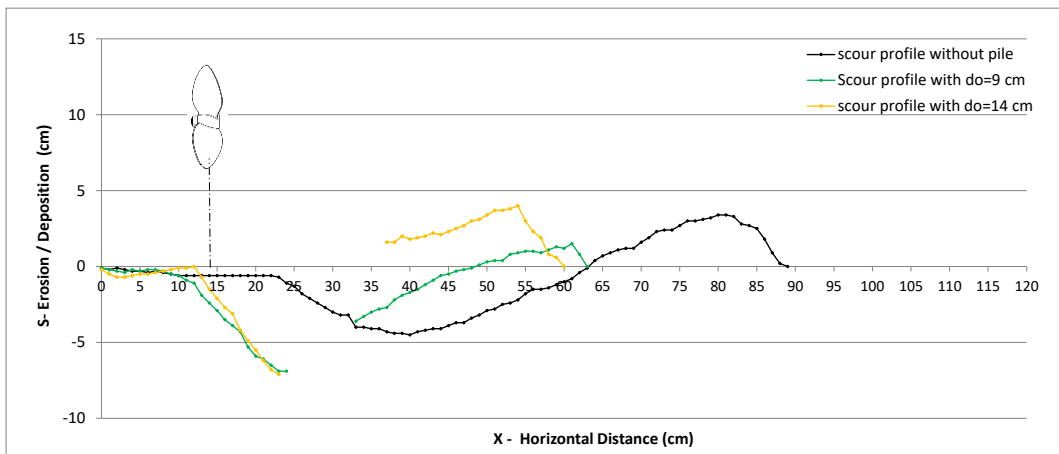


Figure A.104 Scour profiles with pile and without pile conditions ($D_p=6.5$ cm, $G=10$ cm, at 50 Hertz on $d_{50}=0.128$ cm sediment bed)

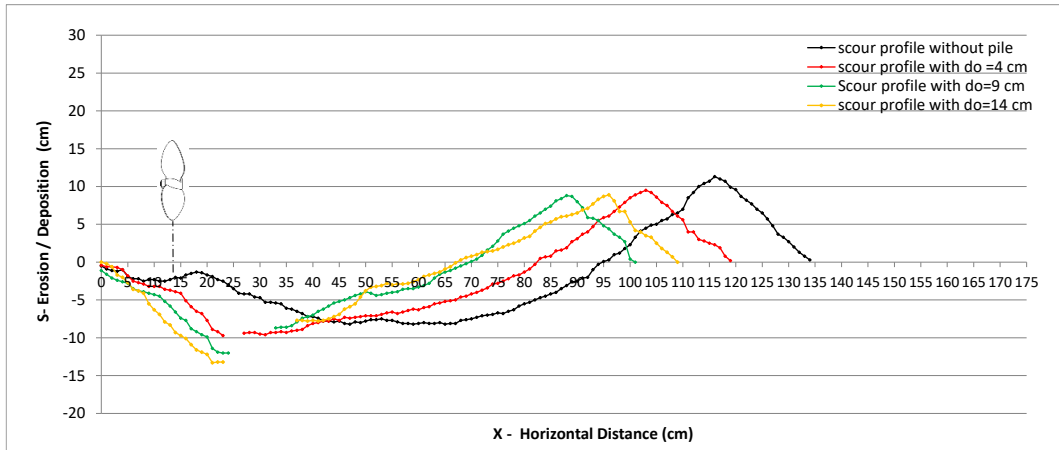


Figure A.105 Scour profiles with pile and without pile conditions ($D_p=10$ cm, $G=10$ cm, at 40 Hertz on $d_{50}=0.128$ cm sediment bed)

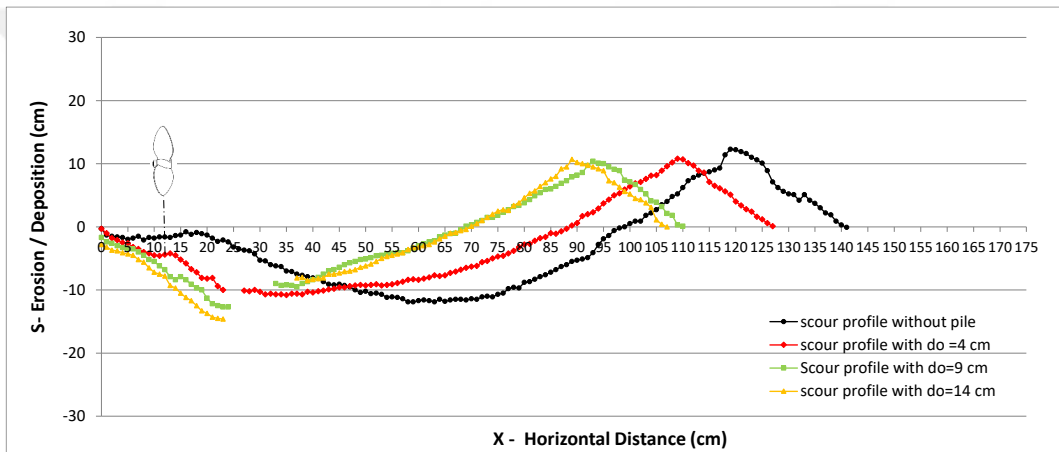


Figure A.106 Scour profiles with pile and without pile conditions ($D_p=10$ cm, $G=10$ cm, at 45 Hertz on $d_{50}=0.128$ cm sediment bed)

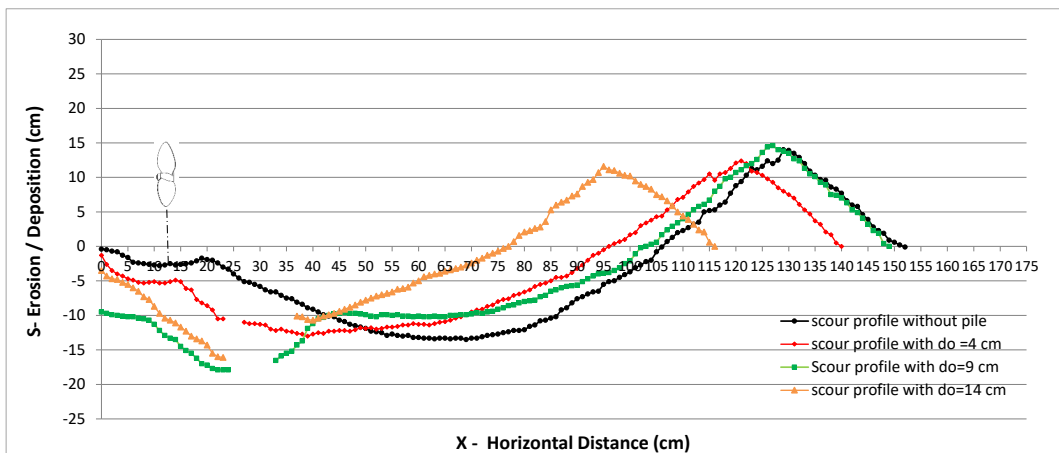


Figure A.107 Scour profiles with pile and without pile conditions ($D_p=10$ cm, $G=10$ cm, at 50 Hertz on $d_{50}=0.128$ cm sediment bed)

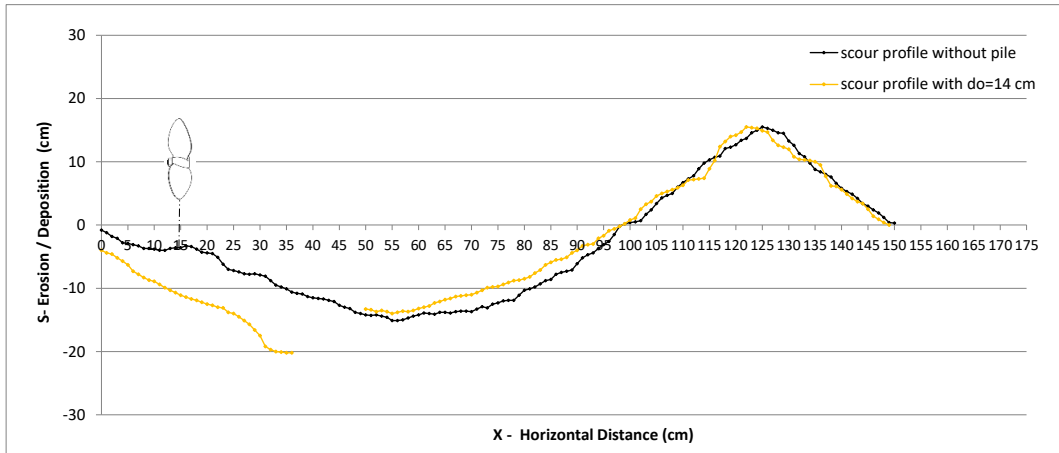


Figure A.108 Scour profiles with pile and without pile conditions ($D_p=13$ cm, $G=10$ cm, at 40 Hertz on $d_{50}=0.128$ cm sediment bed)

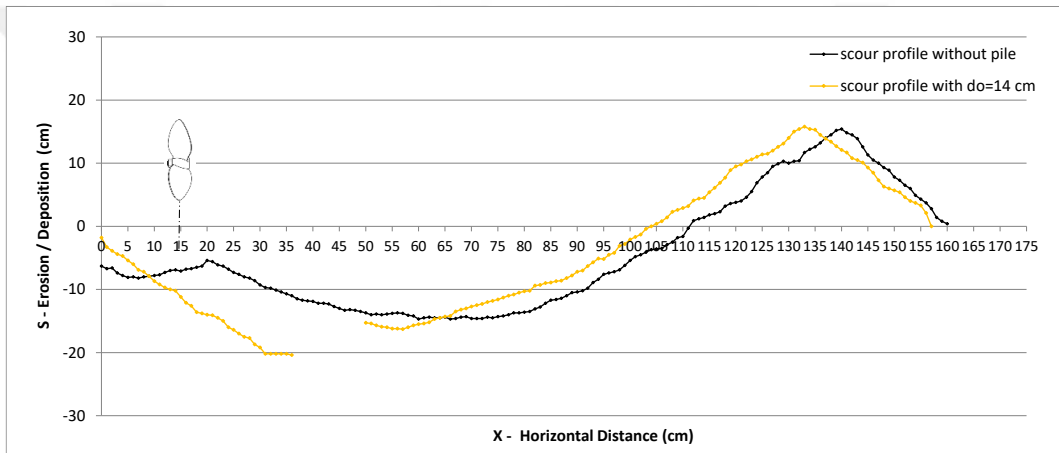


Figure A.109 Scour profiles with pile and without pile conditions ($D_p=13$ cm, $G=10$ cm, at 45 Hertz on $d_{50}=0.128$ cm sediment bed)

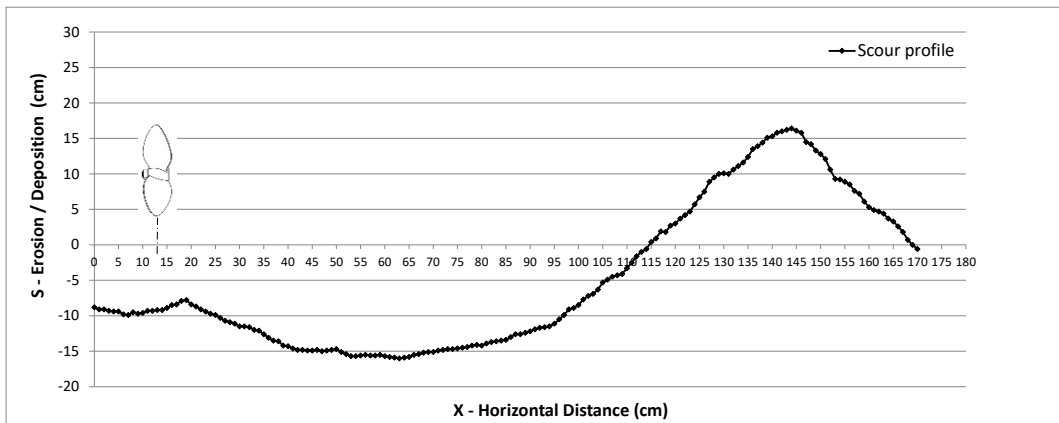


Figure A.110 Scour profiles with pile and without pile conditions ($D_p=13$ cm, $G=10$ cm, at 50 Hertz on $d_{50}=0.128$ cm sediment bed)

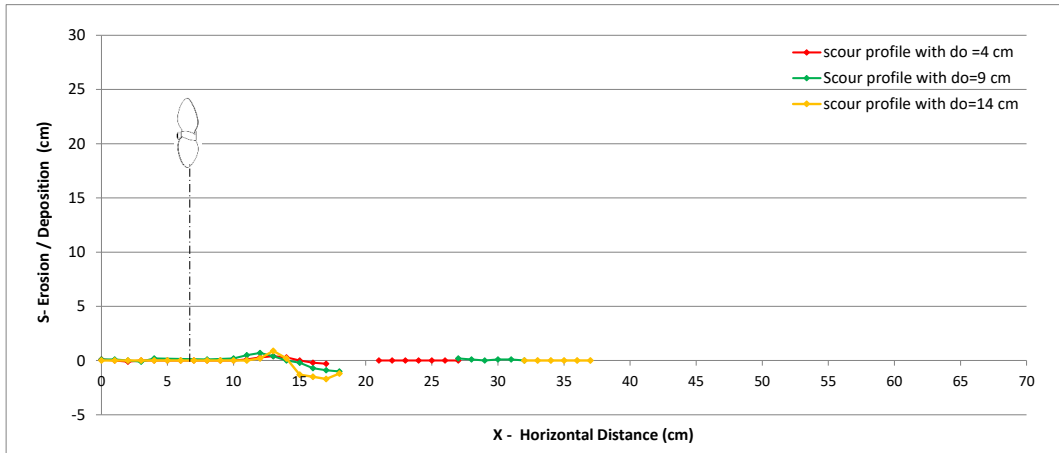


Figure A.111 Scour profiles with pile and without pile conditions ($D_p=6.5$ cm, $G=20$ cm, at 40 Hertz on $d_{50}=0.128$ cm sediment bed)

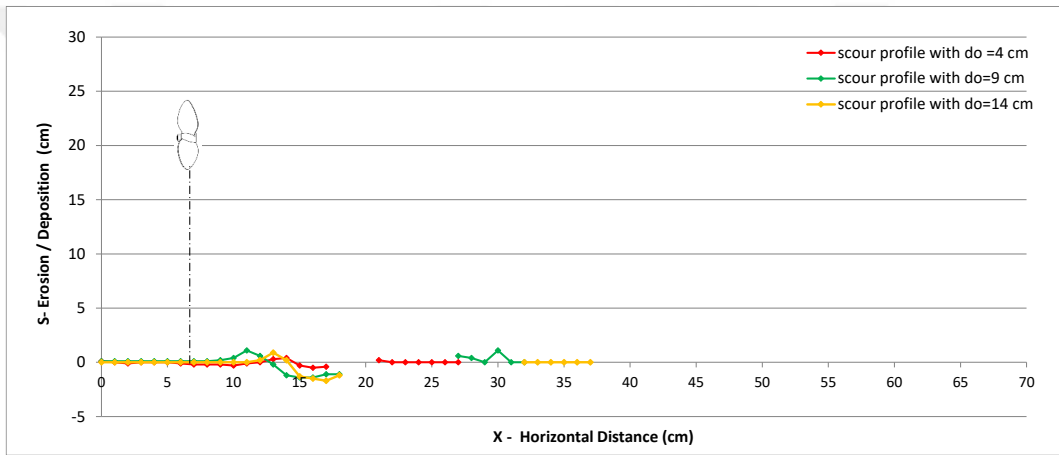


Figure A.112 Scour profiles formation with pile and without pile conditions ($D_p=6.5$ cm, $G=20$ cm, at 45 Hertz on $d_{50}=0.128$ cm sediment bed)

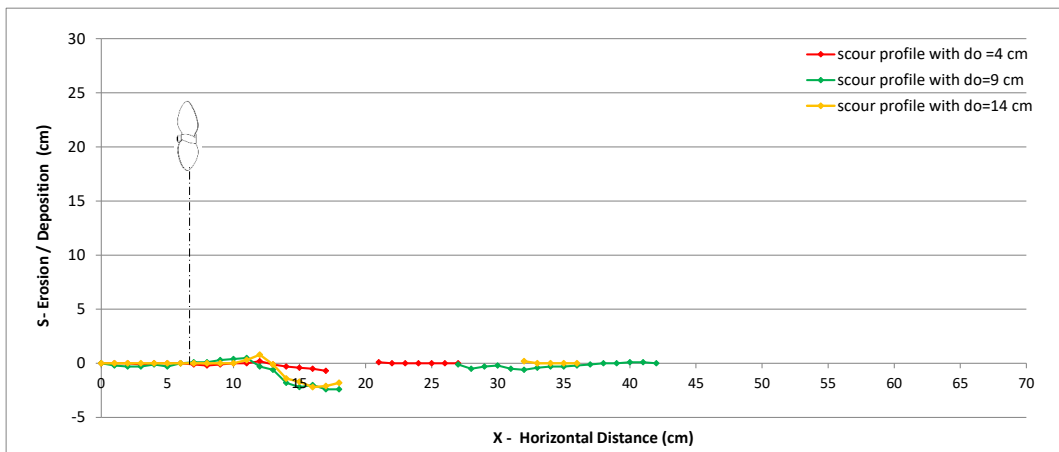


Figure A.133 Scour profiles with pile and without pile ($D_p=6.5$ cm, $G=20$ cm, at 50 Hertz on $d_{50}=0.128$ cm sediment bed)

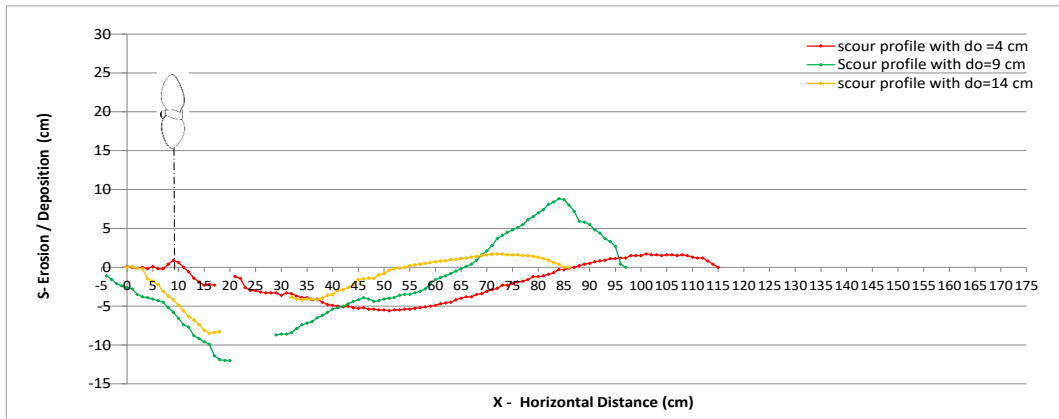


Figure A.114 Scour profiles with pile and without pile conditions ($D_p=10$ cm, $G=20$ cm, at 40 Hertz on $d_{50}=0.128$ cm sediment bed)

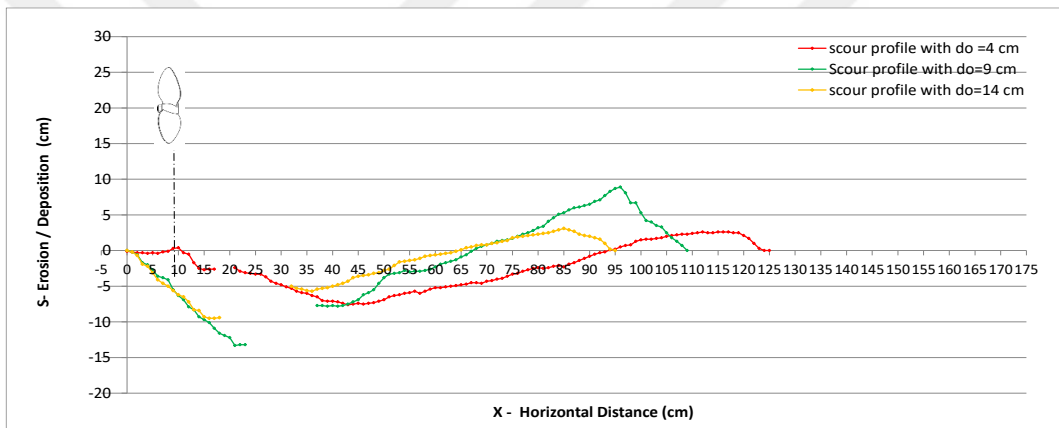


Figure A.115 Scour profiles with pile and without pile conditions ($D_p=10$ cm, $G=20$ cm, at 45 Hertz on $d_{50}=0.128$ cm sediment bed)

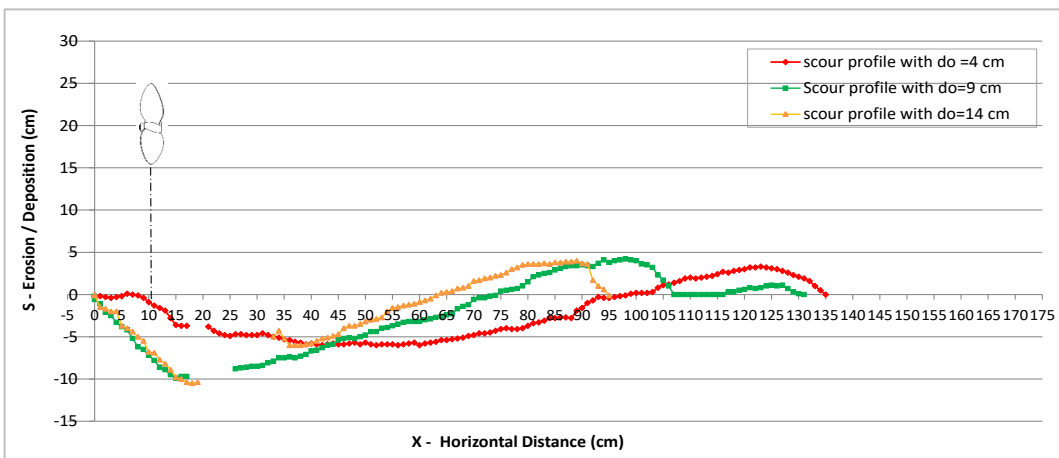


Figure A.116 Scour profiles with pile and without pile conditions ($D_p=10$ cm, $G=20$ cm, at 50 Hertz on $d_{50}=0.128$ cm sediment bed)

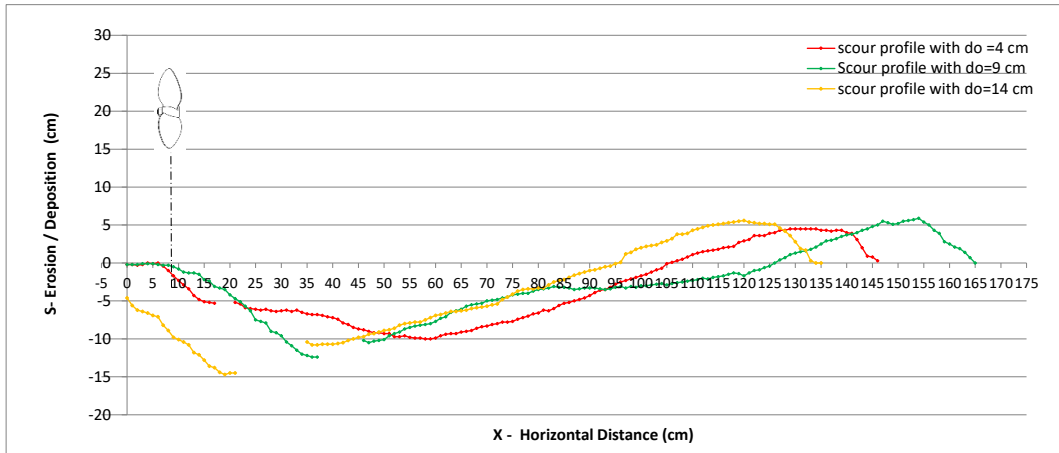


Figure A.117 Scour profiles with pile and without pile conditions ($D_p=13$ cm, $G=20$ cm, at 40 Hertz on $d_{50}=0.128$ cm sediment bed)

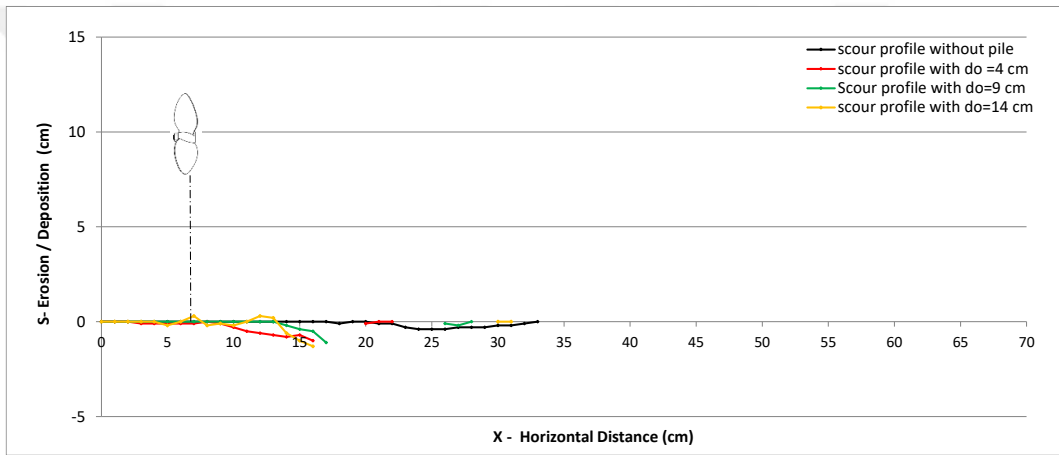


Figure A.118 Scour profiles with pile and without pile conditions ($D_p=6.5$ cm, $G=10$ cm, at 40 Hertz on $d_{50}=0.4$ cm sediment bed)

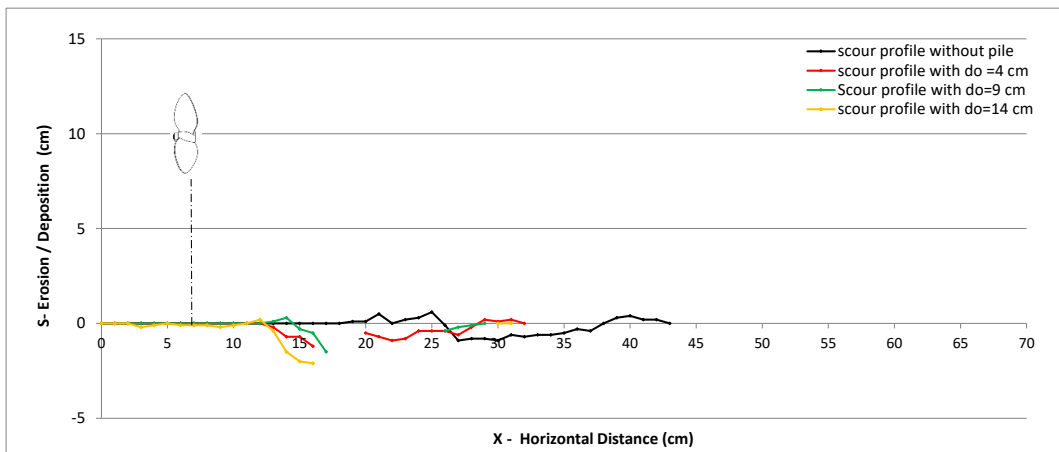


Figure A.119 Scour profiles with pile and without pile conditions ($D_p=6.5$ cm, $G=10$ cm, at 45 Hertz on $d_{50}=0.4$ cm sediment bed)

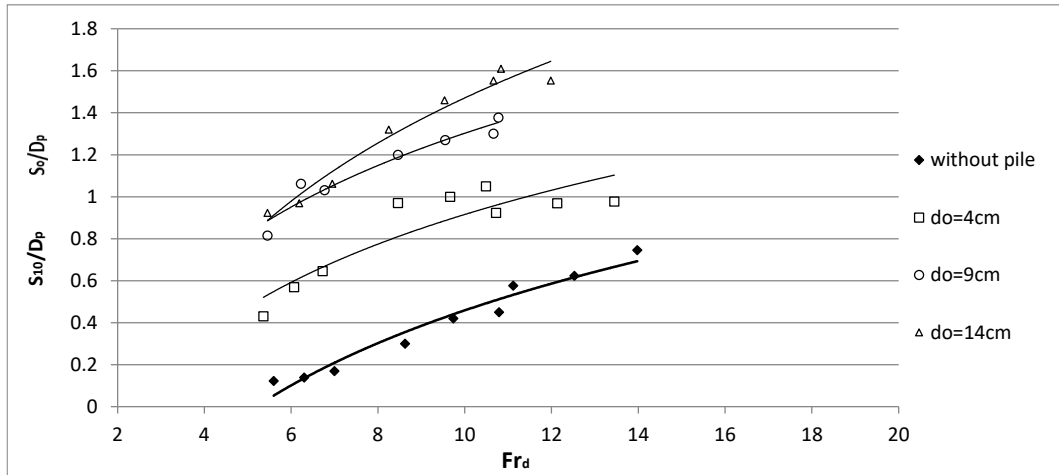


Figure A.120 Variation of S_o/D_p with Fr_d with a pile on sediment bed of $d_{50}=1.28$ mm ($G=10$ cm)

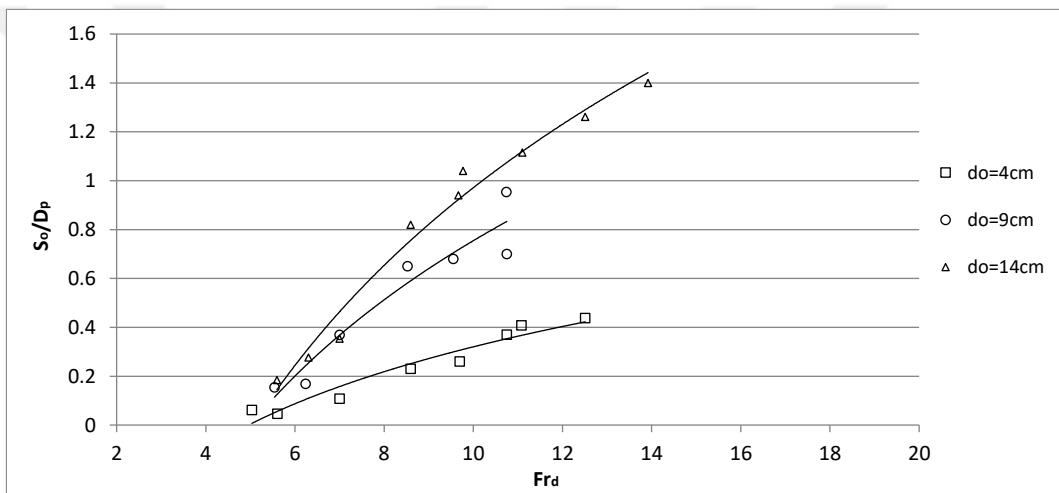


Figure A.121 Variation of S_o/D_p with Fr_d with a pile on sediment bed of $d_{50}=1.28$ mm ($G=20$ cm)

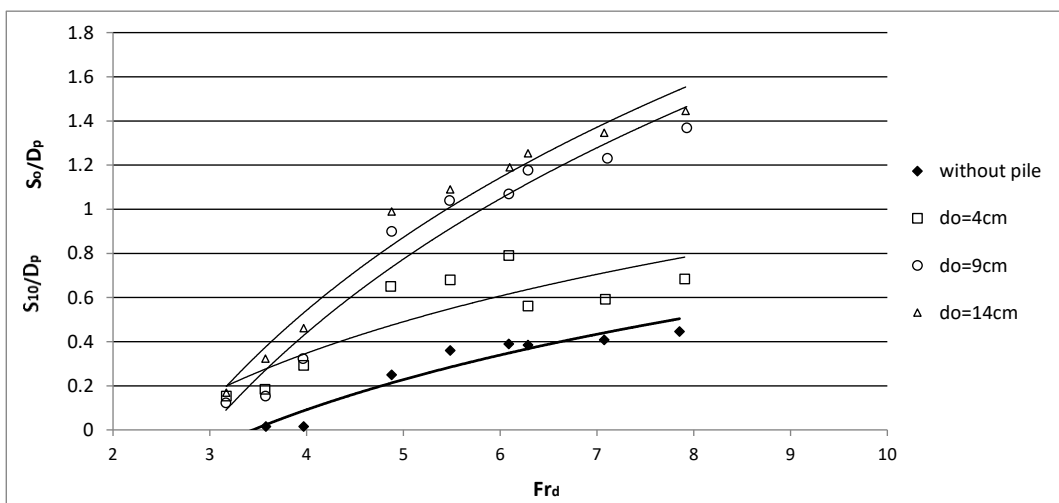


Figure A.122 Variation of S_o/D_p with Fr_d with a pile on sediment bed of $d_{50}=4$ mm ($G=10$ cm)

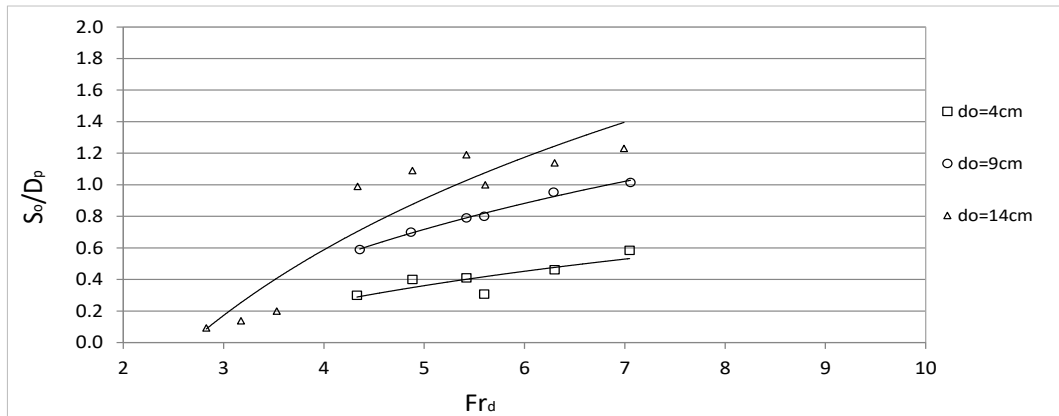


Figure A.123 Variation of S_o/D_p with Fr_d with a pile on sediment bed of $d_{50}=4$ mm ($G=15$ cm)

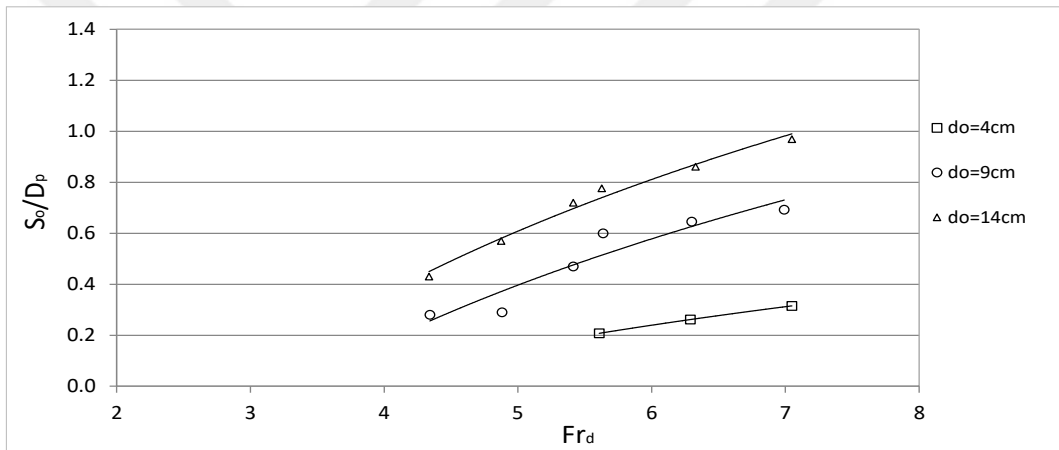


Figure A.124 Variation of S_o/D_p with Fr_d with a pile on sediment bed of $d_{50}=4$ mm ($G=20$ cm)

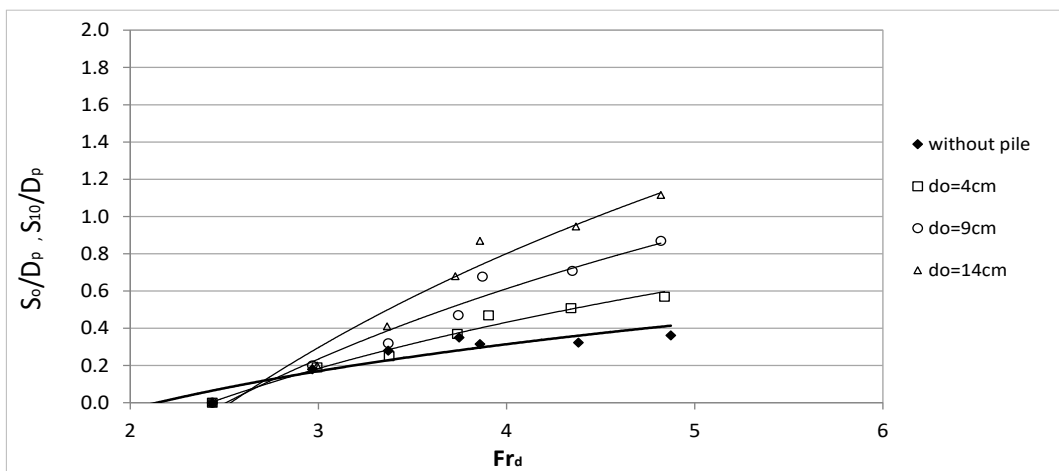


Figure A.125 Variation of S_o/D_p with Fr_d with a pile on sediment bed of $d_{50}=8.3$ mm ($G=10$ cm)

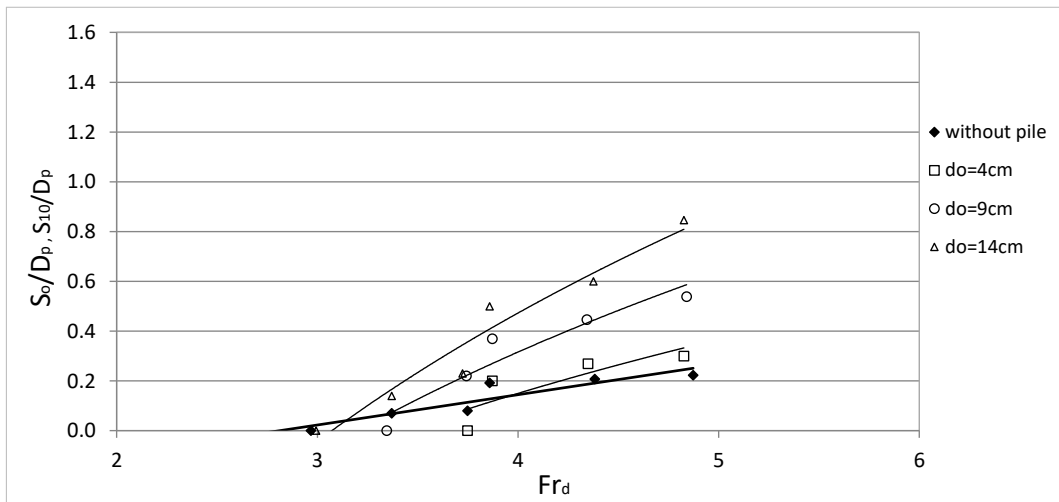


Figure A.126 Variation of S_o/D_p with Fr_d with a pile on sediment bed of $d_{50}=8.3$ mm ($G=15$ cm)

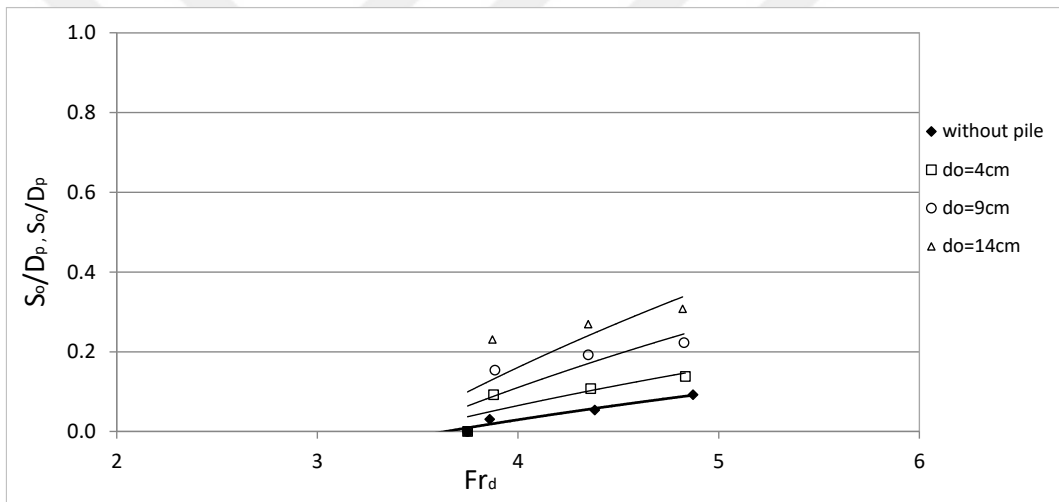


Figure A.127 Variation of S_o/D_p with Fr_d with a pile on sediment bed of $d_{50}=8.3$ mm ($G=20$ cm)

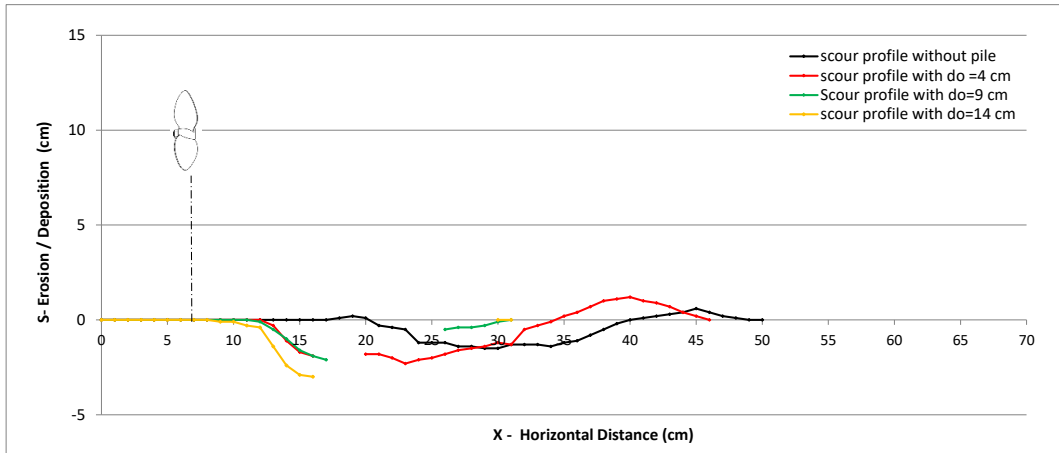


Figure A.128 Scour profiles with pile and without pile conditions ($D_p=6.5$ cm, $G=10$ cm, at 50 Hertz on $d_{50}=0.4$ cm sediment bed)

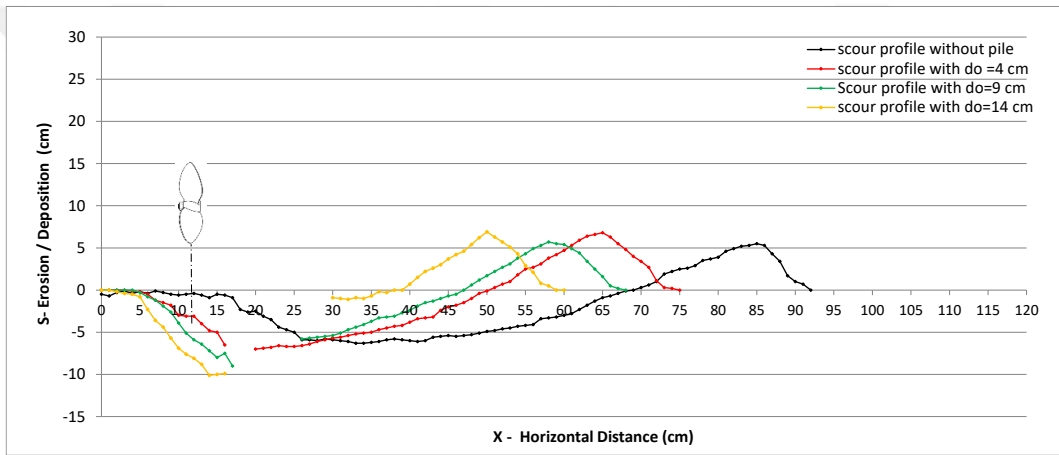


Figure A.129 Scour profiles with pile and without pile conditions ($D_p=10$ cm, $G=10$ cm, at 40 Hertz on $d_{50}=0.4$ cm sediment bed)

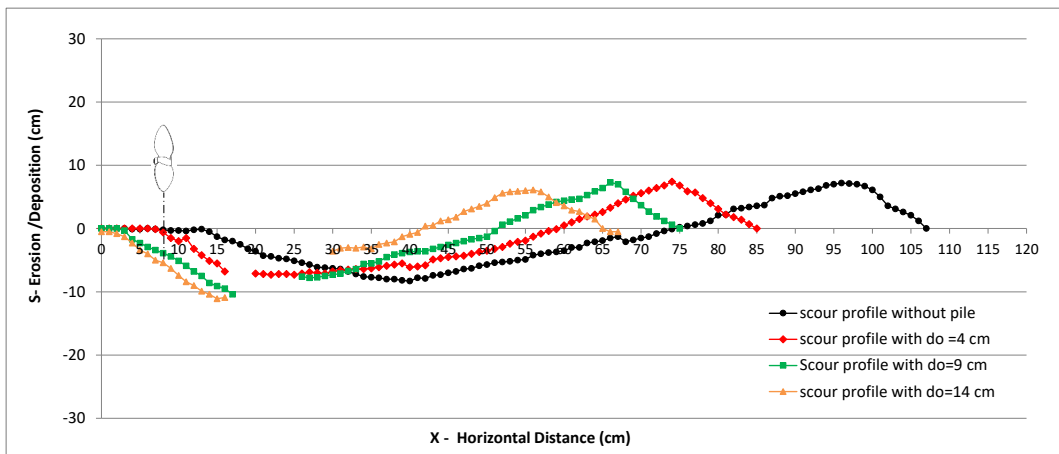


Figure A.130 Scour profiles with pile and without pile conditions ($D_p=10$ cm, $G=10$ cm, at 45 Hertz on $d_{50}=0.4$ cm sediment bed)

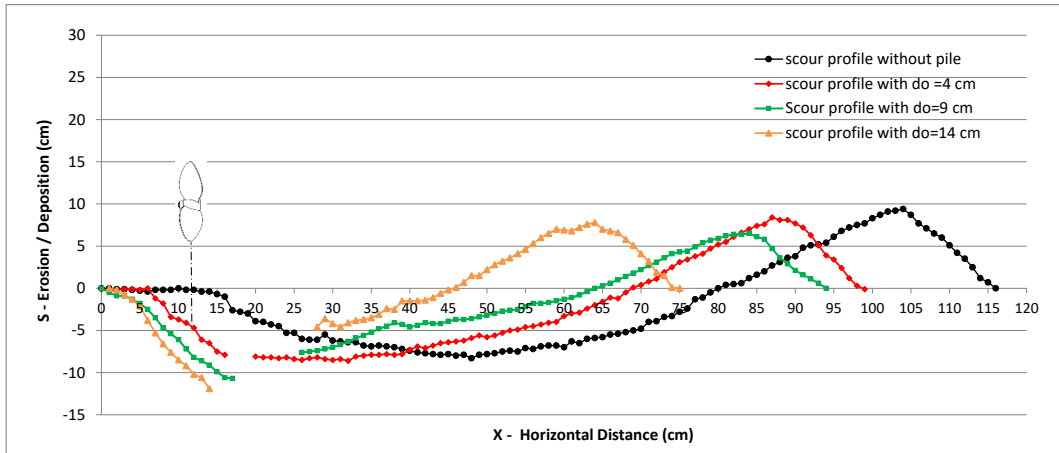


Figure A.131 Scour profiles with pile and without pile conditions ($D_p=10$ cm, $G=10$ cm, at 50 Hertz on $d_{50}=0.4$ cm sediment bed)

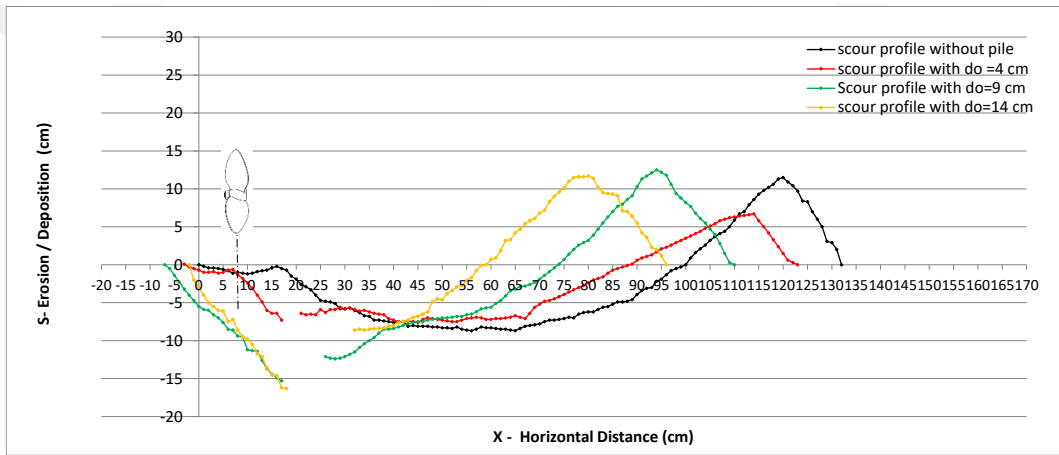


Figure A.132 Scour profiles with pile and without pile conditions ($D_p=13$ cm, $G=10$ cm, at 40 Hertz on $d_{50}=0.4$ cm sediment bed)

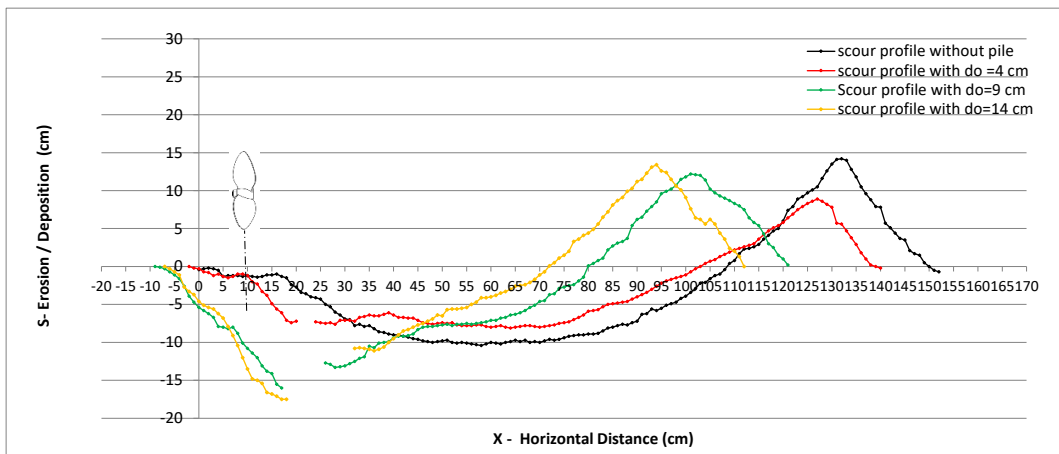


Figure A.133 Scour profiles with pile and without pile conditions ($D_p=13$ cm, $G=10$ cm, at 45 Hertz on $d_{50}=0.4$ cm sediment bed)

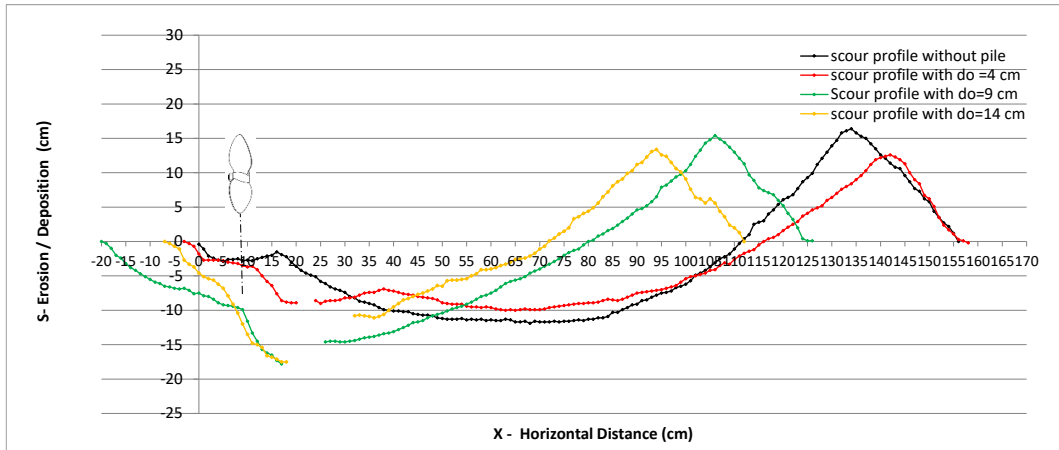


Figure A.134 Scour profiles with pile and without pile conditions ($D_p=13$ cm, $G=10$ cm, at 45 Hertz on $d_{50}=0.4$ cm sediment bed)

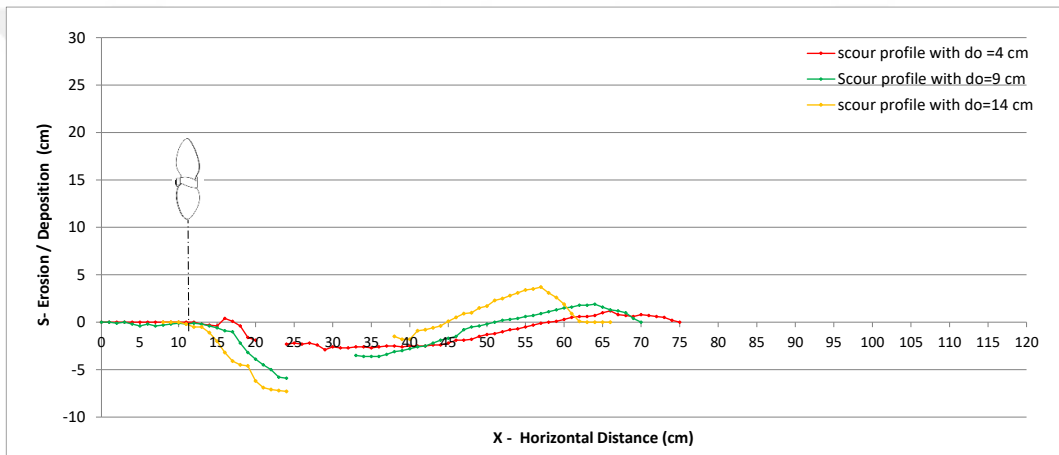


Figure A.135 Scour profiles with pile and without pile conditions ($D_p=10$ cm, $G=15$ cm, at 40 Hertz on $d_{50}=0.4$ cm sediment bed)

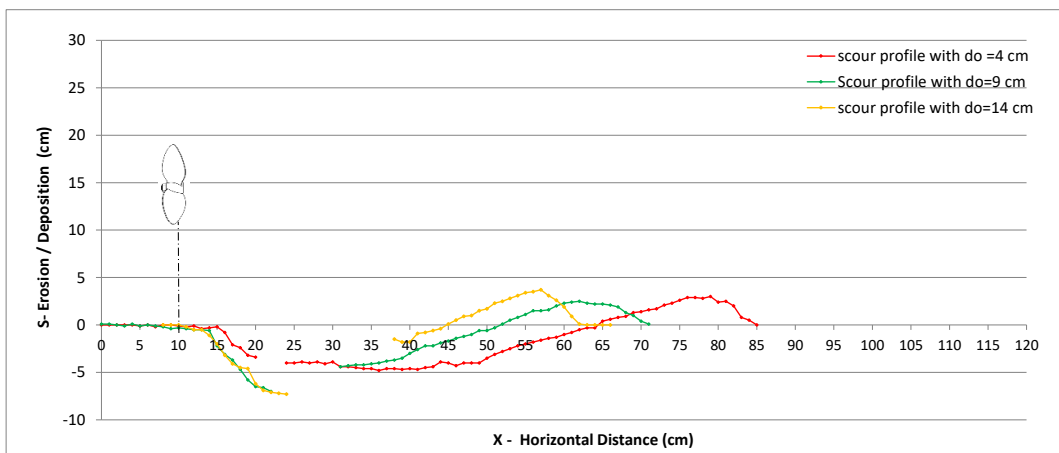


Figure A.136 Scour profiles with pile and without pile conditions ($D_p=10$ cm, $G=15$ cm, at 45 Hertz on $d_{50}=0.4$ cm sediment bed)

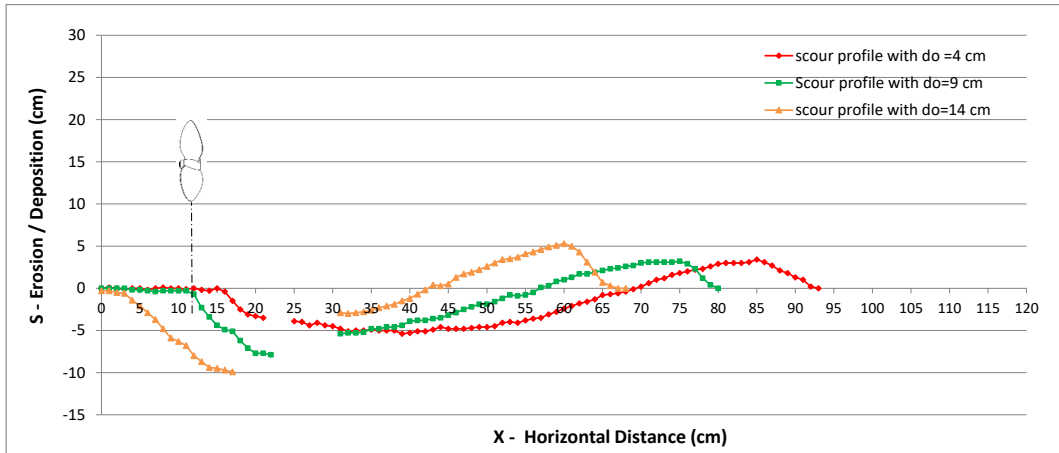


Figure A.137 Scour profiles with pile and without pile conditions ($D_p=10$ cm, $G=15$ cm, at 50 Hertz on $d_{50}=0.4$ cm sediment bed)

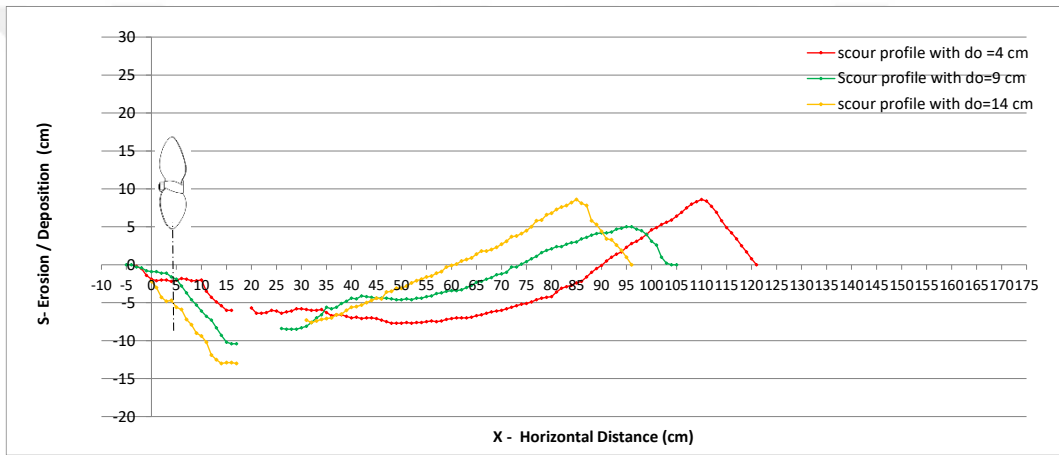


Figure A.138 Scour profiles with pile and without pile conditions ($D_p=13$ cm, $G=15$ cm, at 40 Hertz on $d_{50}=0.4$ cm sediment bed)

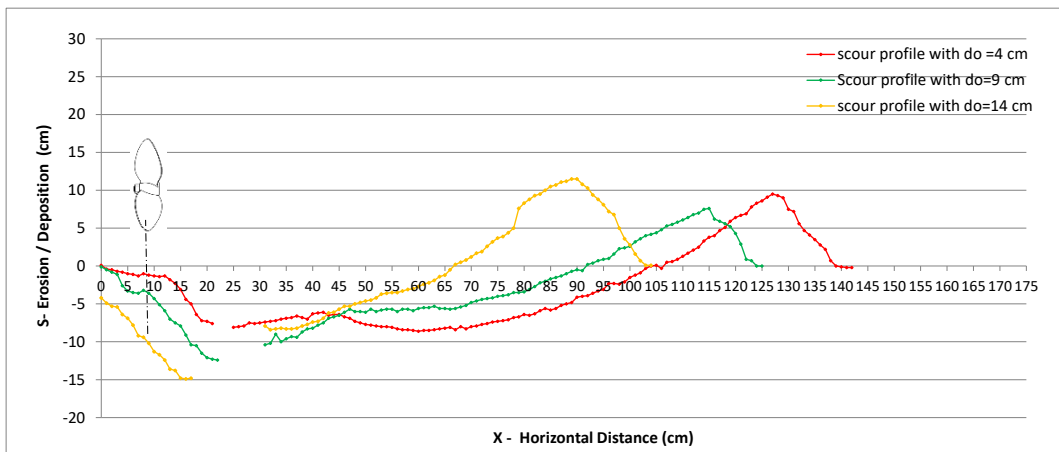


Figure A.139 Scour profiles with pile and without pile conditions ($D_p=13$ cm, $G=15$ cm, at 45 Hertz on $d_{50}=0.4$ cm sediment bed)

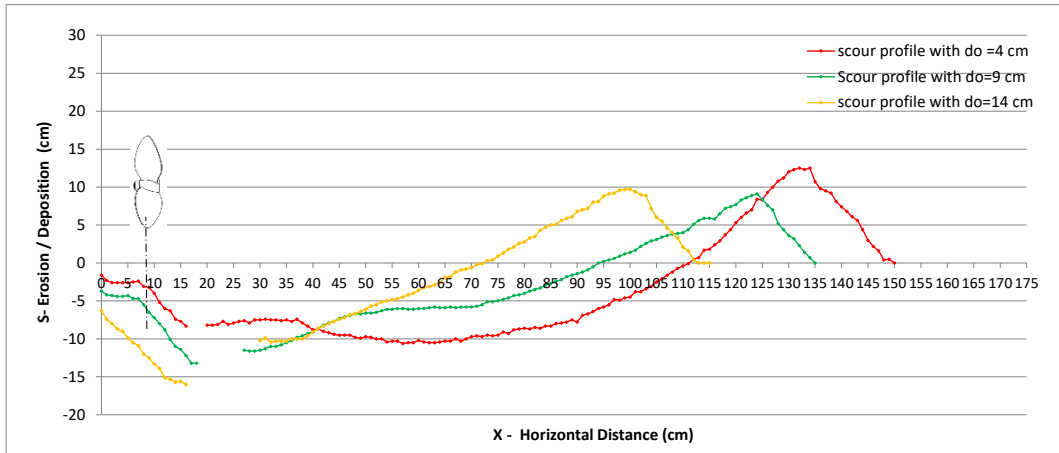


Figure A.140 Scour profiles with pile and without pile conditions ($D_p=13$ cm, $G=15$ cm, at 50 Hertz on $d_{50}=0.4$ cm sediment bed)

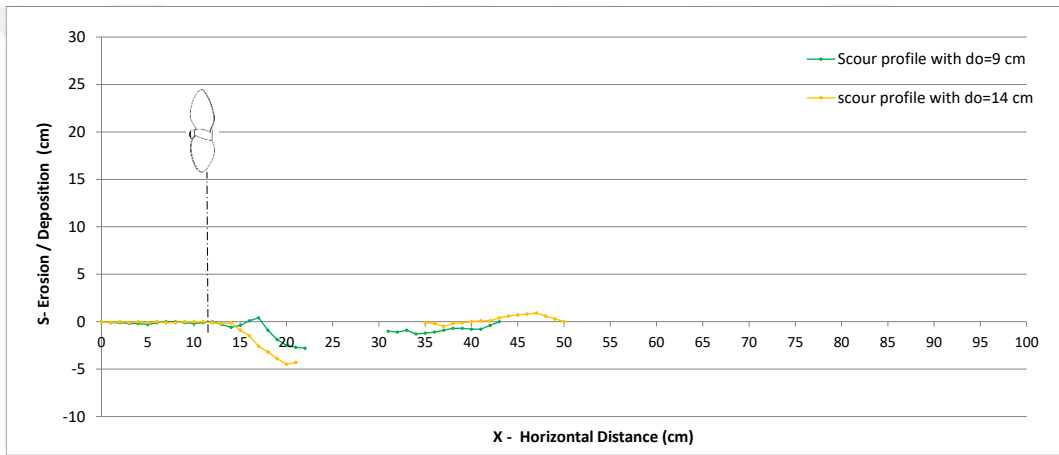


Figure A.141 Scour profiles with pile and without pile conditions ($D_p=10$ cm, $G=20$ cm, at 40 Hertz on $d_{50}=0.4$ cm sediment bed)

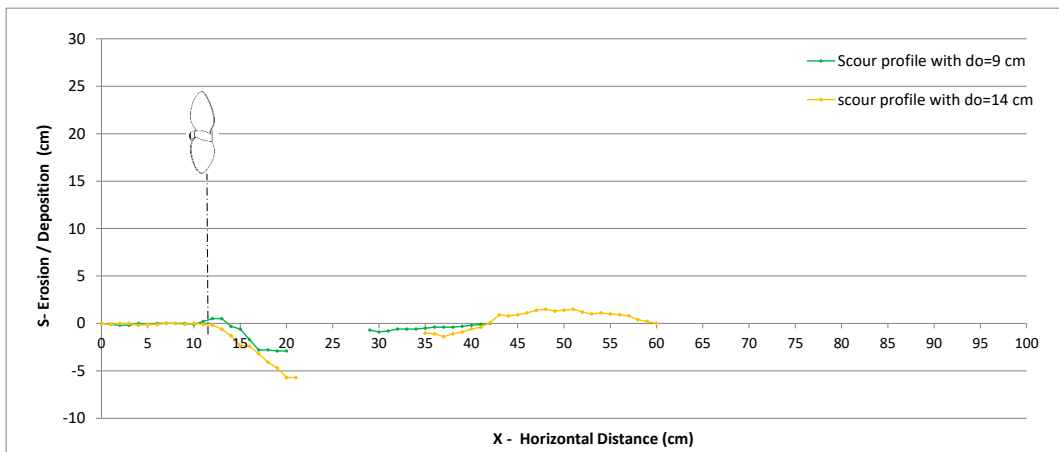


Figure A.142 Scour profiles with pile and without pile conditions ($D_p=10$ cm, $G=20$ cm, at 45 Hertz on $d_{50}=0.4$ cm sediment bed)

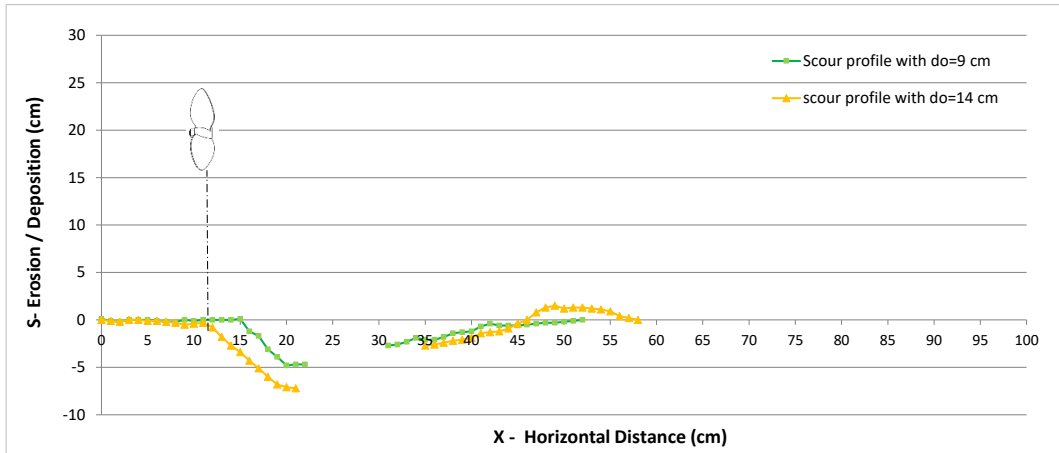


Figure A.143 Scour profiles with pile and without pile conditions ($D_p = 10$ cm, $G = 20$ cm, at 50 Hertz on $d_{50} = 0.4$ cm sediment bed)

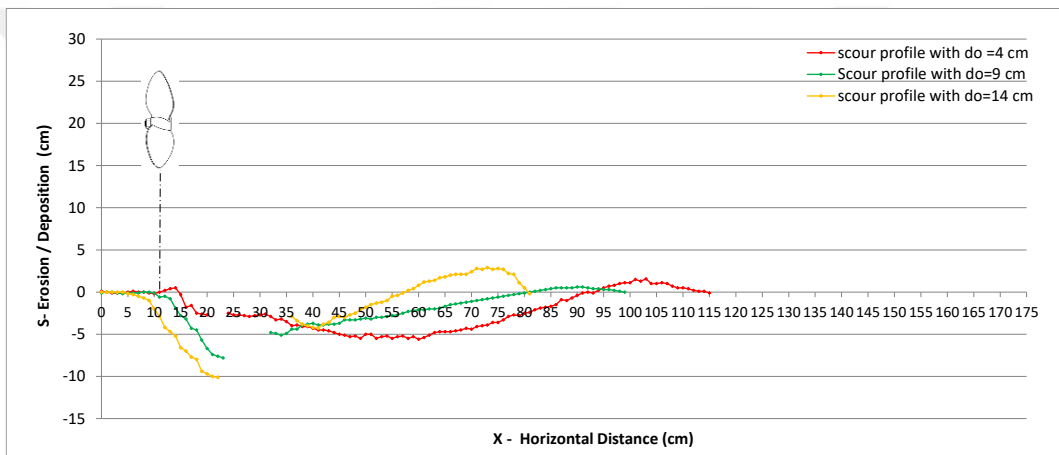


Figure A.144 Scour profiles with pile and without pile conditions ($D_p = 13$ cm, $G = 20$ cm, at 40 Hertz on $d_{50} = 0.4$ cm sediment bed)

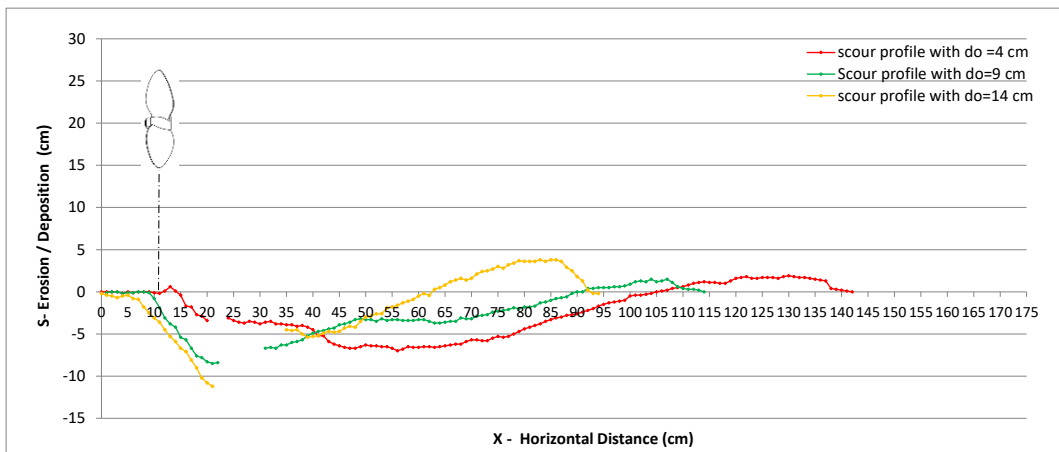


Figure A.145 Scour profiles with pile and without pile conditions ($D_p = 13$ cm, $G = 20$ cm, at 45 Hertz on $d_{50} = 0.4$ cm sediment bed)

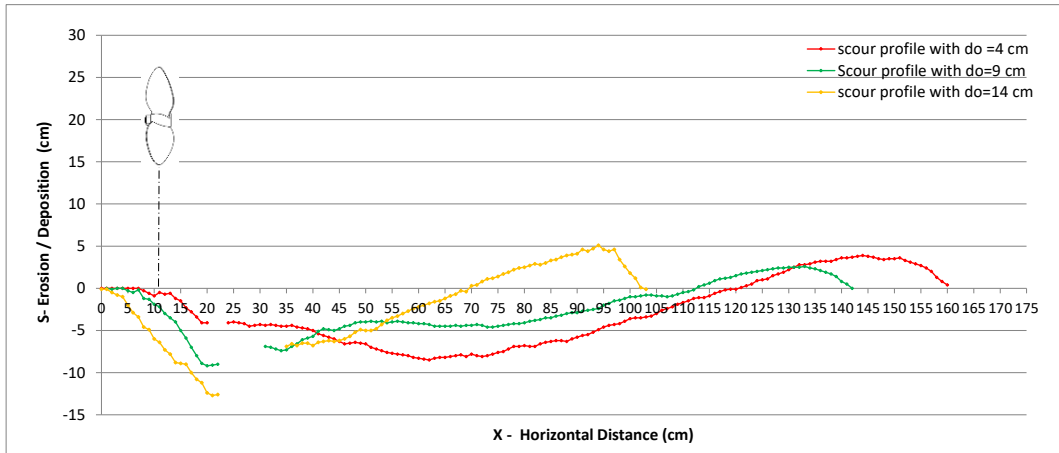


Figure A.146 Scour profiles with pile and without pile conditions ($D_p=13$ cm, $G=20$ cm, at 50 Hertz on $d_{50}=0.4$ cm sediment bed)

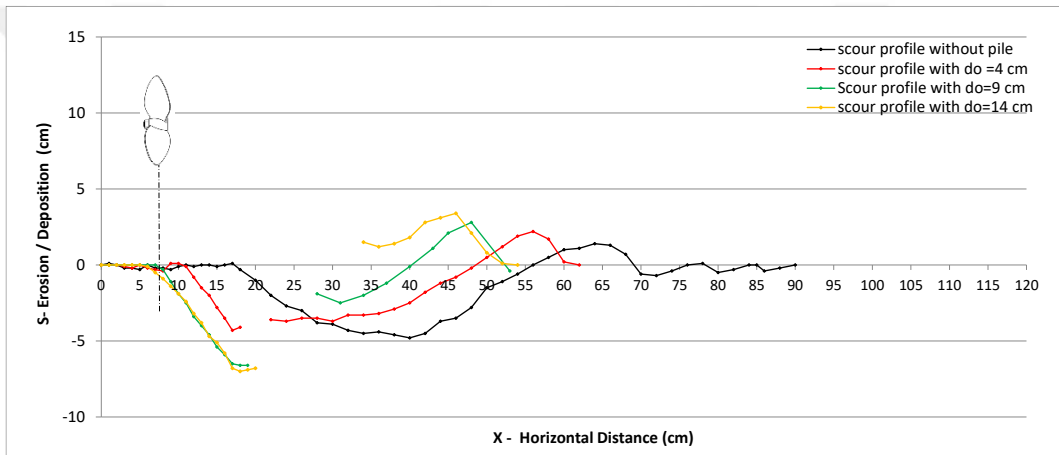


Figure A.147 Scour profiles with pile and without pile conditions ($D_p=6.5$ cm, $G=10$ cm, at 40 Hertz on $d_{50}=0.052$ cm sediment bed)

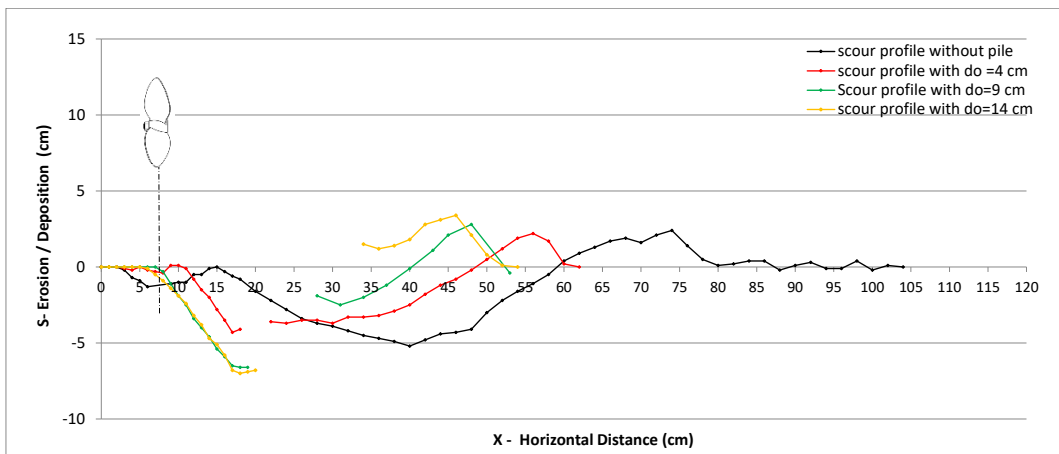


Figure A.148 Scour profiles with pile and without pile conditions ($D_p=6.5$ cm, $G=10$ cm, at 45 Hertz on $d_{50}=0.052$ cm sediment bed)

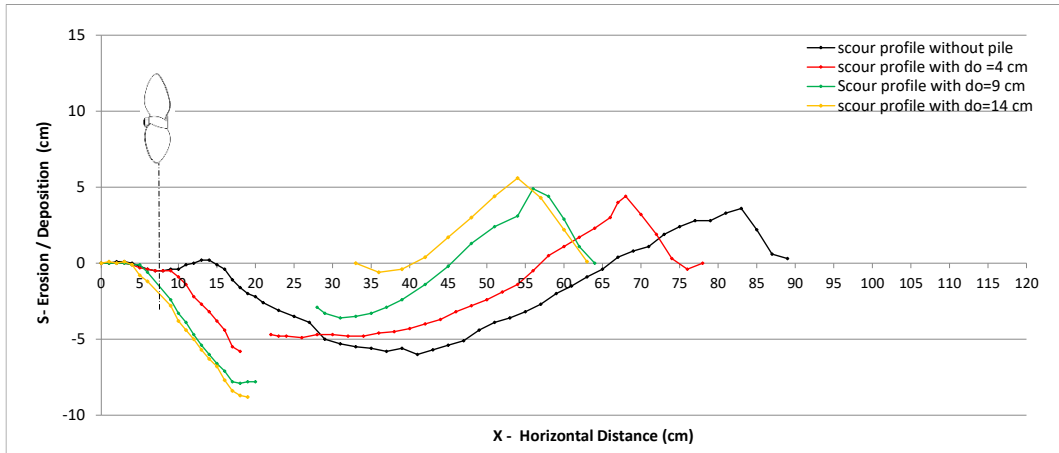


Figure A.149 Scour profiles with pile and without pile conditions ($D_p=6.5$ cm, $G=10$ cm, at 50 Hertz on $d_{50}=0.052$ cm sediment bed)

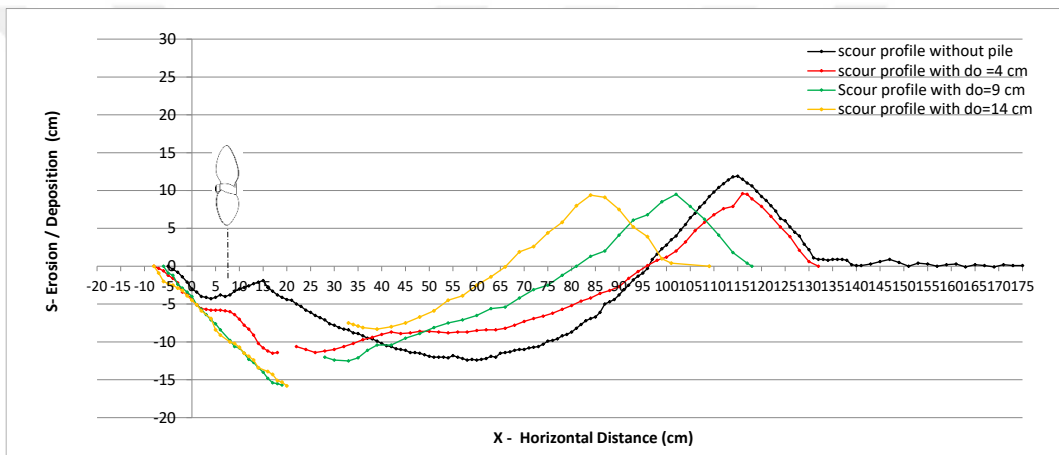


Figure A.150 Scour profiles with pile and without pile conditions ($D_p=10$ cm, $G=10$ cm, at 40 Hertz on $d_{50}=0.052$ cm sediment bed)

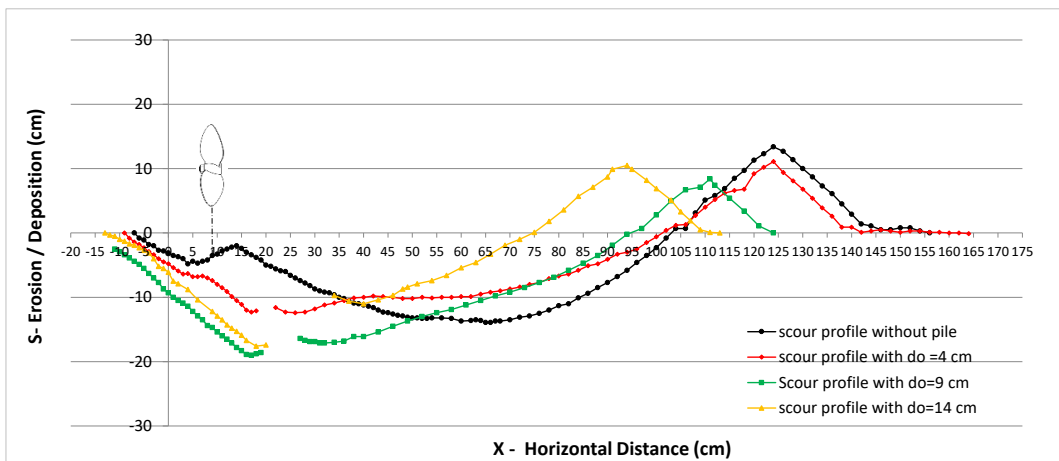


Figure A.151 Scour profiles with pile and without pile conditions ($D_p=10$ cm, $G=10$ cm, at 45 Hertz on $d_{50}=0.052$ cm sediment bed)

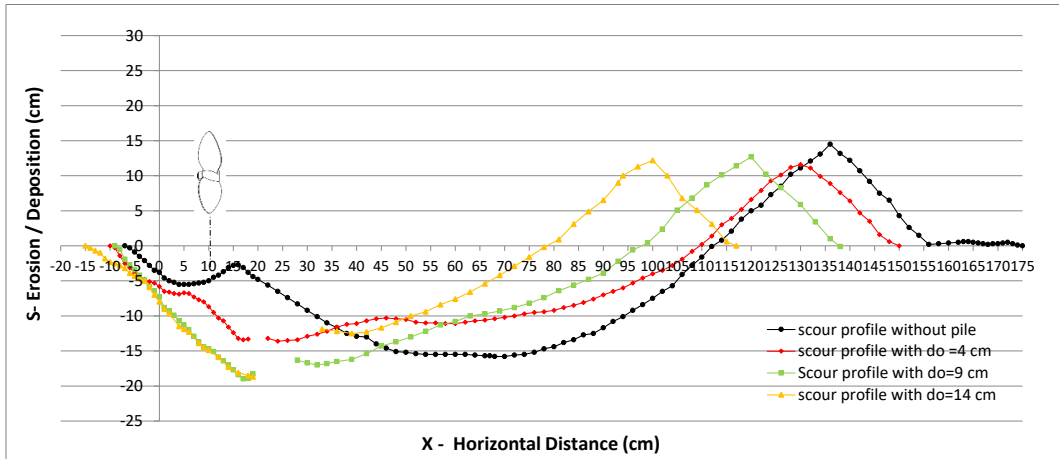


Figure A.152 Scour profiles with pile and without pile conditions ($D_p=10$ cm, $G=10$ cm, at 50 Hertz on $d_{50}=0.052$ cm sediment bed)

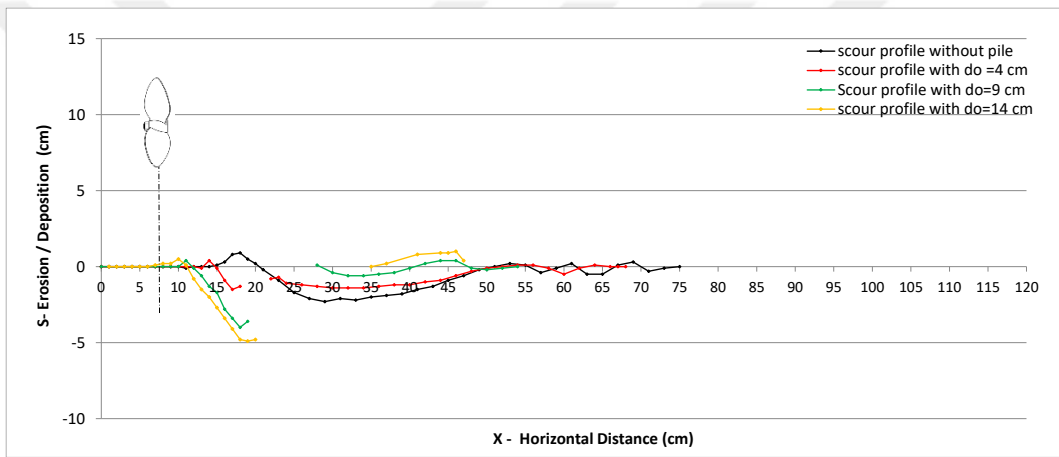


Figure A.153 Scour profiles with pile and without pile conditions ($D_p=6.5$ cm, $G=15$ cm, at 40 Hertz on $d_{50}=0.052$ cm sediment bed)

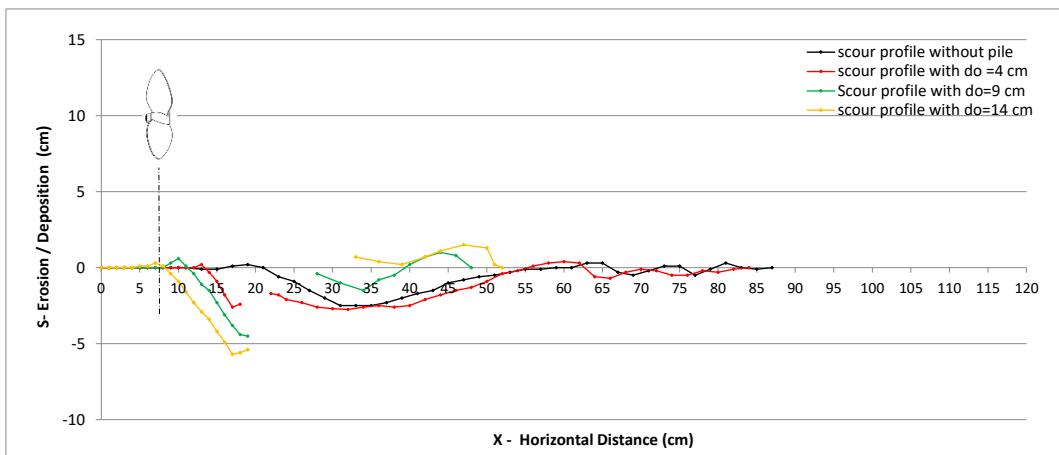


Figure A.154 Scour profiles with pile and without pile conditions ($D_p=6.5$ cm, $G=15$ cm, at 45 Hertz on $d_{50}=0.052$ cm sediment bed)

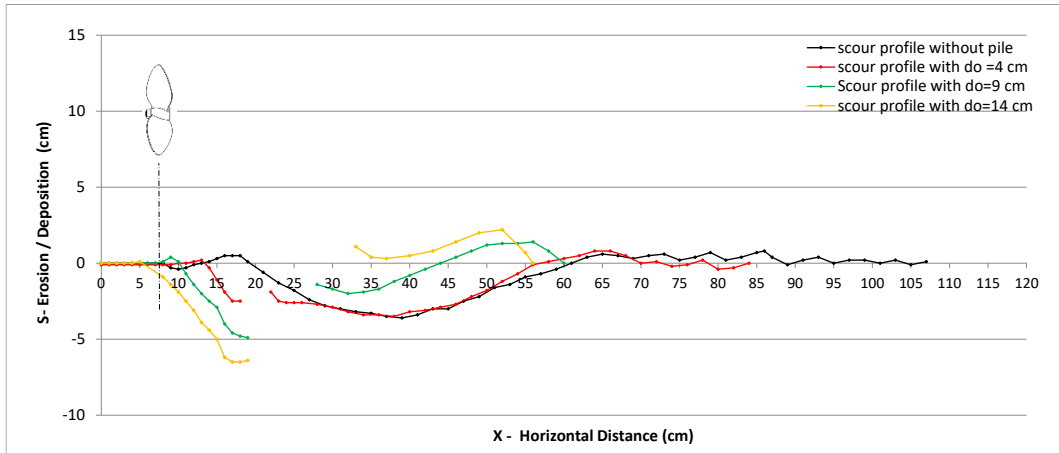


Figure A.155 Scour profiles with pile and without pile conditions ($D_p=6.5$ cm, $G=15$ cm, at 50 Hertz on $d_{50}=0.052$ cm sediment bed)

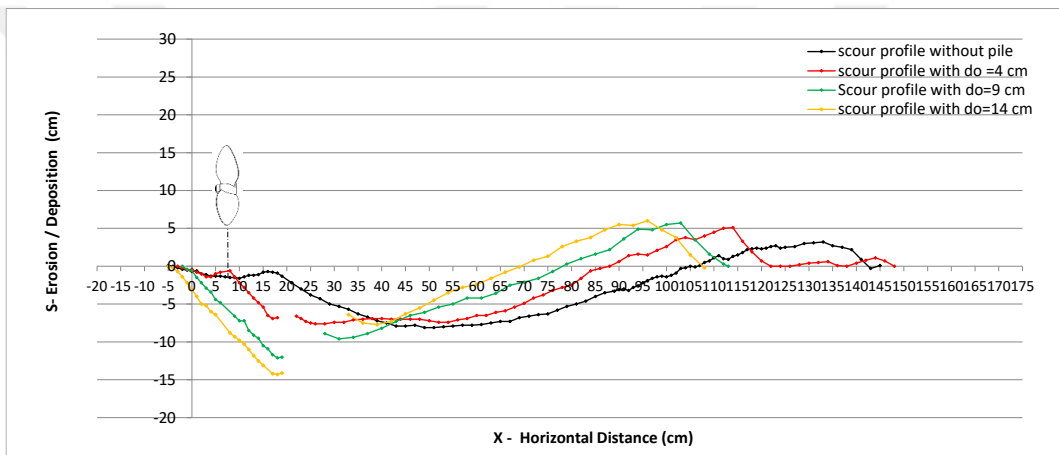


Figure A.156 Scour profiles with pile and without pile conditions ($D_p=10$ cm, $G=15$ cm, at 40 Hertz on $d_{50}=0.052$ cm sediment bed)

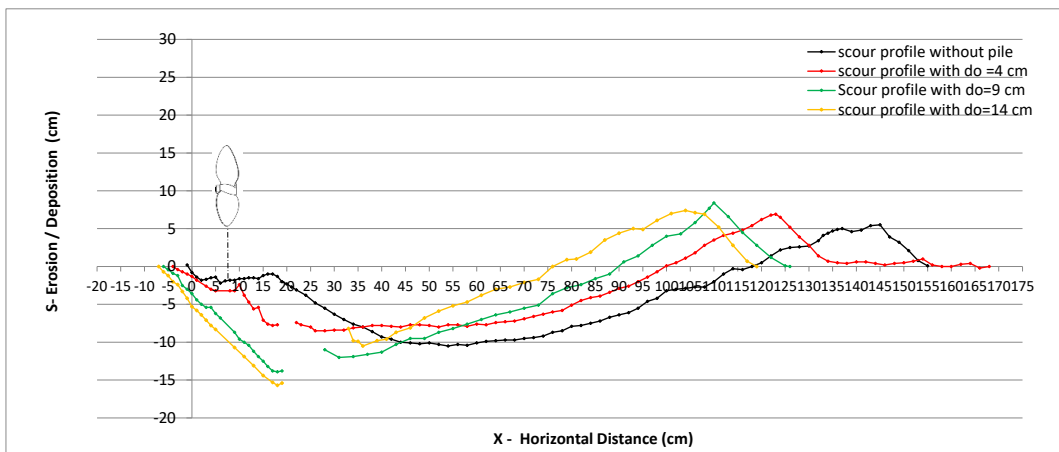


Figure A.157 Scour profiles with pile and without pile conditions ($D_p=10$ cm, $G=15$ cm, at 45 Hertz on $d_{50}=0.052$ cm sediment bed)

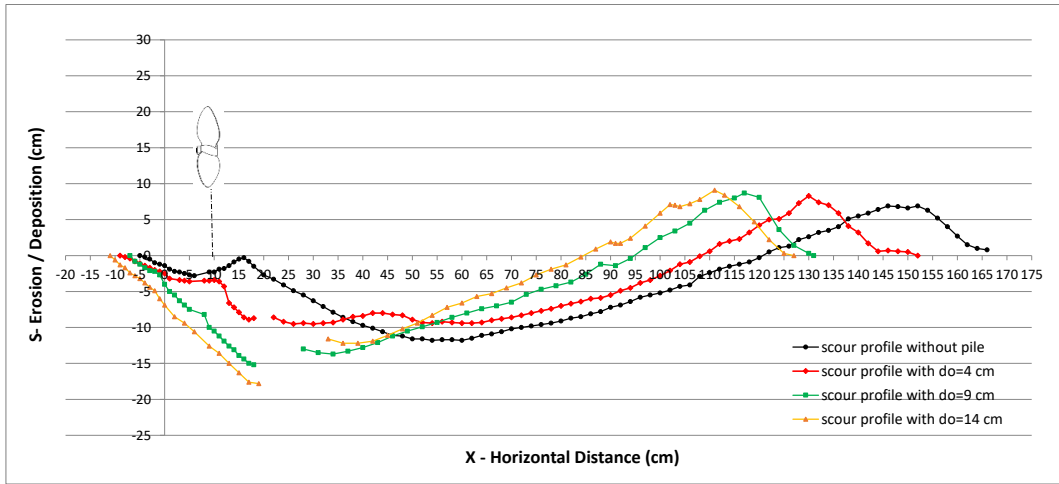


Figure A.158 Scour profiles with pile and without pile conditions ($D_p=10$ cm, $G=15$ cm, at 50 Hertz on $d_{50}=0.052$ cm sediment bed)

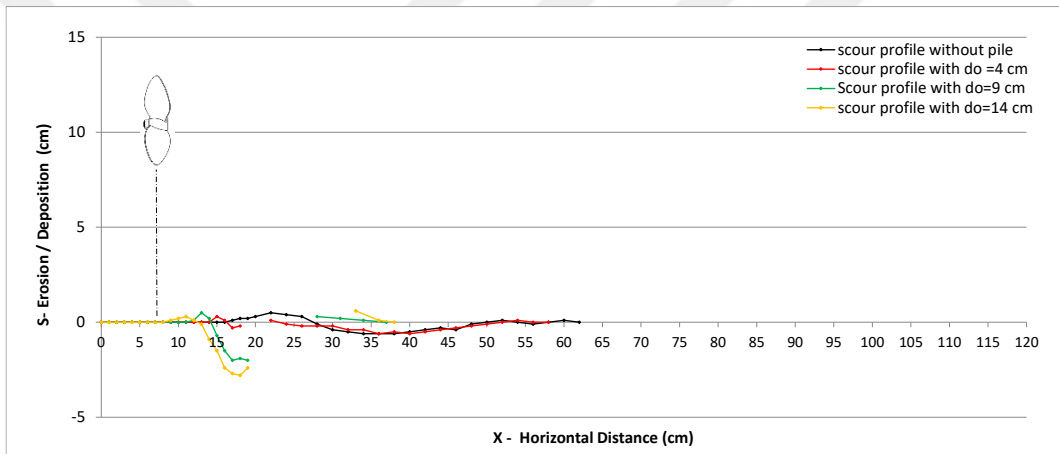


Figure A.159 Scour profiles with pile and without pile conditions ($D_p=6.5$ cm, $G=20$ cm, at 40 Hertz on $d_{50}=0.052$ cm sediment bed)

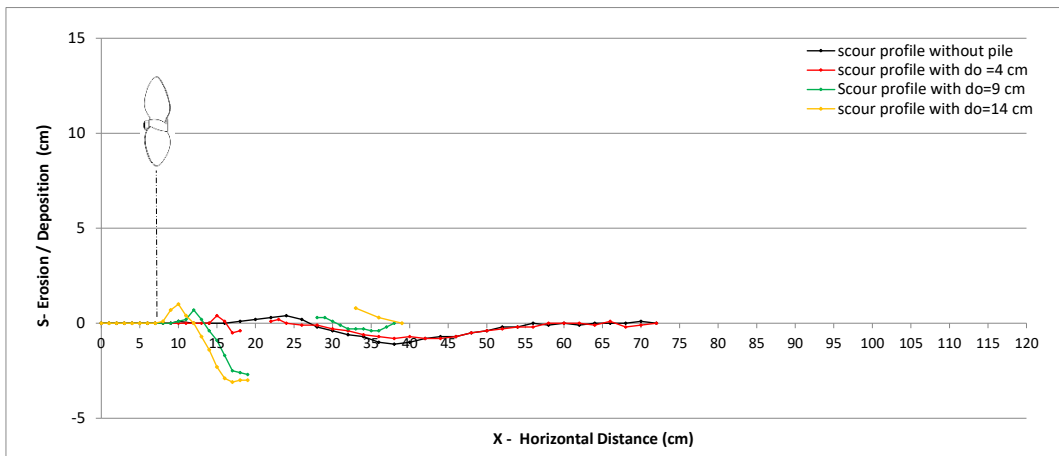


Figure A.160 Scour profiles with pile and without pile conditions ($D_p=6.5$ cm, $G=20$ cm, at 45 Hertz on $d_{50}=0.052$ cm sediment bed)

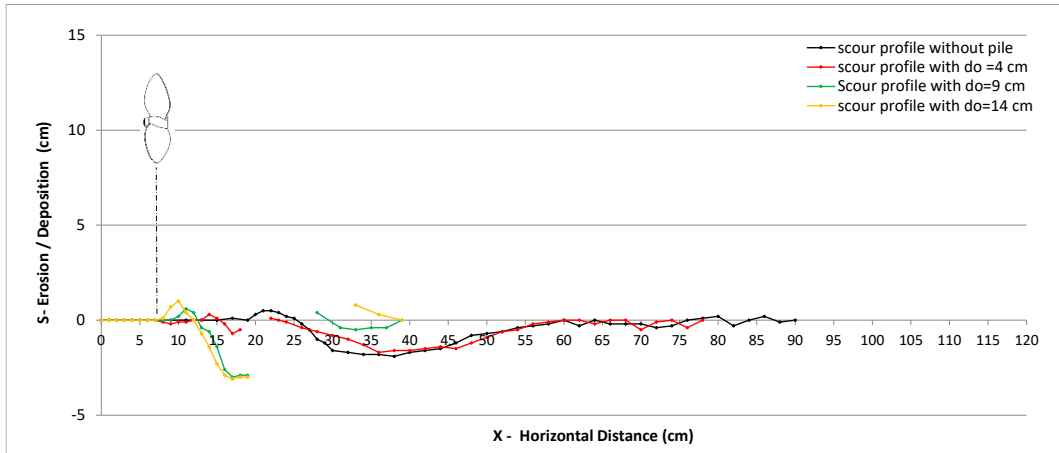


Figure A.161 Scour profiles with pile and without pile conditions ($D_p=6.5$ cm, $G=20$ cm, at 50 Hertz on $d_{50}=0.052$ cm sediment bed)

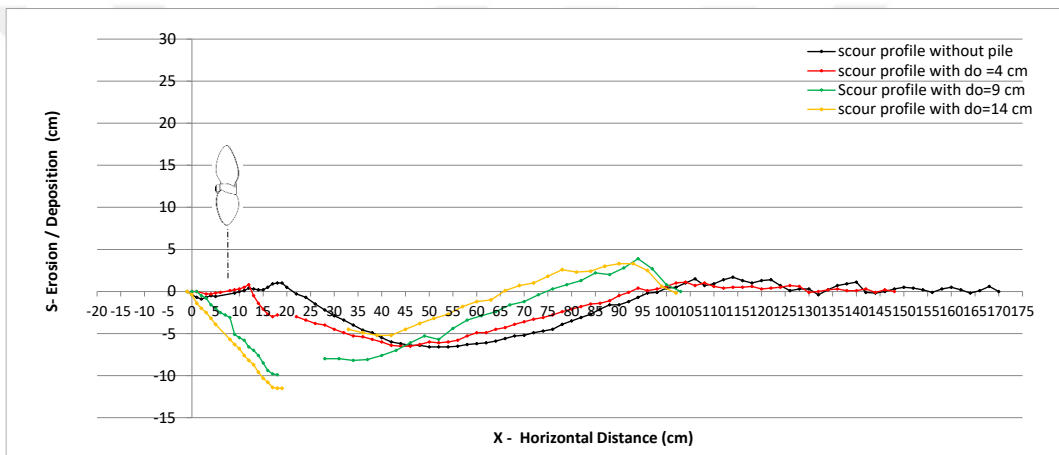


Figure A.162 Scour profiles with pile and without pile conditions ($D_p=10$ cm, $G=20$ cm, at 40 Hertz on $d_{50}=0.052$ cm sediment bed)

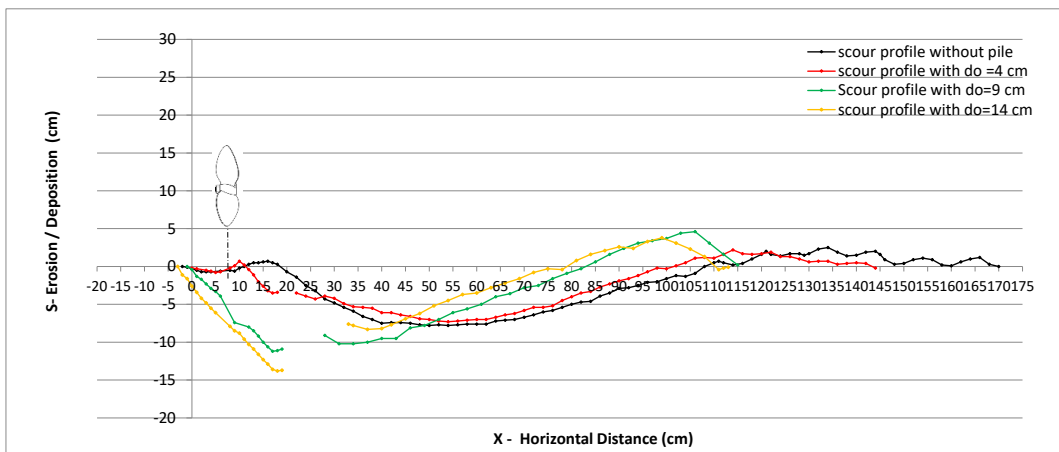


Figure A.163 Scour profiles with pile and without pile conditions ($D_p=10$ cm, $G=20$ cm, at 45 Hertz on $d_{50}=0.052$ cm sediment bed)

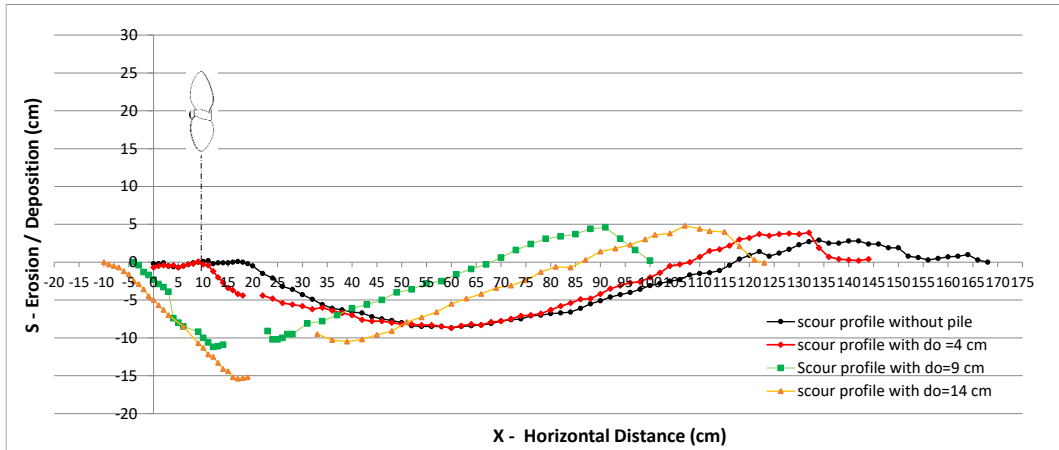


Figure A.164 Scour profiles with pile and without pile conditions ($D_p=10$ cm, $G=20$ cm, at 50 Hertz on $d_{50}=0.052$ cm sediment bed)

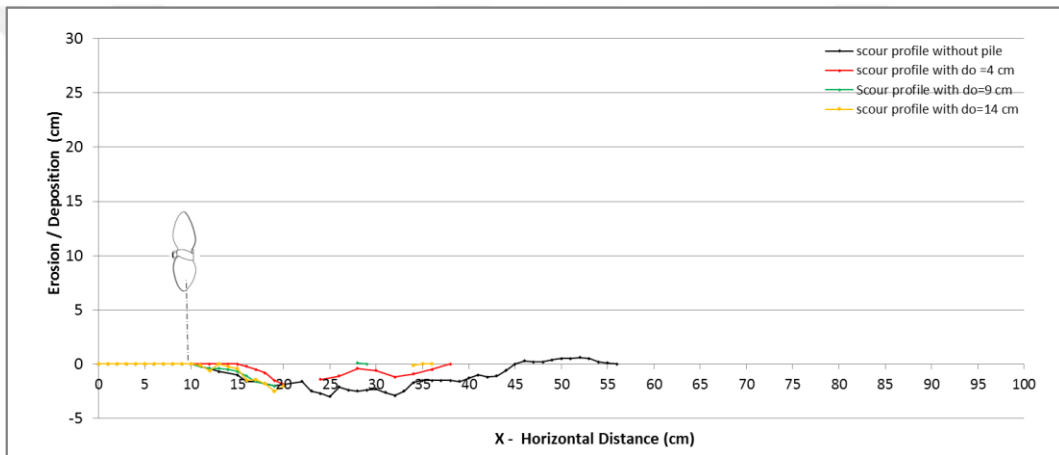


Figure A.165 Scour profiles with pile and without pile conditions ($D_p=10$ cm, $G=10$ cm, at 40 Hertz on $d_{50}=0.83$ cm sediment bed)

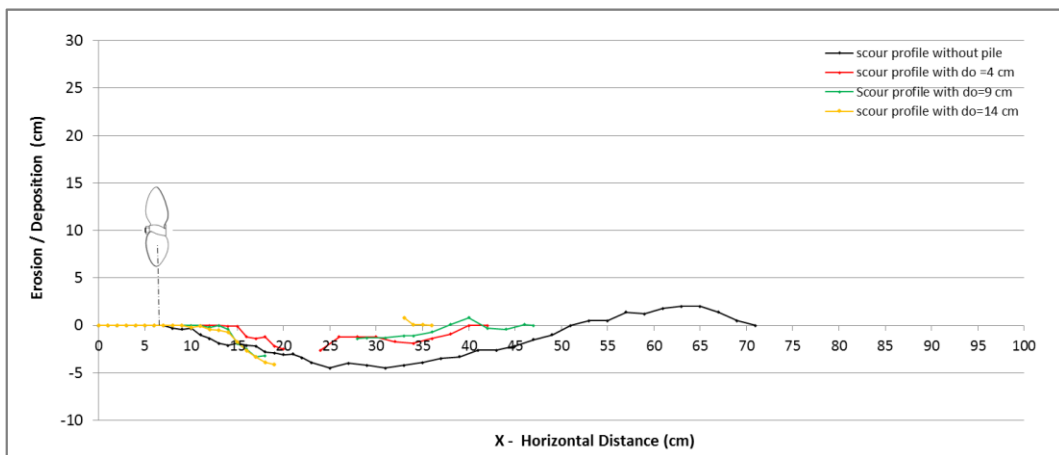


Figure A.166 Scour profiles with pile and without pile conditions ($D_p=10$ cm, $G=10$ cm, at 45 Hertz on $d_{50}=0.83$ cm sediment bed)

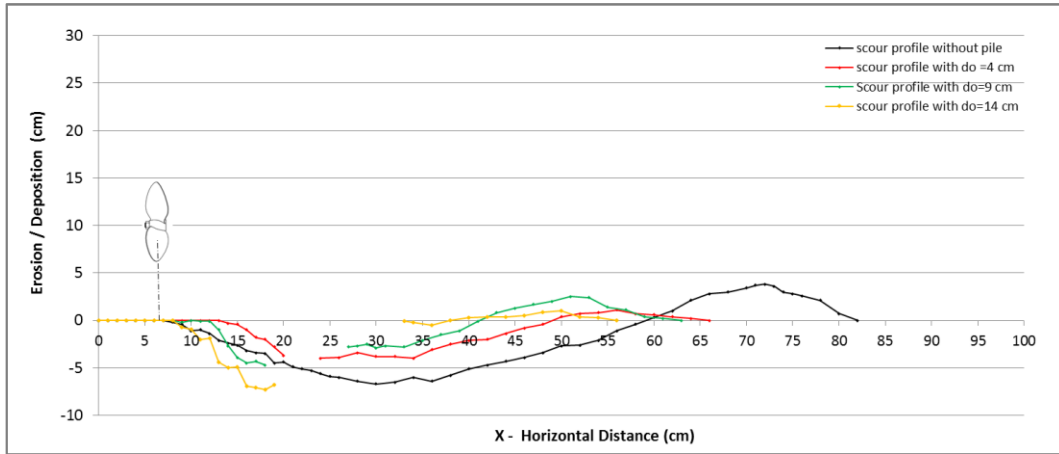


Figure A.167 Scour profiles with pile and without pile conditions ($D_p=10$ cm, $G=10$ cm, at 50 Hertz on $d_{50}=0.83$ cm sediment bed)

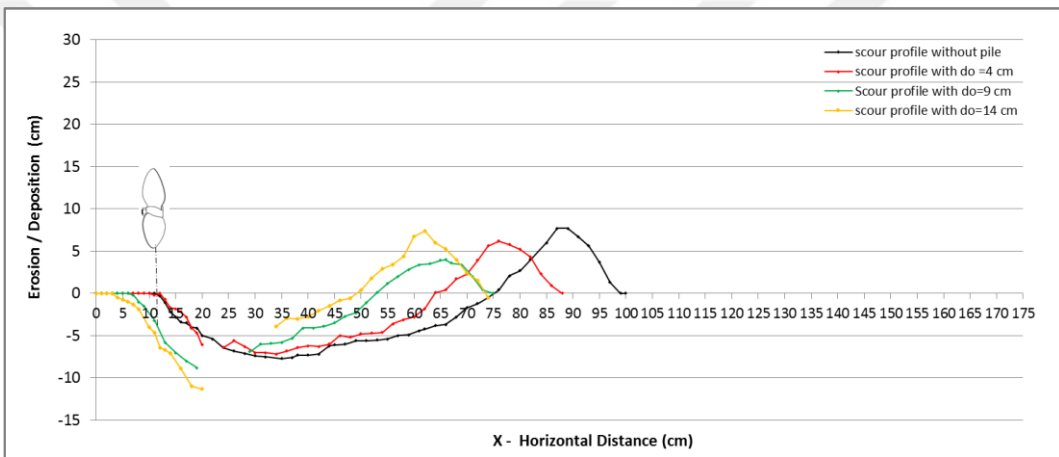


Figure A.168 Scour profiles with pile and without pile conditions ($D_p=13$ cm, $G=10$ cm, at 40 Hertz on $d_{50}=0.83$ cm sediment bed)

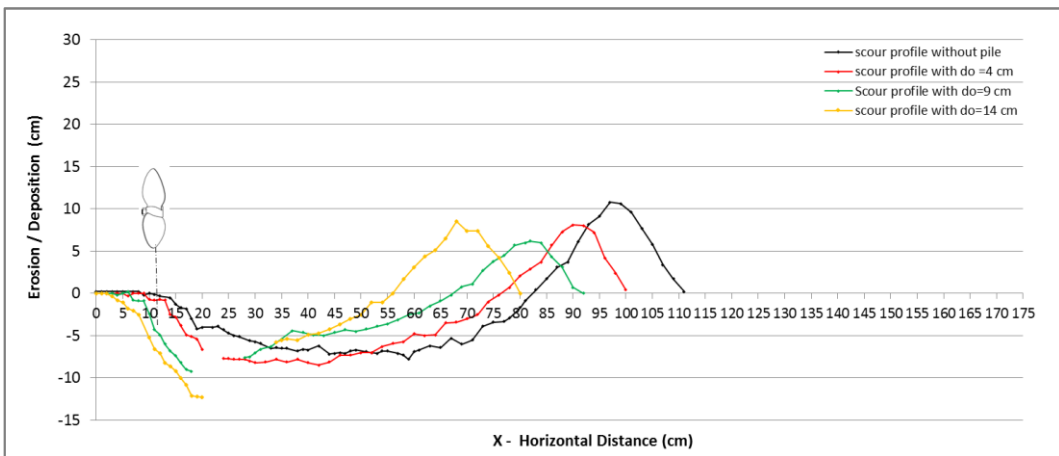


Figure A.169 Scour profiles with pile and without pile conditions ($D_p=13$ cm, $G=10$ cm, at 45 Hertz on $d_{50}=0.83$ cm sediment bed)

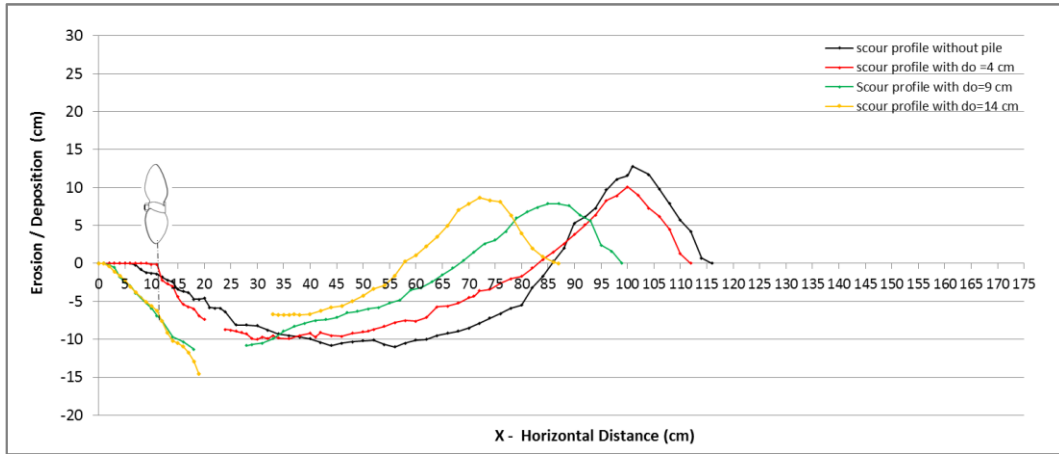


Figure A.170 Scour profiles with pile and without pile conditions ($D_p=13$ cm, $G=10$ cm, at 50 Hertz on $d_{50}=0.83$ cm sediment bed)

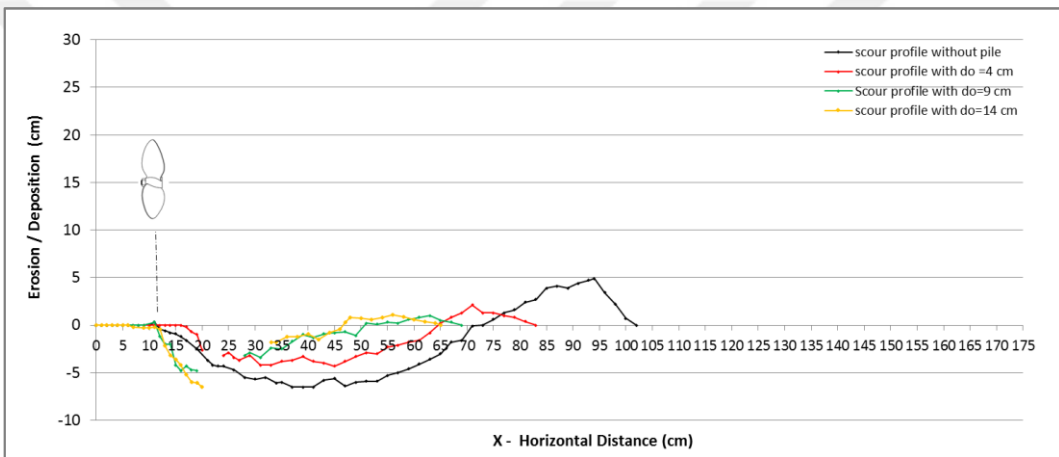


Figure A.171 Scour profiles with pile and without pile conditions ($D_p=13$ cm, $G=15$ cm, at 40 Hertz on $d_{50}=0.83$ cm sediment bed)

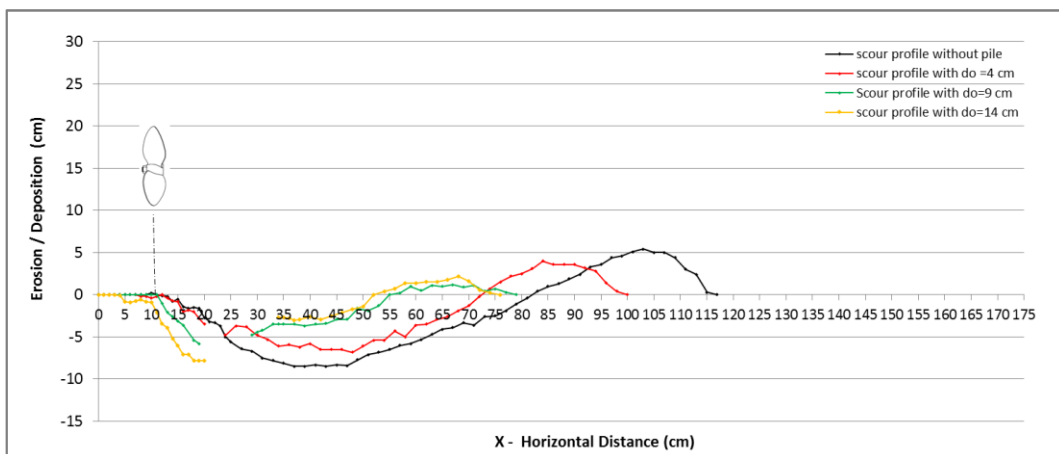


Figure A.172 Scour profiles with pile and without pile conditions t ($D_p=13$ cm, $G=15$ cm, at 45 Hertz on $d_{50}=0.83$ cm sediment bed)

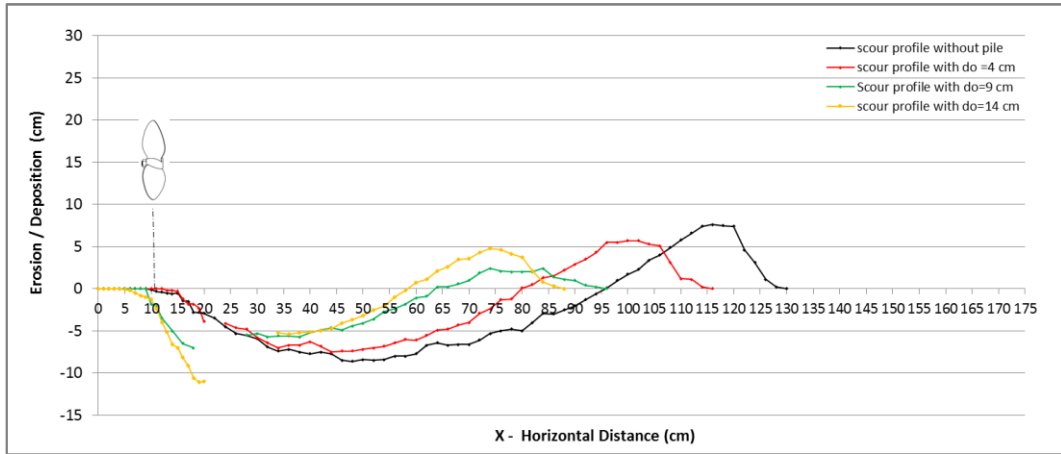


Figure A.173 Scour profiles with pile and without pile conditions ($D_p=13$ cm, $G=15$ cm, at 50 Hertz on $d_{50}=0.83$ cm sediment bed)

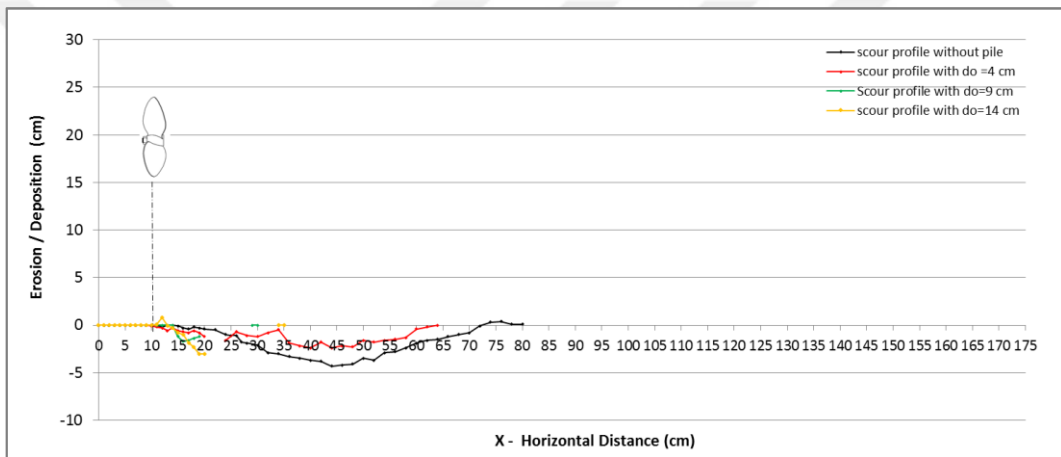


Figure A.174 Scour profiles with pile and without pile conditions ($D_p=13$ cm, $G=20$ cm, at 40 Hertz on $d_{50}=0.83$ cm sediment bed)

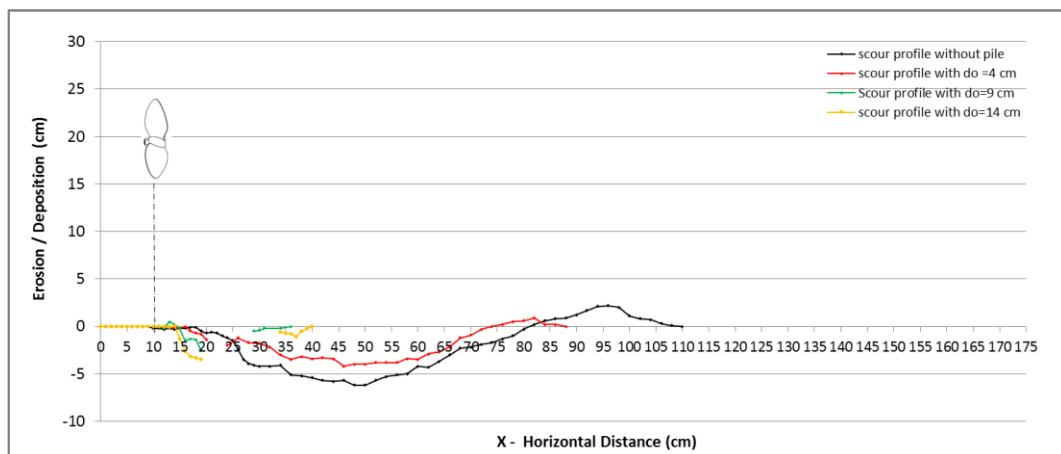


Figure A.175 Scour profiles with pile and without pile conditions ($D_p=13$ cm, $G=20$ cm, at 45 Hertz on $d_{50}=0.83$ cm sediment bed)

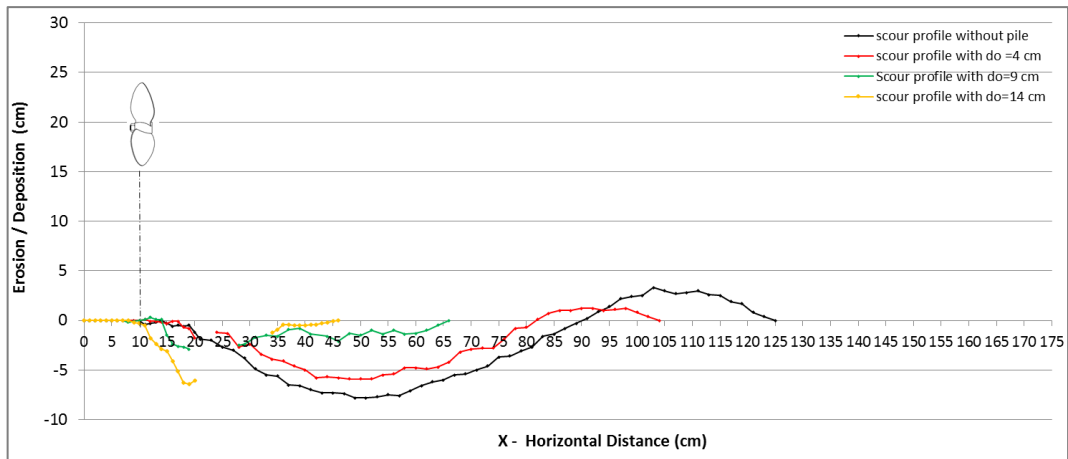


Figure A.176 Scour profiles with pile and without pile conditions ($D_p=13$ cm, $G=20$ cm, at 50 Hertz on $d_{50}=0.83$ cm sediment bed)

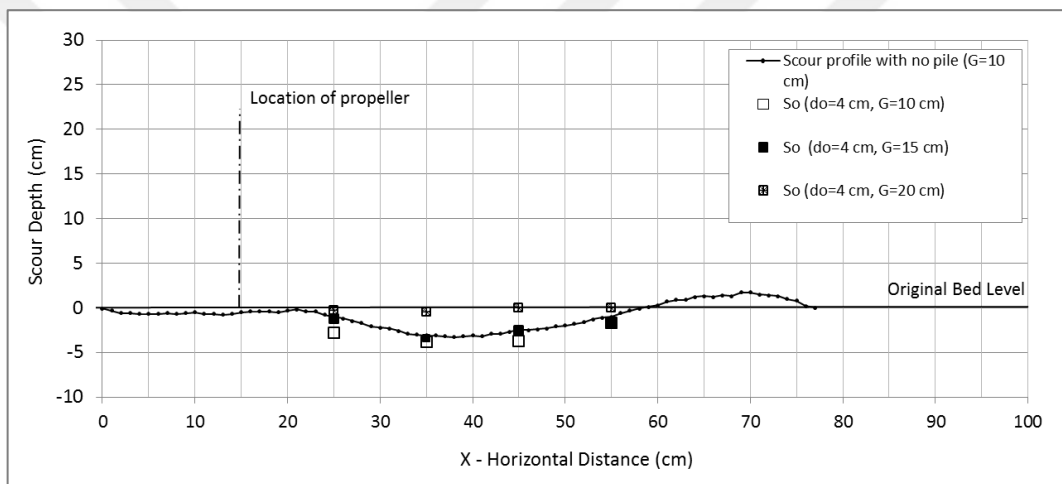


Figure A.177 Scour profile without pile condition and scour depths at the toe of pile (S_o) for different gaps of the propeller on $d_{50}=1.28$ mm bed ($D_p=6.5$ cm with 590 rpm)

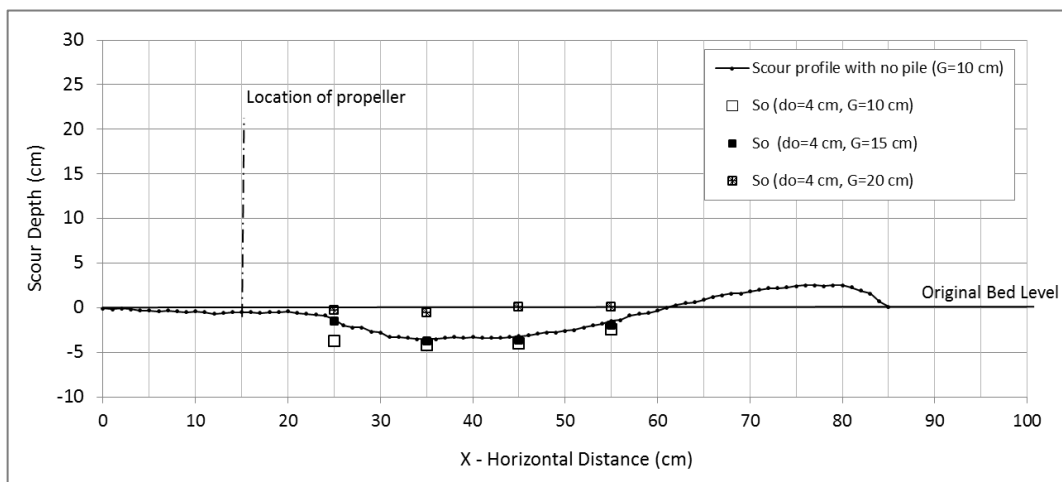


Figure A.178 Scour profile without pile condition and scour depths at the toe of pile (S_o) for different gaps of the propeller on $d_{50}=1.28$ mm bed ($D_p=6.5$ cm with 670 rpm)

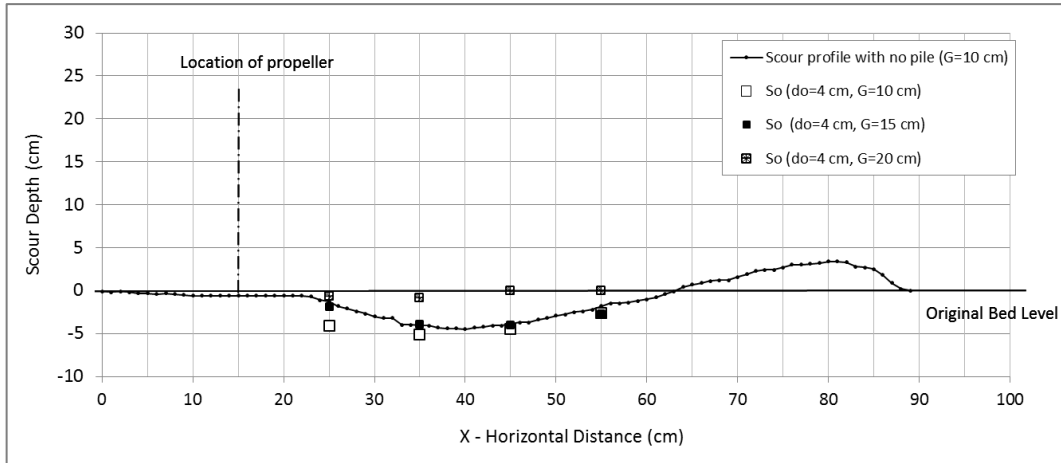


Figure A.179 Scour profile without pile condition and scour depths at the toe of pile (S_o) for different gaps of the propeller on $d_{50}=1.28$ mm bed ($D_p=6.5$ cm with 745 rpm)

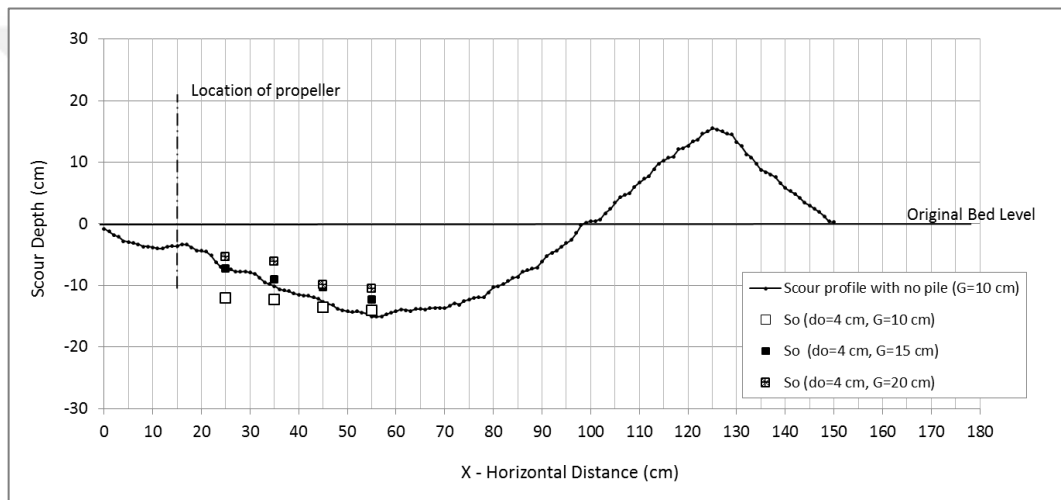


Figure A.180 Scour profile without pile condition and scour depths at the toe of pile (S_o) for different gaps of the propeller on $d_{50}=1.28$ mm bed ($D_p=13$ cm with 590 rpm)

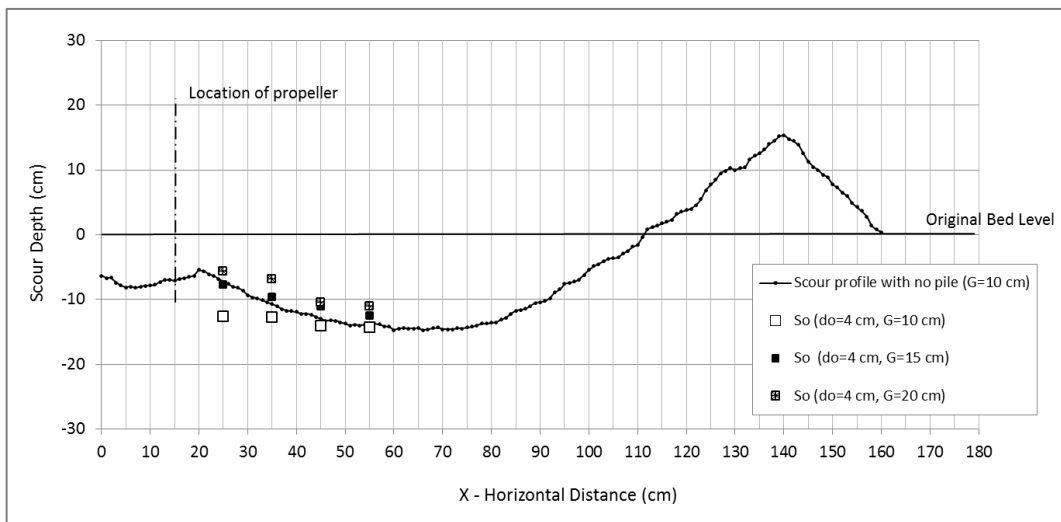


Figure A.181 Scour profile without pile condition and scour depths at the toe of pile (S_o) for different gaps of the propeller on $d_{50}=1.28$ mm bed ($D_p=13$ cm with 670 rpm)

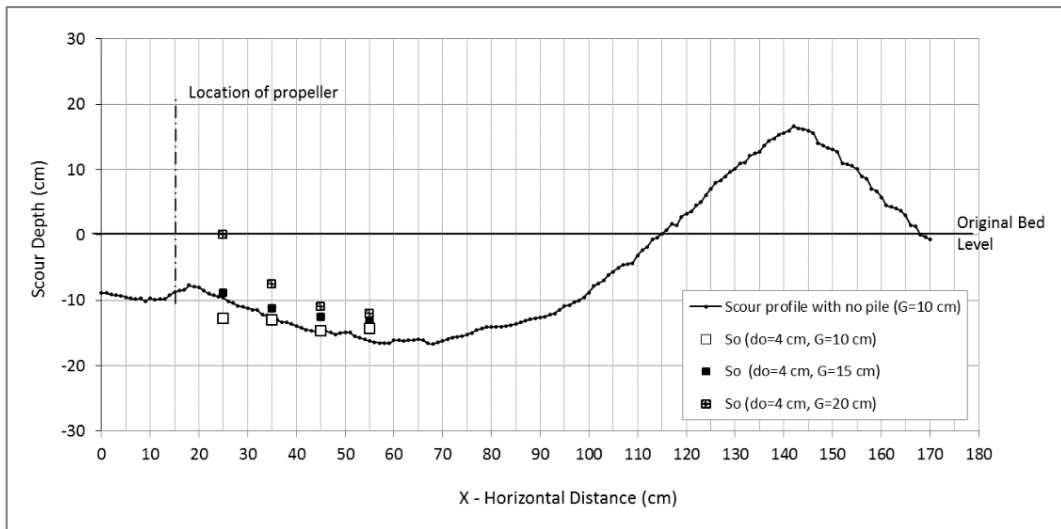


Figure A.182 Scour profile without pile condition and scour depths at the toe of pile (S_o) for different gaps of the propeller on $d_{50}=1.28$ mm Bed ($D_p=13$ cm with 670 rpm)

CURRICULUM VITAE

PERSONAL INFORMATION

Name Surname : Remziye İlayda TAN
Date of birth and place : 24.06.1988, Edirne
Foreign Languages : English
E-mail : itan@inm.yildiz.edu.tr

EDUCATION

Degree	Department	University	Date of Graduation
Master	Civil Engineering	Yıldız Technical University	06.02.2013
Undergraduate	Environmental Engineering	Yıldız Technical University	01.02.2011
Undergraduate	Civil Engineering (Double Major)	Yıldız Technical University	01.02.2011
High School		Beşiktaş Atatürk Anadolu High School	19.06.2006

WORK EXPERIENCE

Year	Corporation / Institute	Enrollment
2014-2019	Yıldız Technical University	

PUBLICATIONS

Papers

1. Tan, R.İ. and Yüksel Y., (2018). “Seabed scour induced by a propeller jet”, *Ocean Engineering*, (160): 132-142.
2. Yüksel, Y., Tan R.İ. and Çelikoğlu Y., (2018). “Propeller Jet Flow Scour Around a Pile Structure”, *Applied Ocean Research*, (79): 160-172.

Conference Papers

1. Yüksel Y., Çelikoğlu Y., Tan R.İ., Atik T., (2018). “Liman Su Alanlarında Gemi Pervanelerinin Etkisinde Tabanda Hareketin Başlangıcı”, 9’uncu Kıyı Mühendisliği Sempozyumu, 1-3 November 2018, Adana.
2. Yüksel Y., Tan R.İ., Çelikoğlu Y., Atik T., (2018). “Scour Mechanism Induced by Propeller Flow Near a Quay Wall”, 36th International Conference on Coastal Engineering, 30 June - 3 August 2018, Baltimore.
3. Yüksel Y., Tan R.İ., Çelikoğlu Y., (2016). “Propeller Jet Flow Around Pile Groups”, IX. PIANC-COPEDEC, 16-21 October 2016, Rio de Janeiro, 84-85.
4. Tan R.İ., Yüksel Y., Çelikoğlu Y., (2017). “Propeller Jet Flow Pile Supported Piers And Sea Bed Interaction”, 35th International Conference on Coastal Engineering, 17-20 November 2017, Antalya, (35): 1-8.
5. Yüksel Y., Tan R.İ., Ayat Aydoğan B., Güner A.A., Aydoğan B., Şeker D.Z., (2014). “Karasu Kıyı Alanının Bütünleşik Modeli”, 8. Kıyı Mühendisliği Sempozyumu, 7-9 November, 1-8 2014, İstanbul.
6. Yüksel Y., Çelikoğlu Y., Saraçoğlu F.A., Tan R.İ., (2014). “Gemi Pervane Jeti Etkisinde Kazık Destekli Yanaşma Yapılarında Oyulma”, 8’inci Kıyı Mühendisliği Sempozyumu, Türkiye.
7. Yüksel Y., Tan R.İ., Ayat Aydoğan B., Güner H.A., Aydoğan B., Şeker D.Z., (2013). “A Coastal Management Case Study in Karasu at Black Sea Region”, Proceedings of the Twenty-Third International Offshore and Polar Engineering, (ISOPE), 30 June - 5 July 2013, USA.
8. Acar U., Tan R.İ., Güler F., Bölükbaş S., Güner A.A., Bayram B., (2011). “Automatic Shore Line Detection and Analyzing Sediment Transport: Case Study İstanbul Terkoz/ Türkiye”, *CoastGIS 2011*, 5-8 September 2011, Oostende, (3): 63-71.